



*Characterization of Arctic Environment by Means of Polarimetric Synthetic Aperture Radar (PolSAR) Data and Digital Elevation Models (DEM)*

*Charakterisierung der arktischen Landoberfläche mittels polarimetrischer Radardaten (PolSAR) und digitalen Höhenmodellen (DEM)*

Doctoral thesis for the doctoral degree

DOCTOR RERUM NATURALIUM (Dr. rer. nat.)

at the

GRADUATE SCHOOL OF SCIENCE AND TECHNOLOGY

JULIUS-MAXIMILIANS-UNIVERSITÄT WÜRZBURG

Submitted by

Tobias ULLMANN

From Sonthofen im Allgäu

Würzburg 2015

Submitted on: .....

(Office stamp)

**Members of the Supervisory Committee:**

Chairperson: .....

Primary Supervisor: Prof. Dr. Roland Baumhauer

Supervisor (Second): Prof. Dr. Stefan Dech

Supervisor (Third): Prof. Dr. Hans-Wolfgang Hubberten

Date of Public Defence: .....

Date of receipt of Certificates: .....

*Für Jutta, Erich, Herbert und Ruppert*



---

---

## Acknowledgments

Foremost, I would like to express my sincere gratitude to my advisers Prof. Dr. Roland Baumhauer and Mr. Achim Roth for the support of my study and the opportunity to do this research. I also sincerely thank my advisers of the thesis committee Prof. Dr. Stefan Dech and Prof. Dr. Hans-Wolfgang Hubberten for their support and encouragement during the last years. I am thankful to my colleagues of the Institute for Geography and Geology and of the German Remote Sensing Data Center for their help and support: Andreas Schmitt, Jens Brauneck, Angela Tintrup gen. Suntrup, Christian Büdel, Daniel Schwindt, Anja Scholten, Andreas Paxian, Birigt Mannig, Doro Schill, Heiko Paeth, Jürgen Kempf, Ibrahim Sani, Tobias Leichtle, Thomas Esch, Michael Thiel, Adrian Emmert and Hannes Taubenböck. My sincere thanks also goes to my colleagues Jason Duffe, Sarah N. Banks and Anne-Marie Demers of the National Wildlife Research Center for their support and for the organization of the field work. I also like to thank Jennifer Sobiech, Wolfgang Dierking, Torsten Sachs and Jörg Hartmann of the Alfred Wegener Institute for the helpful discussions and the support during the fieldwork. I would like to express my gratitude to Reinhold Gröner, Inka Wilhelm and Ole Riemann for their administrative and logistical support.

Especially, I would like to thank my Canadian friend and colleague Blair E. Kennedy. He was the one who made the field work a great experience and a success. He also guaranteed our safe return. I would like to express my sincere gratitude to my family, friends and especially to Chrissi for their patience, encouragement and support during the last years.



---

---

## Abstract

The ecosystem of the high northern latitudes is affected by the recently changing environmental conditions. The Arctic has undergone a significant climatic change over the last decades. The land coverage is changing and a phenological response to the warming is apparent. Remotely sensed data can assist the monitoring and quantification of these changes. The remote sensing of the Arctic was predominantly carried out by the usage of optical sensors but these encounter problems in the Arctic environment, e.g. the frequent cloud cover or the solar geometry. In contrast, the imaging of Synthetic Aperture Radar is not affected by the cloud cover and the acquisition of radar imagery is independent of the solar illumination. The objective of this work was to explore how polarimetric Synthetic Aperture Radar (PolSAR) data of TerraSAR-X, TanDEM-X, Radarsat-2 and ALOS PALSAR and interferometric-derived digital elevation model data of the TanDEM-X Mission can contribute to collect meaningful information on the actual state of the Arctic Environment. The study was conducted for Canadian sites of the Mackenzie Delta Region and Banks Island and in situ reference data were available for the assessment. The up-to-date analysis of the PolSAR data made the application of the Non-Local Means filtering and of the decomposition of co-polarized data necessary.

The Non-Local Means filter showed a high capability to preserve the image values, to keep the edges and to reduce the speckle. This supported not only the suitability for the interpretation but also for the classification. The classification accuracies of Non-Local Means filtered data were in average +10% higher compared to unfiltered images. The correlation of the co- and quad-polarized decomposition features was high for classes with distinct surface or double bounce scattering and a usage of the co-polarized data is beneficial for regions of natural land coverage and for low vegetation formations with little volume scattering. The evaluation further revealed that the X- and C-Band were most sensitive to the generalized land cover classes. It was found that the X-Band data were sensitive to low vegetation formations with low shrub density, the C-Band data were sensitive to the shrub density and the shrub dominated tundra. In contrast, the L-Band data were less sensitive to the land cover. Among the different dual-polarized data the HH/VV-polarized data were identified to be most meaningful for the characterization and classification, followed by the HH/HV-polarized and the VV/VH-polarized data. The quad-polarized data showed highest sensitivity to the land cover but differences to the co-polarized data were small. The accuracy assessment showed that spectral information was required for accurate land cover classification. The best results were obtained when spectral and radar information was combined. The benefit of including radar data in the classification was up to +15% accuracy and most significant for the classes wetland and sparse vegetated tundra. The best classifications were realized with quad-polarized C-Band and multispectral data and with co-polarized X-Band and multispectral data. The overall accuracy was up to 80% for unsupervised and up to 90% for supervised classifications. The results indicated that the

shortwave co-polarized data show promise for the classification of tundra land cover since the polarimetric information is sensitive to low vegetation and the wetlands. Furthermore, co-polarized data provide a higher spatial resolution than the quad-polarized data.

The analysis of the intermediate digital elevation model data of the TanDEM-X showed a high potential for the characterization of the surface morphology. The basic and relative topographic features were shown to be of high relevance for the quantification of the surface morphology and an area-wide application is feasible. In addition, these data were of value for the classification and delineation of landforms. Such classifications will assist the delineation of geomorphological units and have potential to identify locations of actual and future morphologic activity.

## **Zusammenfassung**

Die polaren Regionen der Erde zeigen eine hohe Sensitivität gegenüber dem aktuell stattfindenden klimatischen Wandel. Für den Raum der Arktis wurde eine signifikante Erwärmung der Landoberfläche beobachtet und zukünftige Prognosen zeigen einen positiven Trend der Temperaturentwicklung. Die Folgen für das System sind tiefgehend, zahlreich und zeigen sich bereits heute - beispielsweise in einer Zunahme der photosynthetischen Aktivität und einer Verstärkung der geomorphologischen Dynamik. Durch satellitengestützte Fernerkundungssysteme steht ein Instrumentarium bereit, welches in der Lage ist, solch großflächigen und aktuellen Änderungen der Landoberfläche nachzuzeichnen und zu quantifizieren. Insbesondere optische Systeme haben in den vergangenen Jahren ihre hohe Anwendbarkeit für die kontinuierliche Beobachtung und Quantifizierung von Änderungen bewiesen, bzw. durch sie ist ein Erkennen der Änderungen erst ermöglicht worden. Der Nutzen von optischen Systemen für die Beobachtung der arktischen Landoberfläche wird dabei aber durch die häufige Beschattung durch Wolken und die Beleuchtungsgeometrie erschwert, bzw. unmöglich gemacht. Demgegenüber eröffnen bildgebende Radarsysteme durch die aktive Sendung von elektromagnetischen Signalen die Möglichkeit kontinuierlich Daten über den Zustand der Oberfläche aufzuzeichnen, ohne von den atmosphärischen oder orbitalen Bedingungen abhängig zu sein. Das Ziel der vorliegenden Arbeit war es den Nutzen und Mehrwert von polarimetrischen Synthetic Aperture Radar (PolSAR) Daten der Satelliten TerraSAR-X, TanDEM-X, Radarsat-2 und ALOS PALSAR für die Charakterisierung und Klassifikation der arktischen Landoberfläche zu identifizieren. Darüber hinaus war es ein Ziel das vorläufige interferometrische digitale Höhenmodell der TanDEM-X Mission für die Charakterisierung der Landoberflächen-Morphologie zu verwenden. Die Arbeiten erfolgten hauptsächlich an ausgewählten Testgebieten im Bereich des kanadischen Mackenzie Deltas und im Norden von Banks Island. Für diese Regionen standen in situ erhobene Referenzdaten zur Landbedeckung zur Verfügung. Mit Blick auf den aktuellen Stand der Forschung wurden die Radardaten mit einem entwickelten Non-Local-Means Verfahren gefiltert. Die co-polarisierten Daten wurde zudem mit einer neu entwickelten zwei Komponenten Dekomposition verarbeitet.

Das entwickelte Filterverfahren zeigt eine hohe Anwendbarkeit für alle Radardaten. Der Ansatz war in



der Lage die Kanten und Grauwerte im Bild zu erhalten, bei einer gleichzeitigen Reduktion der Varianz und des Speckle-Effekts. Dies verbesserte nicht nur die Bildinterpretation, sondern auch die Bildklassifikation und eine Erhöhung der Klassifikationsgüte von ca. +10% konnte durch die Filterung erreicht werden. Die Merkmale der Dekomposition von co-polarisierten Daten zeigten eine hohe Korrelation zu den entsprechenden Merkmalen der Dekomposition von voll-polarisierten Daten. Die Korrelation war besonders hoch für Landbedeckungstypen, welche eine double oder single bounce Rückstreuung hervorrufen. Eine Anwendung von co-polarisierten Daten ist somit besonders sinnvoll und aussagekräftig für Landbedeckungstypen, welche nur einen geringen Teil an Volumenstreuung bedingen. Die vergleichende Auswertung der PolSAR Daten zeigte, dass sowohl X- als auch C-Band Daten besonders sensitiv für die untersuchten Landbedeckungsklassen waren. Die X-Band Daten zeigten die höchste Sensitivität für niedrige Tundrengesellschaften. Die C-Band Daten zeigten eine höhere Sensitivität für mittelhohe Tundrengesellschaften und Gebüsch (shrub). Die L-Band Daten wiesen im Vergleich dazu die geringste Sensitivität für die Oberflächenbedeckung auf. Ein Vergleich von verschiedenen dual-polarisierten Daten zeigte, dass die Kanalkombination HH/VV die beste Differenzierung der Landbedeckungsklassen lieferte. Weniger deutlich war die Differenzierung mit den Kombinationen HH/HV und VV/VH. Insgesamt am besten waren jedoch die voll-polarisierten Daten geeignet, auch wenn die Verbesserung im Vergleich zu den co-polarisierten Daten nur gering war. Die Analyse der Klassifikationsgenauigkeiten bestätigte dieses Bild, machte jedoch deutlich, dass zu einer genauen Landbedeckungsklassifikation die Einbeziehung von multispektraler Information notwendig ist. Eine Nutzung von voll-polarisierten C-Band und multispektralen Daten erbrachte so eine mittlere Güte von ca. 80% für unüberwachte und von ca. 90% für überwachte Klassifikationsverfahren. Ähnlich hohe Werte wurden für die Kombination von co-polarisierten X-Band und multispektralen Daten erreicht. Im Vergleich zu Klassifikation die nur auf Grundlage von multispektralen Daten durchgeführt wurden, erbrachte die Einbeziehung der polarisierten Radardaten eine zusätzliche durchschnittliche Klassifikationsgüte von ca. +15%. Der Zugewinn und die Möglichkeit zur Differenzierung war vor allem für die Bedeckungstypen der Feuchtgebiete (wetlands) und der niedrigen Tundrengesellschaften festzustellen.

Die Analyse der digitalen Höhenmodelle zeigte ein hohes Potential der TanDEM-X Daten für die Charakterisierung der topographischen Gegebenheiten. Die aus den Daten abgeleiteten absoluten und relativen topographischen Merkmale waren für eine morphometrische Quantifizierung der Landoberflächen-Morphologie geeignet. Zudem konnten diese Merkmale auch für eine initiale Klassifikation der Landformen genutzt werden. Die Daten zeigten somit ein hohes Potential für die Unterstützung der geomorphologischen Kartierung und für die Identifizierung der aktuellen und zukünftigen Dynamik der Landoberfläche.



---

---

# Contents

<b>Acknowledgments</b>	<b>III</b>
<b>Abstract - Zusammenfassung</b>	<b>VI</b>
<b>List of Figures</b>	<b>XIV</b>
<b>List of Tables</b>	<b>XIX</b>
<b>List of Symbols, Operators and Abbreviations</b>	<b>XX</b>
<b>1 Introduction, State of the Art and Objectives</b>	<b>1</b>
1.1 Motivation . . . . .	1
1.2 State of the Art . . . . .	3
1.2.1 Climate Change of Polar Regions . . . . .	3
1.2.2 Optical Remote Sensing of Arctic Environments . . . . .	5
1.2.3 Polarimetric Synthetic Aperture Radar Data . . . . .	8
1.2.4 Digital Elevation Model Data . . . . .	12
1.3 Objectives . . . . .	16
1.4 Outline . . . . .	17
<b>2 Test Sites and Database</b>	<b>21</b>
2.1 Test Sites . . . . .	21
2.1.1 Site Selection and Overview . . . . .	21
2.1.2 Mackenzie Delta Region . . . . .	22
2.1.3 Banks Island . . . . .	34
2.1.4 James Bay . . . . .	38
2.2 Database . . . . .	40
2.2.1 In situ Data . . . . .	40
2.2.2 Polarimetric Synthetic Aperture Radar Data . . . . .	49
2.2.3 Digital Elevation Model Data . . . . .	52
2.2.4 Multispectral Data . . . . .	53
2.2.5 Airborne Data . . . . .	53

<b>3</b>	<b>Methodology</b>	<b>55</b>
3.1	Imaging, Processing and Feature Extraction . . . . .	55
3.1.1	Synthetic Aperture Radar . . . . .	55
3.1.1.1	Polarimetry . . . . .	59
3.1.1.2	Speckle and Image Filtering . . . . .	75
3.1.1.3	Processing Chain . . . . .	82
3.1.2	Multispectral Data . . . . .	83
3.1.3	Digital Elevation Model . . . . .	84
3.2	Image Classification . . . . .	90
3.2.1	Supervised Land Cover Classification . . . . .	90
3.2.2	Unsupervised Land Cover Classification . . . . .	92
3.2.2.1	Classification of Land Cover . . . . .	92
3.2.2.2	Classification of Water Bodies . . . . .	96
3.2.3	Accuracy Assessment . . . . .	100
3.2.4	Classification of Terrain and Landform . . . . .	101
<b>4</b>	<b>Results</b>	<b>107</b>
4.1	Evaluation of Methodological Concepts . . . . .	107
4.1.1	Non Local Means Filtering . . . . .	107
4.1.1.1	Parametrization . . . . .	108
4.1.1.2	Performance Evaluation . . . . .	110
4.1.1.3	Influence on Class Separability and Classification Accuracy . . . . .	117
4.1.2	Two Component Decomposition . . . . .	119
4.1.3	FKM-ML Unsupervised Land Cover Classifier . . . . .	123
4.2	Land Surface Characterization . . . . .	126
4.2.1	Polarimetric Synthetic Aperture Radar Data . . . . .	126
4.2.1.1	Intensities . . . . .	127
4.2.1.2	Entropy/Alpha Decomposition . . . . .	130
4.2.1.3	Power Decompositions . . . . .	136
4.2.1.4	Influence of the Incidence Angle . . . . .	139
4.2.2	Multispectral Data . . . . .	143
4.2.3	Digital Elevation Model Data . . . . .	148
4.2.3.1	Mackenzie Delta Region - Caribou Hills . . . . .	148
4.2.3.2	Mackenzie Delta Region - Northern Delta . . . . .	158
4.2.3.3	Banks Island . . . . .	162
4.2.3.4	James Bay . . . . .	167
4.3	Land Surface Classification . . . . .	173
4.3.1	Water Bodies . . . . .	173
4.3.2	Land Cover . . . . .	175
4.3.2.1	Mackenzie Delta Region . . . . .	179
4.3.2.2	Banks Island . . . . .	204

4.3.2.3	James Bay . . . . .	208
4.3.3	Terrain and Landform . . . . .	210
4.3.3.1	Mackenzie Delta Region - Caribou Hills . . . . .	211
4.3.3.2	Mackenzie Delta Region - Northern Delta . . . . .	217
4.3.3.3	Banks Island . . . . .	225
4.3.3.4	James Bay . . . . .	232
<b>5</b>	<b>Interpretation and Discussion</b>	<b>239</b>
5.1	Methodological Concepts . . . . .	239
5.1.1	Non-Local Means Filtering . . . . .	239
5.1.2	Two Component Decomposition . . . . .	240
5.1.3	Unsupervised Classifier . . . . .	241
5.2	Land Surface Characterization . . . . .	242
5.2.1	Polarimetric Synthetic Aperture Radar Data . . . . .	242
5.2.2	Digital Elevation Model Data . . . . .	244
5.2.3	Multispectral Data . . . . .	246
5.3	Land Surface Classification . . . . .	246
5.3.1	Water Bodies . . . . .	246
5.3.2	Land Cover . . . . .	247
5.3.3	Terrain and Landform . . . . .	249
<b>6</b>	<b>Conclusions and Outlook</b>	<b>251</b>
6.1	Summary and Conclusions . . . . .	251
6.2	Outlook and Perspectives . . . . .	256
	<b>Bibliography</b>	<b>258</b>
	<b>Appendix</b>	<b>275</b>
	<b>Index</b>	<b>287</b>
	<b>Affidavit</b>	<b>287</b>



---

---

## List of Figures

2.1	Map of permafrost zonation index and location of the selected test sites . . . . .	22
2.2	Climate normals of selected Arctic stations . . . . .	23
2.3	Geographic overview of the Mackenzie Delta Region . . . . .	24
2.4	Geological overview of the Mackenzie Delta Region . . . . .	25
2.5	Permafrost setting of the Mackenzie Delta Region . . . . .	27
2.6	Aerial photography of the Mackenzie Delta Region . . . . .	31
2.7	Aerial photography of the Richards Island . . . . .	32
2.8	Geographic overview of Northern Banks Island . . . . .	34
2.9	Geological overview of Northern Banks Island . . . . .	35
2.10	Quaternary geological overview Northern Banks Island . . . . .	36
2.11	Field and aerial photography of Banks Island . . . . .	37
2.12	Geographic overview of James Bay . . . . .	38
2.13	Mackenzie Delta: Field photographs of the land cover classes . . . . .	42
2.14	Definition of the land cover classes of the Mackenzie Delta Region . . . . .	44
2.15	Occurrence of the land cover classes of the Mackenzie Delta Region . . . . .	45
2.16	Banks Island: Field photographs of the land cover classes . . . . .	47
2.17	Definition of the land cover classes of Banks Island . . . . .	48
2.18	PolSAR Data coverage and in situ data of the test sites - I . . . . .	49
2.19	PolSAR Data coverage and in situ data of the test sites - II . . . . .	50
3.1	Acquisition geometry of a SAR System . . . . .	56
3.2	Acquisition modes of a SAR System . . . . .	57
3.3	Illustration of polarization modes . . . . .	58
3.4	Schematic interaction of electromagnetic wave and tundra land cover . . . . .	61
3.5	Illustration of amplitude, wavelength and intensity and phase . . . . .	63
3.6	Image examples of selected PolSAR features . . . . .	64
3.7	Feature space of Entropy/Alpha/Anisotropy Decomposition . . . . .	73
3.8	Formation of fully and partially developed speckle . . . . .	76
3.9	Estimation of weights in Non-Local Means filtering . . . . .	78
3.10	Process chart of Non-Local Means image filtering . . . . .	80
3.11	Process chart of PolSAR data Processing . . . . .	82
3.12	Digital Elevation Models with different spatial resolutions . . . . .	85
3.13	Calculation of Topographic Position Index . . . . .	88

## List of Figures

3.14	Influence of skip factor on TPI processing time . . . . .	89
3.15	Process chart of unsupervised land cover classification . . . . .	94
3.16	Process chart of iterative water classification . . . . .	97
3.17	Processing examples of iterative water classification . . . . .	98
3.18	Process chart of $k$ -fold cross-validation . . . . .	99
3.19	Example of discrete landform classification . . . . .	104
3.20	Legend of discrete and quasi continuous landform classification . . . . .	105
3.21	Process chart of landform classification . . . . .	106
4.1	Influence of parameter $h$ on the Non-Local Means filtering . . . . .	109
4.2	Parametrization of Non-Local Means filtering (TSX data) . . . . .	110
4.3	Parametrization of Non-Local Means filtering of R-2 data . . . . .	111
4.4	Processing example of Non-Local Means image filtering - I . . . . .	113
4.5	Processing example of Non-Local Means image filtering - II . . . . .	114
4.6	Evaluation of Non-Local Means filtering . . . . .	115
4.7	Processing Example of Non-Local Means filtering - III . . . . .	116
4.8	Influence of image filtering on the separability . . . . .	118
4.9	Influence of image filtering on the classification accuracy . . . . .	119
4.10	Scatterplots of Yamaguchi and Two Component Decomposition features - I . . . . .	120
4.11	Scatterplots of Yamaguchi and Two Component Decomposition features - II . . . . .	121
4.12	Performance analysis via Receiver Operating Characteristic (ROC) - I . . . . .	124
4.13	Performance analysis via Receiver Operating Characteristic (ROC) - II . . . . .	125
4.14	Boxplots of TSX and R-2 sigma nought intensities . . . . .	128
4.15	Boxplots of ALOS PalSAR sigma nought intensities . . . . .	129
4.16	Boxplots of TSX sigma nought intensities . . . . .	129
4.17	Boxplots of Entropy and Alpha - I . . . . .	132
4.18	Boxplots of Entropy and Alpha - II . . . . .	133
4.19	Boxplots of Entropy and Alpha - III . . . . .	135
4.20	Boxplots of Entropy and Alpha - IV . . . . .	136
4.21	Boxplots of TSX and R-2 Power Component Decomposition . . . . .	138
4.22	Boxplots of TSX Power Component Decomposition . . . . .	138
4.23	Influence of the incidence angle - I . . . . .	140
4.24	Influence of the incidence angle - II . . . . .	141
4.25	Influence of she incidence angles on the separability of land cover . . . . .	142
4.26	Boxplots of top-of-atmosphere corrected L-8 features - I . . . . .	145
4.27	Boxplots of top-of-atmosphere corrected L-8 features - II . . . . .	146
4.28	Basic topographic features of the test site Caribou Hills . . . . .	151
4.29	Elevation profiles of the test sites Caribou Hills . . . . .	152
4.30	Slope profiles of the test sites Caribou Hills . . . . .	153
4.31	Topographic Position Indices (TPI) of the test site Caribou Hills . . . . .	155
4.32	Selected TPI Profiles of the test site Caribou Hills . . . . .	156
4.33	TPI Stack profiles of the test sites Caribou Hills . . . . .	157



4.34	Basic topographic features of the Northern Mackenzie Delta . . . . .	159
4.35	Topographic Position Indices (TPI) of the Northern Mackenzie Delta . . . . .	160
4.36	Elevation, slope and TPI Stack profiles of the Northern Mackenzie Delta . . . . .	161
4.37	Basic topographic features of Northern Banks Island . . . . .	164
4.38	Topographic Position Indices (TPI) of Northern Banks Island . . . . .	165
4.39	Elevation, Slope and TPI Stack profiles of Northern Banks Island . . . . .	166
4.40	Basic topographic Features of James Bay . . . . .	169
4.41	Topographic Position Indices (TPI) of James Bay . . . . .	170
4.42	Elevation, slope and TPI Stack profiles of James Bay . . . . .	171
4.43	Classification accuracies of water classification . . . . .	174
4.44	Processing examples of iterative water classification . . . . .	176
4.45	Mackenzie Delta water body and shoreline classification . . . . .	177
4.46	East Channel and Delta Islands: Overall classification accuracies . . . . .	181
4.47	Richards Island and Tuktoyaktuk: Overall classification accuracies . . . . .	182
4.48	Richards Island (RIS) unsupervised classification results . . . . .	183
4.49	Tuktoyaktuk (TUK) unsupervised classification results . . . . .	184
4.50	Normalized unsupervised classification accuracies of all test sites . . . . .	187
4.51	Normalized supervised classification accuracies of all test sites . . . . .	188
4.52	East Channel (ECH) classification results . . . . .	189
4.53	Delta Islands classification results . . . . .	190
4.54	Richards Island classification results . . . . .	191
4.55	Tuktoyaktuk classification results . . . . .	192
4.56	Normalized Jefferys Matusita Distances of all test sites . . . . .	194
4.57	Normalized and the Bhattacharyya Distances of all test sites . . . . .	195
4.58	Scatterplots of separability distances and classification accuracies . . . . .	196
4.59	Mackenzie Delta: Overall classification accuracies . . . . .	198
4.60	Mackenzie Delta unsupervised classification - I . . . . .	200
4.61	Mackenzie Delta unsupervised classification - II . . . . .	201
4.62	Mackenzie Delta supervised classification - I . . . . .	202
4.63	Mackenzie Delta supervised Classification - II . . . . .	203
4.64	Banks Island unsupervised classification results . . . . .	205
4.65	Classification accuracies of Banks Island . . . . .	206
4.66	Banks Island classification results . . . . .	207
4.67	James Bay unsupervised classification results . . . . .	209
4.68	Selection of suitable TPI scales for the test site Caribou Hills . . . . .	212
4.69	Selection of suitable Elevation and slope thresholds for test site Caribou Hills . . . . .	212
4.70	Landform classifications of the test site Caribou Hills - I . . . . .	213
4.71	Landform classifications of the test site Caribou Hills - II . . . . .	214
4.72	Landform classification of the test site Caribou Hills with TPI scale of 2000 m . . . . .	215
4.73	SAGA GIS landform classifications of the test site Caribou Hills . . . . .	216
4.74	Selection of suitable TPI scales for Northern Mackenzie Delta . . . . .	218

*List of Figures*

4.75	Selection of suitable elevation and slope thresholds for Northern Mackenzie Delta . . . . .	219
4.76	Landform classifications of the Northern Mackenzie Delta - I . . . . .	220
4.77	Landform classifications of Northern Mackenzie Delta - II . . . . .	221
4.78	Landform classification of Northern Mackenzie Delta with TPI scale of 1500 m . . . . .	222
4.79	Landform classification of Richards Island based on TPI scale of 1500 m . . . . .	223
4.80	SAGA GIS landform classifications of Northern Mackenzie Delta . . . . .	224
4.81	Selection of suitable TPI scales for Northern Banks Island . . . . .	226
4.82	Selection of suitable elevation and slope thresholds for Northern Banks Island . . . . .	226
4.83	Landform classifications of Northern Banks Island - I . . . . .	228
4.84	Landform classifications of Northern Banks Island - II . . . . .	229
4.85	Landform classification of Northern Banks Island with TPI scale of 2500 m . . . . .	230
4.86	SAGA GIS landform classifications of Northern Banks Island . . . . .	231
4.87	Selection of suitable TPI scales for James Bay . . . . .	233
4.88	Selection of suitable elevation and slope thresholds for James Bay . . . . .	233
4.89	Landform classifications of James Bay - I . . . . .	234
4.90	Landform classifications of James Bay - II . . . . .	235
4.91	SAGA GIS landform classifications of James Bay . . . . .	236



# List of Tables

- 1.1 Overview of selected space borne optical remote sensing methods . . . . . 7
- 1.2 Overview of selected space borne radar remote sensing methods . . . . . 10
- 1.3 Overview of selected DEM remote sensing methods . . . . . 13
  
- 2.1 List of the in situ reference data . . . . . 40
- 2.2 Total number and area of land cover reference data of the Mackenzie Delta Region . . . 43
- 2.3 Total number and area of land cover reference data per class . . . . . 43
- 2.4 Total number and area of land cover reference data of Banks Island . . . . . 46
- 2.5 TSX and TDX data for PolSAR analysis . . . . . 51
- 2.6 R-2 data for incidence angle and land cover analysis . . . . . 52
- 2.7 ALOS data for PolSAR analysis . . . . . 52
- 2.8 Digital elevation model data . . . . . 53
- 2.9 Multispectral data . . . . . 53
- 2.10 Airborne reference data of the Mackenzie Delta Region . . . . . 54
  
- 3.1 Two class Confusion Matrix . . . . . 100
- 3.2 Classification approach of the Nested-Means classification . . . . . 102
- 3.3 Thresholds and class names of the TPI landform classification . . . . . 102
  
- 4.1 Correlation Coefficient of Two and Three Component Decomposition . . . . . 122
- 4.2 List of the data used for classification . . . . . 178
- 4.3 List of the data combinations used for classification . . . . . 178



---



---

## List of Symbols, Operators, Conventions and Abbreviations

### List of Symbols

Symbol	Meaning
$\alpha$	Mean alpha
$A$	Anisotropy
$Am$	Amplitude
$C$	Covariance Matrix
$\phi$	Phase
$E$	Entropy substitute
$ENL$	Equivalent Number of Looks
$f$	Wave frequency
$G_t$	Antenna gain
$H$	Entropy
$I$	Intensity
$k$	Target vector
$K$	Kennaugh Matrix
$\lambda$	Eigenvalue
$\rho$	Alpha substitute
$p$	Probability of eigenvalue
$P_r$	Power detected at receiving system
$P_t$	Power transmitted
$R_r$	Distance between target and receiving system
$R_t$	Distance between transmitting system and target
$S$	Sinclair Matrix
$S_i$	Sinclair Matrix Element
$span$	Total energy
$T$	Coherency Matrix
$U$	Square Matrix
$u$	Eigenvector

## Operators and mathematical conventions

Operator	Meaning
$\Re$	Real part of a complex quantity
$\Im$	Imaginary part of a complex quantity
$\langle \rangle$	Average value
$\ $	Absolute value
$*$	Conjugation of a complex number
$T$	Transpose
$+$	Conjugate transpose
$-1$	Inversion
$E()$	Expected value
$e$	Euler's Number
$\mathbb{R}$	Real number
$\mathbb{C}$	Complex number
$tr()$	Trace of a matrix
$F$	Frobenius norm

## Abbreviations

Abbreviation	Meaning
ALPC	Alpha of C-Matrix
ALPT	Alpha of T-Matrix
AND	Anderson, Northwest Territories, Canada
ANI	Anisotropy
BD	Bhattacharyya Distance
BIS	Banks Island, Northwest Territories, Canada
BRIGHT	Tasseled Cap Brightness
CAH	Caribou Hills, Northwest Territories, Canada
DBL	Double Bounce Scattering
DEM	Digital Elevation Model
DIS	Delta Islands, Northwest Territories, Canada
ECH	East Channel, Northwest Territories, Canada
EEI	Edge Enhancement Index
ENT	Entropy
FKM	Fuzzy-K-Means
FN	Confusion Matrix False Negative
FP	Confusion Matrix False Positive
FPR	Confusion Matrix False Positive Rate
GREEN	Tasseled Cap Greenness

*List of Symbols, Operators and Abbreviations*

HH	Polarization Channel Horizontal-Horizontal
HIS	Herschel Island, Yukon, Canada
HV	Polarization Channel Horizontal-Vertical
IVV	Ivvavik, Northwest Territories, Canada
JAB	James Bay, Québec, Canada
JD	Jefferys Matusita Distance
L-8	Landsat 8
NDVI	Normalized Vegetation Index
NBG	Reference Land Cover Class Bare Ground
NIR	Near Infrared
NWA	Reference Land Cover Class Water
OAI	Overall Filter Evaluation Index
ODD	Odd/Surface Scattering
POM	Preservation of Mean
R-2	Radarsat-2
RED	Red Light
RIS	Richards Island, Northwest Territories, Canada
SAR	Synthetic Aperture Radar
SRI	Speckle Reduction Index
TC	Tasseled Cap Transformation
TDX	TanDEM-X
TDX IDEM	Intermediate DEM of the TanDEM-X Mission
TP	Confusion Matrix True Positive
TPR	Confusion Matrix True Positive Rate
TN	Confusion Matrix True Negative
TSX	TerraSAR-X
TUK	Tuktoyaktuk, Northwest Territories, Canada
UTM	Universal Transverse Mercator
VH	Polarization Channel Vertical-Horizontal
VLD	Reference Land Cover Class Low Tundra
VOL	Volume Scattering
VMD	Reference Land Cover Class Mixed/Medium Tundra
VSD	Reference Land Cover Class Shrub Tundra
VV	Polarization Channel Vertical-Vertical
VWT	Reference Land Cover Class Wetland
WET	Tasseled Cap Wetness
WGS	World Geodetic System
YCP	Yukon Coastal Plain, Yukon, Canada

---





---

## Introduction, State of the Art and Objectives

### 1.1 Motivation

The ecosystem of the high northern latitudes is affected by the recently changing environmental conditions and the Northern Hemisphere has undergone a significant climatic change over the last decades. It was observed that the land coverage of the Arctic ecosystems was changing due to the warming. The measurements of satellites have proven this change as well as the decrease of the annual sea ice extent and the negative mass-balance of the northern ice sheets. Along with this a loss of permanently frozen ground of the northern landmass was determined by long term pan-arctic observations. These variations imply serious changes in the environmental process-response system of the Arctic environment. Numerous studies have therefore been addressed to deepen the understanding of the recent situation and to identify the driving forces and feedback mechanisms. Even though progress was made there is still a demand for a comprehension of the active processes and to map their spatial dimensions. A key role in this field is the reaction of the biosphere and of the periglacial system on the changing climate. The recent warming of the land surface and the near surface atmosphere leads to a deepening of the active layer of permafrost landscapes and this change affects other ecosystem variables like the hydrosphere, the pedosphere, the biosphere or the active geomorphological dynamics. The consequences are, for example, an increase in frequency and magnitude of erosion events and surface movements, the increase in the tundra fire frequency, or the change of the composition of the tundra vegetation. The emission of greenhouse gases increases with a deepening of the active layer since permanently frozen ground acts as a carbon sink. All of these changes have impacts on the recent warming due to feedback mechanisms and nonlinear connections.

A visible indicator of the change of the northern latitudes is, for example, the intensification of coastal erosion processes. The driving force of the intensification is the decrease of the mean annual sea ice extent. The temporal extension of ice free open water conditions results in an increasing storm frequency, in a prolonged heat exchange between water and land and therefore in destabilization of coastal ice-bearing sediments. It was further observed that a substantial greening took place for more than thirty percent of

## *1 Introduction, State of the Art and Objectives*

the Arctic landmass. The augmentation was greatest in the North American High Arctic and along the southern Beaufort Sea. The trend of the photosynthetic activity was positive for these regions and was up to more than eight percent compared to the last decade. The change of the vegetation composition was revealed in a proliferation of the shrub lands as well. Further visible indicators were the degradation of permafrost which manifested, for example, in the formation of thermokarst lakes, the expansion of existing lakes via lateral thawing and erosion and the active layer destabilization and mobilization.

These changes also imply socioeconomic challenges. The warming and the observed decrease of sea ice extent facilitate the utilization of Arctic's resources that were up to now not recoverable. The oil and gas wells detected on- and offshore of the Arctic Shelf have great potential for the world's energy demand. The future scenarios show an intensive terminal development of the northern latitudes and an increase in shipping traffic along the Arctic coasts, for example, due to the opening of the Northwest and Northeast Passages and the extraction of oil and gas in the Canadian Beaufort Sea. These foreseeable challenges cause the necessity to collect information for environmental protection and for decision making. The demand includes high resolution data on the actual state of the land surface in terms of coverage and surface morphology - but also on the temporal development of these parameters on the scale of days, months or years. The remoteness, inaccessibility and vast physical extent of the Arctic are challenges for adequate data collection and it is expensive and time-consuming to collect the required information continuously and for large areas. But it has been demonstrated that valuable information on the Arctic's surface can be collected by the use of remotely sensed data. So far the remote sensing of the Arctic's land surface was predominantly carried out using optical sensors. Information on the spectral reflectance helps to distinguish between different types of vegetation, to show the vegetation development and the greening over time, or to indicate the extent of land cover changes. However, the application of optical remote sensing data encounters problems in the arctic environment which are, for example, the frequent cloud cover, the solar geometry, the fragmentation of land cover boundaries, the fast changing spectral characteristics and the low spectral contrast of the land cover types.

That being said, the imaging of Synthetic Aperture Radar is not affected by the cloud cover and the acquisition of a radar system is independent of solar illumination due to the active sending of the electromagnetic pulses. The Synthetic Aperture Radar sensors are capable to acquire imagery at any time of the year with nearly constant quality and they are independent of the external situation. The radar data were proven to be efficient for various applications in the Arctic environment - such as the detection of land surface changes, the delineation of morphological units, the generation of three-dimensional elevation models, or the characterization and classification of the land cover. Compared to optical sensors the interpretation of Synthetic Aperture Radar data is more challenging and less intuitive since the interpretation of the signal is based on the physical structure and the dielectric properties and not on spectral properties. Furthermore, the information of a radar system varies with the acquisition parameters and geometry. Nevertheless, it is of interest to explore how Synthetic Aperture Radar data can contribute to the collection of the desired land surface information and how they perform compared to optical remote sensing systems. Furthermore, suited acquisition parameters need to be identified and the benefits of the contemporaneous radar systems have to be compared.

## 1.2 State of the Art

The following subsections provide a brief summary of the climate change of the polar regions, the state of the art of the application of multispectral remote sensing of the Arctic environment in general and polarimetric Synthetic Aperture Radar (PolSAR) and digital elevation model (DEM) data in particular. The intention of the following sections is to provide an overview on the recent challenges and to define the research needs with view on the objectives of this study.

### 1.2.1 Climate Change of Polar Regions

Instrumental measurements showed that the land surface of the Arctic has undergone a strong warming over the last century and a further warming is projected for the near future. The implications will be manifold and will have strong impacts on the ecosystem and geosystem. The recently published report of the Intergovernmental Panel on Climate Change (IPCC) underlines the evidence of the change and its significance. The mean land surface winter temperature of the Arctic is increased by about +2°C between 1900 and 2000. Parallel to this the mean sea surface winter temperature of the Arctic increased in the same period about +3°C (IPPC et al. (2014), p. 1322). The scenarios show that the land surface winter temperature will further increase in the next century (2000-2100). The projected temperature increase is in the range of +3°C (Representative Concentration Pathway 2.6 (RCP2.6)) to +10°C (RCP8.5). The moderate emission scenarios of the RCP6.0 and the RCP4.5 show a warming of the land surface in winter of about +5°C to +7°C (IPPC et al. (2014), p. 1322). The projections of the mean sea surface winter temperature show a warming of about +3°C (RCP2.6) to +15°C (RCP8.5) (IPPC et al. (2014), p. 1322). This positive trend is also evident for the summer temperature of the Arctic. The historical mean land surface summer temperature increase between 1900 and 2000 was about +1°C. Further, the scenarios show warming of the land surface in the range from +1°C (RCP2.6) up to +5°C (RCP8.5) by 2100. The change of the projected sea surface summer temperature will be between +1°C (RCP2.6) and +5°C (RCP8.5) by 2100 (IPPC et al. (2014), p. 1323). The IPCC states similar findings for Northern Canada, Alaska and Greenland (IPPC et al. (2014), p. 1326 ff.).

A climate change in the high latitudes has strong impact on other ecosystem variables. It was for example observed that the mean annual sea ice extent was decreasing. A minimum extent was reached in the last decade that was never observed before. The sea ice is an important variable of the system and it is coupled to other variables via feedback mechanisms that are meaningful for the global climate. For instance, the sea ice acts as isolator of the ocean due to its high albedo. It is furthermore a barrier for the exchange of vapor and heat (Vaughan et al. (2013)). The sea ice extent is also important for the climate of the landmass and it is likely an indirect regulator of the permafrost distribution (Lawrence, Slater, Tomas & Holland (2008)).

Another consequences of the changing climate is a change of the periglacial system in general and the degradation of the permafrost in particular. The frozen ground is coupled to the climatic parameters via energy fluxes between atmosphere and ground. It was observed that the ground temperatures of most polar measuring stations were increasing during the last decades (Vaughan et al. (2013), p. 363 ff.). The findings of Romanovsky et al. (2010) and Christiansen et al. (2010) showed an increase in the ground temperature

## 1 Introduction, State of the Art and Objectives

of several degrees for various circumpolar stations. On regional scale the temperature increase in the ground thermal regime was about +1°C to +2°C for the Mackenzie Delta Region as reported by Burn & Kokelj (2009). The warming of the ground causes a degradation of the permafrost which is “[...] a decrease in thickness and/or areal extent.” (Vaughan et al. (2013), p. 364). For example, this degradation manifests in the formation of thermokarst lakes, the expansion of existing lakes via thawing and lateral erosion, the active layer deepening or destabilization and the mobilization of the active layer (Vaughan et al. (2013), p. 364). The destabilization of the ground leads to an intensification of the geomorphological dynamics in frequency and magnitude. The changes are the response of the system to the changing boundary conditions and projections show that the degradation continues and is likely to accelerate - the extent of the near surface permafrost will be significantly lowered during the next decades (Lawrence, Slater, Romanovsky & Nicolsky (2008)).

The composition of vegetation of the Arctic Environment is mainly driven by the mean annual temperature and the number of days with non-negative temperature. It was observed that a phenological response to the warming was apparent by using satellite measurements. Between 1982 and 2012 a substantially greening took place for more than thirty percent of the Arctic landmass. This increase was strongest in the North American High Arctic and along the Beaufort Sea (Anisimov et al. (2014), p. 1578). The trend of the photosynthetic activity was positive for those regions and was up to eight percent compared to the last decade (Xu et al. (2013)). Further changes of the vegetation were related to the expansion of the shrub lands that have generally expanded their ranges and growth - however, the spatial pattern is diverse and negative trends for other Arctic sites have been observed also (Anisimov et al. (2014), p. 1579 and Bonfils et al. (2012)). There is evidence for a displacement of the treeline and a replacement of tundra cover by forest. The projections show a replacement of tundra cover by forest of up to fifty percent by 2100. Along with this it is likely that the forest in sub-polar regions will show an intensive densification (Anisimov et al. (2014), p. 1579). On regional scale these findings were supported by the study of Fraser et al. (2011) that identified a positive and consistent greening for sites in Northern Canada using Landsat time series (1980-2009). Lantz et al. (2013) further showed the recent proliferation of the shrubs in the uplands of the Mackenzie Delta Region by local observation and high resolution airborne photography. The changes of the vegetation coverage will likely result in a positive feedback on the warming due to the overall lowering of the surface albedo (Anisimov et al. (2014), p. 1589). Recent findings on the proliferation and expansion of shrub lands and on the dynamic of the arctic and sub-arctic vegetation are provided by Myers-Smith et al. (2011), Lara et al. (2012), Epstein et al. (2013).

In addition, the warming has strong impacts on the Arctic river deltas. Anisimov et al. (2007), p. 674 note that the “[...] *physical development and ecosystem health of these systems are strongly controlled by cryospheric processes and are thus highly susceptible to the effects of climate change.*” The loss of permanently frozen ground will lead to a destabilization of the sediments caused by intense maritime and fluvial erosion processes. These implications were for example discussed by Solomon (2005) for the Mackenzie Delta Region. The implications of a recent storm surge for the delta ecosystem were shown by Pisaric et al. (2011) and highlighted the interconnections between the climate and the ecosystem. The warming also effects the active geomorphological dynamic of the Arctic’s system. This becomes obvious in an acceleration and intensification of coastal erosion process (Forbes (2011)). On regional scale the warming can also affect the slump activity as shown by Lantz & Kokelj (2008), Lantuit & Pollard (2008)

for the Mackenzie Delta Region and the adjunct Herschel Island. Fast retreating shorelines were reported for the Tuktoyaktuk Peninsular located in the east of the Mackenzie Delta Region by Wolfe et al. (1998) and for the shores of the Mackenzie Delta itself by Solomon (2005).

Climate change and its implications will have also socioeconomic consequences. On the one hand the thawing of permafrost, the mobilization of the near surface and the ground disturbance will affect the northern infrastructure and the related services in a negative way (Larsen et al. (2014)). On the other hand the decreasing sea ice extent offers the opportunity to recover resources that were up to now not accessible and therefore not exploitable. This includes the on- and off-shore oil and gas wells and terrestrial resources that are, for example, located in the Mackenzie Delta Region and on the shelf of the southern Beaufort Sea. In addition, the opening of the Northwest Passage gives new perspectives for the global trading. However, both opportunities will be risks for the Arctic Environment. Especially the sensitive maritime and coastal ecosystems will be endangered in case of oil disasters (Owens (2010), Demers et al. (2011), Banks et al. (2011)). Further aspects of the impact of the climate change of polar regions are comprehensively discussed by ACIA (2005), Anisimov et al. (2007), Forbes (2011), Lemke & Jacobi (2011), Turner & Marshall (2011), Hartmann et al. (2013), Vaughan et al. (2013), Anisimov et al. (2014).

It can be concluded that the current climate change of the Arctic has various implications and is of global relevance. The area-wide identification of the present state of the surface coverage (e.g. vegetation, sea ice, snow cover) is of importance - as well as the monitoring of the changes and the identification of the actual land surface morphology. These information are important to recognize long and short term processes of the system and will help to deepen the understanding of the ongoing transformation process. This is necessary to developed adaption strategies, a sustainable perspective and to avoid negative consequences.

### **1.2.2 Optical Remote Sensing of Arctic Environments**

Optical multispectral remote sensing plays a key role in collecting information on the state of the Arctic land surface and atmospheric conditions. The data of geostationary and polar orbiting satellites are used to determine the atmospherical conditions of the polar regions and are information sources for climate research (Anisimov et al. (2014), Larsen et al. (2014)). Besides, the data of high temporal resolution sensors - such as the Moderate Resolution Imaging Spectroradiometer (MODIS) of the satellites Terra and Aqua, or the Advanced High Resolution Radiometer (AVHRR) - deliver long term information on the state of the surface in general and on the phenological response in particular. The multispectral data of these instruments were used to analyze the long term phenological growth of Arctic vegetation since the 1980s and to examine the start and end of the growing season. Further, these data were used to evaluate the shifts in vegetation production (Stow et al. (2004), Kaeaeb (2008)). Such data were used to quantify the response of the Arctic vegetation on the warming and still have high relevance for the global environmental and climate science as shown by Xu et al. (2013), Anisimov et al. (2014). Comprehensive overviews on the potential of these instruments to map vegetation changes in the Arctic ecosystems are provided by Stow et al. (2004) and Kaeaeb (2008).

In addition to this, high spatial resolution multispectral data were used to characterize Arctic environments on regional and local scales. The frequently used systems were the Landsat and SPOT satellites. The data were successfully applied for various tasks: Multispectral SPOT data were used in the early 1990s

## *1 Introduction, State of the Art and Objectives*

by Markon & Derksen (1994) for the classification of tundra land cover classes based on a supervised Maximum Likelihood approach. The tundra region near Teshekpuk Lake (Alaska) was grouped in twelve land cover classes, e.g. bare ground, sparse vegetated tundra, or different types of wetlands, based on selected sample data. Laidler & Treitz (2003) reviewed the usage of satellite borne multispectral remote sensing systems for the derivation of biophysical parameters of Arctic vegetation and showed the suitability of vegetation indices for mapping and up-scaling tasks. Laidler & Treitz (2003) further summarized key NDVI characteristics of tundra vegetation and discussed the linking of field data and remotely sensed data. Olthof & Fraser (2007) used Landsat data for supervised physically based mixture modeling and estimated the northern land cover fractions using Landsat ETM data. Olthof & Fraser (2007) used linear and multi-linear regression trees to map the fraction of six generalized land cover class. These were water, bare ground, shrub, grass and conifer. The results showed a good visual correspondence to several known vegetation features. The quantitative analysis and comparison with high-resolution IKONS imagery indicated poor performance to predict shrub and bare ground fractions, however. The problems were likely related to phenological difference - and therefore spectral difference - of the shrub vegetation over time and to the high spectral variability of the bare ground classes.

In the late 2000s Landsat ETM data were used by Schneider et al. (2009) for unsupervised and supervised classification of the Russian Lena Delta. The supervised classification approaches were a Minimum Distance and a Maximum likelihood algorithm. Both showed better performance than the unsupervised algorithm and Schneider et al. (2009) were able to classify nine classes of interest - which were, for example, bare ground, grass dominated tundra, tussock tundra and different types of wetlands. The estimated overall classification accuracy was up to 72% and the classification map was used for up-scaling of the greenhouse gas emission from tundra coverage. The spectral information of SPOT was used to estimate the extent of the near-surface permafrost in the Mackenzie Delta by Nguyen et al. (2009). The approach was based on a correlation of land cover types and permafrost properties. The land cover classification was carried out using a Maximum Likelihood classification and in situ reference data were used for the training of the algorithm. The overall classification accuracy was over 80% and a clear correlation between the near surface permafrost properties and the vegetation communities was found. Time series of Landsat was used to identify changes in the vegetation coverage of the Arctic bio-systems by Fraser et al. (2011, 2014), Olthof & Fraser (2014). Multispectral information was proven to be useful for land cover classification of various sites in northern Canada. Furthermore, these data were used to detect landscape disturbance, such as lake erosion or tundra greening (Olthof & Fraser (2014)). Stow et al. (2004) and Kaeaeb (2008) showed further applications of multispectral remote sensing data for land surface characterization. Table 1.1 provides an overview of selected space borne optical remote sensing methods for land surface characterization of Arctic Environments.

In summary the multispectral data were proven to be suited to gain information on the Arctic land surface. The spectral data showed potential classifying generalized land cover categories, such as bare ground, wetlands, or shrub vegetation, on high level of confidence and were well suited to relate land cover information to near-surface properties. This is of importance for the identification of land surface changes and the quantification of permafrost degradation. The information on the land cover is further important for climate sciences, e.g. to provide area-wide estimates of the greenhouse gas emission or to quantify the land surface albedo. As noted by Olthof & Fraser (2007), Schneider et al. (2009), Olthof & Fraser

Table 1.1: Overview of selected space borne optical remote sensing methods for land surface characterization of Arctic Environment

Study Area	Task	Data	Method	Reference
Alaska	Classification of tundra land cover	SPOT	Supervised Maximum Likelihood	Markon & Derksen (1994)
Mackenzie Delta	Mapping of habitats	Landsat TM	Unsupervised Maximum Likelihood	Gratto-Trevor (1996)
Arctic	Review	Multispectral data	n/a	Laidler & Treitz (2003)
Arctic	Review and case studies	Multispectral data	n/a	Stow et al. (2004)
Siberian coast	Mapping of geomorphological features	CORONA	Threshold classification and manual mapping	Grosse et al. (2005)
Lena - Anabar, Russia	Classification of thermokarst-affected terrain types	Landsat and DEM	Supervised Maximum Likelihood and decision tree	Grosse et al. (2006)
Northern Canada	Classification of northern land cover	Landsat	Regression, Mixture Models	Olthof & Fraser (2007)
Polar Regions	Review and case studies	Multispectral, hyperspectral data	n/a	Kaeab (2008)
Lena Delta	Classification of tundra land cover and estimation of methane emission	Landsat ETM+	Unsupervised ISODATA, Supervised Maximum Likelihood & Minimum Distance	Schneider et al. (2009)
Mackenzie Delta	Classification of tundra land cover and estimation of near-surface permafrost	SPOT-5	Supervised Maximum Likelihood	Nguyen et al. (2009)
Lena Delta	Classification of water bodies	Landsat and Rapid Eye	Object-based decision tree Mapping	Hese et al. (2010)
North Siberia	Determination of coastal erosion dynamics	High resolution imagery	Mapping	Lantuit et al. (2011)
Lena Delta	Classification of water bodies	Landsat	Supervised classification	Morgenstern et al. (2011)
Mackenzie Delta Region	Determination of shrub proliferation	High resolution imagery	Mapping	Lantz et al. (2013)
Mackenzie Delta Region	Classification of water bodies and shoreline	Landsat, Radar	Supervised classification	Chenier & Hemmingway (2014)
Mackenzie Delta Region	Classification of tundra land cover and mapping of surface disturbance	Landsat	Decision tree and spectral profile matching	Fraser et al. (2014)

(2014) classes with a high spectral dynamic - such as shrub lands, bare ground or shallow waters - can be difficult to be classified by spectral information alone. Stow et al. (2004) noted in this context that optical multispectral data face the following problems in Arctic environment: The short length of the growing season and the rapid phenological development of the Arctic vegetation require high temporal resolution data. Since the cloud cover of the high latitude regions is nearly persistent it is difficult to acquire suited data and long term time series. A further challenge is the solar geometry. Since the passive multispectral data require the external illumination the acquisitions are restricted to the summer months. The geometry further causes a large range of zenith and azimuth angles that can hinder the image analysis. The low spectral contrast of the cover types and the fragmented boundaries are a challenge (Stow et al. (2004), p. 282-285).

### 1.2.3 Polarimetric Synthetic Aperture Radar Data

In contrast, the imaging of Synthetic Aperture Radar (SAR) is not affected by these circumstances and the acquisition is independent of illumination since SAR systems actively send defined electromagnetic pulses to the earth surface. The radar sensors are capable acquiring data at any time of the year with nearly constant quality. The interpretation of such SAR imagery is more challenging and less intuitive compared to optical and multispectral sensors, however. The analysis has to be done with regard to the physical structure and the dielectric properties of the target. The information of the images varies with the system performance and the acquisition parameters, e.g. frequency, incidence angle, or polarization.

The application of SAR data for characterization of the earth surface has long tradition. It offers a new perspective on the earth surface and goes back to the late 1970s. The first imaging SAR satellite was Seasat (ASF (2014)) that operated in the L-Band and was in orbit for 106 days. Further SAR observations of the earth surface were then conducted during the Space Shuttle Missions in the 1980s (Kramer (2002), p. 1296). The era of operational SAR imaging began with the Japanese Earth Resources Satellite-1 JERS (JAXA (1992)) and the European Remote Sensing Satellites ERS-1 and ERS-2 (ESA (2011)) in the 1990s. Further important missions were the Radarsat-1 Mission (CSA (2014b)), the Shuttle Radar Topography Mission (USGS (2010)), the ENVISAT Mission (ESA (2012)) and the ALOS PALSAR Mission (JAXA (2006)). All of them delivered valuable information on the earth surface. Space borne SAR Systems that operate today are, for example, the Canadian C-Band Radarsat-2 (R-2) (CSA (2014a)), the German X-Band TerraSAR-X (TSX) and TanDEM-X (TDX) (DLR (2007, 2010)), the Japanese ALSO-2 PALSAR (Kankaku et al. (2010), JAXA (2014)), the Italian COSMO-SkyMed (ASI (2014)), the European C-Band Sentinel-1 (ESA (2014b)) and the Korean X-Band Kompsat 5 (Sang-Hoon et al. (2011)). In near future SAR data of the C-Band Radarsat Constellation Mission (CSA (2013)), the X-Band PAZ Mission (Astrium (2011)), or the TSX2 Mission (Janoth et al. (2012)) may be available. A comprehensive summary of the history and development of the radar and SAR technology is provided by Kramer (2002).

New methods for SAR data analysis were developed along with the evolution of the SAR systems. The classical analysis concentrates on single channel SAR imagery that is often used in time series analysis. In addition, the application of SAR interferometry (InSAR) is possible, when more than one SAR acquisition is available and if the data were recorded in suited geometry. The interferometric effect may be used to determine the surface altitude or to detect surface movements. The coherent and simultaneous acquisition



of different polarization channels enables the polarimetric analysis of the radar signal (PolSAR). PolSAR is of high importance for the characterization of the type of the backscatter and for land cover classification. The PolSAR analysis is usually performed using two (dual) or four (quad) polarization channels. Not all of the named SAR systems are capable to acquire the four channels coherently. For example, R-2 and ALOS PALSAR are systems that can acquire quad-polarized imagery (HH/HV/VH/VV). TSX and TDX are capable to acquire dual-polarized imagery - either as co-polarized data (HH/VV) or as cross-polarized data (HH/HV or VH/VH). Further SAR analysis methods are, for example, the polarimetric interferometry (PolInSAR), the radargrammetry, or the SAR tomography. All of them provide information on the third dimension of the target (Richards (2009), Ulaby et al. (2014)).

Focusing on PolSAR analysis, various concepts on the extraction of polarimetric features were developed during the last decades and the frequently used approaches decompose the PolSAR signal in components that are in relation to the type of the backscatter. Such decomposition features help to interpret the signal and to classify the land surface coverage. A model that is still frequently applied was introduced by Freeman & Durden (1998) in late 1990s. The approach decomposes quad-polarized data in the scattering components of volume scattering, odd bounce (surface scattering) and even bounce (double bounce). Further decomposition concepts are, for example, the Hyunen or the Krogager decomposition (Cloude (2010)). Fundamental overviews on the decomposition concepts are provided by Cloude & Pottier (1996) and Touzi et al. (2004). The established models that were developed after this comprehensive review reports were the decomposition models of Yamaguchi et al. (2005) and Yamaguchi et al. (2010) that are advancements of the approach of Freeman & Durden (1998). Further decomposition approaches were described by Wentao et al. (2010), Shan et al. (2012), Cui et al. (2012) - also in context of compact polarimetric (Cloude et al. (2012)). However, most of the methodological work concentrated on the analysis of quad-polarized data and only some concepts dealt with the polarimetric analysis of dual-polarized data, e.g. Cloude (2007), Ainsworth et al. (2008), Shan et al. (2011).

An important application of PolSAR data is the unsupervised land cover classification. Due to the nature of the PolSAR imagery the existing classification strategies - such as the K-Means or Maximum Likelihood approaches - were adapted to the nature and specifics of the polarimetric data. Approaches that were proven to be effective were shown by Lee & Grunes (1992), Cloude (1997), Lee, Grunes, Ainsworth, Du, Schuler & Cloude (1999) and Lee et al. (2004). All of these algorithms were designed to operate with quad-polarized data and evolved as standard techniques for the unsupervised classification of quad-polarized PolSAR data. In contrast, only few researchers have addressed the usage of co-polarized data since only few systems - like TSX or COSMO-Skymed - are capable to acquire the HH and VV channels coherently. The co-polarized data offer the benefit to have a better resolution than quad-polarized data. These data give information on the relation of the HH and VV phases, in contrast to the cross-polarized data. The relation between HH and VV is crucial to discriminate between odd and even bounce. The analysis and exploitation of co-polarized data is a research need - also with view on the fact that the frequently applied eigendecomposition features of quad- and co-polarized data are very similar (Sugimoto et al. (2013)).

Further, research is also needed on the removal of the speckle effect that hinders the radar image analysis and the classification. The effect is a result of the coherent acquisition of the SAR system and it is present in an image in form of a grainy salt-and-pepper texture. A variety of filtering techniques were developed

## 1 Introduction, State of the Art and Objectives

Table 1.2: Overview of selected space borne radar remote sensing methods for land surface characterization of Arctic Environment

Study Area	Task	Data	Method	Reference
Alaska	Bathymetric Mapping of Shallow Water	ERS	Time series - Mapping and modeling	Jeffries et al. (1996)Kozlenko & Jeffries (2000)
Mackenzie Delta Region	Delineation of delta ecozones	ERS	InSAR - Coherence	Hall-Atkinson & Smith (2001)
Canada, Nova Scotia	Mapping of geomorphological units in the intertidal zone	Radarsat	Unsupervised classification	Hughenoltz & Sanden (2001)
Canada, Manitoba	Bathymetric Mapping of Shallow Water	Radarsat	Time series - Mapping	Duguay et al. (2002)
Northern Japan	Discrimination of sea ice thickness	R-2, PALSAR	PolSAR - Analysis and modeling	Nakamura et al. (2006)
Polar Regions	Review and case studies	ERS, Radarsat, PALSAR, TSX	n/a	Kaeab (2008)
Northern Canada	Discrimination of sea ice types and water	ENVISAT ASAR	PolSAR - Analysis and modeling	Geldsetzer & Yackel (2009)
Canada, Quebec	Monitoring of permafrost dynamics	TSX	InSAR - Interferogram	May et al. (2011)
Herschel Island	Monitoring of surface movements	TSX, R-2, ALOS PALSAR	InSAR - Subsidence	Brisco et al. (2009), Short et al. (2011)
Lena Delta	Characterization of melt onset and geomorphological units	R-2, TSX	PolSAR - Analysis	Sobiech et al. (2012)
Alaska	Characterization of post-drainage succession	TSX, Landsat	Time series - Analysis and correlation	Regmi et al. (2012)
Lena Delta	Classification of lake and river ice	R-2, TSX	PolSAR - Unsupervised classification	Sobiech & Dierking (2013)
Mackenzie Delta Region	Classification of water bodies and shoreline	Landsat, R-2	PolSAR - Supervised classification	Chenier & Hemmingway (2014)
Richards Island	Classification of tundra land cover	Landsat, TSX, R-2	PolSAR- Unsupervised and supervised classification	Ullmann et al. (2014)
Baffin Island	Monitoring of surface movements	R-2	InSAR - Subsidence	Short et al. (2014)
Northern Canada	Modeling of Phytomass	R-2, GeoEye	PolSAR- Classification and modeling	Collingwood et al. (2014)
Mackenzie Delta Region	Classification of tundra land cover and shoreline types	R-2	PolSAR - Supervised classification	Banks et al. (2011, 2014)

since this effect has a well-known nature and its reduction is a necessity. Overviews on existing filtering concepts are provided by Dong et al. (2000), Touzi et al. (2004). More recent concepts were shown by Esch et al. (2011) or Schmitt & Wessel (2010), for example. The work of Buades et al. (2005) showed a new promising way to reduce speckle effect very efficiently. The approach is based on the so called Non-Local Means filtering of the image. The main idea is the usage of redundant patches that are present in an image. These patches have a similar gray value arrangement and distribution and are used for the filtering by weighted averaging. This approach is highly efficient and its above-average performance was also shown for SAR and PolSAR imagery, for example, by Deledalle et al. (2010), Parrilli et al. (2010), Torres & Frery (2013), Deledalle et al. (2015). The speckle filtering of PolSAR data has high importance for accurate land cover classification as noted by Lee, Grunes & De-Grandi (1999), Moon-Kyung et al. (2010).

The analysis of PolSAR data was shown previously to be a suited method for land cover characterization - e.g. to estimate biomass (Rignot et al. (1994)) - or for the land cover classification of various ecosystems and anthropogenic disturbed landscapes, such as urban areas (Salehi et al. (2014)) or agricultural regions (Lingli et al. (2014)). The data of SAR sensors were applied for tasks in the Arctic Environment as well. The application of InSAR offers ways to measure the ground movement/subsidence that is related to the freezing and thawing of the active layer (Brisco et al. (2009), Short et al. (2014)), to detect solifluction processes (Rune-Lauknes et al. (2013)), or to quantify mass movements, e.g. caused by coastal erosion slumps (Short et al. (2011)). The InSAR techniques are suited to generate DEMs of the earth surface. The German TSX and TDX satellites performed global InSAR measurements and provide unprecedented elevation information on the entire Arctic landmass. Further, the single polarimetric SAR data were used for the characterization of Arctic landscapes, e.g. shown by Regmi et al. (2012). This study used TSX imagery for the characterization of post-drainage succession in thermokarst lake basins. Park et al. (2010) showed the usage of backscatter characteristics of ASAR data for mapping of freeze and thaw cycles. Radar data were frequently applied for the characterization of snow and ice (e.g. Scheuchl et al. (2002), Sanden et al. (2009), Sobiech & Dierking (2013)) and glacial processes (Rignot et al. (2011)). Also, the data were applied to map the bathymetry of shallow lakes in thermokarst environment, e.g. by Jeffries et al. (1996), Kozlenko & Jeffries (2000), Duguay et al. (2002).

In contrast, few research projects have used PolSAR data for area-wide land cover characterization and classification of tundra environments. Collingwood et al. (2014) showed the usage of quad-polarized R-2 data for the modeling of above-ground phytomass for high Arctic environment. The findings indicated that the data were sensitive for specific cover types of the area of investigation. The PolSAR data of TSX and R-2 were applied to detect snowmelt events in the Lena Delta (Russia) and were identified as meaningful for the delineation of geomorphological units (Sobiech et al. (2012)). The quad-polarized R-2 imagery was shown to be suitable for land cover and shoreline classification of Arctic coastal regions of the southern Beaufort Sea (e.g. Banks et al. (2011), Demers et al. (2013), Banks et al. (2014)). The classification was carried out by supervised Maximum Likelihood classification. The previous work of Ullmann et al. (2014) showed that PolSAR data of quad-polarized R-2 and dual-polarized TSX advance the determination of bare ground and wetland classes and to map the shrub lands based on the physical structure rather than on the spectral information. The applied approaches include unsupervised and supervised Maximum Likelihood classification techniques that were shown to be suited algorithms for the

## 1 Introduction, State of the Art and Objectives

classification of PolSAR data. Table 1.2 provides an overview of selected SAR remote sensing methods for land surface characterization and classification of Arctic Environments.

As summary of this review it was found that further analysis of PolSAR data in land cover classification of Arctic environment is needed. The current SAR systems provide area-wide PolSAR data and it is likely that these data give complementary information on the Arctic land cover and help to come to more accurate classifications. It is further of interest to investigate which frequency and which polarization is best suited for the characterization and classification. Further research is also needed for the application of the Non-Local Means filtering technique. It is likely that this kind of filtering will have positive influence on the signal interpretation and the classification.

### 1.2.4 Digital Elevation Model Data

An important application of remote sensing data is the generation of area-wide DEM. Remotely sensed elevation data are commonly generated via a photogrammetric approach or via SAR interferometry. The application of Light Detection and Ranging Technique (LIDAR) is another a way to generate DEMs. The LIDAR systems are usually operated by aircraft and the coverage is therefore limited. The accurate elevation information assists, for instance, the processing of other remote sensing data. For example, the DEMs are important for orthorectification and geocoding of other remote sensing imagery or for interferometric applications. Further, the DEMs can be used for the characterization and classification of the land surface. The elevation information and its deviates are used for topographic, morphometric or hydrographic modeling and therefore provide information on the surface morphology. DEMs offer the possibility to characterize the landforms and to indicate active dynamics. DEMs are of importance to characterize any process that depends on the topography. Further information and general considerations about the usage of DEM in terrain analysis are provided by Wilson & Gallant (2000) and Hengl & Reuter (2009).

The availability of accurate high resolution digital terrain models derived from remote sensing imagery gives “[...] *a new basis for geomorphological work*” (Evans (2012), p. 94). Chorley et al. (1964) noted that such data will allow the extensive sampling of the earth surface morphology and that this information will support and accelerate the mapping of geomorphological properties. In this context, the geomorphology aims to understand the “[...] *Earth surface processes, geochronology, natural resources, natural hazards and landscape evolution* [...]” (Bishop et al. (2012), p. 5) and is therefore of high importance - taking into account the recent changes and dynamics of the environmental systems. The mapping of physiographical and geomorphological properties has a wide range of applications but its manual creation is expensive and time consuming (Stepinski & Bagaria (2009)). It is of interest to develop automatic mapping techniques that facilitate the creation of geomorphological maps (Stepinski & Bagaria (2009)) and to come “[...] *to automated recognition and delimitation of landforms and elementary forms from DEM* [...]” (Evans (2012), p. 104).

The classification of the earth’s surface into geomorphological forms using remote sensing imagery is therefore a recent field of the physical geographic research. However, the classes that describe the forms of the earth’s surface are difficult to define and differ in the recently presented works. The classification framework “[...] *suffers from a lack of standards*”. (Stepinski & Bagaria (2009), p.94). But the definition of

Table 1.3: Overview of selected DEM remote sensing methods for land surface characterization of Arctic Environments

Study Area	Task	Data	Method	Reference
Alaska	Classification of hydrography	DEM	Hydrographic modeling	Nolan & Prokein (2003)
Lena - Anabar, Russia	Classification of thermokarst-affected terrain types	Landsat and DEM	Supervised Maximum Likelihood and decision tree	Grosse et al. (2006)
Polar Regions	Review and case studies	DEM	n/a	Kaeab (2008)
Alaska	Relation between land cover and hydrographic and topographic features	Optical, DEM	Unsupervised classification, hydrographic modeling	Naito & Cairns (2011)
Arctic	Arctic research	DEM ASTER	n/a	Rees (2012)
Alaska	Characterization of Pingo distribution and morphometry	Interferometric DEM (InSAR)	Mapping and analysis	Jones et al. (2012)
Northern Canada	Classification of land cover and shoreline types	DEM, R-2, SPOT	Object-based decision tree	Demers et al. (2013)
Lena Delta	Characterization of morphometry and thermo-erosional features	DEM (Stereo), GeoEye, ALOS PRISM, RapidEye	Hydrographic modeling,	Stettner et al. (2014)
Northern Canada	Classification of land cover types	LIDAR	Decision tree	Chasmer et al. (2014)

landform classes is necessary to choose suited features and classification techniques for the classification problem. From a geomorphological point of view the geomorphological mapping (which is a classification) “[...] involves the partitioning of the terrain into conceptual spatial units/entities based upon criteria that include morphology (form), genetics (process), composition and structure, chronology, environmental system associations (land cover, soils, ecology), as well as spatial topological relationships of surface features (landforms).” (Bishop et al. (2012), p.5). This definition makes clear that DEMs can assist the geomorphological mapping, but its information is insufficient to characterize of all of the above named criteria. Along with this, the full automation of such mapping - the “Holy Grail” (Chorley et al. (1964), Evans (2012)) - is very complex, since the delineation of the geomorphological units requires expert knowledge and the interpretation of spatial-temporal interconnections.

For this reasons the analysis of DEMs focuses on the characterization and the classification of the geomorphometry (Hengl & Reuter (2009)). In a narrow sense the analysis of landforms in geomorphometry is independent from the analysis of the processes that have formed the observed landforms. Evans (2012), p.95 notes that “[...] landforms are bounded segments of a land surface and may be discontinuous [...]. Specific geomorphometry analyzes the geometric and topological characteristics of landforms.” Evans (2012) provides a comprehensive overview on these considerations and on the question how one can define a landform. The classes of a geomorphometric map - respectively of a landform classification - can

## *1 Introduction, State of the Art and Objectives*

be described by metric features which numerical quantify the form of the surface. Furthermore, the classes have closed boundaries and distinct shape (Evans (2012)). The pixels of an image can, for example, be grouped into one class if they share similar morphometric characteristics. The morphometric features - which are derivatives of the DEM - are used to quantify the similarity between elements of the image. For this work the term “landform” is used to describe groups of elements that share similar morphometric properties. Such landforms have to be interpreted with respect to the spatial resolution of the DEM and the interpretation therefore is scale-dependent. Along with this, the general problem of selecting suited scales arises. This problem has been discussed, for example, by Bishop et al. (2012), Evans (2012).

Examples and case studies that deal with the classification of the surface morphology by means of morphometric features are provided in the following: In the late 1990s Irvin et al. (1997) showed the usage of unsupervised fuzzy and ISODATA classification for the determination of landform units, such as ridges, shoulders and different hill slope positions. The approach was based on the classification of the morphometric features elevation, slope, profile and tangent curvatures and topographic wetness index. Irvin et al. (1997) found that the applied techniques were suited to pick up significant landform elements such as terraces, valleys, hill slopes and summits. The authors noted that the unsupervised classification techniques provided summary information and gave a quick overview on the landform ensemble. Still expert knowledge and experience on the morphology of the area of investigation was needed in order to come to a reasonable interpretation of the unsupervised classes. Burrough et al. (2000) applied a fuzzy approach which was the unsupervised fuzzy k-means classification. The features elevation, slope, curvature and topographic wetness index were used for the classification. Burrough et al. (2000) found that the technique was suited to create spatially coherent landform classes. Further, MacMillan et al. (2000) used fuzzy logic and an unsupervised approach for the classification of defined landform facets.

More frequently used approaches were designed by Weiss (2001) and Iwahashi & Pike (2007). These unsupervised approaches are pixel-based and use threshold divided morphometric features for the classification of generalized landforms - such as ridges, summits, different hill slope positions or valleys. The advantage of these classifiers is the fast computation and the comparable uncomplex interpretation. Further, advanced classifications that use morphometric features were developed by Bolongaro-Crevenna et al. (2005), Prima et al. (2006), Ehsani & Quiel (2008), Saadat et al. (2008). All of these studies highlighted the suitability of DEM and of morphometric features for mapping of generalized landform features. The findings of these studies make clear that expert knowledge and common sense is required for the interpretation. Still, the geomorphological analysis of DEM offers ways to come to a quantitative description of the land surface morphology.

Since landforms can be considered as bounded segments with distinct shape, some approaches try to identify the shape of the landforms prior to the classification by image segmentation techniques. Such investigations were done by Dragut & Blaschke (2006), Dragut & Eisank (2011), Dragut et al. (2011), Dragut & Eisank (2012), Verhagen & Dragut (2012). The segmentation of the landforms offers the opportunity to incorporate the shape and position of the object in the classification process. This advances the classification of any form that has a characteristic and distinct shape. The segmentation process is complex, requires expert knowledge and is dependent on scale and used data. It is therefore difficult to define standards and to design an object-based landform classification framework that has a high transferability.

The characterization of the land surface morphology by means of remote sensing data is especially important for the Arctic environment. As noted by Tinkler (1985) in the mid of the 1980s the vast scale and inaccessibility of the Arctic requires “[...] *at least a decade of accumulated inquiry* [...]” (Tinkler (1985), p. 193). The geomorphology studies of the Arctic therefore relied on the interpretation of airborne remote sensing data. These investigations gave information on the elevation and topographic setting due to stereo imaging. Tinkler (1985) noted in this context: “[...] *In less-well mapped territory of enormous physical extent the practical use of air photographs was developed much earlier. In Canada the National Air Photography Library [...] was founded in 1925* [...]” (Tinkler (1985), p. 174). The vast extent of the Canadian Arctic further led to a change of mind: “[...] *the availability [of the air photographs] produced a revolution in geomorphological thinking in Canada, which marked a departure from the European tradition, with its emphasis on detailed studies of small areas.*” (Tinkler (1985), p.174).

Selected studies that deal with the characterization and classification of the Arctic land surface are listed in Table 3.1.3. Nolan & Prokein (2003) showed the evaluation of hydrological modeling and topographic analysis for the identification of lakes, pingos and river terraces. The analysis was carried out using medium resolution DEM data and the identification relied on hydrographic modeling and manual interpretation. Grosse et al. (2006) used optical and DEM data for the classification of terrain and land cover units in thermokarst environment. The approach was based on Supervised Maximum Likelihood and a decision tree classification. The morphometric information was used to classify units that were bounded to the topographic setting. Naito & Cairns (2011) related the recent shrub dynamics with topographic and hydrographic features and showed that shrubs expand preferentially in regions that have greater water accumulation potential. Jones et al. (2012) used DEM data for area-wide mapping of the pingo distribution on the Arctic Coastal Plain. Demers et al. (2013) noted the importance of DEM data for the classification of coastal low lands, e.g. of shoreline types that have relevance in case of oil disasters (Owens (2010)). Stettner et al. (2014) used DEM data for the characterization of thermo-erosional processes in the Lena Delta and the analysis was based on morphometric features. Chasmer et al. (2014) successfully applied high resolution DEM data to relate surface micro-morphology and meso-morphology with near surface ground conditions.

All of these studies used individual collected DEM data since no standard DEM is available for the entire Arctic. The landmass north than 60° Northern Latitude was not acquired during the SRTM mission. These data have emerged as standard for terrain and surface analysis but are not available for most parts of the Arctic landmass. With the ASTER GDEM (Rees (2012)) a pan-arctic elevation models exists, but it was shown to be of limited value due the varying quality and accuracy (Li, Shi, Li, Muller, Drummond, Li, Li, Li & Liu (2013)) - also for periglacial and glacial research (Nuth & Kääb (2011), Strozzini et al. (2012)). With the TDX Mission a DEM is now available that has a very high vertical and horizontal accuracy and a pan-arctic coverage. Such a high-quality DEM is especially important for mapping vast regions and it offers new perspectives on area-wide terrain analysis and periglacial research. The data of the TDX Mission are likely to become the standard for any application that deals with the area-wide characterization and classification of the land surface morphology, topography or hydrography.

The analysis and classification of the surface morphology was shown to be efficient for the classification of landforms and is capable to provide an initial division of the landscape based on topographic attributes and morphometric features. The interpretation of the classification maps requires expert knowledge and

in situ reference is of importance to improve the quality of the results. The shown studies highlighted that many different approaches exist and that there is a lack of standards in terrain and morphologically surface classification. Instead the strategy to classify the landforms was driven by the site specifics, by the data availability and individual preferences. It was further shown that the TDX Mission delivers high resolution information with high quality and it offers new perspectives on the digital terrain analysis of the Arctic landforms. The data are consistent, truly pan-arctic and of very high precision due to the interferometric generation of the DEM.

### **1.3 Objectives**

The objective of this research is to evaluate the potential of PolSAR X-, C- and L-Band data for land cover characterization and classification of generalized tundra land cover types that are meaningful indicators of the change of the northern high latitude ecosystem. The analysis concentrates on classes that are indicators of ecological sensitive regions and can be mapped area-wide for large parts of the Arctic - such as wetlands, or shrub lands. The analyses are performed with remote sensing data with high to medium spatial resolution (ten and thirty meter). Therefore the data provide a sufficient large coverage to be applicable for area-wide mapping. The study is conducted for selected sites of the Mackenzie Delta Region (Canada), northern Banks Island (Canada) and the east shore of the James Bay (Canada). The imagery used are polarized data of the satellites TSX, TDX, R-2 and ALOS PALSAR. For the assessment of the accuracy in situ collected land cover reference data are available. In addition, the application of DEMs for initial morphometric landform characterization and classification is evaluated. This part of the study concentrates on the usage of the intermediate digital elevation model of the TanDEM-X Mission (TDX IDEM). The major objectives of this study are grouped as follows with regard to the current state of the art of the related fields.

**(1) Evaluation of dual- and quad-polarized PolSAR data for characterization of tundra land cover** - The main goal of this study is to evaluate how dual- and quad-polarized PolSAR features of the X-, C- and L-Band can be used to characterize generalized land cover types of tundra environment. The aim is to identify the potential of different frequencies and polarization modes for the characterization of land surface properties. In addition, it is a aim of this study to evaluate recent advances in SAR data processing - such as the polarimetric decomposition of co-polarized data and the Non-Local Means speckle filtering. It is assumed that PolSAR data facilitate the characterization of tundra land cover types based on the analysis of physical structure and polarimetric characteristic and that PolSAR data provide complementary (synergistic) information to multispectral reflectance properties. For this reason a comparison of PolSAR and multispectral data is of interest in order to evaluate the potential and differences.

**(2) Potential of dual- and quad-polarized PolSAR for supervised and unsupervised classification of tundra land cover** - The second aim of this work is to investigate the potential of X-, C- and L-Band PolSAR data and optical data in unsupervised and supervised land cover classification. The focus lies on the application of unsupervised classification techniques, since in situ reference information on the Arctic land cover are usually sparse due to the limited accessibility. Therefore the circumference of the Arctic makes an automated system desirable. To achieve this objective it is necessary to recapitulate the actual unsupervised classification techniques of PolSAR data and to adapt them so that they can be operated with



dual-polarized SAR data and/or multispectral data in the same way. An unified classification approach will allow to use the classification results in a comparative study (benchmark analysis) and to identify the benefits and limitations of different frequencies and polarization modes for their suitability in land cover classification. The successful and precise classification of meaningful land cover types is of value to accurately map the present state of ecological sensitive regions and to be able to consistently monitor the Arctic land surface properties.

**(3) Potential of high resolution DEM for characterization of the surface morphology** - The third objective of this work is to initially evaluate the potential of TDX IDEM data for the characterization of the surface morphology. The aim is to identify topographic attributes that have a high relevance for environmental processes - like the elevation, slope or relative topographic position - and that have an area-wide application. The assessment will be carried out on selected sites with known characteristics and specifics since the evaluation of the surface morphology is difficult with regard to missing standards.

**(4) Potential of high resolution DEM for classification of the surface morphology and generalized landforms** - It is finally an objective to use topographic attributes for an initial classification of the surface morphology, respectively, of landforms. This task makes the recapitulation of established classification techniques necessary, as well as considerations about the classification framework and about topographic attributes that are suited for the classification of landforms.

A fulfillment of these objects will contribute on the recent exploration of SAR and PolSAR data for the characterization and classification of the Arctic land surface. The comparison of different frequencies and polarization modes is a research need with view on the current state of art. The inclusion of new approaches in PolSAR data processing - such as the Non-Local Means speckle filtering and the analysis of co-polarized data - involves recent advances and research findings in this study. It is further a contribution to the current research on terrain analysis to evaluate and explore the applicability of the TDX IDEM for landform characterization and classification.

## 1.4 Outline

The work is structured in six major parts which are the Introduction and the State of the Art (Part 1, p. 1 ff.), the description of the Test Sites and Database (Part 2, p. 21 ff.), the used Methodology (Part 3, p. 55 ff.), the Results (Part 4, p. 107 ff.), the Interpretation and Discussion (Part 5, p. 239 ff.) and the Conclusions and Outlook (Part 6, p. 251 ff.). The second part of this work shows the data base and the setting that was available to conduct the study. The physical geographic, geologic and climatic situation is shown for the test sites of the Mackenzie Delta, Banks Island and James Bay. It is followed by a description of the collected remote sensing data. These were on the one hand passive multispectral data of the Landsat satellite and optical airborne data and on the other hand space borne quad- and dual-polarized X-, C- and L-Band PolSAR data of the satellites TSX, TDX, R-2 and ALOS PalSAR. The section shows how the land cover of the test sites of the Mackenzie Delta and Banks Island was grouped in generalized land cover categories and how the classes of interest were defined. The section further shows how the in situ ground truth data were collected and processed to be of value for the assessment of the land cover classification accuracy.

## *1 Introduction, State of the Art and Objectives*

The third part shows the methodology that was used in order to characterize and classify the land cover and landforms. In the first section the properties, advances and limitations of SAR and PolSAR data are shown. The concepts of polarimetry and of polarimetric decomposition are summarized and recent advances - such as the usage of Kennaugh Matrix or the Power Decomposition of co-polarized data - are shown. The section gives information on the filtering of PolSAR data since the speckle effect has great impact on the interpretability of the signal and its suitability for classification. In this context, the definition of a fast and robust Non-Local Means filter is shown. This section is followed by a brief description of multispectral data and the definition of frequently used features and indices. Afterward the properties of DEM data are shown and discussed and the derivation of topographic features for the characterization of the land surface is shown. The second section of this part concentrates on the classification of multispectral, radar and DEM data. The supervised classification that was used in this work is presented, followed by the definition of the unsupervised classification techniques. The sections shows the definition of a parametric unsupervised classification approach that is capable to handle optical and dual- and quad-polarized PolSAR data in the same way. This section is followed by a description of the cross-validation technique that was used to assess the accuracy of the supervised and unsupervised land cover classifications. The third section of this part shows how threshold divided topographic features can be used to classify morphometric landforms. The two frequently used approaches of Nested-Means and Topographic Position Index based landform classification are shown. In addition, a new classifier that operates in a similar way is defined. This classifier uses the elevation, slope and the Topographic Position Index to classify landforms of interest. It is operated either discrete detecting a manageable number of classes, or quasi continuous providing an unsupervised classification that supports the manual mapping.

The fourth part presents the results. The evaluation of the developed techniques of Non-Local Means filtering, co-polarized decomposition and unsupervised classification are shown in the beginning. The quality of the filter is evaluated by the visual analysis of exemplary images and by comparing the developed filter to established techniques. The properties of the Non-Local Means filter are quantified by the usage of speckle evaluation indices which allow comparing filters without manual interaction. The differences in co- and quad-polarized Power Decomposition are then quantified by the interpretation of scatterplots and by correlation analysis. Finally, the developed unsupervised classification technique is compared to established unsupervised techniques via a receiver operator characteristic. The next section shows the characteristics of quad- and dual-polarized X-, C- and L-Band data for generalized tundra land cover types of the Mackenzie Delta Region and northern Banks Island. Along with this the reflectance signatures of multispectral data are shown for the land cover types. In the following the basic topographic features and a stack of multi-scale Topographic Position Indices are shown and discussed with respect to the surficial geology and morphometry. This evaluation is done for two sites in the Mackenzie Delta, for Banks Island and for the James Bay. The assessment is based on visual analysis and interpretation. The third major section of this part shows results of the land cover and landform classification. The first part provides the results of the water classification. The benefits and limitations of the chosen water classification approach are shown and quantified. In the following the supervised and unsupervised land cover classifications are shown and evaluated. The accuracy of each test site is assessed via a cross validation using in situ collected land cover reference data. The classification results of multispectral data, radar data and combined radar and optical data are compared and analyzed. Finally, the landform classifications of four selected test sites

are shown and evaluated in context of the site's surface morphology.

The results and main findings of this study are then interpreted and discussed in the following part. This includes a discussion of the methodological concepts, the land surface characterization and classification. The last part summarizes the study and draws conclusions. Finally, an outlook on future perspectives is provided.



---

## Test Sites and Database

### 2.1 Test Sites

The following sections provide an overview on the selection of the test sites and a description of individual sites specifics. The areas of interest were selected sites of the Mackenzie Delta Region (Northwest Territories, Canada), northern Banks Island (Northwest Territories, Canada) and of the James Bay (Quebec, Canada). The main physio-geographic, geologic, climatic and ecologic attributes of each site are presented. The primary test site is the Mackenzie Delta Region and the environmental setting is therefore described in more detail.

#### 2.1.1 Site Selection and Overview

The named sites were selected to achieve a wide spectrum of land coverage types and morphological settings. All sites have in common that they are dominated by periglacial processes and the presence of near surface permafrost. In addition, all sites show the presence of the land cover types that are meaningful indicators of the change of the northern high-latitude ecosystem, e.g. wetland and shrub lands. Figure 2.1 shows the location of the sites, the treeline and the permafrost zonation index of Gruber (2012). Banks Island lies north of the treeline and is part of the continuous permafrost zone and of the High Arctic ecozone (ESWG (1996)). The Mackenzie Delta Region shows a high zonation index and is located close to the treeline. The site therefore shows the transition between the Taiga Plains and the Southern Arctic Tundra ecozone. The ground thermal regime can be considered to be part of the continuous permafrost zone - but discontinuous or even absence of permafrost can be observed due to the complex structure of the delta and the heat exchange between the numerous water bodies and the surrounding. The test site James Bay lies south of the treeline and is part of the Taiga Shield ecozone and of the Sub-Arctic. Permafrost exists and its nature is discontinuous to sporadic - which is also indicated by a low zonation index. Figure 2.2 shows the climate normals of stations that are close to the named test sites. The normals indicate distinct seasonal climates with temperature and precipitation peaks in summer and extreme cold and dry conditions in winter.

## 2 Test Sites and Database

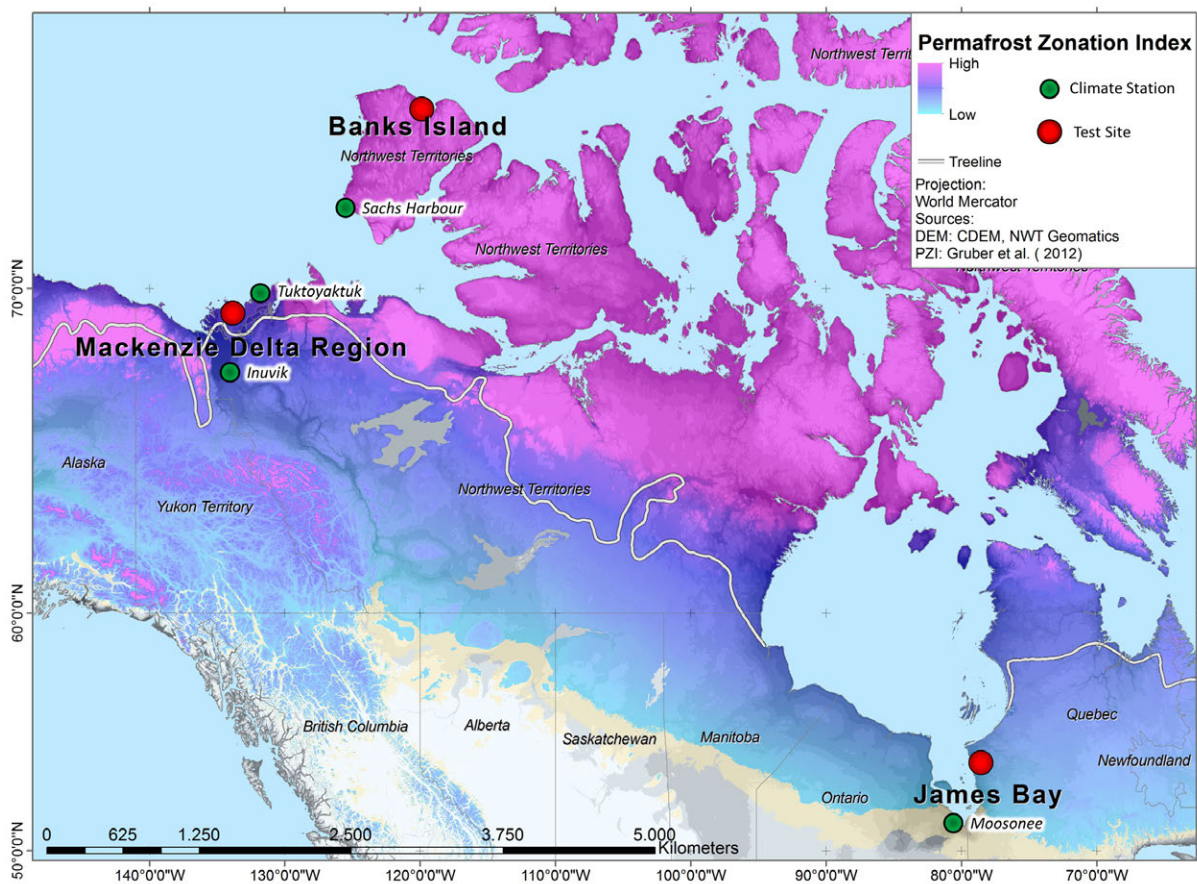


Figure 2.1: Map of permafrost zonation index and location of the selected test sites Banks Island (Northwest Territories, Canada), Mackenzie Delta Region (Northwest Territories, Canada) and James Bay (Québec, Canada). Source: Own figure, on the basis of Gruber (2012), Amante & Eakins (2009).

### 2.1.2 Mackenzie Delta Region

**Geography and Location** - The Mackenzie Delta Region is located close to the northwestern border of the Northwest Territories, Canada, at about 69° Northern Latitude and 133° Western Longitude. The region is part of the Arctic and Sub-Arctic ecosystem and the treeline separates the area in a northern and a southern part. The delta area is more than 200 km long and more than 50 km wide. It is bounded by the Richardson Mountains in the west and the uplands of Richards Island, Tuktoyaktuk Peninsula, Caribou Hills and the Anderson plain in the east (Figure 2.3) (Burn & Kokelj (2009), p. 84). The Mackenzie River system is the largest in Canada and drains most parts of the Canadian inland east of the Rocky Mountains. With a length of more than 1500 km and a watershed area of more than  $1.8 \times 10^6$  km<sup>2</sup> it is one of the largest rivers in the world (Burn & Kokelj (2009), p. 84). The river discharges in the Beaufort Sea (Arctic Ocean) and has built a delta complex at its estuary since the end of the last glaciation. This complex forms the second largest of the Arctic deltas (Burn & Kokelj (2009), p. 87).

**Geology** - The Mackenzie Delta Region is part of the Beaufort-Mackenzie Delta Basin, part of the northern Beaufort Continental Shelf and bounded to the north by the Arctic Ocean. The basin is comprised of

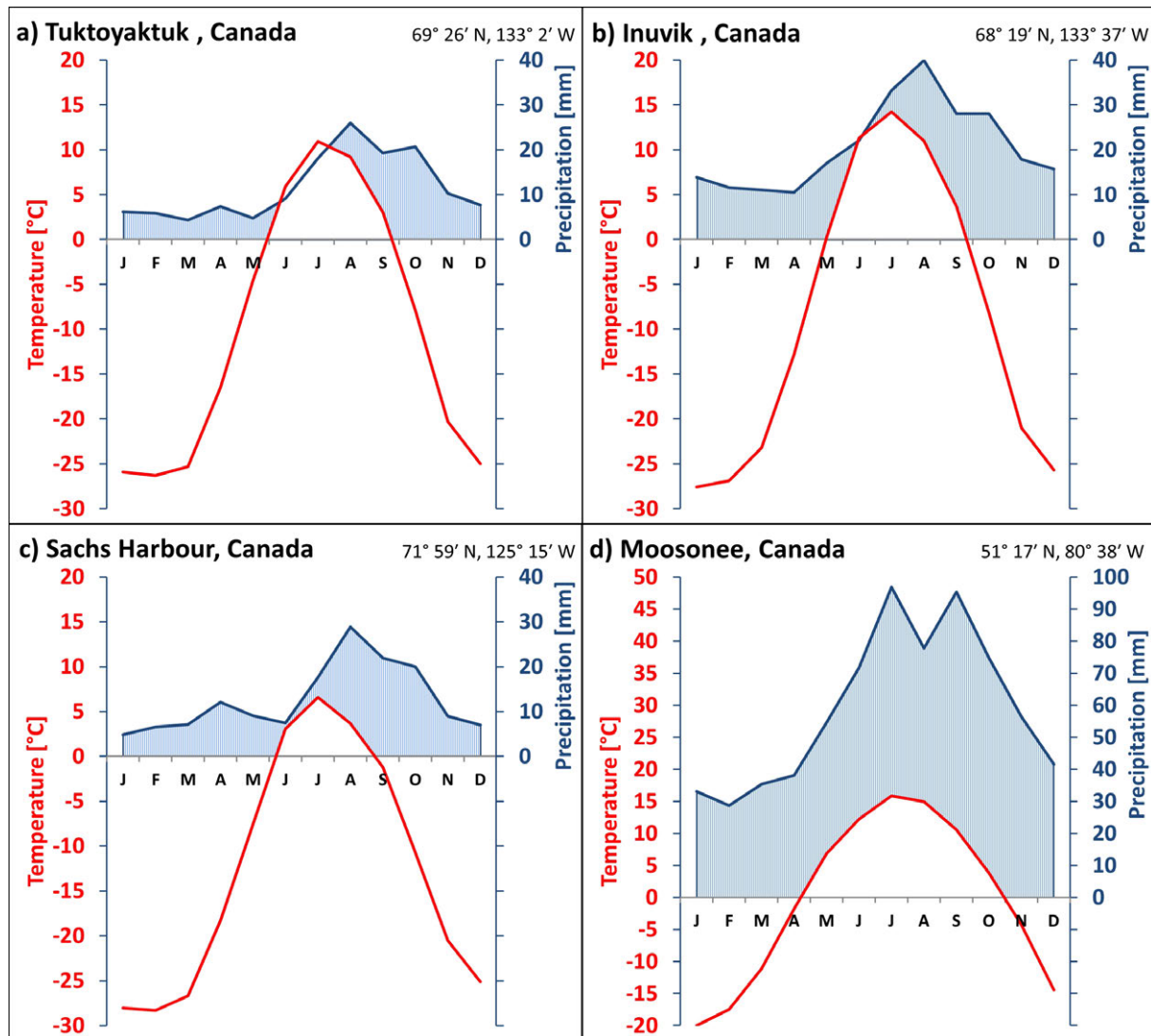


Figure 2.2: Climate normals of selected Arctic stations: a) Tuktoyaktuk, Mackenzie Delta Region, Canada, b) Inuvik, Mackenzie Delta Region, Canada, c) Sachs Harbour, Banks Island, Canada and d) Moosonee, Hudson Bay, Canada. The location of the stations is shown in Figure 2.1. Source: Own figure, on the basis of NWT-Geomatics (2014), Environment-Canada (2014), NOAA (2014).

sub-basins and structural units, e.g. the Yukon Coastal-Plain, the Richards Island Basin, the Tuktoyaktuk Peninsula, the Caribou Hills, the Eskimo Lakes Arch and the Beaufort Shelf. The faults that separate the units are trending northwards and northeastwards. The major faults of the system are the Kaltag-Rapid Fault and the Eskimo Lakes Fault Zone (Hill, Hequette, Ruz & Jenner (1991), p. 7-8) (Figure 2.4). The oldest basement of the area is a Precambrian folded formation of argillites and it is exposed near Inuvik. The estimated age is at about 1 Billion years (Mackay & Dyke (1990), p. 2-4). Hill, Hequette, Ruz & Jenner (1991), p. 7 note that “[t]he Beaufort-Mackenzie Delta Basin is filled with over 6 km of Upper Cretaceous, Tertiary and Quaternary sediments.” Today the Cretaceous shales are exposed south of Remnant Hill and Campbell Lake. The Campbell Lake itself is bedded in Devonian and older limestone formations (Mackay & Dyke (1990), p. 8). Most sediments of the basin are of deltaic or marine genesis.

## 2 Test Sites and Database

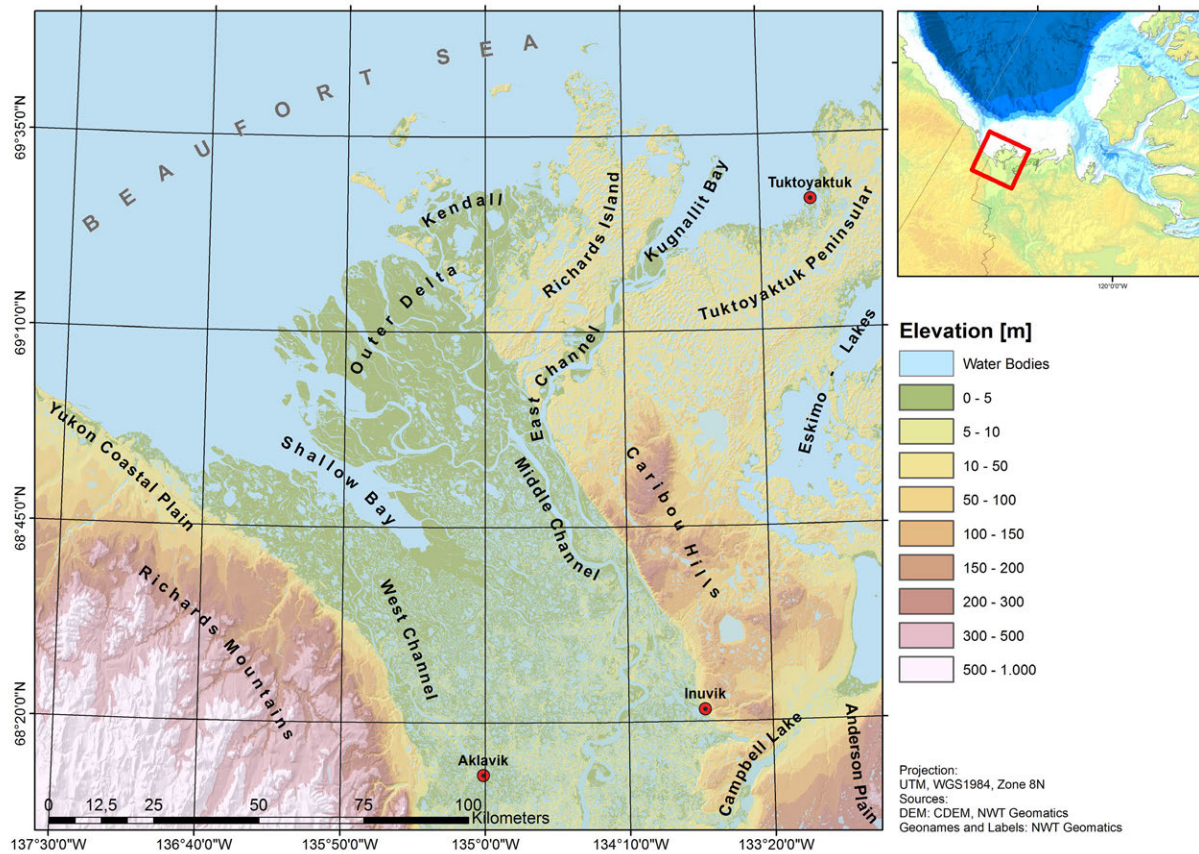


Figure 2.3: Geographic overview of the Mackenzie Delta Region, Northwest Territories, Canada. Source: Own figure, on the basis of NWT-Geomatics (2014), DLR (2013).

They are layered in more than ten sequences (Hill, Hequette, Ruz & Jenner (1991), p. 7). The maximum thickness of the basin sediments is at the offshore shelf break in the north of the delta. There is a rapid decrease of the sediment thickness towards the margins of the Beaufort-Mackenzie Delta Basin - the limit of the former sedimentary basin (Hill, Hequette, Ruz & Jenner (1991), p. 10).

Most of the bedrock is covered by glacial deposits of Quaternary age. The surficial geology shows that most parts of Richards Island, the central part of the Tuktoyaktuk Peninsula, the uplands of the Caribou Hills, the Anderson plain and the Yukon coastal plain are covered by Peistocene sediments. These are mainly of Late and Early Wisconsinan age (Hill, Hequette, Ruz & Jenner (1991), p. 10-13). The genesis of these sediments is associated with the Buckland Glaciation which “[...] represents the maximum all-time limit of the Laurentide ice in the region [...]” (Hill, Hequette, Ruz & Jenner (1991), p. 10). The age of the Buckland Glaciation is Early Wisconsinan (at about 50-100 ka BP) and the last glacial maximum during the Pleistocene was about 30 ka BP. Burn & Kokelj (2009) note that “[...] portions of the outer delta and Richards Island were ice-free throughout much of the [last] glaciation.” (Burn & Kokelj (2009), p. 87). The glacial and glacial-fluvial sediments are visible in form of rolling morainic hills, ridges and kame terraces. Their morphology was modified by active erosion and periglacial processes (Hill, Hequette, Ruz & Jenner (1991), p. 10).

The surficial geology of the delta itself and of the northern and southern part of the Tuktoyaktuk Peninsula



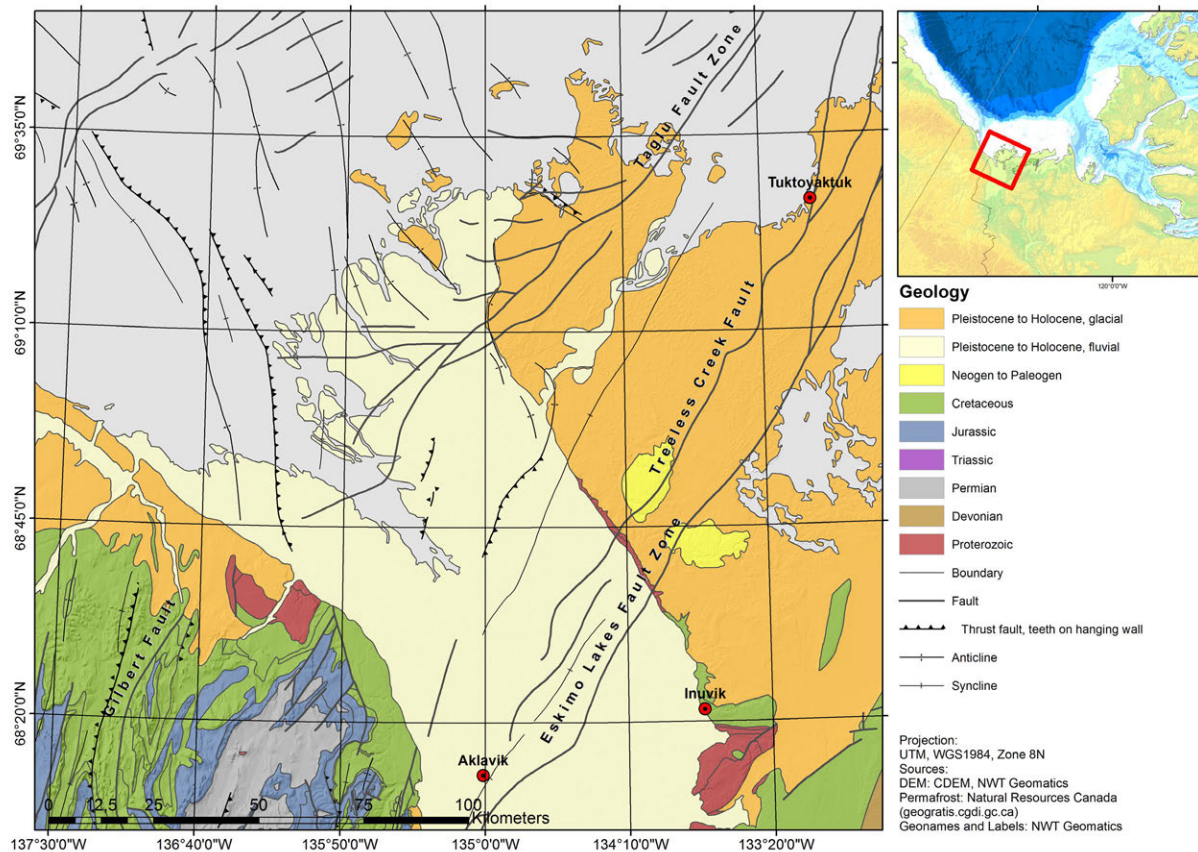


Figure 2.4: Geological overview of the Mackenzie Delta Region, Northwest Territories, Canada. Source: Own figure, on the basis of NWT-Geomatics (2014).

is of Holocene age. The river discharge and the sedimentation of channels of Mackenzie River has formed the present delta complex during the post-glacial and the genesis of the delta started approximately 14 ka BP (Burn & Kokelj (2009), p. 87). The north of the Tukttoyaktuk Peninsula has been formed by aeolian transport and sedimentation. The surficial layers south of the Peninsula were formed by lacustrine deposits (Hill, Hequette, Ruz & Jenner (1991), p. 11). The sea level has risen and an inundation of large parts of the outer delta took place due to the deglaciation in the Holocene. The relative sea level (RSL) shows a rise of at about 70 m in the last 14 ka - taking into account the rate of the isostatic uplift. The discussion on the actual process and the development of the RSL is still ongoing (Hill, Hequette, Ruz & Jenner (1991), p. 60 & 67). In this context Burn & Kokelj (2009), p. 87 name a coastal retreat of the delta shoreline of about 100 km since the begin of the Holocene. Burn & Kokelj (2009) name “[...] *four principal depositional histories for terrestrial sites in the area*” (Burn & Kokelj (2009), p. 87): (1) Areas of the upland terrain that were not affected by the Holocene inundation and therefore show glacial deposits that were developed by geomorphological processes. The composition of that near surface sediments is dominated by sand or till. (2) Areas of the outer delta that were inundated but have emerged as land due to the sedimentation during the Holocene. (3) Most parts of today’s delta that evolved above the sea level. (4) Thermokarst basins of the uplands. The sediments of this regions show lacustrine genesis and are typically covered with organic matter or peat.

## 2 Test Sites and Database

**Climatic situation** - The Mackenzie Delta Region is part of the Arctic and Sub-Arctic ecosystem and the region shows a strong seasonality and distinct summer and winter conditions. The transition time in spring and autumn is relatively short. The summers are short and cool, the winters long and cold. The absolute amount of precipitation is very low at any time of the year and shows a single peak in summer. The precipitation events are typically associated with polar low pressure systems. During the climatic unstable time of the year storms and thunderstorms appear. The storms can have an average wind speed of up to 80 km/h and blow mainly from northwestern direction (Hill, Hequette, Ruz & Jenner (1991), p. 18). The mean annual air temperatures measured at the climate stations of Inuvik and Tuktoyaktuk are between -9 °C and -1 °C (1971-2000). The precipitation varies between 140 mm and 250 mm (Burn & Kokelj (2009), p. 88). The recorded minimum temperature of these stations were -56.7 °C and -50°C. The recorded maximum temperatures were 32.8 °C and 30.0 °C. About 40-60 % of the annual precipitation is in form of snow. The average snow depth in Inuvik is about 26 cm and about 15 cm in Tuktoyaktuk (Environment-Canada (2014), NOAA (2014)). Figure 2.2 shows the average monthly climate normals (1971 - 2000) for climate stations Tuktoyaktuk (Figure 2.2.a) and Inuvik (Figure 2.2.b). Following the effective climate classification of Köppen and Geiger the region may be classified as “Dfc” with a transition to “ET”. The region therefore shows a continental subarctic or boreal climate with a northward transition to Tundra Climate. The coastal regime of Mackenzie Delta Region is in average colder and drier than the upstream locations. In Inuvik the sun is constantly above the horizon for 54 days of a year. On 30 days the sun is constantly below the horizon. In Tuktoyaktuk the sun is above the horizon for 65 days and below the horizon for 46 days (Environment-Canada (2014), NOAA (2014)).

**Permafrost** - The Mackenzie Delta Region is part of the continuous permafrost zone. The ground temperatures are low and range between -10 °C and 0 °C (Allen et al. (1988), p. 3). Today's surface is underlied by ice-bearing permafrost (IBPF) that can have a thickness of several hundred meters - up to a maximum of about 700 m (Allen et al. (1988)). The surrounding sediments, the Mackenzie valley and the delta itself have lower IBPF thicknesses. These low thicknesses - respectively the absence of permafrost - are related to the warming of the numerous water bodies (Nguyen et al. (2009)). The regions of unfrozen ground are also observed at “[...] *newly deposited unconsolidated sediments, where the climate has just begun to impose its influence on the ground thermal regime [...]*” (Allen et al. (1988), p. 3). The estimated IBPF thickness of the region is shown in Figure 2.5. These data were collected by Natural Resource Canada in the 1970s. The measurements were conducted during intensive oil and gas exploration and drilling activities. Burn & Kokelj (2009), p. 94 note that the IBPF thickness may be categorized in four classes: (1) Areas that were unglaciated during the Buckland glacial (parts of Richards Island and the Tuktoyaktuk Peninsula). These show an IBPF thicknesses between 500 m and 700 m. (2) The uplands west and east of the Mackenzie delta that typically show thicknesses of 100 m to 400 m. (3) The delta itself that shows thicknesses of less than 100 m. (4) The outer delta areas that show a discontinuous distribution or even an absence of permafrost. According to Allen et al. (1988), p. 5 a fifth zone can be added: the offshore permafrost which “[...] *is best described as relic degrading permafrost since it exists in a state of disequilibrium with the sea-bottom. In fact, very little offshore permafrost is in equilibrium with negative sea-bottom temperatures.*” The offshore occurrence of permafrost is bounded to former land-fast sediments that today form the Beaufort Shelf. The thicknesses of such sediments are ranging between 0 m and 700 m (Allen et al. (1988), p. 4-5).

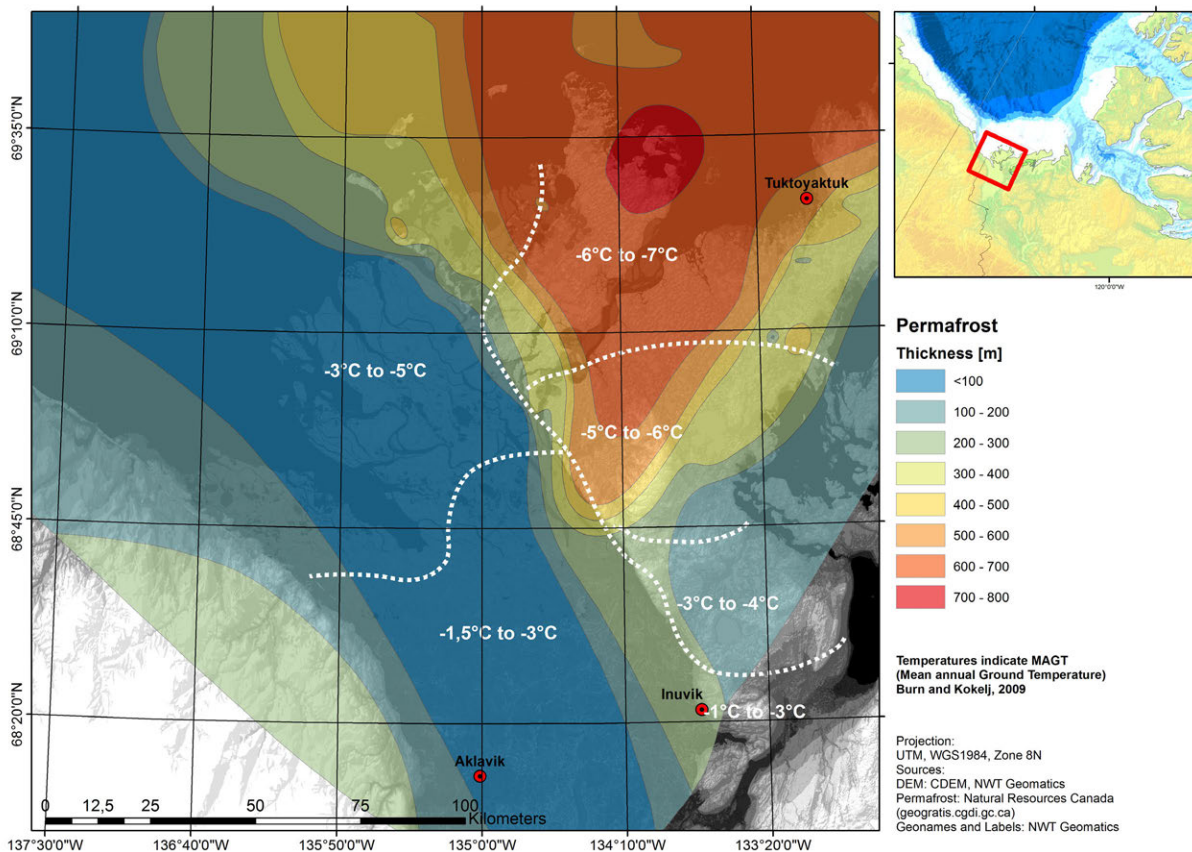


Figure 2.5: Permafrost setting of the Mackenzie Delta Region, Northwest Territories, Canada and estimated mean annual ground temperatures (MAGT). Source: Own figure, on the basis of NWT-Geomatics (2014), Burn & Kokelj (2009).

The distribution of the IBPF thicknesses in the Mackenzie Delta Region are mainly a result of two factors: (1) “[...] *The thermal properties of the subsurface lithologies*” and (2) the “[...] *complex long-term surface temperature history*” (Allen et al. (1988), p. 5). The glaciation of early Wisconsin (about 50-100 ka BP) was covering the entire area. In contrast, the Buckland Glaciation of Late Wisconsin did not cover the entire area - parts of Richards Island and of the Tuktoyaktuk Peninsula remained unglaciated during this event. The near surface temperatures at the base of the glacier were about 0 °C and the ice sheet of the Buckland was likely a wet-base glacier. The unglaciated areas showed a lower near surface temperature since these were not covered by the isolating ice sheet. This may explain the higher IBPF thicknesses of Richards Island and the Tuktoyaktuk Peninsula (Allen et al. (1988), p. 10 - 11). Furthermore, the IBPF thickness is correlating with the thickness of the so called Iperk Strata Sequence. This sequence is a sedimentary layer that evolved during the change from Pliocene to Pleistocene. The sediments of this unit are composed of sand and gravel and were formed by delta-plain deposits. According to Allen et al. (1988), p. 10 - 11 it is likely that the thermal conductivity of this sequence supported the formation of high IBPF thicknesses. The base of the Iperk Sequence shows its maximum on the land-fast regions of Richards Island, of the Tuktoyaktuk Peninsula and the western upland of the modern Mackenzie delta (Allen et al. (1988), p. 10).

## 2 Test Sites and Database

The permafrost environment of the Mackenzie Delta Region shows several types of ground ice. Burn & Kokelj (2009), p. 99 indicated five major types of ice in that region: (1) Pore ice which is observed in association with the sandy sediments of Richards Island and the Tuktoyaktuk Peninsula. (2) Massive tabular ice that developed by ice segregation and is locally present in Pingos. (3) Preserved basal glacier ice that is a residue of the glaciation. (4) Segregation ice that is typical for the upper meters of the near-surface permafrost. (5) Ice wedges. The segregation ice and the ice wedges are common in the entire Mackenzie Delta Region and the typical polygonal networks of the ice wedges are most distinct on drained permafrost lakes and massive ice complexes (Burn & Kokelj (2009), p. 99 - 100). The active layer of the Mackenzie Delta permafrost system shows typically thicknesses between 30 cm and 70 cm. The thickness of the active layer is decreasing with higher latitude. Burn & Kokelj (2009), p. 99 reported a thickness of 45 cm to 65 cm for locations near Inuvik and 35 cm to 55 cm for locations in the south Richards Island. The thickness is greater on dry locations compared to wet locations due to the thermal properties of the pore water in the sediment (Burn & Kokelj (2009), p. 99). The thickness of the active layer is a function of the actual climatic situation, of the surface coverage and of the topographic position (Burn & Zhang (2010), p. 1461). The atmospheric parameters that influence the active layer thickness are the air temperature and the amount and form of the precipitation (rain/snow) (Smith et al. 2001, p. 7). The report of Smith et al. (2001) exemplifies the response of the active layer on the near-surface temperature conditions in the Mackenzie Delta Region.

Permafrost is defined as ground that has a temperature below 0 °C during two consecutive years (Allen et al. (1988), p. 4). The estimated mean annual ground temperatures (MAGT) of the Mackenzie Delta Region are shown in Figure 2.5 and show the following characteristics: (1) The ground of the north of the modern delta and the low-lying coast-lands are colder than the delta areas south of the treeline. (2) The near-shore uplands are colder than the inland uplands east of the delta. The delta complex is warmer than the surrounding terrain. These data were carried out by borehole temperature logger data and were measured between 2003 and 2007 (Burn & Kokelj (2009), p. 98).

**Hydrology** - The Mackenzie River has a mean annual flow rate of about  $10000 \text{ m}^3/\text{s}$  and a sediment load in the order of  $125 \times 10^6 \text{ t}$  (Hill, Blasco, Harper & Fissel (1991), p. 821) to  $150 \times 10^6 \text{ t}$  (Harper (1990), p. 77). The Mackenzie flows in a broad single channel from the Great Slave Lake to Point Separation. On its way to the delta the main tributary is the Liard River. Once the Mackenzie reaches Separation Point the stream splits up in many meandering channels. Three main channels hold most of the flow from Separation Point to the Beaufort Sea. These are from west to east: the West Channel (Aklavik Channel), the Middle Channel and the East Channel. The Middle Channel and the East Channel reunion at the southern end of Richards Island until the streams split up again. The East Channel separates Richards Island from the mainland and the Tuktoyaktuk Peninsula. It is discharging in the Kugmallit Bay (Hill, Hequette, Ruz & Jenner (1991), p. 18 & 23).

From November to April the annual discharge hydrograph of the Mackenzie shows relative constant base flow that is high compared to other Arctic rivers. The discharge increases rapidly in May with the start of the snow-melt in the southern regions of the watershed. It typically shows a peak at the beginning of June. The summer months between July and October are characterized by a high and constant discharge with sporadic peaks that depend on rainfall events (Hill, Hequette, Ruz & Jenner (1991), p. 14- 23). From late October to the beginning of May the Mackenzie River is frozen and the river is covered by ice. Along

with the increasing discharge in late spring, the ice of the river is lifted and the break-up begins (Hill, Hequette, Ruz & Jenner (1991), p. 24). Large areas of the delta are then flooded due to the break-up and the rapidly increasing discharge. The ice breaking can happen within a few days if ice jams are ponding the discharge (Burn & Kokelj (2009), p. 91). Further, storm events and surges can cause local flooding of the outer delta area when the water level of the Mackenzie is low in late summer (Burn & Kokelj (2009), p. 91). The hydrology is characterized by numerous lakes in the delta. The lakes are caused by thawing of underlying permafrost and by flooding of sedges. In summer the color of a lake indicates whether a lake is connected to the actual stream or not. Brown and turbid water indicates a connection to the actual flow. Clear water indicates that the lake is disconnected from the actual river system. Like the Mackenzie itself the lakes are frozen during the winter. The ice may be bottomfast - depending on the bathymetry, geology and local permafrost conditions (Burn & Kokelj (2009), p. 91-92).

**Maritime Environment and Oceanography** - The tidal range of the southern Beaufort Sea is between 0.3 m and 0.5 m during neap and spring tides. The near-shore bathymetry north of the Mackenzie Delta shows depths of less than 100 m - up to an off-shore distance of about 100 km (presumptively the former pre-holocene coastline). This shelf region is mainly formed by land-fast sediments. Ice-free conditions are typically for the summer months from July to October. During the rest of the year the sea is usually frozen. The ice of the Beaufort Sea is characterized by first-year ice, multi-year ice and ice fragments. Three major ice systems are usually present: (1) The Polar Pack Ice of the high latitudes that reaches the shelf break of the Beaufort-Mackenzie Delta Basin in winter. (2) The land-fast ice zone that develops as first-year ice along the northern coast. (3) The active shear and transition zone that lies between the Pack Ice and the land-fast ice. The moving grounding ice can erode the coast in across- and alongshore direction (Hill, Hequette, Ruz & Jenner (1991), p. 24 - 33). The maritime environment of the Beaufort Sea is a low wave energy system since the pack ice is limiting the tidal wave energy. High waves and currents are restricted to the open water season. Nevertheless, waves can reach up to 8 m during storm events. Such situations are typically connected with winds from the northwest. The easterly winds typically cause lower waves and calm water surface conditions in contrast. The limit of the influence of the waves is visible as a band of drift wood (Hill, Hequette, Ruz & Jenner (1991), p. 35 - 43).

**Ecosystems and Vegetation** - During the last glaciation some parts of the Mackenzie Delta Region remained unglaciated. The results of MacDonald (1987), p. 252 indicated that “[...] *the early postglacial sediments are commonly inorganic and often contain pre-Quaternary palynomorphs.*” The initial vegetation developed during the early Holocene as diverse herb community. This development took place on moist areas - sedges and willows settled. At least at 10 ka BP open grasslands were present in the southern part of the Mackenzie Delta Region. The northern part was dominated by shrub formations at this time. These shrubs had their origin in Beringia. From 14 ka to 12 ka BP the shrub communities were already established in Beringia and in the following the shrubs spread from north to south. Along with the warming in the Holocene the treeline of the boreal forest was moving northward. There is evidence for forest communities in the Delta between 9 ka to 5 ka BP. Parallel to this muskeg communities developed between 8 ka and 4 ka BP until the modern level was reached (MacDonald (1987)).

Today the vegetation of the Mackenzie Delta can be categorized in four generalized zones according to ESG (1996), Burn & Kokelj (2009): (1) The open spruce boreal woodlands of the southern Mackenzie valley and on the flanking uplands. (2) A zone with a transition from forest to tundra. (3) The tundra

## 2 Test Sites and Database

formations of the northern delta and of the uplands. (4) The wetlands of the flat outer delta plains. The first zone of the boreal forest shows evenly spread trees and is mainly dominated by spruce species. The density of the trees decreases with higher latitude and altitude. The treeline of the delta valley is located more northward than the treeline of the surrounding uplands. This is caused by the lower altitude of the valley and the different micro climate. The adjacent transition zone may be divided in two sub-formations. Burn & Kokelj (2009), p. 92 note: “[...] *Tundra in the southern part of the transition is dominated by tall shrubs, but to the north the vegetation communities are characterized by sedges and dwarf shrubs less than 75 cm in high [...].*” In the third zone grasses, sedges and small shrubs dominate the land cover. This zone is characterized as Low Arctic Tundra zone. The land cover is dominated by small herbs and mosses. The wetlands of the outer delta are dominated by tussocks, sedges and small reeds (Burn & Kokelj (2009), p. 92).

Important for the ecology of the Mackenzie Delta River system and the surrounding uplands are two processes - namely the wild fires and the flooding. The boreal and tundra fires typically occur during extreme warm summer weeks and can be caused by single lightning storms or anthropogenic. The fires can affect large regions but are limited by water bodies, deficient supply of fuel and high moisture content of organic material. The fires cause a local thawing of the permafrost and a release of organic and nutrient matter is observable (Burn & Kokelj (2009), p. 92). The flooding also plays an important role in the ecology. The areas that are frequently affected by freshwater flooding events show adapted vegetation formations, e.g. wetland vegetation communities. The maritime flooding of low-lying near-shore locations can cause an extinction of vegetation due to salt water intrusion. Pisaric et al. (2011) showed actual results on the impact of recent storm surges and salt water intrusion on the vegetation of the outer Mackenzie Delta.

The Mackenzie Delta Region is characterized by three major ecozones according to ESWG (1996) and the classification of Wiken (1986): the Southern Arctic, the Taiga Cordillera and the Taiga Plains ecozones. (1) The Southern Arctic ecozone is characterized by long and cold winters and short and cool summers. The mean annual temperature is in between  $-11^{\circ}\text{C}$  and  $-7^{\circ}\text{C}$ . The precipitation is varying between 200 mm and 500 mm. The vegetation is dominated by a transition between the taiga forest and the tundra shrub lands. Typically the size of the shrubs decreases with higher latitude and herb communities dominate the land cover. In low lying dips and sedges wetland communities dominate the surface cover. Compared to other ecozones of the Arctic, the Southern Arctic ecozone shows the highest degree of Biodiversity and a sudden greening during the spring and summer. The Southern Arctic ecozone of the Mackenzie is composed of the Yukon Coastal Plain and the Tuktoyaktuk coastal plain ecoregion. The ecozone is entirely part of the continuous permafrost zone and soils are therefore characterized by ground ice and an active layer. The soils are referred as Cryosols (ESWG (1996), p. 37-39). (2) The climate of Taiga Cordillera shows a low annual precipitation less than 300 mm and a mean annual temperature between  $-10^{\circ}\text{C}$  and  $-5^{\circ}\text{C}$ . The precipitation and temperature vary with exposition and altitude (vertical zonation). The vegetation is characterized by alpine tundra vegetation and shrub communities and mixed tundra to taiga communities dominate sites of lower altitude. The ecoregion of the British-Richardson Mountains represents the Taiga Cordillera ecozone of the Mackenzie Delta Region. The soils of this ecozone are dominated by Brunisols, Regosols and - where permafrost is present - by Cryosols (ESWG (1996), p. 97). (3) The ecozone of the Taiga Plains is characterized by a temperatures between  $-10^{\circ}\text{C}$  and  $-1^{\circ}\text{C}$  and a

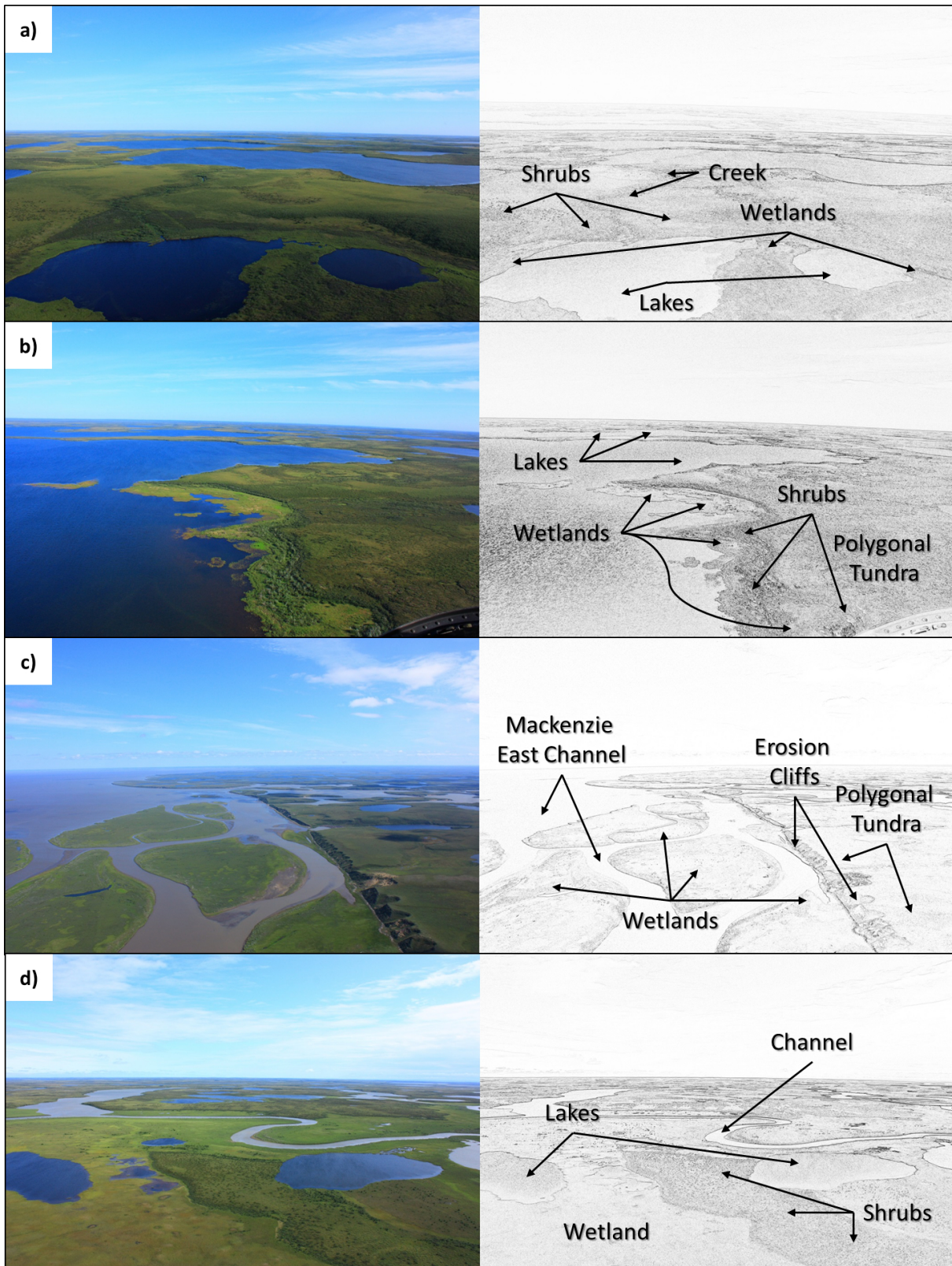


Figure 2.6: Aerial photography of the Mackenzie Delta Region, Northwest Territories, Canada: a) Inland lakes in the south of Richards Island, b) southern shore of the Eskimo Lakes, c) Mackenzie East Channel close to the Kugnallit Bay and d) Channels of Mackenzie close to the southern shore of Richards Island. Source: Own Figure.

2 Test Sites and Database

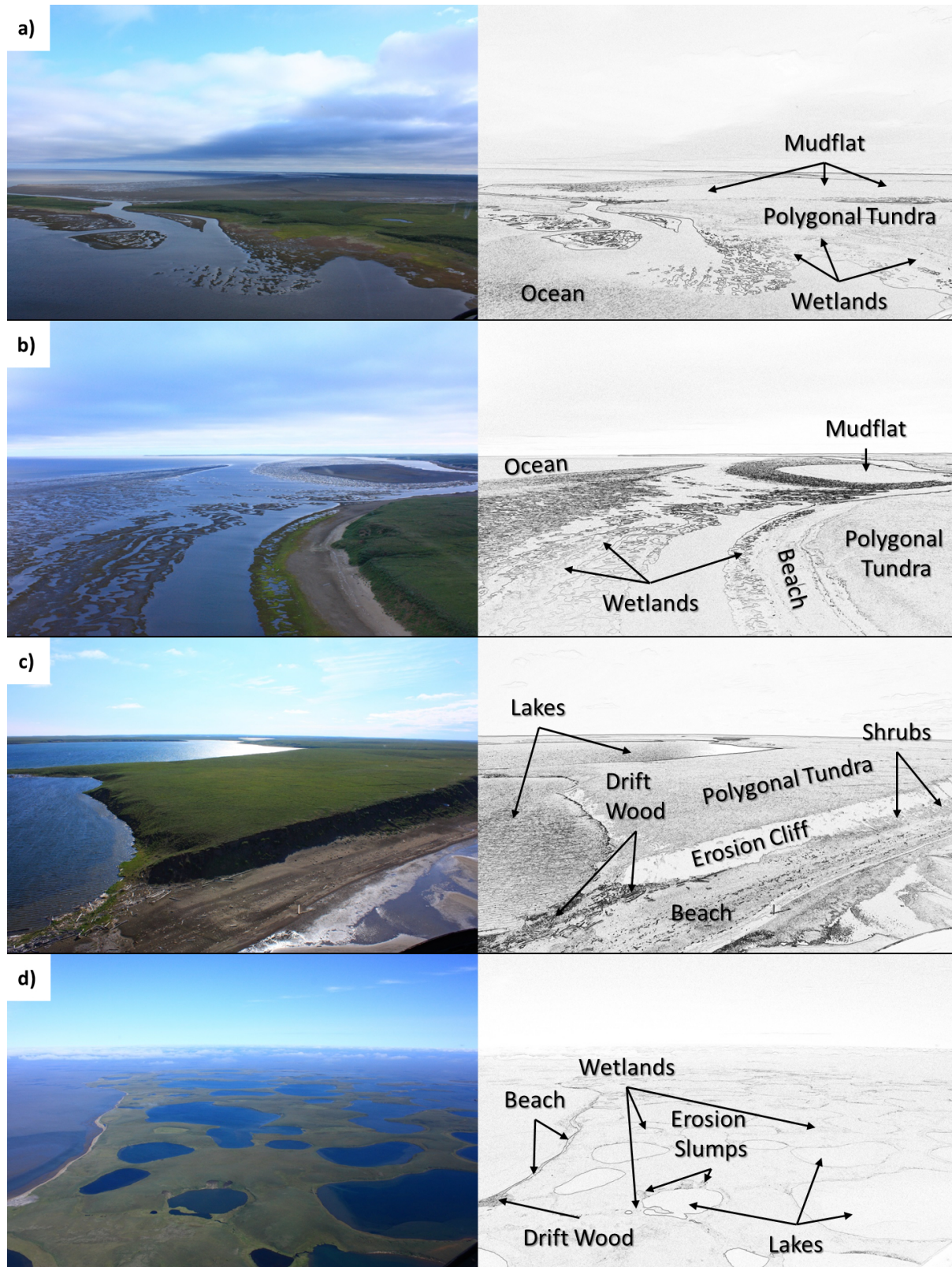


Figure 2.7: Aerial photography of of the Richards Island, Northwest Territories, Canada: a) Coastal wetlands at the western shore of Richards Island, b) Coastal mudflat and beach at the western shore of Richards Island, c) eroding tundra cliff at the western shore of Richards Island and d) inland lakes and erosion slumps of central Richards Island. Source: Own Figure.



low precipitation ranging from 200 to 500 mm (ESWG (1996), p. 45). The vegetation is composed of shrub lands and conifer dominated forests. Mosses, herbs and sedges dominate the vegetation ground layer. Due to the presence of permafrost the typical soils are Cryosolics and Gleysolics. This ecoregion of the Mackenzie Delta Region itself is referred to as Mackenzie Delta and is part of the Great Bear Lake Plain (southeast of Inuvik) (ESWG (1996), p. 45).

**Geomorphology and landforms** - The active morphological dynamics of the Mackenzie Delta Region are dominated by three major processes: (1) The fluvial processes of erosion, transportation and accumulation of the rivers and channels that have an actual flow and discharge. (2) The maritime processes along the shore. These processes have relevance for the outer delta (flooding) and the shores of Richards Island and the Tuktoyaktuk Peninsula (coastal erosion). (3) The dynamics that are related to periglacial processes. These have formed the pingos in the delta and on the uplands and the thermokarst lakes of the delta and the uplands. The periglacial processes are further the reason for the hummocky structure of the land surface and extensive polygonal ice wedge polygons. These are often present on the moraine deposits of the uplands. The thermo-erosional forms are present along the shores of the lakes, the shores of the sea and at steep slopes and cliffs (ESWG (1996), Burn & Kokelj (2009)).

The landforms of the Mackenzie Delta Region can be categorized in four generalized units that have a similar form assemblage: (1) The low-lying flat delta complex of the Mackenzie Valley. It is characterized by low topographic variation and the banks and terraces of the Mackenzie River and its channels and streams. The fluvial and maritime processes have formed extensive flats in the north of the delta. These are non-vegetated mudflats if they lie within the intertidal zone. The flats are covered by low grasslands and wetlands if they lie above the average high-water line. Towards the western shore of Richards Island and close to the settlement of Tuktoyaktuk pingos have formed. (2) The uplands of Richards Island, of the Tuktoyaktuk Peninsula and the surrounding of the Caribou Hills. These areas show a surficial coverage of glacial moraine deposits and a medium topographic variation. Rolling hills, creeks and valleys dominate the landscape. Related to the periglacial processes, numerous lakes and extensive polygonal ice wedge networks are present. Pingos and wetlands developed on drained lakes. Further, wetlands are frequent along the lake shores and at low-lying flat dips. (3) The transition between the uplands and the lowlands. The transition between these units is often distinct and related to the high difference in level. Steep cliffs and slumps are frequent, e.g. along the shores of the Mackenzie East Channel. (4) The higher terrain with structural forms of the exposed bedrock. These show a distinct fluvial drainage network and a high topographic variation. The flanks of the valleys and forms along the faults can be very steep, e.g. the Proterozoic cliffs between the Mackenzie Valley and the eastern uplands, or the Neogen to Paleogen Caribou Hills (ESWG (1996), Burn & Kokelj (2009)).

### 2.1.3 Banks Island

**Geography and Location** - Banks Island is part of the Western Canadian Arctic and belongs to the Arctic Islands of the Canadian Arctic Archipelago. The island is governed by the Northwest Territories of Canada and it is located at about 73° Northern Latitude and 120° Western Longitude. The climate shows a strong seasonality and is dry and cold. The mean annual temperature is about -17 °C and the mean winter temperatures are about -30 °C. The temperature peaks in summer and the mean is between -2 °C and 4 °C. The precipitation is generally low, less than 200 mm and snow can persist the ground the whole year. The ecozone of the Arctic Islands shows the lowest precipitation in Canada (polar desert). Along with this, the tundra vegetation is sparse and dominated by dwarfed forms of herbs and lichen (ESWG (1996), p. 27, ff.). The “[v]egetative cover tends to be greater on wetter sites confined to coastal lowlands, sheltered valleys and most nutrient-rich corridors along streams and rivers.” (ESWG (1996), p. 28). The soils are cryosolic and the site is part of the continuous permafrost zone. The thickness of the permafrost can be up to 500 m, e.g. at Storkerson Bayont (Vincent (1982), p. 213). The land surface morphology is dominated by exposed bedrock of sedimentary rocks, by glacial and marine deposits, or by quaternary fluvial and eolian deposits. Present-day human activities are restricted to trapping, hunting and fishing. The only permanently inhabited settlement on Banks Island is Sachs Harbour (about 71° 60′ N and 125° 15′ W) - located at the southern shore of the island (ESWG (1996), p. 28).

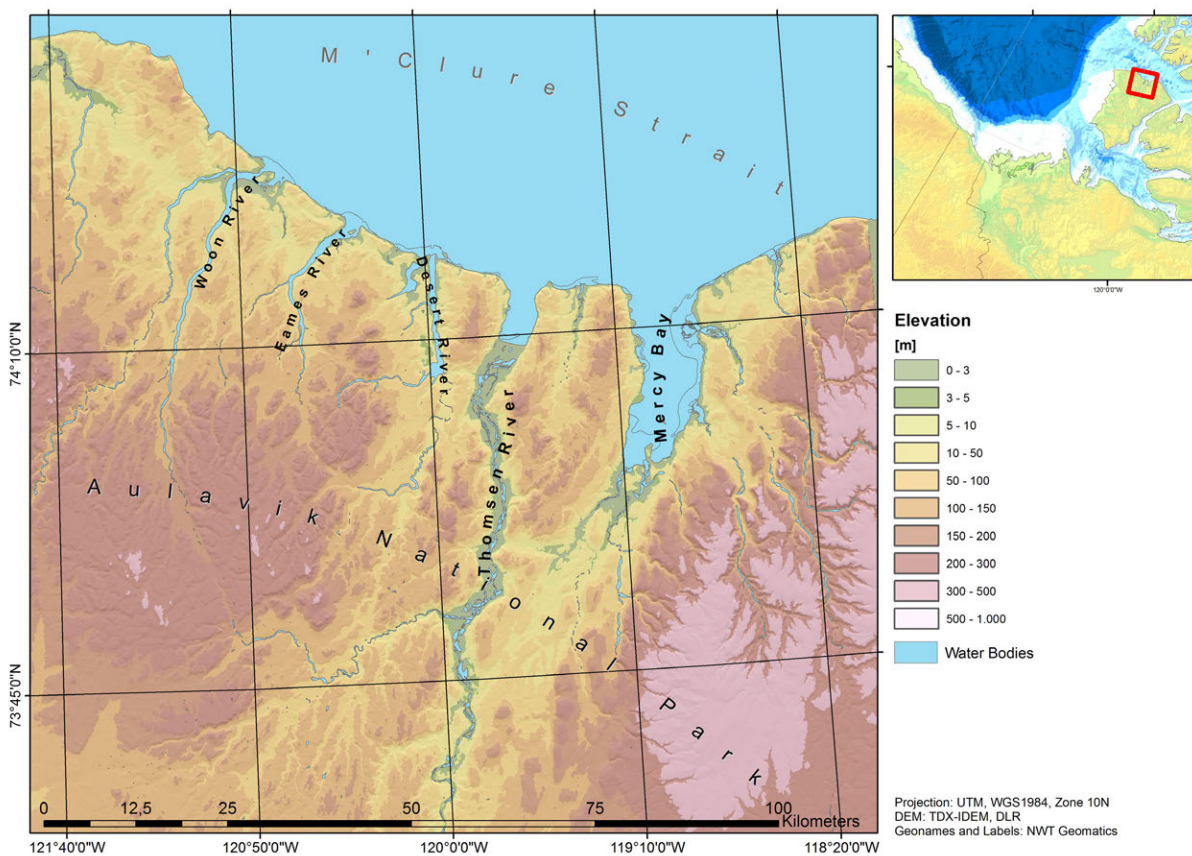


Figure 2.8: Geographic overview of Northern Banks Island, Northwest Territories, Canada. Source: Own figure, on the basis of NWT-Geomatics (2014), DLR (2013).

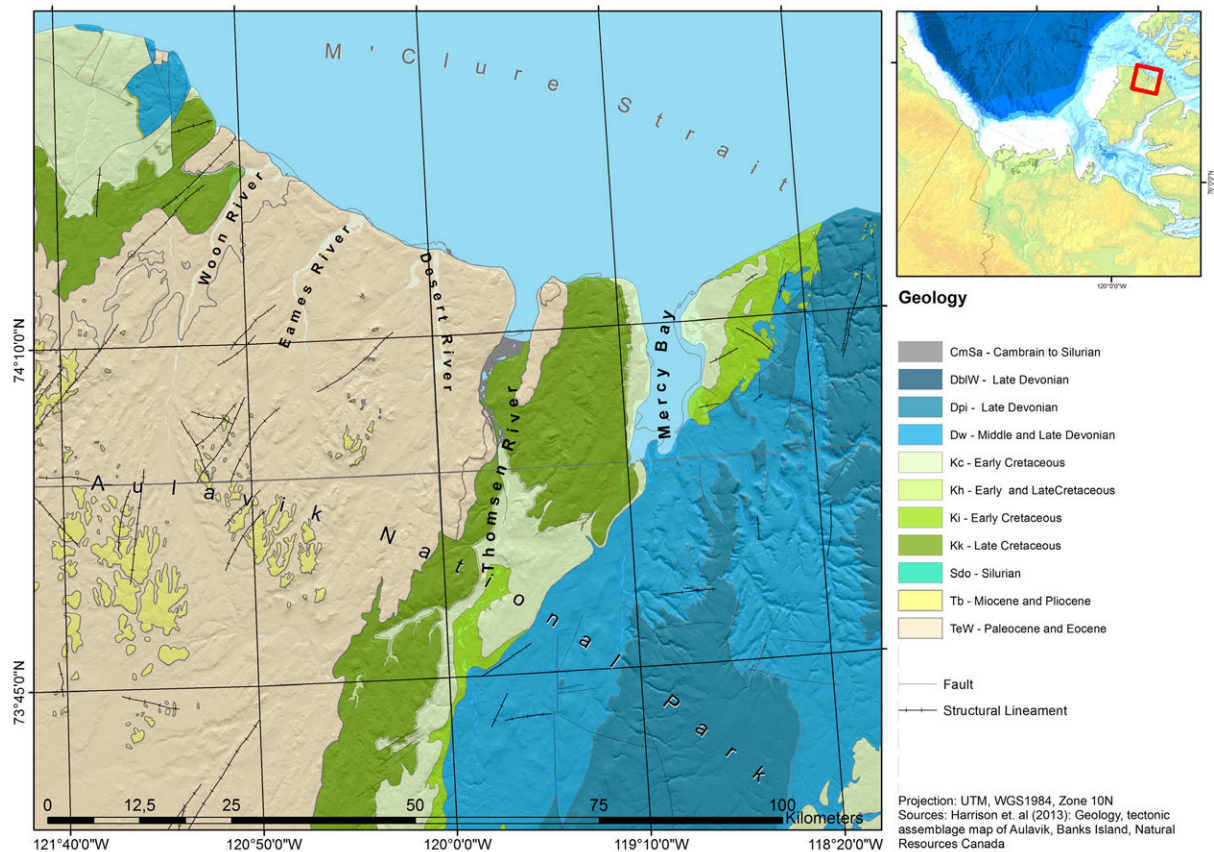


Figure 2.9: Geological overview of Northern Banks Island, Northwest Territories, Canada. Source: Own figure, on the basis of NWT-Geomatics (2014).

**Climate and Vegetation** - The test site of this study is situated in the north of Banks Island and lies inside the district of the Aulavik National Park. The ecoregion is classified as Banks Island Lowlands and comprises the central island and the lowlands of the northern coast lands (ESWG (1996), p. 31 and Larter et al. (2009)). The mean annual temperature of the site is low with  $-16\text{ }^{\circ}\text{C}$  and the mean winter temperature is about  $-30\text{ }^{\circ}\text{C}$ . The sparse tundra vegetation is a mix of mosses, herbs and dwarf shrubs less than 50 cm height. Wetland and marsh communities are common on the coastal lowlands and appear in association with shallow waters and low-lying depressions. The four major rivers of the sites are - from west to east - Woon River, Eames River, Desert River and Thomsen River. These have formed branched river systems with distinct drainage patterns. All rivers discharge in the M'Clure Strait, Arctic Ocean (Figure 2.8).

**Geology and Geomorphology**- The geological setting of the site is dominated by three major units: (1) The bedrock between Woon and Thomsen River is mainly of Paleocene to Eocene age, interrupted by spots of Miocene to Pliocene age. (2) The Thomsen River and its adjunct flanks lie on Cretaceous bedrock. (3) The rocks east of the Thomsen River and of the Mercy Bay are of Devonian age. The elevation of these formations is up to 800 m and the topographic variation is comparable high (see Figures 2.8 & 2.9). The quaternary geology of the site exhibits the glacial history of Northern Banks Island (Figure 2.10). The moraines of the Banks Glaciation, Thomsen Glaciation and Amundson Glaciation are exposed at the

## 2 Test Sites and Database

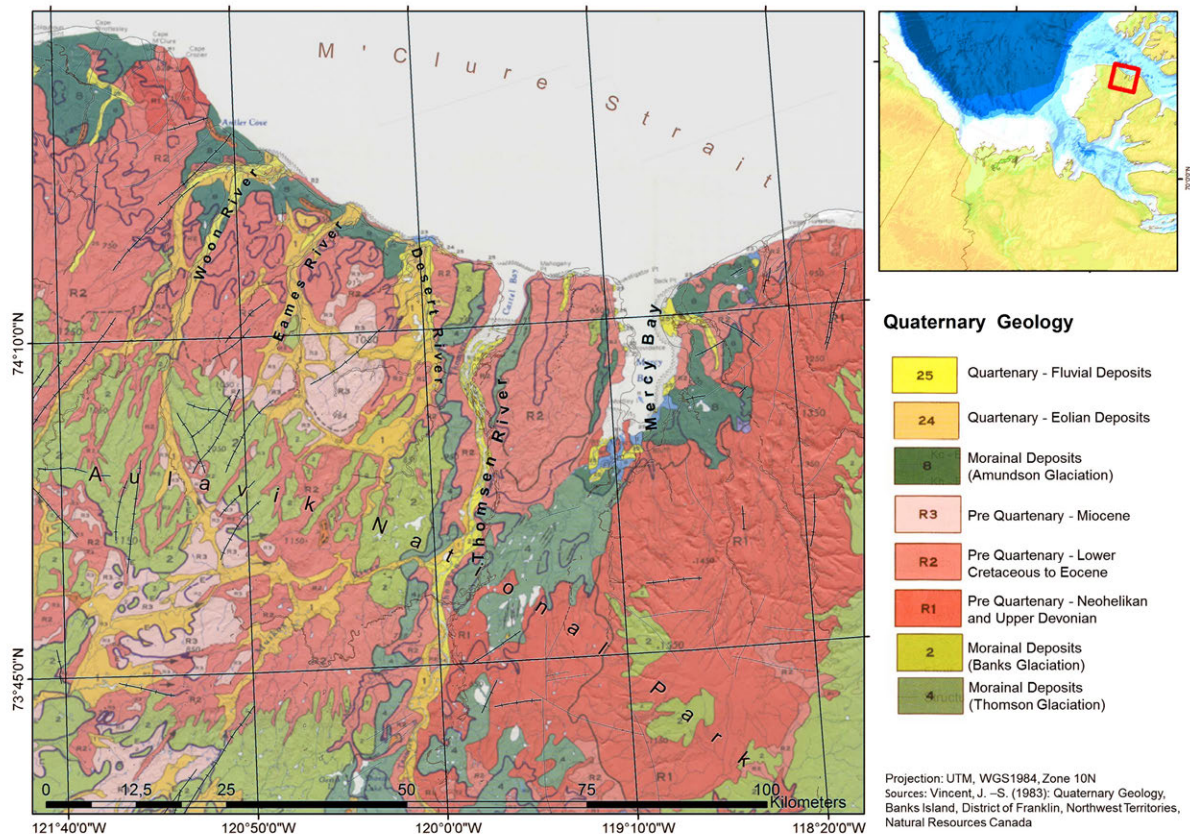


Figure 2.10: Quaternary geological overview Northern Banks Island, Northwest Territories, Canada. Source: Own figure, on the basis of Vincent (1982), NWT-Geomatics (2014).

northern lowlands and in the central part of the site (Vincent (1982), p. 214). The oldest and strongest glaciation event that is evident by land sediments is the Banks Glaciation. The Banks Glaciation took place during the early Pleistocene and the minimum age is of Matuyama with an age of 730 ka BP (Clark & Lea (1992), p. 235 ff) but may be up to 1640 ka BP (Clark & Lea (1992), p. 235 ff.). It was followed by the Thomsen Glaciation. This event is of middle Pleistocene age with about 790-123 ka BP (Clark & Lea (1992), p. 235 ff). Both flowed northwestward and had their origin in the southeast of the island. The Thomsen Glacier covered the Thomsen River basin and deposited stoney and sandy material (Vincent (1982), p. 220). The last glaciation event was the Amundson Glaciation which was of Laurentide origin. The age of this event is Wisconsinan (23 -65 ka BP) (Clark & Lea (1992), p. 235 ff). The event took place in two stades which are the M'Clure Stade and the Russell Stade (Vincent (1982), p. 220 ff.). The north of the island was not glaciated during the Russell Stade. The northwestern area in the west of the Bar Harbour Till was presumptively unglaciated during all glaciation events (Vincent (1982), p. 214, ff.).

The today's surface morphology is dominated by four units: (1) The braided river systems that show a young cover of fluvial and eolian genesis. These wide valleys are covered by sediments of varying grain sizes and are flat to gentle sloped. (2) The zone of the moraine deposits of the glaciations and glacial landforms. These are often of smooth hilly nature and situated on the structural geological units. (3) The coastal land and the shore zone that was formed by today's marine erosion and accumulation processes. (4) The exposed bedrocks of Pre-Quaternary age. Figure 2.11 shows field photographs of exemplary

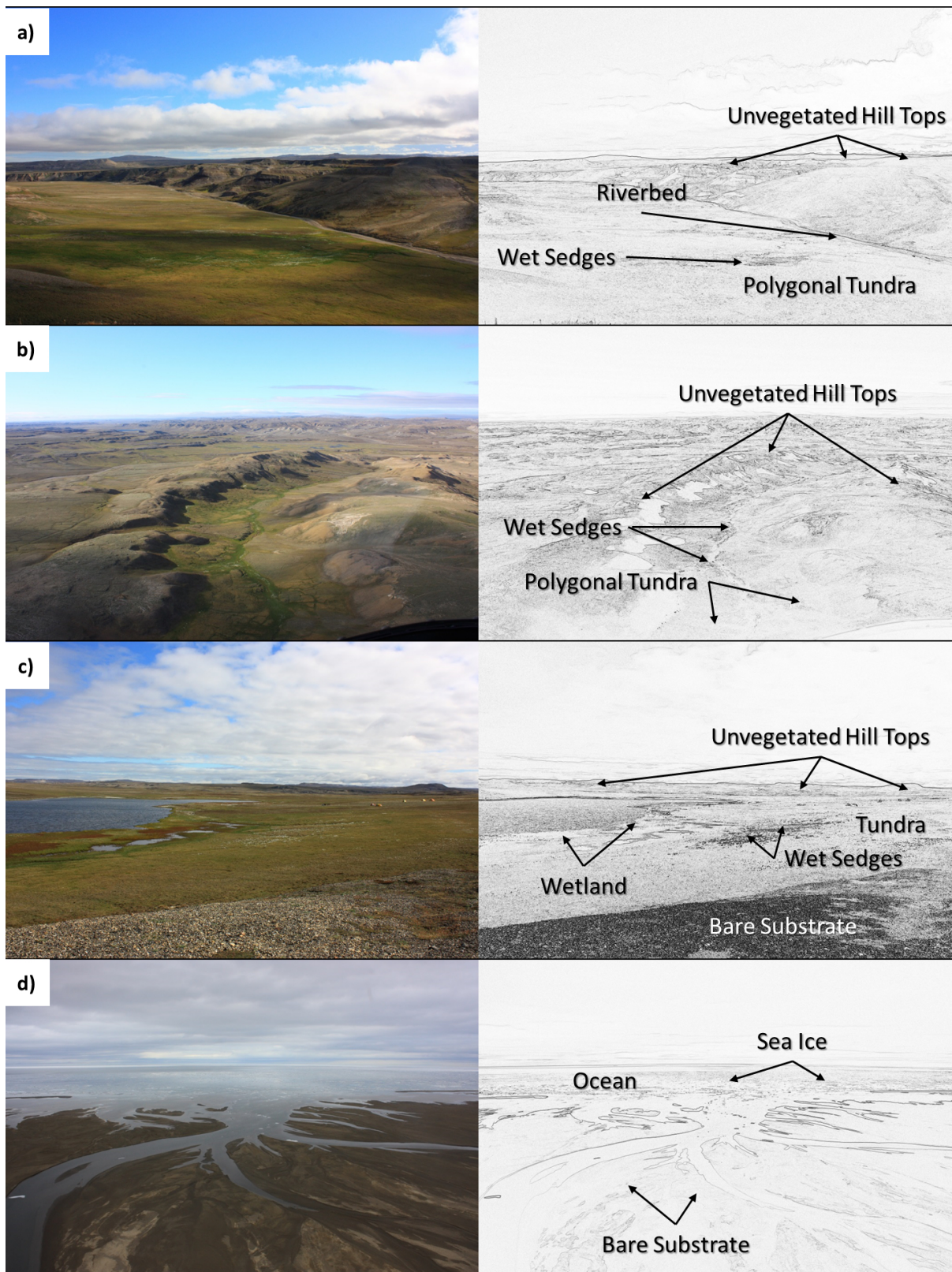


Figure 2.11: Field and aerial photography of Banks Island, Northwest Territories, Canada: a) valley in the Aulavik National Park, b) aerial view on a valley, Northern Banks Island, c) wetland near the campsite, Aulavik National Park and d) estuary of the Eames River. Source: Own Figure.

## 2 Test Sites and Database

sites of Northern Banks Island. Figures 2.11.a & 2.11.b show a valley and ridge sequence that is typical for many parts of the site. The exposed ridges are sparsely vegetated and at the tops the bare ground is exposed. Wetlands are common at the low-lying banks of small rivers and creeks. Figure 2.11.c shows a wetland complex and a lake close to the campsite between Woon and Eames River. Figure 2.11.d shows the estuary of the Eames River pictured from the helicopter.

### 2.1.4 James Bay

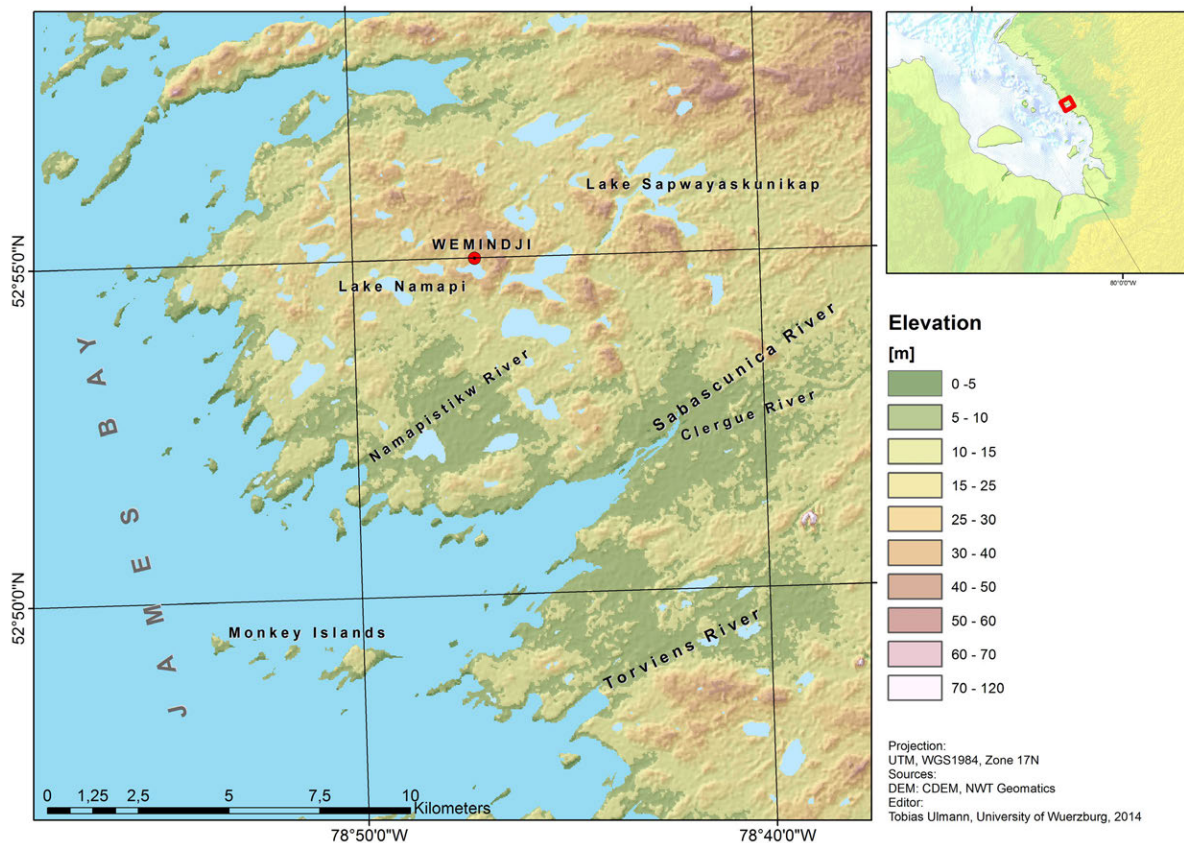


Figure 2.12: Geographic overview of James Bay, Quebec, Canada. Source: Own figure, on the basis of NWT-Geomatics (2014).

The Sub-Arctic test site is located at the eastern shore of the James Bay near the town Wemindji, Quebec, Canada. The region is part of the Taiga Shield ecozone and it is mainly characterized by the presence of Taiga forest and the old bedrocks of the Canadian Shield. The ecoregion is classified as La Grande Hills ecoregion. The climate is Sub-Arctic and characterized by cool and short summers. The mean annual temperatures are between  $-8\text{ }^{\circ}\text{C}$  and  $0\text{ }^{\circ}\text{C}$ . The mean summer temperatures can be up to  $+11\text{ }^{\circ}\text{C}$ , while the mean winter temperatures are up to  $-25\text{ }^{\circ}\text{C}$ . The precipitation is low to medium and between 200 mm and 800 mm (ESWG (1996), p. 53). The vegetative cover is dominated by open taiga forests, tundra vegetation and wetlands that are associated with the numerous lakes. The terrain is composed of rolling hills and low lying depressions and the topographic variation is generally low. The landform ensemble consists of hummocky ground and glacial forms (drumlins and moraines) (ESWG (1996), p. 56 ff). The

site is underlied by discontinuous to sporadic permafrost and Cryosols, Gleysols and Organic Cryosols dominate the pedological setting (ESWG (1996), p. 54). The land use activities are mainly trapping and hunting, fishing. Figure 2.12 shows and geographic overview of the test site and indicates the major rivers and lakes. Figure 2.2 shows the climate normal of the station Moosonee, Canada that is located at the southern limit of the Hudson Bay. Further information on the geologic and physio-geographic setting is provided by ESWG (1996), FOC (2012).

## 2.2 Database

Several data were collected between 2010 and 2013 for the analysis of the tundra landscape of the test sites. Radar remote sensing imagery was acquired by the SAR satellites TSX, TDX and R-2. In addition, polarized data of ALOS PALSAR were available. The multispectral remote sensing data were collected by the Landsat 8 satellite (L-8) for all test sites. High resolution airborne photography of the Mackenzie Delta was provided by Hartmann & Sachs (2012) and NWT-Geomatics (2014). These data were valuable information for the selection of the land cover reference data. Such land cover reference data were also collected in situ during two field campaigns. In 2012 and 2013 selected locations in the Mackenzie Delta Region and on the north of Banks Island were visited and land cover properties were documented and mapped. The data of the TDX IDEM and the ASTER GDEM were available and were used to characterize the land surface morphology. All of the named data are briefly described in the following.

### 2.2.1 In situ Data

For this study in situ data were collected in 2012 and 2013. During the field work locations in the Mackenzie Delta Region and on Northern Banks Island were visited and data of the land coverage were collected. The spectral signatures of selected locations and vegetation formations were measured and the coverage was described. The spectral information was recorded from visible light to near infrared using a field spectrometer. These data provided helpful information for the categorization of the land cover types. These spectral signatures will be used in more detail in upcoming projects. Further, information on the land cover was provided by the National Wildlife Research Center, Environment Canada (NWRC). These data comprised land cover information on selected near-shore locations of Richards Island and of the Tuktoyaktuk Peninsula and were collected during investigations of the NWRC and the Carleton University of Ottawa in 2010. Table 2.1 lists the in situ data that were available for this work. The location of the test sites and their naming is shown in Figure 2.18.

Table 2.1: List of the in situ reference data.

Campaign	Location	Acquisition Year
NWRC & Carleton	Richards Island	2010
NWRC & Carleton	Tuktoyaktuk	2010
NWRC & Carleton	Herschel Island	2011
NWRC & Carleton & Würzburg	Mackenzie Delta	2012
NWRC & Carleton & Würzburg	Banks Island	2012
NWRC & Carleton & Würzburg	Mackenzie Delta	2013

**Mackenzie Delta Region** - The ground truth land cover reference data of the Mackenzie Delta Region were collected in summer 2012 and summer 2013. The first campaign in the Mackenzie Delta Region was conducted between the 19th July and the 28th July 2012. The selected sites were located in the outer Mackenzie Delta, on the uplands close to the East Channel and along the shore of the Tuktoyaktuk Peninsula. The sites were accessed by helicopter and airborne photos were taken during the transits. On the ground the land cover information of representative homogenous plots were recorded, categorized



and mapped. In total more than forty locations were visited in this way. The second campaign in the Mackenzie Delta Region was conducted between the 23th July and the 7th August 2013. The selected sites were located on the central part and along the east shore of Richards Island. The east of Richards Island and the camp location was accessed by boat. The locations of the central island were accessed by foot and land cover information of representative homogenous plots were recorded, categorized and mapped. The shores of the East Channel were recorded by videography during the transit between Inuvik and Richards Island. In total more than thirty locations were visited in 2013.

The data collected during the campaigns were aggregated in six generalized land cover classes with respect to Corns (1974), Ullmann et al. (2014) and with respect to the land cover classification system of GeoBase (2009). The land cover reference data collected by the NWRC in 2010 were aggregated in the same way. Figure 2.18 shows selected locations of the in situ reference data. Exemplary field photographs of the generalized land cover types of the Mackenzie Delta Region are shown in Figure 2.13. The in situ criteria for the categorization and the cut-off between classes were the heights of the formations and the fraction of shrubs. The definition of the classes is provided in Figure 2.14. The occurrence of the selected land cover types is commonly bound to the topography. A schema that shows this interconnection is provided in Figure 2.15. The six generalized land cover classes of interest for the sites of the Mackenzie Delta Region are the following and in accordance to Ullmann et al. (2014):

- Water (NWA): Open water areas such as river, lakes and ocean. Thermokarst processes have led to a high number of small and big inland lakes on the flanks of the Mackenzie Delta and in the delta itself. This class further comprises all permanent water bodies and the ocean.
- Bare Substrate (NBG): Non-vegetated bare substrate of varying grain sizes and exposed bedrock. Extensive mudflats are, for example, present at the west coast of Richards Island, near the bay of West Point and the Burnt Creek. Elongated spits are present east of the North Head of Richards Island.
- Low/Grass and Herb Dominated Tundra (VLD): Closed tundra vegetation of less than 20 cm height dominated by formations of grasses, mosses and small herbs, no shrubs. The low tundra formations are common at the north head of Richards Island, at the surroundings of Madison Bay towards Summer Island and at the hill tops close to the Mackenzie East Channel. The occurrence is observed with increasing elevation and at exposed areas such as hill tops. The locations are usually comparable dry.
- Medium/Herb Dominated Tundra (VMD): Closed tundra vegetation of less than 50 cm height and dominated by formations of herbs and dwarf shrubs. The percent coverage of shrubs is less than 50%. This type of mixed tundra is frequent at the transition between exposed uplands and low lying plains and creeks.
- High/Shrub Dominated Tundra (VSD): Closed tundra vegetation of less than 100 cm height dominated by formations of dwarf shrubs and shrubs. The fraction of shrubs is greater than 50%. Areas of extensive shrub dominance are, for example, present on Richards Island at the leeward side of the hills and brims. The frequency of shrub coverage decreases from south to north, from east to west and from low to high elevation.
- Wetlands (VWT): Vegetated areas in standing water usually dominated by sedge formations. Coastal

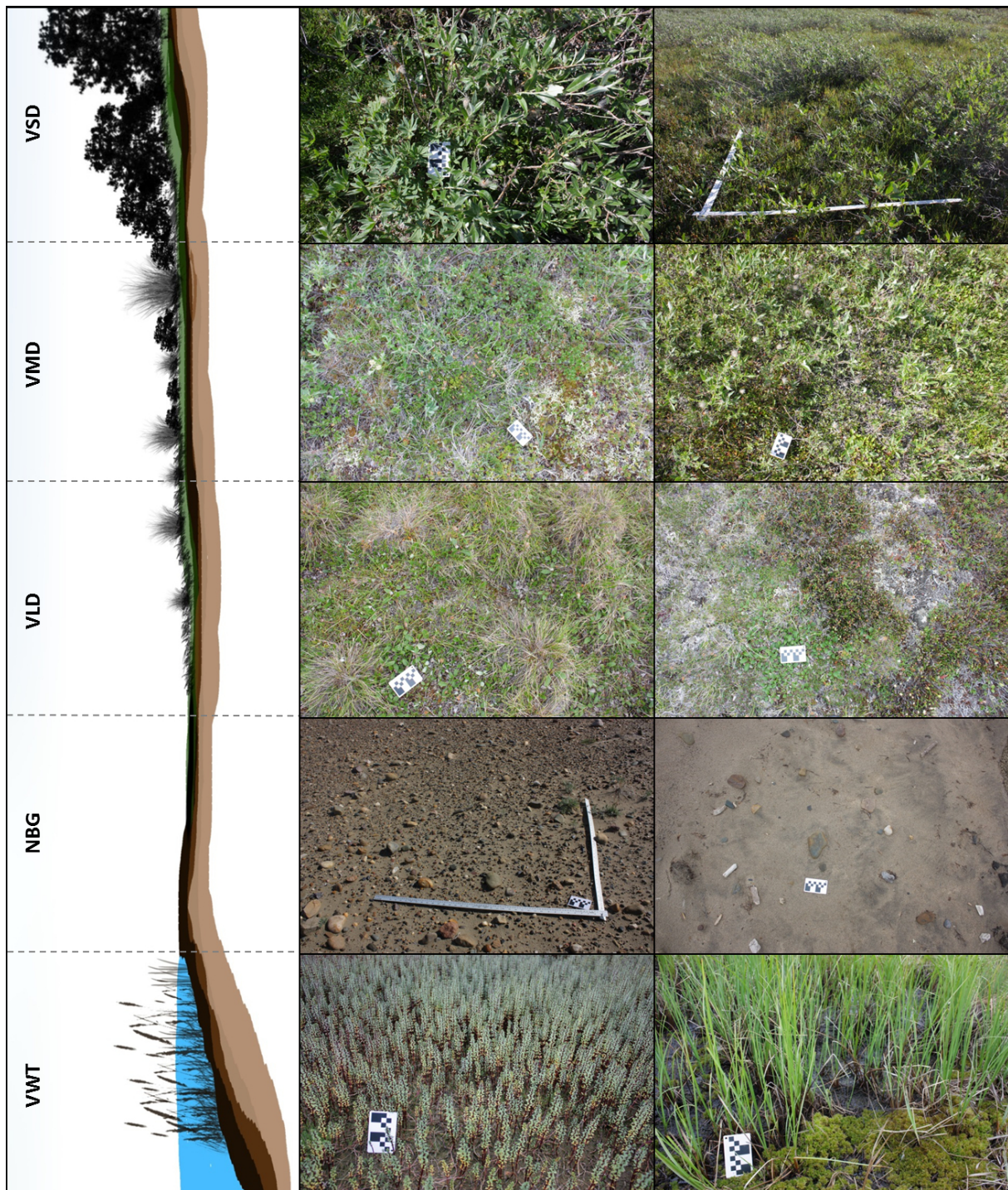


Figure 2.13: Field Photographs showing examples of the land cover classes of the Mackenzie Delta Region: bare ground (NBG), low grass dominated tundra (VLD), mixed tundra (VMD), shrub dominated tundra (VSD) and wetland (VWT) from top view. The meterstick is one by one meter long. The scale (black and white card) has a length of eight centimeters. Source: Own Figure.

Wetlands are present at the western boundary of Richards Island and the outer Mackenzie Delta. Wetlands frequently occur inland at creeks and drained lakes and in association with shallow inshore waters (e.g. the Mackenzie East Channel).

The number of land cover reference samples was increased using airborne reference data. The data used for this task are described in Section 2.2.5. In addition, airborne photos that were taken during the transit between the locations of interest were taken as reference. The new samples were collected from homogeneous regions that were located close to the locations that were visited in situ. These new samples were mapped in ArcGIS using the geocoded airborne photography. After this operation the set of land cover reference data comprised about 1700 polygons for all test sites and all classes of the Mackenzie Delta Region. Table 2.2 shows the number of polygons, the area, the number of pixels of 30 m spaced imagery and the number of pixels of 12 m spaced imagery that was available for the land cover classes. A random stratification was done for each test site using ENVI 5.1. The aim of this operation was to ensure the same number of samples per class. Table 2.3 shows the number of samples that was available for each class of the test sites after this operation. The selected reference data were then validated with the TDX IDEM to avoid systematic topographic effects that may lead to misinterpretation. None of the classes showed a noticeable anomaly (not shown). The stratified random reference data sets were used to assess the accuracy of the land cover classifications (see Section 3.2.3).

Table 2.2: Total number and area of land cover reference data of the test sites of the Mackenzie Delta Region: Bare Substrate (NBG), Low/Grass and Herb Dominated Tundra (VLD), Medium/Herb Dominated Tundra (VMD), High/Shrub Dominated Tundra (VSD) and Wetlands (VWT).

Class	Number of Polygons	Area [sqm]	Area [sqkm]	# Pixels 30m	# Pixels 12m
NBG	201	13653704	14	15171	94817
VLD	301	6059433	6	6733	42079
VMD	244	10308710	10	11454	71588
VSD	450	3978309	4	4420	27627
VWT	209	27097471	27	30108	188177

Table 2.3: Total number and area of random stratified land cover reference data available for each class of the test sites of the Mackenzie Delta Region Richards Island (RIS), Delta Islands (DIS), East Channel (ECH), Caribou Hills (CAH), Tuktoyaktuk (TUK), Anderson (AND), Yukon Coastal Plain (YCP), Herschel Island (HIS), Ivvaivk (IVV) and Banks Island (BIS).

Site	Area [sqm]	Area [sqkm]	# Pixels 30m	# Pixels 12m
RIS	405000	0.41	450	2800
TUK	315000	0.32	350	2200
DIS	135000	0.14	150	950
ECH	360000	0.36	400	2500
CAH	360000	0.36	400	2500
YCP	270000	0.27	300	1900
IVV	288000	0.29	320	2000
AND	432000	0.43	480	3000
BIS	72000	0.07	100	500

2 Test Sites and Database


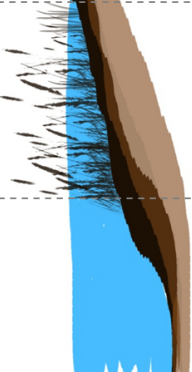


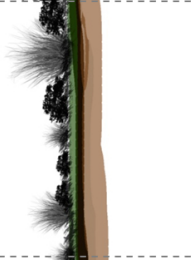

Class Name	NWA	VWT	NBG	VLD	VMD	VSD
						
<b>Shrub Density</b>	0%	0%	0%	0-10 %	10-50%	50-100%
<b>Vegetation Height</b>	n/a	5-40 cm	n/a	0-50 cm	20-50 cm	>50 cm
<b>Vegetation Coverage</b>	0%	10-50%	0%	20-70%	70-100%	100%
<b>Description</b>	<b>Water</b> Open water bodies	<b>Wetlands</b> Vegetated areas in standing water usually dominated by sedge formations	<b>Bare Substrate</b> Non-vegetated open substrate, varying grain sizes and exposed bedrock	<b>Low/Grass and Herb Dominated Tundra</b> Closed tundra vegetation cover dominated by formations of grasses, mosses and small herbs	<b>Medium/Herb Dominated Tundra</b> Closed tundra vegetation cover dominated by formations of herbs and dwarf shrubs	<b>High/Shrub Dominated Tundra</b> Closed tundra vegetation cover dominated by formations of dwarf shrubs and shrubs
<b>Distribution</b>	Rivers, streams, lakes and ocean	Inland at creeks and drained lakes and in association with shallow waters	Beaches, mudflats, spits and young erosion slumps and exposed bedrock	Occurrence with increasing elevation and at exposed areas such as hill tops and at dry locations	Frequent at the transition between exposed uplands and low lying plains and creeks	Leeward side of hills and brims. Decreasing shrub coverage from south to north, from east to west and from high to low elevation

Figure 2.14: Definition of the land cover classes of the Mackenzie Delta Region. Source: Own Figure.

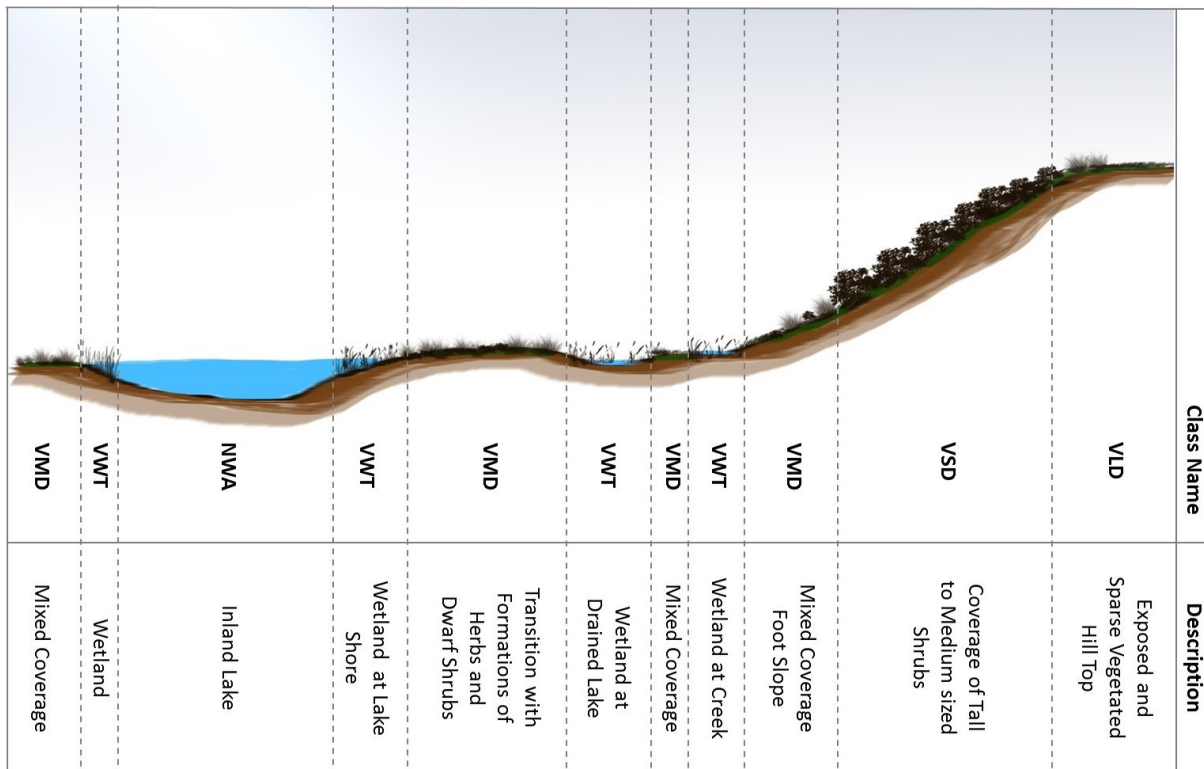


Figure 2.15: Schematic occurrence of the land cover classes in the Mackenzie Delta Region. Source: Own Figure.

**Banks Island** - The ground truth land cover reference data of the test site of northern Banks Island were collected between the 8th July and the 19th July 2012. The north of the island was accessed by helicopter. During the transit from Inuvik to the test sites aerial photography were taken. The sites were then accessed by foot and the land cover properties of representative homogenous plots were recorded, categorized and mapped. In total more than thirty locations were visited in this way. Figure 2.19 shows the locations of the in situ reference data. The data mapped during the campaign were aggregated in six generalized land cover classes. The categorization was done with respect to the properties shown in Figure 2.17 and with respect to the land cover classification system of GeoBase (2009). The in situ criteria for the categorization and the cut-off between classes were the heights of the formations and the appearance of tussock. Exemplary field photographs of the generalized land cover classes of Banks Island are shown in Figure 2.16. The land cover classes of interest of the test site Banks Island are:

- **Water (NWA):** Open water areas such as river, lakes and ocean. Thermokarst lakes are present on the moraine deposits. Further, large open inland waters are relatively seldom due to the high topographic variation and the steep slopes of the site.
- **Bare Substrate (NBG):** Non-vegetated open substrate of varying grain sizes and bedrock. Usually the hill tops and flanks of Northern Banks Island are not vegetated and the bedrock and the weathered material is exposed.
- **Low/Grass and Herb Dominated Tundra (VLD):** Closed tundra vegetation cover of less than 20 cm height dominated by formations of grasses, mosses and small herbs without shrubs. Low tundra

## 2 Test Sites and Database

formations are common at gentle sloped positions and do usually not occur in sheltered valleys. The occurrence is observed with increasing elevation and at exposed areas such as hill tops. The locations are comparably dry.

- Mixed Tussock Tundra (VML): Closed tundra vegetation of less than 40 cm height that is dominated by tussock formations of herbs and grass. This type of mixed tundra is frequent at gentle sloped and low lying plains, creeks and sheltered valleys.
- Mixed non-Tussock Tundra (VMH): Closed tundra vegetation of less than 40 cm height that is dominated by herbs and grass and the absence of tussock formations. This type of mixed tundra is frequent at gentle sloped low lying plains, creeks and sheltered valleys.
- Wetlands (VWT): Vegetated areas in standing water usually dominated by sedge formations. The wetlands of Banks Island frequently occur inland at creeks and lakes and in association with shallow inshore waters. Further, wetlands are common at the low-lying northern coastal lands.

The number of reference samples was increased using remote sensing reference data. The data used for this task were panchromatic SPOT images acquired in summer 2012 and were provided by NWT-Geomatics (2014). The airborne photos that were taken during the outward and the return flight were used as visual reference in addition. The new samples were collected from homogeneous regions that were located close to the locations that were visited in situ. These new samples were mapped in ArcGIS using the geocoded satellite imagery. The identification of representative plots was hindered by the high topographic variation of the site, the small size of homogeneous patches and the comparable low resolution of the auxiliary data. After this operation the set of reference data comprised about 50 polygons. Table 2.4 shows the number of polygons, the area, the number of pixels for 30 m spaced imagery and the number of pixels for 12 m spaced imagery per land cover class. A random stratification was done to generate the same number of samples per class. This operation was done using ENVI 5.1. Table 2.3 shows the number of samples that was available for each class after the random stratification. These land cover reference data were used to assess the accuracy of the land cover classifications (see Section 3.2.3).

Table 2.4: Total number and area of land cover reference data of the test site Banks Island: Bare Substrate (NBG), Low/Grass and Herb Dominated Tundra (VLD), Mixed Tussock Tundra (VML), Mixed non-Tussock Tundra (VMH) and Wetlands (VWT).

Class	Number of Polygons	Area [sqm]	Area [sqkm]	# Pixels 30m	# Pixels 12m
NBG	10	194014	0.19	215	1350
VLD	12	120891	0.12	135	850
VML	10	74787	0.07	85	520
VMH	8	78512	0.08	85	550
VWT	9	286149	0.29	315	1900

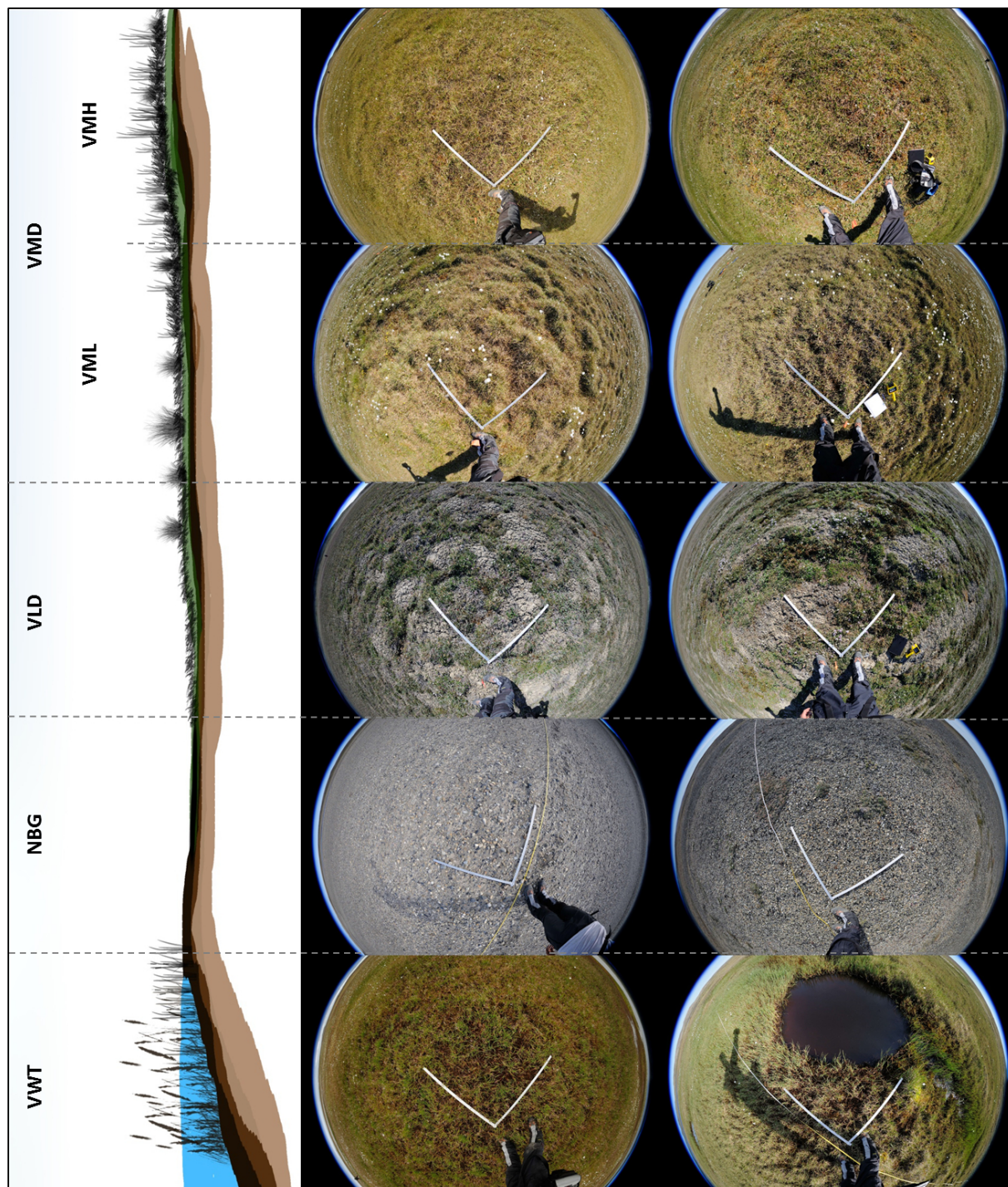


Figure 2.16: Field Photographs showing examples of the land cover classes of Banks Island: bare ground (NBG), low grass dominated tundra (VLD), mixed tussock tundra (VML), mixed non-tussock tundra (VMH) and wetland (VWT) from top view. The meterstick is one by one meter long. Source: Own Figure.

Class Name		VMD	VMH	VLD	NBG	VWT	NWA
		VML					
Vegetation Height		20-40 cm	20-40 cm	0-20 cm	n/a	5-40 cm	n/a
Vegetation Coverage		80-100%	80-100%	10-70%	0%	10-80%	0%
Description		<b>Medium/Non-Tussock Dominated Tundra</b> Closed tundra vegetation cover dominated by non-tussock formations of herbs, and grass	<b>Medium/Tussock Dominated Tundra</b> Closed tundra vegetation cover dominated by tussock formations of herbs and grass	<b>Low/Grass and Herb Dominated Tundra</b> Open tundra vegetation cover dominated by formations of grasses, mosses and small herbs	<b>Bare Substrate</b> Non-vegetated open substrate and bedrock varying grain sizes	<b>Wetlands</b> Vegetated areas in standing water usually dominated by sedge formations	<b>Water</b> Open water bodies
Distribution		Occurrence at sheltered mid-slopes and valleys		Occurrence with increasing elevation and at exposed areas Sparsely vegetated soils with cryptogam crust	Beaches, mudflats, spits exposed bedrock Non-vegetated soils with cryptogam crust	Inland at creeks and drained lakes and in association with shallow waters	Rivers, streams, lakes and ocean

Figure 2.17: Definition of the Land Cover Classes of Banks Island. Source: Own Figure.



## 2.2.2 Polarimetric Synthetic Aperture Radar Data

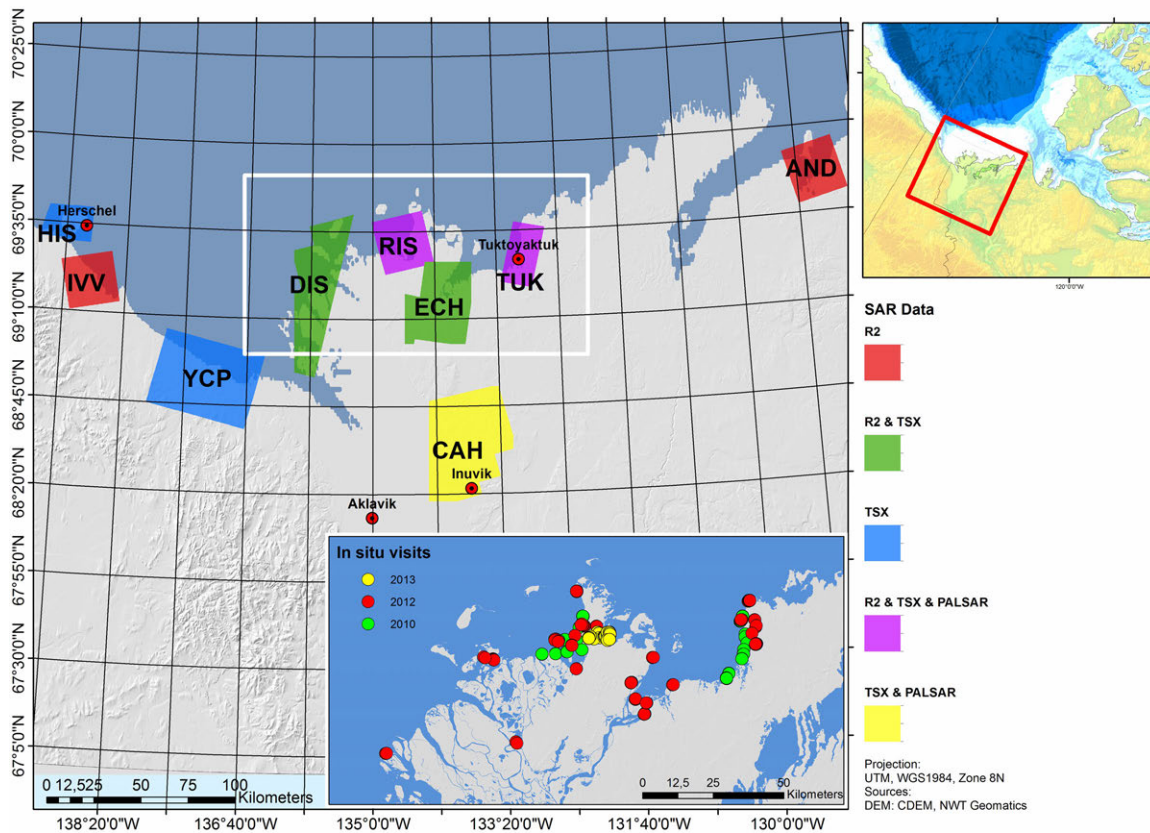


Figure 2.18: Data coverage of R-2, TSX and ALOS PALSAR and location of the in situ data of the test sites Mackenzie Delta Region: Richards Island (RIS), Delta Islands (DIS), East Channel (ECH), Caribou Hills (CAH), Tuktoyaktuk (TUK), Anderson (AND), Yukon Coastal Plain (YCP), Herschel Island (HIS) and Ivvaivk (IVV). Source: Own Figure.

For this study several polarized SAR data were acquired between 2010 and 2013. The data of the X-Band (TSX and TDX), the C-Band (R-2) and the L-Band (ALOS PalSAR) were available as dual- and/or quad-polarized imagery. The location of the test sites and the coverage of the radar data (footprints) of the Mackenzie Delta Region and of northern Banks Island are shown in Figure 2.18 and Figure 2.19. The PolSAR data of the James Bay covered the area shown in Figure 2.12. All of the PolSAR data that were used for land cover characterization and classification were recorded with medium incidence angles between  $30^\circ$  and  $40^\circ$ . In addition, R-2 acquisitions with shallow ( $>40^\circ$ ) and steep ( $<30^\circ$ ) were performed for the test sites Ivvaivk and Anderson to investigate the influence of the incidence angle on the backscatter characteristics of the land cover types. The data products of the named sensors are briefly described in the following. More detailed information on the used PolSAR data and their processing, interpretation and application is provided in Section 3.1.1.

**TSX & TDX** - TSX and TDX are German SAR satellites that operate since 2007 (TSX) and 2010 (TDX). The TDX satellite is constructed in the same way as TSX. Information on both satellites, the specifications of the remote sensing data and satellite and sensor specifics are shown in DLR (2007, 2010, 2013),

## 2 Test Sites and Database

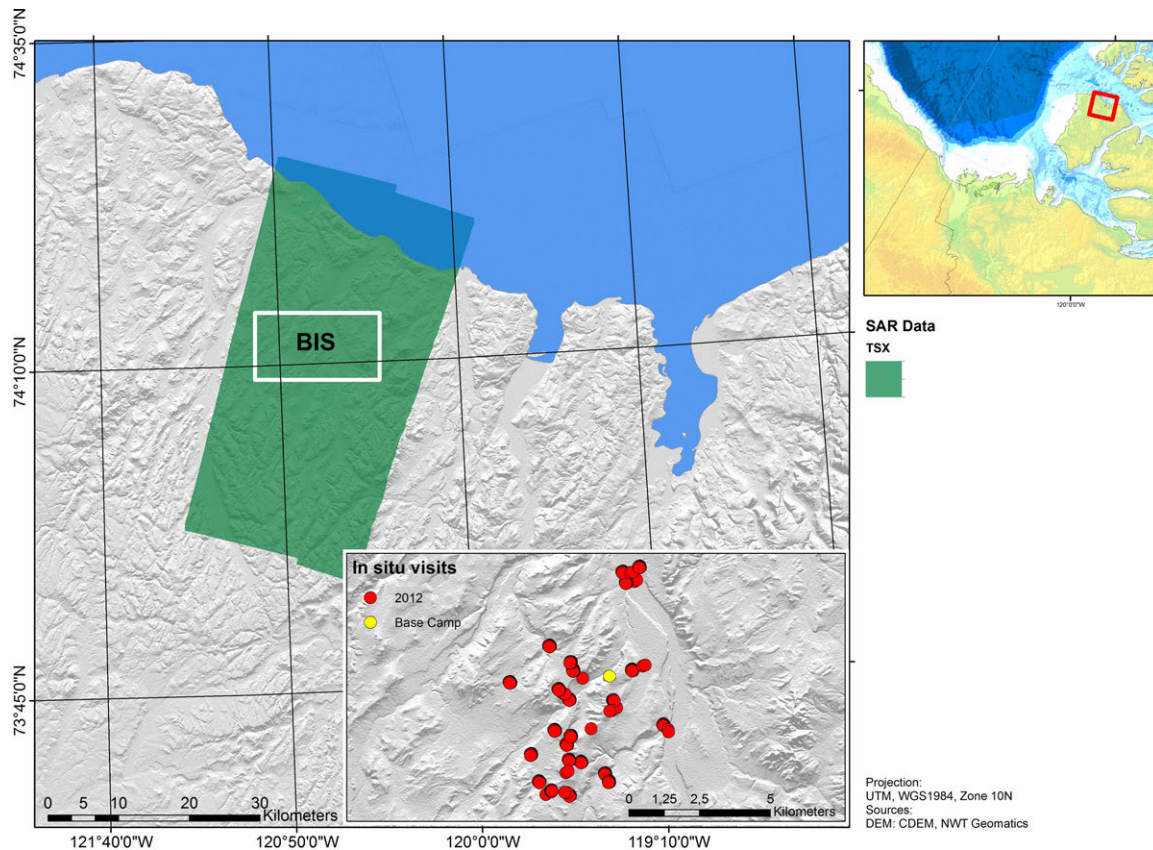


Figure 2.19: Data coverage of R-2, TSX and ALOS PALSAR and location of the in situ data of the test sites northern Banks Island (BIS). Source: Own Figure.

Schattler et al. (2011). The sensors of these satellites operate with short wave X-Band frequency in the microwave spectrum. Therefore the waves have a low penetration depth but a high spatial resolution and high radiometric sensitivity. The X-Band data are known to give information on the top of a surface, e.g. the vegetation canopy, or the coverage of bare ground. The data were acquired in StripMap mode and with five to ten meter spatial resolution. The data were recorded as dual polarimetric imagery in co-polarization mode and the HH and VV channels were phase-coherent and therefore suited for polarimetric analysis. The TSX and TDX data were made available for this project by the German Remote Sensing Data Center (DFD). The corresponding proposals were: „COA1736 - Assessing changes of arctic coastal environments with high resolution SAR data” (Principle Investigator: Achim Roth) and “COA1144 - eSPACE: Assessing the potential for Environmental Sensitivity Index mapping in the Arctic using SAR” (Principle Investigator: Jason Duffe). Table 2.5 lists the TSX and TDX data that cover the Mackenzie Delta and the data used for the characterization of the sites Tuktoyaktuk Peninsula, Banks Island and James Bay.

**R-2** - The satellite R-2 is the follow-on satellite of Radarsat-1. The Canadian satellite operates in the C-Band frequency in the microwave spectrum and is capable to record quad-polarized imagery. The satellite operates since 2007. The waves have a medium penetration depth and a high spatial resolution and high radiometric sensitivity. The C-Band data are known to give information on the top of a surface, e.g. the vegetation canopy, or the coverage of bare ground, but also on the volume of a target and on surface conditions. More information on the system and its specifications is shown in CSA (2014a,b). The

Table 2.5: TSX and TDX data for PolSAR analysis and land cover classification

Sensor	Location	Acquisition Date	Acquisition Mode	Polarization	Incidence Angle [°]	Site Name
TDX	Richards Island	2012.09.04	SM	dual-pol. HH/VV	31.7	RIS
TSX	Richards Island	2012.09.15	SM	dual-pol. HH/VV	32.8	RIS
TSX	Tuktoyaktuk	2011.07.23	SM	dual-pol. HH/VV	38.8	TUK
TSX	Tuktoyaktuk	2011.08.03	SM	dual-pol. HH/VV	38.8	TUK
TDX	East Channel	2012.09.04	SM	dual-pol. HH/VV	31.7	ECH
TDX	East Channel	2012.09.04	SM	dual-pol. HH/VV	31.7	ECH
TSX	East Channel	2012.09.15	SM	dual-pol. HH/VV	32.8	ECH
TSX	East Channel	2012.09.15	SM	dual-pol. HH/VV	32.8	ECH
TSX	Caribou Hills	2012.09.26	SM	dual-pol. HH/VV	33.8	CAH
TSX	Caribou Hills	2012.09.15	SM	dual-pol. HH/VV	32.8	CAH
TSX	Caribou Hills	2012.09.04	SM	dual-pol. HH/VV	31.7	CAH
TSX	Caribou Hills	2012.08.29	SM	dual-pol. HH/VV	32.7	CAH
TSX	Yukon Coastal Plain	2011.08.02	SM	dual-pol. HH/VV	35.8	YCP
TSX	Yukon Coastal Plain	2011.09.04	SM	dual-pol. HH/VV	37.8	YCP
TSX	Yukon Coastal Plain	2011.08.13	SM	dual-pol. HH/VV	36.8	YCP
TSX	Yukon Coastal Plain	2011.09.15	SM	dual-pol. HH/VV	38.8	YCP
TSX	Delta Islands	2012.07.05	SM	dual-pol. HH/VV	35.8	DIS
TSX	Delta Islands	2012.07.27	SM	dual-pol. HH/VV	34.9	DIS
TDX	Delta Islands	2012.08.29	SM	dual-pol. HH/VV	32.7	DIS
TSX	Delta Islands	2012.08.07	SM	dual-pol. HH/VV	33.8	DIS
TSX	Banks Island	2011.07.11	SM	dual-pol. HH/VV	39.7	BIS
TSX	James Bay	2012.07.10	SM	dual-pol. HH/VV	33.7	JAB

R-2 data were acquired in Fine acquisition mode, as quad-polarized imagery and with a spatial resolution of about seven to ten meters. The four channels HH, HV, VH and VV were phase-coherent and therefore suited for polarimetric analysis. The data were recorded for the entire northern Mackenzie Delta region in 2010 and for Tuktoyaktuk in 2011. For the test sites Ivvavik and Anderson data were recorded in 2011 with different incidence angles. No R-2 data were available for this study for Banks Island and James Bay. The R-2 data were made available for this project by the National Wildlife Research Center, Environment Canada, Ottawa under permission of MacDonald Dettwiler and Associates (MDA). The related Multi-User Request Form is “MDA GSI Ref Number: CG0061(2)-12-2011 “eSAPCE””.

**ALOS** - The Japanese satellite Advanced Land Observing Satellite (ALOS) carries multiple instruments and was launched in 2006. The ALOS carries a Phased Array type L-Band Synthetic Aperture Radar (PALSAR) which is a microwave sensor that operates in the L-Band of the microwave spectrum. The PALSAR instrument operates with long wave L-Band frequency and the waves have a high penetration depth but a lower spatial resolution compared to shorter wavelengths. The L-Band data are known to give information on the ground and near surface conditions, e.g. on the soil moisture content. The data were acquired with at a spatial resolution of about 20 m to 30 m. The data were recorded as dual-polarimetric imagery and HH and HV channels were phase-coherent and therefore suited for polarimetric analysis. More information on the system and its specifications is provided by JAXA (2006). The ALOS data were made available for this study by the Japan Aerospace Exploration Agency (JAXA) in the framework of

## 2 Test Sites and Database

Table 2.6: R-2 PolSAR data for incidence angle and land cover analysis.

Sensor	Location	Acquisition Date	Acquisition Mode	Polarization	Incidence Angle [°]	Site Name
R2	Anderson	2011.08.26	Fine	quad-pol.	46.1	AND
R2	Anderson	2011.08.30	Fine	quad-pol.	38.4	AND
R2	Anderson	2011.08.07	Fine	quad-pol.	20.1	AND
R2	Ivvavik	2011.08.04	Fine	quad-pol.	47.6	IVV
R2	Ivvavik	2011.08.08	Fine	quad-pol.	39.3	IVV
R2	Ivvavik	2011.08.09	Fine	quad-pol.	22.7	IVV
R2	Richards Island	2011.07.13	Fine	quad-pol.	35.0	RIS
R2	Tuktoyaktuk	2011.08.19	Fine	quad-pol.	40.5	TUK
R2	Anderson	2011.08.13	Fine	quad-pol.	37.0	AND
R2	Ivvavik	2011.08.08	Fine	quad-pol.	39.3	IVV
R2	East Channel	2010.08.25	Fine	quad-pol.	39.0	ECH
R2	East Channel	2010.08.25	Fine	quad-pol.	39.0	ECH
R2	East Channel	2010.08.05	Fine	quad-pol.	46.5	ECH
R2	East Channel	2010.08.05	Fine	quad-pol.	46.5	ECH
R2	East Channel	2010.08.05	Fine	quad-pol.	46.5	ECH

the ALOS Research Announcement. The data were provided with the Proposal „*PI 1186-Derivation of Environmental Parameters of Arctic Tundra Landscapes from Radar Remote Sensing Data (Principle Investigator: Dr. Jennifer Sobiech*“. The ALOS system has operated until 2011. The L-Band data used in this work were recorded in 2010 and available for the sites Richards Island, Tuktoyaktuk and the Caribou Hills (Table 2.7). The follow-on satellite ALOS-2 was launched in 2014 and acquires PolSAR data in the L-Band (JAXA (2014)).

Table 2.7: ALOS data for PolSAR analysis and land cover classification

Sensor	Location	Acquisition Date	Acquisition Mode	Polarization	Incidence Angle [°]	Site Name
ALOS	Richards Island	2010.09.10	n/a	dual-pol. HH/HV	34.2	RIS
ALOS	Tuktoyaktuk	2010.07.21	n/a	dual-pol. HH/HV	34.3	TUK
ALOS	Caribou Hills	2010.07.26	n/a	dual-pol. HH/HV	34.3	CAH

### 2.2.3 Digital Elevation Model Data

Several DEMs were available for this study. These were the TDX IDEM (DLR (2013), Wessel et al. (2008)), the ASTER Global DEM (GDEM) (Rees (2012)) and the Canadian DEM (GeoBase (2003), NWT-Geomatics (2014)). The TDX IDEM was derived via interferometry, the ASTER DEM via a photogrammetry and the Canadian DEM is a compilation of various elevation models and has a varying quality (Section 3.1.3). The frequently used Shuttle Radar Topography Mission (SRTM) elevation models are not available for regions north of 60° northern latitude, respectively south of 60° southern latitude, and were therefore not available for the Mackenzie Delta and Banks Island. The ASTER GDEM and the TDX IDEM offer currently the best DEMs that cover the entire Arctic. Table 2.8 lists selected properties of the DEMs that were available for the test sites. The specifications of the TDX data are provided by

DLR (2013), of the ASTER GDEM by METI-NASA (2011) and of the Canadian DEM by GeoBase (2003). The TDX data were made available by the German Remote Sensing Data Center (DFD), German Aerospace Center (DLR). The data were requested via the proposal: “*IDEM\_HYDRO0182 “Morphology and Hydrology of Arctic Environments” (Principle Investigator: Tobias Ullmann)*”. The used TDX IDEM data were processed by DFD and the DEM is an intermediate product that was processed using one coverage of the TDX Mission. The release of the final TDX DEM is scheduled for 2015/2016. Further data specifications and information on the TDX IDEM are provided by Zink et al. (2007), Wessel et al. (2008), DLR (2013). More information on the DEM and its usage is provided in Section 3.1.3.

Table 2.8: Digital elevation model data. Note: The used TDX IDEM is an intermediate product and the release of the final TDX DEM is scheduled for 2015/2016.

Sensor	Coverage	Acquisition Year	Resolution [m]	Source
TDX	Mackenzie Delta	2011/2012	12.0	DLR (2014)
TDX	Banks Island	2011/2012	12.0	DLR (2014)
ASTER GDEM	Mackenzie Delta	2012	30.0	METI-NASA (2011)
ASTER GDEM	James Bay	2012	30.0	METI-NASA (2011)
CDEM	Northwest Territories	2003	90.0	GeoBase (2003)
CDEM	Northwest Territories	2003	25.0	GeoBase (2003)
CDEM	Banks Island	2003	25.0	GeoBase (2003)

## 2.2.4 Multispectral Data

The L-8 multispectral data of the sites of the Mackenzie Delta, Banks Island and James Bay were provided by the U.S. Geological Survey. All of the used L-8 data were acquired in summer 2013. The cloud free data were downloaded as geocoded Level 1T products and corrected to the top of atmosphere reflectance (TOA) using the scene specific metadata. The geometric location error between the radar and the optical data was less than 20 m and estimated manually using ENVI 5.1. Table 2.9 lists the used Landsat data. More information on the multispectral data of Landsat and its usage is provided in Section 4.2.2.

Table 2.9: Multispectral data.

Sensor	Coverage	Acquisition Year	Acquired Bands	Resolution [m]	Source
L-8	Mackenzie Delta	2013	1-9	30.0	NASA (2013a)
L-8	James Bay	2013	1-9	30.0	NASA (2013b)
L-8	Banks Island	2013	1-9	30.0	NASA (2013c)

## 2.2.5 Airborne Data

High resolution airborne data of the Mackenzie Delta were available via NWT-Geomatics (2014). The ortho-data were acquired in summer 2007 and have a spatial resolution of less than one meter. The data are terrain corrected ortho-photos. The coverage of the data comprises the entire delta area, the eastern uplands of the delta (Caribou Hills), Richards Island and the Tuktoyaktuk Peninsula. The airborne data of selected spots of the Mackenzie Delta were available via the Alfred Wegener Institute for Marine and

## 2 Test Sites and Database

Polar Research (AWI). These data were recorded during the AirMeth campaign conducted by Dr. Jörg Hartmann and Dr. Torsten Sachs (Hartmann & Sachs (2012)). The relevant RGB ortho-photos covered parts of Richards Island, the lowlands of the northern delta area and spots of the Caribou Hills. The data were recorded with a RGB single lens reflex camera in summer 2012 and summer 2013. Table 2.10 lists the available airborne data.

Table 2.10: Airborne reference data of the Mackenzie Delta Region.

<b>Sensor</b>	<b>Acquisition Year</b>	<b>Acquired Bands</b>	<b>Resolution [m]</b>	<b>Source</b>
Polar 5	2012/2013	R,B,G (VIS)	<1.0	Hartmann & Sachs (2012)
OrthoRGB	2007	R,B,G (VIS)	<1.0	NWT-Geomatics (2014)

---

## Methodology

### 3.1 Imaging, Processing and Feature Extraction

The following section gives information on the background of PolSAR, multispectral and DEM data. The general considerations about these different types of remote sensing imagery are shown and a description of the acquisition principles, the representation of the data, the processing and the feature extraction is provided. The first section highlights the processing of SAR and PolSAR data, the application of polarimetry and the speckle filtering. In the following, the feature extraction of multispectral imagery is shown. Finally, different kinds of digital elevation data are presented and the derivation of topographic attributes is shown.

#### 3.1.1 Synthetic Aperture Radar

The imaging with SAR Systems is based on the active sending and receiving of electromagnetic pulses in the range from about 1 to 20 GHz - the microwave spectrum. The electromagnetic waves are defined by the power, the phase, the direction of propagation, the polarization and the velocity. The received signal shows differences compared to the send signal and these differences are predominantly caused by the interaction of the electromagnetic wave with the object of study (target), respectively the earth's surface. The naming of the SAR Systems is based on the operating wavelength (frequency) and the most frequently used bands of non-military SAR systems are the L-Band, C-Band and X-Band. These operate approximately at wavelengths of 30 cm to 15 cm (L-Band), 7 cm to 5 cm (C-Band) and 4 cm to 3 cm (X-Band) and therefore have much longer wavelengths than the visible light (about 0.5  $\mu\text{m}$ ) or the infrared light (about 0.9  $\mu\text{m}$ ) (Richards (2009), p. 1-6). The microwave radiation can transit targets depending on the properties of the wave and of the target. Thereby the penetration depth increases mainly with the wavelength. The long-wave SAR systems (e.g. L-Band) can even collect information on the sub-surface properties. Dry targets facilitate the penetration, e.g. microwaves can transit dry ice or soil. Therefore the SAR information is not limited to the upper most layer of the earth's surface and the generation of the signal is immanent different from spectral sensors (Richards (2009), 12-52). In addition, the image

### 3 Methodology

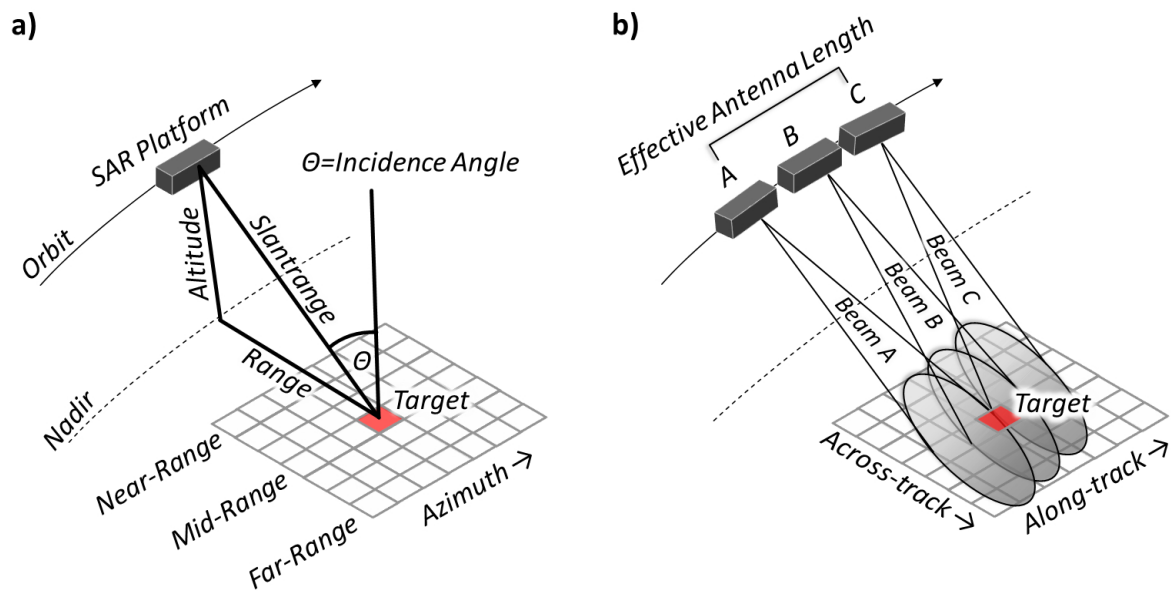


Figure 3.1: Acquisition geometry of a SAR System: a) naming of the elements of the acquisition geometry and b) formation of the synthetic antenna. The synthetic antenna is formed as long as the target is irradiated by pulses of the system. Source: Own figure, on the basis of Richards (2009).

acquisition of a SAR system requires a different acquisition geometry compared to passive optical systems. The recording of the radar signal and the localization of these signals makes an acquisition with a slant geometry necessary. The slant is required to avoid ambiguities since the data are recorded and stored in time domain. This means that the information of the received signal is sorted with respect to the time it needed to travel the distance between the SAR sensor and the target. A downward acquisition on the nadir is not possible since such an acquisition geometry will cause ambiguities: There are always locations to the sensor's left and the sensor's right that have the same distance and therefore the same travel-time (Richards (2009), p. 54-74).

Figure 3.1 shows schematically the acquisition geometry of a SAR system. The angle between the vertical normal of the target and the SAR platform is referred as incidence angle. The SAR systems are usually operated with incidence angles in the range from  $20^\circ$  to  $50^\circ$ . The direct connection between the SAR platform and the target is defined as slant range. This slant range is in direct relation to the time the signal needs to travel between the platform, the target and back to the platform. The geometry that shows the signal in time domain is referred to slant range geometry. The slant range itself is the hypotenuse in a right-angled triangle which is defined by the location of the target, the platform's location on the orbit and the projected platform's location on the nadir. The two cathetus of these triangle are the altitude - the height of the platform above ground - and the range that is defined by the distance between the target and the projected platform's location on the nadir (Richards (2009), p. 54-69).

The principle of the image acquisition is the synthetic extension of the effective antenna length. The longer the synthetic antenna the better is the spatial resolution of the SAR system. Details on the relation between antenna length and the spatial resolution are shown by Richards (2009), p. 53 ff. The extension



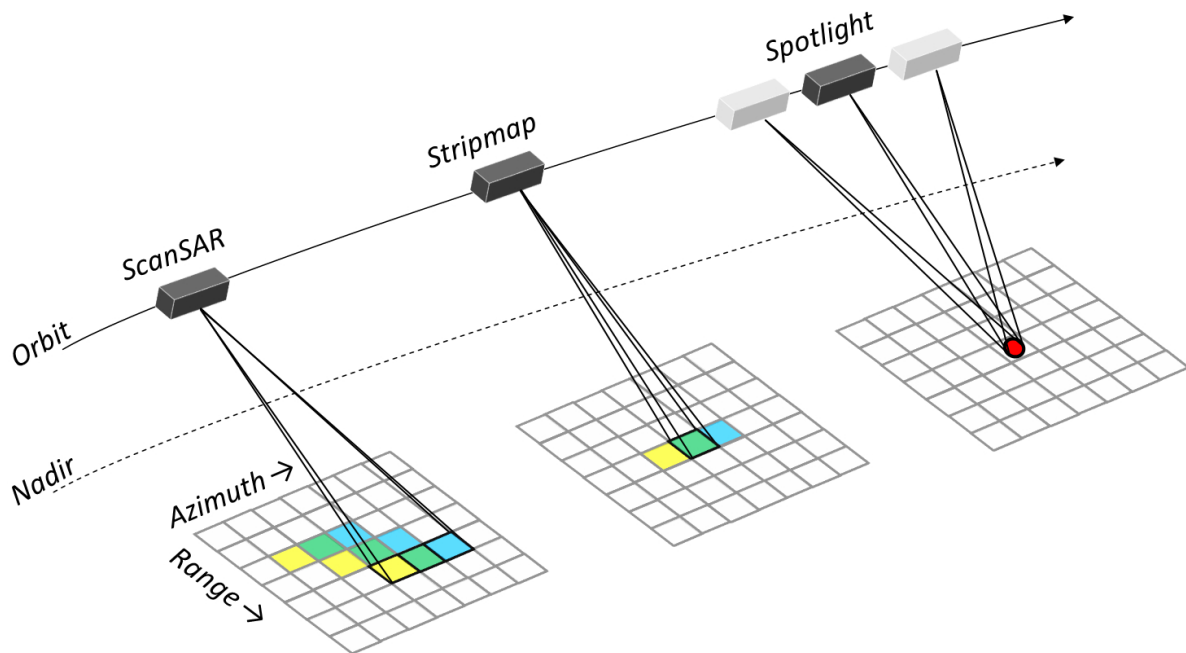


Figure 3.2: Acquisition modes ScanSAR, Stripmap and Spotlight of a SAR System. The best spatial resolution is achieved by the Spotlight mode due to the long integration time and the long effective antenna length. The Stripmap mode offers a trade-off between spatial resolution and coverage. Source: Own figure, on the basis of DLR (2007).

of the antenna is realized by a temporal integration of the signals from the same location. Figure 3.1.b shows how a synthetic antenna is formed. The signals of the target are integrated as long as the target is irradiated by pulses of the system. For example, the target is first irradiated by Beam A. The last irradiation is made with Beam C. This means that the effective antenna length of the system has the length between the platform positions A and C. The synthetic extension of the antenna allows to acquire images with a spatial resolution in the order of several dozens to less than one meter. The acquisitions with a real antenna would not be capable to realize such a high spatial resolution. The direction perpendicular to the range and the direction along the track is defined as azimuth direction. Since the platform is moving while the pulses are sent and received, a Doppler effect is present (Richards (2009), p. 49-53). This Doppler effect is usually corrected during the Level 0 or Level 1 processing.

A SAR system can acquire data in different acquisition modes. Thereby these modes are described by the type of focusing and the duration of illumination. A longer illumination makes a higher spatial resolution possible - the coverage is usually smaller, however. The relation between the spatial resolution and the coverage is reciprocal. That means that a higher spatial resolution usually causes a smaller coverage. The three frequently used acquisition modes are the Stripmap, ScanSAR and Spotlight Mode. For TSX and TDX satellites the best spatial resolution is realized with the so call Staring Spotlight acquisition mode. The Spotlight mode has a high spatial resolution due to a long temporal integration time and a long effective antenna length. The Stripmap mode does a focusing in range and perpendicular to the orbit and at defined repetitive locations. The spatial resolution in range direction is defined by the pulse-repetition-frequency (PRF) and the integration time. The PRF can be modified to enable coherent acquisitions

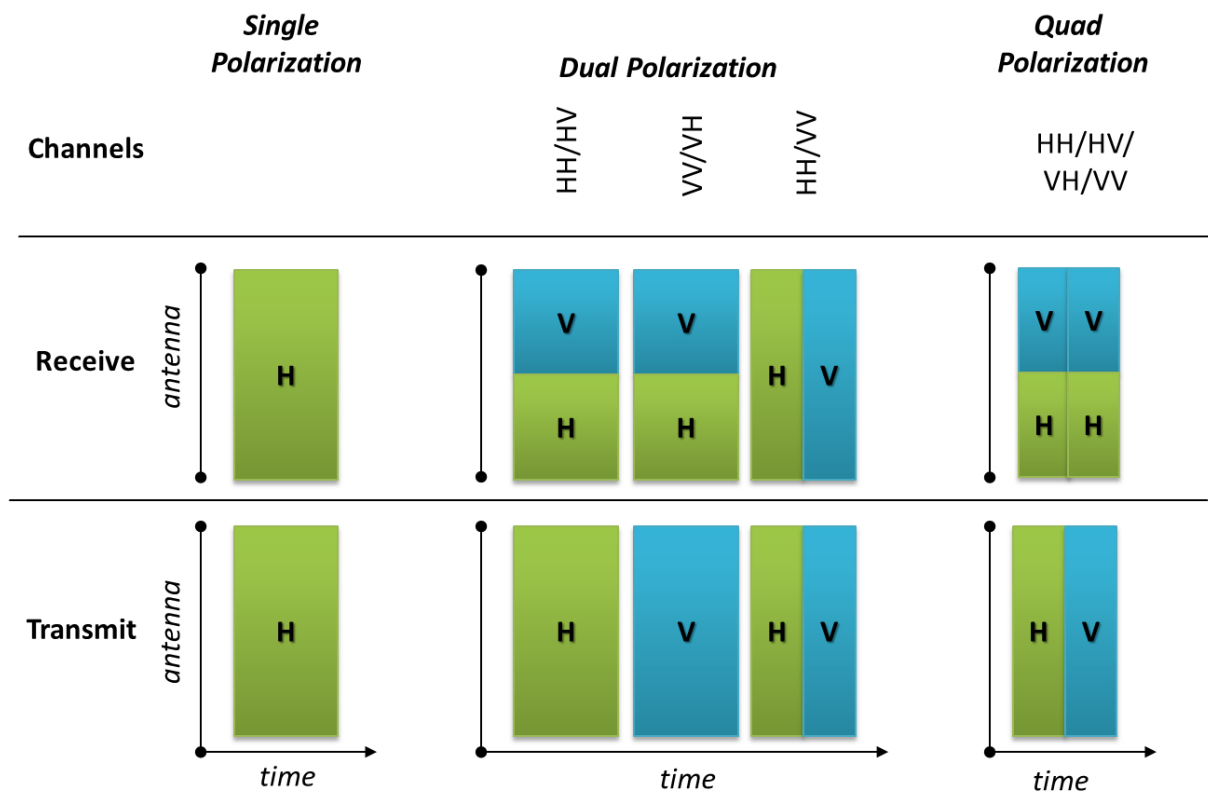


Figure 3.3: Illustration of the polarization modes and the antenna configurations during transmit and receive of the single-, dual- and quad-polarization modes. The split of the antenna and/or the shortening of the acquisition time enables to send and receive different polarimetric channels. These modifications lead to a lower spatial resolution in range by a factor of two (dual) or four (quad) compared to the single-polarization. Source: Own Figure.

with different polarizations. The acquisition of more than one polarization channel reduces usually the width of the swath in range direction. The interval (spacing) between two consecutive measurements in the Stripmap mode defines the spatial resolution in azimuth direction. The spatial resolution in azimuth direction is not affected by the acquisition of polarization channels. The application of the ScanSAR mode allows to generate a large coverage with a lower spatial resolution. The integration time is relatively short since the focusing of the antenna is moving in defined rates from near-range to the far-range. This causes a higher range of incidence angles compared to the Stripmap mode and therefore a wider field of view and a larger coverage (DLR (2007, 2010)). The named acquisition modes are illustrated in Figure 3.2.

The slant acquisition causes distortions that are typical effects of a radar image. These are the shadowing, the foreshortening and the layover. These effects and their implication for analysis and interpretation were widely discussed, e.g. by Richards (2009), Hein (2010), Ulaby et al. (2014). The SAR images are further affected by the so called Speckle Effect, which is also sometimes called Salt-and-Pepper-Effect. This effect is present due to random scattering that happens on a scale that is smaller than the spatial resolution of the system. Information on the nature of the Speckle and its removal is given in the subsequent Section 3.1.1.2. The atmosphere can have distortion effects as well. Usually, these are negligible since the microwaves operate in an atmospheric window with a high transmissibility. Due to this and due to

the active illumination the SAR imaging is nearly unaffected by cloud cover and can take images with constant quality whether it is day or night. The information of SAR data is a function of the acquisition parameters (e.g. incidence angle, polarization, wavelength and acquisition mode) and the target parameters (e.g. dielectric properties, physical structure and orientation). The following subsections give further information on SAR systems, e.g. on the acquisition parameters, the polarimetric feature extraction, the speckle removal and filtering and the processing and the geocoding of SAR imagery.

#### 3.1.1.1 Polarimetry

Some of the properties of the electromagnetic pulse of a SAR system are variable and can be programmed individually prior to an image acquisition. These parameters are, for example, the acquisition mode and the polarization of the antenna during the transmit and the receive. These parameters regulate - among others - the spatial resolution, the coverage and the sensitivity. Usually, SAR systems can send and receive electromagnetic waves in vertical (V) or horizontal (H) polarization. For products of the satellites R-2, TSX, TDX and ALOS PALSAR the polarization used during the image formation is named with two capital letters. The first letter defines the polarization during the transmit and the second letter the polarization during the receive. There are four possible combinations of polarizations: HH, VV, VH and HV. Most SAR systems are able to send and receive not only one single polarization channel but multiple channels in different polarizations simultaneously. Two types of systems are distinguished: (1) The full- or quad-polarized systems and (2) the dual-polarized systems. The former are able to acquire all four polarization channels coherently. For example, the systems R-2, ALOS PALSAR and ALOS-2 are able to acquire data in this mode. TSX and TDX offer an experimental quad-polarization mode (DLR (2006)). The dual-polarized systems acquire two out of the four polarization channels - either the cross-polarized information (HH/HV or VV/VH) or the co-polarized information (HH/VV). The dual-polarized data have a higher spatial resolution compared to the quad-polarized data - if the same wavelength and acquisition geometry is used - since the PRF is higher. The recently launched satellites Sentinel-1, R-2, TDX or TSX are capable to acquire cross-polarized data. Only few systems like TSX, PAZ and COSMO-SkyMed are designed to acquire the co-polarized information coherently. The technique to realize a coherent co-polarized acquisition is comprehensive. Information on the technical details of the co-polarized acquisition mode of TSX are provided by DLR (2010). Figure 3.3 illustrates the polarization modes and the antenna configurations during transmit and receive of the single-, dual- and quad-polarization modes.

The analysis of the Polarimetric Synthetic Aperture Radar (PolSAR) data allows to collect information on the properties of a target by analyzing the relationships and differences in the polarization channels. One of the most important theoretical relations between polarization channels is the difference between the HH phase and the VV phase. These phases are displaced by  $\pi$  if the wave was scattered an odd number of times. These phases are not displaced if the wave was scattered an even number of times. Therefore the co-polarized information can be used to model the type of backscattering, e.g. odd bounce or even bounce. A second important empirical relation is the sensitivity of the HV polarization to random alignment and exposition of surfaces and dipoles. The cross-polarized information is sensitive to scattering processes that are related to the volume of the target, e.g. the type and the structure of vegetation. The

### 3 Methodology

different types of backscattering - double or even bounce scattering, surface or odd bounce scattering and volume scattering - can be related to the properties of a target. Information on the mathematical definition of backscattering models is given in the following sections. A more comprehensive description of the backscattering processes and the relation to the polarization are provided by Richards (2009), Cloude (2010), Ulaby et al. (2014).

Figure 3.4 shows schematically the relation of the wavelength, the type of backscattering and the land cover types of the Mackenzie Delta Region (see Section 2.2.1). The figure shows the types of backscattering that can be expected if the surface is imaged with X-, C- or L-Band SAR data. Regardless of the wavelength it is likely that the wetland vegetation shows a clear double bounce signal. This is due to the interaction of the electromagnetic wave with the water surface and the stem of the vegetation. The law of reflection causes a double bounce signal that is directly returned to the sensor. Due to this a high intensity of the signal and a displacement between the HH phase and the VV phase will be observable. It is likely that this signal is less intense for L-Band data since the long wavelength causes a high penetration: a large portion of the wave will transit the vegetation without interaction. Direct single bounces are likely for the X- and C-Band data for bare ground surfaces without vegetation coverage. The intensity of these single bounces will vary with the dielectric properties (e.g. moisture) and the geometric alignment of the surface (e.g. surface roughness and grain size). For bare ground surfaces the HH phase and the VV phase will not show a meaningful displacement. The L-Band signal of the non-vegetated ground may be caused by sub-surface scattering processes. The wave can transit the upper layer of the ground if the moisture and roughness conditions are suited. The sub-surface scattering process are therefore likely for dry and unconsolidated material with low roughness. For sparse vegetated ground it is expected that the C- and X-Band data will show predominantly surface scattering (ground) and volume scattering (vegetation). It is likely that the X-Band will be more sensitive to the smaller (lower) vegetation than the C-Band. In contrast, the C-Band will be presumptively more sensitive to bigger (higher) vegetation formations than the X-Band. Since the tundra vegetation is dominated by small sized vegetation the L-Band data will only show little volume scattering but mainly surface scattering.

#### Matrix Representations

The signal of a SAR system may be defined by the mathematical framework of the Radar Equation (Equation 3.1). This equation shows the parameters that affect the signal formation and the power returning to the receiving antenna  $P_r$ . The first term characterizes the transmission - the electromagnetic incidence wave  $\vec{E}^i$  - via the transmitted power  $P_t$ , the antenna gain  $G_t$  and the distance between the transmitting system and the target  $R_t$ . The last term of the radar equation describes the scattered electromagnetic wave  $\vec{E}^s$  via the effective length of the receiving antenna  $A_r$  and the distance between target and receiving system  $R_r$ . The middle term describes the influence of the target on the balance between incidence and scattered wave (Richards (2009), p. 75-78). The sign  $\sigma_i$  denotes the complex scattering amplitude of an ideal isotropic target (radar cross section). The scattering amplitude is a function of several parameters - for instance, the frequency and the imaging geometry of the system, the wave polarization, the object's geometry and dielectric properties (Richards (2009), p. 80-83).

$$P_r = \frac{P_t G_t}{4\pi R_t^2} 4\pi |\sigma_i|^2 \frac{A_r}{4\pi R_r^2} \quad (3.1)$$

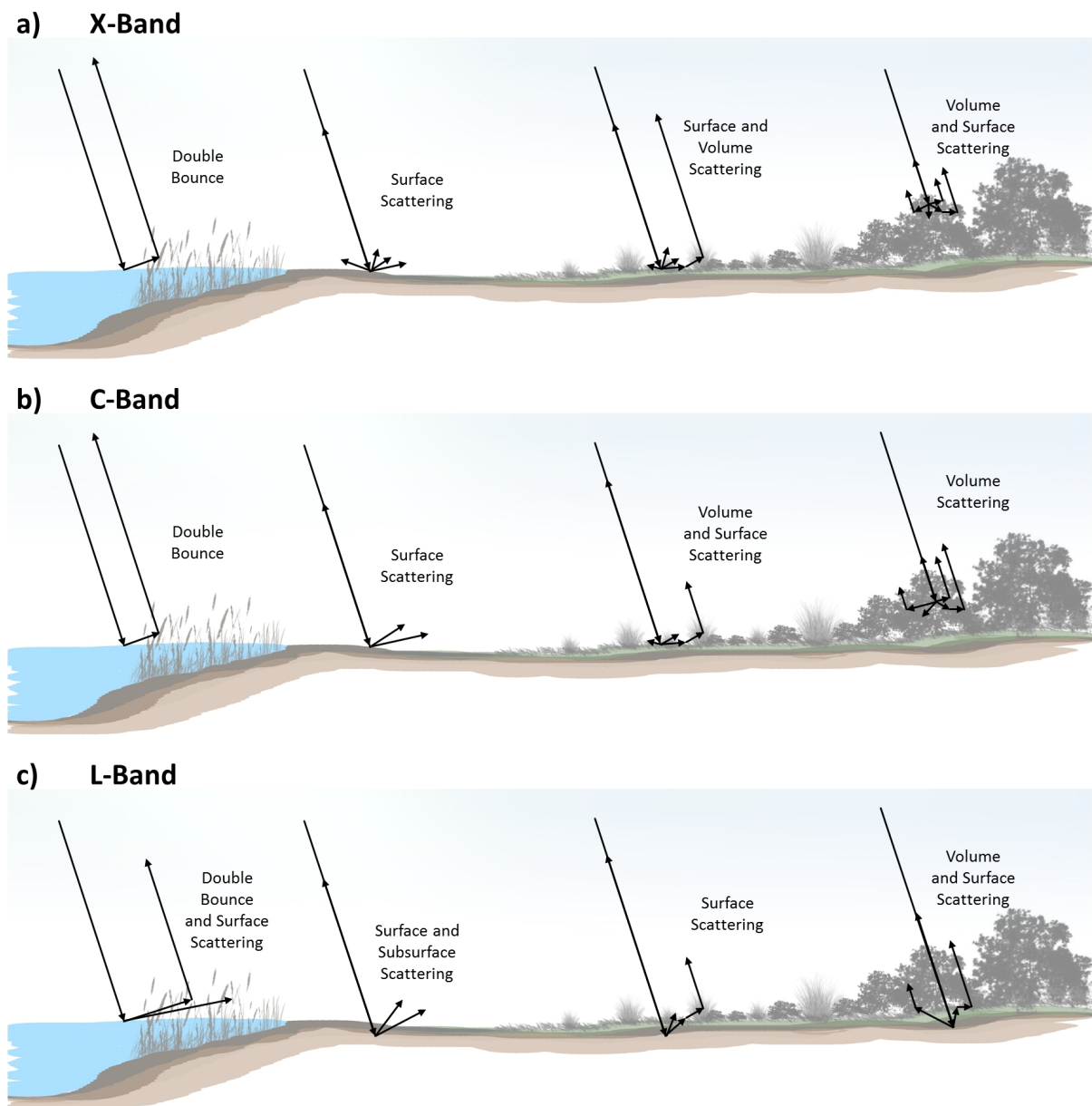


Figure 3.4: Schematic interaction of the electromagnetic wave and tundra land cover: a) X-Band, b) C-Band and c) L-Band. Regardless of the wavelength the wetland vegetation shows a double bounce signal due to the interaction of the electromagnetic wave with the water surface and the vegetation. Surface scattering of the X- and C-Band is likely for bare ground surfaces without vegetation coverage. The L-Band data show only little volume scattering but mainly surface scattering due to the long wavelength. In contrast, X- and C-Band show volume scattering for medium-sized vegetation and shrubs. The description of land cover is shown in Figure 2.13. Source: Own Figure.

### 3 Methodology

The complex scattering amplitude  $\sigma_i$  can be expressed in terms of incidence wave  $\vec{E}^i$  and scattered wave  $\vec{E}^b$  as shown in Equation 3.2.  $R$  denotes the distance between platform and target. Further,  $\vec{R}$  defines the direction of propagation during the transmittance. The scattered wave  $\vec{E}$  therefore has  $-\vec{R}$  direction (Richards (2009), p. 77). This relation between the directions of the scattered and the incidence waves is defined as back scatter alignment (BSA). The alignment that denotes the backscatter wave in direction of its propagation is called forward scatter alignment (FSA). The BSA is usually used and also used in this work because the coordinate systems of transmitting and receiving coincide (Boerner (2008), p.28-29). The polarization of an electromagnetic wave is orthogonal to  $\vec{R}$ . For linear polarizations the vertical component (V) and horizontal component (H) are described as  $\vec{E}_V^b$  and  $\vec{E}_H^b$ , with  $\vec{E}_V^b \perp \vec{E}_H^b \perp \vec{R}$  (Richards (2009), p. 82).

$$\sigma_i = 4\pi R^2 \frac{|\vec{E}^b|^2}{|\vec{E}^i|^2} \quad (3.2)$$

The relationship between incidence and scattered waves (Equation 3.1 and Equation 3.2) is expressed in form of a matrix (Equation 3.3). The vertical and horizontal components of the scattered wave are defined by the scattering amplitudes and the vertical and horizontal components of the incidence wave ( $E_H^i$ ;  $E_V^i$ ). The matrix  $S_2$  is called scattering matrix or Sinclair Matrix. This matrix is the most common form to display the complex polarimetric information. The  $S_2$  matrix of a full-polarimetric linear SAR system is composed by the four individual polarization channels (Equation 3.4). Assuming that HV is equal VH (reciprocity) the matrix  $S_2$  reduces to a symmetric matrix and is shown by Equation 3.4 (Boerner (2008), p.30). For dual-polarized data the scattering matrix  $S_2$  is reduced to the two channels that were acquired by the system.

$$\begin{bmatrix} E_H^b \\ E_V^b \end{bmatrix} = S_2 \begin{bmatrix} E_H^i \\ E_V^i \end{bmatrix} \quad (3.3)$$

$$S_2 = \begin{bmatrix} S_{HH} & S_{HV} \\ S_{VH} & S_{VV} \end{bmatrix} = \begin{bmatrix} S_{HH} & S_{HV} \\ S_{HV} & S_{VV} \end{bmatrix}, S_{HV} = S_{VH} \quad (3.4)$$

A single element ( $S_i$ ) of the Sinclair Matrix stores the complex scattering coefficient of a given target (pixel) and for each polarization (e.g. HH). Each pixel of a SAR image has a complex number for each polarization channel. The scattering coefficient is a complex number and expressed either in Cartesian or Polar Coordinates. The Cartesian Coordinates are the real and imaginary parts of the complex number. These show the signal as two coordinates  $a$  and  $b$  (Equation 3.5) (Richards (2009), p. 322). The Polar Coordinates display the magnitude (or radial coordinate) that is defined as amplitude in power domain  $Am_i$  (Equation 3.6) and as intensity  $I_i$  (Equation 3.7). The polar angle of a Polar Coordinate is defined as phase  $\phi_i$  (Equation 3.8) (Richards (2009), p. 321-322). Figure 3.5 illustrates the amplitude, wavelength, intensity and phase. Examples of the intensity and further selected features are shown in Figure 3.6.

$$S = a + jb, j = \sqrt{-1} \quad (3.5)$$

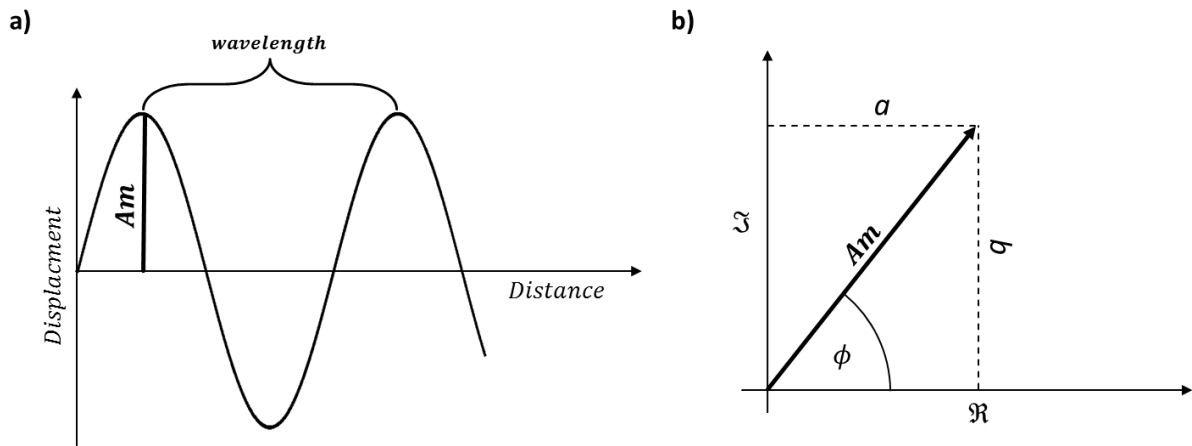


Figure 3.5: Illustration of the SAR signal: a) amplitude  $Am$ , wavelength and b) amplitude  $Am$ , phase  $\phi$ , real part ( $\Re$ ) of the complex number ( $a$ ) and imaginary part ( $\Im$ ) of the complex number ( $b$ ). Source: Own Figure.

$$Am = |S| = \sqrt{a^2 + b^2} \quad (3.6)$$

$$I = Am^2 = a^2 + b^2 \quad (3.7)$$

$$\phi = \tan^{-1} \left( \frac{b}{a} \right) \quad (3.8)$$

The scattering matrix can be transferred to other matrix representations. The intention of such transformations is to get a descriptor that is “[...] *perhaps more suited to [be analyzed] by [...] classification techniques [...]*” (Richards (2009), p. 85). The complex elements of the scattering matrix are commonly transformed to so called target vectors. These target vectors hold the polarimetric information in vector form. A target vector may be defined by combining the complex elements of the scattering matrix. Therefore, an infinite number of representations of the polarimetric information is possible but only some of them are “[...] *convenient to interpret the information [...]*” (ESA (2014a), Chapter 4, p. 1). The information of PolSAR data is usually converted to one of the following matrices: the Coherency Matrix (T-Matrix), the Covariance Matrix (C-Matrix) and the Kennaugh Matrix (K-Matrix). The T-, C- and K-Matrices can be converted into each other by linear transformations.

### Covariance Matrix C

The Covariance Matrix  $C$  is formulated by multiplying the target vector with its conjugated transpose. The Covariance Matrix expresses the “[...] *inter-relationship between the different channels, rather than the channels themselves.*” (Woodhouse (2005) p. 81). The Covariance Matrix can be defined for quad-polarized, co-polarized and cross-polarized data. All polarimetric decompositions can be solved using the Covariance Matrix and the data of the Covariance Matrix are assumed to be Wishart distributed (multivariate Chi-Square Distribution). The following equations show the definition of the Covariance Matrix  $C$  for quad- and dual-polarized systems.

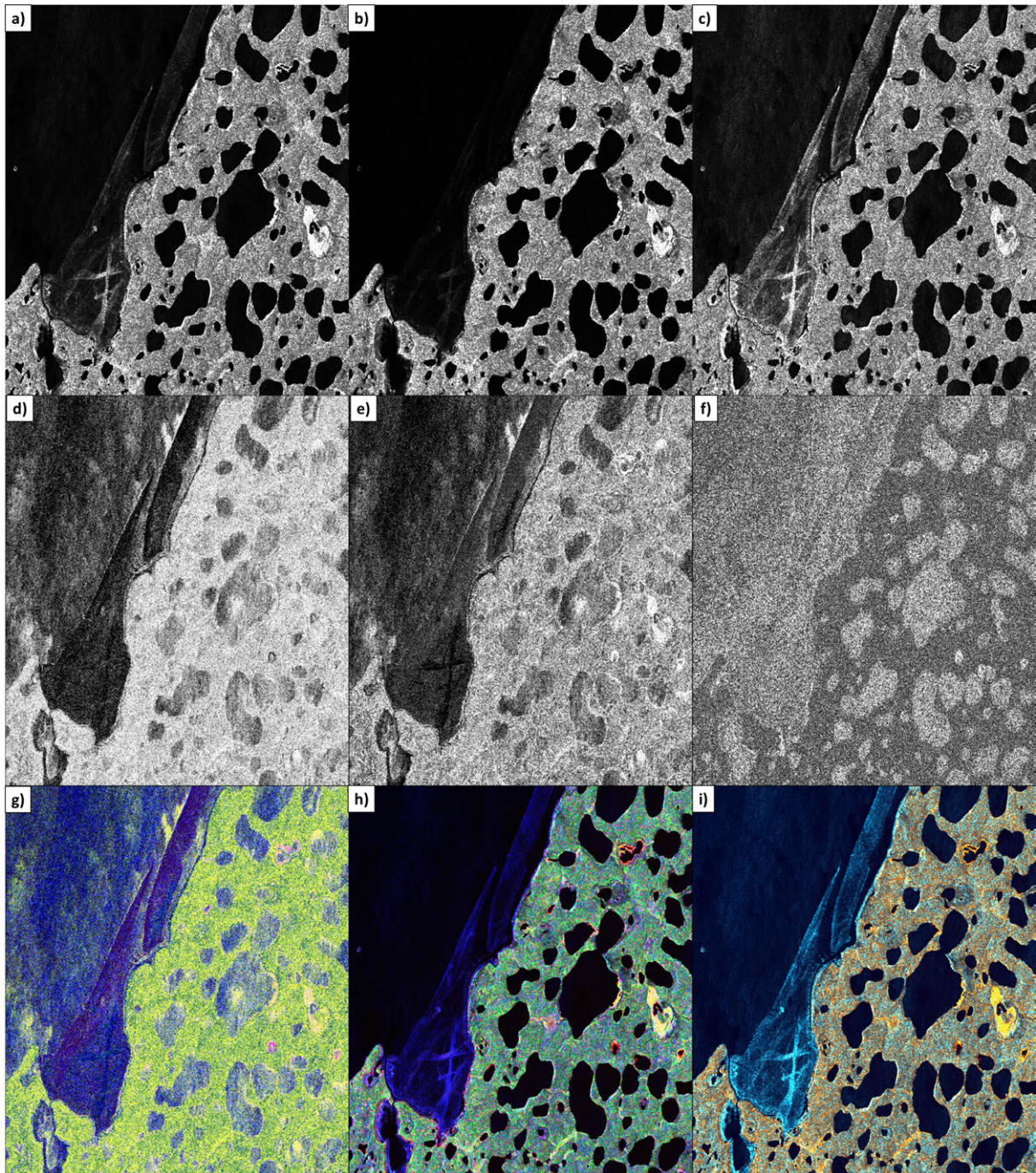


Figure 3.6: Image examples of selected PolSAR features of Radarsat-2: a) HH intensity, b) HV intensity, c) VV intensity, d) Entropy, e) Alpha of T-Matrix, f) Anisotropy, g) false color composite of Entropy/Alpha/Anisotropy Decomposition features (R=Alpha, G=Entropy, B=Anisotropy), h) false color composite of Yamaguchi Decomposition features (R=double bounce, C=volume scattering, B=surface scattering) and i) false color composite of Two Decomposition features (R=double bounce, C=surface scattering, B=difference between surface scattering and double bounce). Source: Own Figure.



**Quad-Polarized** - Invoking reciprocity ( $S_{HV} = S_{VH}$ ), the target vector  $k_c$  of  $C$  reduces to three complex elements (Equation 3.9):

$$k_c = \begin{pmatrix} S_{HH} \\ \sqrt{2}S_{HV} \\ S_{VV} \end{pmatrix} \quad (3.9)$$

The Matrix  $C$  is defined by the multiplication of  $k_c$  with its conjugated transpose  $k_c^+$  (Equation 3.10). The result is a matrix with 3x3 elements. The off-diagonal elements of this matrix show the inter-relationships between the three channels and are complex numbers. The diagonal elements are the absolute intensities of the channels and real numbers (Equation 3.10).

$$C = \langle k_c k_c^+ \rangle = \begin{bmatrix} |S_{HH}|^2 & \sqrt{2}S_{HH}S_{HV}^* & S_{HH}S_{VV}^* \\ \sqrt{2}S_{HV}S_{HH}^* & 2|S_{HV}|^2 & \sqrt{2}S_{HV}S_{VV}^* \\ S_{VV}S_{HH}^* & \sqrt{2}S_{VV}S_{HV}^* & |S_{VV}|^2 \end{bmatrix} \quad (3.10)$$

**Dual-Polarized** - For dual-polarized data  $C$  is computed by multiplying the reduced target vector  $k_c$  (Equation 3.11) with its conjugated transpose  $k_c^+$ .

$$k_c = \begin{pmatrix} S_{HH} \\ S_{VV} \end{pmatrix} \text{ or } k_c = \begin{pmatrix} S_{XX} \\ S_{XY} \end{pmatrix} \quad (3.11)$$

The Covariance Matrix  $C$  is a 2x2 hermitian matrix. It either shows the co-polarized (Equation 3.12) or cross-polarized  $C$  (Equation 3.13) information. The off-diagonal elements of this matrix show the inter-relationships between the two channels and are complex numbers. The diagonal elements are the absolute intensities of the two channels and are real number. All elements of a dual-polarized  $C$  are elements of a quad-polarized  $C$ .

$$C = \langle k_c k_c^+ \rangle = \begin{bmatrix} |S_{HH}|^2 & S_{HH}S_{VV}^* \\ S_{VV}S_{HH}^* & |S_{VV}|^2 \end{bmatrix} \quad (3.12)$$

$$C = \langle k_c k_c^+ \rangle = \begin{bmatrix} |S_{XX}|^2 & \sqrt{2}(S_{XX}S_{XY}^*) \\ \sqrt{2}(S_{XY}S_{XX}^*) & |S_{XY}|^2 \end{bmatrix} \quad (3.13)$$

### Coherency Matrix T

One other common descriptor of polarimetric information is the Coherency Matrix  $T$ . It is defined by the multiplication of the target Pauli Vector with its conjugated transpose. The Coherency Matrix is defined for quad-polarized and co-polarized data. It can directly be converted to the Covariance or the Kennaugh Matrix. All polarimetric decompositions can be solved using this matrix. The distribution of the Coherency Matrix is assumed to be a complex Wishart Distribution. The following equations show the definition of the Coherency Matrix  $T$  for quad- and co-polarized data.

**Quad-Polarized** - The Coherency Matrix  $T$  is computed by multiplying the target Pauli Vector  $k_\tau$  (Equation 3.14) with its conjugated transpose  $k_\tau^+$  and assuming reciprocity. The Pauli Vector is used with the emphasis to highlight the phase difference between the HH channel and the VV channel. The phase

### 3 Methodology

relation of these two channels is a key discriminator for the differentiation of the type of backscatter (Richards (2009), p. 81).

$$k_\tau = \frac{1}{\sqrt{2}} \begin{pmatrix} S_{HH} + S_{VV} \\ S_{HH} - S_{VV} \\ 2S_{HV} \end{pmatrix} \quad (3.14)$$

The Coherency Matrix  $T$  is a 3x3 hermitian matrix. The element  $T_{11}$  is known to be sensitive to surface scattering, element  $T_{22}$  to double bounce scattering and element  $T_{33}$  to volume scattering. In case of non reflection symmetry the off-diagonal element  $T_{23}$  is a discriminator for helix scattering. In case of ideal reflection symmetry the elements  $T_{12}$ ,  $T_{13}$  and  $T_{23}$  reduce to zero (Richards (2009), p. 89). The off-diagonal elements of this matrix show the inter-relationships between the elements of the Pauli Vector and are complex numbers. The diagonal elements are the absolute intensities of the Pauli Vector and are real numbers.

$$T = \langle k_\tau k_\tau^+ \rangle = \begin{bmatrix} T_{11} & T_{12} & T_{13} \\ T_{12}^* & T_{22} & T_{23} \\ T_{13}^* & T_{23}^* & T_{33} \end{bmatrix} \quad (3.15)$$

$$T = \frac{1}{2} \begin{bmatrix} |S_{HH}|^2 + 2\Re(S_{HH}S_{VV}^*) + |S_{VV}|^2 & |S_{HH}|^2 - 2j\Im(S_{HH}S_{VV}^*) - |S_{VV}|^2 & 2S_{HH}S_{HV}^* + 2S_{VV}S_{HV}^* \\ |S_{HH}|^2 + 2j\Im(S_{HH}S_{VV}^*) - |S_{VV}|^2 & |S_{HH}|^2 - 2\Re(S_{HH}S_{VV}^*) + |S_{VV}|^2 & 2S_{HH}S_{HV}^* - 2S_{VV}S_{HV}^* \\ 2S_{HV}S_{HH}^* + 2S_{HV}S_{VV}^* & 2S_{HV}S_{HH}^* - 2S_{HV}S_{VV}^* & 4|S_{HV}|^2 \end{bmatrix} \quad (3.16)$$

**Dual-Polarized** - For co-polarized data  $T$  is computed using the reduced complex Sinclair Matrix elements.  $T$  is defined by the multiplication of the reduced Pauli Vector  $k_\tau$  (Equation 3.17) with its conjugated transpose  $k_\tau^+$ .

$$k_\tau = \frac{1}{\sqrt{2}} \begin{pmatrix} S_{HH} + S_{VV} \\ S_{HH} - S_{VV} \end{pmatrix} \quad (3.17)$$

The Coherency Matrix  $T$  of co-polarized data is a 2x2 hermitian matrix (Equation 3.18). The element  $T_{11}$  is known to be sensitive to surface scattering and the element  $T_{22}$  to double bounce scattering. No information on HV and on the volume or helix scattering can be derived since the cross-polarized information is missing. All elements of a co-polarized  $T$  are elements of a quad-polarized  $T$ . The elements of the co-polarized  $T$  are the upper left 2x2 elements the quad-polarized  $T$ .

$$T = \langle k_\tau k_\tau^+ \rangle = \begin{bmatrix} T_{11} & T_{12} \\ T_{12}^* & T_{22} \end{bmatrix} \quad (3.18)$$

$$T = \frac{1}{2} \begin{bmatrix} |S_{HH}|^2 + 2\Re(S_{HH}S_{VV}^*) + |S_{VV}|^2 & |S_{HH}|^2 - 2j\Im(S_{HH}S_{VV}^*) - |S_{VV}|^2 \\ |S_{HH}|^2 + 2j\Im(S_{HH}S_{VV}^*) - |S_{VV}|^2 & |S_{HH}|^2 - 2\Re(S_{HH}S_{VV}^*) + |S_{VV}|^2 \end{bmatrix} \quad (3.19)$$

### Kennaugh Matrix $K$

The polarimetric information can be expressed by the Mueller or Kennaugh Matrix (Guissard (1994)). The Kennaugh Matrix is the BSA form of the Mueller Matrix (FSA). The Kennaugh Matrix describes the relation between the radiated and received wave in form of a 4x4 matrix using only real elements (Schmitt (2009), Schmitt et al. (2015)). The Kennaugh Matrix is also called Stokes Matrix and can be converted to the Covariance or Coherency Matrix. The formulation and definition of the Kennaugh Matrix is shown here in accordance to Schmitt (2009), Schmitt et al. (2015). The Matrix is symmetric and the single elements of the matrix are linear combinations of the Sinclair Matrix elements. The Kennaugh Matrix can be expressed in the same form for coherent and incoherent scattering processes - in contrast to  $T$  or  $C$ . Schmitt (2009), Schmitt et al. (2015) showed different ways to transform the  $K$ -Matrix and furthermore showed the anticipated distributions (probability density functions) of the elements of the Kennaugh Matrix.

**Quad-Polarized** - The Kennaugh Matrix  $K$  shows the relationship between received  $\begin{bmatrix} g_0 \\ g_1 \\ g_2 \\ g_3 \end{bmatrix}_{received}$  and radiated waves  $\begin{bmatrix} g_0 \\ g_1 \\ g_2 \\ g_3 \end{bmatrix}_{radiated}$  using the Stokes Vector  $\vec{g}$  (Equation 3.20). The Kennaugh Matrix  $K$  of quad-polarized data is defined by ten elements (Equation 3.20). The first element  $K_0$  holds the total received power (Schmitt (2009)).

$$\begin{bmatrix} g_0 \\ g_1 \\ g_2 \\ g_3 \end{bmatrix}_{received} = \begin{bmatrix} K_0 & K_4 & K_5 & K_6 \\ K_4 & K_1 & K_9 & K_8 \\ K_5 & K_9 & K_2 & K_7 \\ K_6 & K_8 & K_7 & K_3 \end{bmatrix} \begin{bmatrix} g_0 \\ g_1 \\ g_2 \\ g_3 \end{bmatrix}_{radiated}, \text{ with } \quad (3.20)$$

$$K_0 = \frac{1}{2}(|S_{xx}|^2 + |S_{xy}|^2 + |S_{yx}|^2 + |S_{yy}|^2)$$

$$K_1 = \frac{1}{2}(|S_{xx}|^2 - |S_{xy}|^2 - |S_{yx}|^2 + |S_{yy}|^2)$$

$$K_2 = \Re(S_{xy}S_{xy}^* + S_{xx}S_{yy}^*)$$

$$K_3 = -\Re(S_{xy}S_{xy}^* - S_{xx}S_{yy}^*)$$

$$K_4 = \frac{1}{2}(|S_{xx}|^2 - |S_{xy}|^2 + |S_{yx}|^2 - |S_{yy}|^2)$$

$$K_5 = \Re(S_{xx}S_{xy}^* + S_{xy}S_{yy}^*)$$

$$K_6 = \Im(S_{xx}S_{xy}^* + S_{xy}S_{yy}^*)$$

$$K_7 = \Im(S_{xx}S_{yy}^*)$$

$$K_8 = \Im(S_{xx}S_{xy}^* - S_{xy}S_{yy}^*)$$

$$K_9 = \Re(S_{xx}S_{xy}^* - S_{xy}S_{yy}^*)$$

**Dual-Polarized** - The Kennaugh Matrix  $K$  is defined for co-polarized data by Equation 3.21 and by Equation 3.22 for cross-polarized data. In both cases  $K$  is a symmetric 4x4 matrix with real elements.

$$K_{co} = \begin{bmatrix} K_0 & K_4 & 0 & 0 \\ K_4 & 0 & 0 & 0 \\ 0 & 0 & 0 & K_7 \\ 0 & 0 & K_7 & K_3 \end{bmatrix}, \text{ with } \quad (3.21)$$

### 3 Methodology

$$K_0 = \frac{1}{2}(|S_{xx}|^2 + |S_{yy}|^2)$$

$$K_3 = -\Re(S_{xx}S_{yy}^*)$$

$$K_4 = \frac{1}{2}(|S_{xx}|^2 - |S_{yy}|^2)$$

$$K_7 = \Im(S_{xx}S_{yy}^*)$$

$$K_{cross} = \begin{bmatrix} K_0 & 0 & K_5 & K_6 \\ 0 & K_1 & 0 & 0 \\ K_5 & 0 & 0 & 0 \\ K_6 & 0 & 0 & 0 \end{bmatrix}, \text{ with} \quad (3.22)$$

$$K_0 = \frac{1}{2}(|S_{xx}|^2 + 2|S_{xy}|^2)$$

$$K_1 = \frac{1}{2}(|S_{xx}|^2 - 2|S_{xy}|^2)$$

$$K_5 = \Re(S_{xx}S_{xy}^*)$$

$$K_6 = \Im(S_{xx}S_{xy}^*)$$

#### Polarimetric Decompositions

The information of PolSAR data can further be transformed to other features that facilitate the interpretation of the PolSAR signal in terms of the backscattering processes and properties. The most common way to transform the data is the application of a decomposition model. A decomposition model thereby decomposes the total received energy - which is called span and the sum of all acquired channels - into individual components (Cloude & Pottier (1996)). The aim of a decomposition is to display the span at a certain location (pixel) as the sum of a finite number of elements, e.g. as a sum of double bounce, surface bounce and volume scattering intensities. The frequently used decomposition models are the Power Decompositions (e.g. Freeman-Durden Decomposition, the Yamaguchi Decomposition) and the eigendecompositions (e.g. Cloude Pottiers' Entropy/Alpha decomposition).

The most decomposition models were designed to be used with quad-polarized data. The idea of the decomposition is to derive features that help to characterize the backscattering process and to facilitate the interpretation and classification of the PolSAR data. Thereby the decomposition features help to evaluate the relation between signal and physical properties of the earth surface, e.g. moisture conditions or land cover properties. For example, the identification of a double bounce scattering will likely help to identify wetlands since the shape and arrangement of the wetland vegetation facilitates the generation of a double bounce signal. A single bounce signal will likely be in relation to plan surfaces - such as bare or sparsely vegetated ground.

Since PolSAR data are operationally available numerous decomposition models have been developed (Cloude & Pottier (1996), Touzi et al. (2004)). These models can be grouped in incoherent and coherent models (Richards (2009)). The coherent models are applied to characterize the scattering from pure targets that truly have a polarized backscatter (e.g. single isolated targets). In contrast, the incoherent models are applied to characterize distributed targets. The targets of natural landscapes are usually considered as distributed and the analysis of the PolSAR signal is not based on the information of a single pixel but on the sample statistics of that pixel's neighborhood. This is realized by spatial averaging of the Covariance, Coherency or Kennaugh Matrices with an estimation window. The landscape of the Arctic

can generally be considered as natural landscape in the sense of the named discrimination. The incoherent models used for this work were the Entropy/Alpha decomposition of quad- and dual-polarized data and the Yamaguchi Decomposition. The Yamaguchi Decomposition Model was applied to the quad-polarized data and the co-polarized data (Two-Component Decomposition Model shown by Ullmann et al. (2014)). These decomposition models were selected since they are frequently used, have a comparable uncomplex interpretation, help to understand the relation between observation and process and can be applied to quad- and dual-polarized data. The following subsections show how the decomposition models are defined for quad- and dual-polarized data. The sections further give information on the interpretation of the decomposition features with regard to the land cover. All of the decomposition models shown in the following were implemented in a PolSAR Toolbox in IDL and ENVI. The IDL/ENVI models were verified by comparing the results to PolSARpro (ESA (2014a)) and the Radar-Tools (RAT).

**Quad-Polarized - Yamaguchi Decomposition** - The first who introduced a power decomposition model in the classical sense were Freeman and Durden (Freeman & Durden (1998)). Yamaguchi et al. (2005) developed an adapted form of this model. The model is a four component decomposition model but it is usually applied as a three component model. The four component model is decomposing the span into the scattering power components (intensities) of surface scattering  $P_s$ , double bounce scattering  $P_d$ , volume scattering  $P_v$  and helix scattering  $P_h$ . The model is solved using the spatially averaged Coherency Matrix  $\langle |T| \rangle$ . It may also be solved using the Covariance or Kennaugh Matrix. The native Yamaguchi model is designed for quad-polarized data and invokes reciprocity (HV=VH). The modeling of double bounce and surface scattering is based on the utilization of the phase difference between HH and VV. This phase relation is expressed by the coefficients  $\alpha$  and  $\beta$ . The model is further based on the criteria of Bragg scattering and uses the reflection coefficients  $R_h$  and  $R_v$ . Further information on the Bragg scattering is provided by Richards (2009), p. 136 ff.

The three component model decomposes the span into the intensities of double bounce, surface and volume scattering. Yamaguchi et al. (2005) further showed how this decomposition model can be modified to take the rotation of the Coherency Matrix into account (Yamaguchi et al. (2010)). The rotation is used to minimize the cross-polarized component. The Yamaguchi Decomposition of quad-polarized data was processed here using the original definition. The decomposition equation is shown in Equation 3.23 for the four component model. If the three component model is used  $P_h$  is set to zero. Equation 3.24 and Equation 3.25 show the extended decomposition approach introducing the expansion coefficients  $f_s, f_d, f_v, f_h$  and the surface, double bounce, volume and helix scattering models  $|T|_{surface}, |T|_{double}, |T|_{vol}, |T|_{helix}$ . The surface and double bounce models are defined by the coefficients  $\alpha$  and  $\beta$ . These are defined as shown by Yamaguchi et al. (2005). The approach therefore has five equations and the six variable  $f_s, f_d, f_v, f_h, \alpha, \beta$ . The definition of two cases allows to reduce the variables. Then the system is overdetermined and solvable. These cases are  $\Re(S_{xx}S_{yy}^*) \geq 0$ , with  $\alpha = 0$  and  $\Re(S_{xx}S_{yy}^*) < 0$ , with  $\beta^* = 0$ . The term  $\Re(S_{xx}S_{yy}^*)$  is used to distinguish between dominant surface scattering (first case) and dominant double bounce (second case). Image examples of the Three Component decomposition features are shown in Figure 3.6.h.

$$span = P_s + P_d + P_v + P_h \quad (3.23)$$

### 3 Methodology

$$\langle |T| \rangle = f_s |T|_{surface} + f_d |T|_{double} + \frac{f_v}{4} |T|_{vol} + \frac{f_h}{2} |T|_{helix} \quad (3.24)$$

$$\langle |T| \rangle = f_s \begin{bmatrix} 1 & \beta^* & 0 \\ \beta & |\beta|^2 & 0 \\ 0 & 0 & 0 \end{bmatrix} + f_d \begin{bmatrix} |\alpha|^2 & \alpha & 0 \\ \alpha^* & 1 & 0 \\ 0 & 0 & 0 \end{bmatrix} + \frac{f_v}{4} \begin{bmatrix} 2 & 0 & 0 \\ 0 & 1 & 0 \\ 0 & 0 & 1 \end{bmatrix} + \frac{f_h}{2} \begin{bmatrix} 0 & 0 & 0 \\ 0 & 1 & \pm j \\ 0 & \pm j & 1 \end{bmatrix}, \text{ with} \quad (3.25)$$

**Dual-Polarized - Two Component Decomposition** - The models of surface scattering and double bounce are based on the co-polarized information. A straight forward approach is to decompose the span of co-polarized data into the scattering power components of surface  $P_s$  and double bounce  $P_d$  (Equation 3.26) (Ullmann et al. (2014)). The scattering power components volume and helix scattering are not obtainable due to the missing cross-polarized information. Therefore the features  $P_s$  and  $P_d$  are different to the features  $P_s$  and  $P_d$  of quad-polarized data since they are not adjusted to the cross-polarized information. The model is based on the expansion coefficients  $f_s, f_d$  and the surface and double bounce scattering models  $|T|_{surface}, |T|_{double}$  (Equation 3.28). The scattering models are defined via the coefficients  $\alpha$  and  $\beta$  as shown by Yamaguchi et al. (2005).

$$span = P_s + P_d \quad (3.26)$$

$$\langle |T| \rangle = f_s |T|_{surface} + f_d |T|_{double} \quad (3.27)$$

$$\langle |T| \rangle = f_s \begin{bmatrix} 1 & \beta^* \\ \beta & |\beta|^2 \end{bmatrix} + f_d \begin{bmatrix} |\alpha|^2 & \alpha \\ \alpha^* & 1 \end{bmatrix}, \text{ with} \quad (3.28)$$

This approach leads to three equations and the four variable  $f_s, f_d, \alpha, \beta$ . The left hand side of each equation is given by the values  $T_{11}, T_{12}$ , and  $T_{22}$  (coefficients  $A, B$  and  $C$ ) of the spatially averaged co-polarized Coherency Matrix  $\langle |T| \rangle$  (Equation 3.29, Equation 3.30 and Equation 3.31).

$$A = T_{22} = \frac{1}{2} \langle |S_{HH} - S_{VV}|^2 \rangle = f_s |\beta|^2 + f_d \quad (3.29)$$

$$B = T_{11} = \frac{1}{2} \langle |S_{HH} + S_{VV}|^2 \rangle = f_s + f_d |\alpha|^2 \quad (3.30)$$

$$C = T_{12} = \frac{1}{2} \langle (S_{HH} + S_{VV})(S_{HH} - S_{VV})^* \rangle = f_s \beta^* + f_d \alpha \quad (3.31)$$

Again two cases are distinguished to solve the equation system: Case 1 when surface scattering is dominant ( $\Re(S_{xx}S_{yy}^*) \geq 0$ , with  $\alpha = 0$ ) and Case 2 when double bounce scattering is dominant ( $\Re(S_{xx}S_{yy}^*) < 0$ , with  $\beta^* = 0$ ). The unknowns  $f_s, f_d, \alpha, \beta$  are then defined by Equation 3.32, Equation 3.33 and Equation 3.34 for Case 1 and by the Equation 3.35, Equation 3.36 and Equation 3.37 for Case 2.

**Case 1:**  $\Re(S_{xx}S_{yy}^*) \geq 0$ , with  $\alpha = 0$

$$f_s = B \quad (3.32)$$

$$f_d = A - \left( \frac{|C|^2}{B} \right) \quad (3.33)$$

$$\beta^* = \frac{C}{B} \quad (3.34)$$

**Case 2:**  $\Re(S_{xx}S_{yy}^*) < 0$ , with  $\beta^* = 0$

$$f_d = A \quad (3.35)$$

$$f_s = B - \left( \frac{|C|^2}{A} \right) \quad (3.36)$$

$$\alpha = \frac{C}{A}, \text{ with} \quad (3.37)$$

The scattering power components of surface  $P_s$  and double bounce  $P_d$  are finally derived via Equation 3.38 and Equation 3.39. Image examples of the Two Component decomposition features are shown in Figure 3.6.i.

$$P_s = f_s(1 + |\beta|^2) \quad (3.38)$$

$$P_d = f_d(1 + |\alpha|^2) \quad (3.39)$$

**Quad-Polarized - Entropy/Alpha decomposition** - The Coherency and Covariance Matrix of dual or quad-polarized systems can be decomposed using the eigendecomposition approach that is described by Cloude (2010), p. 192 ff and Richards (2009), p. 288 ff. The eigendecomposition utilizes the diagonal matrix of the eigenvalues  $\Lambda$  and the unitary matrix of the eigenvectors  $U$ . Assuming reciprocity, three eigenvalues  $\lambda$  and three eigenvectors  $u$  are obtained for quad-polarized data (Equation 3.40). The spatially averaged Coherency Matrix  $\langle |T| \rangle$  is then displayed as the summed product of all eigenvectors and eigenvalues. The eigenvalues of the Coherency and the Covariance Matrix are real and are the same - the eigenvectors differ from each other.

$$\langle |T| \rangle = U\Lambda U^+ = U \begin{bmatrix} \lambda_1 & 0 & 0 \\ 0 & \lambda_2 & 0 \\ 0 & 0 & \lambda_3 \end{bmatrix} U^+ = \lambda_1 u_1 u_1^+ + \lambda_2 u_2 u_2^+ + \lambda_3 u_3 u_3^+ \quad (3.40)$$

These eigenvalues and eigenvectors were used by Cloude and Pottier to derive further parameters that describe the properties of the scattering process (Cloude & Pottier (1996)). This approach is the frequently

### 3 Methodology

applied Entropy/Alpha Decomposition. The features Entropy  $H$  and Alpha  $\underline{\alpha}$  describe the backscattering properties of a pixel in an incoherent way. The Entropy (Equation 3.41) can be interpreted as the degree of randomness of the scattered signal (Equation 3.42). It is described by the logarithmic sum of the pseudo probabilities  $p$  of the eigenvalues and ranges from zero to one. The scattering angle Alpha  $\underline{\alpha}$  is the sum of inverse cosine of the absolute value of the eigenvectors and is weighted by the pseudo probabilities  $p$  (Equation 3.43). The Alpha of the T-Matrix indicates the type of backscattering since Alpha is a descriptor of the Pauli feature space (see Equation 3.14): a low Alpha value can be interpreted as dominant single bounce, a medium Alpha value as volume scattering and a high Alpha value as dominant double bounce. The Alpha of the C-Matrix quantifies the relation between the polarization channels and its calculation is based on the channel information (see Equation 3.9). Alpha is usually shown between zero and ninety degree. In the following Alpha is shown in the value range from zero to one. Cloude and Pottier also showed a third feature that is calculated via the ratio between the difference and the sum of the second and third eigenvalue. This feature is defined as Anisotropy  $A$  (Equation 3.44) and indicates the relevance of secondary scattering processes. Image examples of the decomposition features are shown in Figure 3.6.g.

$$H = -\sum_{i=1}^3 p_i \log_3(p_i) \quad (3.41)$$

$$p_i = \frac{\lambda_i}{\sum_{k=1}^3 \lambda_k} \quad (3.42)$$

$$\underline{\alpha} = \sum_{i=1}^3 p_i \cos^{-1}(|u_i|) \quad (3.43)$$

$$A = \frac{\lambda_2 - \lambda_3}{\lambda_2 + \lambda_3} \quad (3.44)$$

The three features Entropy  $H$ , Alpha  $\underline{\alpha}$  and Anisotropy  $A$  form a three dimensional feature space. The relation between the features and the feasible regions of this space are shown in Figure 3.7. More information on the relation of the features and how the feasible regions are defined is provided by Cloude (1997, 2010).

**Dual-Polarized - Entropy/Alpha decomposition** - The eigendecomposition can be applied to dual-polarized data as well. The decomposition is done following Equation 3.45 and Equation 3.46. For dual-polarized data two eigenvalues  $\lambda$  and two eigenvectors  $u$  are calculated. The approach decomposes the Coherency or Covariance Matrix of co-polarized data. It is also applicable for the Covariance Matrix of cross-polarized data.

$$T = U \Lambda U^+ = U \begin{bmatrix} \lambda_1 & 0 \\ 0 & \lambda_2 \end{bmatrix} U^+ = \lambda_1 u_1 u_1^+ + \lambda_2 u_2 u_2^+ \quad (3.45)$$

$$U = \begin{bmatrix} u_{11} & u_{12} \\ u_{21} & u_{22} \end{bmatrix} = \begin{bmatrix} u_1 & u_2 \end{bmatrix} \quad (3.46)$$



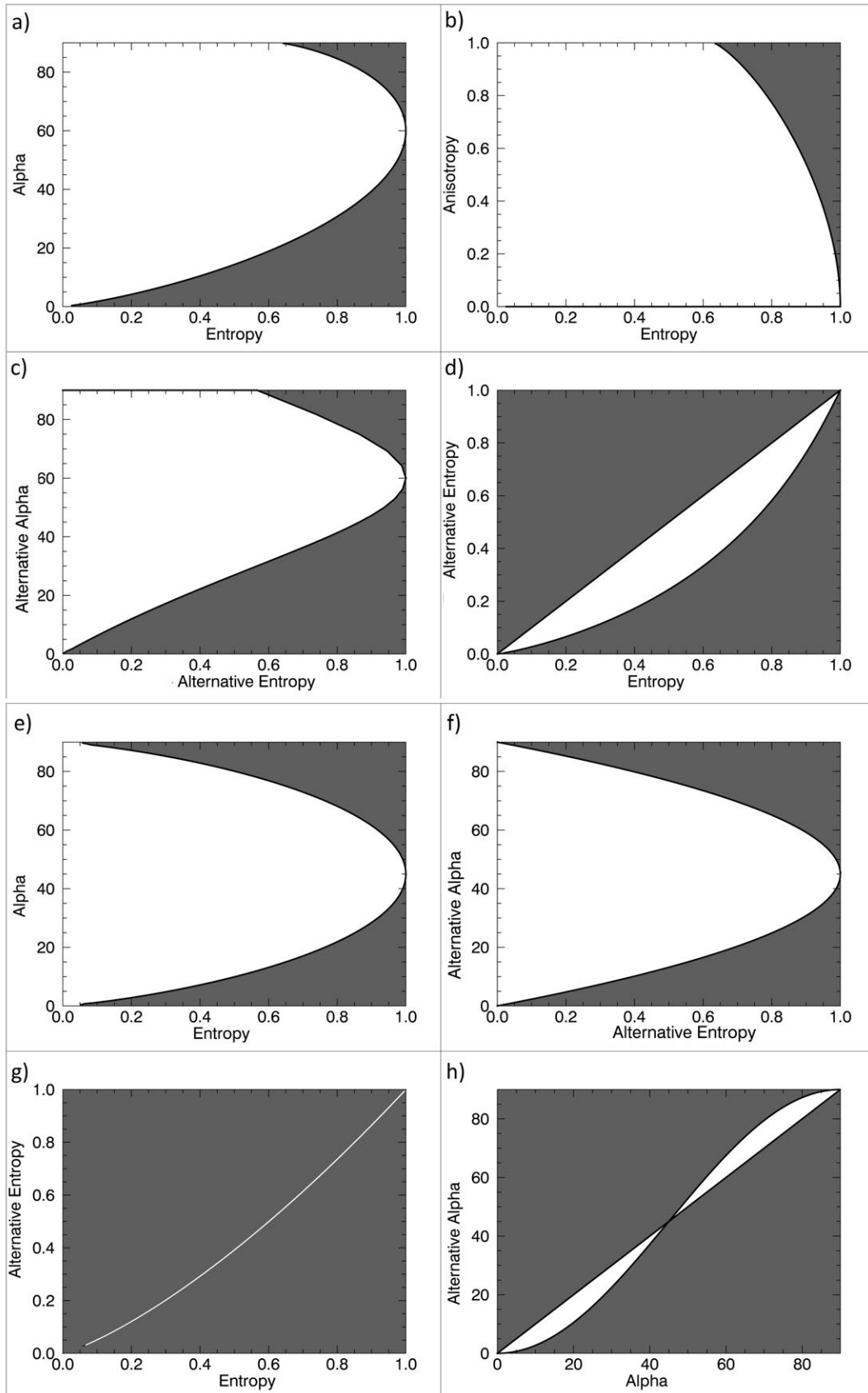


Figure 3.7: Feature spaces of: a) quad-polarized Entropy/Alpha, b) quad-polarized Entropy/Anisotropy, c) quad-polarized alternative Entropy/Alpha, d) quad-polarized classic and alternative Entropy, e) dual-polarized Entropy/Alpha, f) dual-polarized alternative Entropy/Alpha, g) dual-polarized classic and alternative Entropy and h) quad-/dual-polarized classic and alternative Alpha. Feasible regions are shown in white. Source: Own Figure.

### 3 Methodology

Cloude (2007) described the Entropy/Alpha decomposition of dual-polarized data. According to Shan et al. (2011) the decomposition may be done for co- and cross-polarized data. The Entropy  $H$  is calculated via the pseudo probabilities  $p$  of the eigenvalues (Equation 3.47). The Entropy describes the logarithmic sum of the pseudo probabilities and ranges from zero to one (Equation 3.47). The scattering angle Alpha  $\alpha$  has the same definition as above and is the sum of inverse cosine of the absolute value of the eigenvectors. It is weighted by the two pseudo probabilities (Equation 3.49). The interpretation must be done with regard to the two polarimetric channels (two eigenvalues and two eigenvectors). The Alpha angle of the T-Matrix indicates dominate double bounce if Alpha is greater 0.5 (45°). It indicates dominate surface scattering if the value is less than 0.5 (45°). Any value close to 0.5 indicates mixed scattering. The Alpha angle of the C-Matrix shows the relation between the two channels of the dual-polarized scattering matrix. If the Alpha angle of the C-Matrix of co-polarized data is greater than 0.5 (45°) HH scattering is dominant. If the value is less than 0.5 (45°) VV scattering is dominant.

$$p_i = \frac{\lambda_i}{\sum_{k=1}^2 \lambda_k} \quad (3.47)$$

$$H = -\sum_{i=1}^2 p_i \log_2(p_i) \quad (3.48)$$

$$\alpha = \sum_{i=1}^2 p_i \cos^{-1}(|u_i|) \quad (3.49)$$

**Quad-Polarized - Alternative Entropy/Alpha Decomposition-** An et al. (2010) suggested a fast way to receive parameters that have a very similar interpretation as the features Entropy and Alpha of Cloude's decomposition. The idea of this approach is to reduce the high computation load of the eigendecomposition (Shan et al. (2011)). The retrieval of this alternative features is shown in the following for quad- and dual-polarized data. For quad-polarized data the alternative features are defined by the Entropy subscript  $E$  (Equation 3.50) and the subscript of the Alpha of the T-Matrix  $\rho$  (Equation 3.51). Both features range from zero to one and have a fast processing. The computation is simply based on the ratios of Coherence Matrix elements. Further, Equation 3.51 and Equation 3.52 show how the Kennaugh Matrix elements can be used to define the subscript  $\rho_1$  of the Alpha of the T-Matrix and the subscript  $\rho_2$  of the Alpha of the C-Matrix. The subscripts have a very similar feature space compared to the classical features (see Figure3.7.c).

$$E = \frac{(Ea - 1)}{(\sqrt{3} - 1)} \text{ with, } Ea = \frac{span}{\sqrt{\sum_{i=1}^3 \sum_{j=1}^3 |T_{ij}|^2}} \quad (3.50)$$

$$\rho = \rho_1 = 1 - \frac{T_{11}}{span} = 1 - \frac{(K_0 - K_3)}{2K_0} \quad (3.51)$$

$$\rho_2 = 1 - \frac{(K_0 - K_4)}{2K_0} \quad (3.52)$$

**Dual-Polarized - Alternative Entropy/Alpha Decomposition-** The alternative Entropy/Alpha Decomposition can be applied to the dual-polarized data as well. The Entropy subscript  $E$  is then defined by the Equation 3.53 and the symbol  $F$  denotes the Forbenius norm. The subscript  $\rho$  of the Alpha T-Matrix is defined by Equation 3.51. The subscript  $\rho_1$  may be directly defined with the elements of a co-polarized Kennaugh Matrix (Equation 3.51). The subscript  $\rho_2$  is likewise defined by Equation 3.52. The feature space of subscript  $E$  and subscript  $\rho$  is very similar to the classical feature space (Figure 3.7.f). The classical Entropy  $H$  and the Entropy subscript  $E$  nearly have a linear correlation (Figure 3.7.g). The classical Alpha angle  $\underline{\alpha}$  and the Alpha angle subscript  $\rho$  form a sine feature space (Figure 3.7.h) (An et al. (2010), Shan et al. (2011)). Hereafter, the alternative Entropy and the alternative Alpha angle are referred to as Entropy and Alpha.

$$E = 2 \left( 1 - \left\| \frac{T}{span} \right\|_F^2 \right) \quad (3.53)$$

### 3.1.1.2 Speckle and Image Filtering

**Speckle Effect** - One of the most important effects that hinders the SAR data interpretation is the speckle effect. The speckle effect is frequently called multiplicative noise, however, Richards (2009), p. 124-125 notes: “[...] [speckle] is in reality just the way the reflections appear because of the irradiation with coherent energy [...]”. The speckle appears in form of (apparently) random brightness variations over homogenous regions. The effect is present because of the random distribution of targets within a resolution cell (pixel). These targets are incremental scatters and form the observed raw signal. That means that the signal is composed of individual components that come from individual targets. The more dominant a scattering of a certain target is, the less dominant is the speckle effect and the scattering from the other targets becomes negligible. The speckle is fully developed if the scattering of none of the targets is dominant. The distribution of the phase angles of such targets is then assumed to be uniform since the targets are randomly distributed in the pixel (Richards (2009), p.122). Figure 3.8.a illustrates the formation of fully developed speckle without a dominant target. Figure 3.8.b illustrates the formation of partially developed speckle with one dominant target.

The speckle effect can be reduced by averaging cells with similar speckle characteristics. This can be done either by temporal or spatial aggregation. The spatial aggregation is frequently applied and reduces the size and the spatial resolution of a SAR image by aggregating the information of neighboring pixels. The process of aggregation thereby enhances the radiometric quality of the image, it reduces the variance and is called multi-looking. The number of looks gives information on the number of cells that were aggregated. For example, the information of a pixel of an image with four looks is composed by aggregating four neighboring pixels. This may be done by halving the range and azimuth dimensions.

The total number of looks is the number of looks in range multiplied with those in azimuth. The original size of the image without any looks is called single-look (Richards (2009), p.124-127). More information on the application of multi-looking and the consequences for the SAR signal and its interpretation are provided by Richards (2009), p.342-345. Further information on the nature of speckle, its importance in SAR image analysis and also on the utilization of the speckle effect for the image classification is

### 3 Methodology

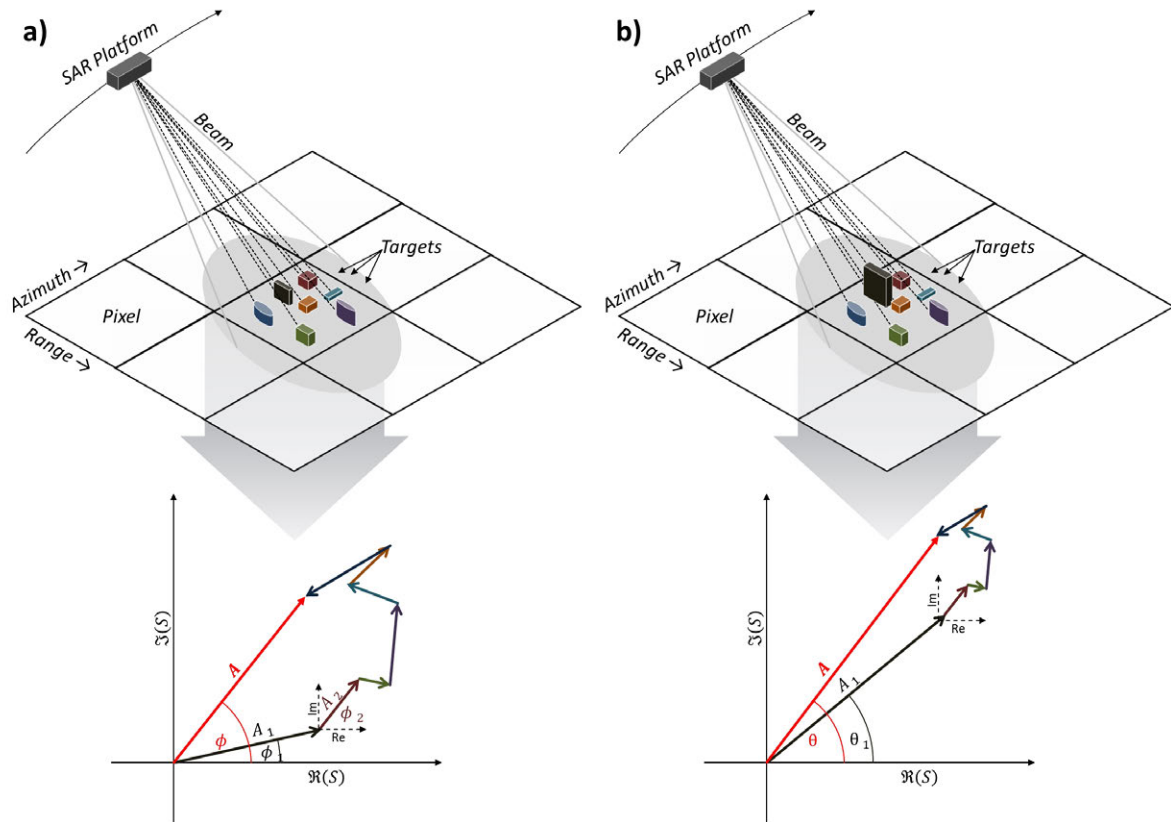


Figure 3.8: Formation of: a) fully and b) partially developed speckle. The targets are randomly distributed in the pixel. In a) none of the targets has a dominant scattering. In b) the scattering of the black target is dominant and the scattering of the other targets becomes negligible. Source: Own Figure.

provided by Lee & Grunes (1992), Richards (2009), Esch et al. (2011). The speckle can also be reduced by using so called speckle filters. These further “[...] improve the potential interpretability of the data.” (Richards (2009), p. 128) and enhance the suitability of the data for image classification (see Lee, Grunes & De-Grandi (1999), Moon-Kyung et al. (2010)). Richards (2009), p. 127 ff. illustrated that the averaging of neighboring pixels is an effective way to reduce the variance and speckle effect. This filtering may be done by moving window operators (convolutions). The two frequently applied and important speckle filters that operate in this way are the Boxcar and the Lee filter. Both are briefly described in the following.

**Boxcar Filter** - The Boxcar Filter is the most simple way of averaging the neighborhood of a pixel. A box of a certain size is centered on a pixel of interest and all of the pixels inside the box are averaged and form the new image value. The box is then moved to the next location (pixel) until all pixels of the image were visited. The size of the box regulates the number of elements that are used for the averaging. This method is very effective to reduce the variance but the Boxcar Filter also causes a blurring of the image. For example, this blurring is present at boundaries between two or more different land cover units, e.g. at the boundary between land and water. The blurring is also present if strong and weak scatterers are averaged. The size of the estimation window is typically between 3x3 and 21x21 pixels (Richards (2009), p.128-129). The algorithm of the Boxcar Filter is implemented in ENVI 5.1.

**Lee Filter** - The so called Lee Filters are methods to overcome this blurring. The principle of the Lee

Filter is to use more pixels for the averaging of homogeneous regions and less pixels for the averaging of heterogeneous regions. The application is similar to the Boxcar Filtering: A moving window is used, the values inside the box are averaged and form the new filtered pixel value. Not all of the pixels inside the box are used, however. Instead only pixels are used that are within a certain range around the mean value of the window. When using the Sigma Lee Filter, this range is defined by two standard deviations under assumption of a Gaussian Normal distribution (Richards (2009), p. 129-131). If the Enhanced Lee Filter is used then the cut-off values (thresholds) are estimated by values of the coefficient of variation. This coefficient is the ratio between the standard deviation and the mean (Esch et al. (2011)). The pixels under observation are classified in one of the three categories: "Homogeneous", "Heterogeneous" or "Point Target" - based on their coefficient of variation. If the pixel is of type "Homogeneous" the new filtered pixel value is the average of the filter window. If it is "Heterogeneous", then the new value is formed by weighted averaging. If it is "Point Target", the new value is the same as the old value. The thresholds used to define the classes are based on the number of looks of the radar image or on user defined values. The Enhanced Lee Filter preserves edges of the image, e.g. the edge between different land cover units, or between strong and weak scatterers, since the power of the filter is adapted by the coefficient of variation that indicates the appearance and the power of the speckle effect (Esch et al. (2011)). The size of the estimation window of a Lee Filter is typically between 5x5 and 21x21 pixels - but does not have an upper limit. Large windows will cause an blurring of the image and a longer computation time, however. The algorithms of the Sigma Lee Filter and the Enhanced Lee Filter are implemented in ENVI 5.1.

**Non-Local Means Filters** - The state of practice tends to use so called Non-Local Means filters that preserve the original image information, keep edges and reduce the speckle effect. This method was introduced by Buades et al. (2005). Its application for SAR and PolSAR data was shown by Deledalle et al. (2010), Parrilli et al. (2010), Deledalle et al. (2015), for example. The Non-Local Means filter thereby characterizes the similarity between a pixel under observation and any other pixel in the image or an adequate search window or an image patch. Compared to the neighborhood filters the number of elements that are used for the filtering is much higher and the elements used are not necessarily adjacent neighbors but potentially far apart and not connected. The similarity is usually defined by absolute differences of the image patches. The new filtered pixel value is the sum of all pixels in the image or the search window and weighted by the similarity. According to Deledalle et al. (2015) this similarity is based on adaptive selection of potential similar pixels. The approaches can be grouped into two categories: (1) The point-wise methods estimate the similarity between pixels by directly comparing the pixel value of interest to any pixel value inside the search window. If the difference is less than a certain threshold the pixels are averaged. This approach guarantees that only similar values are used for the averaging but it "[...] *suffers from a selection bias* [...]" (Deledalle et al. (2015), p. 2). That means that suited thresholds are unknown and have to be defined. The Lee Filters are local approaches that use a Point-Wise method to select suited pixels for the averaging. (2) The second approach used in Non-Local Means filtering is based on the patch-wise estimation of the similarity. "*Rather than selecting pixels with similar intensities, the relative importance of pixels can be weighted by comparing their surrounding neighborhoods.*" (Deledalle et al. (2015), p. 2). This is realized by comparing the local neighborhood of the pixels. This neighborhood is called similarity window. The size of this window is smaller than the search window and regulates the number of elements that can be used for the averaging. Usually the size of the search window ranges from

### 3 Methodology

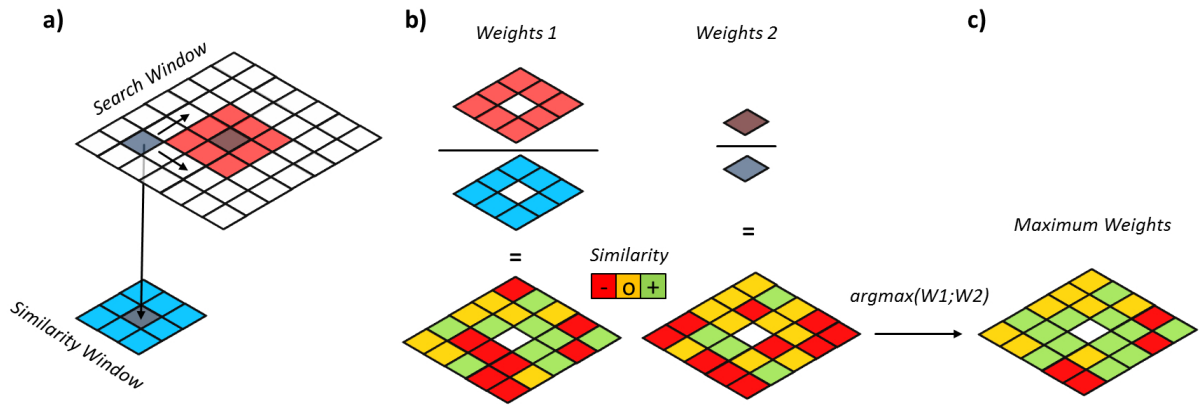


Figure 3.9: Estimation of weights in Non-Local Means filtering: a) search and similarity window, b) estimation of the first patch-wise weights (Weights 1) and point-wise weights (Weights 2) and c) the resulting maximum weights. Source: Own Figure.

21x21 pixels to more than 99x99 pixels. The size of the similarity window usually varies between 5x5 and 31x31 pixels. Therefore the Non-Local Means filters have a very high computational load.

Buades et al. (2005) define a patch-wise method: The approach of the Non-Local Means filter is based on the decomposition assumption that the original image value  $v(i)$  is composed of the true value  $u(i)$  and the noise contribution  $n(i)$  (Equation 3.54). This decomposition can be rewritten introducing a denoising method (filter)  $D_h v$ . The parameter  $h$  is the filtering parameter and  $v$  the observed noisy original image (Equation 3.55). In Buades Non-Local framework the term  $D_h v$  is defined by the product of the original noisy image  $v(j)$  and a family of weights  $w(i, j)$  that defines the similarity between the pixel at location  $i$  and any pixel  $j$  in the image. The individual weight at a location  $i$  is a number between zero and one. The sum of the weights of any pixel  $i$  in the image or the search window is one (Equation 3.56).

$$v(i) = u(i) + n(i) \quad (3.54)$$

$$v = D_h v + n(D_h v) \quad (3.55)$$

$$D_h v = \sum_{j \in I} w(i, j) v(j), \text{ with } v = \{v(i) \mid i \in I\} \text{ and } w(i, j) \in [0, 1] \text{ and } \sum_j w(i, j) = 1 \quad (3.56)$$

Buades et al. (2005) define the weights  $w(i, j)$  via the normalization constant  $Z(i)$  and the squared difference of the local neighborhood of the location of interest  $u(v_i)$  and any other local neighborhood of the image  $u(v_j)$  (Equation 3.57). The normalization constant  $Z(i)$  is the sum of all the differences. The differences are measured as weighted Euclidean distances with a Gaussian Kernel  $\|\dots\|_{2,a}^2$  and with a standard deviation of  $a$ . The standard deviation is usually set to a fixed value.

$$w(i, j) = \frac{1}{Z(i)} e^{-\frac{\|u(v_j) - u(v_i)\|_{2,a}^2}{h^2}}, \text{ with } Z(i) = \sum_j e^{-\frac{\|u(v_j) - u(v_i)\|_{2,a}^2}{h^2}} \quad (3.57)$$

The similarity between two patches (or similarity windows) is defined by the parameter  $h$  that acts as the degree of filtering (Buades et al. (2005)). “*It controls the decay of the exponential function and therefore the decay of the weights as a function of the Euclidean distances.*” (Buades et al. (2005), p.3). A large (small) value of parameter  $h$  will cause a strong (weak) filtering. The parameter  $h$  can be either set manually or automatically with more comprehensive methods (e.g. shown by Deledalle et al. (2010, 2015)). The idea of Buades et al. (2005) is independent of the type of the image and is designed for Gaussian distributed noise (Buades et al. (2005), Deledalle et al. (2010)). In contrast, the distribution of the (single-look) SAR images and the speckle can be modeled with several non-gaussian statistical distributions, e.g. the Reighley, K-distribution or Weibull Distribution (Gao (2010)). Therefore the Non-Local Means filtering of Buades et al. (2005) was adapted to the nature of SAR and PolSAR imagery as mentioned by Deledalle et al. (2010), Parrilli et al. (2010), Deledalle et al. (2015). Nevertheless, the SAR and PolSAR data can be assumed to be Gaussian normal distributed if the number of looks is high and if the targets are natural landscapes with moderate roughness. For these data the original model of Buades et al. (2005) is appropriate. More information on the statistical modeling of SAR and PolSAR images is shown by Gao (2010), Cloude (2010).

A Non-Local Means filter was designed for this work in order to realize a fast, robust and comprehensible algorithm that is capable to handle quad- and dual-polarized PolSAR data in the same way. The design of this filter is in the sense of Buades et al. (2005) and restricted to multi-looked pre-processed SAR and PolSAR data. Therefore the filter is a post-filter and an image filtering technique. This has the following consequences: (1) The processing of the filter will be fast since the image dimensions were reduced during the multi-looked. (2) The data are assumed to be Gaussian Normal distributed because of the high number of looks. (3) A point-wise estimation of the similarity is more reliable since the variances are reduced due to the averaging. The bias is therefore smaller compared to single-look data. (4) The size of the search window and of the similarity window can be reduced since the data were already averaged during the processing, e.g. less samples are required to get an unbiased estimate.

The designed Non-Local Means filter combines a point-wise and a patch-wise method for the estimation of the similarity (weights). The first weights  $w_1(i, j)$  are estimated patch-wise using the original formula of Buades et al. (2005) (Equation 3.58). The second weights  $w_2(i, j)$  are estimated point-wise using Equation 3.59. The final weights  $w_3(i, j)$  used for the denoising method  $D_h v$  are the maxima of  $w_1(i, j)$  and  $w_2(i, j)$  (Equation 3.60). Therefore the similarity between the pixel at location  $i$  and any pixel  $j$  in the image is high if the pixels have similar values or if their local neighborhood is similar. Again the similarity and power of the filtering is regulated via parameter  $h$ . The parameter  $h$  was set manually to keep the algorithm flexible and simple. This further makes the computation robust. The parametrization of parameter  $h$  is shown in the Section 4.1.1.1. This algorithm is fast since it is applied to the multi-looked data and since small sizes of the search and similarity windows are used. If this Non-Local Means filter is applied to PolSAR data, the weights of each polarimetric channel are multiplied prior to the averaging to guarantee the independence of the information. If applied with PolSAR data, the filter will fulfill the principles of a speckle filter defined by Lee, Grunes & De-Grandi (1999): (1) The elements are filtered independently in the spatial domain, (2) every element of the matrix is filtered by the same amount and (3) the filtering has an adaptive nature. The algorithm was programmed in IDL 8.3 and implemented in the PolSAR ENVI Toolbox. Figure 3.9 illustrates the formation of the weights and Figure 3.10 shows

### 3 Methodology

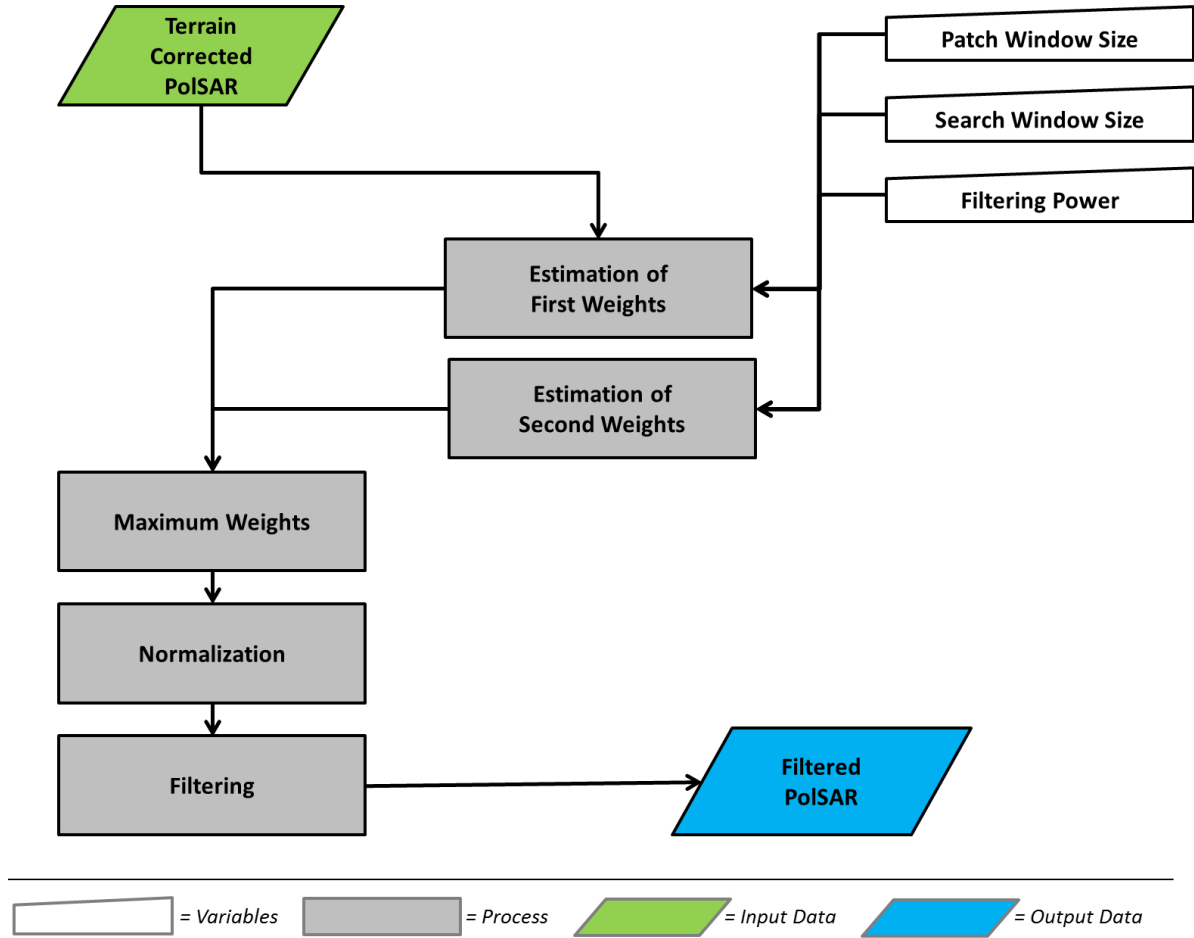


Figure 3.10: Process chart of Non-Local Means image filtering. Source: Own Figure.

the process chart of the Non-Local Means image filter. The user defined parameters are the sizes of the patch and similarity windows and the filtering parameter  $h$ . These are used to estimated the patch- and the point-wise weights. The maximum weights are normalized with respect to the number of polarimetric channels.

$$w_1(i, j) = \frac{1}{Z(i)} e^{-\frac{\|u(v_j) - u(v_i)\|_{2,\alpha}^2}{h^2}}, \text{ with } Z(i) = \sum_j e^{-\frac{\|u(v_j) - u(v_i)\|_{2,\alpha}^2}{h^2}} \quad (3.58)$$

$$w_2(i, j) = \frac{1}{Z(i)} e^{-\frac{|u(v_j) - u(v_i)|^2}{h^2}}, \text{ with } Z(i) = \sum_j e^{-\frac{|u(v_j) - u(v_i)|^2}{h^2}} \quad (3.59)$$

$$w_3(i, j) = \text{argmax}(w_1(i, j); w_2(i, j)) \quad (3.60)$$

The effect of filtering can be characterize by the usage of so called speckle evaluation indices. These are used to quantify the effect of filtering in terms of preservation of the mean value or the reduction of the variance. The index Preservation of Edges shows how good a filter is capable to preserve edges and boundaries in the image. The quantitative assessment of filtering was discussed in Huang & Genderen



(1996), Nyoungui et al. (2002), Leichtle (2013). In accordance to Nyoungui et al. (2002) and Leichtle (2013) the following speckle evaluation indices were selected for the quantification of the developed speckle filter.

**Preservation of Mean** - The Preservation of Mean (POM) is a measurement for the ability of the filter to keep the original mean value. In optimal case the filter does not bias the mean and the POM is one. Any value less than one shows that the original mean value was modified during the filtering. The POM is defined by the ratio of the original mean value  $\mu_{orig}$  and the filtered mean value  $\mu_{filt}$  (Equation 3.61).

$$POM = 1 - \left| 1 - \frac{\mu_{filt}}{\mu_{orig}} \right| \quad (3.61)$$

**Reduction of Speckle** - The Reduction of the Speckle Index (RSI) can be measured by comparing the coefficient of variation of the filtered  $COV_{filt}$  and the original image  $COV_{orig}$  (Equation 3.62). This ration directly quantifies the reduction of the variance (standard deviation).

$$RSI = 1 - \left| \frac{COV_{filt}}{COV_{orig}} \right|, \text{ with } COV = \frac{\sigma}{\mu} \quad (3.62)$$

**Preservation of Edges** - The preservation of edges can be quantified by the so called Edge Enhancement Index (EEI). The index used as described in detail by Leichtle (2013), p. 57- 62 and its IDL source code was provided by Leichtle (2013), p. 126-128. The index is formed by the ratio of the absolute differences between the left and right side of an edge of the filtered ( $I_{right}^{filt} - I_{left}^{filt}$ ) and the original image ( $I_{right}^{orig} - I_{left}^{orig}$ ) (Equation 3.63). An EEI greater than one indicates that the contrast of the edge was enhanced during the filtering. That means that the absolute difference between the left and the right side was increased by the filter. An EEI less than one shows a blurring of the edge and means that the difference between the left and the right side was reduced by the filter. The EEI requires the definition of edges in the image. This edge detection was realized by the usage of the CANNY edge-detection algorithm. This algorithm is capable to automatically detect edges in an image and is implemented in IDL 8.3.

$$EEI = \frac{\left| I_{right}^{filt} - I_{left}^{filt} \right|}{\left| I_{right}^{orig} - I_{left}^{orig} \right|} \quad (3.63)$$

**Overall Evaluation Index** - The described indices can be aggregated to an Overall Evaluation Index (OAI) by multiplication of POM, RSI and EEI (Equation 3.64). All of the described speckle evaluation indices were programmed in IDL 8.3 and implemented in the PolSAR ENVI Toolbox.

$$OAI = POM * RSI * EEI \quad (3.64)$$

### 3.1.1.3 Processing Chain

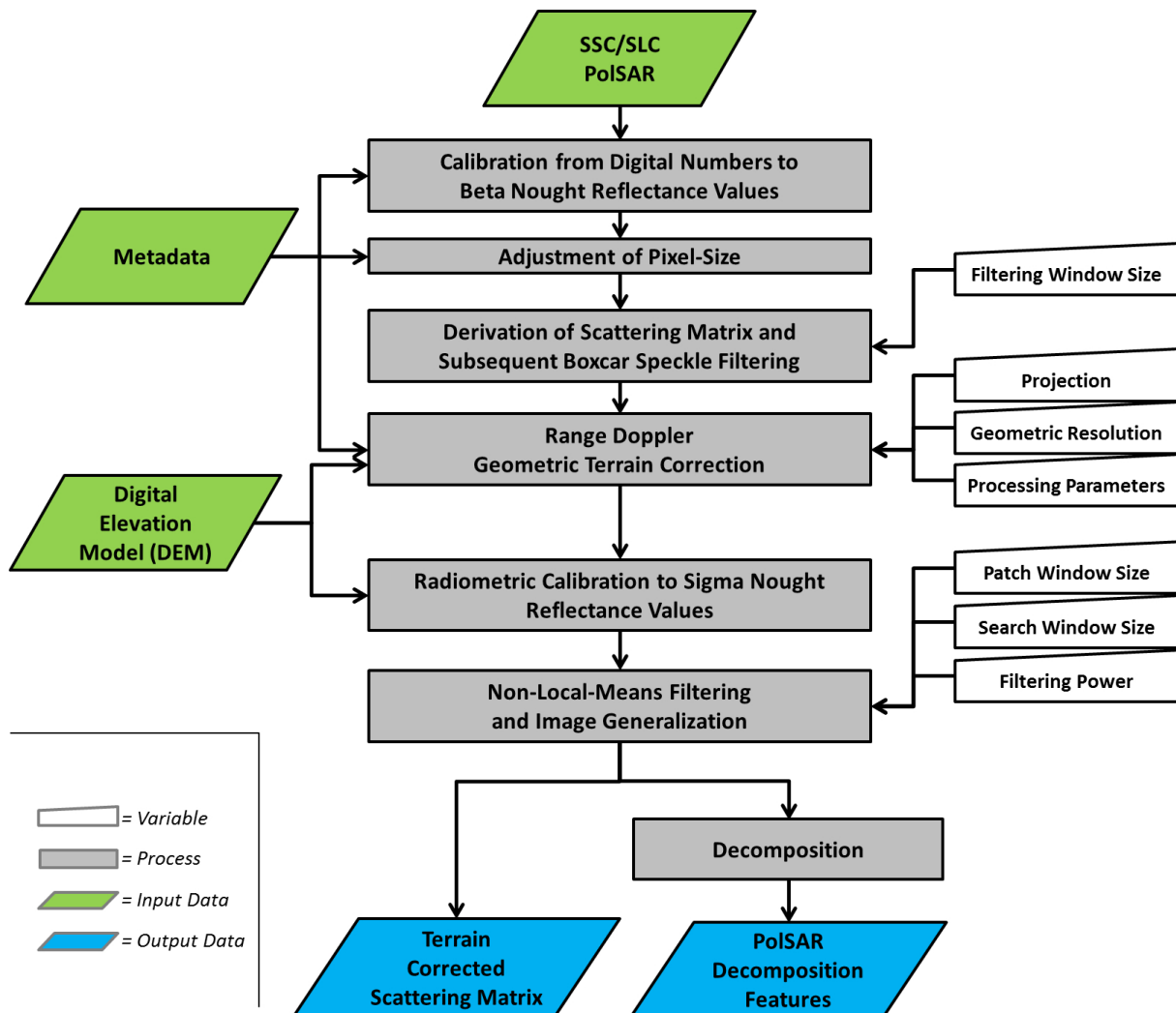


Figure 3.11: Process chart of PolSAR data processing. Source: Own Figure.

All of the PolSAR data used in this work were ordered as single-look complex images (SLC) (R-2, PALSAR) or single-look slant range complex (SSC) images (TSX, TDX). The data of each polarimetric channel were complex numbers and the geometry of the data was in time domain and in slant range geometry. For mapping applications the SAR data must be geocoded and processed to ground range detected products. It is further beneficial to perform an orthorectification and to radiometrically calibrate the data in order to achieve a high comparability and transferability. The used processing chain is illustrated in Figure 3.11. The first step was the import of the level 1 data (SSC, SLC) and the calibration from digital numbers to beta nought reflectance values. This calibration was done using the meta-data enclosed to the image data. The import and the beta nought calibration was realized in NEST 5.1. In the following the pixel-size was adjusted with respect to the meta-data in order to achieve square pixels on the ground. The image dimensions in range and azimuth were reduced (multi-looking) and the information was aggregated. Both steps were done in NEST 5.1. The third step was the deviation of the Kennaugh

Matrix with an estimation window size of 5x5 pixel. The elements were calculated in NEST 5.1 using the Graph Builder. In the following the Geometric Terrain Correction was performed to Universal Transverse Mercator (UTM) using the WGS84 ellipsoid.

The spatial resolution was set to twelve meter and calculated with bilinear interpolation. The geocoding was done with the Range Doppler approach (e.g. Roth et al. (2004), Richards (2009), Hein (2010)) and TDX IDEM data in NEST 5.1. The projected local incidence angles were derived from the TDX IDEM and the elevation information was used to calibrate the data to sigma nought intensities. All of these steps were processed in NEST 5.1. The data were then exported and the Non-Local Means filtering of the Kennaugh Matrix intensities was done in ENVI 5.1 with a similarity window size of 3x3 pixels and search window size of 31x31 pixels. These values were shown to provide a good trade-off between processing time and quality of the filtering (not shown). The parameter  $h$  was parametrized semi-automatically (see Section 4.1.1.1). Finally, the decomposition products of the Entropy/Alpha and the Three and Two Component Power Decomposition were processed with the functions of the PolSAR ENVI Toolbox. The geometric location error after terrain correction between R-2 and TSX data was less than ten meters. The ALOS data were manually registered to the TSX and R-2 due to geometric distortions of the ALOS data. The PolSAR data listed in Section 2.2 were mosaiced to cover the test sites. ENVI's mosaic function was used for this task and the statistics were calculated from the overlap: a gain and bias correction was performed.

#### 3.1.2 Multispectral Data

The usage of optical multispectral sensors for the characterization of the earth surface has one of the longest traditions in remote sensing. The multispectral systems operate passively and record the intensities of specific electromagnetic wavelengths that were either reflected or emitted from the earth surface (Jensen (1995)). The coverage of today's systems range from several hundreds to thousands of square kilometers and some geostationary systems are capable to image an entire hemisphere. Therefore the spatial resolution ranges from less than one meter to more than one hundred meter pixel spacing. The multispectral systems record the reflectance of the sunlight with up to about ten channels (bands) in the range from the visible light to the medium infrared light. In addition, some systems like the later Landsat satellites can record the thermal emission of the earth surface. The received signal varies with respect to the spectral properties of the earth surface and in reverse way the analysis of the spectral signatures can be used to characterize and classify the coverage and properties of the surface. For example, the reflectance of the near infrared light is high for intact green vegetation. This circumstance can be used to characterize and map green vegetation via the infrared band. Further information on the history of the multispectral sensors, their operation, the technical framework and possible applications is provided by Jensen (1995), Kramer (2002), Jensen (2007).

The position of the multispectral bands is usually bounded to atmospheric windows that have a high transmissibility for electromagnetic waves. Before the signal is recorded, the wave has to pass the atmosphere twice. Due to interactions of the wave in the atmosphere the signal is altered which hinders the interpretation. The transferability is also limited due to changing atmospheric conditions, e.g. the content of water vapor. In worst case no observation of the earth surface is possible due to cloud coverage or

### 3 Methodology

missing insolation. The altering of the signal by the atmosphere can be corrected by so called Atmosphere Corrections (Jensen (2007)). These corrections usually require user interaction and the knowledge of a sufficient high number of true reflectance signatures - at least the knowledge of the most likely signatures. If no such information is available, the reflectance values can be corrected to the top of the atmosphere. This type of correction called Top of Atmosphere Correction (TOC).

There are many features that can be derived from the multispectral information. The purpose of such features is to facilitate the interpretation, characterization and classification of the image. An overview on the frequently used features in context of the polar regions is provided by Laidler & Treitz (2003). The Normalized Difference Vegetation Index (NDVI) and the features of the Tasseled Cap Transformation are examples for features that facilitate the interpretation of the multispectral signal. Both are briefly described in the following and were used in this work for the land cover characterization of the test sites. The computation is implemented in ENVI 5.1 and information on the algorithms and their application is provided by Jensen (1995, 2007), Olthof & Fraser (2007), Fraser et al. (2011).

**NDVI** - The NDVI is calculated via the difference between the infrared and red reflectance and is normalized by the sum of the red and infrared reflectance. The NDVI is one of the most frequently used features for the characterization of vegetation since the bands of red and infrared light are indicators for the so call red-edge (Laidler & Treitz (2003), Jensen (2007)). The information of the NDVI can be related to bio-physical properties of the vegetation. The NDVI is an indicator for the Leaf Area Index, or the net primary production. Several studies have used the NDVI for the characterization of the Arctic land surface (Laidler & Treitz (2003), Kaeab (2008)).

**Tasseled Cap Transformation** - The multispectral data can be transformed by using the so called Tasseled Cap Transformation (Jensen (1995)). The purpose of this feature space transformation is to characterize the image in terms of Brightness, Greenness and Wetness. The Greenness has been shown to be a suitable feature to characterize different vegetation communities in context of arctic environment (Fraser et al. (2011), Olthof & Fraser (2014)). The parameters used for the transformation are sensor specific. The Tasseled Cap Transformation for data of the Landsat Satellites 1 to 7 is implemented in ENVI 5.1. The Tasseled Cap Transformation of L-8 data was realized in this work by recalculating the spectral information of the Operational Land Imager (OLI) to the spectral information of the Enhanced Thematic Mapper (ETM). Necessary computing steps were programed in IDL 8.3 (not shown).

#### 3.1.3 Digital Elevation Model

DEMs have become an important information source for the analysis of the earth surface and are widely used in many disciplines of the environmental sciences. The application of DEM ranges from ecosystem and environmental analysis to climate modeling. The information on the terrain assesses the characterization of the geomorphology and helps mapping units that show similar processes, genesis or shape. The derivatives of the elevation can be used to quantify the land surface in terms of morphometry or to model hydrographic properties - such as the size and location of the catchment, or the potential stream network (Wilson & Gallant (2000), Hengl & Reuter (2009)). Therefore the data are suited to characterize and classify the surface morphology on different scales, depending on the coverage and the resolution of the DEM.

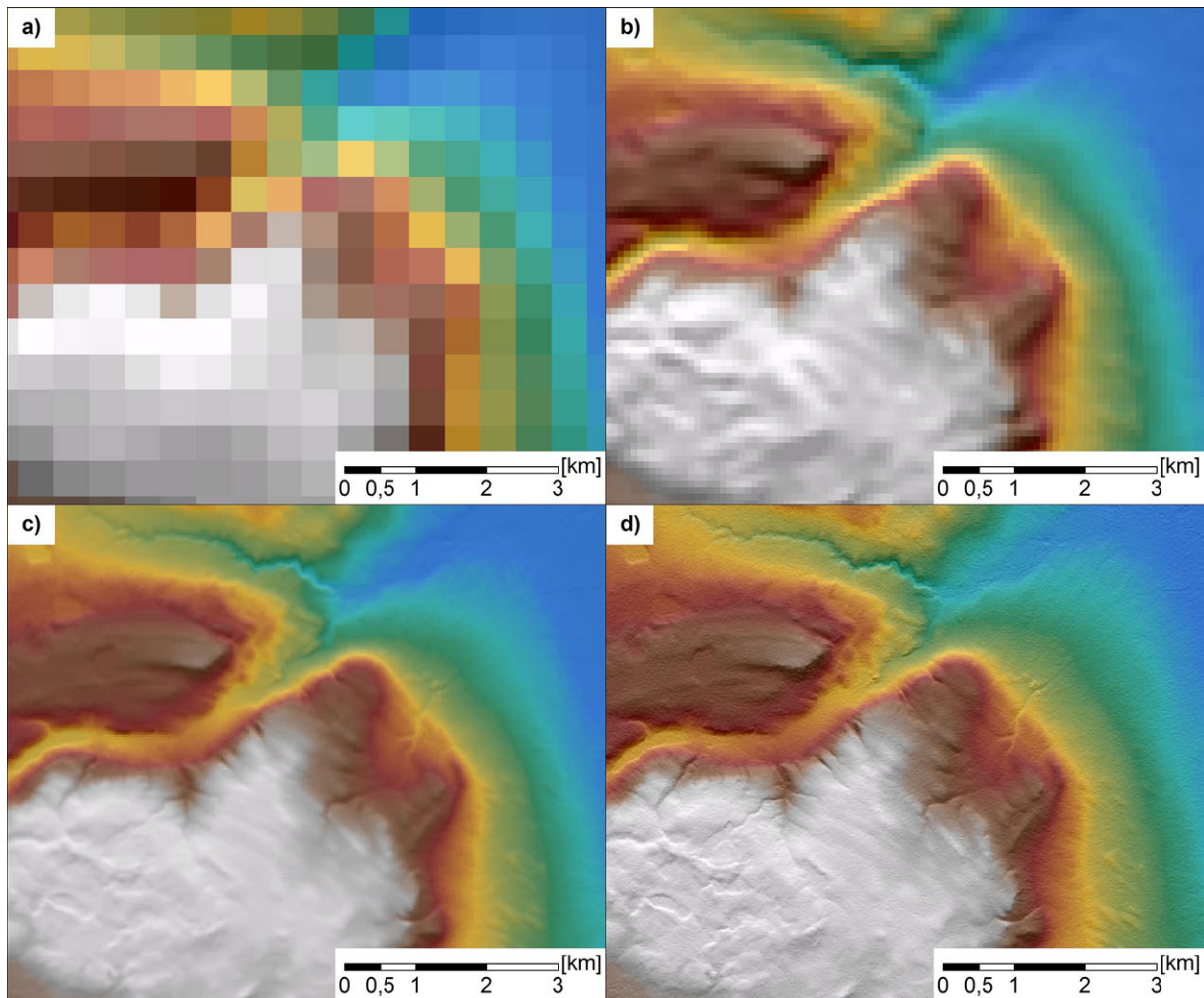


Figure 3.12: Digital Elevation Models with a) 500 x 500 m resolution , b) 90 x 90 m resolution, c) 30 x 30 m resolution and d) 12 x 12 m resolution. Source: Own Figure.

The elevation information can be stored in different data formats such as points, contour lines or grids. No matter which data format is present, the spacing of the information defines the scale on which the data can be interpreted. Figure 3.12 exemplary shows DEMs with 500 m pixel spacing, 90 m pixel spacing, 30 m pixel spacing and 12 m pixel spacing. The potential to discriminate landforms and landform elements varies with the spatial resolution.

DEMs that cover large areas, or even the entire land surface of the earth, can be derived by remote sensing techniques. Generally, there are three ways to generate the elevation information. The oldest approach is the application of photogrammetry (El-Garouani et al. (2014)). This method is based on the stereoscopic effect. The area of interest is imaged from different viewing positions and the shift of the parallaxes determines the elevation. The imaging systems are usually passive spectral cameras but the approach can be used with radar data and is then called radargrammetry (Crosetto & Perez Aragues (2000)). The coverage and the spatial resolution of the photogrammetric DEM depend on the acquisition system. The space borne systems can provide coverages of several hundreds of square kilometers with a single acquisition and up to five meter spatial resolution. The spatial resolution of airborne systems can be

### 3 Methodology

less than one meter but the coverage is usually smaller. The optical photogrammetric DEMs are surface models since the electromagnetic waves are reflected from the top surface and not from the ground. The determination of the altitude via the shift of the parallaxes requires common points in the images. For this reason the quality of photogrammetric DEMs is limited in untextured and flat terrain. In contrast, the quality of the DEM is usually high for textured and rough terrain. The ASTER GDEM is an example for a global DEM that was derived via a photogrammetric approach (METI-NASA (2011), Rees (2012)).

A further way to derive the altitude of a location of interest is the Light Detection and Ranging Technique (LIDAR). Laser pulses are sent to the surface and a system records the time the signal needed to travel between the emitter and the receiver. The time is in direct relation to the distance between the platform and the object of study. The LIDAR systems have a high accuracy and a high spatial resolution (less than one meter). Further, they can be used to generate digital terrain models that truly show the altitude of the ground and not of the upper surface, e.g. the top of canopy. The LIDAR systems are usually operated from air-borne platforms and therefore the coverage is limited. The space borne LIDAR systems, like ICESAT and ICESAT2, have a very small coverage and sample the altitude data point-wise and not as image (NASA (2014)).

The SAR interferometry (InSAR) is another way to generate area-wide information on the elevation. The InSAR approach requires the imaging from a minimum of two different viewing positions to induce an interferometric effect. The generation of DEM further needs a high coherence of the signals. The elevation is derived via the analysis of the phase shifts between two or more repeat or simultaneous SAR observations (Hein (2010)). The quality of an InSAR derived DEM is much higher if the temporal delay between the acquisitions is very short (nearly single-pass), or if the same sent signal is recorded at two spatially separated receivers (single-pass). Still the application is possible with repeat observations and in repeat pass geometry. The SRTM DEM is an example for a DEM that was derived with single-pass InSAR (Hein (2010)). The recent TDX DEM is an example for the application of nearly single-pass InSAR. The space-borne InSAR derived DEMs can have a spatial resolution less than 15 m and a global coverage. The quality of the InSAR DEM is limited for rough terrain since the SAR signal is acquired in slant range and areas of the surface may be shadowed. No information on the elevation of such shadowed areas is then available. This problem can be solved if InSAR acquisitions are taken from different viewing positions, e.g. by changing the side of the look, or the incidence angle of the SAR system. The quality of InSAR derived DEMs is high for flat terrain. InSAR DEMs are known to have a relatively small location error in every spatial direction. The benefits of the space-borne SAR interferometry is of importance for the imaging of the Arctic since this regions has a frequent cloud cover.

**Topographic Attributes** - The information of the DEM can be used to generate further land surface features (land surface parameters) that facilitate the interpretability and help to group and classify elements of the terrain that share similar characteristics (Hengl & Reuter (2009)). In this context, the information on the elevation is considered to be a continuous three dimensional surface. As a consequence the features can be derived via geometric and algebraic analysis (Wilson & Gallant (2000)). These derivatives then show primary or secondary attributes of the surface, such as the rate of change, or the skewness. The primary and secondary derivatives of the DEM that are frequently used to characterize the morphometry of a landscape are briefly described in the following. The features were programmed in IDL 8.3 and implemented in a Terrain ENVI Toolbox.

**Slope** - The slope is the first derivative of the elevation information and measures the gradient at a location of interest with respect to the spacing of the grid in map units. The slope can be expressed in percent or as angle in degree (ESRI (2014)). For raster data slope can be calculated with a moving window operation (convolution). The slope is significant for various applications of geographical terrain analysis, e.g. the determination of overland flow, the estimation of the rate and velocity of the runoff and the characterization of the geomorphology, the vegetation or the soil (Wilson & Gallant (2000), p.7).

**Aspect**- The aspect is defined as “[...] *the orientation of the line of the steepest descent and is usually measured in degrees clockwise from north.*” (Wilson & Gallant (2000), p.54). The aspect is calculated with a moving window operation (ESRI (2014)). The aspect has a significance for the estimation of the solar insolation and for any process that can be related to the exposure. It is a frequently used attribute for ecological surveys as well (Wilson & Gallant (2000), p.7).

**Curvature** - Wilson & Gallant (2000), p. 56 define the curvature attributes as “[...] *the rate of change of a first derivative such as slope or aspect, usually in a particular direction.*” . Two curvature attributes are frequently used in terrain analysis. The first one is the plan or contour curvature that measures the rate of change along a contour line. The second one is the profile curvature that measures the rate of change along the steepest down-stream flow line (Wilson & Gallant (2000), p. 56). The profile curvature gives information on the flow acceleration or the erosion and accumulation rate. The plan curvature is important in hydrographic modeling. It is further an indicator for converging or diverging of flows and for the potential soil water content (Wilson & Gallant (2000), p.7). The calculation of these two topographic attributes is shown in detail by Wilson & Gallant (2000), p. 57-58.

**Convexity** - The convexity is a measurement of the land surface curvature and approximates the second moment of the elevation. It can be estimated with a Laplacian filter (Iwahashi & Pike (2007)). Positive convexity indicates convex surfaces and negative convexity indicates concave surfaces. Values around zero indicate elongated or planar surfaces. The convexity has significance for the characterization of the flow acceleration, the erosion and the accumulation rate and is related to the profile curvature.

**Texture** - The topographic texture is an attribute to measure the local variations of the terrain. Also, the texture can be interpreted as the roughness of the surface and there are various approaches to characterize the texture and roughness (e.g. Shawn et al. (1999)). Iwahashi & Pike (2007) showed a texture attribute that is defined by “*extracting grid cells [...] that outline the distribution of valleys and ridges in the DEM.*” (Iwahashi & Pike (2007) , p. 413). The calculation of this texture is based on the comparison of the original mean value and the median value of the same DEM that was smoothed with a moving window approach. The valleys (ridges) are present if the original elevation value is lower (higher) than the surrounding median elevation. Therefore, the texture is similar to the Topographic Position Index of Weiss (2001), to the difference from the mean elevation (Wilson & Gallant (2000), p.74) and the deviation from the mean elevation (Wilson & Gallant (2000), p.75).

**Topographic Position Index (TPI)** - The name “Topographic Position Index” was introduced by Weiss (2001) and the feature is also known as “difference from the mean elevation” (Wilson & Gallant (2000), p.74) and the “deviation from the mean elevation” (Wilson & Gallant (2000), p.75). “*The attribute measures the relative topographic position as a fraction of the local relief, and so is normalized to the local surface roughness.*” (Wilson & Gallant (2000), p.75). The TPI can be expressed as the difference of the actual elevation  $x_i$  from the mean elevation of the surrounding  $\bar{x}$  (Equation 3.65) and as a dimensionless

### 3 Methodology

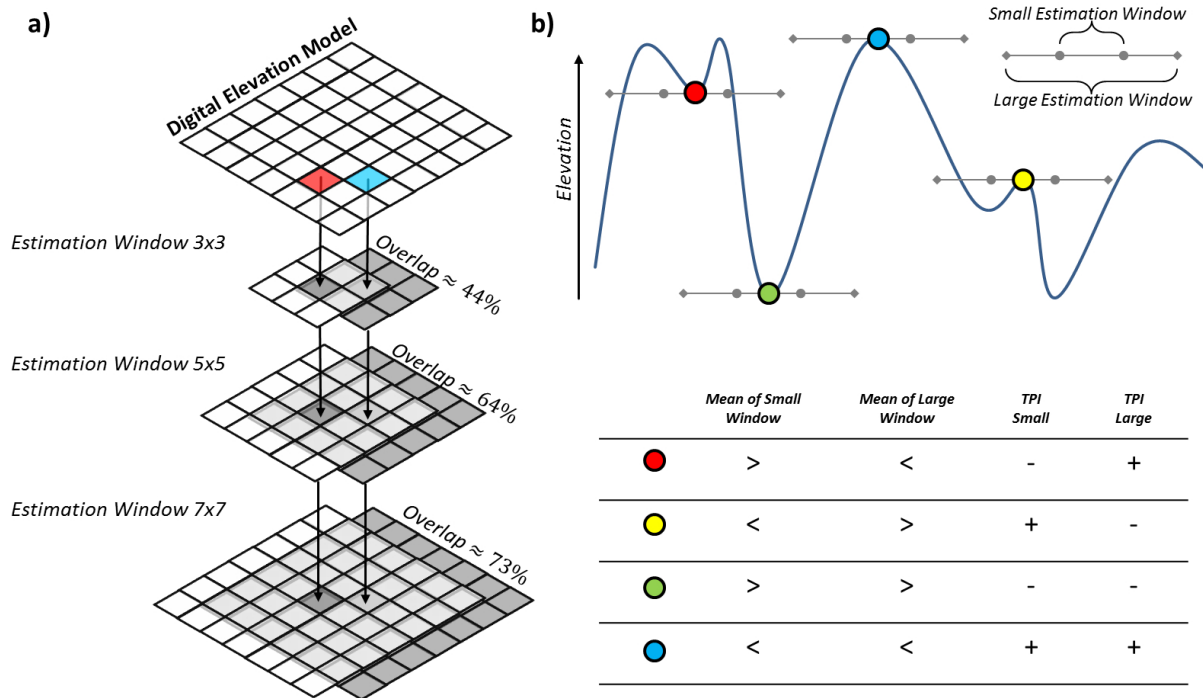


Figure 3.13: Calculation of the Topographic Position Index: a) estimation window sizes of 3x3, 5x5 and 7x7 pixels and corresponding percentage overlap, b) interpretation of the values for small and large estimation window sizes. Source: Own Figure.

index showing the deviation of the actual elevation from the mean elevation normalized by the standard deviation  $SD$  (Equation 3.66). Due to this normalization values outside the range -1 to +1 are seldom and indicate “[...] irregularities in the DEM, where the elevation is significantly outside the typical range in that region.”(Wilson & Gallant (2000), p.75).

$$TPI_{diff} = x_i - \bar{x} \quad (3.65)$$

$$TPI = \frac{(x_i - \bar{x})}{SD} \quad (3.66)$$

Like the texture attribute of Iwahashi & Pike (2007), positive (negative) TPI values indicate ridges (valleys) and the original elevation value is higher (lower) than the surrounding region. The TPI is estimated with a convolution (moving window approach) and the size of the window regulates the scale on which TPI has to be interpreted. For example, a positive TPI close to +1 derived with a small window may be a local, regional or global feature. A positive TPI value close to +1 derived with a very large window is definitely a first-order landform, like a high mountain top. Figure 3.13 illustrates how the estimation window size of the TPI is connected to the interpretation of the TPI value.

**Fast Calculation of Topographic Position Indices (TPIs)** - Usually the TPI is calculated using the classical moving window approach. The mean and the standard deviation are calculated using every element inside the kernel and for every pixel of the image. This process has a high computational load when large scales (estimation windows) are used and if the spatial resolution of the DEM is high.



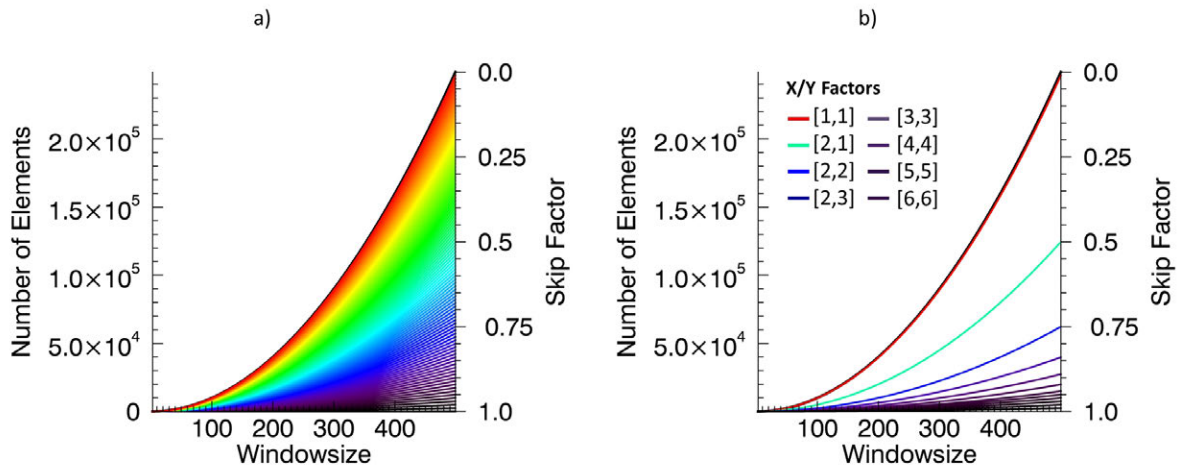


Figure 3.14: Influence of the skip factor on TPI processing time: a) size of the estimation window size and resulting number of calculations with respect to the skip factors and b) selected skip factors and their x and y factors. Source: Own Figure.

The computational load increases further if many TPIs are calculated, e.g. if the scales that are suitable to characterize the landforms are unknown. The current publications that used the TPI were therefore limited to a small number of scales (Reu et al. (2011), Re et al. (2013)). The problem of selecting suitable scales has been discussed and is still ongoing (Dragut & Eisank (2011), Dragut et al. (2011)) but only insufficient in context of the TPI. It will be an advance to calculate the TPI fast and for many scales. Such TPI stacks will help to select scales that are suitable to characterize the landforms and will further offer the opportunity to derive new second-order topographic features.

The calculation of the TPI can be accelerated by interleaving pixels in the mean estimation and by applying a rapid calculation of the standard deviation. It is sufficient to calculate the mean and the standard deviation of selected locations since the moments of neighboring pixels are similar due to their spatial closeness. The overlap between the estimation windows of two adjunct locations is high and the redundancy is high if the estimation window is large (compare Figure 3.13). The interleaving of pixels can be realized by introducing a skip factor. This skip factor expresses the fraction of pixels in the image for which the mean and the standard deviation was not calculated. For example, a skip factor of 0.5 indicates that the moments were calculated for every second pixel in the image. The skip factor  $Sf$  is defined by the number of interleaved pixels in x- ( $Sx$ ) and y-dimension ( $Sy$ ) (Equation 3.67). For example, the skip factor is 0.75 when every second pixel in the x-dimension ( $Sx = 2$ ) and every second pixel in the y-dimension ( $Sy = 2$ ) is interleaved. The gaps can be closed afterward by interpolation. The skip factor should only be applied if the estimation window size has a sufficient large size in order to avoid a bias. In this work the skip factor was applied only for window sizes greater than 15x15 pixel. The computation of the TPI can further be accelerated by using the rapid calculation of the standard deviation (Equation 3.68). The computing of the standard deviation in this way is fast since it is not necessary to store all  $x_i$  in the memory. The relation between the skip factor, the window size and the processing time is illustrated in Figure 3.14. Calculating many TPIs fast and with different window sizes, enables the generation of TPI stacks. The analysis of these stacks helps to detect scales that are suited to describe landforms. The indicators for a changing size

### 3 Methodology

of the landforms can be derived by analyzing the statistics of the TPI stack, e.g. the change of the mean TPI, the change of the variance, the rate of variance changes between two adjunct scales or the direction of the TPI changes from scale to scale.

$$Sf = 1 - \left( \frac{1}{SxSy} \right) \quad (3.67)$$

$$SD^2 = \sum_{i=1}^n (x_i - \bar{x})^2 = \sum_{i=1}^n (x_i^2) - n\bar{x}^2 = \sum_{i=1}^n (x_i^2) - \frac{1}{n} \left( \sum_{i=1}^n x_i \right)^2 \quad (3.68)$$

**Further Topographic and Hydrographic Attributes** - There are further topographic attributes that can be processed using the DEM. Wilson & Gallant (2000) and Hengl & Reuter (2009) provide broad overviews on topographic attributes. In particular, these reports show the definition of features that are derived with respect to the catchment area and the watershed. However, the hydrographic modeling of Arctic landscapes is difficult due to the frequent endorheic nature of the hydrographic elements and requires new and elaborated approaches.

## 3.2 Image Classification

The information of remote sensing imagery can be characterized as a spatial continuous set of measurements of the earth surface. These continuous information can be classified into groups by defining classification rules. All elements of a class then share similar characteristics with respect to the defined rules. An infinite number of classifications (solutions) is possible due to the continuous nature of the information and the number of potential rules. Therefore the task of discrete classification can be considered as a pattern recognition problem (Canty (2006), p. 187). *“Pattern recognition problems, in turn, are usually approached by developing appropriate machine learning algorithms. Broadly speaking, machine learning involves tasks for which there is no known direct method to compute a desired output from a set of inputs. The strategy adopted is for the computer to “learn” from a set of representative examples.”* (Canty (2006), p. 187). The classification of remote sensing data aims usually to classify the coverage of the surface into a finite number of classes. Two classification strategies exist to realize such classifications: the supervised and the unsupervised classification.

### 3.2.1 Supervised Land Cover Classification

The supervised classification approaches require having reference information on the land cover and on the classes of interest. The information must necessarily be of representative nature, e.g. that means that the information include data of all classes of interest, their variances and their spatial distribution in the area of interest. These information can be used in a training phase to adopt and develop a suited classification procedure. Such a classification algorithm will then learn the classification rules form the representative samples. The found rules are then extrapolated to the entire image and each pixel is assigned to one land cover class. Canty (2006), p. 187 names three ways to define a suited classification procedure (model): parametric models, nonparametric models and semi-parametric models. Examples of nonparametric

models are the Gaussian Kernel Classification, or the Support Vector Machines classification. The semi-parametric models are also called mixture models and the Feed-Forward Neural Network classification is an example (Canty (2006), p. 187). However, the more frequently used approaches utilize parametric models.

If supervised parametric models are used for a classification, it is assumed that the statistics of the classes follow known probability distributions. The reference information can then be used to estimate the parameters of these distributions. Frequently the multivariate Normal Distribution is assumed to facilitate the computation. The reference information is used for the training of the classifier and to define the multivariate class-specific probability density functions. The number of variables (e.g. bands, polarimetric channels) defines the dimensionality of the Normal Distribution. It is recommended to standardize the data if more than one source of information is used, e.g. if multispectral and PolSAR data are used in combination. The classification is based on the estimated multivariate probability density functions and the class label for a pixel of interest is assigned by the maximum observed probability. For such a Maximum Likelihood classification (MLC) the probability  $u_{kv}$  at location  $v$  to belong to class  $k$  is defined as shown in Equation 3.69. The probability is calculated via the Covariance Matrix  $C$ , the mean vector  $m$  and the a priori information  $p$ . In most cases the reference information is insufficient to estimate the a priori probability and the usage of  $p$  is rejected (Canty (2006)).

$$u_{kv} = \frac{1}{\sqrt{|C_k|}} \exp \left[ -\frac{1}{2} (v - m_k)^T C_k^{-1} (v - m_k) \right] p_k \quad (3.69)$$

Each pixel in the image then has a tuple of values that shows the probabilities to belong to a classes. For example, if the number of classes is five then every pixel has five probabilities that define the class-memberships of that pixel. These memberships sum up to one and the logic is therefore fuzzy. The images that display the membership values of the pixels are called rule images. The discrete classification is realized by the maximum observed membership value. The supervised classification was done in this work using the MLC approach implemented in ENVI 5.1. This method was shown in previous work to be efficient to classify generalized land cover types with remote sensing imagery and is frequently used (Section 1.2). It was also chosen since this classification strategy is well known and the traceability of the classification process is high.

The MLC is processed in the three steps: (1) The land cover reference data are used to create the training data statistics. That includes the calculation of Covariance matrices and the mean vectors for each training sample and each land cover class. These data define the multivariate class-specific probability density functions. (2) These class-specific probability density functions are used to calculate the rule images. The usage of the a priori information  $p$  is rejected and equal  $p$  is assumed for all classes. (3) The discrete classification is realized by searching for the maximum observed probability of the rule images. In ENVI's algorithm this operation is done by searching for the the minimum Mahalanobis distance (Canty (2006), p. 194). The final classification has one class label for every pixel in the image. The supervised classifiers need precise and comprehensive training data in order to achieve an accurate and reliable classification. The number of the elements of the training data must be sufficient high to represent the land cover information of all classes of interest for the entire study area. Especially for Arctic regions these requirements are hard to full-fill due to the limited accessibility.

## 3.2.2 Unsupervised Land Cover Classification

A further way of discrete classification is the usage of unsupervised classification techniques. In unsupervised classification “[...] *the attempt is made to find an underlying class structure automatically by organizing the data into groups sharing similar [...] characteristics*” (Canty (2006), p. 267) and without reference information. The unsupervised classifiers do not require any manually selected training samples - in contrast to the supervised classification techniques. This is favorable when little reference information exists. The approach of unsupervised classification separates the feature space in a user-defined number of classes. “[...] *The members of each class are to be in some sense more similar to one another than to the members of the other classes.*” (Canty (2006), p. 267). The process that defines these classes is called clustering. Frequently used unsupervised approaches are the K-Means classification (Canty (2006), p. 271), the Initial Arbitrary Cluster Allocation (ISODATA) (Jensen (1995), p. 236 ff.) - which is an extension of the classical K-Means approach - and the Fuzzy-K-Means Clustering (Jensen (1995), p. 240 ff. and Canty (2006), p. 280, ff.). Overviews on these and other techniques are provided by Jensen (1995), Thanh et al. (2005), Canty (2006).

### 3.2.2.1 Classification of Land Cover

The unsupervised classification techniques are frequently applied to classify the land coverage with remote sensing imagery, if reference information is sparse. The application is not restricted to a specific type of image and the techniques may be adapted to take data specifics into account. In the following approaches of the unsupervised classification of PolSAR data are shown. Overviews on the unsupervised classification of multispectral data is provided by Jensen (1995), Thanh et al. (2005), Canty (2006). Further, examples of the unsupervised classification of multispectral data in context of the Arctic environment are shown in Section 1.2.2.

The classes of an unsupervised PolSAR classification can be interpreted in terms of polarimetric scattering properties. The classifiers - developed for PolSAR data - group pixels that share similar scattering properties. As shown in Section 3.1.1 the determination of the scattering properties can help to distinguish different types of the land cover. The unsupervised classification of PolSAR data is often performed with parametric models since the probability distribution of the SAR and PolSAR data can be approximated (see Section 3.1.1.2). The frequently used unsupervised PolSAR classification techniques are based on parametric models and the approach can be simplified to two principles:

(1) The first principle is the classification of scattering types by applying thresholds to the feature space of a decomposition. These thresholds should be applied to normalized features such as the Entropy, Alpha or the ratio of the Power Decomposition features (Cloude (1997), Lee et al. (2004)). The thresholds are usually not set with respect to the actual distribution of the data but with a priori knowledge. Examples for threshold classification techniques are the Entropy/Alpha segmentation and the Entropy/Alpha/Anisotropy segmentation. Both techniques are implemented in the RAT Toolbox and in the PolSARpro software (ESA (2014a)):

**Entropy/Alpha segmentation classifier** - The Entropy/Alpha Segmentation can be used to group pixels that share similar properties in the features space of the eigendecomposition. This approach was shown by Cloude (1997) and uses the features Entropy and Alpha (see Section 4.2.1.2). The feature space of

these two variables is separated in regions that are believed to reflect scattering properties. In the original approach of Cloude (1997) nine zones are defined, e.g. a Zone 2 that shows high Entropy Vegetation Scattering, or a Zone 7 that shows low Entropy Multiple Scattering Events. The nine zones are defined by thresholds and these are fixed. The approach was developed for quad-polarized data but may be applied to dual-polarized data as well.

**Entropy/Alpha/Anisotropy segmentation** - This scheme can be extended with the Anisotropy of the eigendecomposition of quad-polarized data (see Section 4.2.1.2). The segmentation of the Entropy and Alpha feature space remains the same and the feature space is further separated into low and high Anisotropy environments using a threshold. The number of classes is then increased to eighteen and the approach can only be applied to quad-polarized data since the information on three eigenvalues is needed.

(2) The second principle is the application of more comprehensive parametric models, such as the unsupervised MLC technique. As shown and discussed by Canty (2006) the MLC can be initialized with random class statistics rather than with manually selected training data and is then an unsupervised technique. “[B]ecause of the exponential dependence of the memberships [...] the computation is very sensitive to initialization conditions and can even become unstable.” (Canty (2006), p. 283). Therefore it is necessary to initialize the MLC with other classifiers in advance that are more robust. Canty (2006) notes: “To avoid this problem, one can first obtain initial values [...] by preceding the calculation with the FKM algorithm” (Canty (2006), p. 283). The initialization of MLC with other classifiers is a frequently applied approach. However, the MLC process remains the same as the one described in Section 3.2.1. In unsupervised classification the MLC process is usually iteratively repeated until a certain convergence criterion is met, e.g. if less than a defined number of valid pixels changed their class labels between two iterations. The intention of the iterative process is identification of an (local) optimum in the feature space (Canty (2006), p. 284). The three established PolSAR classification techniques that operate in this way are described in the following. The classifiers are implemented in the RAT Toolbox and in the PolSARpro software (ESA (2014a)):

**Wishart classifier** - The classifications of the Entropy/Alpha segmentation or the Entropy/Alpha/Anisotropy segmentation can be used to initialize an iterative MLC as shown by Lee, Grunes, Ainsworth, Du, Schuler & Cloude (1999). The class statistics of the segmentation are used to calculate the covariance matrices and the mean vectors. This approach utilizes a complex Wishart Distribution and it can be applied to both quad- and dual-polarized imagery. The application of this approach is seldom shown for dual-polarized imagery, however.

**K-Means Wishart classifier** - The iterative MLC can be initialized by a K-Means pre-classification. This approach is similar to the technique shown by Lee, Grunes, Ainsworth, Du, Schuler & Cloude (1999). The initialization is based on the classical K-Means clustering and not on the segmentation of the eigendecomposition feature space. The clustering is usually performed on the scattering matrix and the data are assumed to follow a complex Wishart Distribution.

**Lee Terrain Classification** - The classification of Lee et al. (2004) is based on the Power Decomposition features of the decomposition of Freeman & Durden (1998). These are used for a pre-classification of scattering types. The number of pre-classes of each scattering type is extended by a K-Means clustering. Afterward this K-Means classification is used to initialize an iterative MLC. The approach is only suited for quad-polarized data since it requires three Power Decomposition features.

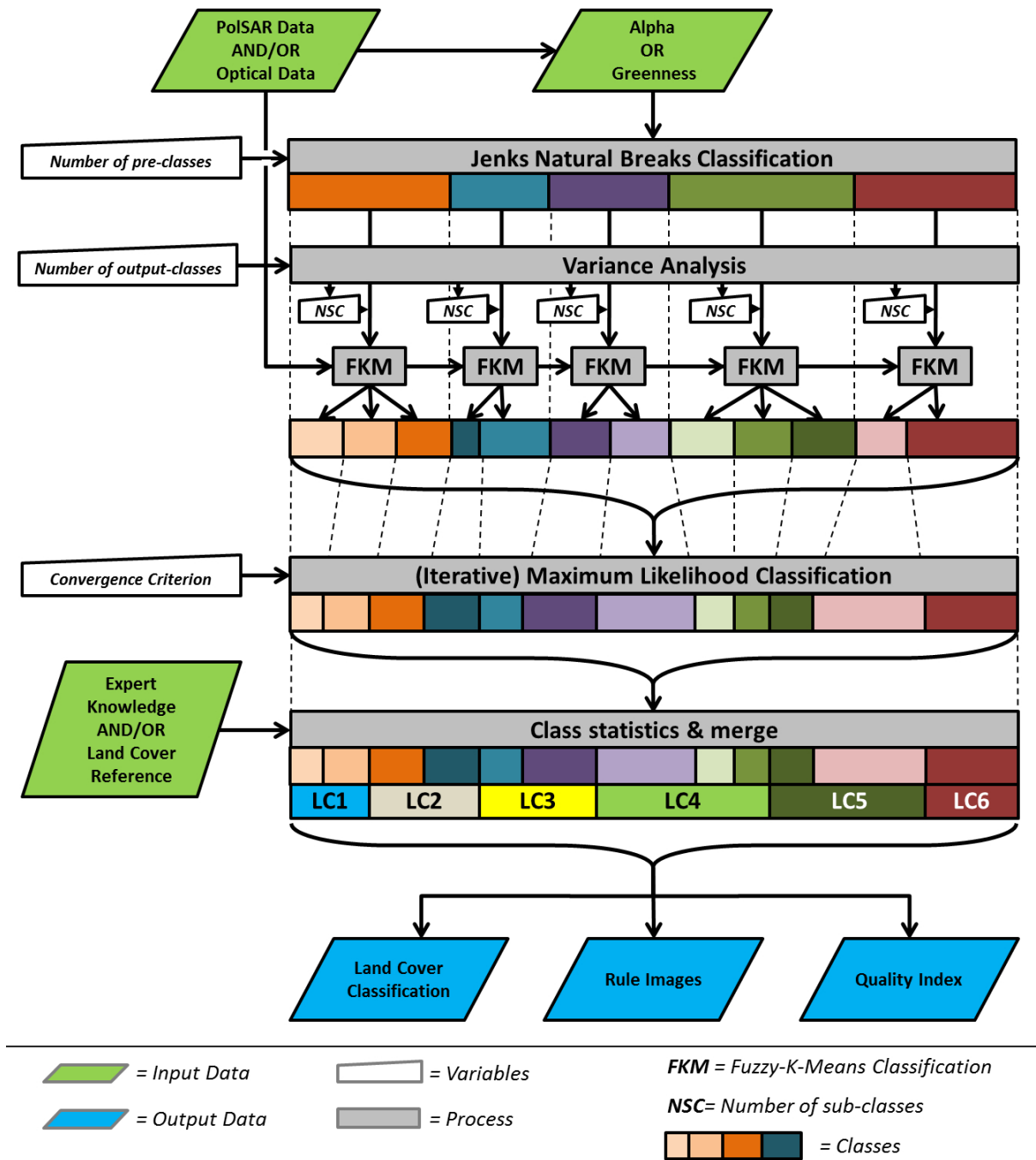


Figure 3.15: Process chart of FKM-ML unsupervised land cover classification. The iterative Maximum Likelihood classification is initialized with the Jenks-Natural-Breaks and the Fuzzy-K-Means classification. The approach handles PolSAR and multispectral data in the same way and is capable to analyze polarimetric and optical imagery. The unsupervised classes can be merged using expert knowledge and/or reference data in order to assess the accuracy of the classification in conventional way. Beside the classification map, the classifier outputs the rule images of the Maximum Likelihood Classification and an index that indicates the quality of the classification for each pixel. Source: Own figure, on the basis of Ullmann et al. (2014).

All of the shown classifiers were originally designed to operate with quad-polarized PolSAR data. Ullmann et al. (2014) showed an unsupervised classification technique that is capable to operate with dual- and quad-polarized PolSAR data and may also be applied to multispectral imagery and combined stacks of PolSAR and multispectral imagery. The unsupervised classifier (FKM-ML) is similar to the unsupervised PolSAR MLC of Lee et al. (2004). The algorithm uses a combination of the Jenks-Natural Breaks classification (Jenks (1967)), the Fuzzy-K-Means (FKM) classification (Canty (2006)) and the classical MLC. The intention of the approach is a robust classification of dual- and quad-polarized PolSAR and/or multispectral data. The approach is initialized by classifying categories using the Jenks-Natural-Breaks classifier. This algorithm is based on a single feature. *“This feature should be identified as sensitive and meaningful for characterization of the land cover in advance (e.g. the Alpha angle or the NDVI).”* (Ullmann et al. (2014), p. 8576). Afterward the FKM classification of Canty (2006) is applied to each pre-class separately and finally the statistics of the FKM classes are used to initialize an iterative MLC. The process chart is illustrated in Figure 3.15. The classifier was programmed in IDL 8.3 and implemented in the PolSAR ENVI Toolbox. The classification is performed in the following five steps according to Ullmann et al. (2014):

- (1) The classification is initialized by classifying a single feature with the Jenks-Natural-Breaks logarithm in an user defined number of classes. This technique searches for natural breaks in the histogram of the feature by comparing the variances of the potential classes and by shifting the class boundaries. The process is iterative and ends when the variances of all classes reach a local minimum. The classes can be interpreted as generalized categories of the reflectance (multispectral data), or as generalized scattering types of PolSAR data. In accordance to Ullmann et al. (2014) it was chosen to initialize the classification with the Tasseled Cap Greenness whenever multispectral data were used in the classification and to initialize the classification with the Alpha of T-Matrix for co- and quad-polarized data and with the Alpha of the C-Matrix for cross-polarized data. The default number of classes was set to six. This value was shown to be suited for the classification of the land cover in pretests (not shown).
- (2) In the following the standard deviations of the pre-classes are calculated with regard to all bands and channels. The total number of output-classes is then apportioned to each category with respect to the standard deviations. Each pre-class now has a number of sub-classes. The sum of all number of sub-classes is the total number of output-classes.
- (3) Each pre-class is then classified in the number of these sub-classes separately using the FKM algorithm of (Canty (2006)). This algorithm searches iteratively for a local minimum in the feature space and automatically defines the rules for the classification. This iterative process is stopped when the difference of the fuzzy class membership's matrices between two iterations reaches a small value. The FKM and K-Means algorithms are known to be weak when the number of output-classes is high and when the feature space has many dimensions. Ullmann et al. (2014) note: *“Since the FKM is applied to a subset of the feature space the calculation is fast and robust. This classification preserves the categories of the pre-classification [...]”* (Ullmann et al. (2014), p. 8577).
- (4) The statistics of the FKM classification are the input of the iterative MLC. During the MLC the covariance matrices and the mean vectors of all classes are analyzed. A multivariate Gaussian Normal Distribution is assumed in this context to facilitate the calculation and to make the computation the same for all types of input data (PolSAR and multispectral). Each class is now defined by multivariate Gaussian

### 3 Methodology

probability density functions. These are used to calculate the class memberships of every pixel in the image. The used logic is fuzzy and each pixel has a membership value for each class. The memberships of all classes of a certain pixel sum up to one. This continuous classification can be converted to a discrete classification by assigning the class with the highest membership (probability) value.

(5) This intermediate classification is now again the input for the MLC and the covariance matrices and the mean vectors are calculated. This process is iteratively repeated until less than five percent of all valid pixels change their class label between two iterations.

In unsupervised classification the number of output-classes is usually set to be higher than the number of target land cover classes. Therefore the number unsupervised classes must be reduced either by expert knowledge or reference data. In the latter case the unsupervised classes can be reduced (merged) with respect to percentaged occurrences of the reference land cover classes. Each unsupervised class can be assigned to the land cover class with the highest occurrence and with respect to the dominating coverage. The merging of unsupervised classes was done using the collected ground-truth reference data. The main intention was to be able to estimate the accuracy of the classification in the common way and to make the unsupervised classification result comparable to the supervised classifications.

#### 3.2.2.2 Classification of Water Bodies

The water surfaces can be delineated in a comparable uncomplex way by remote sensing image analysis and classification. The spectral reflectance and the polarimetric scattering characteristics of water surfaces are usually very different from non-water surfaces. However, the appearance of the water surface can be highly variable over time, e.g. the color and roughness of the water can change very fast. In radar imagery the differentiation of water and land is hindered since calm water and other smooth surfaces cause similar low intensity values. The same is true for areas that are shadowed. In contrast, the surface of rough water causes high intensity values and it is often difficult to distinguish between rough water and land surface. A way to overcome these limitations is the usage of polarimetric information - the type of the scattering is of importance: Water surfaces are characterized by a dominant single bounce signal and the intensity of double bounce or volume scattering is very low. The single bounce is also dominant if the surface is rough and therefore the double bounce and the volume scattering components (e.g. of the Two or Three Component Power Decomposition) can be used to identify water areas. The water bodies can have several different positions in the feature space due to the high variability of the water surface. Therefore it is an advance to classify water bodies prior to an unsupervised land cover classification and to reduce the variance of the feature space.

In this work the water bodies of the test sites were classified by an iterative threshold classifier that uses co- or quad-polarized PolSAR data. The process chart of that classifier is shown in Figure 3.16. The classification uses terrain corrected and sigma-nought calibrated PolSAR data. The Two or Three Component Decomposition is applied and the double bounce or volume bounce intensity is classified using a threshold that separates water and land (binary classification). However, the threshold needed for an optimal classification is unknown. The classifier is therefore applied iteratively and the threshold is increased after each iteration by adding a small value. The binary classification is done during each iteration and after a user defined number of iterations the algorithm counts how often a pixel was classified



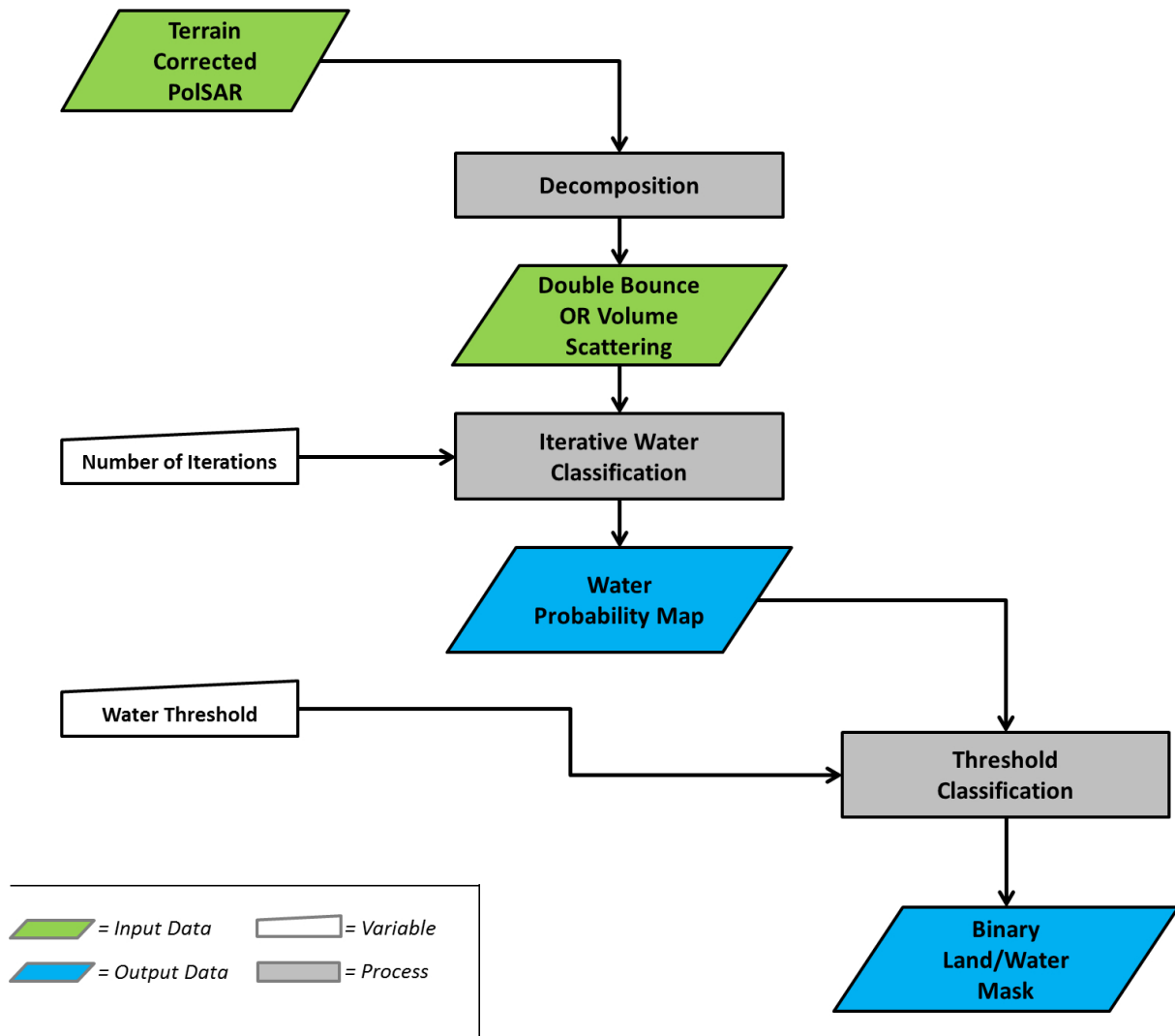
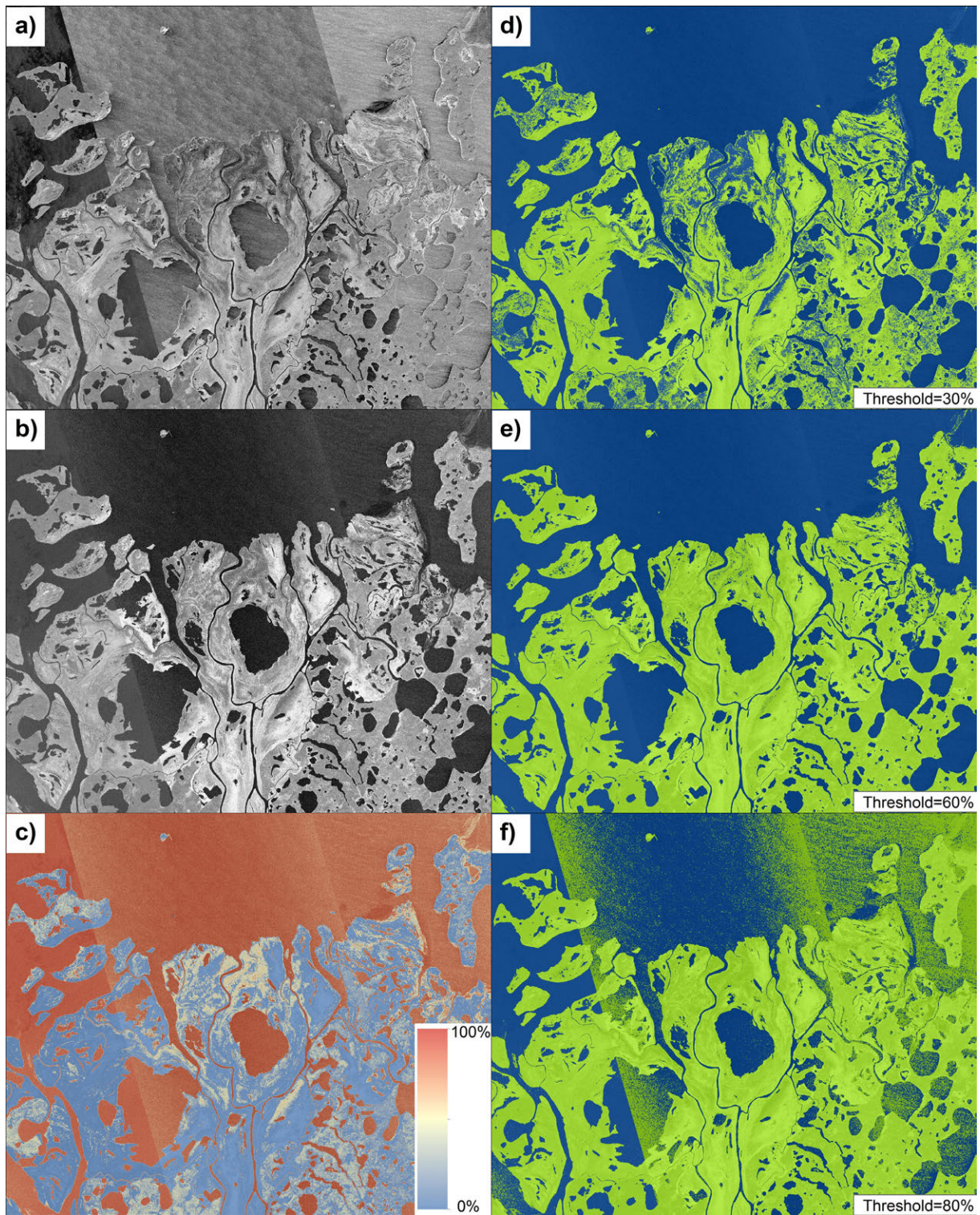


Figure 3.16: Process chart of iterative water classification. The water classification is based on the double bounce or volume scattering intensity of PolSAR data. The intensity information is recoded and transformed to the water probability map using an upper and lower thresholds. The upper threshold is increased during each iteration. The binary water classification is realized by thresholding the water probability map. Source: Own Figure.

as water and how often it was classified as land. These information are stored in a so called water probability map and the map is normalized with respect to the number of iterations. Therefore this step performs a recoding and transforming of the intensity information similar to a stretching. The final binary water classification is then obtained by applying a water threshold. This threshold is either set by the user or by suited algorithms, e.g. the OTSU algorithm (IDL8.1).

Figure 3.17 shows an example of the iterative water classification. Figure 3.17.a shows the span of three mosaiced co-polarized TSX images. It is visible that the water surface of the left scene is calm, the surface of the middle image is medium rough and the surface of the right image is very rough. Therefore the intensity of the span shows a high variety. In contrast, the intensities of the double bounce feature of the Two Component Decomposition (same data) are very low and all water surfaces appear dark in the



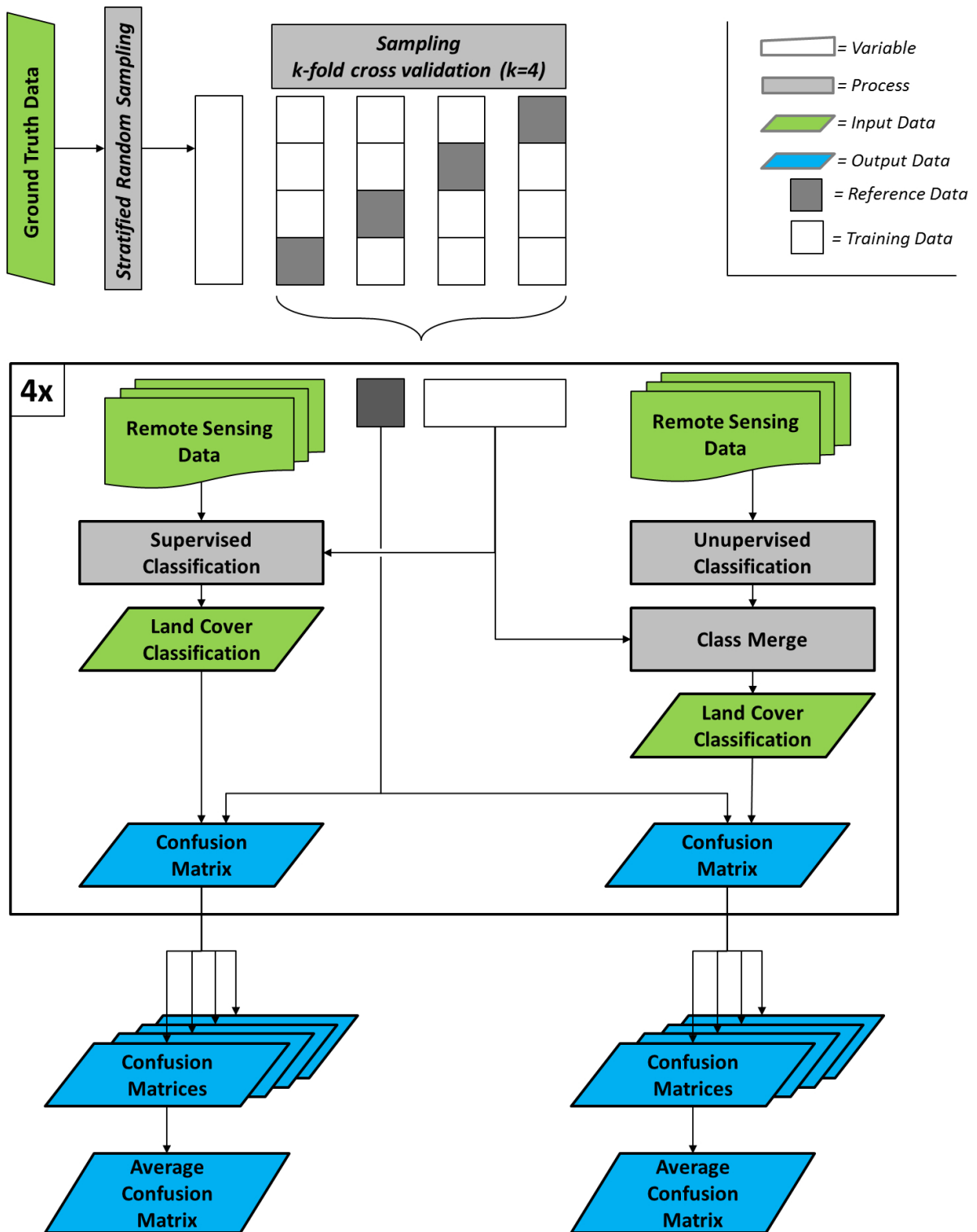


Figure 3.18: Process chart of the  $k$ -fold cross-validation with  $k=4$  for supervised and unsupervised classification. The classifications and the estimation of the classification accuracies are performed four times in order to take the variation of the data during the training and referencing into account. Source: Own Figure.

### 3 Methodology

image and have a low intensity (Figure 3.17.b). Figure 3.17.c shows the water probability map that was calculated with 300 iterations, a lower threshold of zero intensity and an upper threshold of an intensity of 0.075. These two thresholds were carried out in pretests and showed a satisfying transferability to other sites if sigma nought calibrated intensities were used (not shown). The example shows the binary classification if a threshold of 30% (Figure 3.17.d), 60% (Figure 3.17.e) or 80% (Figure 3.17.f) was used. The 60% threshold is visually the one that is best suited separate water bodies from land surfaces.

#### 3.2.3 Accuracy Assessment

One of the most important steps of image classification is the assessment of the classification accuracy. The accuracy can be estimated by comparing two data sets that show the same location of interest and have the class information in common. These sets are on the one hand the classification itself and on the other hand a set of independent reference data. These two data sources can be used to form an error matrix - or confusion matrix - which displays the relation between the classification and the reference in form of a table. Such an assessment makes it necessary to separate the reference data that are used in the classification process from the reference data that will be used to estimate the accuracy. The intention of this separation is to be able to independently quantify the quality of the classification and to avoid any blurring of the classification accuracy or over-fitting (Congalton & Green (2008)).

Table 3.1: Two class Confusion Matrix.

		Prediction		
		Class1	Class2	Row Total
Observation	Class1	A	B	e
	Class2	C	D	f
Column Total		g	h	I

A two class confusion matrix is shown in Table 3.1. Indices that characterize the accuracy of a classification can be calculated using the elements of the confusion matrix. For example, these indices are the Overall Classification Accuracy (*OAC*) (Equation 3.70), the False Positive Rate (*FPR*) (Equation 3.71) or the True Positive Rate (*TPR*) (Equation 3.72). In addition, the confusion matrix can be used to define the producer's accuracy *PA* (omission error) and the user's accuracy *UA* (commission error) of each class (Equation 3.73&3.74) (Jensen (1995), p.248). The accuracy matrices can be used to estimated the significance between paired observations, e.g. via the McNemer's test (McNemar (1947)). This test indicates if the inclusion of additional data had significant impact on the classification accuracy.

$$OAC = \frac{A+D}{I}, \text{ with } I = e + f = g + h \quad (3.70)$$

$$FPR = \frac{B}{A+B} \quad (3.71)$$

$$TPR = \frac{D}{C+D} \quad (3.72)$$

$$PA_{Class1} = \frac{A}{g} \quad PA_{Class2} = \frac{D}{h} \quad (3.73)$$

$$UA_{Class1} = \frac{A}{e} \quad UA_{Class2} = \frac{D}{f} \quad (3.74)$$

The accuracies of the unsupervised and supervised classification can be assessed in more comprehensive way by a  $k$ -fold cross-validation (Congalton & Green (2008)). The number of experiments  $k$  depends on the absolute number of the available reference pixels. A reasonable minimum of samples must be provided to ensure statistical significance. Usually the number of experiments is between three and five. During each experiment the total number of samples is apportioned into a training and a reference set. Each reference set is used to estimate the classification accuracy. Each training set is used to train the supervised classifier or to assign the land cover classes to the unsupervised classes. The samples can be selected with a stratified random approach. For this work the number of elements used for training or referencing were the same for each class to avoid misleading results. The cross-validation experiments are applied in order to take the variation of the data during the training and referencing into account. The confusion matrices can be calculated for each experiment in the classical way and the final assessment is done by averaging the confusion matrices of all experiments (Congalton & Green (2008)).

Figure 3.18 shows exemplary the process chart of the  $k$ -fold cross-validation. A random stratification is applied to the collected ground-truth data. The number of samples per class is the same and points are randomly selected to avoid spatial coherence. These data are then split in  $k$  reference and training sets. The size of the sets is regulated by the number of experiments. The training sets are used to classify the data in supervised way and to merge the classes of the unsupervised classification. These land cover classifications are then compared to the reference set and the confusion matrices are calculated. This process is repeated four times and the training and reference sets are permuted. Finally, all confusion matrices are averaged.

### 3.2.4 Classification of Terrain and Landform

The DEMs and topographic features can be used to classify the surface morphology and landforms in an unsupervised way (see Section 1.2.4). In the following two established pixel-based approaches of unsupervised landform classification are shown. These are the Nested Means landform classification of Iwahashi & Pike (2007) and the TPI based landform classification of Weiss (2001). In addition, a third classification technique is shown that operates in similar way but is more flexible and involves elevation in the classification processes. All of these algorithms are examples for classification techniques that operate with threshold divided variables. The thresholds are set by expert knowledge or automated algorithms. These approaches are a native way to use the actual value of a topographic attribute for a classification. They do not use any further comprehensive multivariate clustering to define the classes, but are useful for an initial evaluation and data exploration.

### 3 Methodology

Table 3.2: Classification approach of the Nested-Means Landform classification. The classification of Iwahashi & Pike (2007) is based on the three part geometric signature of the elevation, convexity and texture.

Feature	Classes and Feature Division															
	Very Steep				Steep				Moderate				Gentle			
Slope																
Convexity	-	+	-	+	-	+	-	+	-	+	-	+	-	+	-	+
Texture	-	+	-	+	-	+	-	+	-	+	-	+	-	+	-	+
Class	1	2	3	4	5	6	7	8	9	10	11	12	13	14	15	16

Table 3.3: Thresholds and class names of the TPI based landform classification. The landform classification of Weiss (2001) uses the slope, a small scale TPI and a large scale TPI to classify ten landform classes. The naming of these landforms is on the basis of Jenness (2006).

Name	Slope	Small TPI	Large TPI
Canyons, Deeply Incised Streams		$< -1$	$< -1$
Midslope Drainage, Shallow Valleys		$< -1$	$-1 < TPI < +1$
Upland Drainages, Headwaters		$< -1$	$> +1$
U-shaped Valleys		$-1 < TPI < +1$	$< -1$
Plains	$< 5^\circ$	$-1 < TPI < +1$	$-1 < TPI < +1$
Open Slopes	$> 5^\circ$	$-1 < TPI < +1$	$-1 < TPI < +1$
Upper Slope, Mesas		$-1 < TPI < +1$	$> +1$
Local Ridges / Hills in Valleys		$> +1$	$< -1$
Midslope Ridges / Small Hills in Plains		$> +1$	$-1 < TPI < +1$
Mountain Tops / High Ridges		$> +1$	$> +1$

**Nested-Means landform classification** - The Nested-Means Landform classification approach of Iwahashi & Pike (2007) uses three topographic features to classify the morphometry. The features used are the slope, the texture and the convexity (see Section 3.1.3). These form a three-part geometric signature and are used to classify eight, twelve or sixteen landform classes. The classification is initialized by classifying the slope into four classes based on the histogram information, if sixteen classes are distinguished. Each of these slope classes is divided into two classes based on the histogram of the convexity. Finally, the histogram of the texture is used to divide these eight classes again into two sub-classes. Table 3.2 shows the principle of the classification approach. The sixteen classes can be denominated by their landform class, for example, a class can be named “steep slope, low convexity, fine texture”. The approach can be applied to any kind of gridded DEM, but Iwahashi & Pike (2007) note that the size of the estimation window that defines the values of the topographic features has a strong impact on the classification result. This can directly be addressed to the scale problem discussed by Evans (2012). The approach is implemented in SAGA GIS 2.1 and the standard estimation window sizes of the texture and the convexity are 21x21 pixel. The standard estimation window size of the slope is 5x5 pixel. These standard values are in accordance to the values used by Iwahashi & Pike (2007) and were shown to provide reasonable results for the TDX IDEM and the ASTER GDEM in pretests (not shown).

**Topographic Position Index (TPI) based landform classification** - A further landform classification approach was presented by Weiss (2001). The approach can be used in two different ways: The first one uses the slope and one TPI. The second one uses the slope, a small scale TPI and a large scale TPI. The

classification is based on user-defined or fixed thresholds and the segmentation of the feature space is done without any further application of clustering techniques. The more frequently used classification is the second one that utilizes the two TPIs. In total Weiss (2001), Jenness (2006) classify the surface morphology into ten landform classes. These are defined by their slope values and both TPI values. Table 3.3 lists the used thresholds and the names of the landform classes in accordance to Jenness (2006). The approach is implemented in SAGA GIS 2.1 and the standard estimation window sizes of the TPIs are 200x200 m and 2000x2000 m.

**Modified TPI and Nested-Means landform classification** - The slope, the curvature and the relative topographic indices were shown to be meaningful topographic features to classify the morphometry of a landscape. Further features have been used in landform classification as shown by Hengl & Reuter (2009), p. 411. The classification of landforms is often based on threshold divided variables and therefore the number of landform classes is increasing very fast if many features are used. Seldom more than three features are used. For this work a landform classification technique was investigated that operates with three threshold divided variables. These variables are the elevation, the slope and a TPI. The technique can be applied in two different ways which are a quasi continuous classification and a discrete classification. The quasi continuous classification shows a large number of classes. These classes are not suited to be interpreted individually but provide an enhanced visualization of the landform ensemble. The discrete classification classifies the named topographic features in a manageable number of classes. These classes can be used for further classification or interpretation. Both approaches can be operated manually, e.g. by using thresholds that were identified to be meaningful in advance or thresholds with geomorphological relevance (e.g. provided by Barsch & Liedtke (1985)). A further way is to set the thresholds automatically, e.g. with the Jenks-Natural-Breaks algorithm (Jenks (1967)). This algorithm is suited for this task since the estimation of the thresholds is done individually for each feature. This classification approach was programmed in IDL 8.3 and implemented in the Terrain ENVI Toolbox. The process of the classification is schematically illustrated in Figure 3.21. The elevation information of the DEM, the slope and the TPI are classified using the threshold classification. The thresholds are variable inputs and can be defined manually or by the Jenks-Natural-Breaks algorithm. The number of thresholds regulates the number of landform classes. Further, the number of thresholds is used to modify the provided discrete colormap (legend). The colors are interpolated in accordance to the classification and the RGB vector is stored as a look-up table in the header of the classification file or external.

The intention of this classification is to provide a simple and applicable classification schema that shows the main morphometric attributes (elevation and slope) in combination with a scale dependent feature (TPI). The landforms and processes are often bounded to the altitude and therefore the elevation is a meaningful feature that should be included in the morphometric classification. Since the TPI information is scale dependent the named classifications can be drawn for several scales. The elevation and the slope are used independently of the chosen scale. That means that no averaging of the elevation or slope is performed when the scale of the TPI is changed.

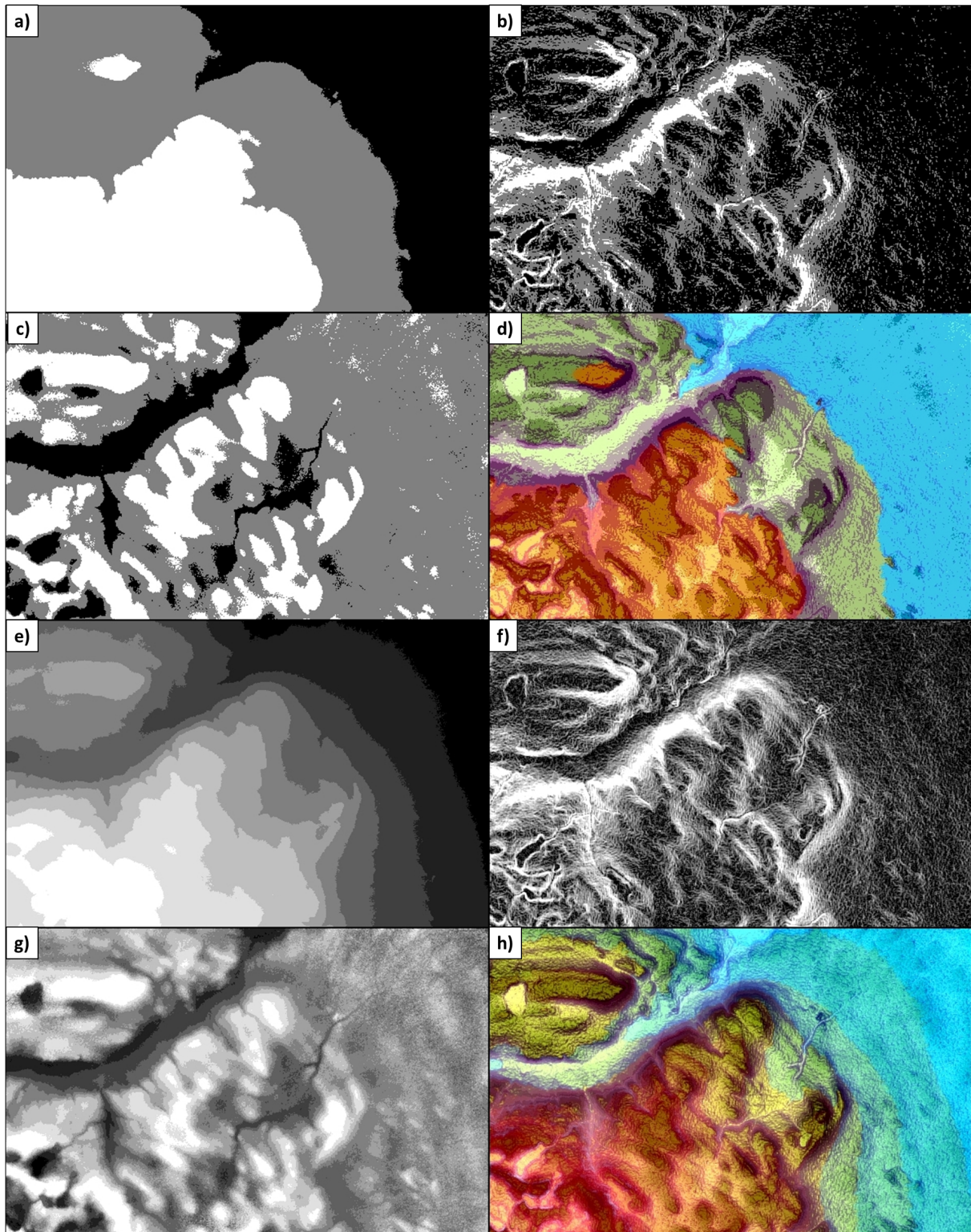


Figure 3.19: Example of discrete landform classification of elevation, slope and TPI: a) three elevation classes, b) three slope classes, c) three TPI classes, d) the combined landform classification with 27 potential classes, e) ten elevation classes, f) ten slope classes, g) ten TPI classes and h) the combined landform classification with 1000 potential classes. The thresholds used for the classification were estimated with Jenks-Natural-Breaks algorithm. Source: Own Figure.



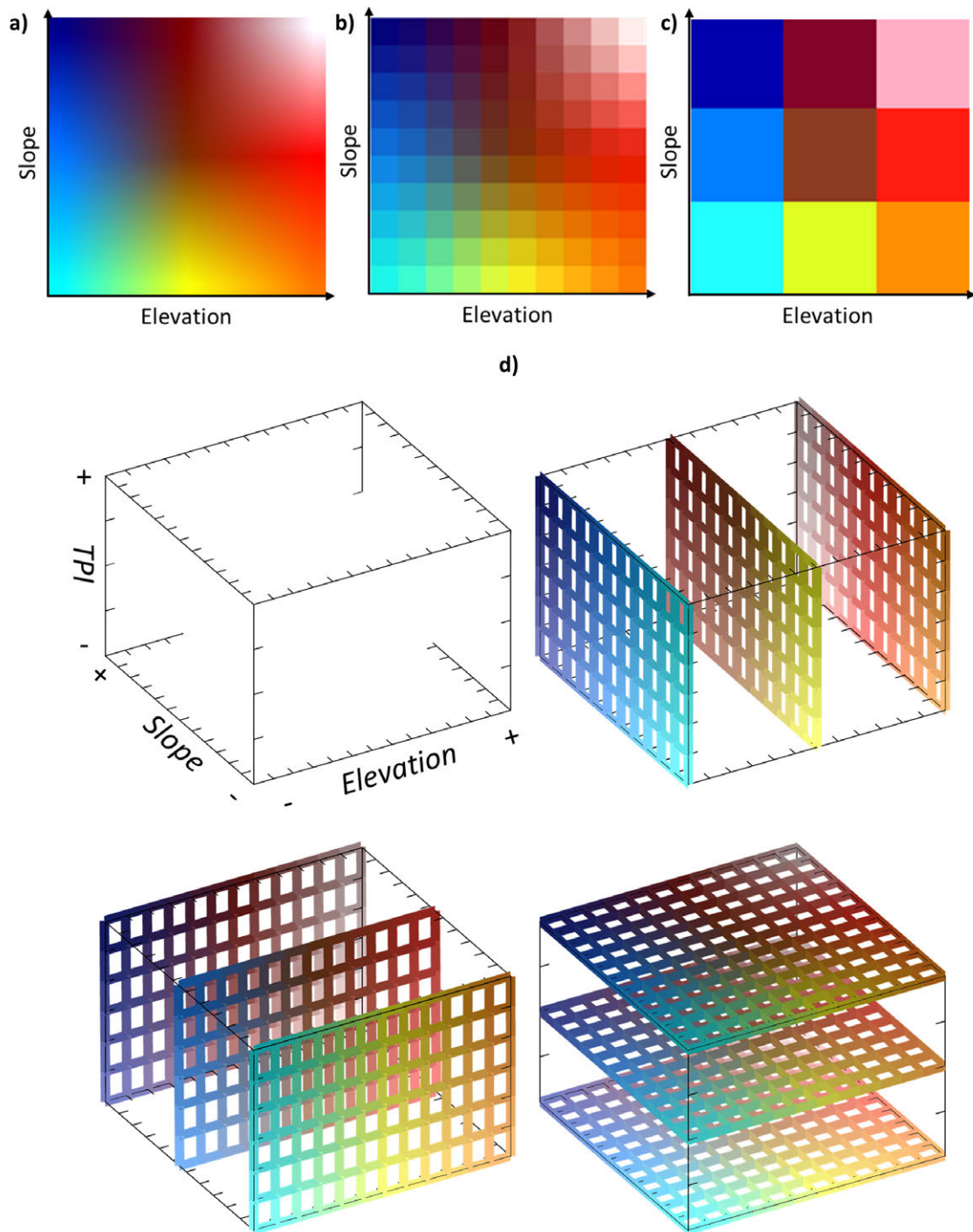


Figure 3.20: Legend of discrete and quasi continuous landform classification: a) 256 elevation and 256 slope classes, b) 10 elevation and 10 slope classes, c) 3 elevation and 3 slope classes and d) quasi continuous color cube of the elevation, slope and TPI. The color (hue) is defined by the slope and the elevation. The TPI changes the brightness and the darker (brighter) a color is the higher (lower) is the TPI value. Source: Own Figure.

### 3 Methodology

Figure 3.19 shows exemplary the discrete landform classification composed of three elevation classes (Figure 3.19.a), three slope classes (Figure 3.19.b) and three TPI classes (Figure 3.19.c). In total the classification has 27 (3x3x3) classes (Figure 3.19.d). The thresholds were estimated using the Jenks-Natural-Breaks classification algorithm. Figure 3.19.e shows exemplary the quasi continuous landform classification composed of ten elevation classes, ten slope classes (Figure 3.19.f) and ten TPI classes (Figure 3.19.g). In total the classification has 1000 (10x10x10) classes (Figure 3.19.h). The colors of such a landform classification are defined by a colormap. The color (hue) is defined here by the slope and the elevation and is fix for any scale. The TPI values modifies the brightness of the color and therefore the actual color vectors change with the scale. Figure 3.20 shows the interpolation of a initial colormap (Figure 3.20.a) to ten slope and ten elevation classes (Figure 3.20.b) and to three slope and three elevation classes (Figure 3.20.c). Figure 3.20 shows the color cube that provides the colors of the continuous landform classification for the elevation, the slope and the Topographic Position index. For better visibility the colors are shown as grids and only for selected sections. The figure indicates how the TPI categories affect the colors. The darker (brighter) a color is the higher (lower) is the TPI value. Therefore the TPI values do not change the hue (color) but the brightness.

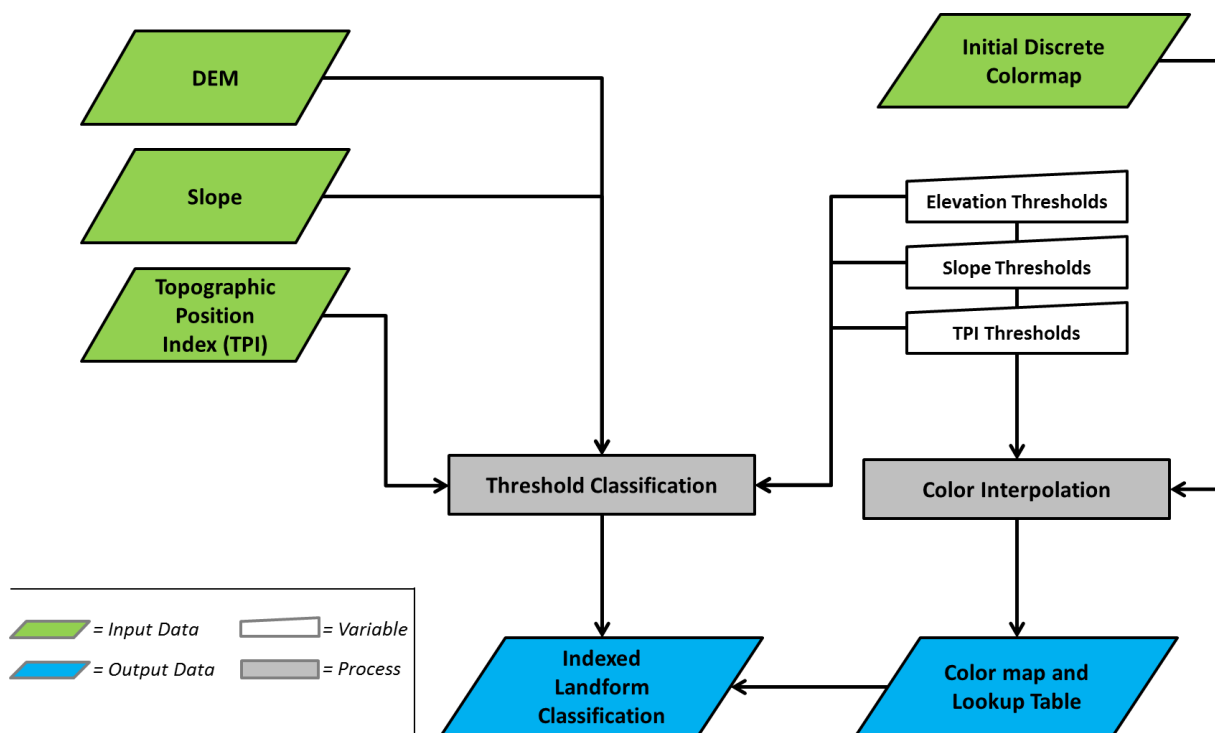


Figure 3.21: Process chart of the landform classification of elevation, slope and TPI. The approach is based on threshold divided variables. The thresholds are set manually or by the use of the Jenks-Natural-Breaks algorithm. The colors of the classification are set automatically (compare Figure 3.20). Source: Own Figure.

---

## Results

### 4.1 Evaluation of Methodological Concepts

The first part of this chapter shows results of the evaluation of the Non-Local Means image filtering. The parametrization of the filter and its performance were evaluated via speckle evaluation indices and qualitative visual analysis. The provided image examples highlight the benefits of the filtering for the interpretation of PolSAR data. In the following the influence of the filtering on the classification is shown. Afterward, the features of the Two Component Decomposition are evaluated by comparing the decomposition features of quad-polarized R-2 data. The scatterplot analysis and the correlation analysis were carried out for two test sites of the Mackenzie Delta Region. The third section presents results of the unsupervised FKM-ML classifier. The performance of this classifier was compared to other standard unsupervised classification techniques via a Receiver Operating Characteristic (ROC).

#### 4.1.1 Non Local Means Filtering

As shown in Section 3.1.1.2 the aim of the developed Non-Local Means filter is to provide a fast and effective filtering of a PolSAR images and to enhance the suitability of these data for the classification. The developed Non-Local Means filter can be applied to any kind of input data and requires the definition of three parameters: the patch window size, the search window size and the filtering power (parameter  $h$ ). The patch window size defines the size of the patches that are compared. The number of patches is regulated via the size of the search window. The smaller the patches and the smaller the search window, the faster is the processing. There is a trade-off between an adequate filtering and the processing time, however. Therefore the first aim was to find parameters that provide good results and have an acceptable computation load. With view to the recent literature the patch window size and the search window size were set to fixed parameters and the patch window size was fixed to 31x31 pixels. This size has been shown to be sufficient to find enough similar pixels for the filtering and to provide an acceptable processing time (not shown). In this context the search window size was fixed to a size of 3x3 pixels (see Section 3.1.1.2). The parameter of interest that has to be defined via a parametrization is therefore the parameter  $h$ .

## 4 Results

This parameter regulates the strength - or power - of the filtering and it defines the similarity of the patch of interest and any other patch in the search window. The parameter  $h$  has no influence on the processing time. The parametrization of the parameter  $h$  has been extensively discussed during the last years (see Section 1.2). Since the aim of this filter is an application of processed and detected data the estimation of the parameter  $h$  was done here in an empirical way and will not include any further modeling.

### 4.1.1.1 Parametrization

The PolSAR data of TSX and R-2 were processed in accordance to the processing chain described in Section 3.1.1.3 in order to find an adequate value for parameter  $h$ . This was done for the test sites Richards Island (RIS), Tuktoyaktuk (TUK) and East Channel (ECH). For each site the data were filtered as described in Section 3.1.1.2 and the parameter  $h$  was altered during the processing. In total ten filtered images were derived for each site and  $h$  was increased by 0.005 after each iteration. Figure 4.1.a shows the unfiltered span after processing. Figure 4.1.b shows the Non-local Means filtered span with  $h=0.005$ . Figure 4.1.c the Non-local Means filtered span with  $h=0.010$ . Figure 4.1.d the Non-local Means filtered span with  $h=0.015$ . Figure 4.1.e the Non-local Means filtered span with  $h=0.020$  and Figure 4.1.f the Non-local Means filtered span with  $h=0.030$ . It is obvious that  $h$  has strong influence on the filtering and that details of the image get lost with the increment of parameter  $h$ . The filtered images still show that main features are preserved and the blurring is moderate.

These data were used to quantify the influence of parameter  $h$  on the image quality. Each filtered image was split in a set of 40 image chips with a size of 300x300 pixels to increase the test statistics. In total a set of 120 image chips of TSX and R-2 data were processed. In the following the speckle evaluation indices Preservation of Mean (POM), Speckle Reduction Index (SRI), Edge Enhancement Index (EEI) and the Overall Evaluation Index (OAI) were calculated for each filtered image chip and summarized (see Section 3.1.1.2). Figure 4.2.a shows that the POM was decreasing with an increment of the parameter  $h$ . The POM was about 0.95 for  $h=0.01$  and about 0.85 for  $h=0.04$ . The range of POM was less than 0.15 for each set. The SRI (Figure 4.2.b) was increasing with an increment of parameter  $h$ . The SRI was on a high level of about 0.8 if parameter  $h$  was greater than 0.025. The EEI decreased with an increment of parameter  $h$  (Figure 4.2.c). This indicated a blurring of edges with increasing parameter  $h$ . The OAI (Figure 4.2.d) indicated that the best trade-off between POM, SRI and EEI was observed for parameter  $h$  being in the range from 0.025 to 0.030.

Very similar observations were made for the R-2 data (Figure 4.3). The POM of R-2 data was decreasing with an increment parameter  $h$  (Figure 4.3.a). The SRI was increasing for parameter  $h$  values between 0.005 and 0.025 and the SRI was on a high level of about 0.75 if parameter  $h$  was greater than 0.025 (Figure 4.3.b). The EEI decreased linearly with an increment of parameter  $h$  (Figure 4.3.c) and the variances were increasing as well. As observed for the TSX data the OAI (Figure 4.3.d) indicated that the best trade-off between POM, SRI and EEI was observed for parameter  $h$  being in the range from 0.025 to 0.030. Based on this evaluation the Non-Local Means filtering of all following operations was done with a parameter  $h$  equal to 0.025 for TSX and R-2 data. In terms of the speckle evaluation indices this means that the mean values will be preserved on a level of about 85%, the speckle will be reduced on a level of about 65% and the edges will be slightly blurred with an average EEI of about 90%.

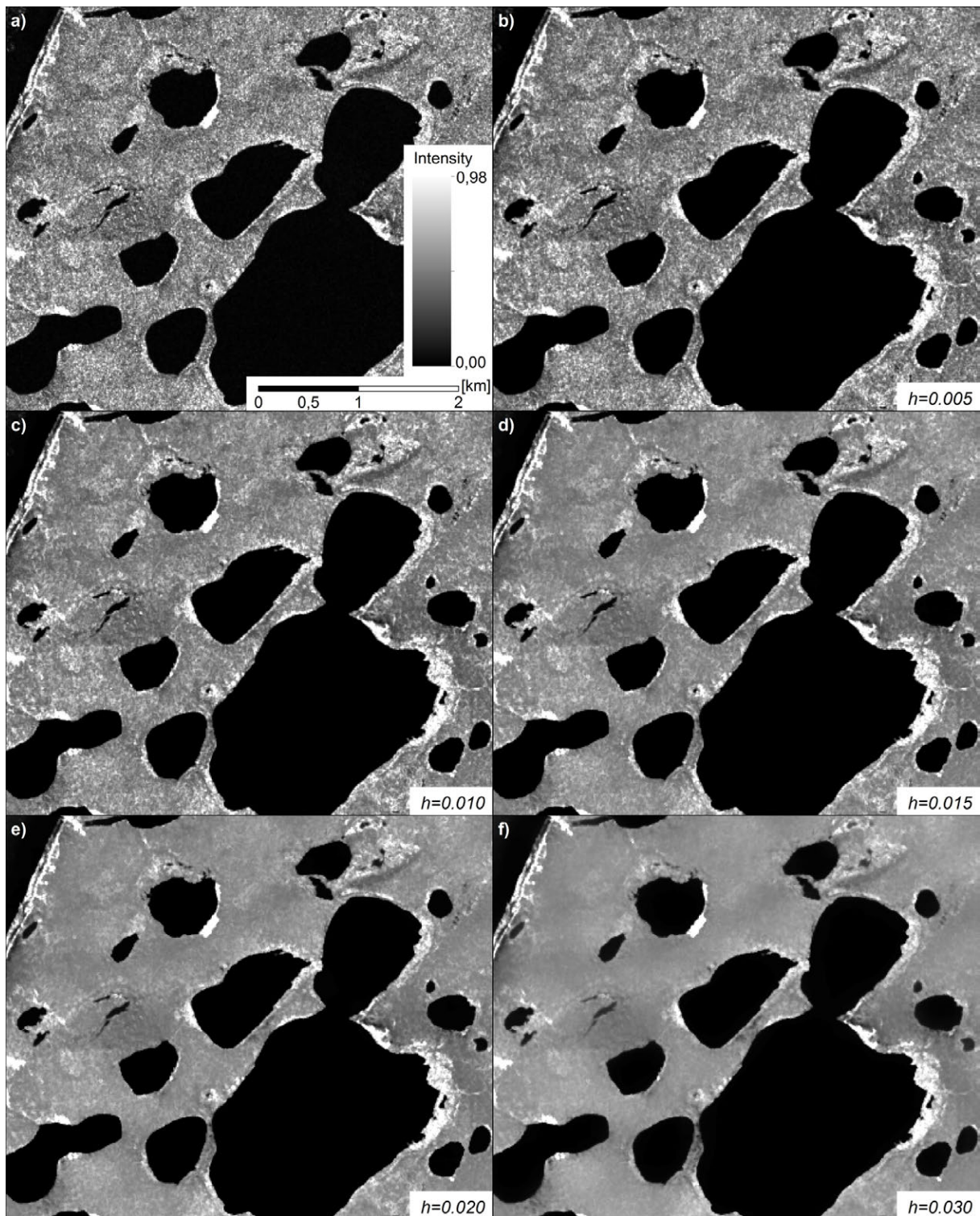


Figure 4.1: Processing examples of Non-Local Means filtering and influence of parameter  $h$  on the filtering: a) original unfiltered image, b) filtered image with  $h=0.005$ , c) filtered image with  $h=0.010$ , d) filtered image with  $h=0.015$ , e) filtered image with  $h=0.020$  and f) filtered image with  $h=0.030$ . Details get lost with an increment of parameter  $h$ . The filtered images still show the main features and the blurring of edges and boundaries is moderate. Source: Own Figure.

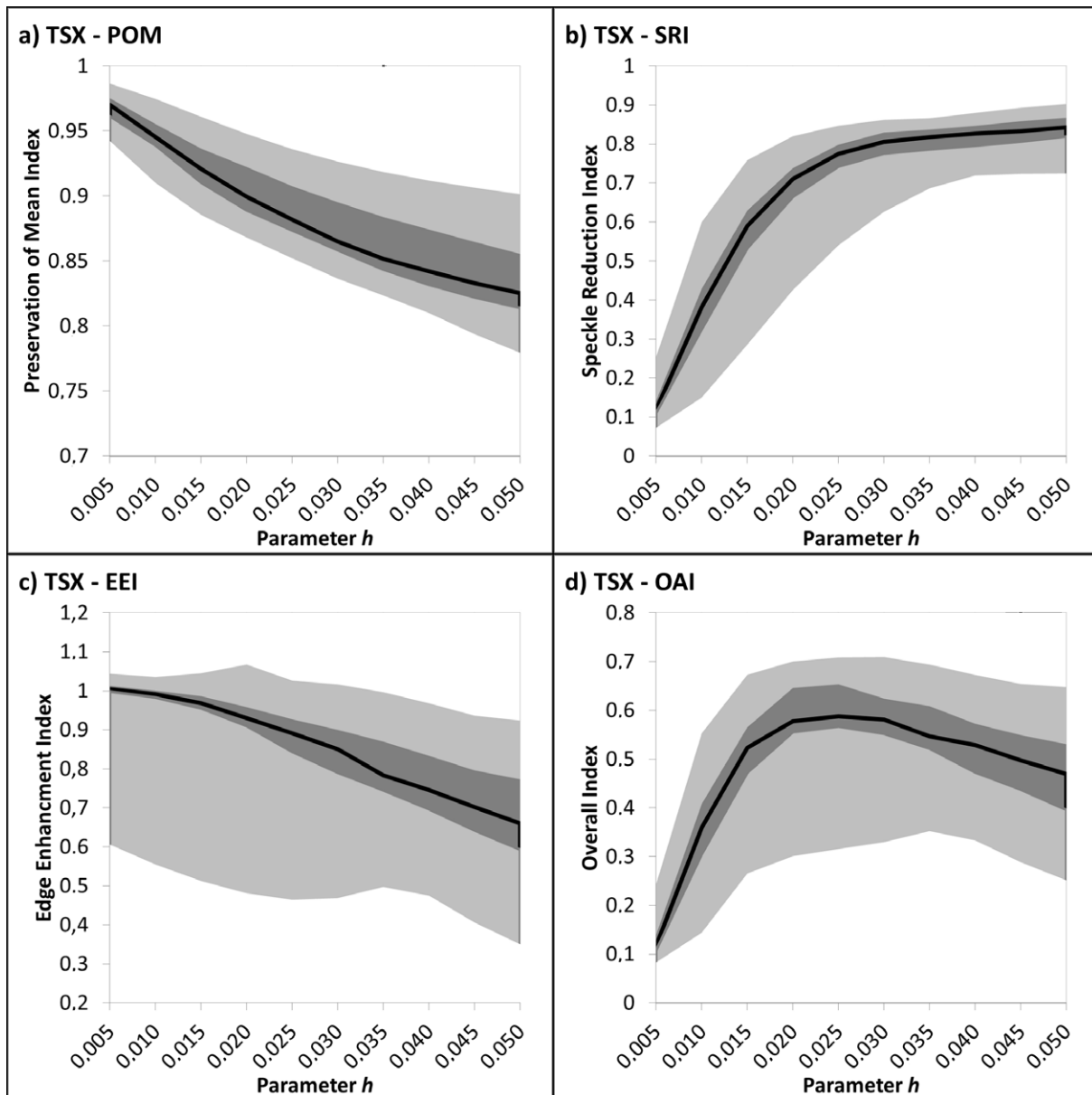


Figure 4.2: Parametrization of Non-Local Means filtering (TSX data). Mean values (black line), 25%-50% quartiles (dark gray) and 1%-99% quartiles (light gray) of: a) Preservation of Mean (POM), b) Speckle Reduction Index (SRI), c) Edge Enhancement Index (EEI) and d) Overall Evaluation Index (OAI) of TSX co-polarized imagery. Source: Own Figure.

#### 4.1.1.2 Performance Evaluation

The performance of the Non-Local Means filtering was evaluated visually in the following. The data of the test sites of the Mackenzie Delta Region, of Banks Island and of the City of Ottawa (data provided by DFD, DLR 2013) were filtered with the Non-Local Means filter. The processing parameters were fixed as described in the former section. The data analyzed in this way were quad-polarized R-2 data and co-polarized TSX data. Figure 4.4 shows a processing example of co-polarized TSX imagery of the northern Mackenzie Delta. Figure 4.4.a shows the unfiltered image after the pre-processing (multi-looking

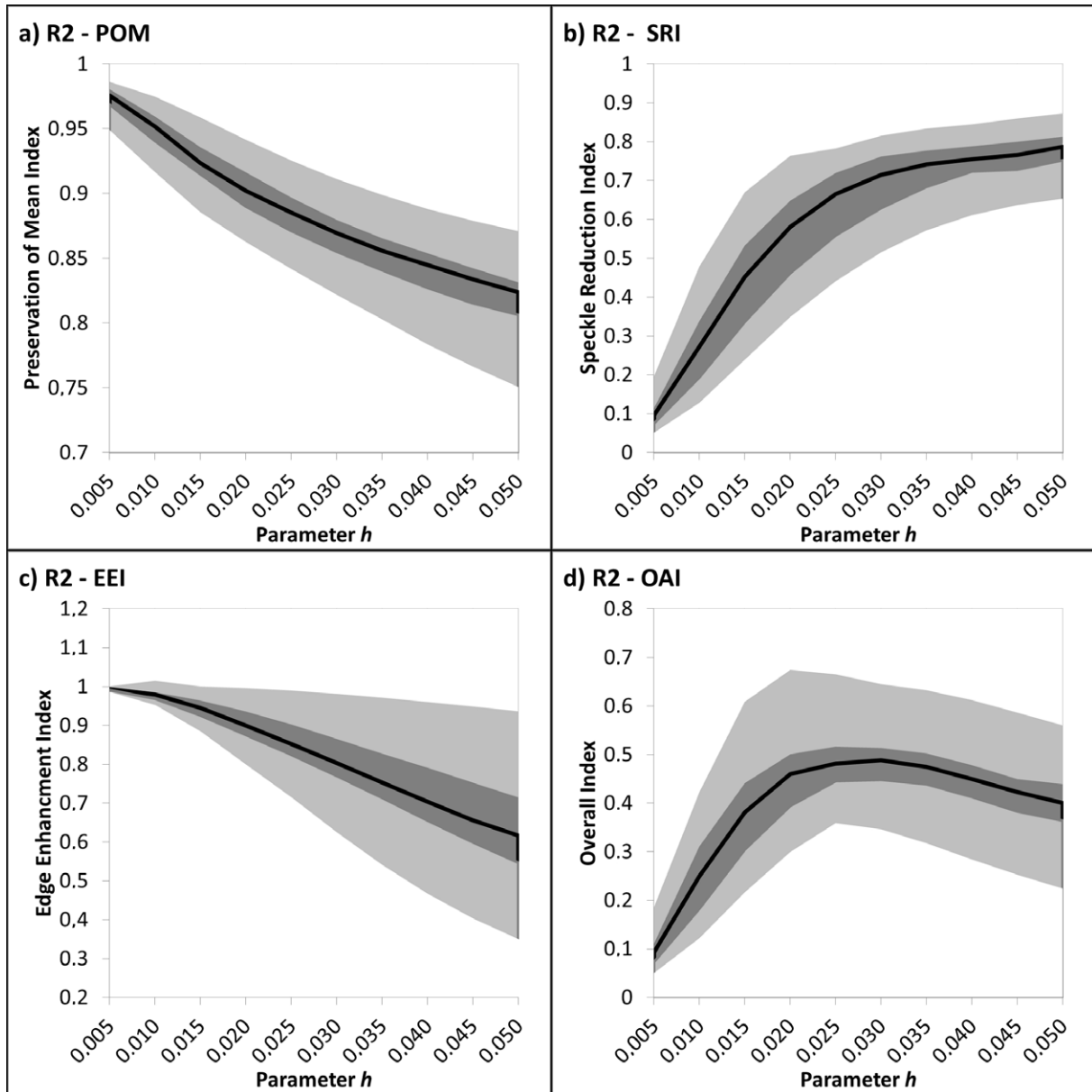


Figure 4.3: Parametrization of Non-Local Means filtering of R-2 data. Mean values (black line), 25%-50% quartiles (dark gray) and 1%-99% quartiles (light gray) of: a) Preservation of Mean (POM), b) Speckle Reduction Index (SRI), c) Edge Enhancement Index (EEI) and d) Overall Evaluation Index (OAI) of R-2 data. Source: Own Figure.

and geocoding). The image is shown as a RGB false color composite of the Kennaugh Matrix elements K0 (R), K3 (G) and K4 (B). It is visible that the image had a noisy texture and the water areas appeared grainy. Figure 4.4.b shows the same image after Non-Local Means filtering. The image was much smoother and the effect of filtering was clearly visible. The example shows that the boundaries between water and land were preserved and there was no blurring of the edges. This is best visible comparing Figure 4.4.c and Figure 4.4.d: These two images show the contour lines of the sigma nought intensity of the unfiltered and filtered image. It was observed that the filtering was strongest on the noisy and grainy parts of the image. The number of counter lines was reduced. The same was visible for the hillshaded values that

#### 4 Results

were derived from the unfiltered (Figure 4.4.e) and filtered (Figure 4.4.f) sigma nought intensity data.

The developed Non-Local Means filtering was applied to the Scattering Matrix as discussed in Section 3.1.1.2. Because of this all derivatives of the Scattering Matrix will be smoothed and filtered as well. The following example illustrates this for the intensity, the Entropy and the Alpha of the eigendecomposition (Figure 4.5). The left side of Figure 4.5.a&c&e shows the unfiltered data and the right side (b, d, f) the filtered data. The figure shows co-polarized TSX data of Ottawa City, Banks Island and Richards Island. Again the filtering removed noisy and grainy texture and the edges of the images were well preserved. This is visible in the example of Ottawa (first row): The noisy but homogeneous regions of the parking area were filtered while the shape of the buildings and cars remained sharp and clearly visible. The filtering helped to enhance the image interpretation: The small valleys of the Banks Island data (second row) were hardly visible in the unfiltered Entropy. They appeared much more pronounced and distinct in the filtered image. This was also shown for the erosion slumps in the Richards Island scene (third row). This landscape feature appeared with low values in the image at the shore of inland lake. The slumps were hard to be identified in the unfiltered image. After the filtering the slumps were clearly highlighted by unique low values and a sharp and distinct shape.

Beside the visual analysis the performance of the Non-Local Means filtering was evaluated by comparing the Non-Local Means filtering to standard filtering techniques. It was chosen to compare the filter to the standard Boxcar and the Lee Filter. These two well-known filters were selected since they provide a comprehensible computation and as they are known to be efficient and often used for image filtering (Section 3.1.1.2). The Lee Filter is further more a standard processing technique to filter SAR and PolSAR imagery and to preserve the edges in an image.

The following analysis was performed for TSX and R-2 data of the test sites RIS, TUK and ECH. The Boxcar and Lee filtering were applied with window sizes of 3x3, 5x5, 7x7 and 9x9 pixels. The Equivalent Number of Looks (ENL) needed for the Lee filtering was estimated with the functions of the Radar Tool Box (RAT). The Boxcar and Lee filters were processed in ENVI 5.1. The Non-Local Means filtering was processed with parameter  $h$  equal 0.025 using a search window size of 31x31 pixels and a patch window size of 3x3 pixels. Each filtered image was split in a set of 40 image chips with a size of 300x300 pixels. In total a set of 120 image chips of TSX and 120 image chips of R-2 data were obtained. Afterward the speckle evaluation indices POM, SRI, EEI and OAI were calculated for the Boxcar filtered chips (M3, M5, M7 and M9), the Lee filtered chips (L3, L5, L7 and L9) and the Non-Local Means filtered chips (NL) for all sites and both sensors. The results of this analysis are shown in Figure 4.6. It was observed that the POMs of the Boxcar filtered and Lee filtered image chips were decreasing when the size of the window was increased (Figure 4.6.a). The reduction of POM was stronger for the Boxcar filtering. The best values of the POM were observed for M3, L3 and NL. The evaluation of the SRI (Figure 4.6.b) showed that both Boxcar and Lee filter led to a similar reduction of speckle. The SRI was increasing when the size of the window was increased. The highest values (about 0.85) were observed for M9 and L9. The average SRI of the NL filtered image chips was about 0.8 and the performance was comparable to M7 and L7. The highest EEI was observed for the NL filtered image chips with a value of about 0.9 (Figure 4.6.c). The EEI of NL was higher than the EEIs of the Boxcar or Lee filtered image chips. The index decreased for both Boxcar and Lee filter when the size of the window was increased. The decrease of the EEI was strongest when the Boxcar filter was used. This indicated that the Lee filtering was better suited to preserve the



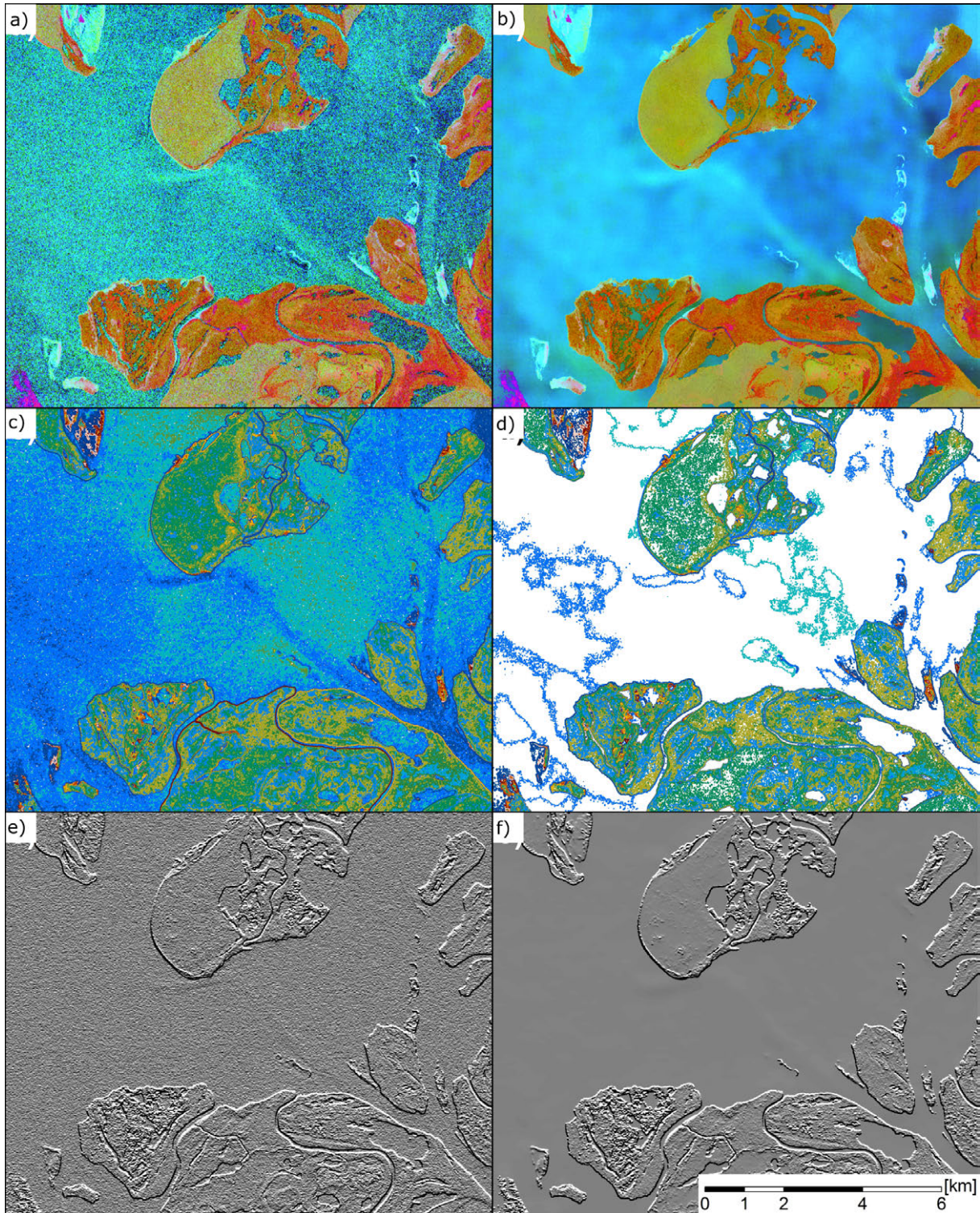


Figure 4.4: Processing example of Non-Local Means image filtering: a) original image, b) Non-Local Means filtered image, c) intensity-isolines of original image, d) intensity-isolines of Non-Local Means filtered image, e) hillshaded intensity of original image and f) hillshaded intensity of Non-Local Means filtered image. Source: Own Figure.

#### 4 Results

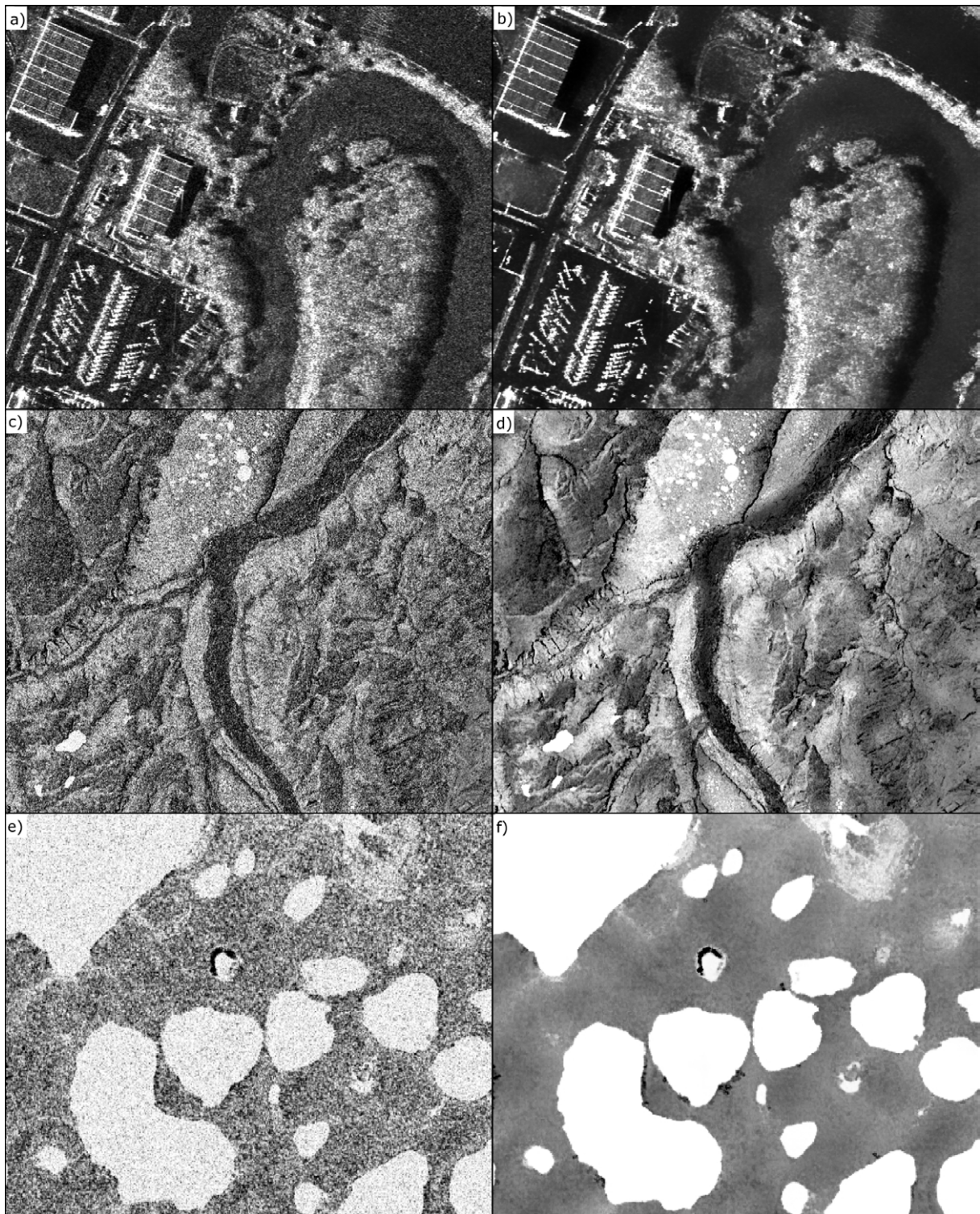


Figure 4.5: Processing example of Non-Local Means image filtering: a) original HH intensity [dB], b) Non-Local Means filtered HH intensity [dB], c) original Entropy, d) Non-Local Means filtered Entropy, e) original Alpha and f) Non-Local Means filtered Alpha. Source: Own Figure.

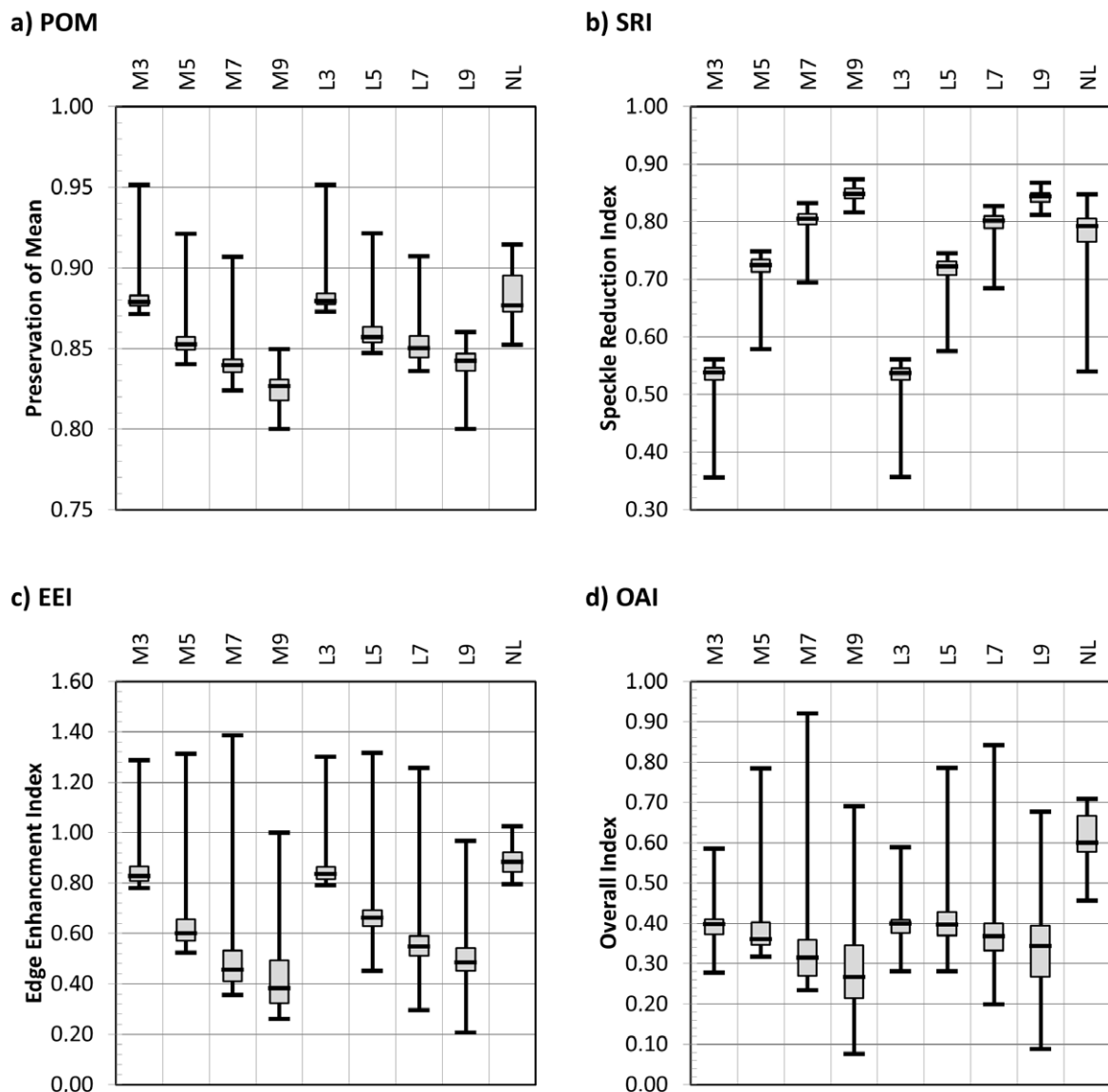


Figure 4.6: Evaluation of Non-Local Means filtering. Comparison of Boxcar Filter filtered images (M3-M9), Lee Filter filtered images (L3-L9) and Non-Local Means filtered images (NL). Boxplots of: a) Preservation of Mean (POM), b) Speckle Reduction Index (SRI), c) Edge Enhancement Index (EEI) and d) Overall Evaluation Index (OAI). Source: Own Figure.

edges in the image. The evaluation of the OAI revealed that the best trade-off between the indices was realized with NL, followed by L5 and M3 (Figure 4.6.d).

The Non-Local Means filter defined in Section 3.1.1.2 does not require any specific type of input data. The algorithm is capable to handle any multilayer or single layer input. The Non-Local Means filtering can therefore also be used to filter DEM data. In this case the first weight can be interpreted as the height difference between the pixel of interest and any other pixel in the search window. The second weight can be interpreted as the difference between the patch of interest and any other patch in the search window. The parameter  $h$  is then defined in the unit meters and can be interpreted as a topographic tolerance. The

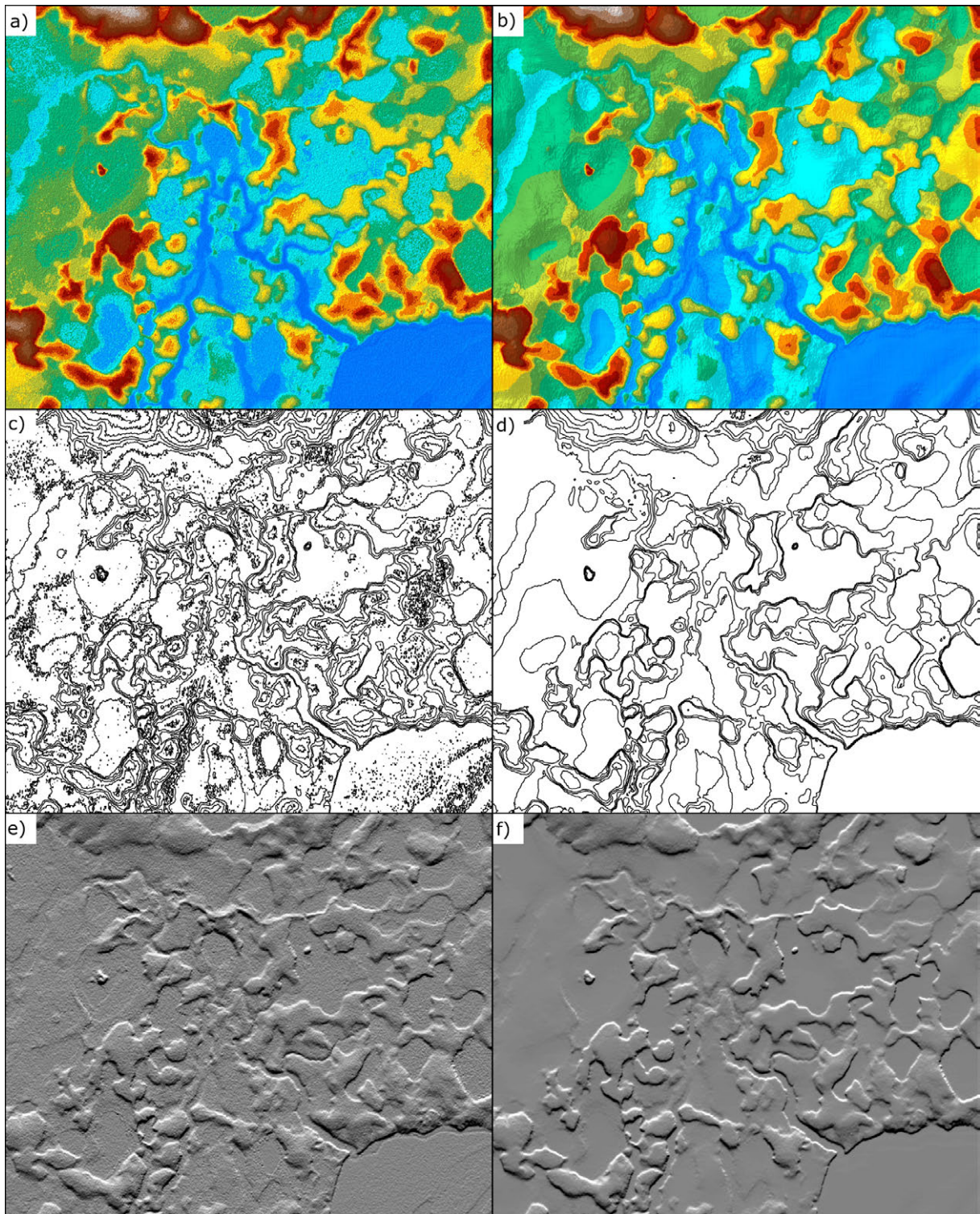


Figure 4.7: Processing Example of Non-Local Means filtering: a) original TDX IDEM, b) Non-Local Means filtered TDX IDEM, c) contour lines of original TDX IDEM, d) contour lines of Non-Local Means filtered TDX IDEM, e) hillshade of original DEMTDX IDEM and f) hillshade of Non-Local Means filtered TDX IDEM. Source: Own Figure.

filtering of DEM data was investigated using the TDX IDEM data. The parametrization was performed manually and a parameter  $h$  in the range from one to three meters was identified to provide meaningful results (not shown). Figure 4.7 shows a processing example of a site in the north-east of Inuvik (Mackenzie Delta Region). Figure 4.7.a shows the unfiltered IDEM and Figure 4.7.b the filtered IDEM. The contour lines of both images are shown in Figure 4.7.c and Figure 4.7.d. The hillshades are drawn in Figure 4.7.e and Figure 4.7.f. The Non-Local Means filtering was most effective for regions with gentle slopes and for regions with a low topographic variation. This is visible in the image for the wetland areas in the lower right corner of the image and the gentle mid slopes in the upper left corner of the image. The contour lines and the hillshade appear much smoother in these regions and provide a better view on the topography.

##### 4.1.1.3 Influence on Class Separability and Classification Accuracy

The influence of the Non-local Means filtering on the separability and the land cover classification was investigated. The separability of the classes was estimated using the Jefferys Matusita Distance (JM) and the Bhattacharyya Distance (BD) (Jensen (1995, 2007)). The separability analysis was conducted for the test sites RIS, TUK and ECH using co-polarized TSX, quad-polarized R-2, cross-polarized ALOS data and the land cover reference data (see Section 2.2.1). The JM and BD were calculated using the unfiltered images, the Boxcar filtered images and the Non-local Means filtered images. The results of this comparative analysis are shown in Figure 4.8. The analysis of the JM (Figure 4.8.a) showed that both Boxcar filter (M7) and Non-Local Means filter (NL) increased the separability of the classes. The JM of filtered data was in average about 0.1 higher than the JM of the unfiltered data. This was observed for data of all sensors, however, the JM values showed a fast saturation and values close to 1.4. This is the maximum value of the JM. The analysis of the BD (Figure 4.8.b) offered a more complete picture and showed that the separability of classes was highest for Non-Local Means filtered images. This was observed for the TSX, R-2 and ALOS data. In average the BD was about +2.0 higher compared to the unfiltered images and the Boxcar and Lee filtered images. The results indicated that the filtering of the PolSAR data had a positive influence on the separability and the Non-Local Means filtering was shown to provide the highest increase in the separability among the investigated filters.

The direct influence on the classification accuracy was investigated in the following and several supervised classifications were calculated using co-polarized TSX data of the three sites RIS, TUK and ECH. The images were classified using ENVI's Maximum Likelihood classification (MLC) (see Section 3.2.1). The training statistics and the classification accuracies were derived and assessed with the land cover reference data (see Section 4.1.3). In total three classifications were processed for each site: a MLC that used the unfiltered data, a MLC that used the Boxcar filtered data and a MLC that used the Non-Local Means filtered data. The classification accuracies were derived as normalized confusion matrices (see Section 3.2.3). Figure 4.9 shows the influence of the Boxcar filtering and of the Non-local Means filtering on the classification accuracies of the supervised MLC. Figure 4.9.a shows the average accuracies of the unfiltered data versus the accuracies of the Non-Local Means (NL) and the Boxcar filtered data (M7). It was noticeable that both classifications showed a better classification performance. The classification accuracy was in average +10% higher for the Non-Local Means filtered data and in average +5% higher for the Boxcar filtered data. Figure 4.9.b shows the average accuracies of the Non-Local Means filtered

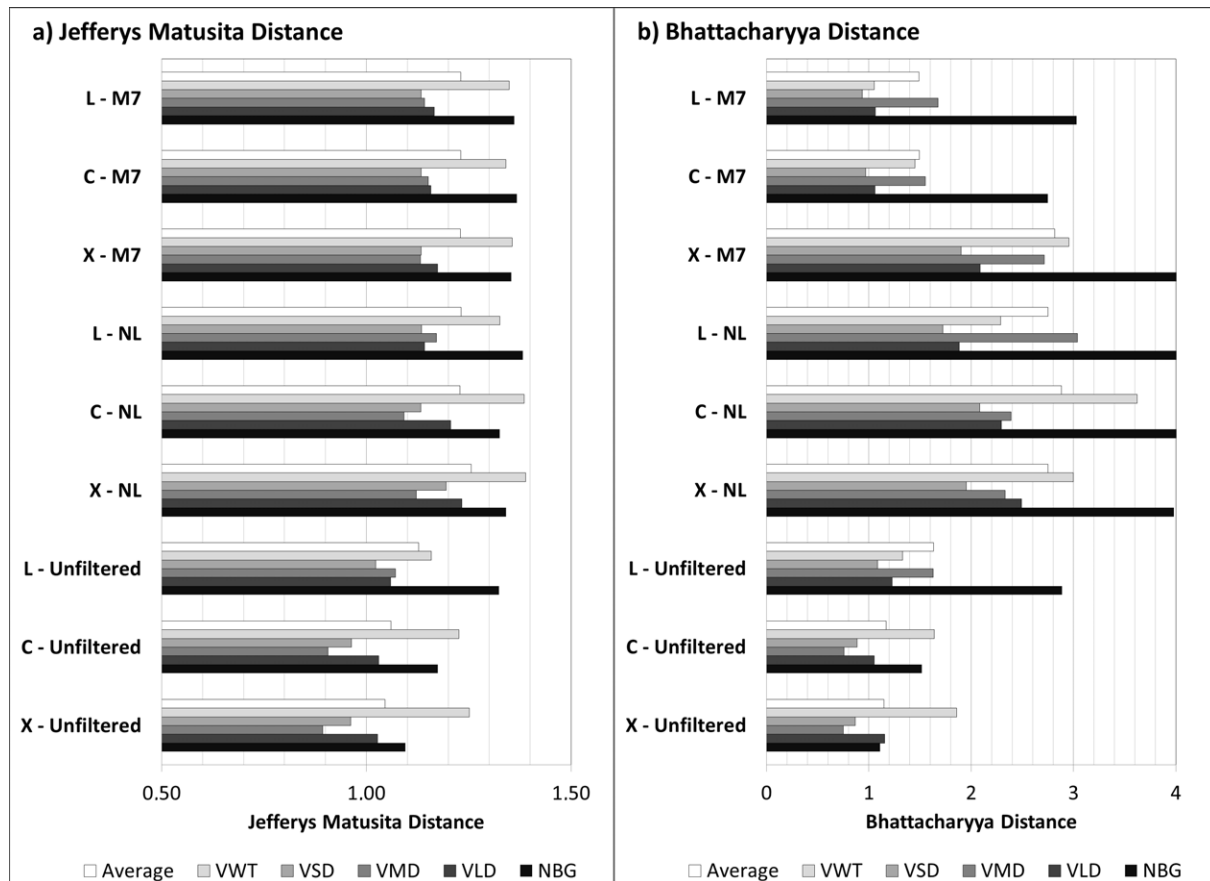


Figure 4.8: Influence of image filtering on the separability of land cover reference data: a) Jefferys Matusita Distance and b) Bhattacharyya Distance. Estimation was done for X-Band (X), C-Band (C) and L-Band (L) PolSAR data of TSX, R-2 and ALOS PALSAR. The filtering was performed with Boxcar Filters (M3-M9), Lee Filters (L3-L9) and the Non-Local Means filter (NL). Source: Own Figure.

data versus the accuracies of the Boxcar filtered data. The accuracies of NL were in average +5% higher than the accuracies of M7.

In this Section the performance of the developed Non-Local Means filter was evaluated. It was shown that both TerraSAR-X and Radarsat-2 data showed the best trade-off in terms of preservation of mean, reduction of speckle and enhancement of edges for a Non-local Means filtering with a parameter  $h$  of about 0.025 - if a patch window size of 3x3 and a search window size of 31x31 pixels were used. Based on this evaluation the Non-Local Means filtering of TerraSAR-X and Radarsat-2 was done for all the following analyses with these settings. The analysis of the Non-Local Means filter further revealed that this kind of filtering was better suited than the Boxcar and Lee filters. The preservation of the mean of the Non-Local Means filter was comparable to the performance of Boxcar and Lee filters with a window size of 3x3 pixels. The reduction of the speckle was as high as observed for a Boxcar filter with a window size of 7x7 pixels. The enhancement of the edges was shown to be highest among all tested filters and its performance can be compared to a Lee filter with 3x3 pixels. The influence of the Non-Local Means filtering on the class separability was found to be positive and the filtering offered

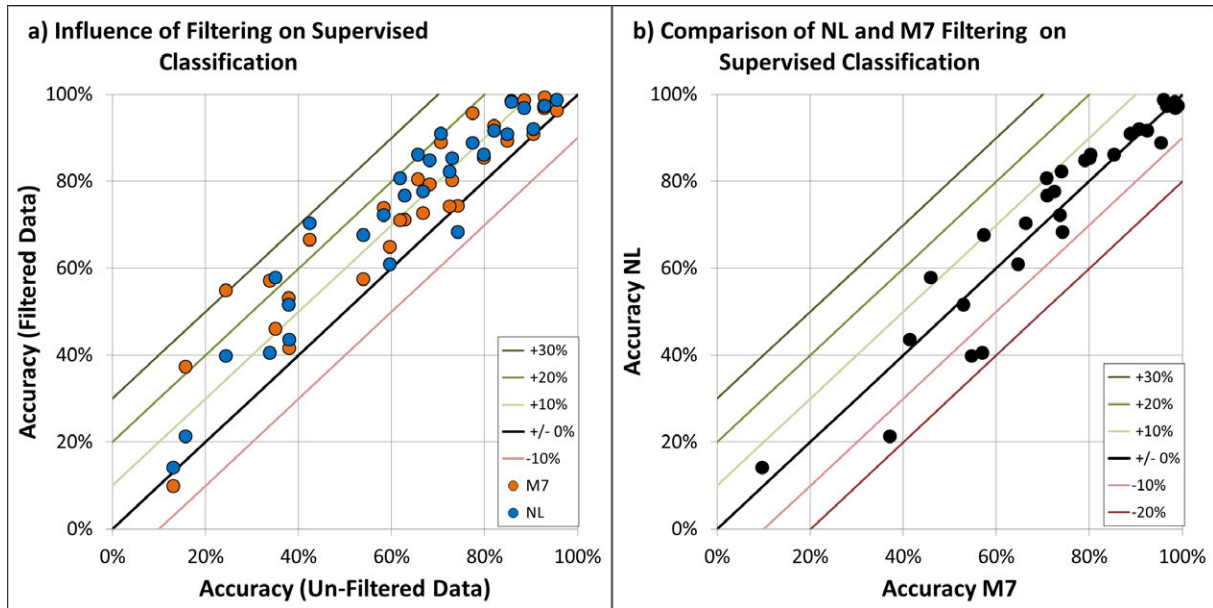


Figure 4.9: Influence of image filtering on the classification accuracy: a) classification accuracy of unfiltered data vs. classification accuracy of Boxcar filtered data (M7) and Non-Local Means filtered data (NL) and b) classification accuracy of Boxcar filtered data (M7) vs. Non-Local Means filtered data (NL). Source: Own Figure.

more distinct class positions. The accuracies of the supervised classifications of filtered images were therefore about +10% higher compared to the accuracies of supervised classifications of unfiltered images.

#### 4.1.2 Two Component Decomposition

The Two Component Decomposition was evaluated by comparing the Two Component Decomposition features double bounce (DBL2) and odd bounce (ODD2) and the Three Component Yamaguchi Decomposition features double bounce (DBL3), odd bounce (ODD3) and volume scattering (VOL3). These two data sets were processed for the two test sites RIS and TUK using quad-polarized R-2 data. The features DBL3, ODD3 and VOL3 were processed by the use of the quad-polarized R-2 data and the Three Component Yamaguchi Decomposition. The same quad-polarized R-2 data were used to form a co-polarized Scattering Matrix. The features DBL2 and ODD2 were processed by the use of these synthetic co-polarized R-2 data and the Two Component Decomposition. Any difference between the decomposition features is than related to differences in the models since the decompositions were solved using the same data (no temporal decorrelation). In the following the linear correlation between the decomposition features of co- and quad-polarized data were investigated for both test sites using the Squared Linear Pearson Correlation Coefficient  $R^2$ . The correlation values were calculated in IDL8.3 with the CORRELATE function. The analysis was carried out for each land cover class separately and for all reference data. The averaged results of both test sites are shown in Table 4.1.

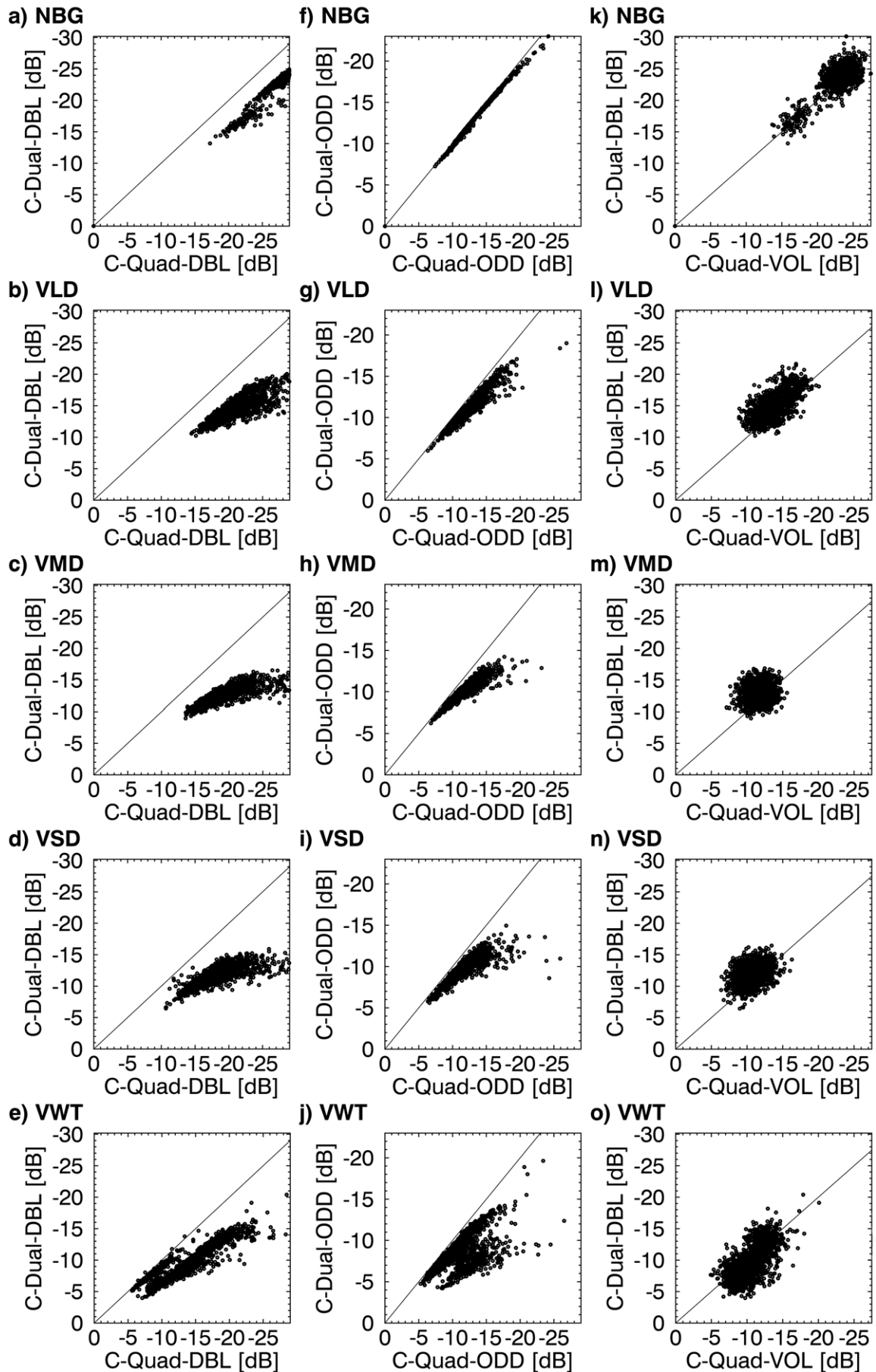


Figure 4.10: Scatterplots of Yamaguchi and Two Component Decomposition features for different land cover classes of test site Richards Island. Source: Own Figure.



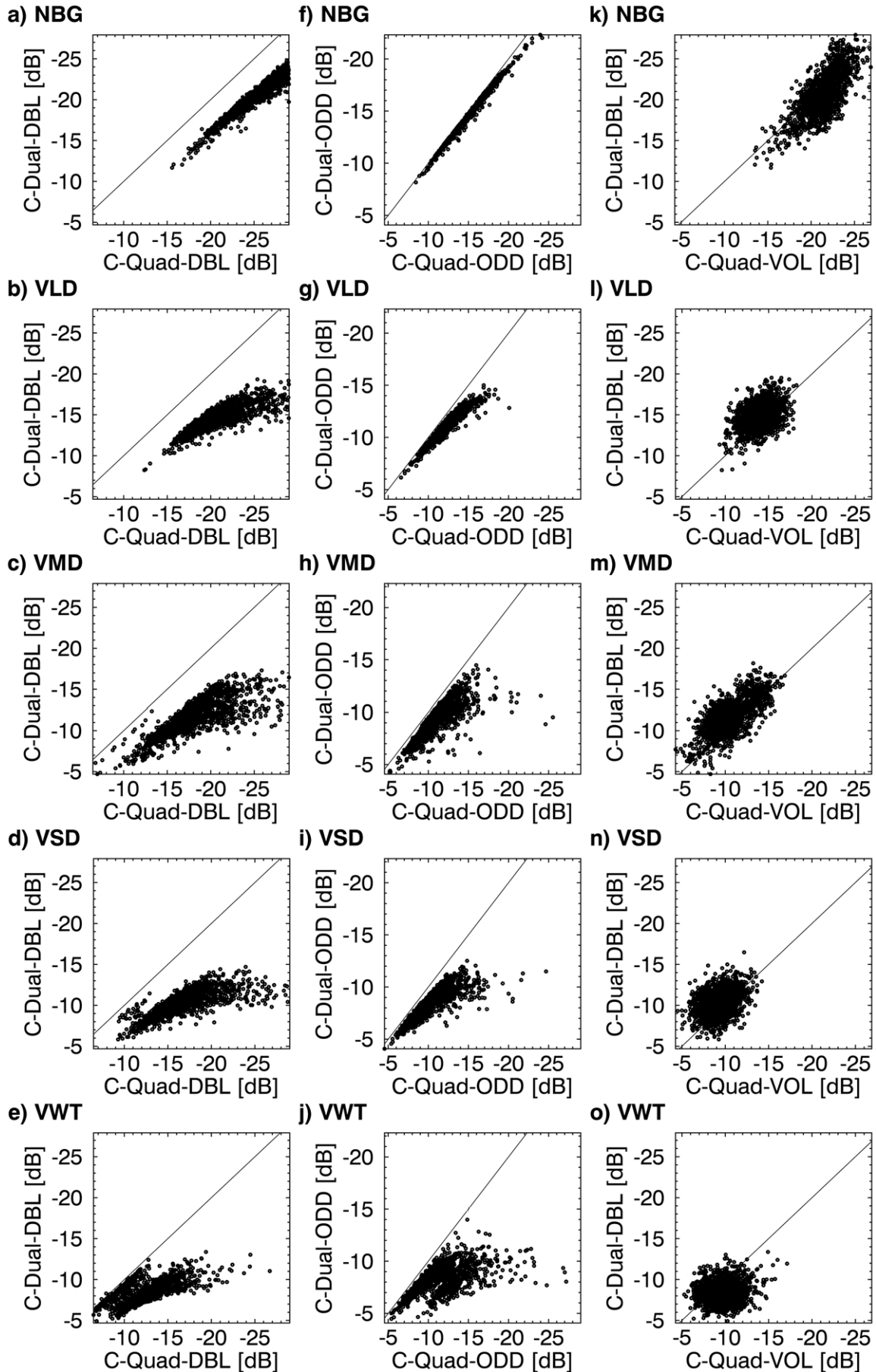


Figure 4.11: Scatterplots of Yamaguchi and Two Component Decomposition features for different land cover classes of test site Tuktoyaktuk. Source: Own Figure.

#### 4 Results

Table 4.1: Squared Linear Pearson Correlation Coefficient of Two Component Decomposition Features (DBL2, ODD2) and Three Component Decomposition Features (DBL3, VOL3, ODD3) for land cover classes bare ground (NBG), low grass dominated tundra (VLD), mixed tundra (VMD), shrub dominated tundra (VSD) and wetland (VWT).

ALL	DBL3	VOL3	ODD3	DBL2	ODD2	VMD	DBL3	VOL3	ODD3	DBL2	ODD2
<b>DBL3</b>	1	0.3	0.2	0.7	0.3	<b>DBL3</b>	1	0.2	0.1	0.5	0
<b>VOL3</b>		1	0.1	0.5	0.5	<b>VOL3</b>		1	0.1	0	0
<b>ODD3</b>			1	0.2	0.7	<b>ODD3</b>			1	0	0.6
<b>DBL2</b>				1	0.5	<b>DBL2</b>				1	0
<b>ODD2</b>					1	<b>ODD2</b>					1
NBG	DBL3	VOL3	ODD3	DBL2	ODD2	VSD	DBL3	VOL3	ODD3	DBL2	ODD2
<b>DBL3</b>	1	0.5	0.5	0.9	0.5	<b>DBL3</b>	1	0.1	0	0.5	0
<b>VOL3</b>		1	0.6	0.7	0.7	<b>VOL3</b>		1	0	0.1	0.1
<b>ODD3</b>			1	0.6	0.9	<b>ODD3</b>			1	0	0.5
<b>DBL2</b>				1	0.6	<b>DBL2</b>				1	0.1
<b>ODD2</b>					1	<b>ODD2</b>					1
VLD	DBL3	VOL3	ODD3	DBL2	ODD2	VWT	DBL3	VOL3	ODD3	DBL2	ODD2
<b>DBL3</b>	1	0	0.1	0.6	0.1	<b>DBL3</b>	1	0	0	0.6	0.1
<b>VOL3</b>		1	0.1	0.4	0.3	<b>VOL3</b>		1	0	0.3	0.3
<b>ODD3</b>			1	0.2	0.9	<b>ODD3</b>			1	0.1	0.6
<b>DBL2</b>				1	0.3	<b>DBL2</b>				1	0.2
<b>ODD2</b>					1	<b>ODD2</b>					1

Figure 4.10 shows the scatterplots of Two Component DBL2 and Three Component DBL3 features of different land cover classes of test site RIS (Section 2.2.1). The plots show that the intensities of DBL2 were lower than the intensities of DBL3. There were clear linear trends between both features for the classes NBG and VWT, but the class VWT showed two clusters: one close to the one-to-one line and a second one slightly shifted and below the first cluster. The vegetation classes (VLD, VMD and VSD) showed no distinct linear trends and diverse scattering was present. The second column of Figure 4.10 shows the scatterplots of ODD2 and ODD3. The linear correlation was very high for the class NBG (Figure 4.10.f) and the data lied very close to the one-to-one line. The linear trend was less pronounced for the other land cover classes VLD, VMD and VSD. The scattering of class VWT was diverse. The third column shows the scatterplots of VOL3 and DBL2 (Figure 4.10.k-o). None of the classes showed a linear trend.

Figure 4.11 shows the scatterplots of DBL2 and DBL3 of different land cover classes of test site TUK. The results were comparable to the results of test site RIS. The plots showed that the intensities of the Two Component features were again lower than the scattered intensities of the Three Component features. Distinct linear trends were observed between DBL3 and DBL2 for the classes NBG and WTL. The two clusters in the scatterplot of class VWT were again visible: one close to the one-to-one line and second one slightly below the first cluster. The vegetation classes (VLD, VMD and VSD) showed no clear linear correlation and diverse scattering. The variance of the scattering was higher compared to plots of test site RIS. The second column of Figure 4.11 shows the scatterplots of ODD2 and ODD3 features. The linear correlation was again very high for the classes NBG and VLD (Figure 4.11.f-g) and the data lied

close to the one-to-one line - similar to the observations made for test site RIS. The linear trend was less pronounced for the other land cover classes VMD and VSD. The scattering of class VWT was again diverse. The third column shows the scatterplots of VOL3 and DBL2 (Figure 4.11.k-o). Again none of the classes showed a linear trend and random scattering was dominant.

Table 4.1 summarizes the averaged  $R^2$  values of the features of Two (DBL2, ODD2) and Three Component Decomposition (DBL3, VOL3, ODD3). The highest correlation was observed between ODD2 and ODD3 for the classes NBG and VLD with  $R^2$  values greater than 0.6. In average the correlation between these two features was about 0.7. The correlation between DBL2 and DBL3 was highest for the classes NBG and WTL with  $R^2$  values greater than 0.6. The average correlation was estimated to be around 0.7. The analysis revealed that the correlations between ODD2 and DBL2, ODD3 and DBL3, ODD3 and VOL3 and between VOL3 and DBL3 were in average low and  $R^2$  values were less than 0.5. These findings supported the model approach. Orthogonal scattering mechanisms - like odd bounce and double bounce - should not show a linear correlation. The results of correlation and scatterplot analysis indicated that the features of the Two Component Decomposition can be interpreted similar to the Three Component Yamaguchi Decomposition features if the dominant backscattering was either of type surface scattering or double bounce. It was observed that the correlation was low for land cover classes that facilitated volume scattering, e.g. for shrub dominated land cover.

In this section the correlations between the Two Component Decomposition features double bounce and odd bounce and the Three Component Yamaguchi Decomposition features double bounce and odd bounce were investigated. It was shown that features of both decomposition models showed a distinct linear trend for land cover classes of bare ground and wetlands. The correlation was low for the other vegetation classes, e.g. shrub dominated tundra. The double bounce and odd bounce features of the two Component Decomposition showed no correlation with the volume scattering of the Three Component Yamaguchi Decomposition. The features of the Two Component Decomposition provided a similar interpretation as the Three Component Yamaguchi Decomposition features. The information of the Two Component Decomposition features was not adjusted to the volume scattering contribution and therefore the differences between both models were maximized when the volume scattering contribution was high.

### 4.1.3 FKM-ML Unsupervised Land Cover Classifier

The intention of the unsupervised classification approach (FKM-ML) shown in Section 3.2.2.1 is to provide a classification scheme that is capable to handle quad- and dual-polarized PolSAR data and multispectral data in the same way. The classifier does not require any training samples and operates unsupervised. The aim of the following analysis was to compare the performance of the FKM-ML to other standard PolSAR classifiers. The evaluation was done using a Receiver Operating Characteristic (ROC). The ROC is calculated via the False Positive Rate (FPR) and True Positive Rate (TPR) of a confusion matrix (see Section 3.2.3). The ROC diagram shows the FPR on the abscissa and the TPR on the ordinate. The closer a classification result is to FPR=0 and TPR=1 the better is the performance of a classifier. The ROC diagrams are frequently used to identify the best classification technique or to parametrize classifiers. The one-to-one line in the ROC diagram indicates a random classification. This means that a classification

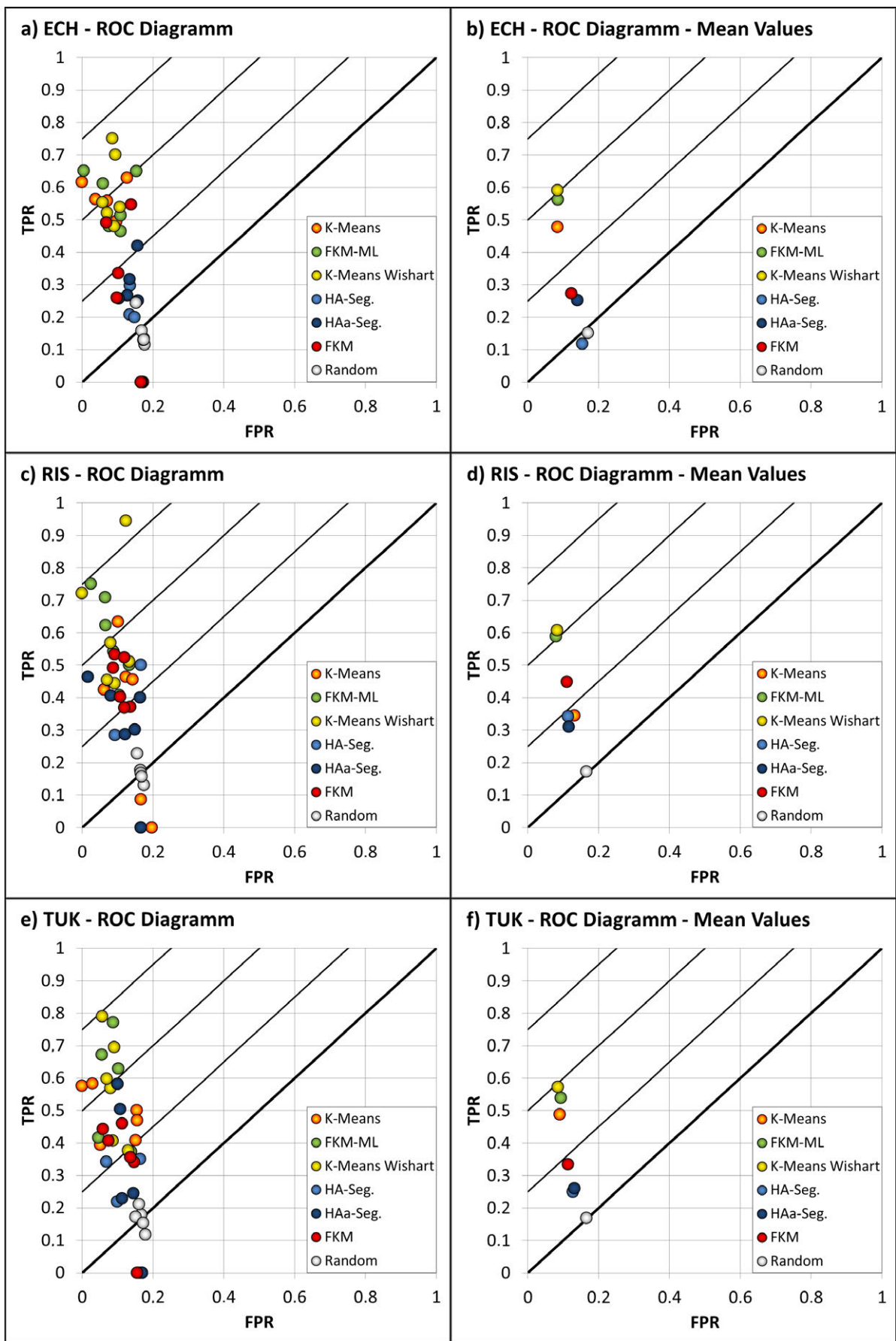


Figure 4.12: Classification performance analysis via Receiver Operating Characteristic (ROC) - False Positive Rate (FPR) vs. True Positive Rate (TPR): a)-b) East Channel (ECH), c)-d) Richards Island (RIS), e)-f) Tuktoyaktuk (TUK). The closer a point is to FPR=0 and TPR=1 the better is the classification. Source: Own Figure.

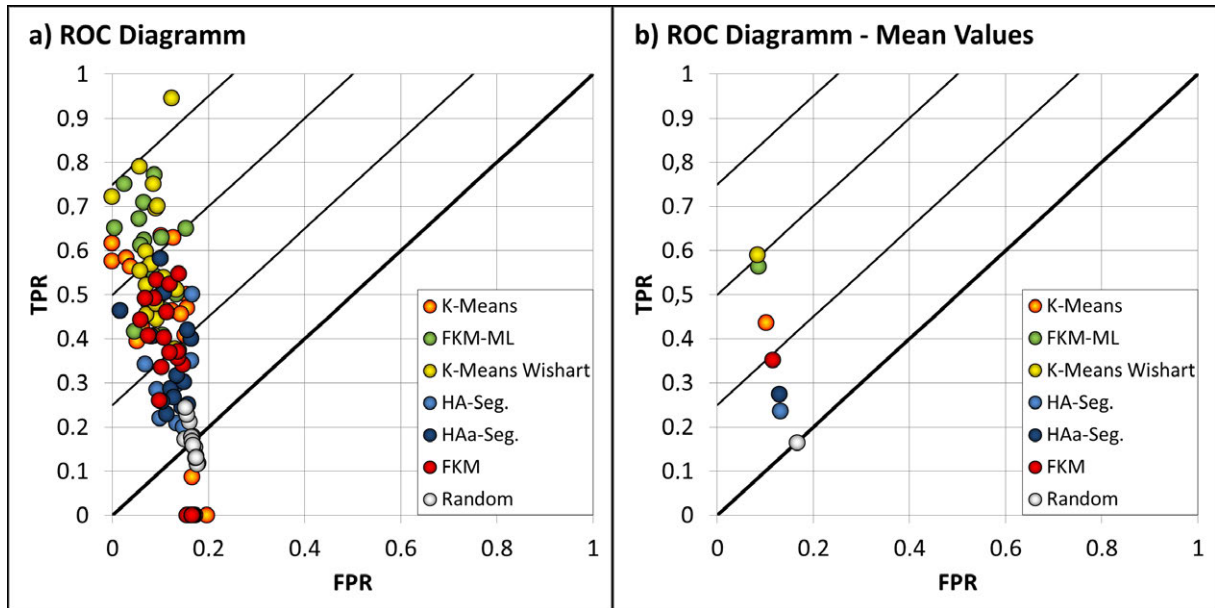


Figure 4.13: Overall classification performance analysis via Receiver Operating Characteristic (ROC) - False Positive Rate (FPR) vs. True Positive Rate (TPR): a) single values of all test sites and b) mean values of all test sites. The closer a point is to FPR=0 and TPR=1 the better is the classification. Source: Own Figure.

results on the one-to-one line has a fifty to fifty percent chance of correct classification. The area below the one-to-one line in a ROC diagram indicates therefore systematic errors.

In the following the FKM-ML classifier was compared to the standard K-Means, the Fuzzy-K-Means (FKM), the K-Means Wishart classifier, the Entropy/Alpha segmentation classifier (HA-Seg.) and the Entropy/Alpha/Anisotropy classifier (HAa-Seg.) (see Section 3.2.2). The performance of the ROC calculation was validated via a random classification. If the ROC is calculated properly the random classification results lies on - or very close to - the one-to-one line. The test was arranged using quad-polarized R-2 data of the test sites ECH, RIS and TUK. The classifications of K-Means, FKM, K-Means Wishart, HA-Seg. and HAa-Seg. were calculated with standard parameters in the Radar Tool Box (Rat). The FKM-ML was applied with the following settings: The unsupervised Jenks-Natural-Breaks classification was initialized with six pre-classes using the Alpha values of the T-Matrix. The total number of output-classes was fixed to twenty classes and these were used to initiate the iterative MLC. The convergence criterion was fixed to five percent and the classifier showed a convergence (see Section 3.2.2.1). The unsupervised classes of these unsupervised classifications were merged with regard to the land cover reference (see Section 3.2.2.1). This operation was necessary to calculate the classification accuracy in conventional sense (see Section 3.2.2.1 and Section 3.2.3). Each final classification had five land cover classes and the confusion matrices were calculated.

These confusion matrices were used to calculate FPR and TPR for each class and method. Figure 4.12 shows the results of the ROC analysis of the test site ECH (Figure 4.12.a-b), of the test site RIS (Figure 4.12.c-d) and of the test site TUK (Figure 4.12.e-f). The left side of each figure shows the FPR and TPR values of all classes for each classifier. The right side of each figure shows the average FPR and TPR values of each classifier. It was observed that FPR was less than 0.2 for all test sites and all classifiers.

## 4 Results

The TPR values ranged between zero and one. The random classification lied close to the one-to-one line. The results showed that the FPR and TPR values of the HA-Seg. and HAa-Seg. were low and TPR values were between 0.2 and 0.3. The FPR was relatively high and showed values greater 0.1. The performance of the K-Means and the FKM classifier was in mid-range of the spectrum and TPR values between and 0.2 and 0.3 were observed. The FPR values were in average around 0.1 for all test sites. The best performance was observed for the K-Means Wishart and the FKM-ML classification. The TPR values of both classifiers were in average about 0.5 and the FPR values were close to 0.1. The values were similar for all test sites and indicated that both classifiers had a similar classification performance and the best performance among all tested classifiers. These findings also revealed in the averaged results (Figure 4.13). The TPR values increased and the FPR values decreased from Random, HAa Seg., HA Seg., FKM, K-Means, FKM-ML to K-Means Wishart.

In this Section the performance of the unsupervised classifier FKM-ML was evaluated. The performance of the classifier was compared to five frequently used unsupervised classifiers. These were the standard K-Means, the Fuzzy-K-Means, the K-Means Wishart classifier, the Entropy/Alpha segmentation classifier and the Entropy/Alpha/Anisotropy classifier. The evaluation was conducted with Radarsat-2 quad-polarized data. The performance was investigated via a Receiver Operating Characteristic. The results showed that the FKM-ML and the K-Means Wishart classifier had the best classification performance among all tested classifiers. The differences between these two classifiers were small. The K-Means and the Fuzzy-K-Means classifiers showed good performance but the values of the True Positive Rate were about 0.15 lower than the results of FKM-ML and K-Means Wishart classifiers. The lowest performance was observed for the Entropy/Alpha segmentation classifier and the Entropy/Alpha/Anisotropy segmentation classifier.

## 4.2 Land Surface Characterization

This chapter shows results of the land surface characterization. The first section provides results of the analysis of PolSAR data of the test sites of the Mackenzie Delta Region and Banks Island. The ground truth reference data that were recorded during the field work were used to estimate the individual class statistics of each polarimetric feature. The results of this statistical assessment are shown in form of a boxplots analysis. The second section shows results of the analysis of multispectral data of the test sites of the Mackenzie Delta Region and Banks Island. The analysis shows the spectral characteristics of the individual classes. The last section of this chapter provides results of the analysis of the DEM data. The shown examples highlight the application of DEMs for the characterization of the land surface morphology and include the qualitative evaluation of direct and relative topographic features.

### 4.2.1 Polarimetric Synthetic Aperture Radar Data

The following results show the statistical characteristics of the PolSAR sigma nought intensities, the alternative Entropy, Alpha of C-Matrix, Alpha of T-Matrix and the Two and Three Component Decomposition features of the land cover classes defined in Section 2.2.1. The analysis was performed using the geocoded and orthorectified X-, C- and L-Band data (Section 2.2.2). The processing of these data

was done as described in Section 3.1.1.3 and the Non-Local Means filtering was performed as described in Section 3.1.1.2 and with respect to the findings of Section 4.1.1. All of the data were processed to a geometric resolution of twelve meter. The PolSAR data of all Mackenzie Delta test sites had similar acquisition geometries and all data were acquired at the same time of the year with less than one month temporal delay (see Section 2.2.2). The boxplots of the following figures display the average 1% (lower horizontal black line), 25% (lower boundary of the gray box), 50% (middle horizontal black line), 75% (upper boundary of the gray box) and 99% (upper horizontal black line) percentiles. The aim of this analysis was to identify the benefits and limitations of the different wavelengths (X-, C-, L-Band) and polarization modes (co-, cross-, quad-polarization) for the characterization of the investigated generalized tundra land cover types (Section 2.2.1).

### 4.2.1.1 Intensities

The analysis of the boxplots showed following characteristics of the sigma nought calibrated intensities of the X-, C- and L-Band data of the Mackenzie Delta test sites (ECH, DIS, TUK, RIS):

- **X-Band - HH** The median values of the HH intensity of the X-Band increased from NBG to VLD to VMD to VSD and to WTL. The highest backscatter values were observed for the class WTL with a median value of about -10 dB. The variance of the class NBG was high and the boxplot of class WTL showed high overlap with the boxplot of class VLD. The overlaps of the boxes were high for the vegetation classes VLD, VMD and VSD (Figure 4.14.a).
- **X-Band - VV** The position of the class WTL was less pronounced in the VV intensity of the X-Band data. The median value of this class was about -11 dB and the box showed a high overlap with the box of class VSD. The variance of NBG was again high and the median was about the same as the median of class VSD. The median intensity values increased from VLD to VMD to VSD (Figure 4.14.b).
- **X-Band - HV** The HV intensities of the X-Band were sensitive to the type of vegetation and land cover. The HV values were increasing from NBG to VLD to VMD to VSD to VWT and showed similar characteristic as the HH intensity. The variances of the classes were low and the overlap of the boxes was smaller compared to the HH and VV intensities. The classes NBG and VLD had a distinct statistic and the values of the 25% and the 75% quartiles showed no overlap with any other class. The median intensity of VWT was again comparable high with a value of about -8 dB (Figure 4.14.c). The analysis of the HV intensity was carried out for the test site TUK. No cross-polarized data were available for the test sites RIS, ECH and DIS.
- **C-Band - HH** The characteristics of the C-Band HH intensity were comparable to the characteristics of the X-Band. The median values were increasing from NBG to VLD to VMD to VSD to VWT. The values of VWT were high with a median of about -15 dB. The overlaps between the boxes of the vegetation classes VLD, VMD and VSD were high. Compared to the X-Band HH intensity the variance of class NBG was smaller and no overlap between NBG and VLD was observed for the 25% and 75% quartiles (Figure 4.14.d).
- **C-Band - VV** The boxplots of the C-Band VV intensity showed three major results: The difference between the classes VLD and VMD were small and the overlaps of the boxes was high. The class

#### 4 Results

WTL and the class NBG showed comparable high median values of -10 dB and -8 dB. The class VSD showed no overlap with the class VWT and only small overlap with the class VMD (Figure 4.14.e).

- **C-Band - HV** The C-Band HV intensity was sensitive to the vegetation classes and showed increasing median intensity values from VLD to VMD to VSD. The differences between VLD and VMD were small. The boxes of the classes VSD and VWT showed an overlap and similar statistics. The differences between these classes were smaller compared to the results of the X-Band HV intensity (Figure 4.14.f).
- **L-Band - HH** The HH intensity of the L-Band showed no sensitivity to the vegetation classes VLD, VMD and VSD. The class VWT had a similar median value compared to the other vegetation classes but a higher variance. In contrast, the class NBG showed a high median intensity value and the box of the 25% and the 75% quartile had no overlap with any of the other classes (Figure 4.15.a).
- **L-Band - HV** Similar observations were made for the HV intensity of the L-Band. The differences between the classes VLD, VMD and VSD were small and the class NBG showed again low values and no overlap with any of the other classes (Figure 4.15.b).

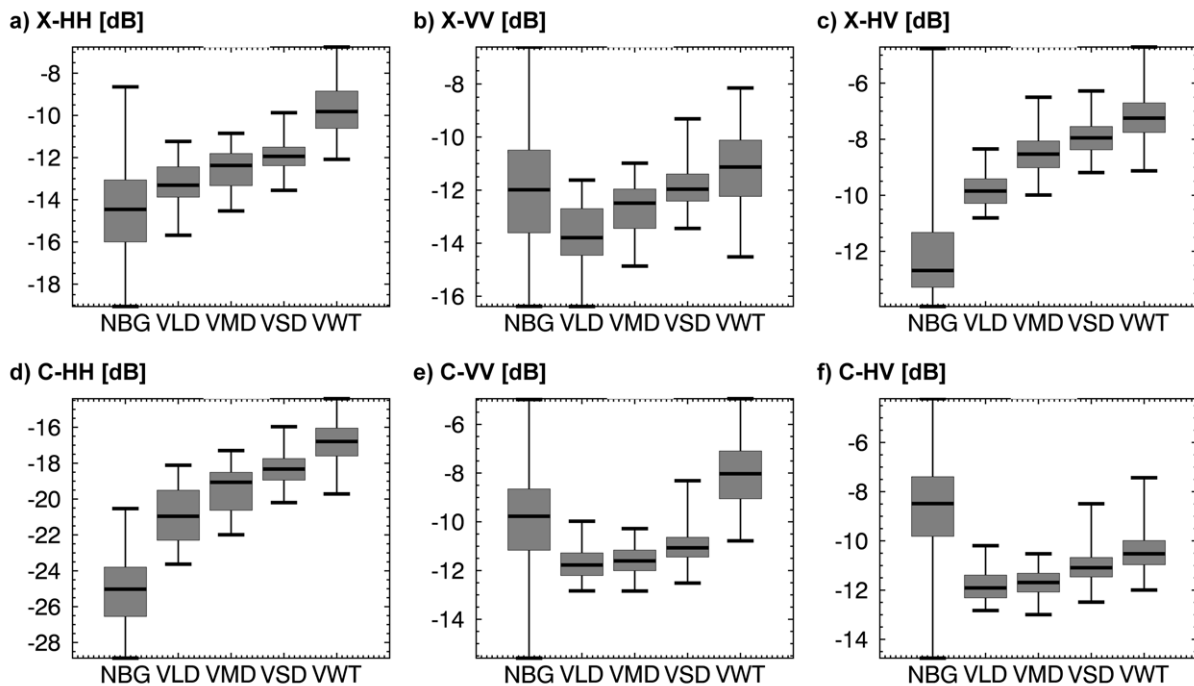


Figure 4.14: Average boxplots of TSX (X) and R-2 (C) sigma nought intensities (HH, VV and HV) of the Mackenzie Delta test sites (RIS, ECH, DIS and TUK). Source: Own Figure.

The following characteristics were found for the sigma nought calibrated intensities of the X-Band data of the test site Banks Island (BIS):

- **X-Band - HH** The overlaps between the boxes was generally high and the individual characteristics of the land cover classes were less clear compared to the Mackenzie Delta test sites. The class NBG showed a high variance and the boxplot had an overlap with all other classes. The HH intensity was



comparable high for class VWT with a median intensity value of about -10.5 dB. The median values increased from class VML to class VMH. The intensity was high for class VLD with a median value of about -11 dB (Figure 4.16.a).

- **X-Band - VV** The VV intensity showed similar characteristic compared to the characteristic of the HH intensity. The class NBG had a high variance and values were ranging from -7 to -15 dB. The class VWT had a lower median value than the class NBG. Again the median value of the class VLD was high and about -11.5 dB (Figure 4.16.b).



Figure 4.15: Average boxplots of ALOS PalSAR (L) sigma nought intensities (HH and HV) of the Mackenzie Delta test sites (RIS, ECH, DIS and TUK). Source: Own Figure.

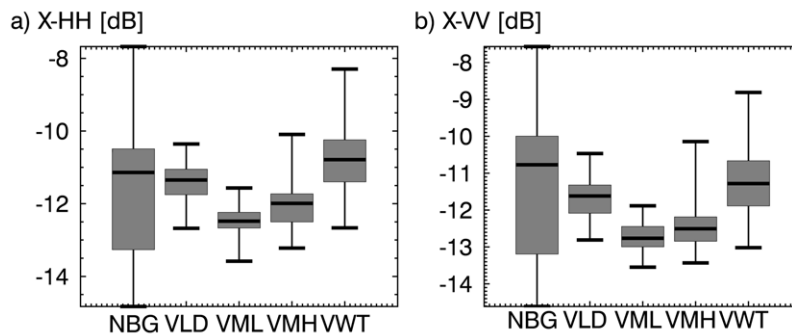


Figure 4.16: Average boxplots of TSX (X) sigma nought intensities: a) HH, b) VV of test site Banks Island. Source: Own Figure.

The results of the boxplot analysis indicated that the intensities of X- and C-Band were sensitive to the different land cover types. The class VWT showed high intensity values. This was related to the double bounce signal due to the interaction of the electromagnetic wave with the water and the stem of the vegetation (see Figure 3.4). It was observed that the variance of the class NBG was high. This was likely related to differences in the substrate, e.g. different grain sizes, and differences in the moisture regime. The reference data were not suited to investigate the differences and to explain the high variance. It was further observed that the X-Band HV intensity showed a clear separation of the class VLD and the values of the 25% and the 75% quartiles showed no overlaps with any other class. In contrast, the C-Band HV intensity was more sensitive for the separation of the class VSD. For both X- and C-Band an increment of the median intensity values was observed from VLD to VMD to VSD. The L-Band intensities HH and HV were shown to be not sensitive to the different vegetation types of the test sites. The differences

## 4 Results

in the statistics of the classes were small and only the classes NBG and VWT showed noticeable and meaningful differences. The X-Band intensities HH and VV were analyzed for the test site Banks Island and showed a lower sensitivity to the land cover types and the variances were higher. This might be a result of the higher topographic variation of the site. Nevertheless the class VWT had a clear position and a high median intensity value. The median values of both intensities (HH and VV) increased from VML to VMH to VLD.

The intensities of X-, C- and L-Band PolSAR data were analyzed in this section via a boxplot analysis. It was shown that X- and C-Band intensities showed the highest sensitivity to the land cover classes. Both frequencies were identified to be sensitive to the wetland vegetation and to the different types of non-wetland vegetation. The X-Band showed higher sensitivity to the low tundra formations and the C-Band was more sensitive to the medium and high tundra formations. The L-Band intensities HH and HV showed no sensitivity to the non-wetland vegetation classes but to bare ground and to some degree to wetland vegetation.

### 4.2.1.2 Entropy/Alpha Decomposition

The following characteristics of Entropy, Alpha of C-Matrix and Alpha of T-Matrix were found for the sigma nought calibrated scattering matrices of X-, C- and L-Band data of the Mackenzie Delta test sites (ECH, DIS, TUK, RIS). The data analyzed were the co-polarized X-Band data and the quad-polarized C-Band data. Further, the quad-polarized data were used to form a scattering matrix of co-polarized C-Band data.

- **X-Band - HH/VV-polarized Entropy** The Entropy of the X-Band data showed a sensitivity to all land cover classes. The values of Entropy increased from NBG to VLD to VMD to VSD and VWT and indicated therefore an increasing randomness of the scattering process. The Entropy was found to be lowest for the class NBG. The median values of vegetation classes showed comparable high Entropy values in the range from 0.6 to 0.7 and the boxes had overlaps. The highest Entropy was observed for class VWT with a 25% to 75% quartile in the range from 0.75 to 0.9. Such a high Entropy value indicated that different scattering types contributed to the signal (Figure 4.17.a).
- **X-Band - HH/VV-polarized Alpha of C-Matrix** The analysis of the Alpha of the C-Matrix showed three major results: Alpha was high for the class NBG, Alpha showed only little differences between the vegetation classes VLD, VMD and VSD and Alpha was low for the class VWT. HH scattering was therefore dominant for class NBG and VV scattering was dominant for class VWT. The remaining classes showed no dominant scattering of a polarization channel and median Alpha values of 0.5 were observed. These results were in accordance to the analysis of the intensity data (Figure 4.17.b).
- **X-Band - HH/VV-polarized Alpha of T-Matrix** The analysis of the Alpha of the T-Matrix showed that this feature was sensitive to the land cover classes. The scattering of the class NBG was identified as single bounce scattering with low Alpha values. The median values of the Alpha increased from VLD to VMD to VSD and were in the range from 0.15 to 0.25. This indicated an increasing volume or mixed scattering component. The highest Alpha values were observed for the

class VWT with values of the 25% to 75% quartile in the range from 0.3 to 0.45. This indicated mixed scattering and a double bounce scattering component (Figure 4.17.c).

- **C-Band - HH/VV-polarized Entropy** The analysis of the C-Band co-polarized Entropy showed nearly identical results compared to the analysis of the X-Band co-polarized Entropy. The variances of the boxplots were higher but still the classes NBG and VWT had a clear position and the Entropy values were ranging from 0.3 to 0.4 and from 0.75 to 0.9 (Figure 4.17.d).
- **C-Band - HH/VV-polarized Alpha of C-Matrix** The results of the analysis of the C-Band co-polarized Alpha of the C-Matrix were comparable to the X-Band co-polarized Alpha of the C-Matrix. The vegetation classes VLD, VMD and VSD showed that VV scattering was more dominant than the HH scattering and the median Alpha values were less than 0.5. The contribution of the VV scattering decreased from VLD (0.45) to VMD (0.48) to VSD (0.5) (Figure 4.17.e).
- **C-Band - HH/VV-polarized Alpha of T-Matrix** The co-polarized C-Band Alpha of T-Matrix showed very similar characteristics compared to the co-polarized X-Band Alpha of T-Matrix. Again the variances were higher but the separation of the classes NBG and VWT was still distinct (Figure 4.17.f).
- **C-Band - quad-polarized Entropy** It was observed that the quad-polarized Entropy was nearly identically to the Entropy of the co-polarized C-Band data. The values were lower but the characteristics of the land cover classes were comparable (Figure 4.17.g).
- **C-Band - quad-polarized Alpha of C-Matrix** The quad-polarized C-Band Alpha of T-Matrix showed similar characteristics compared to the co-polarized C-Band Alpha of T-Matrix. The differences between the vegetation classes VLD, VMD and VSD were more pronounced in the quad-polarized data since the HV information was integrated. The dominance of HH scattering was clearly visible and Alpha values were therefore greater 0.5 and the overlaps of the 25% to 75% quartiles were lower compared to the co-polarized data (Figure 4.17.h).
- **C-Band - quad-polarized Alpha of T-Matrix** The high similarity between quad-polarized and co-polarized Entropy/Alpha decomposition features was furthermore supported by the results of the analysis of the quad-polarized Alpha of T-Matrix. The characteristics of the land cover classes were nearly identical. However, the quad-polarized Alpha values were higher compared to the co-polarized data (Figure 4.17.i).

The following characteristics of Entropy, Alpha of C-Matrix and Alpha of T-Matrix were observed for the sigma nought calibrated scattering matrix of co-polarized X-Band data of the test site Banks Island (BIS):

- **X-Band - HH/VV-polarized Entropy** The Entropy of the co-polarized X-Band data showed a sensitivity to all investigated land cover classes. However, the boxes of all classes (25% to 75% quartiles) were overlapping and the Entropy values were high and above 0.5. This indicated a high randomness and mixed scattering of all classes. The lowest Entropy was observed for the class NBG. The Entropy values increased from VLD to VML to VMH and were highest for the class VWT (Figure 4.18.a).
- **X-Band - HH/VV-polarized Alpha of C-Matrix** The analysis of the Alpha of the C-Matrix showed three major results that were comparable to the findings of the Mackenzie Delta test sites: Alpha was high for class NBG, the Alpha values of the vegetation classes VLD, VML and VMH

#### 4 Results

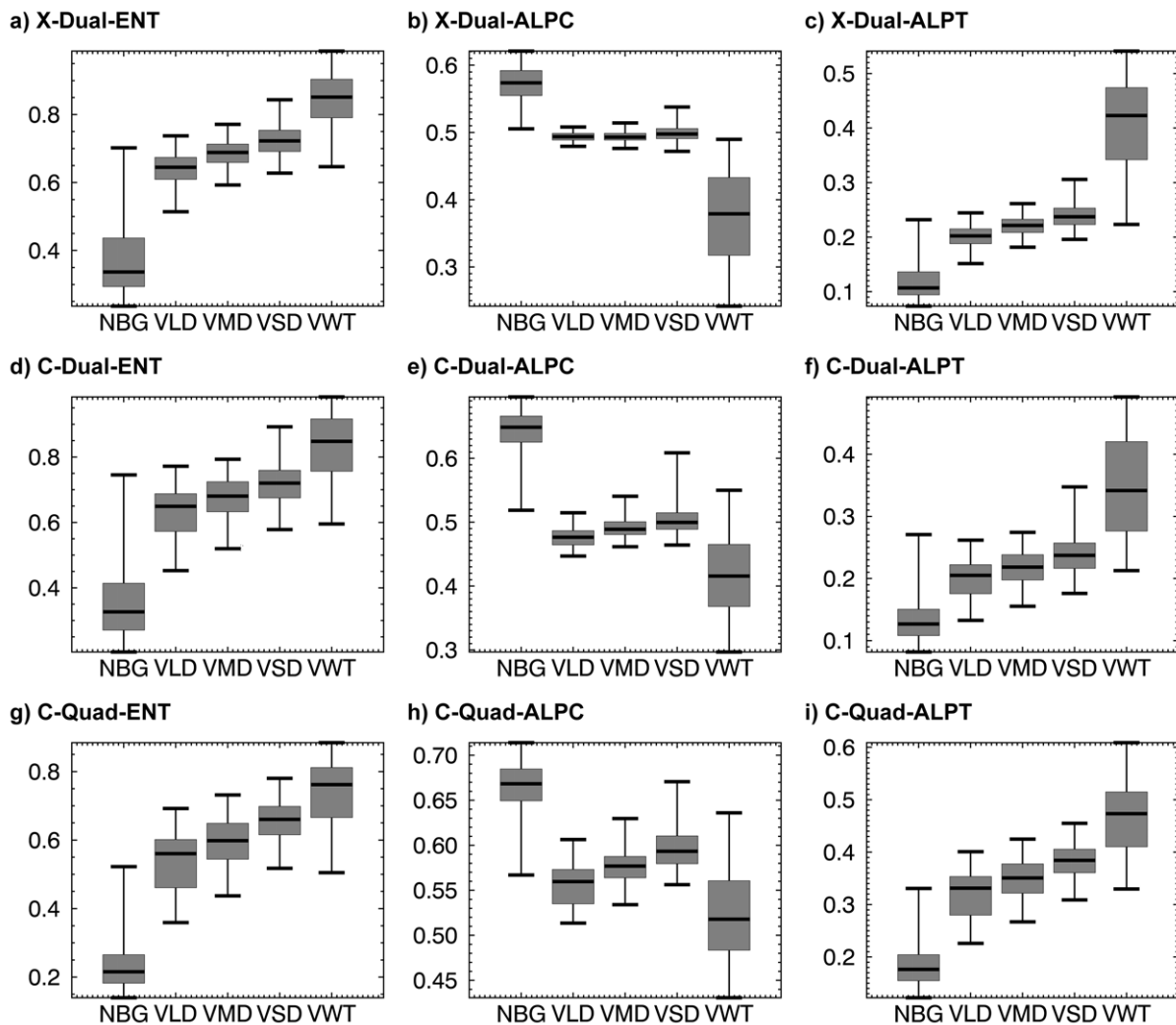


Figure 4.17: Average boxplots of Entropy (ENT), Alpha of Covariance Matrix (ALPC) and Alpha of Coherency Matrix (ALPT): a)-c) co-polarized TSX (X), d)-f) co-polarized R-2 (C) and g)-i) quad-polarized R-2 of all Mackenzie Delta test sites (RIS, ECH, DIS and TUK). Source: Own Figure.

were similar and Alpha was low for the class VWT. HH scattering was therefore dominant for class NBG and VV scattering was dominant for class VWT. The remaining classes showed no dominant scattering of a polarization channel and the median Alpha values were around 0.5. (Figure 4.18.b).

- X-Band - HH/VV-polarized Alpha of T-Matrix** The analysis of the Alpha of the T-Matrix showed that this feature was sensitive to the land cover classes but the variance was high. The scattering of class NBG was identified as single bounce scattering with low Alpha values. The median Alpha values increased from VLD to VML to VMH and showed a high overlap of the 25% to 75% quartiles. This indicated an increasing volume or mixed scattering component. The highest Alpha values were observed for the class VWT but the 25% to 75% quartile was completely overlapping with the 25% to 75% quartile of class VMH. This indicated volume or mixed scattering and no dominant double bounce scattering component (Figure 4.18.c).

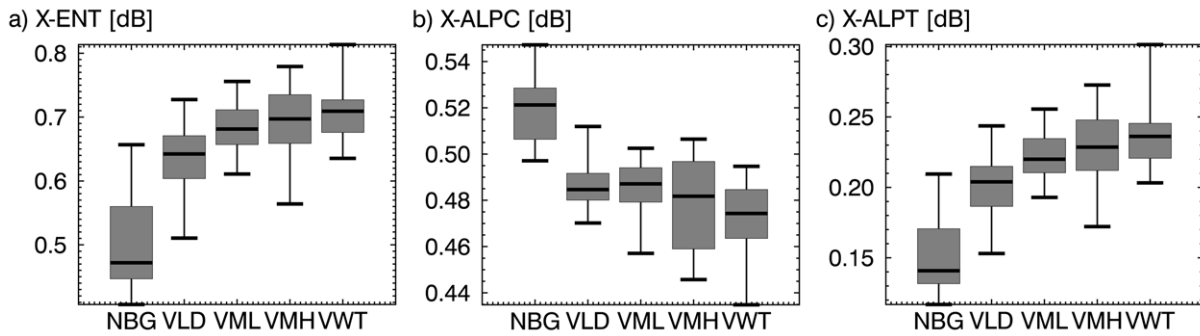


Figure 4.18: Average boxplots of Entropy (ENT), Alpha of Covariance Matrix (ALPC) and Alpha of Coherency Matrix (ALPT): a)-c) co-polarized TSX (X) of test site Banks Island. Source: Own Figure.

The PolSAR data analyzed in the following were the cross-polarized X-, C- and L-Band data. The quad-polarized data were used to form a scattering matrix of HH/HV-polarized C-Band data and VV/VV-polarized C-Band data.

- **C-Band - VV/VH-polarized Entropy** The analysis of the Entropy showed an increase in the median Entropy values from NBG to VLD to VMD to VSD and VWT. The overlaps between the 25% to 75% quartiles of the vegetation classes were high and the degree of randomness was high as well. The class NBG had distinct Entropy values lower than 0.4 (Figure 4.19.a).
- **C-Band - VV/VH-polarized Alpha of C-Matrix** The Alpha of the C-Matrix showed that the VV scattering was dominant and the contribution of HV scattering was higher for the vegetation classes VLD, VMD and VSD and highest for VWT (Figure 4.19.b).
- **C-Band - VV/VH-polarized Alpha of T-Matrix** The Alpha of T-Matrix did not give relevant information on the characteristics of the land cover classes. The overlaps between the 25% to 75% quartiles of all classes were very high and therefore Alpha values of about 0.5 were observed (Figure 4.19.c).
- **C-Band - HH/HV-polarized Entropy** The results of the analysis of the C-Band Entropy showed two main differences to the VV/VH-polarized Entropy: The ranges of the class statistics were higher and the Entropy values of the class VWT were lower. (Figure 4.19.d).
- **C-Band - HH/HV-polarized Alpha of C-Matrix** The analysis of the HH/HV-polarized C-Band Alpha of C-Matrix values showed a high variance of all classes. The HH scattering was dominant and the contribution of HV scattering increased from VLD to VMD to VSD (Figure 4.19.e).
- **C-Band - HH/HV-polarized Alpha of T-Matrix** The Alpha of T-Matrix did not give relevant information on the characteristics of the land cover classes and all Alpha values were about 0.5 (Figure 4.19.f).
- **X-Band - HH/HV-polarized Entropy** The analysis of the HH/HV-polarized X-Band Entropy showed a high variance of the class NBG. In contrast, the C-Band data the Entropy decreased from VLD to VMD to VSD and was highest with values close to 1.0 for the class VWT. (Figure 4.19.g). The analysis of the HH/HV-polarized Entropy was carried out for the test site TUK. No cross-polarized data were available for the test sites RIS, ECH and DIS.

#### 4 Results

- **X-Band - HH/HV-polarized Alpha of C-Matrix** The analysis of the HH/HV Alpha of C-Matrix showed dominant HV scattering for the classes NBG, VLD, VMD and VSD. The median values were similar and the overlaps of the 25% to 75% quartiles were high. The HH scattering was dominant for the class VWT with values close 0.5. These observations supported the findings from the analysis of the intensity values (Figure 4.19.h). The analysis of the HH/HV-polarized Alpha of C-Matrix was carried out for the test site TUK. No cross-polarized data were available for the test sites RIS, ECH and DIS.
- **X-Band - HH/HV-polarized Alpha of T-Matrix** The Alpha of T-Matrix did not give relevant information on the characteristics of the land cover classes and Alpha values were close to 0.5. Slightly higher values were observed for the class VWT. (Figure 4.19.i). The analysis of the HH/HV-polarized Alpha of T-Matrix was carried out for the test site TUK. No cross-polarized data were available for the test sites RIS, ECH and DIS.
- **L-Band - HH/HV-polarized Entropy** The median values of the Entropy of the HH/HV-polarized L-Band data were increasing from class VLD to VMD to VSD to VWT and high overlaps of the 25% to 75% quartiles were observed. The class NBG showed a high variance and no distinct values. The Entropy values of all classes were high and values greater 0.5 were observed. A high randomness was therefore present (Figure 4.20.a).
- **L-Band - HH/HV-polarized Alpha of C-Matrix** The Alpha of C-Matrix showed that HH scattering was dominant. The HV scattering contribution increased from VLD to VMD to VSD and VWT. The Alpha values of C-Matrix were low and less than 0.3 (Figure 4.20.b).
- **L-Band - HH/HV-polarized Alpha of T-Matrix** The Alpha of T-Matrix did not give relevant information on the characteristics of the land cover classes and Alpha values were close to 0.5 (Figure 4.20.c).

The results of the boxplot analysis of the Entropy/Alpha decomposition features showed that the X- and C-Band data were more sensitive to the land cover than the L-Band data. The best characterization of the classes was observed for the quad-polarized and the co-polarized data. The Alpha values of the T-Matrix of both polarization modes were distinct for the classes NBG and VWT and showed increasing values from VLD to VMD to VSD. The Alpha values of the C-matrix were less suited to characterize the land cover. The vegetation classes VLD, VMD and VSD showed a higher contribution of the HH scattering. The class VWT showed higher contribution of the VV scattering. The position of the class NBG was distinct and the HH scattering was dominant. The differences between the quad-polarized and co-polarized C-Band decomposition features were very small and nearly identical results were observed. The X-Band data showed comparable results to the C-Band data but the X-band data were more sensitive to the wetland vegetation. All of the three decomposition features were shown to be of value to characterize the land cover.

In contrast, the cross-polarized data were shown to be less suited for the characterization of the land cover. The overlaps of the 25% to 75% quartiles were high for all classes and features. Along with this the positions of the classes NBG and VWT were less distinct. Comparing the different cross-polarized data (HH/HV and VV/VH) the HH/HV-polarized data were the favorable polarization for the characterization of the land cover types. The HH/HV data were more sensitive to the classes VWT and NBG and the

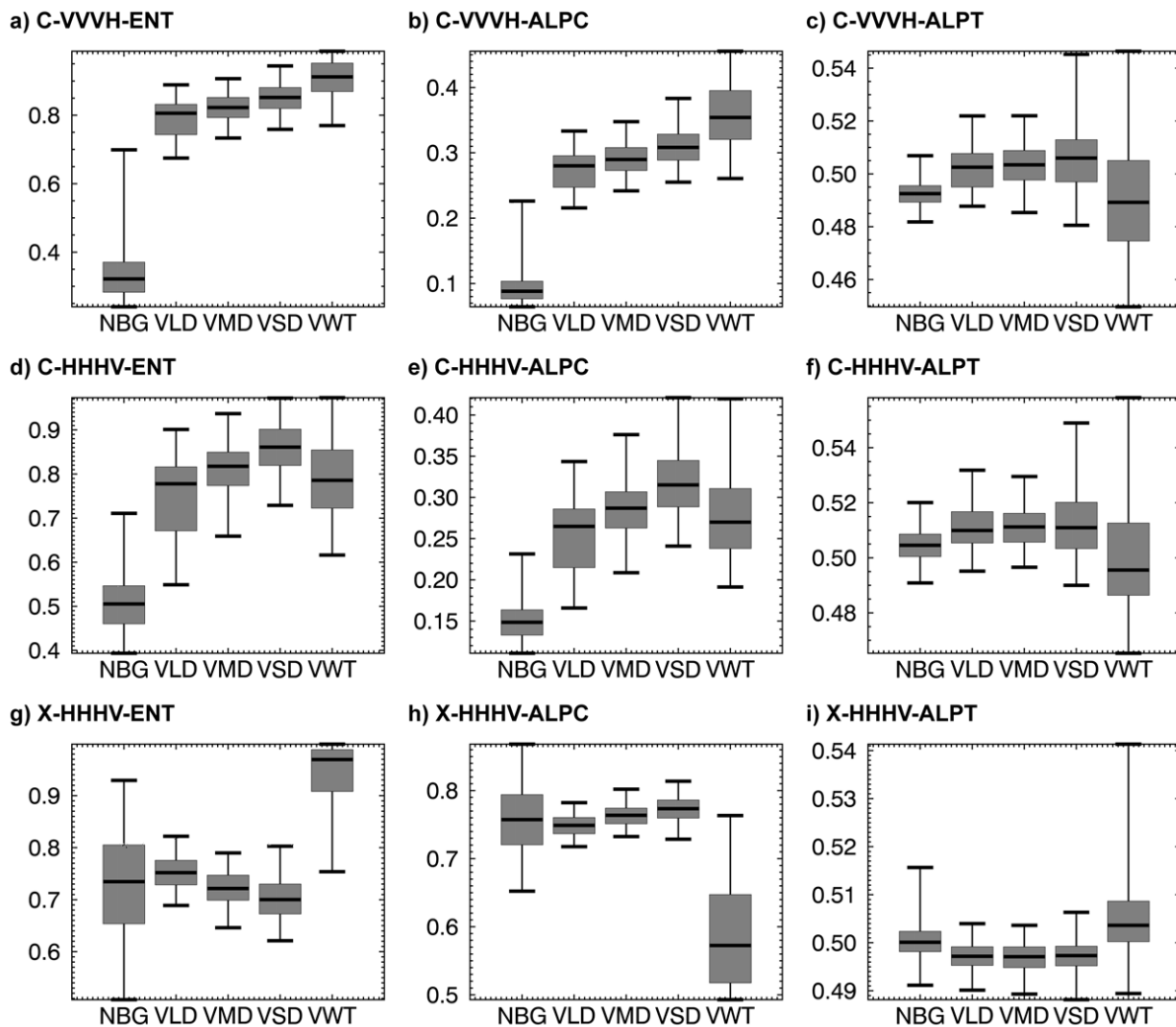


Figure 4.19: Average boxplots of Entropy (ENT), Alpha of Covariance Matrix (ALPC) and Alpha of Coherency Matrix (ALPT): a)-c) cross-polarized R-2 VV/VH (C), d)-f) cross-polarized R-2 HH/HV and g)-i) cross-polarized TSX HH/HV of the Mackenzie Delta test sites (RIS, ECH, DIS and TUK). Source: Own Figure.

differences between the vegetation classes VLD, VMD and VSD were more pronounced. Among the analyzed decomposition features the Entropy and the Alpha of C-matrix were shown to be of value for the characterization. The Alpha of T-Matrix did not give any reasonable information.

The analysis of X-Band, C-Band and L-Band Entropy/Alpha decomposition features showed that X- and C-Band data were best suited for the characterization of the tundra land cover. The best results were observed for quad-polarized and co-polarized data and the differences between both were very small. All three analyzed features (Entropy, Alpha of C-Matrix and Alpha of T-Matrix) were shown to be of value for the characterization of the land cover types. The HH/HV-polarized data were the favorable cross-polarization for the characterization of the land cover types. Especially the characterization of the wetlands was more distinct with the HH/HV data. The cross-polarized Entropy and the Alpha of C-Matrix were identified to be helpful for the characterization of land cover classes.

## 4 Results

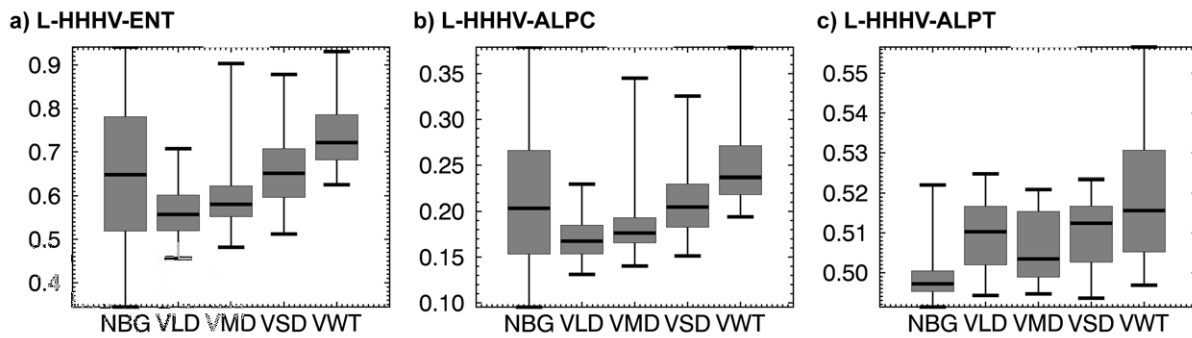


Figure 4.20: Average boxplots of Entropy (ENT), Alpha of Covariance Matrix (ALPC) and Alpha of Coherency Matrix (ALPT): a-c) cross-polarized ALOS PaLSAR HH/HV of the Mackenzie Delta test sites (RIS, ECH, DIS and TUK). Source: Own Figure.

### 4.2.1.3 Power Decompositions

In the following the characteristics of the Two and Three Component Power Decompositions features double bounce (DBL), odd bounce (ODD) and volume scattering (VOL) were evaluated. For this analysis the data were processed for the test sites of the Mackenzie Delta Region and for the test site Banks Island. The Three Component Decomposition features were directly derived from the quad-polarized C-Band data. The data were processed and Yamaguchi Decomposition was performed. The same quad-polarized C-Band data were used to form a co-polarized Scattering Matrix. This data were processed and the Two Component Decomposition was performed. Any differences between the co- and quad-polarized features were then only caused by the differences in the models and the missing HV information (see Section 4.1.2). The co-polarized X-Band data were analyzed and Two Component Decomposition was calculated. The following characteristics of double bounce, odd bounce and volume scattering were observed for the sigma nought calibrated data of the test sites of the Mackenzie Delta Region (ECH, DIS, TUK, RIS):

- **C-Band - quad-polarized Double Bounce** The double bounce of quad-polarized C-Band data showed a high sensitivity to the land cover classes. The median values of class NBG were low. The median values increased from VLD to VMD to VSD and were high for the class VWT. The 25% to 75% quartiles of the non-wetland vegetation showed high overlaps (Figure 4.21.a).
- **C-Band - quad-polarized Volume Scattering** The median volume scattering values were increasing from NBG to VLD to VMD to VSD to VWT. The lowest values were observed for the class NBG and the highest median values for the class VWT. The classes VLD and VMD showed a high overlap of their 25% to 75% quartiles. The position of the class VSD was more distinct and the overlap of its 25% to 75% quartile with the quartiles of the classes VMD and VWT was small (Figure 4.21.b).
- **C-Band - quad-polarized Surface Scattering** All classes showed a high contribution of surface scattering and the overlaps of the 25% to 75% quartiles were high. The highest median values were observed for the class NBG. The median surface scattering values were increasing from VLD to VMD to VSD to VWT (Figure 4.21.c).
- **C-Band - HH/VV-polarized Double Bounce** The analysis of the co-polarized C-Band double



bounce showed comparable results to the quad-polarized double bounce. The feature showed increasing median values from NBG to VLD to VMD to VSD. The highest values were observed for class VWT (Figure 4.21.d).

- **C-Band - HH/VV-polarized Surface Scattering** Along with this the characteristics of the co-polarized odd bounce feature were similar to the characteristics of the quad-polarized odd bounce feature. The differences in the class statistics were small (Figure 4.21.e) and supported the findings of the correlation analysis (Section 4.1.2).
- **X-Band - HH/VV-polarized Double Bounce** The double bounce of the co-polarized X-Band data showed a high sensitivity to the land cover classes. The classes VSD and VWT showed distinct positions of the 25% to 75% quartiles and no overlap with any other class. Like the C-Band data the median values were increasing from NBG to VLD to VMD to VSD to VWT (Figure 4.21.f).
- **X-Band - HH/VV-polarized Surface Scattering** The analysis of the surface scattering of co-polarized X-Band data showed a distinct position of the classes NBG and VWT. Both showed a small overlap of their 25% to 75% quartiles. The median values of both classes were comparable high and the values were greater than -8 dB. The classes VLD and VMD showed nearly identical statistics. The class VSD showed a higher median value but its 25% to 75% quartile showed overlaps with the other classes (Figure 4.21.g).

The following characteristics of double bounce (DBL) and odd bounce (ODD) were obtained for the sigma nought calibrated scattering matrices of the co-polarized X-Band data of the test sites Banks Island (BIS):

- **X-Band - HH/VV-polarized Double Bounce** The double bounce of the co-polarized X-Band data showed sensitivity to the class VWT. The median values were high and the 25% to 75% quartile showed a distinct position. The class NBG showed lower values and a high variance. The classes VLD, VML and VMH showed overlapping 25% to 75% quartiles. Among these classes the median values were highest for the class VLD - followed by VMH and by VML (Figure 4.22.a).
- **X-Band - HH/VV-polarized Surface Scattering** The analysis of the surface scattering of co-polarized X-Band data showed higher sensitivity of this feature to the land cover classes compared to the double bounce. The positions of the 25% to 75% quartiles of the classes VLD and VWT were more distinct but the range of the values of the class NBG was still very high and comprised the 25% to 75% quartiles of all other classes. The median values were highest for class VLD - followed by VMH and VML (Figure 4.22.b).

The analysis of the Two and Three Component Power Decompositions features double bounce, odd bounce and volume scattering showed that these features were sensitive to the different types of the land coverage. Generally, the differences between the C- and X-Band were small - as well as the differences between the double bounce and surface scattering of co- and quad-polarized data. This supports the findings of Section 4.2.1.1. The classes NBG and VWT had the most distinct statistics compared to the other examined features. The statistics of the classes VLD, VMD and VSD were more diverse and variable. It was observed that the intensity values increased from VLD to VMD and VSD. This was best visible for the volume scattering of the quad-polarized data. Since the calculation of volume scattering was based on the HV information (compare Figure 4.21.b and Figure 4.21.f) this can also be anticipated

4 Results

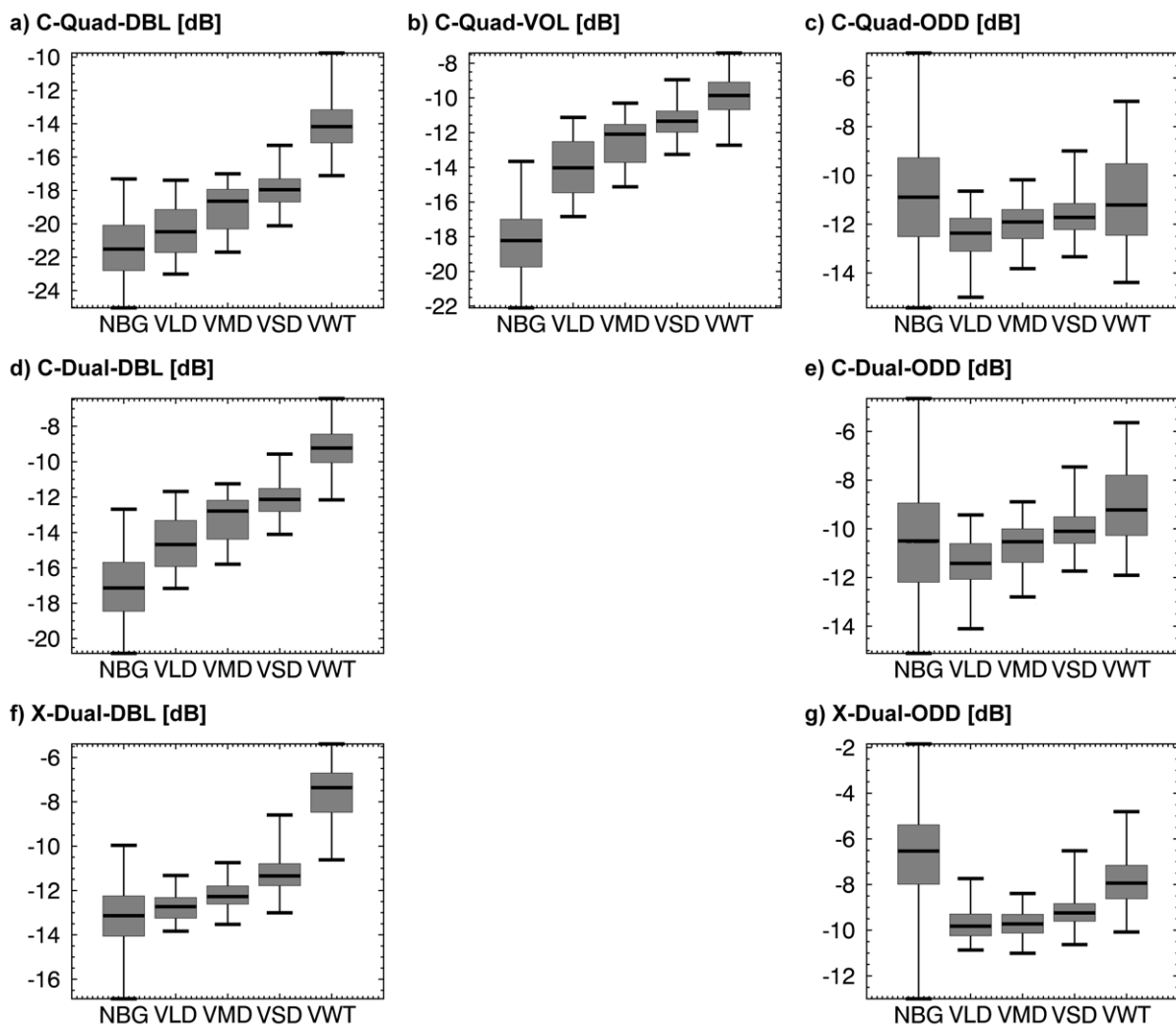


Figure 4.21: Average boxplots of TSX (X) and R-2 (C) Yamaguchi and Two Component Decomposition features double bounce (DBL), volume scattering (VOL) and surface scattering (ODD): a)-c) quad-polarized R-2 (C), d)-e) co-polarized R-2 and f)-g) co-polarized TSX of the Mackenzie Delta test sites (RIS, ECH, DIS and TUK). Source: Own Figure.

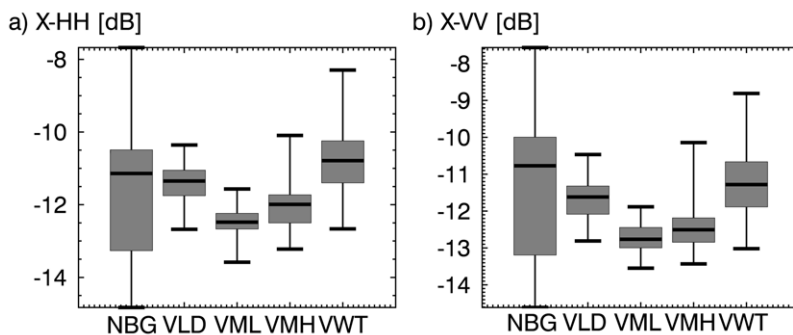


Figure 4.22: Boxplots of co-polarized TSX (X) Two Component Decomposition features a) double bounce (DBL). b) surface scattering (ODD) and c) Difference between ODD and DBL of test site Banks Island. Source: Own Figure.

for the volume scattering of the X-Band. The double bounce feature was more sensitive to the land cover types than the surface scattering feature.

The Two Component Decomposition features (X-Band) and Three Component Power Decompositions features (C-Band) were shown to be sensitive to the type of land cover. The double bounce and surface scattering intensities provided a good interpretation and helped to explain the observed PolSAR signal. The differences between the C- and X-Band decomposition features were small, as well as the differences between the double bounce and surface scattering of co- and quad-polarized data. The volume scattering feature was nevertheless shown to be highly sensitive to the vegetation classes and was increasing with increasing vegetation height and changing composition, respectively shrub density.

#### 4.2.1.4 Influence of the Incidence Angle

The chosen incidence angle strong has influence on the image content of SAR imagery. It was demonstrated that certain incidence angles highlight certain classes (see Section 3.4 and Richards (2009), p. 267). The volume scattering is decreasing and the surface scattering is increasing with a steepening of the incidence angle. The shallow incidence angles facilitate the volume scattering in contrast. There are lower and upper incidence angles that can be used for a SAR acquisition. The incidence angles lower or higher than these boundaries will lead to artifacts in the image and are usually referred as “out-of-performance”. For TSX the lower boundary is about 20° and the upper boundary is about 50° (DLR 2007). The aim of the following analysis was to investigate the influence of the incidence angle on the separability of tundra land cover classes. For this task quad-polarized data of R-2 were acquired for the test sites Anderson (AND) and Ivvavik (IVV). The data were recorded with three different incidence angles. The images of AND were taken between the 07. and the 30. August 2011 with incidence angles of 46°, 38° and 20°. The images of IVV were taken between the 04. and the 09. August 2011 with incidence angles of 47°, 39° and 22°. Both sites were not visited during the field work and therefore the reference data were selected using high resolution optical ortho-imagery (Section 2.2.5). Due to the northern location no reference information on the distribution of class VSD was available and class VSD was not included in the analysis.

Figure 4.23 shows the scatterplots of the sigma nought intensities HH and HV of the test site AND of the three incidence angles 46° (Shallow), 38° (Medium) and 22° (Steep). The plots are shown for the land cover classes NWA, NBG, VLD, VMD and VWT. It was observed that the HH intensities of the shallow and medium incidence angles were low for the class NWA and values between -22 and -33 dB were observed (Figure 4.23.a & f). In contrast, the HH intensity of class NWA of the steep incidence angle was high, ranging from -5 to -13 dB and was therefore as high as the intensity ranges of the other classes (Figure 4.23.k & o). That indicated a poor separation of land and water when steep incidence angle are used. The intensity of HV of class NWA was low for all incidence angles and ranging from -28 to -35 dB (Figure 4.23.a & f & k). The HV intensities of shallow, medium and steep incidence angles were similar to all other classes and the intensities ranged from -22 to -33 dB for class NBG (Figure 4.23.b & g), between -15 to -25 dB for class VLD (Figure 4.23.c & h), between -15 to -25 dB for class VMD (Figure 4.23.d & i) and between -10 and -33 dB for class WTL (Figure 4.23.e & j). The HH intensities of the shallow and medium incidence angles were comparable: For both the intensities ranged between -10

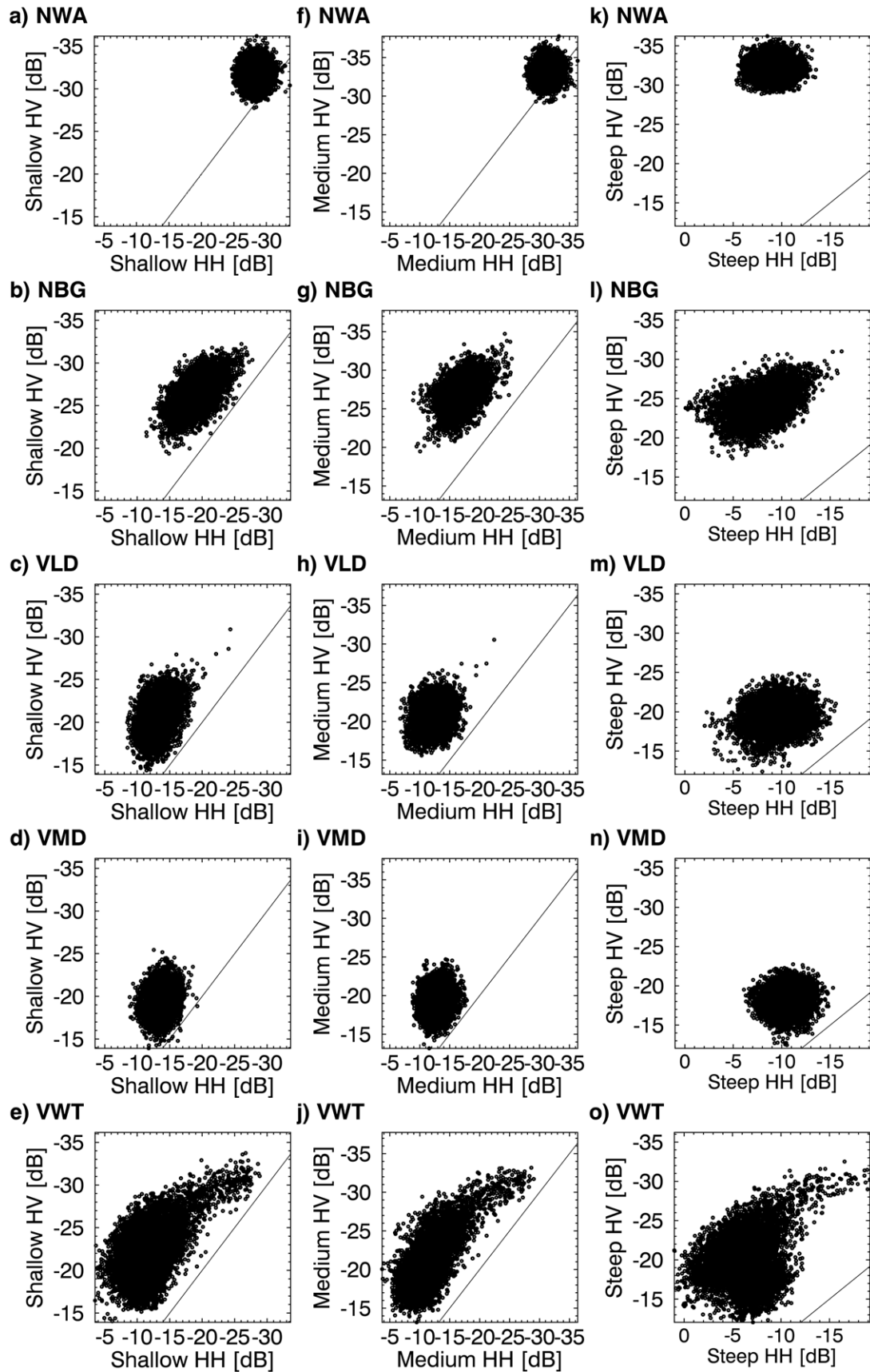


Figure 4.23: Influence of the incidence angle and scatterplots of HH and HV Radarsat-2 sigma nought intensities of test site Anderson (AND): a)-e) shallow incidence angle ( $46^\circ$ ), f)-j) medium incidence angle ( $38^\circ$ ) and k)-o) steep incidence angle ( $20^\circ$ ). Source: Own Figure.

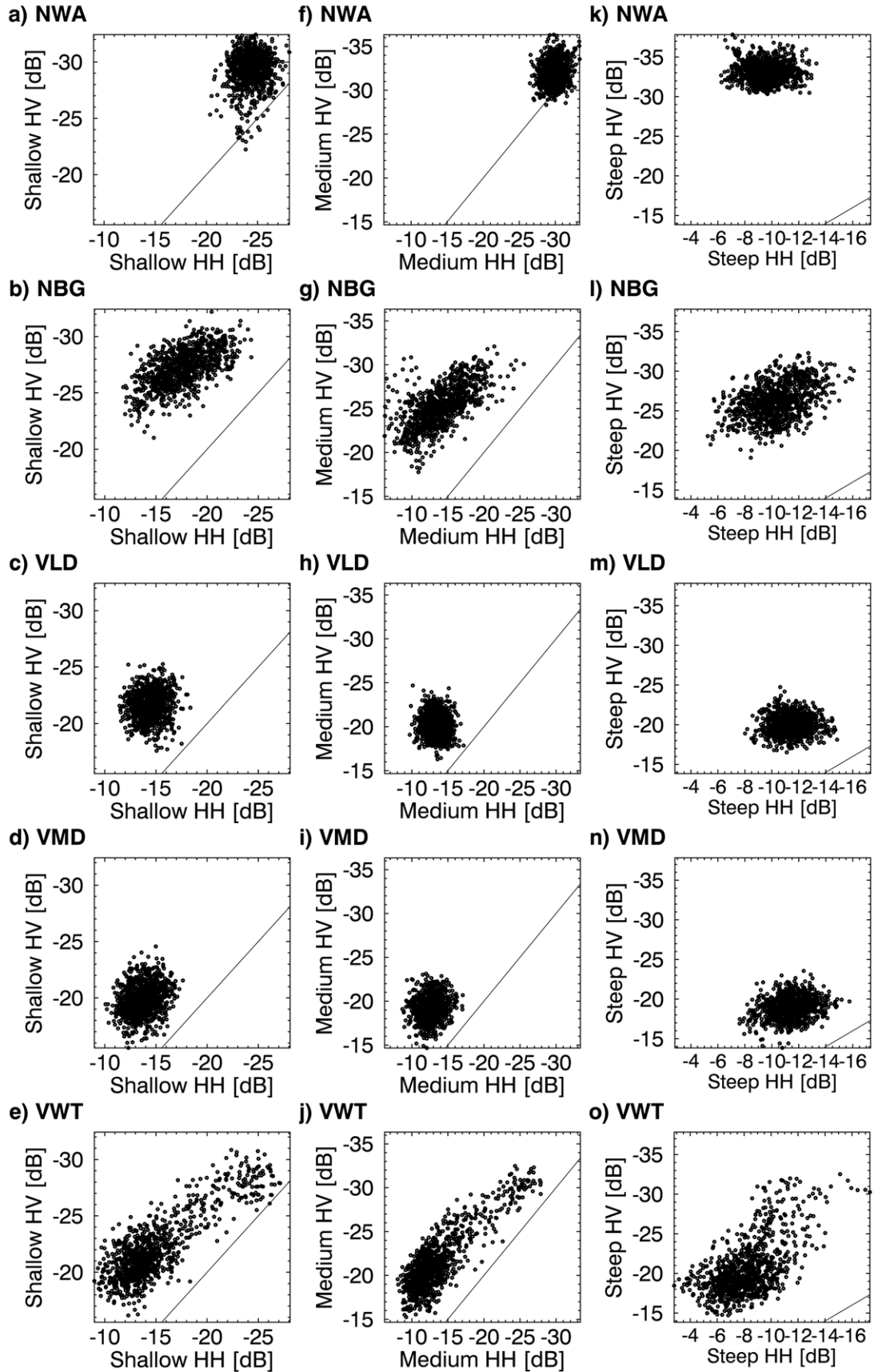


Figure 4.24: Influence of the incidence angle and scatterplots of HH and HV Radarsat-2 sigma nought intensities of test site Ivvavik (IVV): a)-e) shallow incidence angle ( $47^\circ$ ), f)-j) medium incidence angle ( $39^\circ$ ) and k)-o) steep incidence angle ( $22^\circ$ ). Source: Own Figure.

#### 4 Results

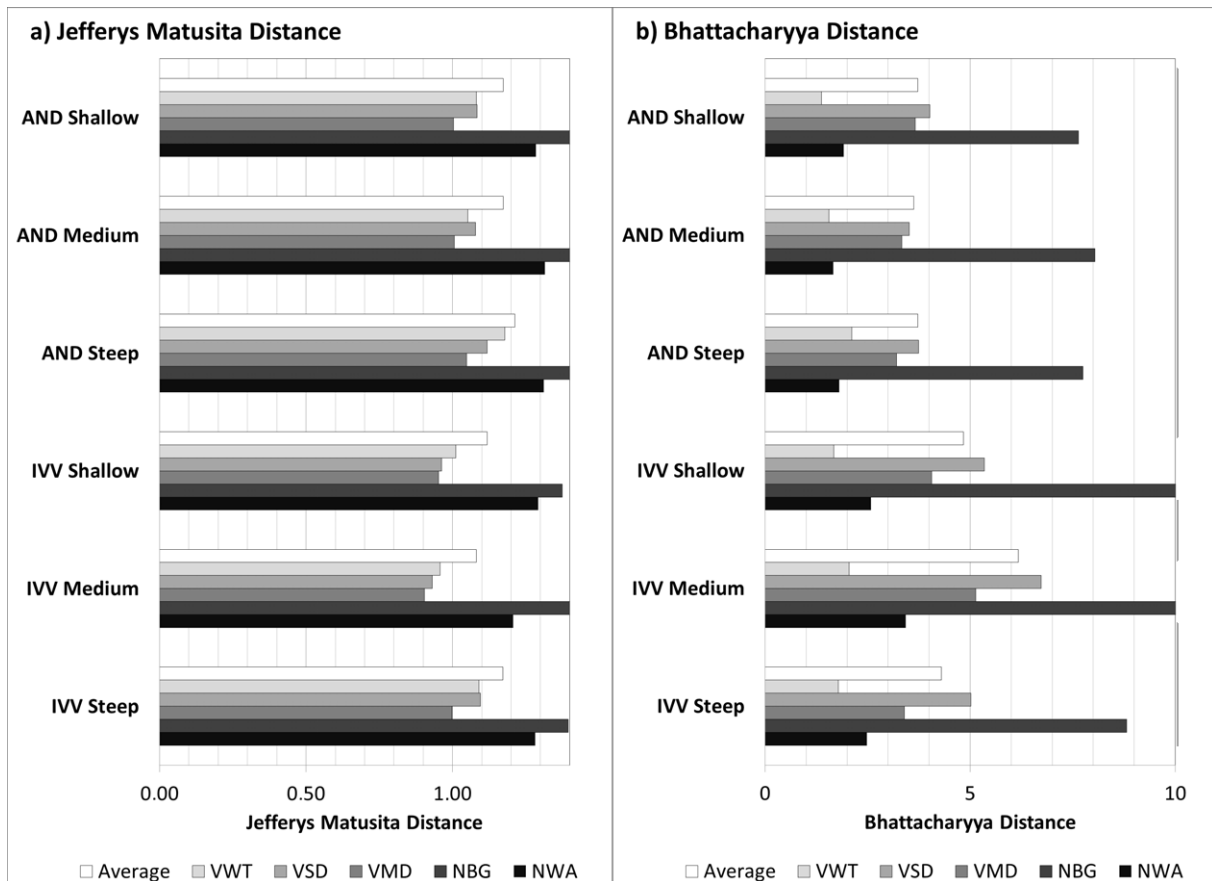


Figure 4.25: Influence of shallow, medium and steep incidence angles on the separability of land cover reference data: a) Jefferys Matusita Distance and b) Bhattacharyya Distance for test sites Anderson (AND) and Ivvavik (IVV). Source: Own Figure.

and -33 dB for class NBG (Figure 4.23.b & g), between -8 and -18 dB for class VLD (Figure 4.23.c & h), between -8 and -18 dB for class VMD (Figure 4.23.d & i) and between -5 to -25 dB for class VWT (Figure 4.23.e & j). The HH intensities of the steep incidence angles showed three major differences compared to shallow and medium incidence angles: (1) The intensity was high for class VWT and the values ranging from +2 to -18 dB (Figure 4.23.o). (2) The intensity of class NBG was high and the values ranging from 0 to -13 dB (Figure 4.23.l). (3) The intensities of class VLD (-3 to -13 dB) showed higher values compared to class VMD (-8 to -13 dB) (Figure 4.23.m & n).

Figure 4.24 shows the scatterplots of the intensities HH and HV of test site IVV of the three different incidence angles 47° (Shallow), 39° (Medium) and 22° (Steep) and of the land cover classes NWA, NBG, VLD, VMD and VWT. The findings were comparable to the results of test site AND. The HH intensity was low for the class NWA and the shallow and medium incidence angles were ranging from -25 to -35 dB (Figure 4.24.a & f). The HH intensity of the steep incidence angle of class NWA was ranging from -5 to -13 dB and was as high as the intensity range of all other classes (Figure 4.24.k & o). The intensity of HV of all incidence angles of class NWA was low and ranging from -28 to -35 dB (Figure 4.24 a & f & k). The HV intensities of shallow, medium and steep incidence angles were comparable for all other classes. The HH intensities of the steep incidence angles showed again major differences compared to the HH

intensities of shallow and medium incidence angles. The intensity values were higher and ranged from -4 to -16 dB. The values of class VWT and NBG were comparable high (Figure 4.24.l & o). The difference between the classes VLD and VMD were very small but the mean value of the VMD cluster was slightly lower than the mean values of the VLD cluster (Figure 4.24.m & n).

The influence of the different incidence angles on the class separability was investigated using the separability distances Jefferys Matusita Distance (JD) and Bhattacharyya Distance (BD) (Jensen (1995, 2007)). Figure 4.25 shows the JD and BD of the classes NWA, NBG, VLD, VMD and VWT for the shallow, medium and steep incidence angles. The JD and BD were calculated using the quad-polarized scattering matrices. The analysis showed that JD was on the same level for all incidence angles (Figure 4.25.a). The best separability was observed for the class NWA for all incidence angles and both test sites. There was only small difference of the average JD among the different incidence angles and no favorable incidence angle for the class separation could be identified. The analysis of the BD (4.25.b) showed a similar picture for test site AND. The classes' BD were on the same level for all incidence angles and the average BD values were around 2.5. The results of test site IVV showed that the highest average BD value of about 3.2 was observed for the medium incidence angle. The BD values of the shallow and steep incidence angle were around 2.5. These findings indicated that the medium incidence angle was best suited to separate among all different classes. However, the differences were small and no favorable incidence angle for the class separation could be identified.

The influence of the incidence angle on the class separability was analyzed for the two test sites Anderson and Ivvavik. Both sites are located in the Mackenzie Delta Region and land cover reference data were collected using high resolution optical ortho-imagery. The analysis of the scatterplots showed that the differences between the shallow and medium incidence angles were small and that the classes' intensity values showed very similar characteristics. The intensity values of data acquired with steep incidence angle were higher and the class positions were slightly different. The separability of the land cover classes was analyzed using the Jefferys Matusita Distance and Bhattacharyya Distance. None of these features indicated a favorable incidence angle for the class separation. The analysis of Bhattacharyya Distance for test site Ivvavik showed that the medium incidence angle was in average best suited to separate among all land cover classes, however.

### 4.2.2 Multispectral Data

In the following the characteristics of the multispectral optical data of L-8 were evaluated. The data were processed to top of atmosphere corrected reflectance values using the meta-information (see Section 3.1.2). The L-8 data of the Mackenzie Delta Region and of Banks Island were cropped to the extent to the PolSAR data and sampled to a spatial resolution of 12 m using bilinear interpolation (see Section 2.2.2). The same land cover reference data used for the PolSAR analysis were used to calculate the statistics of the classes. The boxplots of the following figures display the average locations of the 1% (lower horizontal black line), 25% (lower boundary of the gray box), 50% (middle horizontal black line), 75% (upper boundary of the gray box) and 99% (upper horizontal black line) percentiles. Figure 4.26 shows the average top of atmosphere corrected reflectance values, NDVI, rightness, greenness and wetness of the tasseled cap transformation of L-8 data of the Mackenzie Delta test sites (DIS, ECH, RIS) of the land

#### 4 Results

cover classes NBG, VLD, VMD, VSD and VWT. In summary the following findings were made:

- **NDVI** The NDVI of class NBG was low with values less than 0.3. The NDVI values were increasing from VLD to VMD to VSD up to a maximum of about 0.7. The NDVI of class VWT was low and was around 0.5. The 25% to 75% percentile of this class showed an overlap with the classes VLD and VSD (Figure 4.26.a).
- **Brightness (BRIGHT)** The brightness of the classes NBG and VWT was low and the reflectance values were less than 0.30. The classes VLD, VMD and VSD showed brightness values between 0.30 and 0.35. The 25% to 75% percentiles of these classes were overlapping and none of the classes showed a distinct distribution of brightness values (Figure 4.26.b).
- **Greenness (GREEN)** The greenness range of values of class NBG was distinct and very low with negative values. Like the NDVI the greenness values were increasing from VLD to VMD to VSD and ranged from about 0.05 to 0.12. The 5% to 75% percentiles of these classes were overlapping and showed a poor separation. The class VWT showed lower greenness values. These were ranging from 0 to 0.05. In addition, the 25% to 75% percentile of VWT showed no overlap with any other class (Figure 4.26.c).
- **Wetness (WETNESS)** The highest wetness values were observed for the class NBG and the class VWT. Both showed a median value of about -0.07. The wetness values were lowest for the class VLD and values less than -0.1 were observed. The median values of the wetness were increasing from VLD to VMD to VSD. The 25% to 75% percentiles of classes VLD and VMD were overlapping. In contrast, the 25% to 75% percentile of the class VSD showed no overlap with any other class (Figure 4.26.d).
- **Reflectance of red light (RED)** The class NBG showed the highest reflectance values of the red light and the median value was about 0.09. The median values of the classes VLD, VMD and VSD were lower and about 0.065, 0.06 and 0.05. The 5% to 75% percentiles of these classes showed overlaps and poor separation. The class VWT had a median value of about 0.05 and the 5% to 75% percentiles of classes VWT and VSD were overlapping (Figure 4.26.e).
- **Reflectance of near-infrared light (NIR)** The near-infrared reflectance of class NBG was distinct, very low and values were less than 0.15. The differences between the classes VLD, VMD and VSD were small and the median reflectance values of these classes were about 0.27. The class VWT showed, in contrast, a distinct position and its median value was about 0.2 (Figure 4.26.f).

Figure 4.27 shows the top of atmosphere corrected reflectance values of L-8 data of the test sties Banks Island. The land cover classes NBG, VLD, VML, VMH and VWT were analyzed using the Normalized Difference Vegetation Index (NDVI), the brightness, greenness and wetness of the tasseled cap transformation, the reflectance of red and the reflectance of near-infrared light.

- **NDVI** The median NDVI of class NBG was lowest with values less than 0.2. The NDVI values of the classes VLD and VWT were about 0.28 and the 5% to 75% percentiles of both classes were overlapping. The highest NDVI values were observed for classes VML and VMH. Both showed median values of about 0.32 and the 5% to 75% percentiles of both classes were overlapping (Figure 4.27.a).
- **Brightness (BRIGHT)** The class NBG showed a high range of brightness values. The lowest



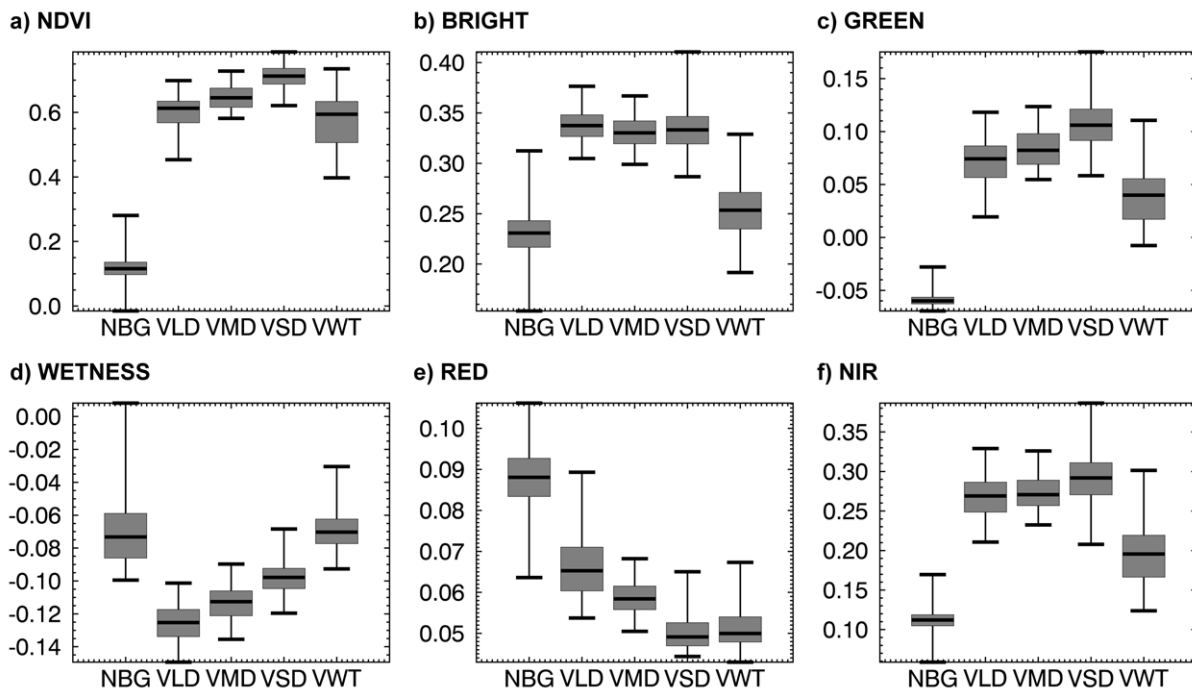


Figure 4.26: Boxplots of top-of-atmosphere corrected L-8 features: a) NDVI, b) Brightness, c) Greenness, d) Wetness of Tasseled Cap Transformation, e) reflectance of red and f) reflectance of near-infrared of the Mackenzie Delta test sites (RIS, ECH, DIS). Source: Own Figure.

brightness values were observed for class VWT with a median brightness of about 0.3. The other vegetation classes showed brightness values in the range from 0.35 to 0.4 and the 5% to 75% percentiles were overlapping (Figure 4.27.b).

- **Greenness (GREEN)** Positive greenness values were observed for the classes VML and VMD. The greenness was lowest for class NBG and showed a distinct position of the 5% to 75% percentile (Figure 4.27.c).
- **Wetness (WETNESS)** Among all analyzed features the wetness showed the lowest variation of the reflectance values. The median values of the classes NBG, VLD, VML, VMH were about the same and around -0.16. The 5% to 75% percentiles of these classes showed a similar range of values. In contrast, the class VWT had a distinct position and wetness values were ranging from -0.16 to -0.05 (Figure 4.27.d).
- **Reflectance of red light (RED)** The highest reflectance values of red light were observed for class NBG. The reflectance was low for the classes VLD, VML, VMH and VWT. The class VWT had the lowest median value with less than 0.1 (Figure 4.27.e).
- **Reflectance of near-infrared light (NIR)** The class NBG showed a high range of near-infrared reflectance values. The 5% to 75% percentile of the class NBG comprised the 5% to 75% percentiles of the classes VLD, VML and VMH. The median reflectance of class VWT was lower than the median of any other class and a value of about 0.16 was observed (Figure 4.27.f).

It was observed that the class NBG has the most distinct position of all investigated features and it was characterized by a low NDIV, low greenness, low brightness and low near-infrared reflectance. The class

#### 4 Results

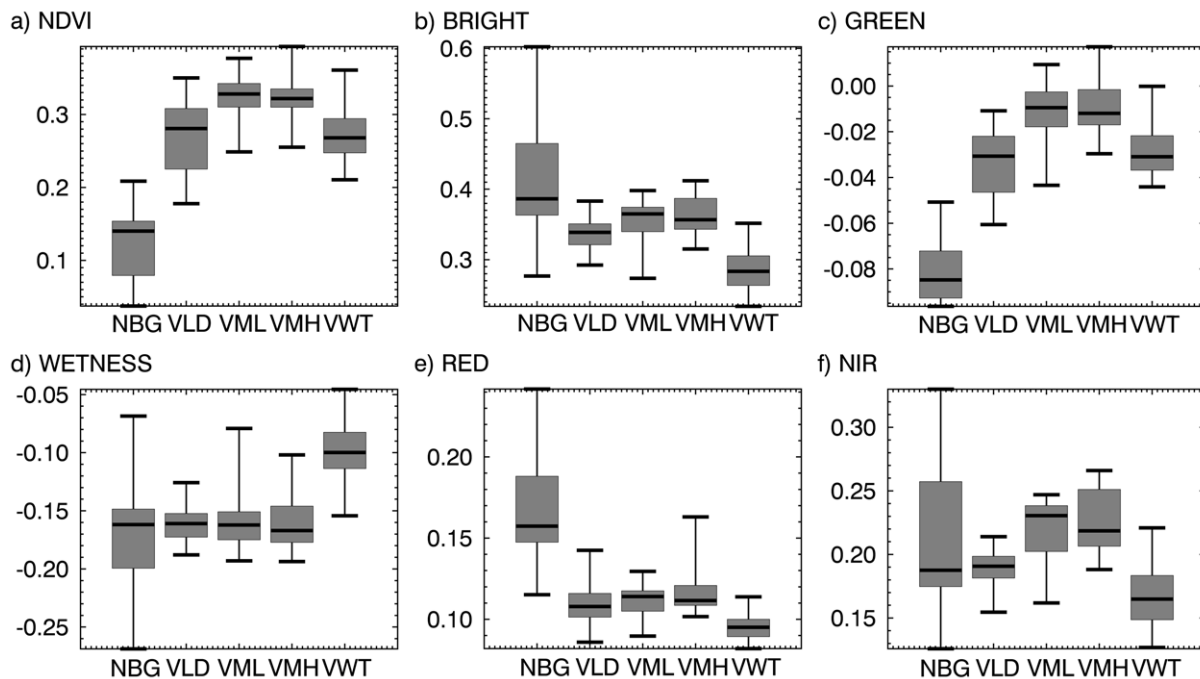


Figure 4.27: Boxplots of top-of-atmosphere corrected L-8 features: a) NDVI, b) Brightness, c) Greenness, d) Wetness of Tasseled Cap Transformation, e) reflectance of red and f) reflectance of near-infrared of the test site Banks Island (BIS). Source: Own Figure.

showed a comparable high wetness and a high reflectance of the red light. The NDVI, the greenness, the wetness and the reflectance of near-infrared had increasing median values from VLD to VMD to VSD. These classes showed comparable high brightness values. The reflectance of the red light was decreasing from VLD to VMD to VSD. The class VWT was characterized by comparable low NDVI, low brightness, low greenness and low near-infrared reflectance values. For all of analyzed features the median of VWT was lower than the median of VLD and the 25% to 75% percentile showed no - respectively only a small - overlap with the percentiles of the other classes. The reflectance of red light was low and the percentile of class VWT overlapped the percentile of class VSD.

The greenness of the tasseled cap transformation and the NDVI were identified to be suitable to characterize the land cover classes. Both features showed the best differentiation of the classes reflectance characteristics and increasing values for the the land cover classes VLD, VMD and VSD. This was likely related to increasing shrub density and the higher vegetation fraction. These features clearly differentiated the vegetated and non-vegetated ground. The greenness showed the best differentiation of the class VWT and of the other vegetation classes. The analysis of the test site Banks Island showed that the characteristics of the land cover classes were less clear compared to the Mackenzie Delta test sites. The 5% to 75% percentiles of all classes showed similar values and data ranges. In particular the classes VML and VMH had very similar ranges of values among all investigated features. The wetness and the near-infrared reflectance were best suited to characterize the class VWT. In contrast, the class NBG showed the most distinct class statistic of all investigated features - beside the wetness and the near-infrared reflectance.

The analysis of the multispectral Landsat 8 data was conducted for the test sites of the Mackenzie Delta Region and the test site Banks Island. The features analyzed were the Normalized Difference Vegetation Index, the brightness, greenness and wetness of the tasseled cap transformation, the reflectance of red and the reflectance of near-infrared light. The boxplot analysis of the land cover reference data showed that NDVI and the greenness of the tasseled cap transformation were best suited to characterize the land cover. Both features showed increasing values for increasing vegetation density and coverage. The features were suited to differentiate between bare and vegetated ground. The results of the test sites Banks Island were less clear and showed that other features than NDVI and the greenness were better suited to characterize some of the land cover types, e.g. the wetland vegetation (wetness).

### 4.2.3 Digital Elevation Model Data

The following section shows results of the characterization of the land surface morphology based on DEM data. The focus of this analysis was to visually and qualitatively show the information content and the benefits of the DEM data (TDX IDEM and ALSO GDEM) for the characterization of different types of polar landforms using topographic and morphometric features. Four test sites were selected that represent different landforms: the Caribou Hills of the Mackenzie Delta Region, the coastal low-lands of the northern Mackenzie Delta and uplands of Richards Island, the coastal zone and the sloped inland of northern Banks Island and the shore zone of the James Bay. The following subsections are dedicated to the individual test sites and are structured as follows: (1) The first part of each section provides a description of the landform arrangement of the chosen subset of the test site and is based on the information of Section 2.1. This part therefore highlights the structural geological setting, the surficial setting and the morphology of the surface. (2) In the following the basic topographic features of the site are shown. These are the elevation, the slope, the convexity and the aspect (Section 3.1.3). This part also shows the TPIs calculated with different estimation window sizes (TPI stack). (3) Further, the final subsection provides results of the analysis of profiles that were drawn along meaningful topographic variations. These profiles show the elevation, the slope, TPIs of selected scales and the interpolated TPI values of all investigated scales.

The key findings are summarized at the end of Section 4.2.3.4 on page 168. The DEM data shown in the following underwent the processing as specified in Section 3.1.3. The data were filtered with the Non-Local Means filter (see Section 3.1.1.2) and with respect to the findings of Section 4.1.1.2. The TPIs were processed as described in Section 3.1.3 and the fast TPI calculation was used to form a stack of TPIs with different estimation window sizes (scales). The TPI stack is composed of twenty-five TPIs that were calculated individually with scales ranging from 100 m to 3000 m. The findings of the following sections were integrated in the landform classification (see Section 4.3.3).

#### 4.2.3.1 Mackenzie Delta Region - Caribou Hills

The site between the Mackenzie Delta and the uplands of the Caribou Hills shows four major landform units: (1) The steep ridges and cliffs of the proterozoic formations. (2) The low lying pleistocene to holocene alluvial sediments of the Mackenzie River and Delta. (3) The pleistocene to holocene uplands and (4) the neogen to paleogen uplands of the Caribou Hills (compare Figure 2.3). The landform arrangement of the uplands is dominated by structural forms of the geology such as hills with exposed bedrock and valleys along faults. The low lying part of the site is dominated by fluvial sediments of the delta and by periglacial landforms. This ensemble is visible in form of banks, terraces and thermokarst lakes. The pleistocene to holocene uplands show landforms caused by periglacial processes. The thermo-erosion processes have led to numerous thermokarst lakes with comparable steep shores, in-situ presence of ice-bearing permafrost and with wetlands at shallow slopes and drained lakes. The active periglacial forming is visible in form of polygonal ice wedge networks and in the formation of pingos and hummocks (see Section 2.1.2).

Figure 4.28 shows the basic topographic features of the test site Caribou Hills derived from TDX IDEM with a spatial resolution of 13 m. The elevation of the site varies between -5 m and 250 m (Figure 4.28.a&f). The steep slopes of the proterozoic formations were clearly visible and showed an elevation

ranging from 100 m at the top-slope to 0 m at the foot-slope. The slope angle was very steep and up to 30° (Figure 4.28.b). Along with this the convexity was concave (positive) at the ridges and convex (negative) at the valleys and gullies (Figure 4.28.c). The aspect clearly showed the two main direction of the valley-and-ridge sequences of the pleistocene to holocene uplands. These were the northwest-southeast and northeast-southwest directions. The alluvial delta complex had low relief energy and was flat to gently sloped and the aspect directions were varying. Figure 4.28.e shows the hillshade of the site and highlighted the landform features. Again the valleys and ridges of the steep sloped proterozoic formations were clearly visible and separated the hilly landscape of the uplands from the flat alluvial channels and banks of the delta complex. Further, the figure shows the location of four profiles that were analyzed in the following: Profile 1 (A-B) was perpendicular to the front of the proterozoic formation and showed the transition between delta lowland and pleistocene to holocene upland. Profile 2 (C-D) showed a cross section along the main valley direction of the neogen to paleogen Caribou Hills. Profile 3 (G-H) showed a cross section perpendicular to the main valley direction of the neogen to paleogen Caribou Hills. Profile 4 (E-F) was located close to the foot-slope of the Caribou Hills and was situated on the hilly pleistocene to holocene upland.

**Elevation** - Figure 4.29 shows the elevation values of the Profiles 1-4. The first approx. 2.0 km of Profile 1 (Figure 4.29.a) showed the flat delta complex lying on a level of about 0 m. The exposition of the proterozoic formations caused a rapid increase in the elevation up to 100 m - followed by small-scale variations in the range from 10 m to 25 m. Between 2.0 km and 3.8 km the landscape was smooth and nearly constant leveled on an altitude of about 90 m. The elevation profile showed more variations from 3.8 km to 7.0 km with a sequence of three major valleys and hills with an elevation range of about +/-25 m. From 7.0 km to 9.0 km the elevation was climbing nearly constantly up to a maximum peak of about 160 m. From 9.0 km to the end of the profile the elevation was varying on high level and showed the head of a small valley situated on the neogen to paleogen Caribou Hills (9.5 km to 10.0 km). The elevation values of Profile 2 (Figure 4.29.b) showed the cross section along a ridge of the neogen to paleogen Caribou Hills. The elevation range of the profile was approximately 180 m (50 m to 230 m). The profile showed a rapid increase in the elevation along the southern side of the hills (0.0 km to 3.0 km). This increase was followed by a decay of the elevation towards the northern side of the hills (3.0 km to 9.0 km). The small-scale topographic variations of the northern side were in the range of about +/- 15 m and were caused by local valley heads and local divides (ridges). The most northern part of the profile (9.0 km to 11.0 km) showed the foot-slope of the neogen to paleogen hills and the flat surfaces of the lakes. The Profile 3 (Figure 4.29.c) followed the same direction as Profile 2 (Figure 4.29.c) but it was situated on the foot-slope of the Caribou Hills and in pleistocene to holocene sediments. The variations of the elevation were lower and in the range from 50 m to 125 m. The small-scale changes were related to the shores of the thermokarst lakes and the lakes themselves. The last part of the profile showed the smooth lake surface (5.5 km to 6.8 km). The Profile 4 showed the cross section of the lower northern part of the Caribou Hills. The elevation range of the profile was about 125 m, ranging from the level of the pleistocene to holocene upland (about 50 m) to the level of the neogen to paleogen hills (about 175 m). The elevation profile showed three major valleys and four major ridges located at about 1.0 km, 2.8 km, 4.0 km and 5.9 km. Therefore the widths of the valleys were approximately 1.5-2.0 km. The small-scale variations of the elevation were related to the local drainage.

#### 4 Results

**Slope** - The slope variations of Profile 1 followed the main variations of the elevation (see Figure 4.30). The slope was more sensitive to small scale variations since it was independent of the actual elevation value. This was visible in Profile 1 (Figure 4.30.a) with higher variability of the value range. The slope values of the steep transition between alluvial delta complex and the uplands were up to  $30^\circ$  (0.0 km to 2.0 km). The ridges and the heads of the valleys of proterozoic top-slope were deeply cut and showed fast variations on a high level. The terrain of this section was very rough (2.0 km and 3.8 km). In contrast, the slope variations were small and less than  $5^\circ$  for the flat upland between 2.0 km and 3.8 km of the profile. The sequence of three major valleys and hills (3.8 km to 7.0 km) caused high slope variations and values up to  $15^\circ$ . This indicated local small-scale peaks and troughs. The slope variations were moderate and up to  $10^\circ$  for the climbing elevation between 7.0 km to 9.0 km. The head of a small valley - situated on the neogen to paleogen Caribou Hills - was clearly indicated by high slope variations that showed a steepness of the valley of up to  $15^\circ$ . The Profile 2 (Figure 4.30.b) showed slope variations less than  $5^\circ$  for most parts of the profile. The slope was up to  $10^\circ$  for five locations at the distances 0.8 km, 2.5 km, 7.0 km, 9.0 km and 9.8 km. The first peak was caused by a depressed u-shaped valley situated in perpendicular direction to the profile direction. This valley lied at the steep southern side of the Caribou Hills. The third peak showed the head of a secondary valley that was located perpendicular to the main valley direction. All of the remaining peaks were related to the steep shores of thermokarst lakes. These can occur on high elevation level due to the endorheic drainage. The slopes of Profile 3 (Figure 4.30.c) reached values up to  $20^\circ$  between 0.5 and 1.0 km. These variations were caused by the steep shores of the southern lake and two steep ridges separating the southern lake from the two small lakes between 1.0 km and 2.0 km. The following part (2.0 km to 5.0 km) showed a variable slope with values greater  $5^\circ$  and up to  $15^\circ$ . These variations highlighted the small-scale variations of the landscape and were not related to any higher-ranking landform. The last part of the profile (5.0 km to 6.8 km) showed the comparable steep shore of the northern thermo-erosion lake and the flat lake surface. The Profile 4 (Figure 4.30.d) showed a rapid increase in the slope values which was a result of the fast climbing elevation - from the lake level to the exposed western ridge of the neogen to paleogen hills. The slope values were up to  $15^\circ$  (0.0 km to 0.5 km). The following part of the profile (0.5 km to 5.0 km) showed gentle to moderate slope variations up to  $10^\circ$ . These were related to the drainage system and were composed of higher ranking northwest-southeast oriented valleys and ridges and the secondary valleys and ridges in northeast-southwest direction. The last part of the profile showed the high slopes of the continuously climbing elevation of the steep flank (5.0 km to 6.0 km).

**Topographic Position Index (TPI)** - Figure 4.31 shows TPI values processed with scales of 100 m, 500 m, 1000 m, 1500 m, 2000 m and 3000 m. The corresponding estimation window sizes were 9x9, 41x41, 83x83, 125x125, 149x149 and 249x249 pixels. A skip factor of 0.75 was used for the estimation of the TPI values (see Section 3.1.3). The analysis of the TPIs showed that small-scale valleys and ridges were best pronounced if the estimation window size was less than 500 m (Figure 4.31.a & b). This was best visible for the valley-ridge sequence of the proterozoic formation and for the drainage system of the neogen to paleogen Caribou Hills (local hills and local valleys). The TPI values calculated with an estimation window size of 1000 m highlighted the local tops of the Caribou Hills and the first-order valleys and of the pleistocene to holocene upland. The small-scale differences - e.g. the local hills and local valleys of the Caribou Hills - got lost on this scale (Figure 4.31.c). Figures 4.31.d, e & f showed that

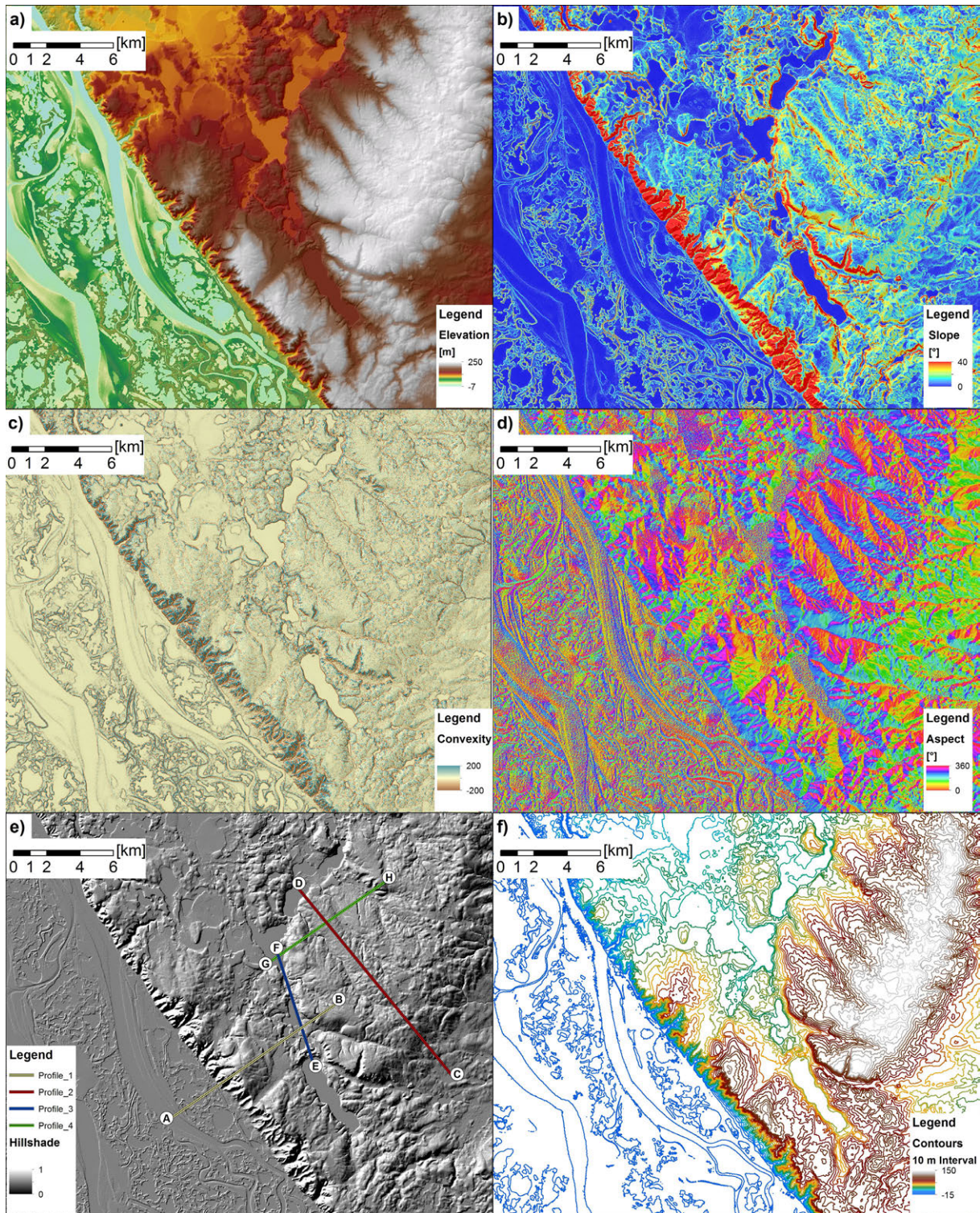


Figure 4.28: Basic topographic features of the test site Caribou Hills (CAH): a) Elevation, b) Slope, c) Convexity, d) Aspect, e) Hillshade and location of profiles and f) contour map. Data Source: TDX IDEM with a spatial resolution of 13 m. Source: Own Figure.

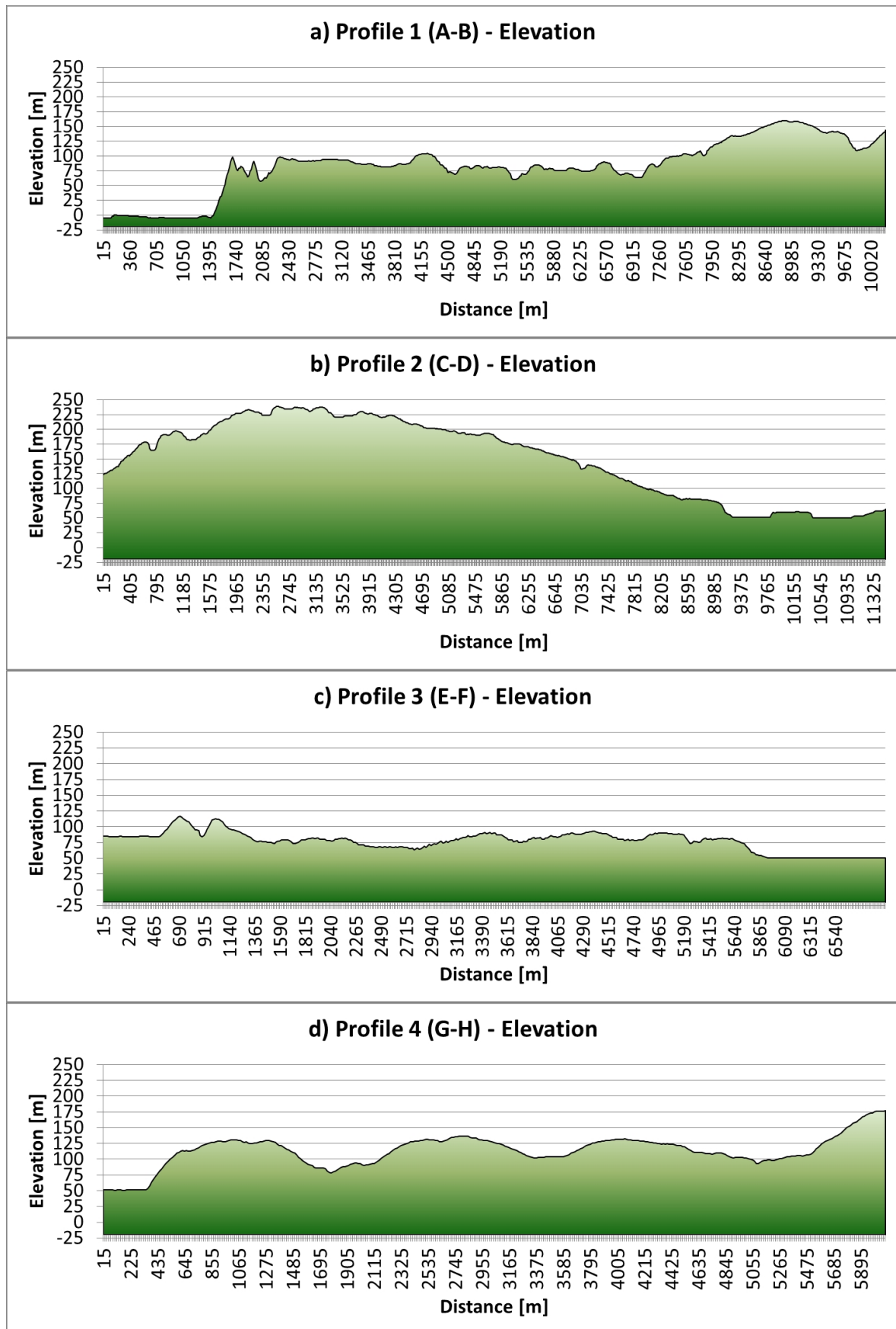


Figure 4.29: Elevation profiles of the test sites Caribou Hills: a) Profile 1 (A-B), b) Profile 2 (C-D), c) Profile 3 (E-F) and d) Profile 4 (G-H). Locations of the profiles is shown in Figure 4.28. Data Source: TDX IDEM with a spatial resolution of 13 m. Source: Own Figure.



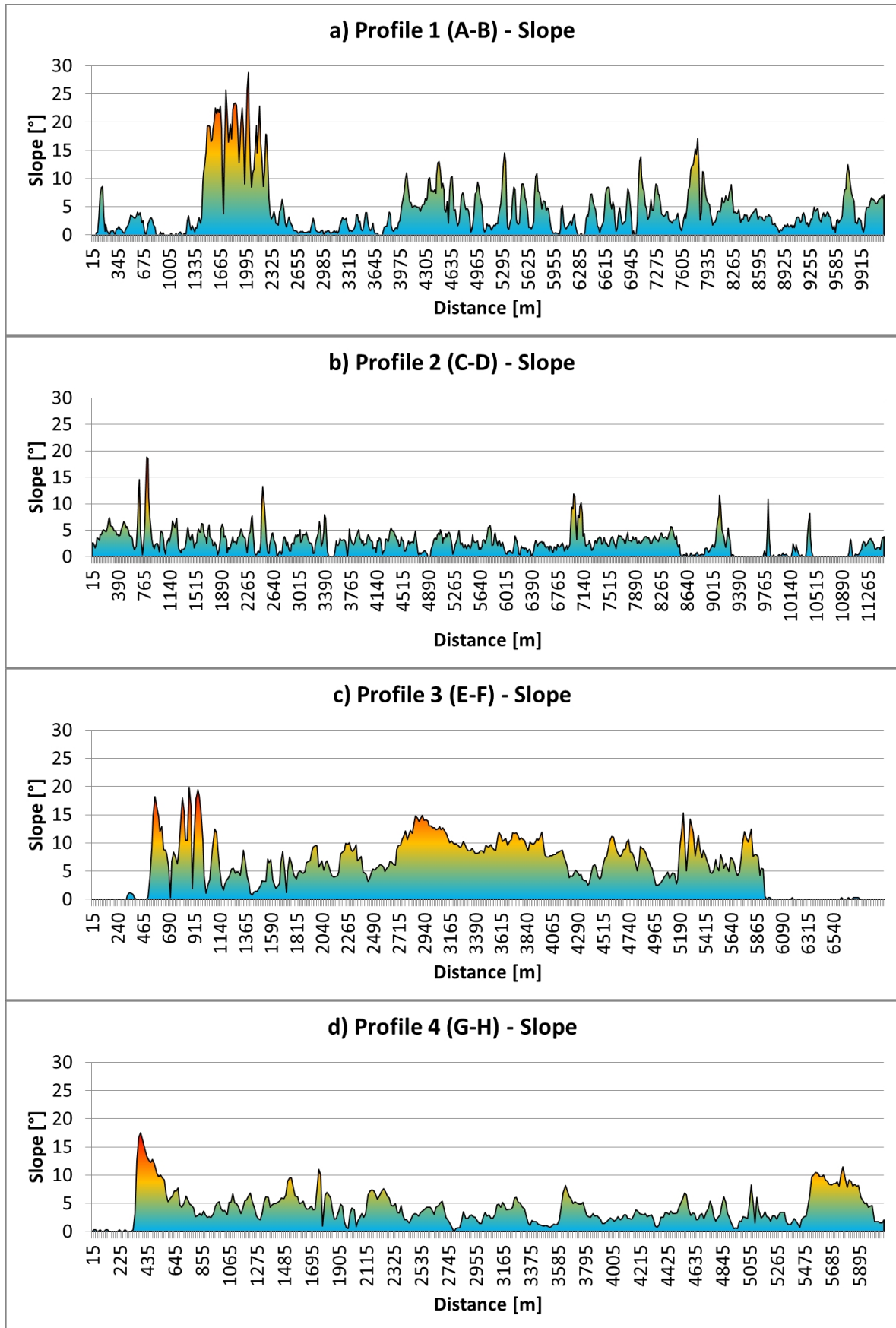


Figure 4.30: Slope profiles of the test sites Caribou Hills: a) Profile 1 (A-B), b) Profile 2 (C-D), c) Profile 3 (E-F) and d) Profile 4 (G-H). Locations of the profiles is shown in Figure 4.28. Data Source: TDX IDEM with a spatial resolution of 13 m. Source: Own Figure.

#### 4 Results

the increase in the estimation window size had only small effect on the distribution and range of the TPI values. The large-scale features highlighted especially the first order landforms of the site - which were the top and mid slopes of the Caribou Hills, the plains and lakes of the pleistocene to holocene upland and the steep proterozoic formation itself.

The systematic increase in the TPI estimation window size showed some limitations of the TPI feature for the landscape analysis. The TPIs estimated with large window sizes (1500 m, 2000 m and 3000 m) showed a systematically blurring of regions close the proterozoic formation. This blurring was caused by the fast changing elevation between the alluvial delta and the upland. This led to a systematically blurring of the foot-slopes (Figures 4.31.d-f). Beside this the TPI is a relative feature and therefore it did not provide any information on the actual elevation of the landscape. For this reason the TPI variations of the lower alluvial delta complex took place in the same range of values as the TPI variations of the uplands or Caribou Hills. An assignment of landforms will therefore essentially require information on the actual elevation to separate landforms on different elevation levels.

The Figure 4.32 shows TPI values of selected window sizes (100 m, 1000 m and 2500 m) for the Profiles 1 to 4. The effect of the blurring (systematic error) was clearly visible in Figure 4.32.a. Between the distances 0.0 km and 1.4 km the TPI values systematically decreased for scales of 1000 m and 2500 m. That was an effect of the fast changing elevation. It was visible that the TPI values of the scale 100 m were very noisy in the flat delta area and that the range of the values was the same as the one of the upland and Caribou Hills. Comparing the TPI profiles with the elevation (Figure 4.29.a) and slope profiles (Figure 4.30.a), it was observed that small scales of the TPI highlight the small-scale variations of the land surface and that the large scales of the TPI were useful to highlight medium to higher order landforms. Very similar observations were made for the Profile 2 (4.32.b) and the Profile 3 (4.32.c). It was noticeable that noisy TPI values were again observed for the flat surfaces of the lakes. The Profile 4 (4.32.d) illustrated the effect of the different scales on the TPI values. It was observed that a minimum estimation window size of 1000 m was needed to detect the major valleys and the major ridges located at about 1.0 km, 2.8 km, 4.0 km and 5.9 km. The TPIs of this scale were therefore sensitive to the width of the valleys (1.5-2.0 km). In contrast, the small estimation window sizes were suited to delineate the small-scale variations of the local drainage patterns.

The Figure 4.31 shows the interpolated TPI values of the Profiles 1 to 4 for all estimation window sizes between 100 m and 3000 m. The observations made for the three selected TPI scales were confirmed. Moreover all of the profiles showed that scales less than 250 m were very sensitive for any small-scale changes of the surface morphology and that the noise component was very high. This sensitivity was caused by the small number of elements (pixels) used for the estimation of the TPI and by the small sample size. It was observed that the TPI signal was clear for scales above 250 m. The analysis of the TPI stack was useful to estimate the effective size of a landform element. For example, it was observed that the ridges and valleys of the Caribou Hills (4.31.d) showed high - respectively low - TPI values on all scales up to a scale of 3000 m. In contrast, the same figure shows that the local variations of the ridges and valleys - e.g. located at distances of 2.0 km, 2.6 km and 3.4 km - were only detectable using scales of more than 1000 m.

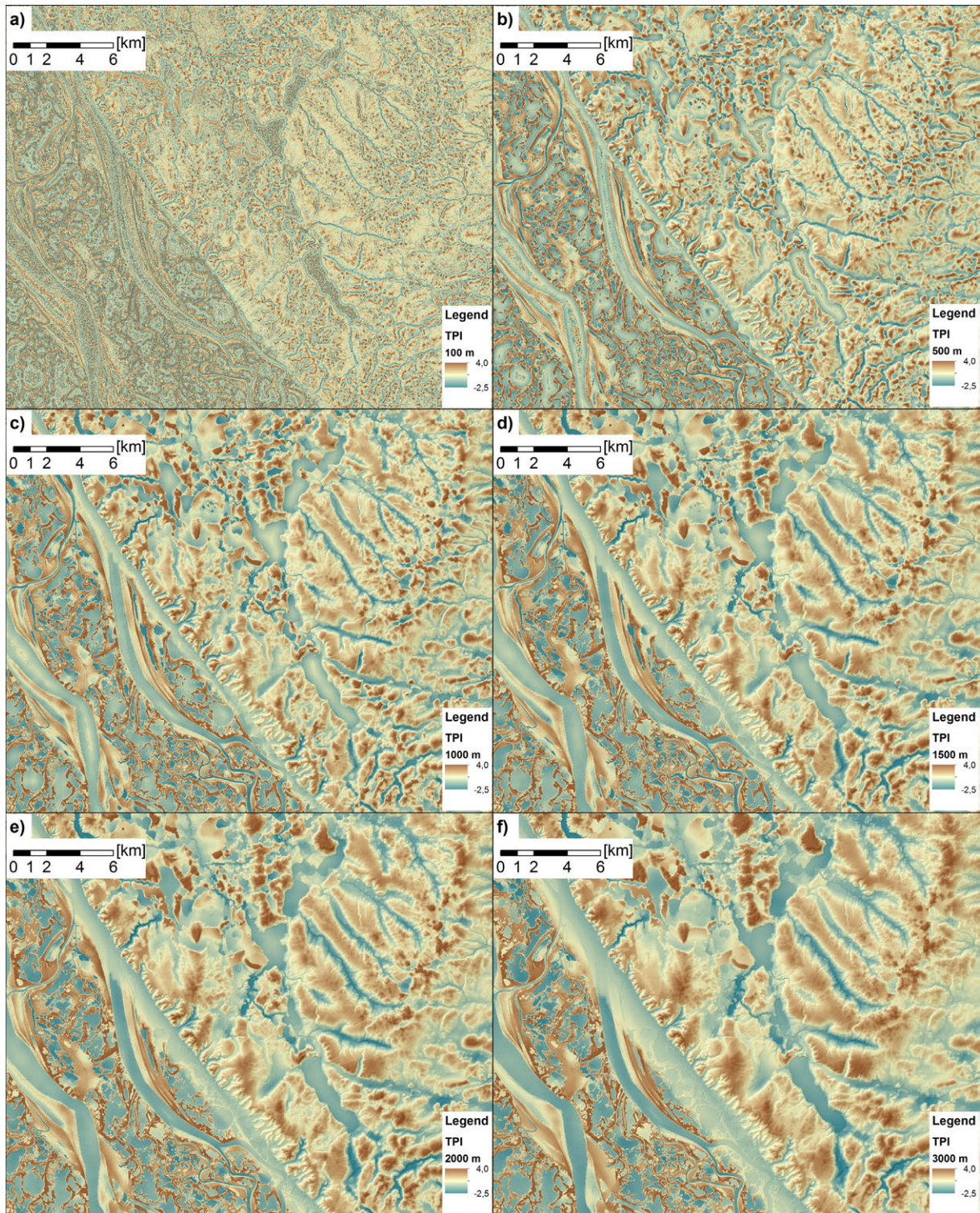


Figure 4.31: Topographic Position Indices (TPI) of the test site Caribou Hills (CAH) for TPI scales of: a) 100 m, b) 500 m, c) 1000 m, d) 1500 m, e) 2000 m and f) 3000 m. Data Source: TDX IDEM with a spatial resolution of 13 m. Source: Own Figure.

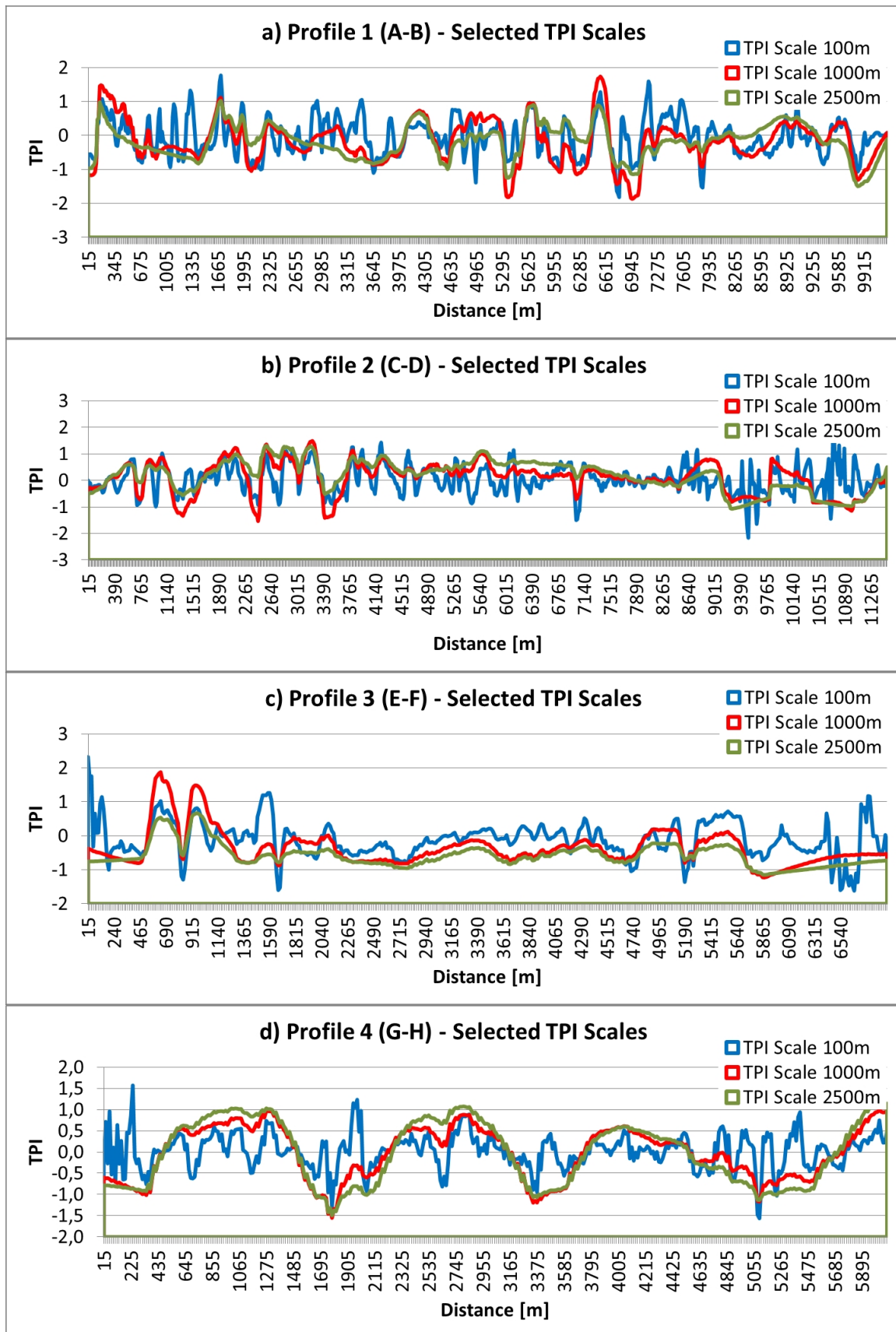


Figure 4.32: Selected TPI Profiles of the test sites Caribou Hills: a) Profile 1 (A-B), b) Profile 2 (C-D), c) Profile 3 (E-F) and d) Profile 4 (G-H) for the TPI scales of: 100 m (blue), 1000 m (red) and 2500 m (green). The Z-Axes displays the TPI values. Locations of the profiles are shown in Figure 4.28. Data Source: TDX IDEM with a spatial resolution of 13 m. Source: Own Figure.

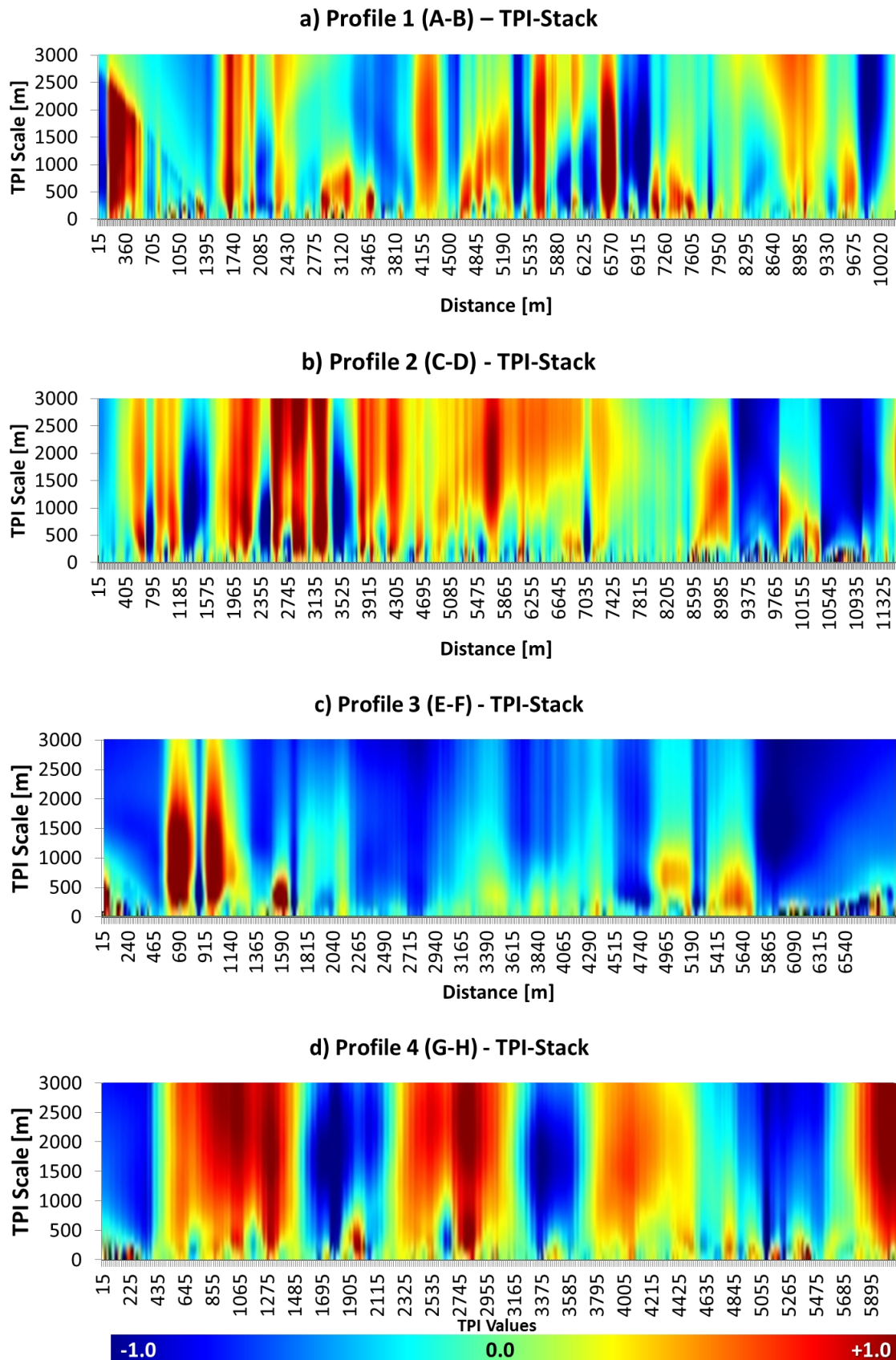


Figure 4.33: TPI stack profiles of the test sites Caribou Hills: a) Profile 1 (A-B), b) Profile 2 (C-D), c) Profile 3 (E-F) and d) Profile 4 (G-H). The colors from dark blue to dark red show the TPI values. The Z-Axis displays the scale used for the TPI estimation. Locations of the profiles are shown in Figure 4.28. Data Source: TDX IDEM with a spatial resolution of 13 m. Source: Own Figure.

### 4.2.3.2 Mackenzie Delta Region - Northern Delta

The coastal region of the Northern Mackenzie Delta and of Richards Island can be categorized in two major landform units: (1) The first one is the low lying land of the Mackenzie Delta. This unit shows lower thickness of the permafrost body (see Section 2.1.2 and Figure 2.4) and is characterized either by exposed flat to gentle sloped non-vegetated sediments (e.g. banks, beaches, mudflats of the shore zones) or by low vegetation of wetlands or consolidated grass dominated tundra. The delta complex is of pleistocene to holocene age and shows mainly fluvial deposits with small grain sizes (Figure 2.4). (2) The second unit is dominated by periglacial forms and lies on higher altitude compared to the delta. These regions are underlied by continuous permafrost with an IBPF thickness of more than 500 m (see Section 2.1.2 and Figure 2.5) and the surface morphology is dominated by periglacial forms, such as thermokarst lakes, erosion slumps (thaw slumps), wetland complexes, pingos, polygonal ice wedge networks and hummocks. The uplands are of pleistocene to holocene age, show mainly surficial glacial deposits and are situated on an level between 20 m and 70 m. Fast elevation changes and steep slopes of the uplands are related to the presence of near surface permafrost and active erosion. The hills of central part of Richard Island are consolidated ice-complexes and are often associated with lateral erosion features. The transition between the uplands and the delta is characterized by areas of accumulation in the west of the test site. This is visible in form of non-vegetated and extensive mudflats. The areas of active erosion are present along the northwestern shore, the North Head of Richards Island and at the western shores of Summer Island. The erosion is visible in form of large-scale erosion slumps and of steep eroding tundra cliffs with heights up to several meters (see Owens 2010, Hill, Blasco, Harper & Fissel 1991, Hill, Hequette, Ruz & Jenner 1991).

Figure 4.34 shows the basic topographic features of the test site Northern Delta derived from TDX IDEM with a spatial resolution of 13 m. The elevation model showed that the low-lands of the delta were present between -10 m to 20 m. The elevation of the uplands was up to 70 m (Figure 4.34.a&f). The steep slope values were bounded to the presence of the ice complexes of the uplands and to the eroding shores and cliffs (transition between low- and up-land). The flanks of the central hills, the eroding tundra cliffs, the thawing slumps and the pingos showed slope values of up to 40° and represented the dominating vertical landform features. In contrast, the low lands of the alluvial delta complex were flat with slope values less than 1°. This was also true for the lake surfaces that were clearly distinguishable by very low slope values (Figure 4.34.b). The convexity highlighted the upper slopes of the hills and the eroding tundra cliffs as concave (positive) and the foot-slopes and creeks as convex (negative) (Figure 4.34.c). The aspect of the DEM (Figure 4.34.d) showed that the hills of central Richards Island were mainly aligned in southwest-northeast direction. Therefore these forms followed the main direction of the faults. The expositions of the hill flanks were mainly in northwestern and southeastern directions. In addition, these observations were visible in the hillshade of the elevation model (Figure 4.34.e). The position of the lightning was north and surfaces exposed to the north had bright values. The figure shows the location of a profile (Profile A-B) that will be analyzed in the following.

Figure 4.35 shows the TPI values processed with scales of 100 m, 500 m, 1000 m, 1500 m, 2000 m and 3000 m. The corresponding estimation window sizes were 9x9, 41x41, 83x83, 125x125, 149x149 and 249x249 pixels and a skip factor of 0.75 was used for the estimation of the TPIs (see Section 3.1.3). It was

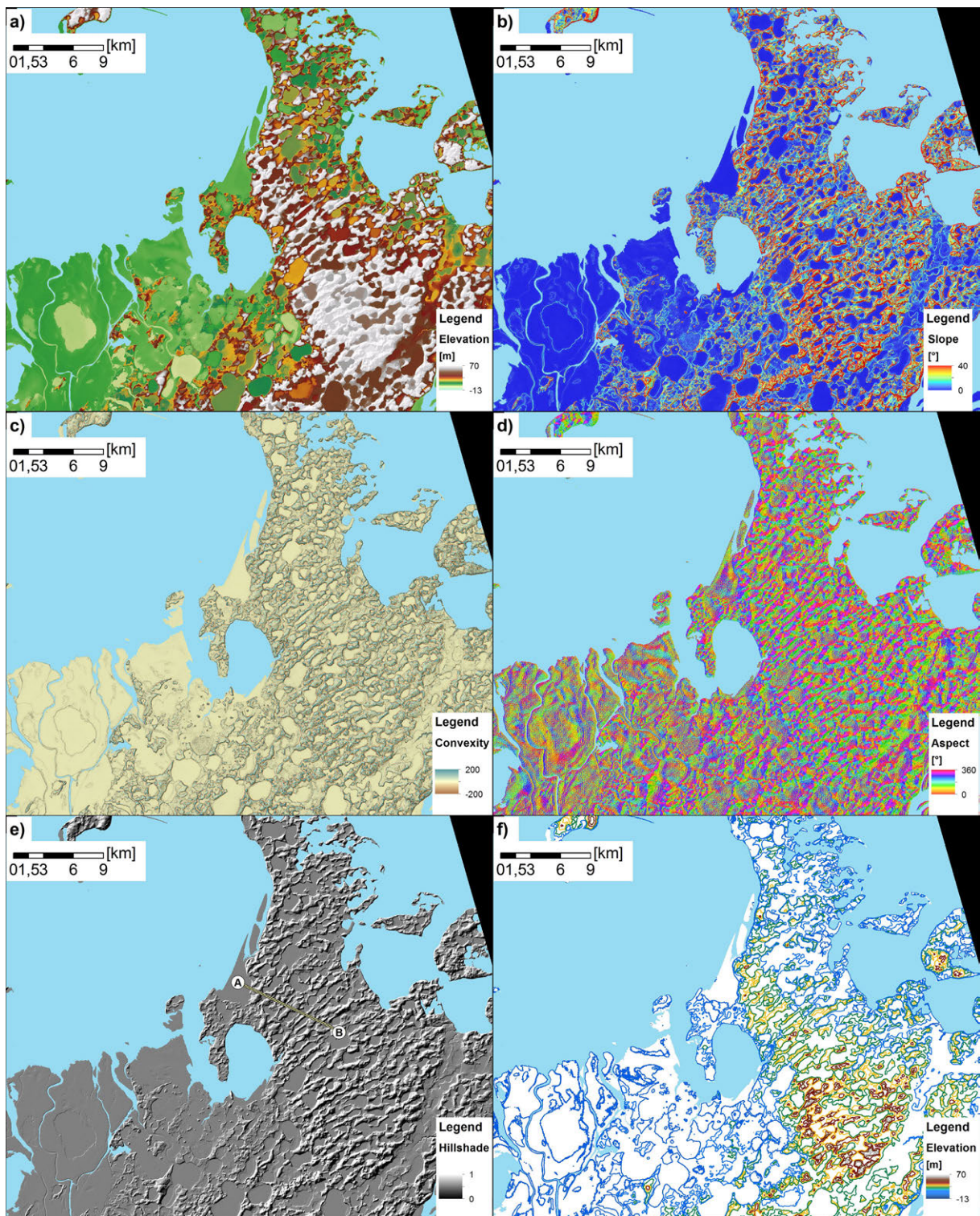


Figure 4.34: Basic topographic features of the Northern Mackenzie Delta: a) Elevation, b) Slope, c) Convexity, d) Aspect, e) Hillshade and location of profile and f) contour map. Data Source: TDX IDEM with a spatial resolution of 13 m. Source: Own Figure.

#### 4 Results



Figure 4.35: Topographic Position Indices (TPI) of the of the Northern Mackenzie Delta for TPI scales of: a) 100 m, b) 500 m, c) 1000 m, d) 1500 m, e) 2000 m and f) 3000 m. Data Source: TDX IDEM with a spatial resolution of 13 m. Source: Own Figure.



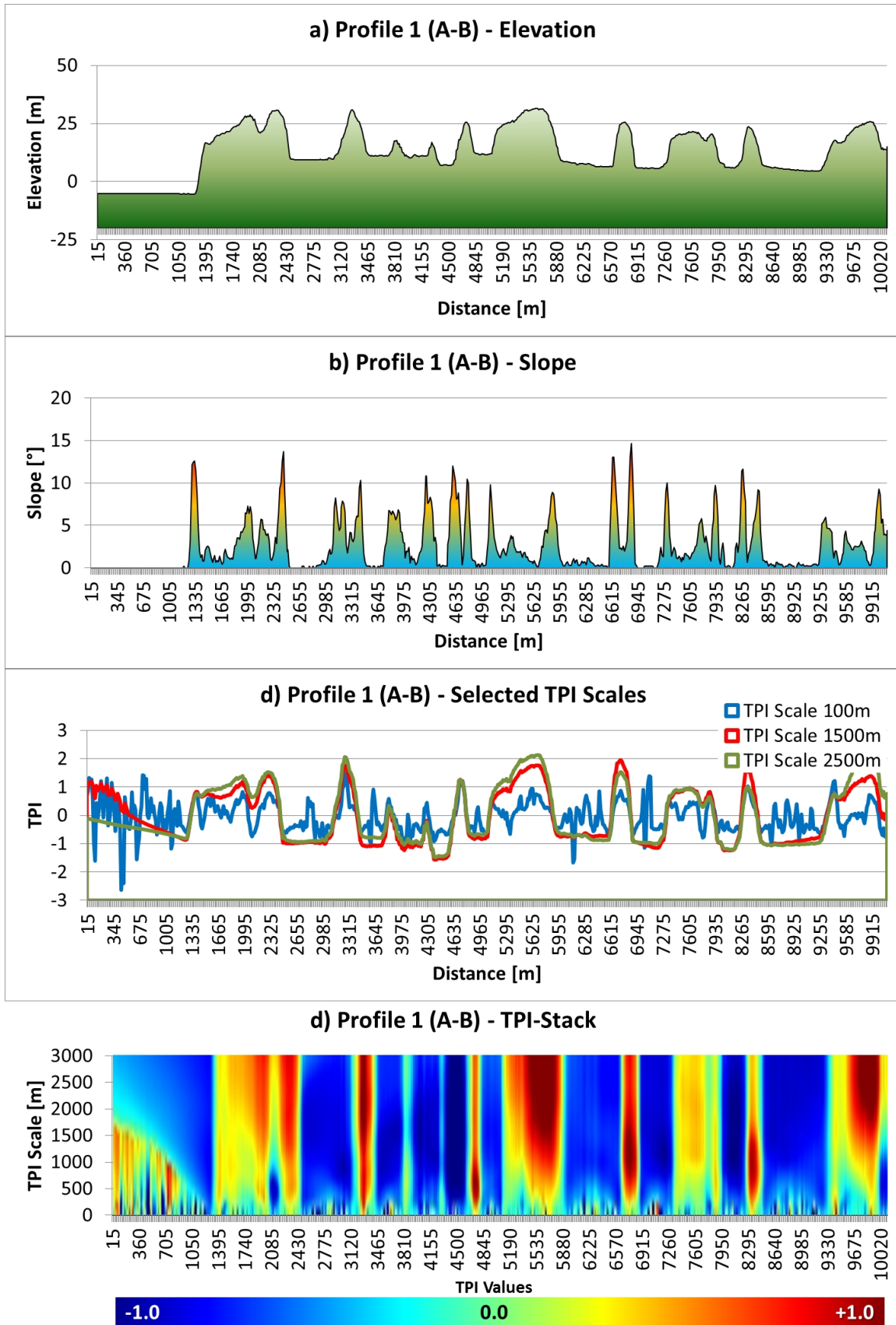


Figure 4.36: Elevation, slope and TPI stack profiles of the Northern Mackenzie Delta: a) Elevation Profile, b) Slope Profile, c) selected TPI profile and d) TPI stack profile. The colors from dark blue to dark red show the TPI values. The Z-Axes displays the scale used for the TPI estimation. Location of the profile is shown in Figure4.34. Data Source: TDX IDEM with a spatial resolution of 13 m. Source: Own Figure.

## 4 Results

observed that a TPI scale of 100 m highlighted the local tops of the hills of the central part of Richards Island (Figure 4.35.a). The variation of the TPI values was very high and a high noise contribution was present. This was also observed for the extensive flat areas of the alluvial delta complex. This supported the findings made for the test site Caribou Hills: small scales were unsuited to characterize flat areas and plains. The scales greater 500 m suppressed the noise and showed clear positions of the hill tops and ridges of the central island and the channels of the delta (Figure 4.35.b). The TPI values calculated with scales of 1000 m and 1500 m (Figure 4.35.b&c) provided a good characterization of the local tops (e.g. pingos, hills) and the lake-and-valley system of the main island. The scales of 2000 m and 3000 m were suited to overview the arrangement of the landforms. These features clearly highlighted sequences of the hills, ridges, valleys, lakes and plains of the test site.

**Elevation** - Figure 4.36.a shows the elevation values of the profile. The mudflat (0.0 km to 1.2 km) showed constant low elevation values of about -5 m. The following shore-zone was steep and elevation climbed up to 30 m until distance 2.2 km. The following part of the profile (2.2 km to 10.0 km) showed a sequence of nine major hills (related to permafrost ice complexes) and nine thermokarst erosion lakes. It was observed that the transitions between the top and the foot-slopes were very rapid and that the lake surfaces were on different levels and between 10 m to 15 m elevation. **Slope** - The slope variations of the profile followed the main variations of the elevation (Figure 4.36.b). The shores, as well as the hill flanks, were steep and showed slope values between 10° and 15°. The surfaces of the lakes and the mudflat were flat and showed slope values less than 2°. **Topographic Position Index (TPI)** - The selected TPI values of the profile are shown in Figure 4.36.c. The interpolated TPI values of the TPI stack were estimated with window sizes between 100 m and 3000 m and are shown in Figure 4.36.d. The results were similar to the findings made for the test site Caribou Hills. The TPI values were highly variable and very noisy if the scale was less than 250 m which meant that the estimation window size was less than 19x19 pixels. The signal was more clear for higher TPI scales and clearly showed the position of top, mid and foot-slopes. These can be associated with the hill tops, the flanks and the valleys and plains. In addition, the analysis of the profile showed the systematically blurring of the TPI values of flat surface areas (distance 0.0 km to 1.2 km). The appearance of this anomaly was similar to the observations made for the foot-slope of the proterozoic formation of the test site Caribou Hills (Figure 4.33.d).

### 4.2.3.3 Banks Island

The high arctic test site of Northern Banks Island has a higher relief energy than the sites of the Mackenzie Delta and is dominated by the structural forms of the geological units. Three morphological units can be divided: (1) The first one are the low-lying coastal lands that are either flat to gentle sloped or steep. The plain surfaces were formed by accumulation of fluvial sediments at the mouths of the Woom, Eams, Desert and Thomson Rivers. The steep cliffs were formed by active thermokarst erosion processes - such as erosion slumps (thaw slumps) and eroding cliffs (see Figure 2.10). The surficial material of this unit is composed of eolian, fluvial and morainal deposits. The low-lands are mainly situated on plaeocene to eocene bedrock. (2) The second unit is the non-vegetated to sparse vegetated upland which shows exposed bedrock and regoliths. The elevation is up to 500 m and the upland is the collecting basin of the Woom, Eams, Desert and Thomson Rivers. The unit is embedded in paleocene to eocene

bedrock and high elevation peaks are usually related to exposed miocene to pliocene bedrock (see Figure 2.9). The surficial material is composed of either regoliths of the bedrock material or morainal deposits of the Banks Glaciation. The valleys and creeks are usually vegetated by low grasses and sedges at local sinks and the valleys are nutrient-rich corridors. The micro-topography is influenced by small to medium-sized hummocks and tussocks - if vegetation is present. The mid-slopes and top-slopes are usually non-vegetated and show exposed bedrock. (3) The banks and river beds of the Woom, Eams, Desert and Thomson Rivers can be classified as separate unit. The braided river systems show abrasive fluvial materials and fine eolian deposits. The shores of the rivers are usually steep and cut deeply in the sediments via lateral fluvial-erosional and thermo-erosional processes.

Figure 4.37 shows the basic topographic features of Northern Banks Island derived from TDX IDEM with a spatial resolution of 13 m. The elevation model showed that the low-lands were present on a level of -10 m to 20 m elevation. The valleys of the braided rivers were wide - up to an elevation of about 100 m. With higher elevation the valleys got narrow and branched in smaller secondary-valleys. The uplands in the south of the site showed elevation values greater than 250 m (4.37.a&f). The steep slopes of the site were bounded to the northern shore, to the lateral banks of the rivers and local peaks and ridges. The slope values were high and reached values of more than 45°. In contrast, the northern low-lands - as well as the river beds - were smooth and flat with slope values less than 2° (4.37.b). The convexity was positive (concave) for the upper slopes of the hills and the steep erosional features. In contrast, convexity was negative (convex) at the foot-slopes of hills and at small creeks and valleys (4.37.c). The valleys of the site showed mainly a north-south or a northeast to southwest alignment. Therefore the valleys followed the main directions of the fault-system. The orientation of the secondary and tributary valleys was diverse and showed no systematical orientation (4.37.d). The orientation of these valleys was in relation to the local drainage. The same facts were visible in the hillshade of the test sites (4.37.e). The hillshade highlighted the steep flanks of the pre-quadernary hills and the flat quadernary sediments of the braided river systems. 4.37.e shows the location of the profile that will be analyzed in the following. The profile started at the upper hill top of a western pre-quadernary hill, crossed the two braided river beds of the Woon River and finally cut the northern shore between the mouth of Woon and Eames River (compare Figure 2.8).

Figure 4.38 shows TPI values processed with scales of 100 m, 500 m, 1000 m, 1500 m, 2000 m and 3000 m. The corresponding estimation window sizes were 9x9, 41x41, 83x83, 125x125, 149x149 and 249x249 pixels and a skip factor of 0.75 was used for the estimation of the TPI values (see Section 3.1.3). In contrast to the findings of the test sites Caribou Hills and Northern Mackenzie Delta, the small scale of 100 m was suited to detect the small creeks and valleys of Northern Banks Island. The TPI calculated with a scale of 100 m was suited to mark the local hill tops and ridges (Figure 4.38.a). The scales 500 m and more highlighted the valleys and the ridges of the pre-quadernary hills (Figure 4.38.b). The distribution of the TPI values of scales of 1000 m and 1500 m showed a trade-off between local and regional landscape features. The major and secondary valleys showed negative TPI values and the ridges and exposed hill tops showed positive TPI values. The mid slopes were identified in both features with values around zero (Figure 4.38.c&d). TPI scales of 2000 m and 3000 m showed the major valleys and hill of the test site (Figure 4.38.e&f) and a blurring of the values at the shore. The effect of this blurring was comparable to the systematic effects observed for the test sites of the Northern Mackenzie Delta and the Caribou Hills. The effect was caused here by the rapid elevation change between coast and flat near-shore water.

## 4 Results

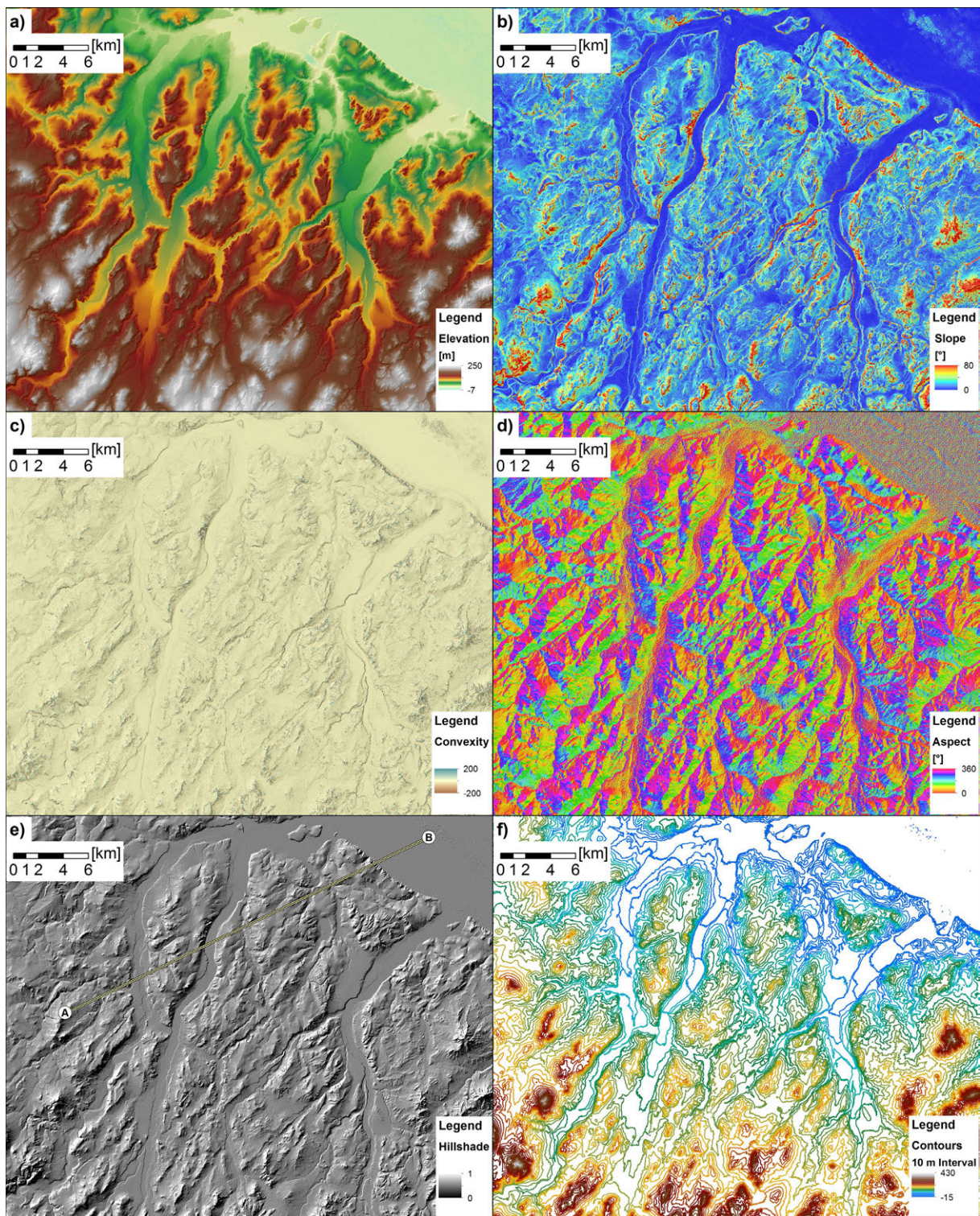


Figure 4.37: Basic topographic features of Northern Banks Island: a) Elevation, b) Slope, c) Convexity, d) Aspect, e) Hillshade and location of Profile and f) contour map. Data Source: TDX IDEM with a spatial resolution of 13 m. Source: Own Figure.

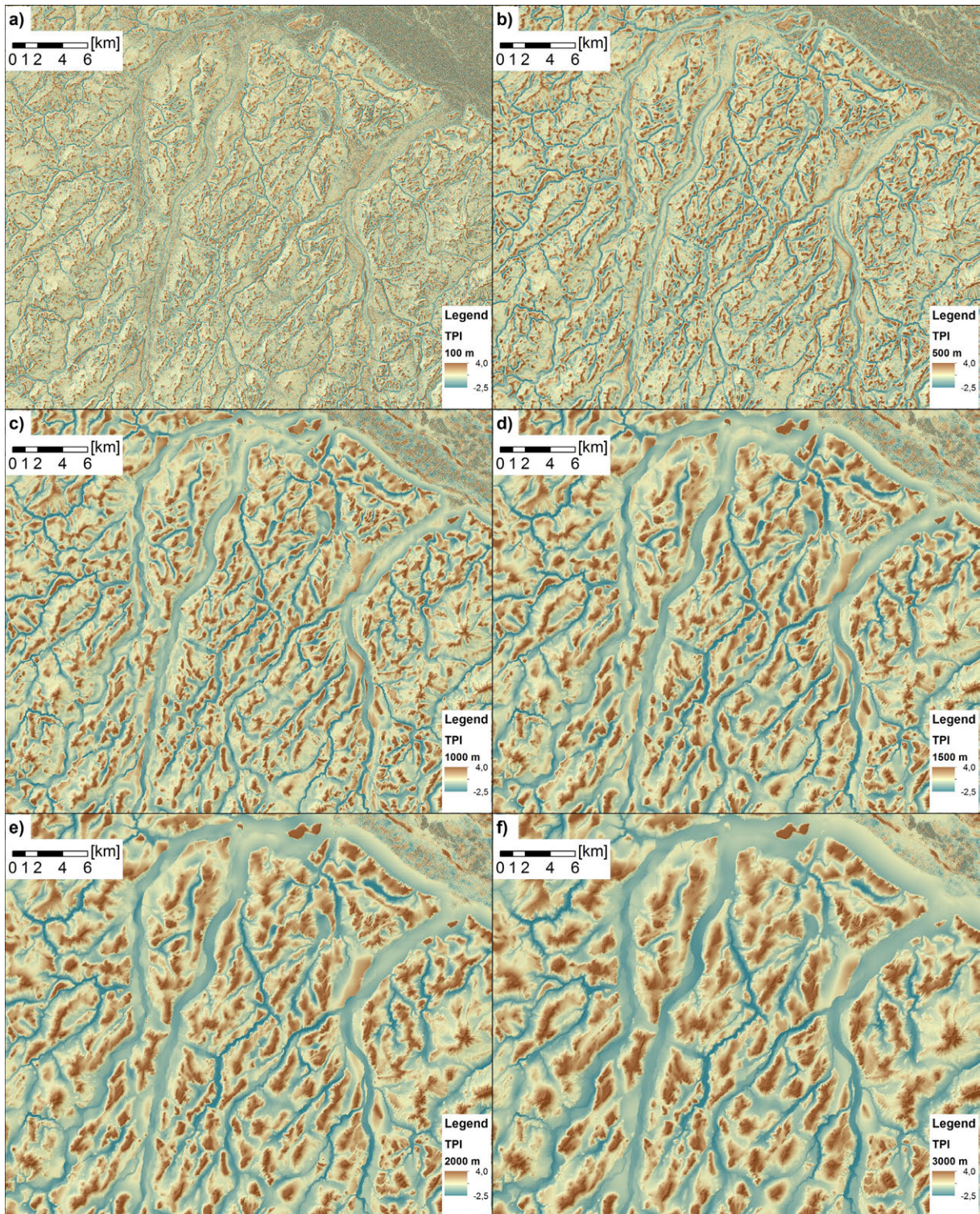


Figure 4.38: Topographic Position Indices (TPI) of the of Northern Banks Island for TPI scales of: a) 100 m, b) 500 m, c) 1000 m, d) 1500 m, e) 2000 m and f) 3000 m. Data Source: TDX IDEM with a spatial resolution of 13 m. Source: Own Figure.

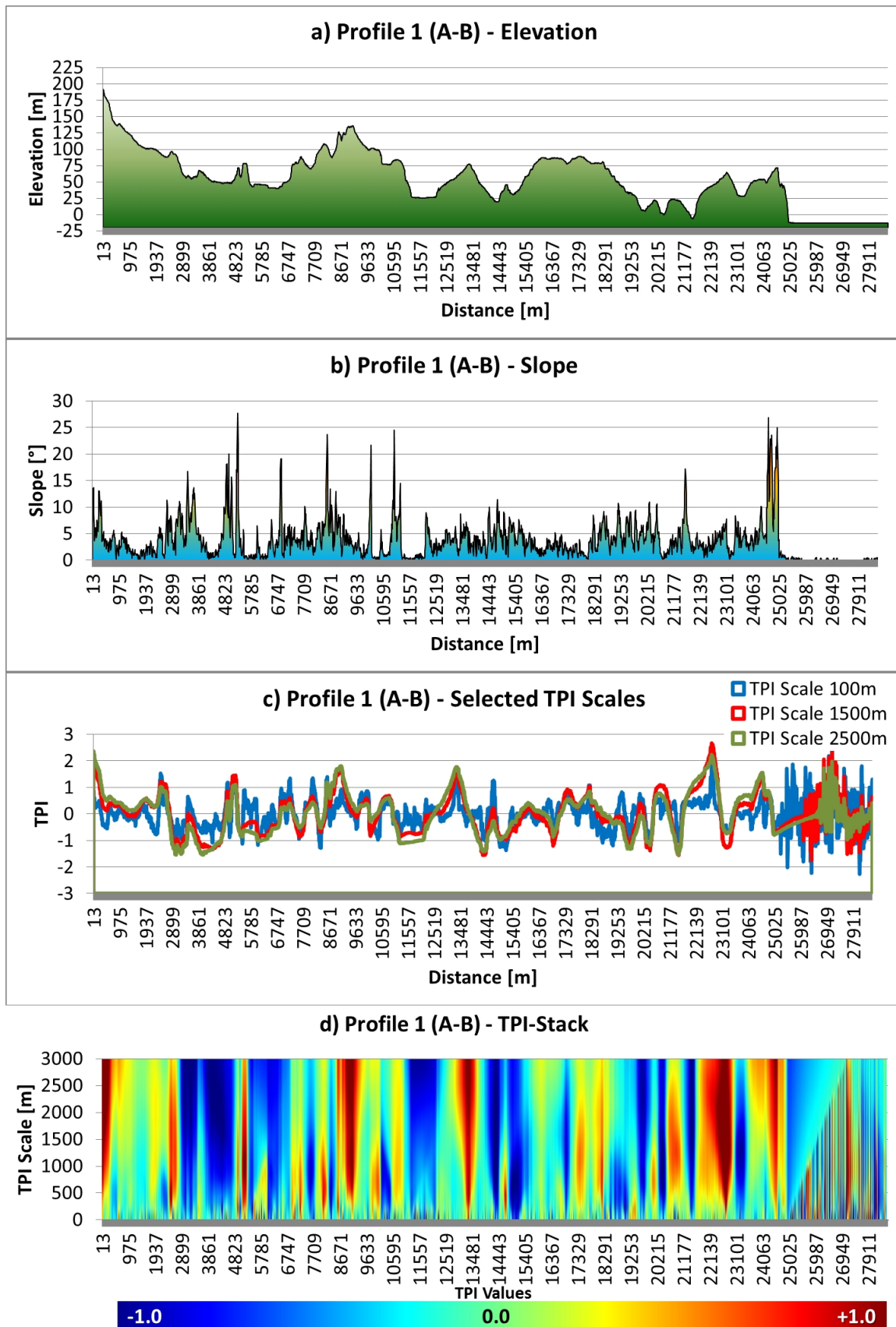


Figure 4.39: Elevation, slope and TPI stack profiles of Northern Banks Island: a) Elevation profile, b) Slope profile, c) Selected TPI profile and d) TPI Sstack profile. The colors from dark blue to dark red show the TPI values. The Z-Axes displays the scale used for the TPI estimation. Location of the profile is shown in Figure 4.37. Data Source: TDX IDEM with a spatial resolution of 13 m. Source: Own Figure.

**Elevation** - Figure 4.39.a shows the elevation values of the profile. The first part between distances 0.0 km and 4.9 km showed the top of a western pre-Quaternary hill and the hill flank which was interrupted by the flanks of a secondary valley. The following part of the profile showed the valley and riverbed of the western Woon River (4.9 km to 6.5 km). The elevation climbed up to 130 m at the Paleocene to Eocene formations (6.5 km to 11.0 km). The local depressions and tops were the results of the local drainage system. The profile showed the flat valley and riverbed of the eastern Woon River between distances 11.0 km and 12.0 km. The riverbed was bounded to the east by the pre-Quaternary hills. The following part of the profile between distances 12.0 km and 22.0 km showed a sequence of small secondary valleys and hills. The near-shore morainal deposits were located on a level of up to 75 m and bounded to the north by the steep cliffs of the northern shore between Woon and Eames River (22.0 km to 25.0 km). The profile showed the flat water surface between distances 25.0 km and 28.0 km. **Slope** - The slope variations of profile are shown in Figure 4.39.b. The high slope values of around  $25^\circ$  were observed for the lateral banks of the Woon and Eames River and the cliffs of the northern shore. The minimum slope values of less than  $2^\circ$  were observed for the flat riverbeds of Woon River and Eames River and for the plateau-like top-slope of the northern hills. The variations of the slope were high and indicated therefore a high topographic variation and roughness. **Topographic Position Index (TPI)** - The selected TPI values of the profile (Figure 4.39.c) and the interpolated TPI values estimated with window sizes between 100 m and 3000 m are shown in Figure 4.39.d. The scales larger than 1500 m showed very similar TPI values and were highly correlated. Further, this was visible in Figure 4.38. The scales less than 250 m were again highly variable and noisy. The scales between 500 m and 1000 m showed local peaks and valleys that were dissolved on larger scales. The systematic blurring of the TPI values was again present at the northern shore. The effect was comparable to the observations made for the test sites of the Mackenzie Delta Region.

### 4.2.3.4 James Bay

The topographic variations of the sub-polar test site James Bay are mainly caused by the geological setting. The low-lands appear near the shore and at the mouths of the Sabasunica, Clergue and Torviens River. The intertidal is non-vegetated and extensive flat areas of the back-shore are covered by wetland vegetation. The hinterland is characterized by hilly landscape and the elevation is up to 120 m. The hills close to the village Wemindj reach up to 50 m. The top-slopes and hill tops are usually not vegetated and the bedrock of the Canadian Shield is exposed. The mid and foot-slopes, as well as the creeks and valleys, are vegetated and often covered by spruce and shrub. The near-surface permafrost of the area occurs isolated or sporadic. The major lakes occur at the area around Wemindj (e.g. Lake Namapi and Lake Sapwayaskunikap).

Figure 4.40 shows the basic topographic features of the test site James Bay derived from ASTER GDEM with a spatial resolution of 31 m. The elevation showed that low-lying coastal plains less than 10 m altitude were present at the mouths of Namapistikw, Sabasunica, Clergue and Torviens River (4.40.a&f). The steep areas with slope values greater  $30^\circ$  were observed at the isolated hills and at the shores of the peninsula north of Wemindj. The slope values were up to  $40^\circ$  and therefore very steep. This high range of values was likely caused by the noise of the ASTER GDEM. The slope values were less than  $5^\circ$  at the

#### 4 Results

mouths of Namapistikw, Sabascunica, Clergue and Torviens River (4.40.c). The high convexity values were observed at the steep sloped areas and the noise contribution was high. The convexity therefore had a grainy texture. However, convexity values around zero and with less grainy texture were observed for the low-lands of the river estuaries. (4.40.c). The aspect showed random exposition of pixels located at flat and gentle sloped areas (Figure 4.40.d). Figure 4.40.e shows the hillshade of the test site and the location of a profile line. The profile started at the bay close to the mouth of Namapistikw (A), crossed the hilly mid slopes of the hinterland, the Lake Sapwayaskunikap and ended in the upland approximately 12 km northeast of Wemindj (B).

Figure 4.41 shows TPI values processed with scales of 100 m, 500 m, 1000 m, 1500 m, 2000 m and 3000 m. The corresponding estimation window sizes were 3x3, 15x15, 31x31, 49x49, 63x63 and 97x97 pixels and a skip factor of 0.75 was used to estimate the TPI values (see Section 3.1.3). The size of the estimation window per scale of the GDEM was therefore about the seventh part of the size of the estimation window used for the TDX IDEM. The lower spatial resolution of the GDEM led to a lower sample size. Therefore it was observed that scales of 100 m and 500 m (Figure 4.41.a-b) had a grainy texture and a high noise contribution. Still, the scales highlighted the local peaks and depressions - but did not provide a clear regional overview of the landforms and the interpretation of the TPI values was limited. In contrast, the scales of 1000 m, 1500 m and 2000 m provided a regional overview and showed the top, mid and foot-slope positions - as well as the peaks, ridges and valleys (Figure 4.41.c-e). However, a high noise contribution was observed. The scale of 3000 m highlighted the higher order landform elements, such as the low-lying estuaries of Namapistikw, Sabascunica, Clergue and Torviens River and the hills close to Wemindj (Figure 4.41.f). The flat lake surfaces were less clear visible in the GDEM compared to the TDX IDEM data. This indicated again that the noise contribution was high in the GDEM data.

**Elevation** - Figure 4.39.a shows the elevation values of the profile. The first part showed the gentle increase in the low-lands close to the mouth of Namapistikw River. The elevation was less than 20 m (0.0 km to 5.0 km). This section was followed by a sequence of four major peaks and secondary valleys (5.0 km to 8.6 km). The elevation climbed from about 10 m up to a 75 m high peak of the upland (8.6 km to 15.3 km). Between distances 15.0 km and 18.0 km the elevation declined to a level of about 40 m. **Slope** - The slope variations of profile are shown in Figure 4.39.b. The slope values close to 10° were observed for the hill-and-valley sequence in the south of Wemindj village. The slope values of about 5° were observed for the flanks of the peaks and valleys, e.g. at distances 7.1 km, 8.5 km or 15.7 km. The values of the slope were low and less than 3° for the majority of the profile but high variations were visible and were likely a result of the noisy texture. **Topographic Position Index (TPI)** - The selected TPI values of the profile (Figure 4.39.c) and the interpolated TPI values were estimated with scales between 100 m and 3000 m and are shown in Figure 4.39.d. It was observed that the noise was high for scales less than 500 m. This meant that a minimum estimation window size of 15x15 pixels and a sample size of about 200 elements was necessary to detect a TPI signal of relevance. A clear signal of the landforms was observed for TPI scales greater than 1000 m. This was in correspondence to the visual analysis of the TPIs (Figure 4.41). The differences between the scales greater than 1000 m were small and the profile lines of the TPI scales 1000 m and 2500 m showed very similar shape and high correlation.



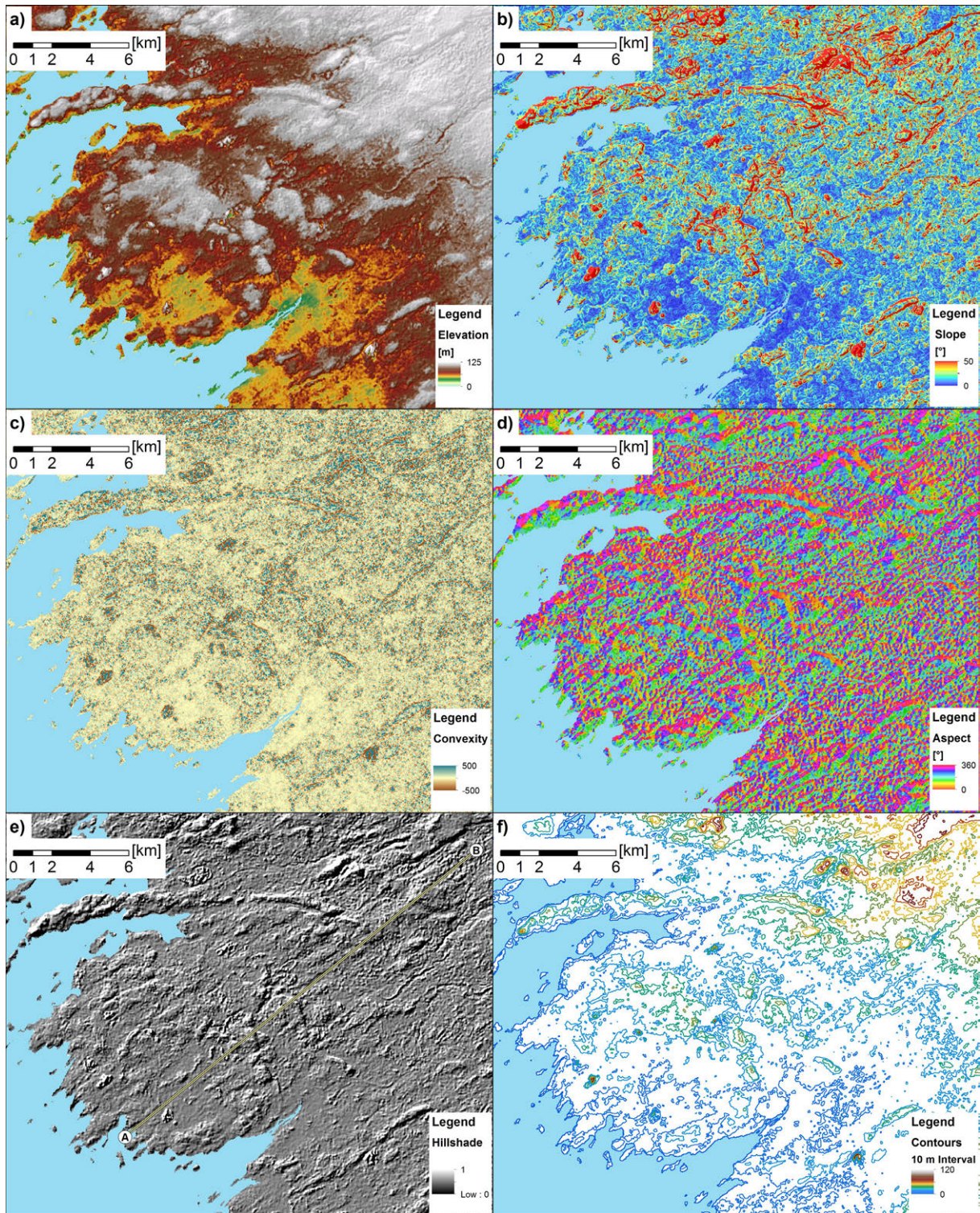


Figure 4.40: Basic topographic Features of James Bay: a) Elevation, b) Slope, c) Convexity, d) Aspect, e) Hillshade and location of Profile and f) contour map. Data Source: ASTER GDEM with spatial resolution of 31 m. Source: Own Figure.

4 Results



Figure 4.41: Topographic Position Indices (TPI) of the of James Bay for TPI scales of: a) 100 m, b) 500 m, c) 1000 m, d) 1500 m, e) 2000 m and f) 3000 m. Data Source: ASTER GDEM with spatial resolution of 31 m. Source: Own Figure.

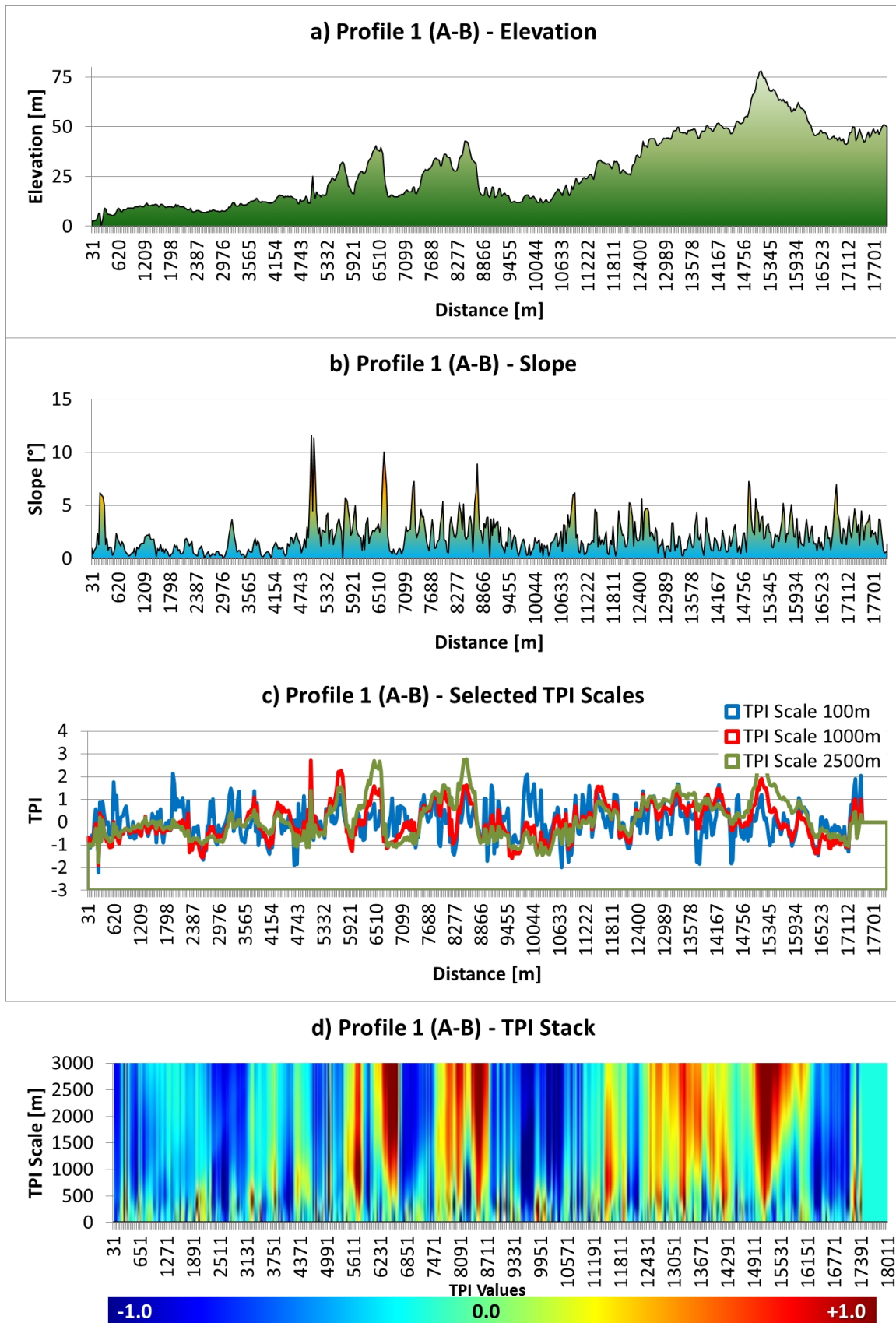


Figure 4.42: Elevation, Slope and TPI stack profiles of James Bay: a) Elevation profile, b) Slope profile, c) Selected TPI profile and d) TPI stack profile. The colors from dark blue to dark red show the TPI values. The Z-Axis displays the scale used for the TPI estimation. Location of the profile is shown in Figure 4.40. Data Source: ASTER GDEM with spatial resolution of 31 m. Source: Own Figure.

#### 4 Results

In this section basic topographic features and the relative Topographic Position Indices (TPI) estimated for different scales were analyzed. The investigations were done for four test sites using TanDEM-X intermediate digital elevation models with a spatial resolution of 13 m and ASTER GDEM data with a spatial resolution of 31 m. It was shown that the elevation, the slope and the aspect offer important information on the arrangement of the landscape elements and surface morphology and that the actual values of these features were suited for the morphometric quantification of the landforms. It was shown that TPIs calculated with small estimation windows were suited for the characterization of local forms. The TPIs derived on medium scale were identified to be useful to characterize the regional arrangement of landforms - such as the elements of the drainage system or the slope position. The large scales were suited to characterize first-order and higher-ranking landforms - such as primary valleys ridges, peaks and hills. It was found that the small scales were better suited for relief with high variation and less suited for relief with low topographic variation. The TPIs estimated on medium and large scales showed robust values and high applicability for all test sites - independent from the topographic variation and roughness. However, the extensive flat surfaces showed a noisy texture on all investigated scales. The TPI feature was therefore less suited for the characterization of these flat forms. It was observed that a systematical blurring of the TPI values was present if rapid elevation changes took place on short distance. The effect was caused as long as the signal of a high elevation location was part of the sample used for the TPI estimation. The TPI was shown to be meaningful for the identification and characterization of the landforms but not with respect to the actual elevation or slope. The comparison of the GDEM and the TanDEM-X intermediate digital elevation model showed that the GDEM data had a higher noise contribution. Further, the higher spatial resolution of the TanDEM-X intermediate digital elevation model was essentially important to derive robust and reliable TPI values on small scales - due to the high sample size that is offered by the high spatial resolution.

## 4.3 Land Surface Classification

The following chapter summarizes the results of the classification of the land cover and surface morphology. The first section shows results of the semi-automated iterative water classification. The accuracies of these classifications were evaluated and examples are shown to highlight the benefits and limitations of the technique. The second section shows the land cover classifications of PolSAR and multispectral data. The absolute and relative accuracies of the supervised and unsupervised classification and image examples of the classifications maps are shown. The last section summarizes first findings of the landform classification based on the TDX IDEM and ASTER GDEM data.

### 4.3.1 Water Bodies

The iterative water classifier described in Section 3.2.2.2 was applied to the data of the test sites of the Mackenzie Delta region (RIS, TUK, DIS, ECH, CAH, YCP), Banks Island (BIS) and James Bay (JAB). The classifications were processed with co-polarized TSX data and the double bounce feature of the Two Component Decomposition was used for the classification. In addition, the water classification was performed with quad-polarized Rardarsat-2 data for the test sites RIS, TUK, ECH and DIS. The classifications of quad-polarized data was based on the double bounce feature of the Three Component Yamaguchi Decomposition. All of the PolSAR data were processed as described in Section 3.1.1.3. The data were filtered with the Non-Local Means filter specified in Section 3.1.1.2 and with respect to the findings shown in Section 4.1.1. The threshold needed for the masking of land and water was set manually by analyzing the water probability maps defined Section 3.2.2.2 (not shown). The accuracies of the classification results were then assessed using the vector data of NWT-Geomatics (2014).

Figure 4.43 shows results of the accuracy assessment. The water classification had an average overall classification accuracy of about 96% for co-polarized TSX data and about 96% for quad-polarized R-2 data. The best classification of TSX and R-2 was found for the test site DIS with accuracies of up to 98.6%. The lowest classification accuracy of TSX data was observed for the test site CAH with about 90%. The lowest classification accuracy of R-2 data was observed for the test site RIS with about 94.5%. The misclassifications of water bodies were related to an overestimation of the water bodies. This overestimation was observed for areas of low double bounce - such as beaches and mudflats - that were labeled as class “land” in the reference and classified as class “water” . Further, the over- and underestimation was caused by shadowing effects of steep shores and slopes. The shadows of these landforms were classified as water and led to lower classification accuracies. The final water masks of the test site RIS, TUK and JAB are shown in Figure 4.48, Figure 4.49 and Figure 4.67.

Figure 4.44 shows processing examples of the iterative water classifier for the northern shore of the Mackenzie Delta (RIS, DIS). The first row of the figure shows the total received intensities (span) of the co-polarized TSX data. The second row shows the sigma nought intensities of the double bounce of the Two Component Decompositions. The third row shows the water probability maps. The red colors show high, yellow colors medium and blue colors low probability. The fourth row shows the final water masks that were delineated from the water probability maps. The threshold was set manually and was 60% for all of the shown images. The last row shows the vector data of NWT-Geomatics (2014) that were used as

#### 4 Results

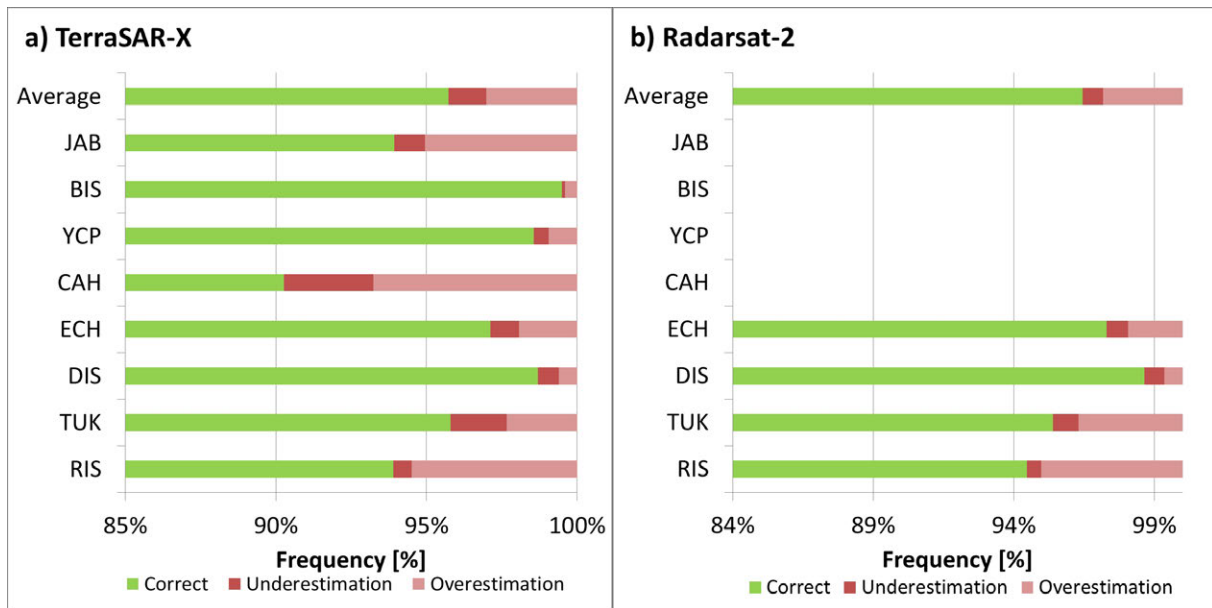


Figure 4.43: Classification accuracies of water classification for: a) TSX and b) R-2. Source: Own Figure.

reference. The results showed that the double bounce feature was well suited for the characterization of the water bodies. This was also true if the water surface was rough. This can be seen best by comparing Figure 4.44.f and Figure 4.44.k. The water surface of the Figure 4.44.k was calm and appeared dark in the span image (low intensity). The water surface of Figure 4.44.k was very rough and appeared with bright colors (high intensity). The rough water surface was caused by stormy winds during the image acquisition. The double bounce features showed very low intensity values of the water bodies in both images. The scattering of rough water surfaces did not cause a double bounce signal and the energy of double bounce scattering was therefore low. The probability maps clearly indicated water bodies in red color and with high probability and the land in blue colors and with low probabilities. The areas of low double bounce - such as beaches and mudflats - showed yellow color and medium probability. The visual comparison of the final water masks and the reference data indicated that water bodies were identified on a high level of confidence. The location and shape of the ocean and inland lakes were corresponding - as well as the shape of the main channels. The differences were related to the areas of medium probability. The intertidal mudflats in the middle of Figure 4.44.o and Figure 4.44.m were not classified as water bodies in the reference data since they did not appear permanently.

The Figure 4.45 shows the final water mask of the Mackenzie Delta. The classification was based on all available co-polarized TSX data (see Table 2.5). The classification was processed with the double bounce of the Two Component Decomposition and the data were filtered with the Non-Local Means filter in advance (see Section 3.1.1.2). The water classification threshold was set to 60% and was the same for every image. The mosaicing of the data was done in ENVI 5.1. The non-permanent water bodies, such as mudflats, were included manually in the classification using the reference data of NWT-Geomatics (2014). In addition, the TDX IDEM was used to distinguish between inland water bodies (light blue) without connection to the ocean of the Beaufort Sea (dark blue) and the main channels of the Mackenzie Delta

(dark blue). The binary classification was converted to vector format and the coastline (shoreline) was delineated. This line is shown in red color in the figure.

The iterative water classifier was applied to the test sites of the Mackenzie Delta, Banks Island and the James Bay. The classifications were processed using the double bounce feature of the Two Component Decomposition of co-polarized TerraSAR-X data and the double bounce feature of the Three Component Yamaguchi Decomposition of quad-polarized Rardarsat-2 data. The results showed that the double bounce feature was well suited for the detection of the water bodies since the water surface did not cause a double bounce signal. The water classification had an average overall classification accuracy of about 96% for both co-polarized TerraSAR-X data and quad-polarized Rardarsat-2 data and the classifier was capable to perform homogeneous classifications of large areas. The missed detections were related to shadowed areas and to non-permanent water bodies of the intertidal. The combination of these water masks and DEM data was suited to differentiate between inland water and the ocean - based on the elevation of the vectorized water polygons. In addition, the shape information was used to delineate the shorelines of lakes, river or ocean - as was shown for the entire Mackenzie Delta. The thresholds needed for the masking of the water was set manually but the used thresholds were the same for all of the classifications and therefore showed a high transferability.

#### 4.3.2 Land Cover

The classification of the land cover was performed for the test sites of the Mackenzie Delta, Banks Island in supervised and unsupervised way. In addition first preliminary unsupervised classifications of the and James Bay were performed. The overall process of the land cover classification is illustrated in Figure 3.15 and described in Section 3.2.2.1. All of the data were processed as described in Section 3.1.1.3. The PolSAR data were filtered with the Non-Local Means filter specified in Section 3.1.1.2 and with respect to the findings of Section 4.1.1. Prior to the land cover classification the water bodies of the test sites were classified as shown in the previous Section 4.3.1. The data of L-8 were manually registered to the PolSAR data and showed in average a location error of less than 20 m and therefore of less than one pixel. The data were sampled to a spatial resolution of 30 m using the pixel aggregate function of ENVI 5.1.

The unsupervised classification was done using the unsupervised FKM-ML classifier described in Section 3.2.2.1. The FKM-ML was applied with the following settings for all classifications: The unsupervised Jenks-Natural-Breaks classification was initialized with six pre-classes and these were derived from the Alpha values of T-Matrix of the PolSAR data. The pre-classes were derived from the greenness of the tasseled cap transformation (Section 3.1.2) whenever L-8 data were used in the classification process. The total number of output-classes was fixed to twenty classes and FKM classification was performed afterward. The data used in FKM were the sigma nought calibrated and Range-Doppler geocoded Kenough Matrices of the PolSAR data and/or the TOC reflectances of the multispectral data. The statistics of these twenty classes were calculated and the iterative MLC was initialized. The convergence criterion was fixed to five percent and convergence of the classifier was observed for all performed classifications. A standardization of the data was performed with respect to the mean and the standard deviation whenever PolSAR and optical data were combined. The unsupervised classes

#### 4 Results

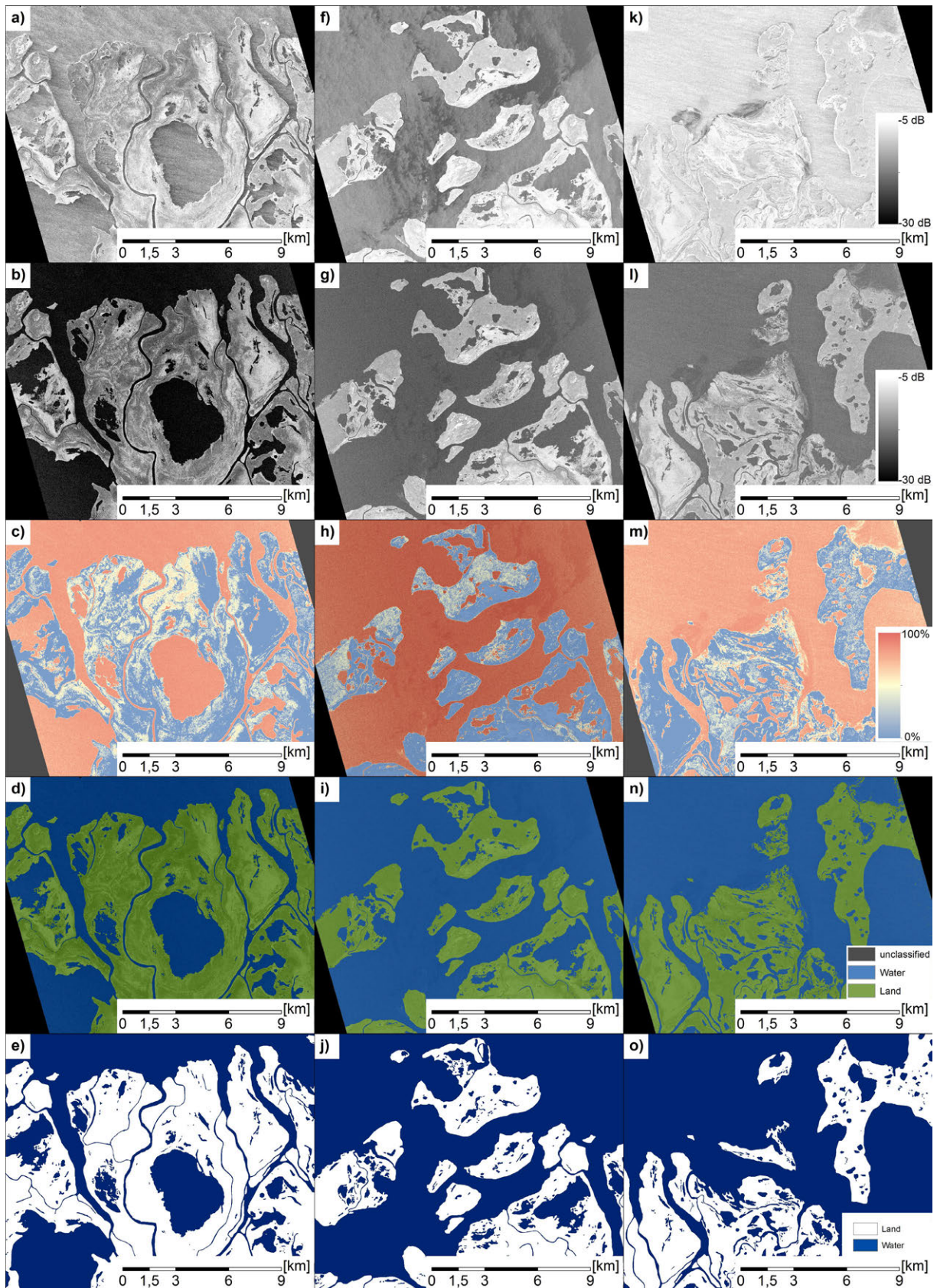


Figure 4.44: Processing examples of iterative water classification: a), f), k) span, b), g), l) double bounce, c), h), m) water probability map, d), i), n) final water mask, e), j), o) reference data of NWT-Geomatics (2014). Source: Own Figure.



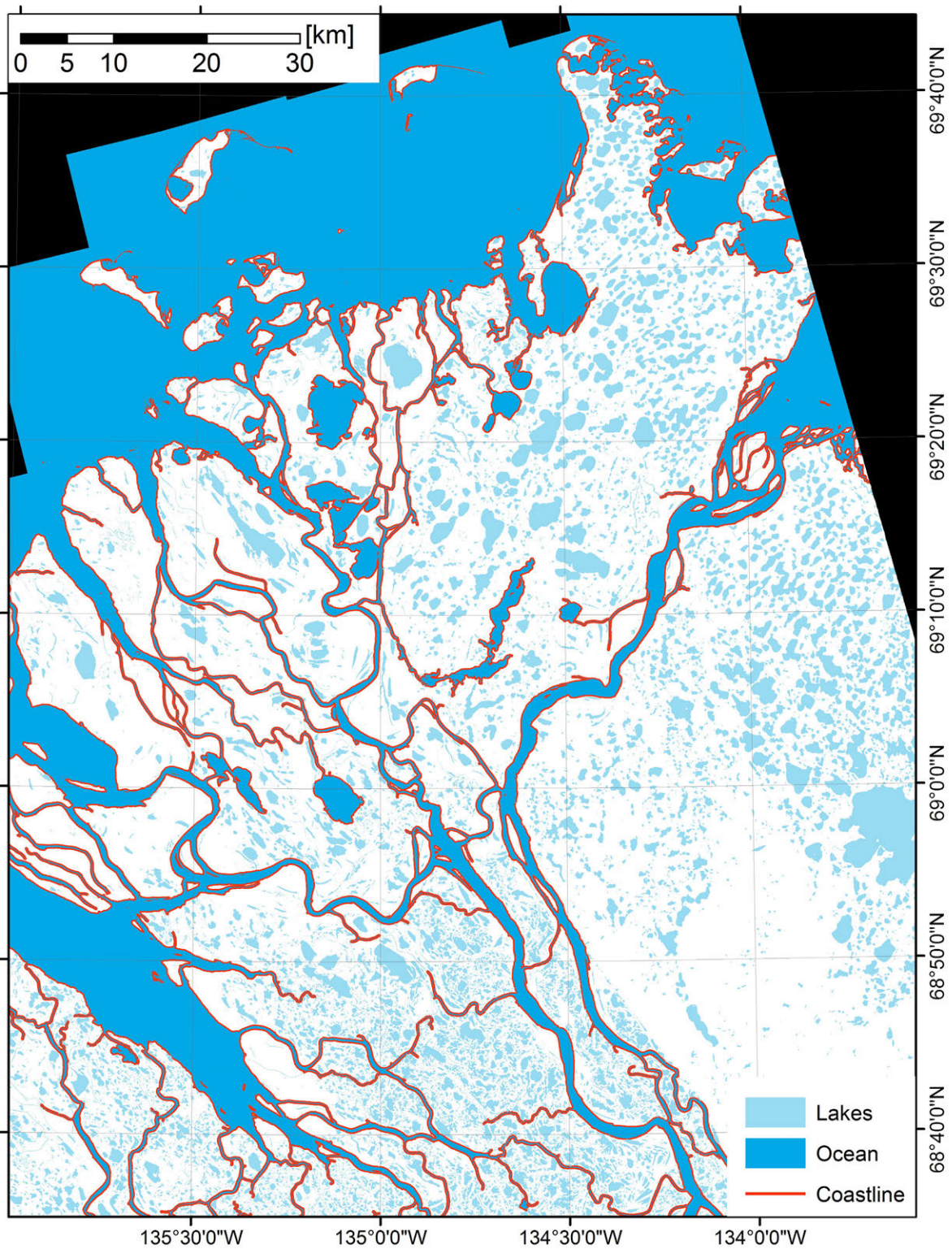


Figure 4.45: Mackenzie Delta water body and shoreline classification of co-polarized TSX and TDX IDEM. The initial classification was processed with the iterative water classifier and had an overall classification accuracy of about 93%. The classification was manually enhanced afterward using reference data of NWT-Geomatics (2014). Source: Own Figure.

#### 4 Results

were finally merged with respect to each training set defined by the experiments of the cross validation (see Section 3.2.3). Each final land cover classification had five land cover classes (NBG, VLD, VMD, VSD, VWT) and the masked water bodies (NWA). The default settings of the FKM-ML classifier (six pre-classes, twenty output classes and a five percent convergence threshold) were carried out in pre-tests (not shown) and showed a high applicability.

Table 4.2: List of the data used for unsupervised and supervised land cover classification of the test sites of the Mackenzie Delta (RIS, TUK, ECH, DIS) and Banks Island (BIS). The table shows the availability of TerraSAR-X and TanDEM-X (X-Band), Radarsat-2 (C-Band), ALOS PALSAR (L-Band) and multispectral Landsat 8 (L-8).

Location	X-Band (HH/VV)	X-Band (HH/HV)	C-Band (HH/HV/VH/VV)	L-Band (HH/HV)	L-8
RIS	✓	✗	✓	✓	✓
TUK	✓	✓	✓	✓	✓
ECH	✓	✗	✓	✓	✓
DIS	✓	✗	✓	✓	✓
BIS	✓	✗	✗	✗	✓

Table 4.3: List of the data combinations used for unsupervised and supervised land cover classification of the test sites of the Mackenzie Delta (RIS, TUK, ECH, DIS) and Banks Island (BIS).

Data	RIS	TUK	ECH	DIS	BIS
X - HHHV	✗	✓	✗	✗	✗
X - HHVV	✓	✓	✓	✓	✓
C - HHHV	✓	✓	✓	✓	✗
C - HHVV	✓	✓	✓	✓	✗
C - VVVH	✓	✓	✓	✓	✗
C - Quad	✓	✓	✓	✓	✗
L - HHHV	✓	✓	✗	✗	✗
L8	✓	✓	✓	✓	✓
X - HHHV + L8	✗	✓	✗	✗	✗
X - HHVV + L8	✓	✓	✓	✓	✓
C - HHHV + L8	✓	✓	✓	✓	✗
C - HHVV + L8	✓	✓	✓	✓	✗
C - VVVH + L8	✓	✓	✓	✓	✗
C - Quad + L8	✓	✓	✓	✓	✗
L - HHHV + L8	✓	✓	✗	✗	✗
X - HHVV + L - HHHV	✓	✓	✗	✗	✗
C - Quad + L - HHHV	✓	✓	✗	✗	✗
C - Quad + X - HHVV	✓	✓	✓	✓	✗
X - HHVV + C - HHHV	✓	✓	✓	✓	✗

The supervised classification was done using ENVI's Maximum Likelihood classification described in Section 3.2.1 and water bodies were masked prior to the classification. A standardization of the data was performed with respect to the mean and the standard deviation whenever PolSAR and optical data were combined. The training sets used for the supervised classification were defined by the experiments of the

cross validation (see Section 3.2.3). Again each land cover classification had the five land cover classes (NBG, VLD, VMD, VSD, VWT) and the masked water bodies (NWA).

The unsupervised and supervised classifications were processed and assessed with respect to the  $k$ -fold cross validation (see Section 3.2.3). The parameter  $k$  was set to three. This meant that three unsupervised and three supervised classifications were calculated for each test site and each data set. The accuracy assessment was performed three times and the final accuracies were estimated by averaging the accuracies of all cross validation experiments. The assessments of the unsupervised and supervised classification accuracies were performed for the test sites RIS, TUK, ECH, DIS and BIS. The classifications were performed for all available X-, C- and L-Band PolSAR data, the multispectral data of L-8 and the combination of PolSAR and optical data - depending on the availability of the data. Table 4.2 gives an overview which data were used for the evaluation. Table 4.3 shows which data combinations were evaluated for the test sites. The results of the assessment are shown in the following sections.

#### 4.3.2.1 Mackenzie Delta Region

Figure 4.46 shows the average overall classification accuracies of the test sites ECH and DIS for unsupervised (Figure 4.46.a & b) and supervised classification (Figure 4.46.c & d). It was found that the highest accuracies of the unsupervised classification were observed for the combination of PolSAR and L-8 data. The highest overall classification accuracies were obtained for the combination of L-8 and co-polarized C-Band, co-polarized X-Band, cross-polarized C-Band and quad-polarized C-Band data. The absolute accuracies of these unsupervised classifications ranged from about 66% to 75% for test sites ECH and from about 75% to 80% for test site DIS. For both test sites it was observed that the unsupervised classification of PolSAR data alone had lower overall classification accuracies than the classification of L-8 data. The accuracy of L-8 classification was about 66% for test site ECH and about 75% for test site DIS. The accuracies of the classifications of the PolSAR data ranged from 52% to 62% for test site ECH and from 52% to 70% for test site DIS. Among the PolSAR data the co-polarized C-Band data showed the highest accuracies. The combination of quad-polarized C-Band or HH/HV-polarized C-Band and co-polarized X-Band data for unsupervised classification showed classification accuracies comparable to L-8 data for the test site DIS. The classification accuracies of these data were low for the test site ECH and were less than 56%. The single classification accuracies of all classes and data combinations are shown in the Appendix Figure A1 & A2 on page 276.

For the test sites ECH the highest classification accuracies of supervised classification were observed when L-8 data and quad-polarized C-Band, co-polarized X-Band or co-polarized C-Band data were used. The accuracies of these classifications were above 80% and higher than the classification accuracy of L-8 data alone. It was observed that the supervised classifications of PolSAR data showed again lower overall classification accuracies than the classification of L-8 data. The accuracies were less than 70% and therefore more than 10% lower than the accuracy of L-8 data. The lowest overall classification accuracies of the PolSAR were observed for the VV/VH-polarized C-Band and the co-polarized X-Band data. The best classification was realized with quad-polarized and co-polarized C-Band data. The analysis of the overall classification accuracies of supervised classification of test sites DIS showed different results. The best classification results were observed for the combination of L-8 data and co-polarized X-Band,

#### 4 Results

quad-polarized C-Band or cross-polarized C-Band data. All of these classifications - as well as the classification accuracies of L-8 data and co-polarized C-Band data - showed accuracies of more than 92%. The accuracies of PolSAR alone showed lower overall classification accuracies. The best classification of PolSAR data was observed for the co-polarized X-Band, the quad-polarized C-Band and the co-polarized C-Band data with accuracies of about 85%, 80% and 75%. The accuracies of the cross-polarized C-Band data were lower than 70%. The combination of quad-polarized C-Band or HH/HV-polarized C-Band and co-polarized X-Band data showed accuracies close to 90%.

Figure 4.47 shows the average classification accuracies of the test sites RIS and TUK of unsupervised (Figure 4.47.a & b) and supervised classification (Figure 4.47.c & d). The best unsupervised classification results were observed for the combination of L-8 and quad-polarized C-Band with an overall classification accuracy of about 78% for both test sites. For RIS it was observed that only the combination of L-8 and cross-polarized or co-polarized C-Band showed overall classification accuracies comparable to the accuracy of L-8 data alone. The combination of L-8 and X-Band, or L-Band data showed lower accuracies. This was also true for any classification of the PolSAR data. The lowest accuracies were observed for the cross-polarized L-Band and the VV/VH-polarized C-Band data. For test site TUK it was observed that any combination of PolSAR and L-8 data had higher classification accuracies than the L-8 classification. The accuracies of these classifications ranged from about 75% to 78% and were up to +5% higher than the accuracy of the L-8 classification. The lowest accuracies were observed for the VV/VH-polarized C-Band, the HH/HV-polarized X-Band and the HH/HV-polarized L-Band data. Among the combination of different PolSAR data the combination of co-polarized X-Band and quad-polarized C-Band - as well as the combination of co-polarized X-Band and HH/HV-polarized C-Band data - showed the highest accuracies. Figure 4.48 and Figure 4.49 show processing examples of the unsupervised FKM-ML classification of the test sites RIS and TUK. The class number is sorted with respect to the greenness (L-8) and to the Alpha of the T-Matrix (TSX) from low to high.

The results of the supervised classification showed that the best classification of RIS and TUK was observed for the combination of L-8 and quad-polarized C-Band data with an overall accuracies close to 90% for both test sites. Further, it was observed that the combination of any of the PolSAR data and L-8 data had higher accuracies than the classification of L-8 data. The increase in the overall accuracy was up to +6% for both test sites. Among the PolSAR data the best classification was observed for the quad-polarized C-Band data. The accuracies of co-polarized X-Band, cross-polarized C-band and HH/HV-polarized L-Band data showed lower classification accuracies with values ranging from 65% to 75%. For both sites it was found that the combination of co-polarized X-Band and quad-polarized C-Band data showed high overall accuracies of more than 85%. The single classification accuracies of all classes and data combinations are shown in the Appendix Figure A3 & A4 on page 278.

The aim of the following analysis was to integrate the unsupervised and supervised classification results of the accuracy assessments of the test sites DIS, ECH, RIS and TUK. The accuracies of each test site were set in relation to the classification accuracies of the L-8 data in order to make the results comparable and to exclude systematic errors. This normalization of the accuracies showed the ratio of an accuracy to the accuracy of the L-8 data. This was done for the classification results of the PolSAR data of co-polarized X-Band and C-Band and the combination of X- and C-Band PolSAR data and/or L-8 data. The ratios were calculated for each class and each test site separately and an average was formed for each class and

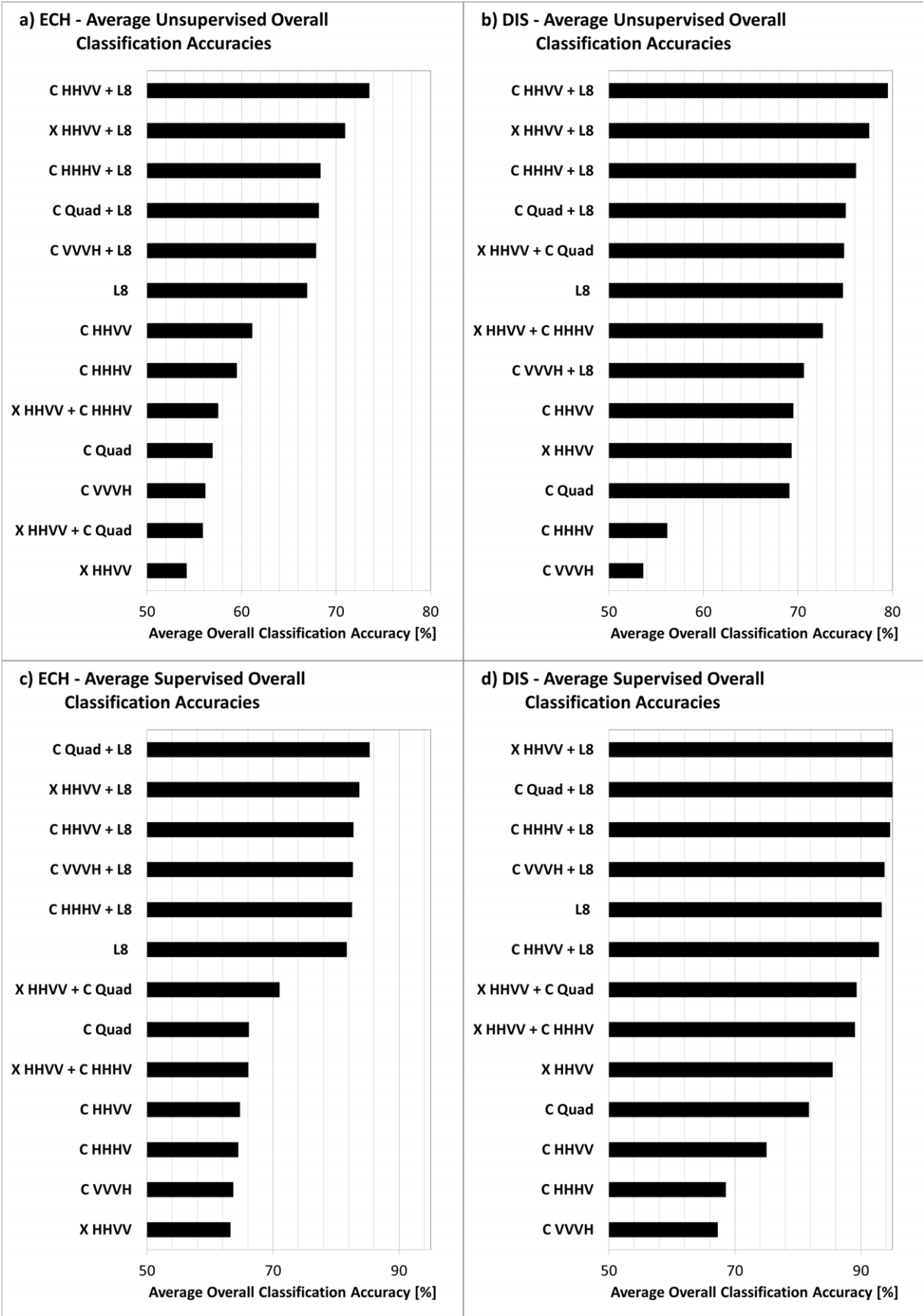


Figure 4.46: East Channel (ECH) and Delta Islands (DIS): Overall unsupervised and supervised classification accuracies. Source: Own Figure.

4 Results

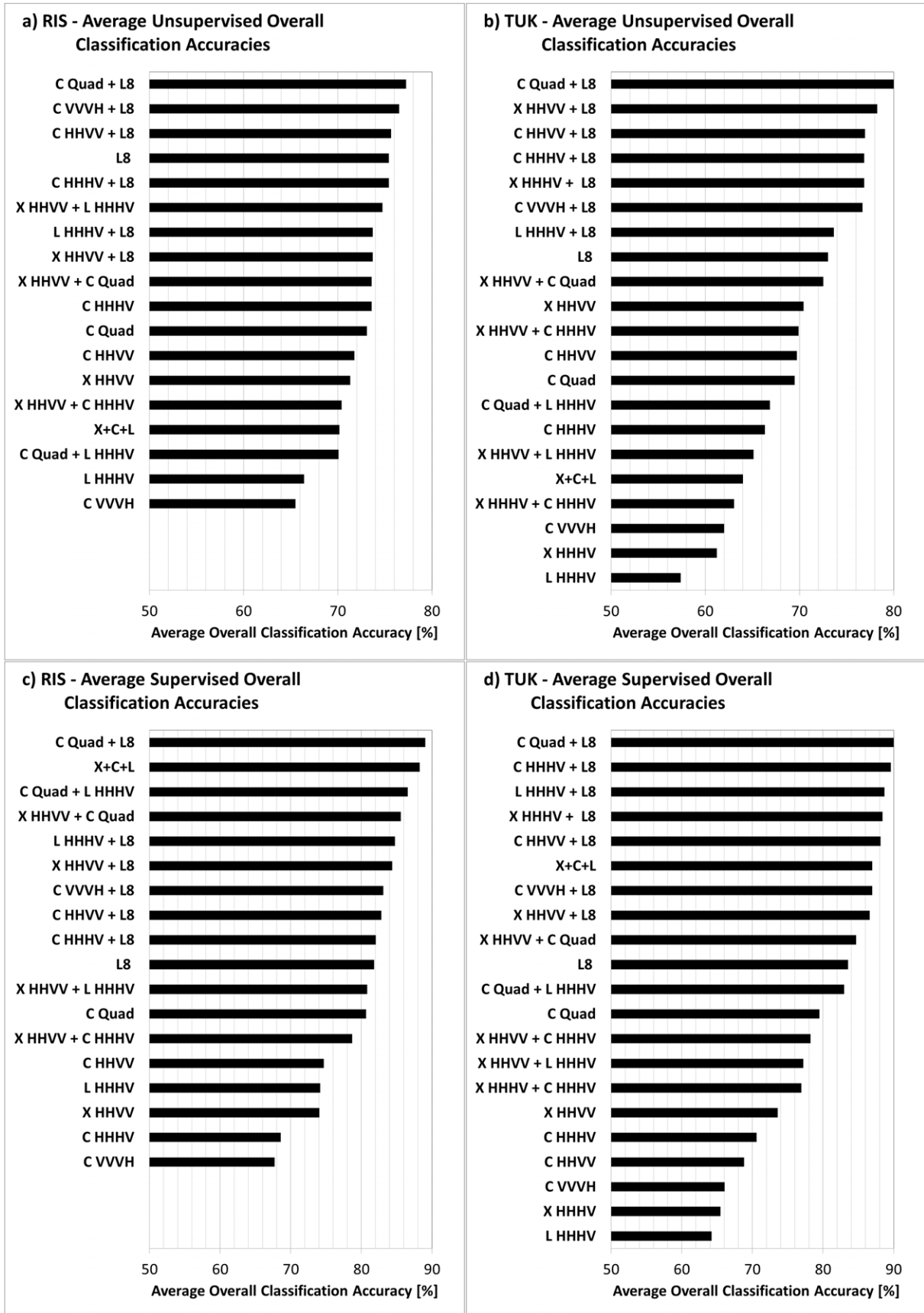


Figure 4.47: Richards Island (RIS) and Tuktoyaktuk (TUK): Overall unsupervised and supervised classification accuracies. Note: The abbreviation “X+C+L” means “X HHV + C Quad + L + HHHV”. Source: Own Figure.

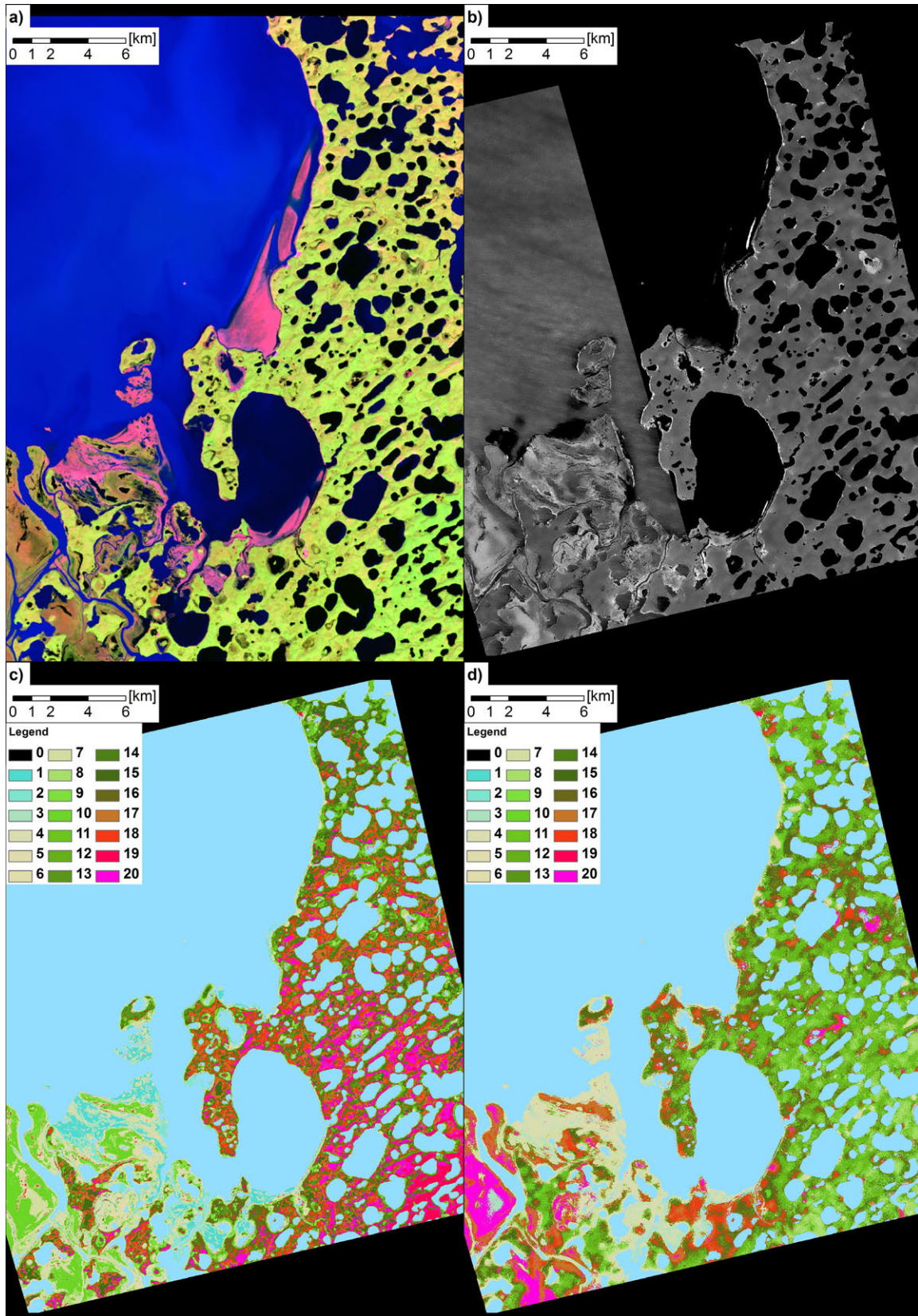


Figure 4.48: Richards Island (RIS) unsupervised classification results: a) false color composite of L-8 (R=Band 7, B=Band 5, G=Band 4), b) Span of co-polarized TSX, c) unsupervised classification of L-8 and d) unsupervised classification of co-polarized TSX. The water bodies were classified with the iterative water classifier based on the co-polarized TSX data. Source: Own Figure.

#### 4 Results

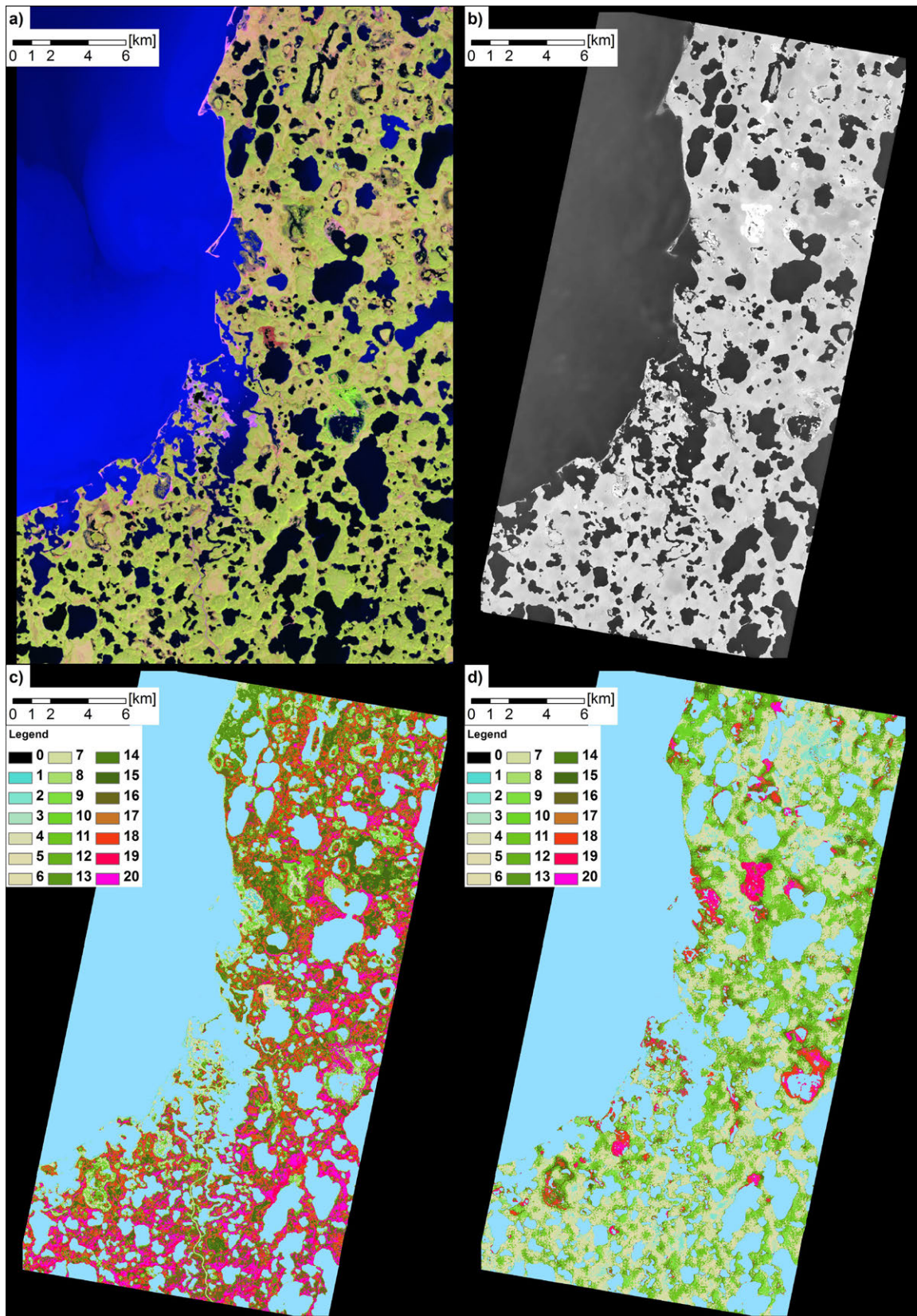


Figure 4.49: Tuktoyaktuk (TUK) unsupervised classification results: a) false color composite of L-8 (R=Band 7, B=Band 5, G=Band 4), b) Span of co-polarized TSX, c) unsupervised classification of L-8 and d) unsupervised classification of co-polarized TSX. The water bodies were classified with the iterative water classifier based on the co-polarized TSX data. Source: Own Figure.



the overall classification accuracies. The ratio was transformed to percent with respect to the L-8 accuracy. Negative values therefore indicated accuracies that were lower than the accuracy of L-8 classification. Positive values indicated accuracies that were higher than the accuracy of L-8 classification. The absolute value shows how much percent a classification was better or worse than the L-8 classification.

Figure 4.50 shows the results of this analysis for the unsupervised classification results and for the classes NBG (Figure 4.50.a), VLD (Figure 4.50.b), VMD (Figure 4.50.c), VSD (Figure 4.50.d), VWT (Figure 4.50.e) for each test site and the total average (Figure 4.50.f). It was found that the classification accuracies of class NBG were high in all of the L-8 classifications. Figure 4.50.a shows mainly negative anomalies for any other classification. The positive anomalies were observed for some of the test sites when combining L-8 and PolSAR data. The classification accuracy of any of the L-8 classifications was low for class VLD in contrast. Figure 4.50.b shows mainly positive anomalies. This means that PolSAR data and the combination of PolSAR and L-8 data were better suited to classify the class VLD than L-8 data alone. The negative anomalies were observed for the test site TUK. The unsupervised classification of class VMD had again a high accuracy when the L-8 data and some combinations of L-8 and PolSAR data were used. None of the PolSAR data beside the combination of co-polarized X-Band and quad-polarized C-Band of test site TUK showed classification accuracies higher than the L-8 classification. The combination of L-8 and PolSAR data showed positive anomalies for some of the test sites. Figure 4.50.d shows that the classification accuracy of the class VSD was high for the L-8 data and the anomalies were mainly negative. In contrast, it was found that a combination of cross-or quad-polarized C-Band data and L-8 data increased the classification accuracy of this class. Figure 4.50.e shows that the PolSAR data were suited to classify the class VWT. The anomalies were mainly positive. This was true for the co-polarized X-Band and the co-polarized C-Band. Along with this the average anomalies of this class were positive when combining PolSAR and L-8 data. The total average (Figure 4.50.f) showed that any combination of PolSAR and L-8 data was in average better suited for the unsupervised classification of the land cover than L-8 alone. Among the PolSAR data the co- and quad-polarized C-Band, as well as the co-polarized X-Band data, were best suited. The classification accuracy was low for HH/HV- and VV/VH-polarized data.

Figure 4.51 shows the normalized classification accuracies of the supervised classification results and for the classes NBG (Figure 4.51.a), VLD (Figure 4.51.b), VMD (Figure 4.51.c), VSD (Figure 4.51.d), VWT (Figure 4.51.e) for each test site and the total average (Figure 4.51.f). The results showed that the classification of class NBG with PolSAR data was in average worse compared to the classification of L-8 data. The combination of the PolSAR and L-8 data showed strong positive anomalies of this class, however. Figure 4.51.b shows the results of class VLD. The classifications of quad-polarized data and the classifications of X- and C-Band data showed higher classification accuracies than the accuracies of L-8 data. All combinations of PolSAR and L-8 data showed positive anomalies and the accuracy of this class was in average +5% higher than the classification accuracy of L-8 data alone. The PolSAR data showed in average lower accuracies of class VMD than the L-8 data (Figure 4.51.c). The only positive anomaly of the average of all test sites was found for the combination of co-polarized X-Band and quad-polarized C-Band data. The anomalies were positive when L-8 and PolSAR data were combined. Figure 4.51.d shows that the L-8 data were suited to classify the class VSD. The only positive anomalies of the PolSAR data were found for test site TUK for the combination of co-polarized X-Band and quad-polarized C-Band

#### 4 Results

data. The combination of L-8 data and co-polarized X-Band, as well as the combination of L-8 data and quad-polarized C-Band data, showed a positive anomaly of this class with values of between +1% and +5%. The results of Figure 4.51.e showed that the PolSAR data were again suited to classify the class VWT. The average anomalies were positive for all PolSAR data beside the cross-polarized C-Band data. Along with this the combination of L-8 and PolSAR data showed only positive anomalies. The average increment of the classification accuracy was up to +5% for the combination of L-8 and quad-polarized C-Band data. The total average values showed that any combination of PolSAR and L-8 data was in average better suited for the supervised classification of the land cover than L-8 alone. The average increase in the classification accuracy was about +5% for the combination of L-8 and quad-polarized data. Among the PolSAR data it was found that the best classification was obtained with quad-polarized C-Band data, followed by the co-polarized X- and C- Band data, the HH/HV-polarized C-Band data and the VV/VH-polarized C-Band data.

Figure 4.52, Figure 4.53, Figure 4.54 and Figure 4.55 show the classification results of the test sites ECH, DIS, RIS and TUK. Figures a) show the supervised classification of quad-polarized R-2 and L-8. Figures b) shows the unsupervised classification of quad-polarized R-2 and L-8. Figures c) show the supervised classification of co-polarized TSX and L-8. Figures d) show the unsupervised classification of co-polarized TSX and L-8. Figures e) show the supervised classification of quad-polarized R-2 and co-polarized TSX. Figures f) show the unsupervised classification of quad-polarized R-2 and co-polarized TSX. The results visually prove the findings of the accuracy assessment. The classification of the class VWT was on high level of confidence for all supervised and unsupervised classifications and for all test sites. All of the classifications detected the wetlands of the Mackenzie East Channel (Figure 4.52), the wetlands of the outer Mackenzie Delta Complex (Figure 4.53), the coastal and inland wetlands of Richards Island and the adjunct eastern Mackenzie Delta (Figure 4.54) and the inland wetlands of the Tuktoyaktuk Peninsular (Figure 4.55). The results showed that all of the supervised and unsupervised classifications classified the class NBG on high level of confidence. This can be shown for the exposed non-vegetated hill tops of the East Channel Region, the sparse vegetated areas and flats of the outer Mackenzie Delta, the mudflats and beaches of Richards Island and the beaches and mudflats of the Tuktoyaktuk Peninsular. The classifications revealed that the main differences in the class locations were related to the vegetation classes VLD and VSD, e.g. for the test site ECH. For the test site DIS the main differences between the supervised and the unsupervised classifications were related to the classification of the class VLD and VMD. This was best visible for the island north of the main delta complex. The land cover was classified as VMD in all of the supervised classifications and as class VLD in all of the unsupervised classifications. The main differences in the classifications were observed for the test site RIS for class VSD. The supervised classification showed the location of this class mainly at low lying creeks and at the western shore of West Point. In contrast, the unsupervised classifications showed many misclassified pixels. The supervised and unsupervised classifications of the test site TUK showed a good correspondence of the classes VLD and VSD. The accuracy assessments of the classifications showed that the accuracies of these classes were high.

In addition to this analyses, the average separability distances Jefferys Matusita Distance (JD) and Bhattacharyya Distance (BD) were calculated and analyzed for the Mackenzie Delta test sites ECH, RIS and TUK. The same reference data were used to process the distance-features and the multispectral and

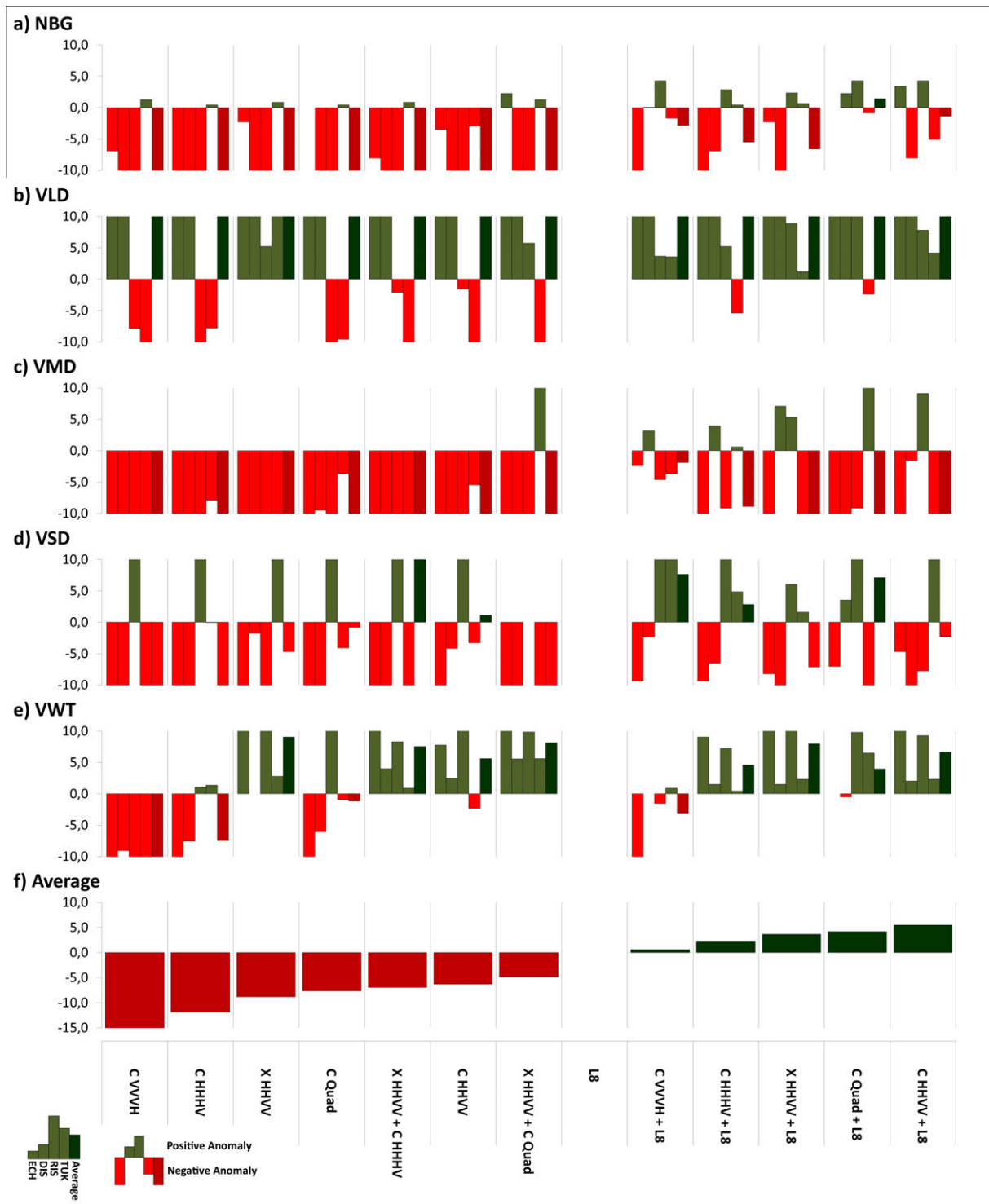


Figure 4.50: Normalized unsupervised classification accuracies of the Mackenzie Delta test sites DIS, ECH, RIS and TUK. The accuracies of each test sites were set in relation to the classification accuracies of the L-8 data. The ratios were calculated for each class and each test sites separately. The ratio is shown in percent. Negative values (red) indicate accuracies that were lower than the accuracy of the L-8 classification. Positive values (green) indicate accuracies that were higher than the accuracy of the L-8 classification. The absolute value shows how much percent a classification was better or worse than the L-8 classification. Source: Own Figure.

#### 4 Results

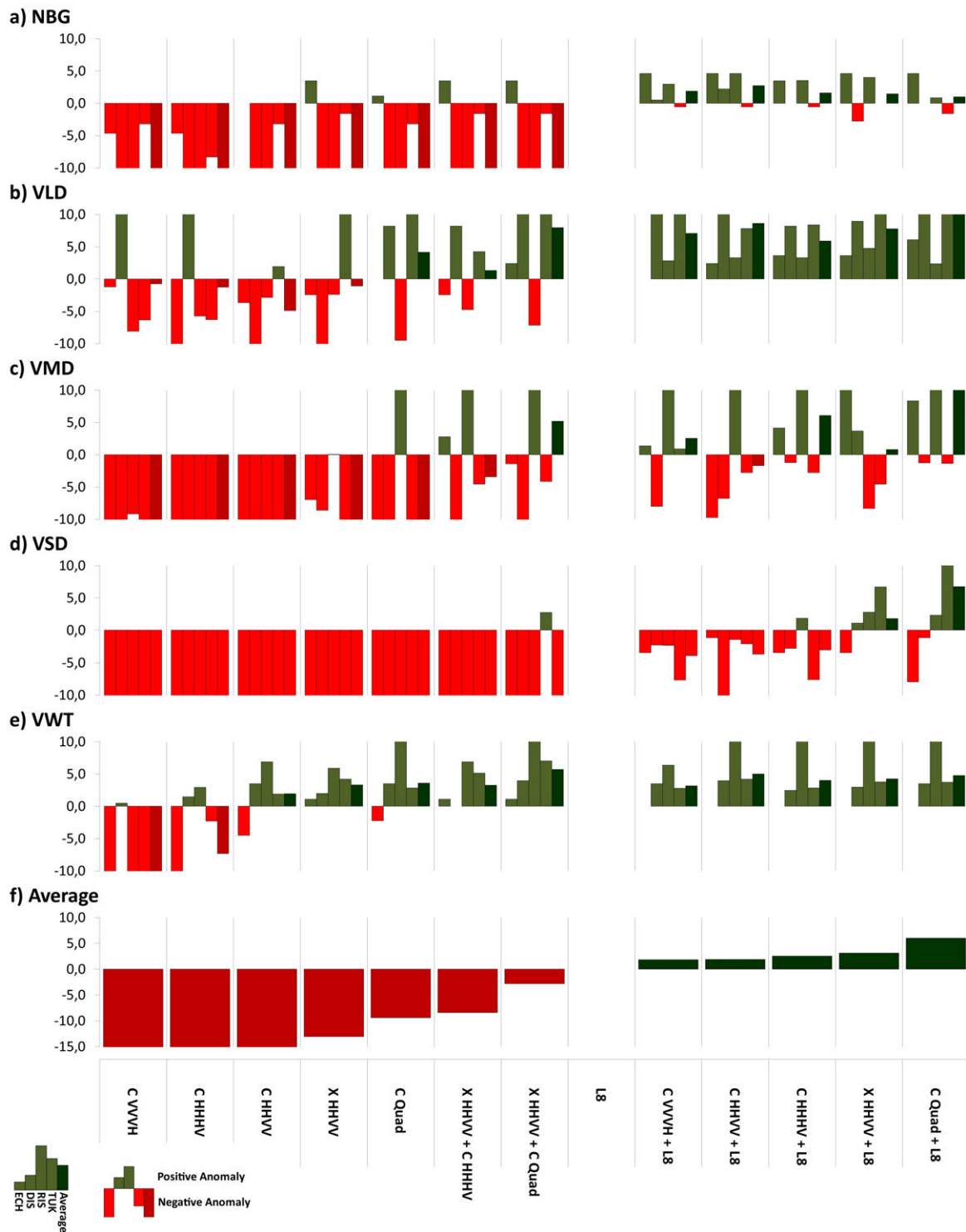


Figure 4.51: Normalized supervised classification accuracies of the Mackenzie Delta test sites DIS, ECH, RIS and TUK. The accuracies of each test sites were set in relation to the classification accuracies of the L-8 data. The ratios were calculated for each class and each test sites separately and averaged. The ratio is shown in percent. Negative values (red) indicate accuracies that were lower than the accuracy of the L-8 classification. Positive values (green) indicate accuracies that were higher than the accuracy of the L-8 classification. The absolute value shows how much percent a classification was better or worse than the L-8 classification. Source: Own Figure.

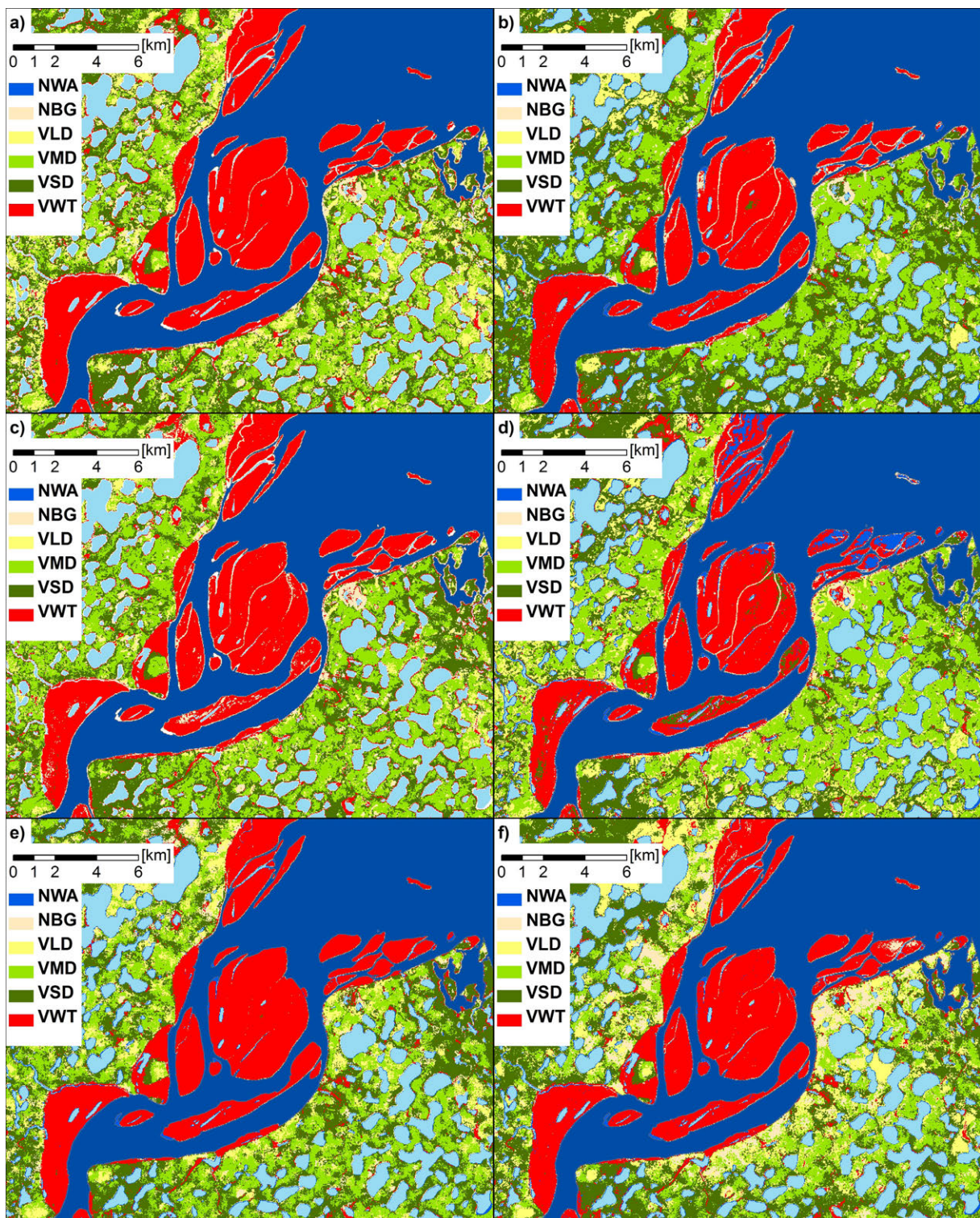


Figure 4.52: East Channel (ECH) classification results of: a) supervised classification of quad-polarized R-2 and L-8, b) unsupervised classification of quad-polarized R-2 and L-8, c) supervised classification of co-polarized TSX and L-8, d) unsupervised classification of co-polarized TSX and L-8, e) supervised classification of quad-polarized R-2 and co-polarized TSX and f) unsupervised classification of quad-polarized R-2 and co-polarized TSX. Source: Own Figure.

#### 4 Results

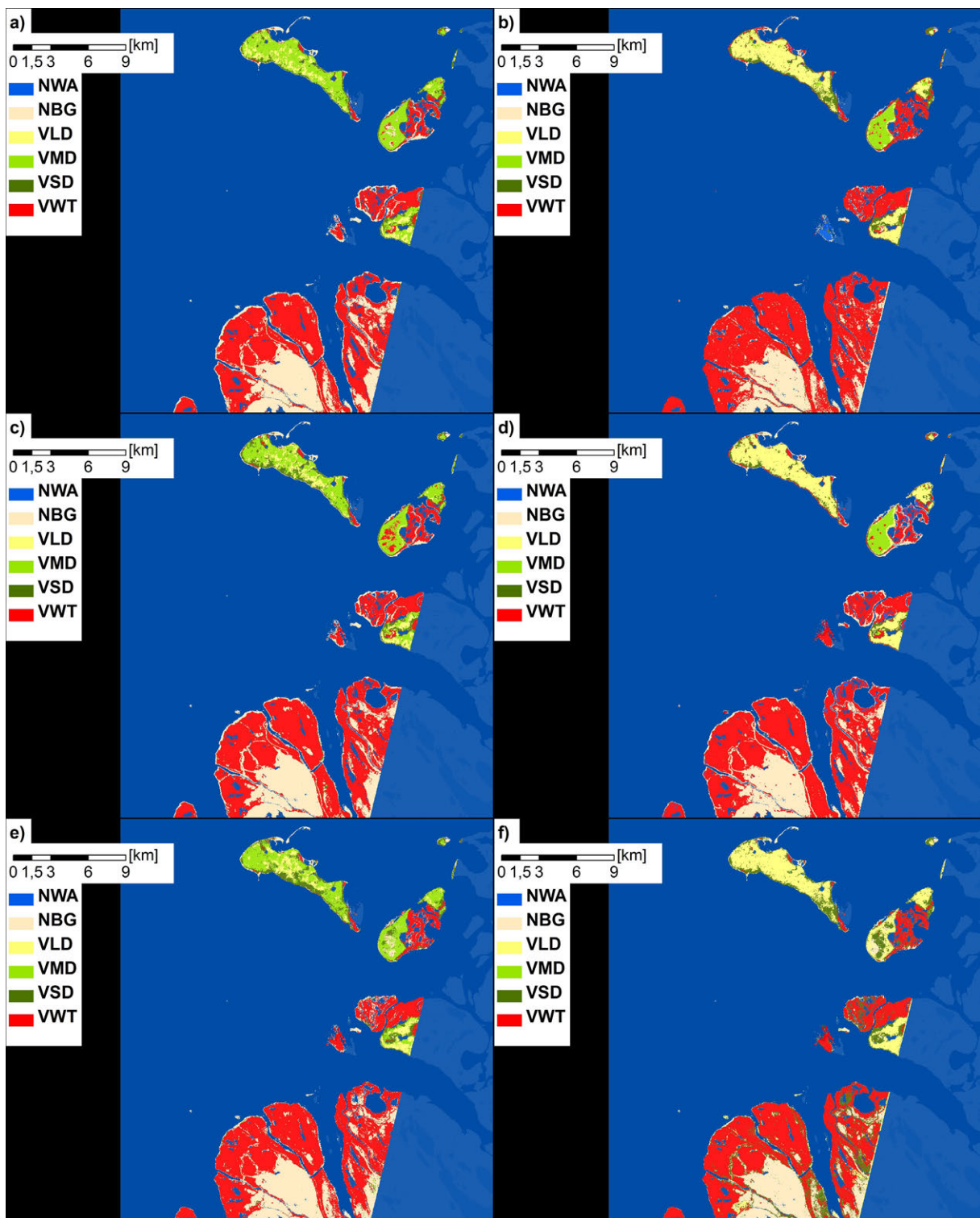


Figure 4.53: Delta Islands (DIS) classification results of: a) supervised classification of quad-polarized R-2 and L-8, b) unsupervised classification of quad-polarized R-2 and L-8, c) supervised classification of co-polarized TSX and L-8, d) unsupervised classification of co-polarized TSX and L-8, e) supervised classification of quad-polarized R-2 and co-polarized TSX and f) unsupervised classification of quad-polarized R-2 and co-polarized TSX. Source: Own Figure.

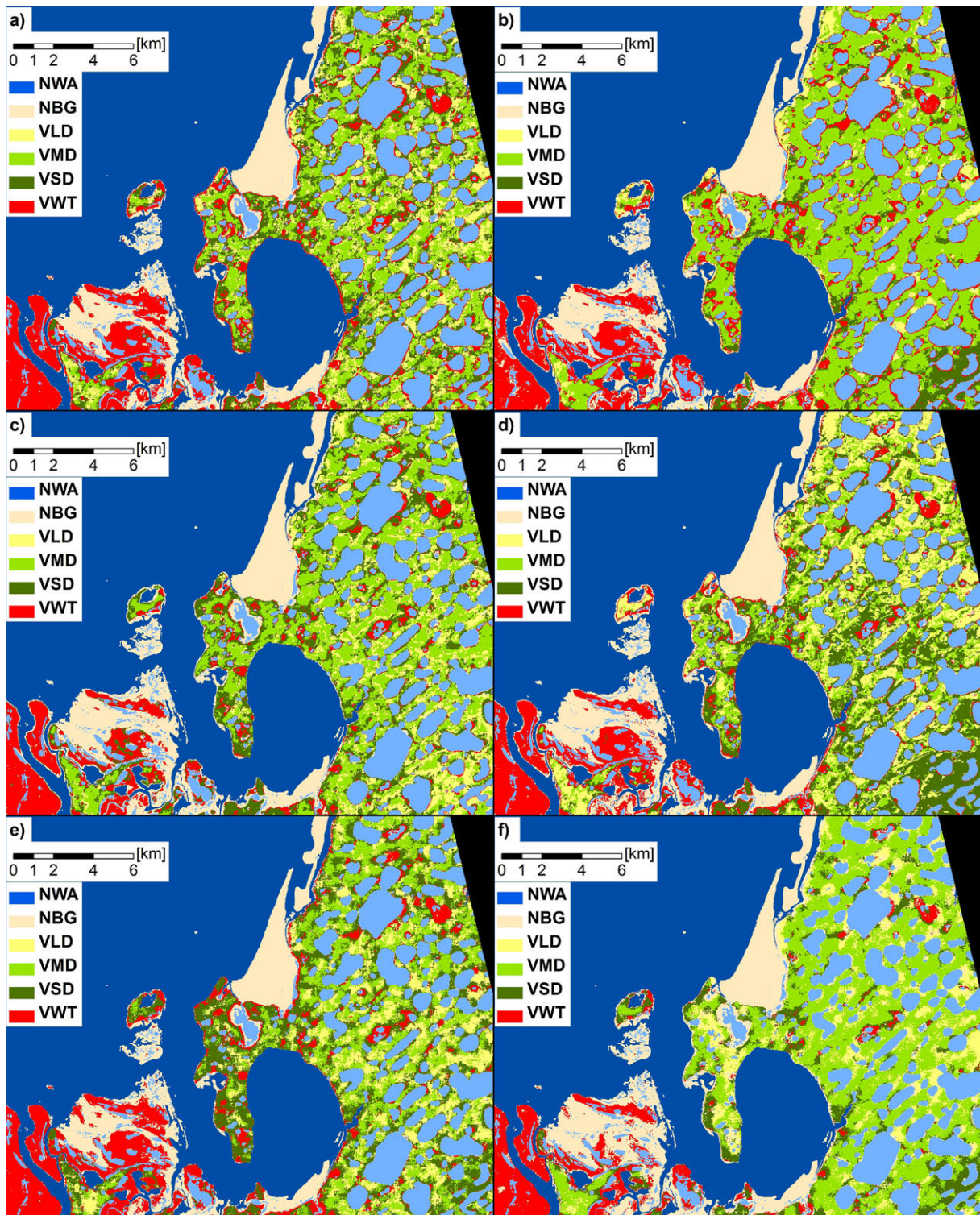


Figure 4.54: Richards Island (RIS) classification results of: a) supervised classification of quad-polarized R-2 and L-8, b) unsupervised classification of quad-polarized R-2 and L-8, c) supervised classification of co-polarized TSX and L-8, d) unsupervised classification of co-polarized TSX and L-8, e) supervised classification of quad-polarized R-2 and co-polarized TSX and f) unsupervised classification of quad-polarized R-2 and co-polarized TSX. Source: Own Figure.

#### 4 Results

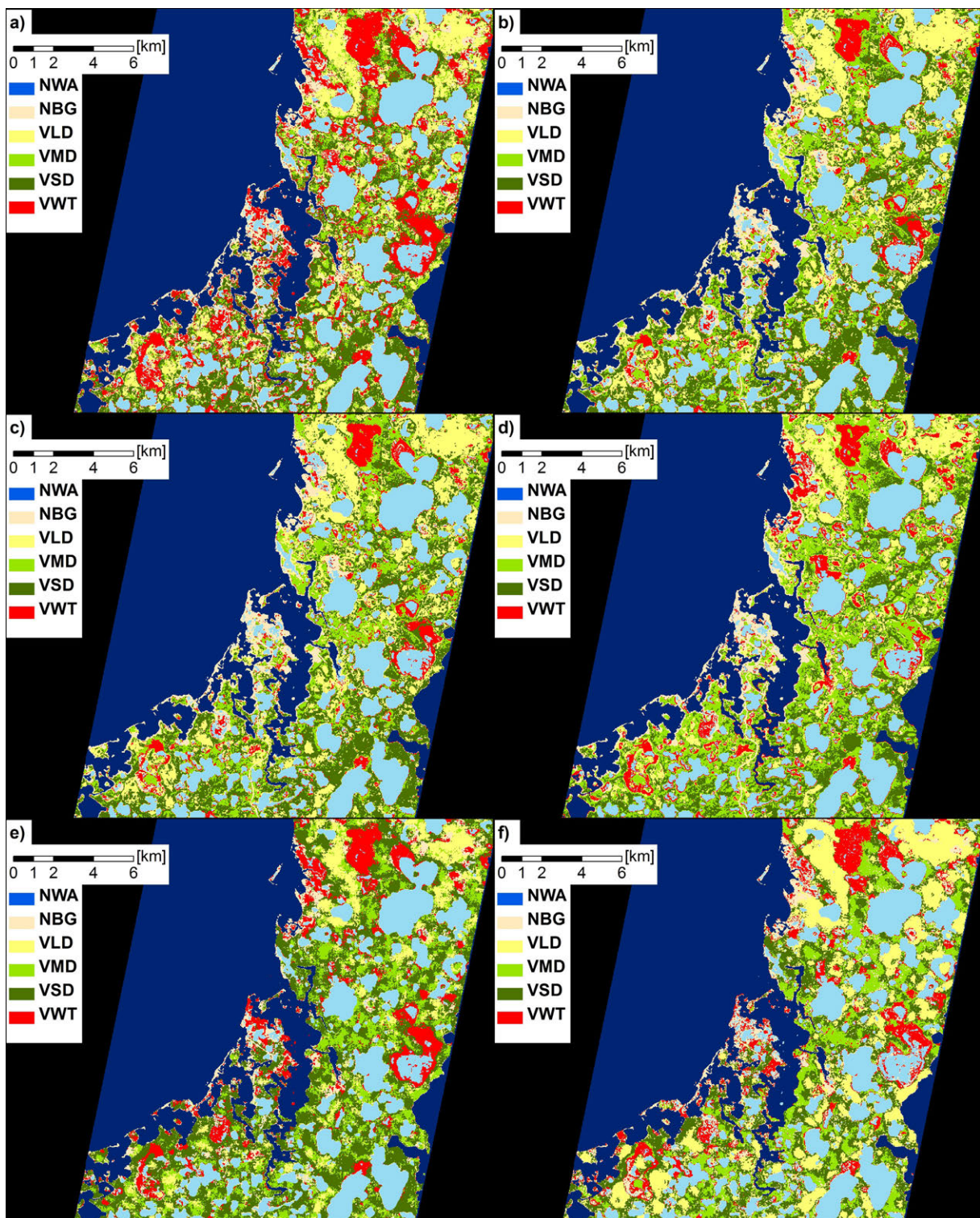


Figure 4.55: Tuktoyaktuk (TUK) classification results of: a) supervised classification of quad-polarized R-2 and L-8, b) unsupervised classification of quad-polarized R-2 and L-8, c) supervised classification of co-polarized TSX and L-8, d) unsupervised classification of co-polarized TSX and L-8, e) supervised classification of quad-polarized R-2 and co-polarized TSX and f) unsupervised classification of quad-polarized R-2 and co-polarized TSX. Source: Own Figure.



PolSAR data were normalized prior to the separability analysis using the mean and the standard deviation. The JD and BD were normalized in the same way as it was done for the classification accuracies. Therefore the normalized values of JD and BD show the separability of a class in relation to the separability offered by the L-8 data. The ratios were calculated for each class and each test site separately and an average was formed. Negative (positive) values therefore indicated separabilities that were lower (higher) than the separability of L-8 data. The absolute value showed how much percent a JD or BD was higher or lower than the JD or BD of L-8 data. The single separabilities of all classes and data combinations of the test sites RIS and TUK are shown in the Appendix Figure A5 & A6 on page 280.

Figure 4.56 shows the normalized JDs. It was found that the combination of multispectral and PolSAR data enhanced the separability of classes in the feature space. Again the PolSAR data showed nearly the same ranking: The best separation was realized with quad-polarized C-Band data, followed by co-polarized C- and X- Band data, HH/HV-polarized and VV/VH-polarized C-Band data. Remarkably, the quad-polarized C-Band data - as well as the multi-frequency data of co-polarized X-Band and C-Band - showed a higher overall JD than the L-8 data. Among the combined PolSAR and multispectral data the best JD was realized with L-8 and quad-polarized C-Band, followed by L-8 and co-polarized X-Band, L-8 and HH/HV-polarized C-Band, L-8 and co-polarized C-Band and L-8 and VV/VH-polarized C-Band data. The JD variations of the classes were low. However, it was found that PolSAR data showed high JDs of class VWT - if the PolSAR data had the co-polarized information. This indicated again the suitability of the co- and quad-polarized data for the characterization and separation of the wetlands. Figure 4.57 shows the normalized BDs. Again the PolSAR data showed nearly the same ranking: The best separation was realized with quad-polarized C-Band data, followed by co-polarized X- Band data, HH/HV-polarized, co-polarized and VV/VH-polarized C-Band data. Among the combined PolSAR and multispectral data the best BD was realized with L-8 and quad-polarized C-Band, followed by L-8 and co-polarized X-Band, L-8 and co-polarized C-Band, L-8 and HH/HV-polarized C-Band and L-8 and VV/VH-polarized C-Band data. The BD values of class VWT were high if co-polarized information was added and the BDs were up three-times higher than the BD of L-8 data. As stated before this indicated the suitability of the co-polarized information for the characterization and separation of the wetlands.

The following analysis was dedicated to the question if separability distances can act as predictor for the classification accuracy. The JDs, BDs and unsupervised and supervised classification accuracies were therefore plotted and the  $R^2$  coefficients were calculated. Figure 4.58.a shows that the JD and BD had a weak correlation with a  $R^2$  value of about 0.4. The analysis further revealed that BD values had a high range of values for saturated JDs. Figure 4.58.b shows the scatterplot of the JD and the supervised classification accuracies and indicated a clear linear trend with a  $R^2$  value of about 0.6. The correlation between the BD and the supervised classification accuracies was weak with a  $R^2$  value of about 0.4 (Figure 4.58.c). Finally the correlation between unsupervised and supervised classification accuracies was investigated. The correlation was positive and a  $R^2$  value of about 0.5 was observed. The unsupervised accuracies were lower and the correlation was better for accuracies higher than 70 %.

Finally, the supervised and unsupervised classifications were performed for the entire Mackenzie Delta using co-polarized TSX and L-8 imagery (see Table 2.5 and Table 2.9) in order to test the applicability of the approach for large areas. The TSX data were processed as described in Section 3.1.1.3. They were filtered with the Non-Local Means filter as specified in Section 3.1.1.2 and with respect to the findings of

#### 4 Results

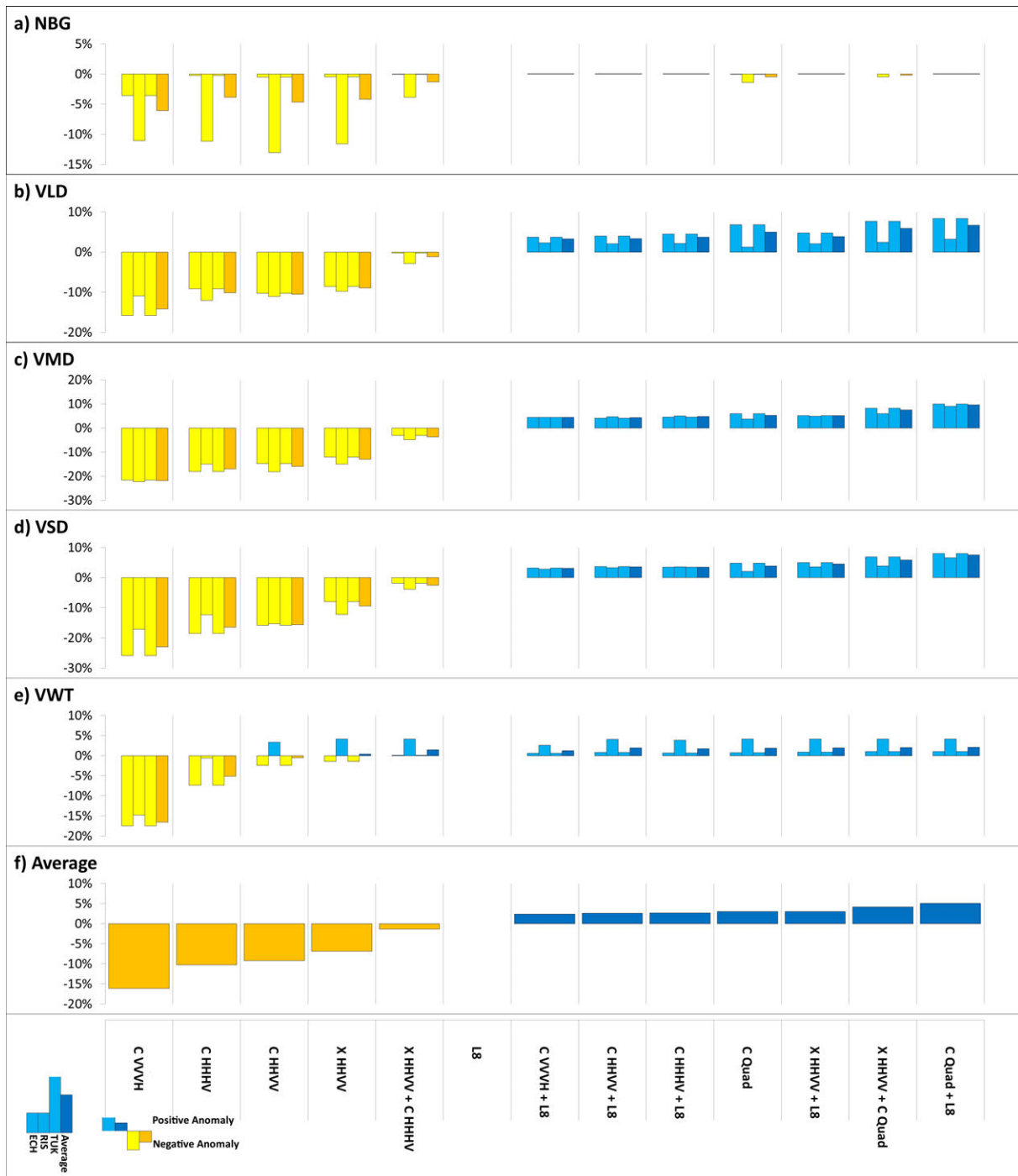


Figure 4.56: Normalized Jefferys Matusita Distances (JD) of the Mackenzie Delta test sites ECH, RIS and TUK. The JDs of each test sites were set in relation to the JD of the L-8 data. The ratios were calculated for each class and each test sites separately and averaged. The ratio is shown in percent. Negative values (orange) indicate JDs that were lower than the JD of the L-8 data. Positive values (blue) indicate JDs that were higher than the JD of the L-8 data. The absolute value shows how much percent a JD was higher or lower than the JD of L-8 data. Source: Own Figure.

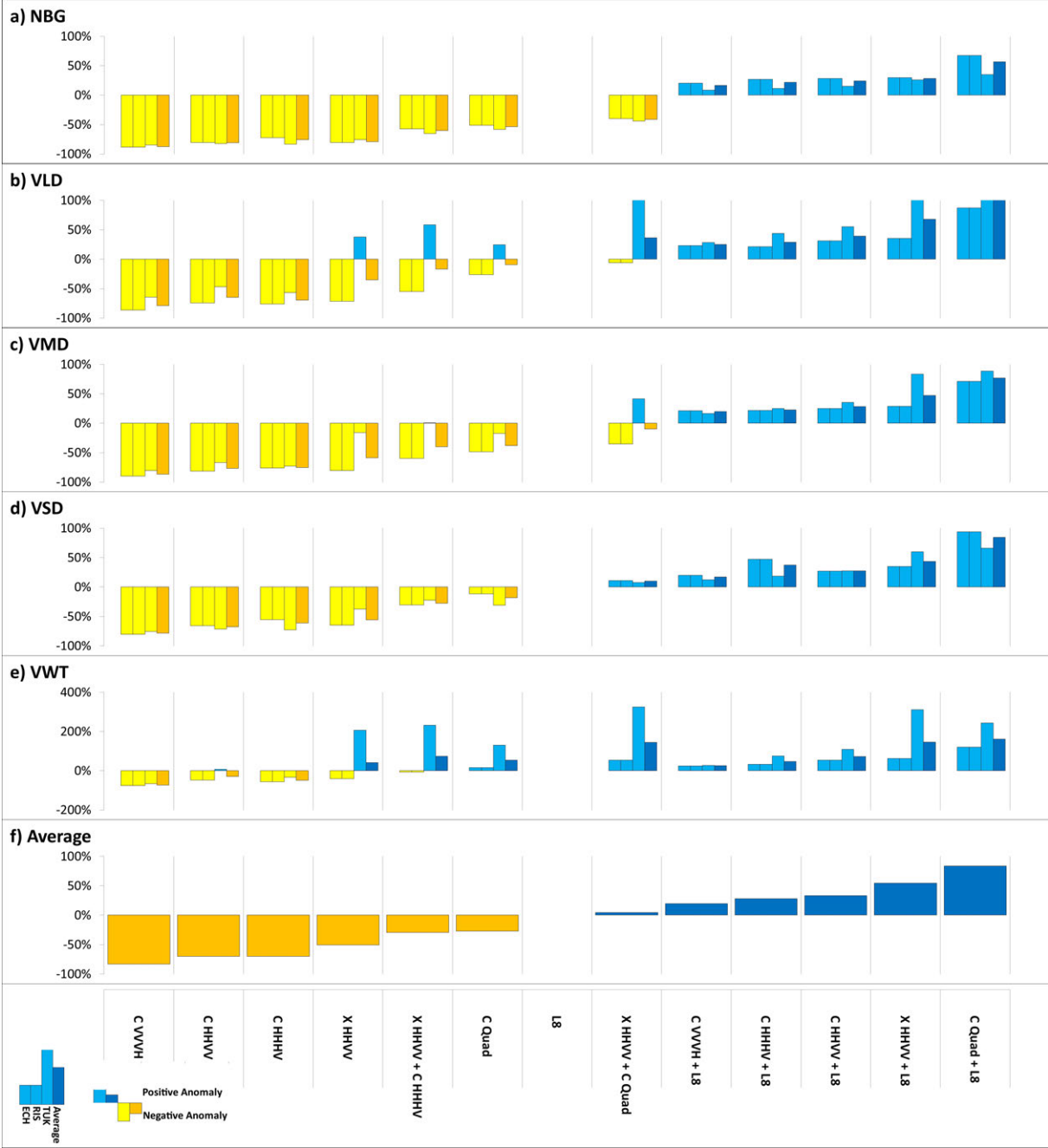


Figure 4.57: Normalized Bhattacharyya Distances (BD) of the Mackenzie Delta test sites ECH, RIS and TUK. The BDs of each test sites were set in relation to the BD of the L-8 data. The ratios were calculated for each class and each test sites separately and averaged. The ratio is shown in percent. Negative values (orange) indicate BDs that were lower than the BD of the L-8 data. Positive values (blue) indicate BDs that were higher than the BD of the L-8 data. The absolute value shows how much percent a BD was higher or lower than the BD of L-8 data. Source: Own Figure.

#### 4 Results

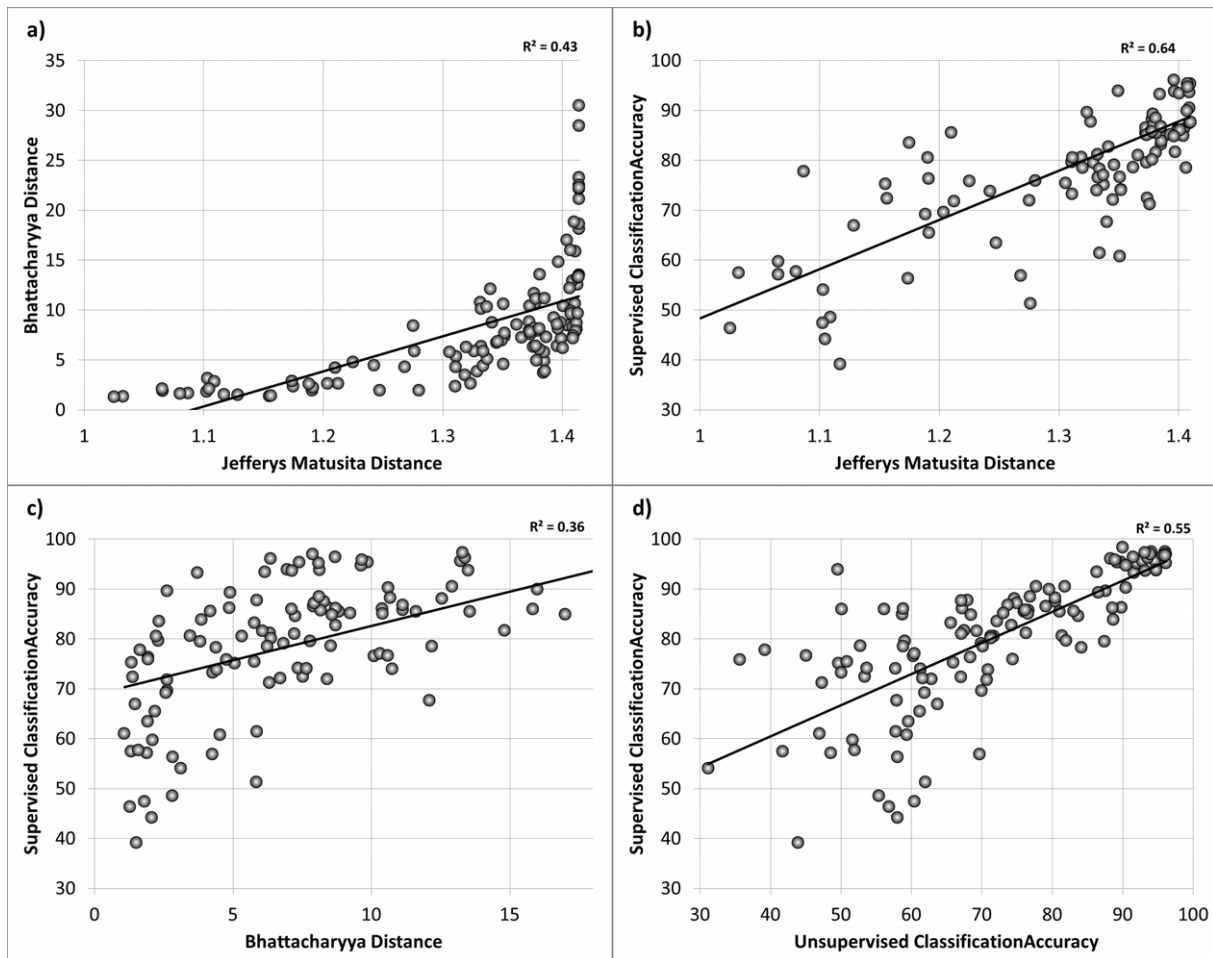


Figure 4.58: Scatterplots of separability distances and classification accuracies: a) Jefferys Matusita Distances versus Bhattacharyya Distances, b) Jefferys Matusita Distances versus supervised classification accuracies, c) Bhattacharyya Distances versus supervised classification accuracies and d) unsupervised classification accuracies versus supervised classification accuracies. The plots show the average accuracies of the cross validation and were derived from the Mackenzie Delta test sites ECH, RIS and TUK. Source: Own Figure.

Section 4.1.1. Prior to the land cover classification the water bodies of the test site were classified based on the iterative water classifier and reference data of NWT-Geomatics (2014). The final water mask used is shown in Figure 4.45. The data of TSX were mosaiced in ENVI 5.1 using the mosaic function and the color balancing option (not shown). The statistics needed for the color balancing were derived from the overlapping parts of the scenes. The order of the scenes in the mosaicing process was selected manually. The L-8 data were sampled to a geometric resolution of 15 m using the bilinear resampling function of ENVI 5.1. The TSX data were sampled to a geometric resolution of 15 m using the pixel aggregate function of ENVI 5.1. The data of L-8 and TSX were manually registered and showed in average and mean location error of less than 20 m and of less than two pixels. All of the available reference and in situ data of all test sites of the Mackenzie Delta (RIS, DIS, ECH, CAH and YCP) were used to assess the classification accuracies. Because of this it was necessary to introduce a new land cover class. The land coverage of the upper Mackenzie Delta and of the regions south of Inuvik is dominated by the presence of

spruce trees and therefore this class was introduced as VTR (tree vegetation). The reference data for this class were collected using high-resolution airborne photography and imagery that was taken during the helicopter flights in 2012 (see Section 2.2.5 and Section 2.2.1).

The unsupervised classification was done using the unsupervised FKM-ML classifier. The FKM-ML was used with the same settings as the classification of the single test sites. The unsupervised Jenks-Natural-Breaks was initialized again with six pre-classes and the Alpha values of T-Matrix were used. Again the pre-classes were derived from the greenness of the tasseled cap transformation when L-8 data were used in the classification process. The total number of output-classes was again fixed to twenty classes and FKM classification was performed afterward. The data used in FKM were the sigma nought and terrain corrected Kennaugh Matrix of PolSAR data and/or the TOC reflectance values of the multispectral data. The statistics of these FKM twenty classes were calculated and the iterative the ML was initialized. The convergence criterion was fixed to five percent and convergence of the classifier was observed for all performed classifications. A standardization of the data was performed with respect to the mean and the standard deviation whenever PolSAR and optical data were combined. The unsupervised classes were finally merged with respect to each training set derived from the experiments of the cross validation (see Section 3.2.3). Each final land cover classification has six land cover classes (NBG, VLD, VMD, VSD, VTR, VWT) and the masked water bodies (NWA).

The supervised classification was done using ENVI's Maximum Likelihood classification described in Section 3.2.1. The classification was initialized on the data and water bodies were masked prior to the classification. A standardization was performed with respect to the mean and the standard deviation whenever PolSAR and optical data were combined. The training sets used for the supervised classification were derived from the experiments of the cross validation. Each final land cover classification had six land cover classes (NBG, VLD, VMD, VSD, VWT, VTR) and the masked water bodies (NWA). The unsupervised and supervised classifications were processed and assessed with respect to the cross validation (see Section 3.2.3). The parameter  $k$  was again set to three. The accuracy assessment was performed three times and the final accuracies were estimated by averaging the accuracies of all cross validation experiments. The classifications were performed for the co-polarized TSX, L-8 and the combined stack of TSX and L-8.

The average unsupervised classification accuracies are shown in Figure 4.59.a. It was found that the best classification was obtained for the combination of L-8 and TSX data. The average was about 72% and was as high the average accuracy of L-8 data alone. The average overall classification accuracy of TSX was about 67%. All of the unsupervised classifications showed high classification accuracies of the classes NBG, VWT and VTR. The unsupervised classifications accuracies of class VMD were low in all classifications and it was not possible to delineate this class on a high level of confidence for the entire Mackenzie Delta. The average accuracy was less than 50% and indicated systematic errors in the unsupervised classification process. The classification accuracies of classes VLD and VSD were about 60% for the classification of L-8 and TSX, about 80% for L-8 and higher than 60% for TSX.

The best supervised classification result was processed using the data of L-8 and TSX. An average overall classification accuracy of about 90% was observed (Figure 4.59.b). The accuracies of the classes VWT, VTR and NBG were higher than 95%. The accuracy of class VLD was comparable low and about 70%. The classes VMD and VSD were classified with about 85% accuracy. These values were in average

#### 4 Results

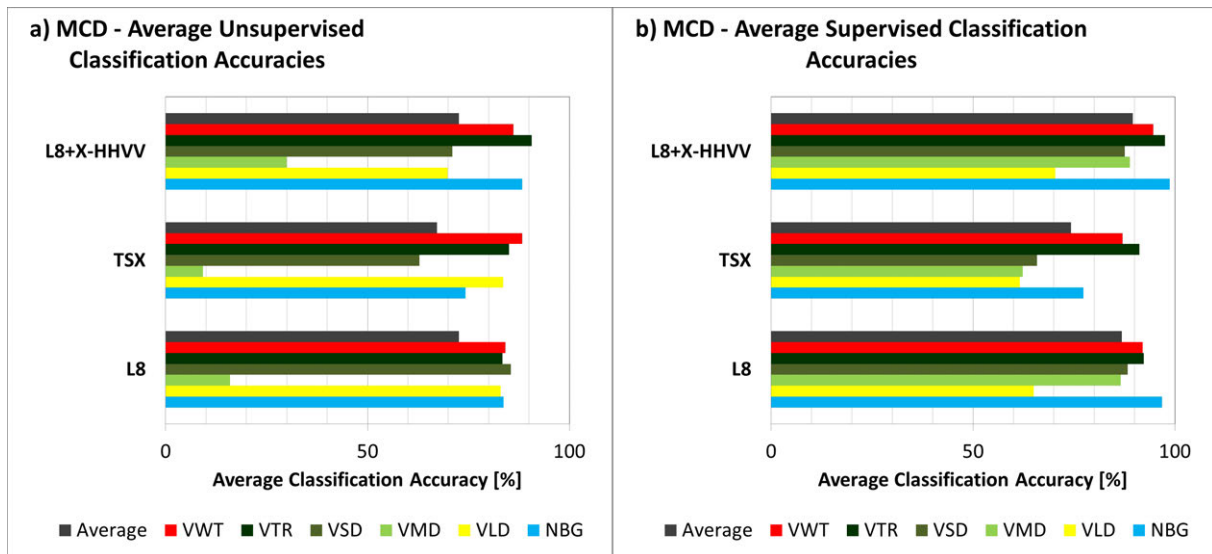


Figure 4.59: Mackenzie Delta: Overall unsupervised and supervised classification accuracies. Source: Own Figure.

+5% higher than the classification accuracies of L-8 classification. This classification showed an overall classification accuracy of about 85% and accuracies were high for the classes NBG, VTR and VWT. The class VLD showed a low accuracy of about 60%. The lowest accuracies were found for the TSX classification. The overall accuracy was about 70% and classes VLD, VMD and VSD were classified with accuracies in the range from 60% to 65%. The accuracies of classes VWT and VTR were estimated with 88% and 91%.

Figure 4.60 shows exemplary the unsupervised FKM-ML classification of the Mackenzie Delta based on the data of L-8 and TSX. The classes were sorted with respect to their average greenness value. Therefore the non-vegetated and sparse vegetated areas of the outer delta complex, of mudflats and beaches and the exposed hill tops were drawn in blueish and grayish colors. The wetlands of the delta complex and the inland wetlands showed up with greenish color. The different tundra vegetation classes of Richards Island, the East Channel Region and the Caribou Hills are shown in orange, violet and red colors due to their high greenness values. The spruce trees of the upper delta are shown in violet and red colors. Figure 4.61 shows the result of unsupervised land cover classification of L-8 and TSX data. The classification was based on the unsupervised classification (Figure 4.60) and the classes were merged using the land cover reference data. The classification showed that the wetlands of the Mackenzie Delta and of the East Channel were well detected. The same was true for the spruce vegetation of the northern delta and the classification clearly showed the treeline. Further, the classification highlighted the location of bare ground and mudflats of the Outer Delta and of the west side of Richards Island.

Figure 4.62 shows the result of supervised land cover classification of L-8 and TSX data. The classification of the classes NBG, VTR and VWT was nearly identical to the unsupervised classification. Main differences between the supervised and the unsupervised classifications were observed for the classes VMD and VLD. The differences were best visible for the central part of Richards Island. The land cover of this region was classified as VLD in the unsupervised classification and as VMD in the supervised

classification. The locations of class VSD were comparable but showed some variations, e.g. again visible in the central part of Richards Island and the East Channel Region. Figure 4.63 shows the result of supervised land cover classification of TSX data. As indicated in the accuracy assessment, the land cover classes NBG, VWT and VTR were mainly in correspondence to the supervised classification of TSX and L-8 data (Figure 4.62). The main differences between these classifications were related to the classes VMD and VSD. The classification of TSX data showed many missed detections of the class VSD. This was best visible for the central part of Richards Island and the northern lowlands of the Caribou Hills.

The data of X-, C- and L-Band PolSAR data and multispectral data of Landsat 8 were evaluated with respect to their suitability in land cover classification of generalized tundra land cover types of the Mackenzie Delta Region. The unsupervised classification was done using the unsupervised FKM-ML classifier and the supervised classification was done using ENVI's Maximum Likelihood classification. The unsupervised and supervised classifications were processed and assessed with respect to a  $k$ -fold cross validation. The assessments of the unsupervised and supervised classification accuracies were performed for the test sites RIS, TUK, ECH and DIS. The classifications were processed for all available X-, C- and L-Band PolSAR data, the multispectral data of Landsat 8 and the combinations of PolSAR and multispectral data - depending on the coverage of the data. The assessment of the PolSAR data indicated that the classification of the generalized land cover types was best realized with quad-polarized data followed by co- and cross-polarized data of C- and X-Band. Among the cross-polarized data the HH/HV-polarized data were shown to be better suited for the classification than the VV/VH-polarized data. The L-Band data were shown to be less sensitive to the land cover and therefore the classifications accuracies were low. It was further found that the information of PolSAR data was not sufficient to clearly differentiate between different types of tundra vegetation. The best results were obtained when spectral information and polarimetric information were used synergistically for the land cover classification. Among the different combinations of PolSAR and multispectral data, the quad-polarized data followed by the co-polarized and cross-polarized data of the C- and X-Band were found to be best suited for the classification. These results were also confirmed by the analysis of the Jefferys Matusita and Bhattacharyya Distances. The unsupervised classification of co-polarized TSX and Landsat-8 data showed in average classification accuracies of more than 80% for the classes of sparse vegetated tundra and shrub dominated tundra. This indicated that the combination of shortwave radar and optical data had a high potential to classify the generalized tundra land cover types of the sites in an unsupervised way and with high accuracy. The classes of bare ground and wetland had the highest classification accuracies of all investigated classes.

4 Results

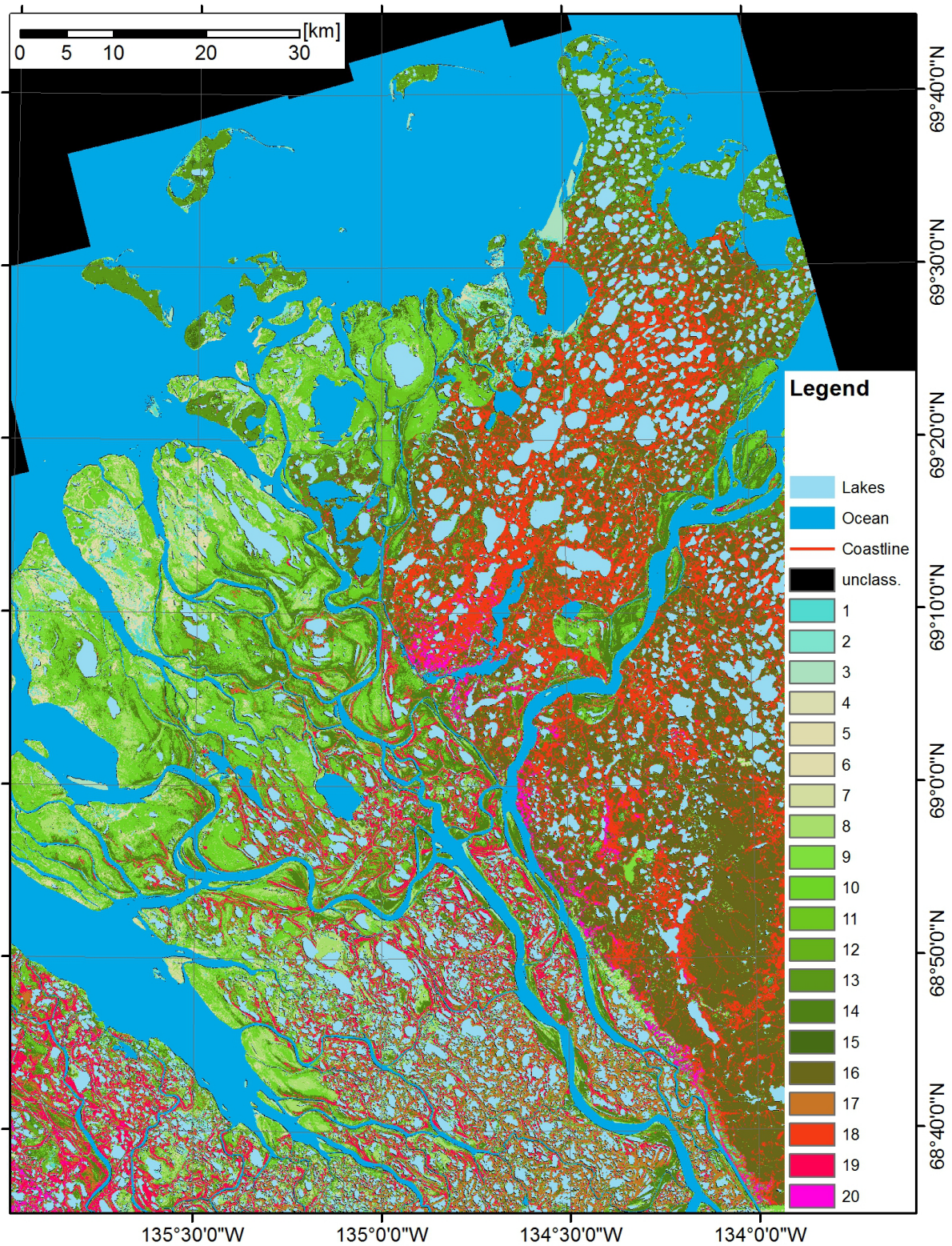


Figure 4.60: Mackenzie Delta classification result of unsupervised classification of co-polarized TSX and L-8. The classification was processed using the FKM-ML classifier and it is based on the greenness of the tasseled cap transformation. The classes are sorted according to their average greenness value from blue to gray to green to red. Source: Own Figure.



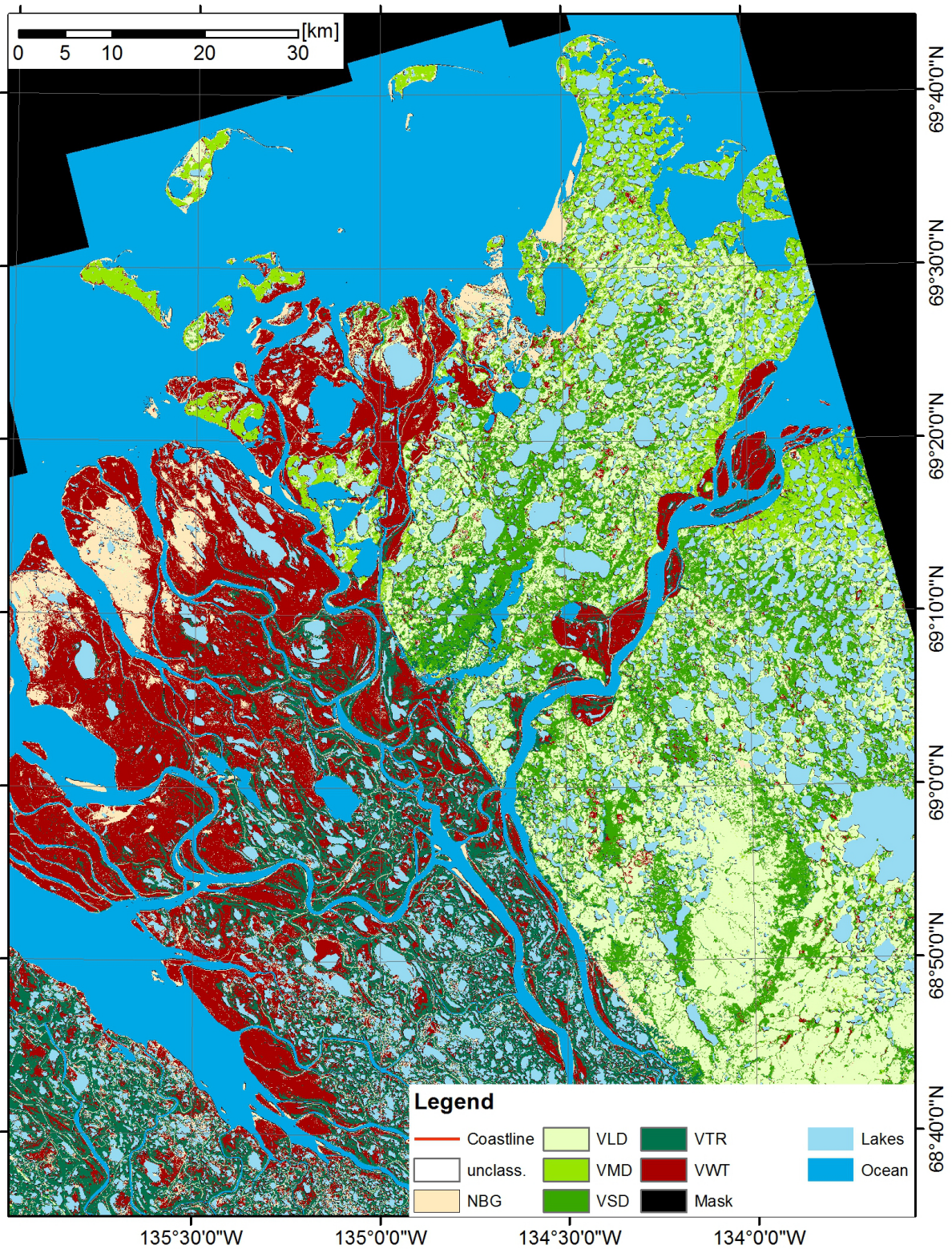


Figure 4.61: Mackenzie Delta classification result of unsupervised classification of co-polarized TSX and L-8 data. The classification was processed using the FKM-ML classifier and it is based on the greenness of the tasseled cap transformation.. The classes are sorted according to their average greenness value from blue to gray to green to red. The classes of Figure 4.60 were merged to the land cover classes in accordance to the in situ reference data. The overall classification accuracy was estimated with a cross validation and is about 72%. Source: Own Figure.

#### 4 Results

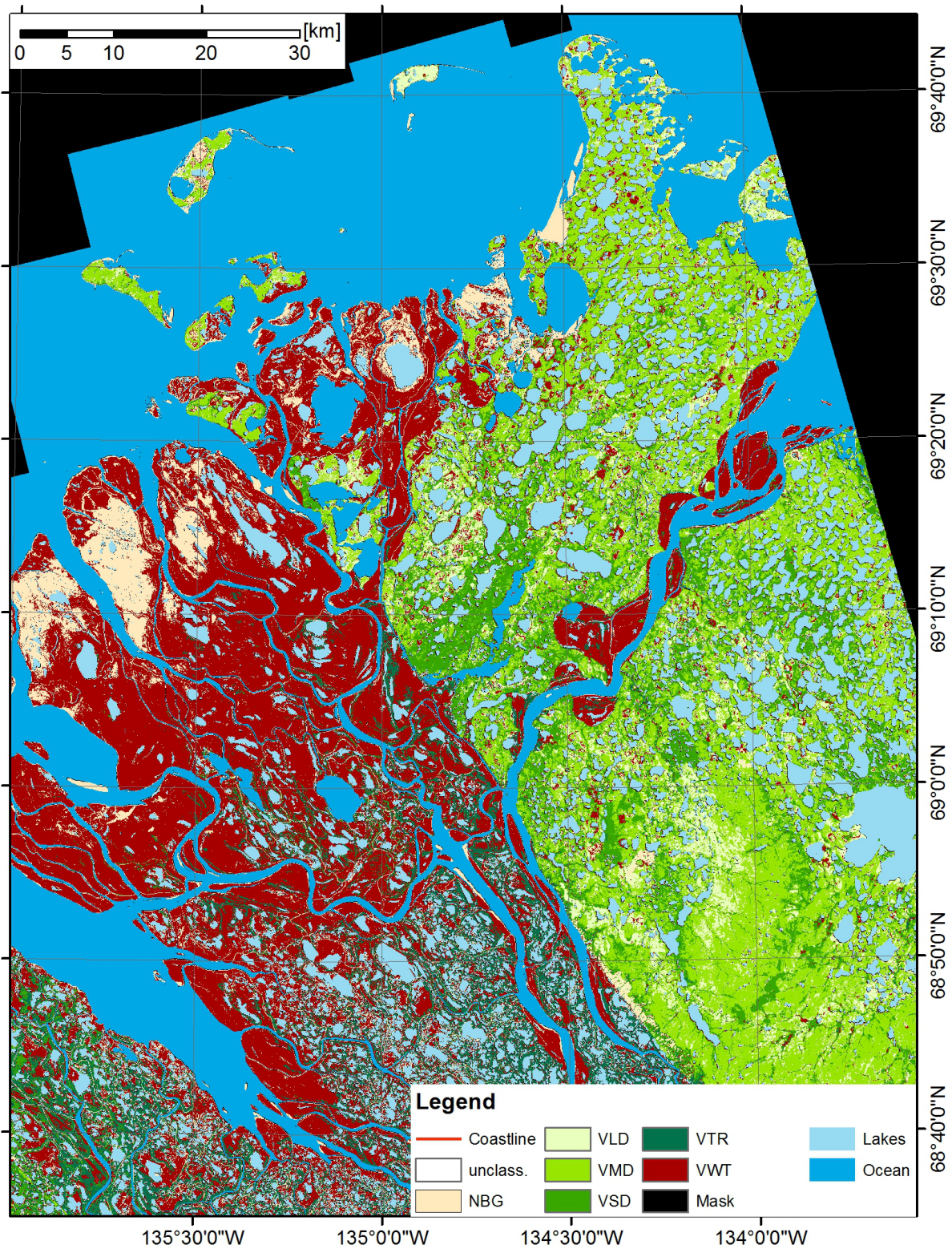


Figure 4.62: Mackenzie Delta classification result of supervised classification of co-polarized TSX and L-8 data. The classification was processed using the standard Maximum Likelihood classification. The training data were collected during in situ fieldwork and using high resolution airborne photography. The overall classification accuracy was estimated with a cross validation and is about 90%.

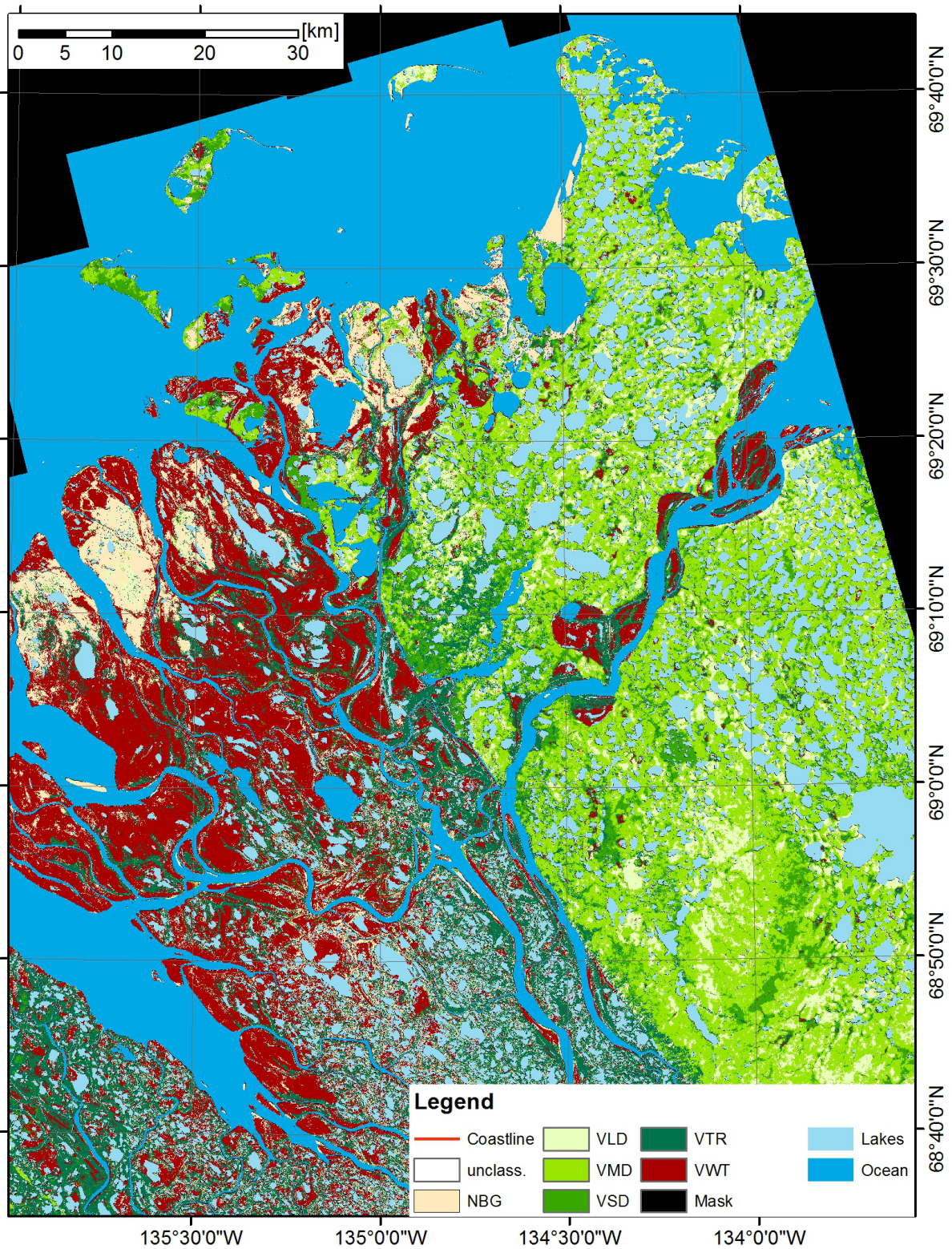


Figure 4.63: Mackenzie Delta classification result of supervised classification of co-polarized TSX was processed using the standard Maximum Likelihood classification. The training data were collected during in situ fieldwork and using high resolution airborne photography. The overall classification accuracy was estimated with a cross validation and is about 68%. Source: Own Figure.

## 4 Results

### 4.3.2.2 Banks Island

The supervised and unsupervised classifications were performed for the test site Banks Island to test the transferability of the approach and of the results. The classifications were done using co-polarized TSX and L-8 imagery (see Table 2.7). The TSX data were processed as described in Section 3.1.1.3. The data were filtered with the Non-Local Means filter specified in Section 3.1.1.2 with respect to the findings of Section 4.1.1. Prior to the land cover classification the water bodies of the test site were classified based on the iterative water classifier and reference data of NWT-Geomatics (2014). The L-8 data were sampled to a geometric resolution of 15 m using the bilinear resampling function of ENVI 5.1. The TSX data were sampled to a geometric resolution of 15 m using the pixel aggregate function of ENVI 5.1. The data of L-8 and TSX were manually registered afterward and showed in average a mean location error of less than 20 m, respectively, of less than two pixels.

The classification process of unsupervised and supervised classification was the same as described for the test sites of the Mackenzie Delta Regions. Each final land cover classification of a cross validation experiment had five land cover classes (N BG, VLD, VML, VMH, VWT) and the masked water bodies (NWA). The supervised classification, the merging of unsupervised classes and the assessment was carried out using the ground truth reference data collected during the field work in 2012 (see Section 2.2.1). Figure 4.64.a shows the L-8 false color composite of test sites Banks Island. The image indicated that the spectral differences between the land cover types were small and the image mainly showed brownish and dark greenish colors. Figure 4.64.b shows the span of the TSX co-polarized data. The backscatter variations were mainly related to the up and low lands and the water areas. Figure 4.64.c and Figure 4.64.d show the results of unsupervised FKM-ML classification with twenty classes. Both classifications clearly highlighted the valleys of the Eams and Woon River and the sparse vegetated uplands of the Aulavik National Park with low class values. IN addition, the low lying valleys of northern Banks Island were pronounced with higher class numbers in both classifications. This indicated comparable high greenness and Alpha T-Matrix values.

The results of the unsupervised and supervised classification are shown in Figure 4.65. As observed for the test sites of the Mackenzie Delta, the highest overall classification accuracy was realized when TSX and L-8 data were combined. The average accuracy of the unsupervised classification was about 68% (Figure 4.65.a) and high for the classes N BG, VLD and VWT - this is in correspondence to the results of the Mackenzie Delta test sites. The classification accuracies were lower for the classes VML and VMH with values of 61% and 15%, however. The results of class VML indicated again a systematic error of the unsupervised classifier since the accuracy was less than 50%. The classification of TSX data alone showed the suitability of the co-polarized for the classification of the classes N BG and VLD. The accuracy of class VWT was comparable low with an accuracy of 65%. The classes VML and VMH showed low accuracies of about 35%. As noted before this indicated systematic errors in the classification process or during the merging of the unsupervised classes. The average overall classification accuracy was estimated with a value of about 62%. The classification of L-8 data showed that the multispectral data were suited to classify N BG, VLD and VWT on a high level of confidence with classification accuracies of about 78%. The classification of VML and VMH was on lower level of confidence with accuracies of 63% and 69%. The accuracies of the supervised classification of the site Banks Island showed that the average overall

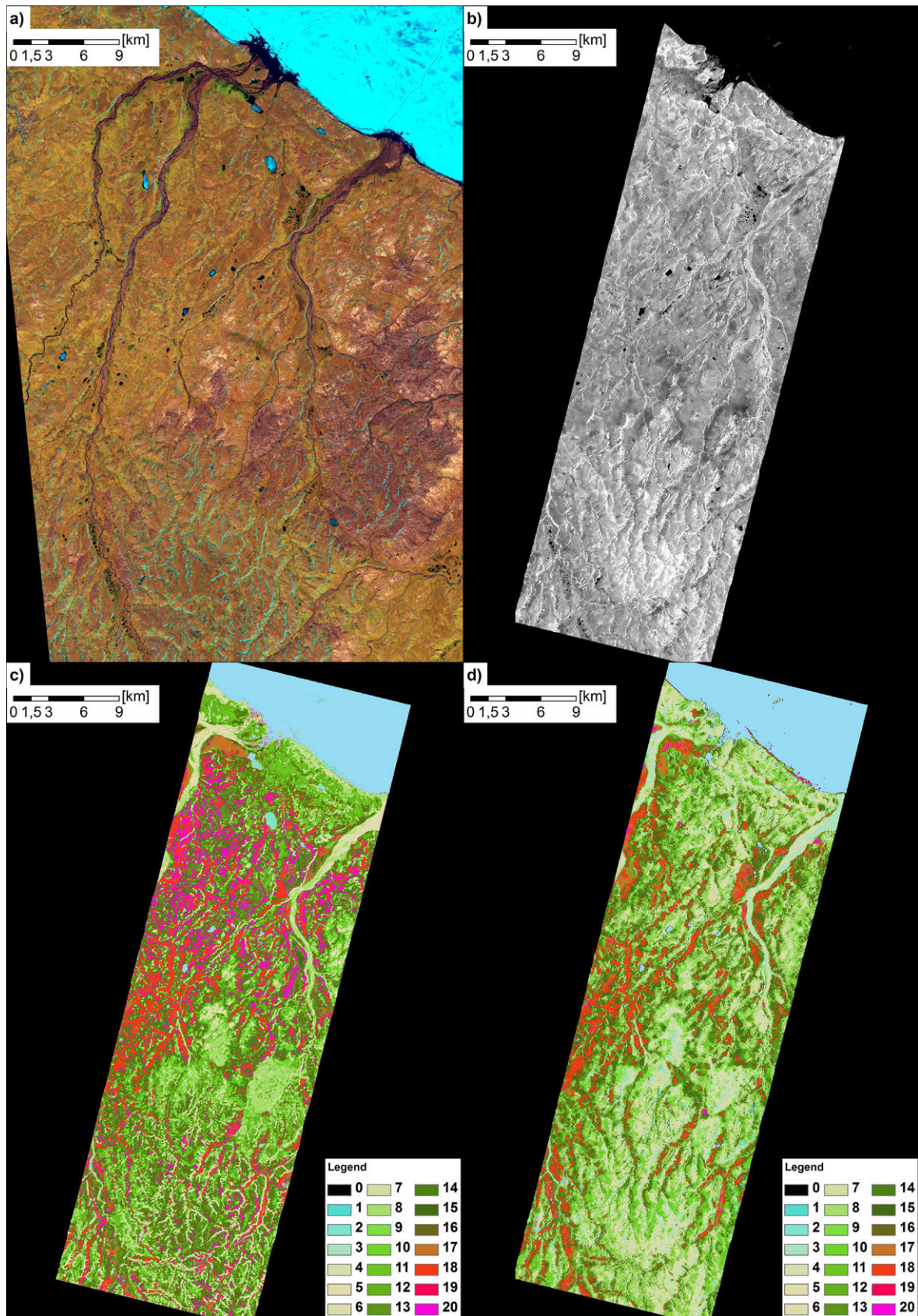


Figure 4.64: Banks Island (BIS) unsupervised classification results: a) false color composite of L-8 (R=Band 7, B=Band 5, G=Band 4), b) Span of co-polarized TSX, c) unsupervised classification of L-8 and d) unsupervised classification of co-polarized TSX. The water bodies were classified with the iterative water classifier based on the co-polarized TSX data. Source: Own Figure.

#### 4 Results

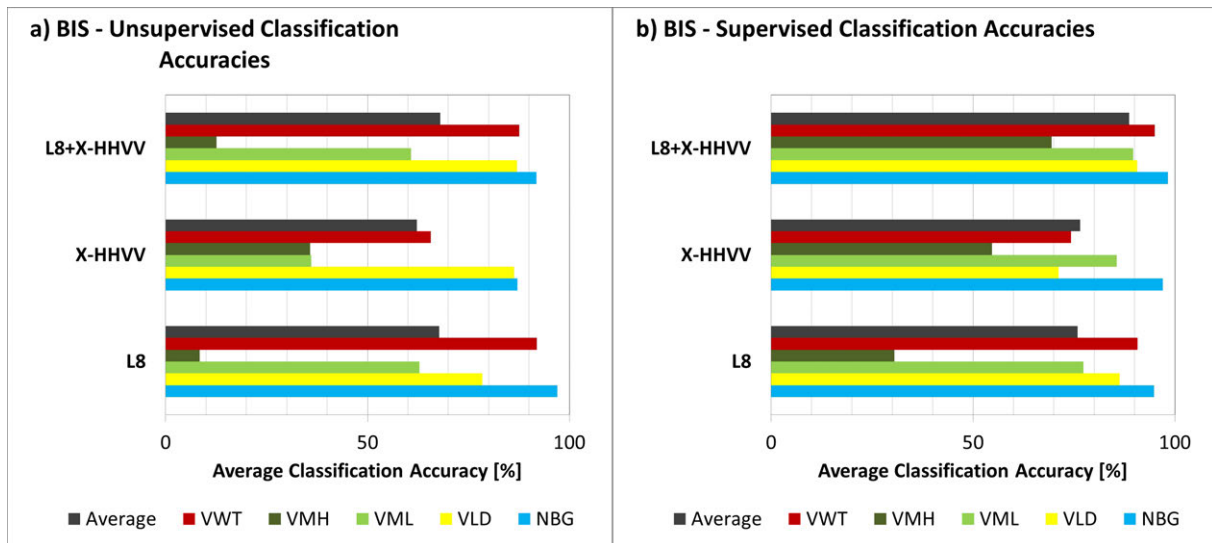


Figure 4.65: Classification accuracies of Banks Island land cover classifications: a) accuracies of unsupervised FKM-ML classification and b) accuracies of supervised Maximum Likelihood classification of L-8 (L8) and TSX co-polarized data (X-HHV). Source: Own Figure.

classification accuracy of TSX data was as high as the accuracy of L-8 data (Figure 4.65.b). Both classifications showed high accuracies of more than 75% for the classes NBG, VLD, VML and VWT. The classification of TSX data showed an accuracy of class VMH of 55%. The classification of L-8 data provided an accuracy of 30% for this class. The classifications accuracies increased when both data sources were used for the classification. The overall classification accuracy was then up to 88% and the class VMH had an accuracy of 69%. The accuracies of the other classes were high and above 88%. These results compare well to the findings of the Mackenzie Delta. However, the mixed tundra was difficult to be identified with either optical or PolSAR data. The combination of both data enhanced the classification accuracy but the unsupervised classification was still on low level of confidence. The unsupervised classification showed good performance for the classes NBG, VLD and VWT in contrast. Examples of the unsupervised and supervised classifications of TSX and L-8 are shown in Figure 4.54. The differences between supervised and unsupervised classifications were bigger, compared to sites of the Mackenzie Delta - especially the classification of the norther wetlands differed.

The unsupervised classification was performed for the test site Banks Island to test the transferability of the approach. The analysis was performed using co-polarized TSX and Landsat 8 imagery. The in situ data collected during the field work 2012 were used as reference and training of the supervised classifier. The results showed that the accuracies of both supervised and unsupervised were lower compared to the results of the Mackenzie Delta Region. The best result among the supervised classifications was observed for the combination of Landsat 8 and co-polarized TSX data and the overall classification accuracy was about 88%. The best unsupervised classification was observed for this data combination and was up to 68%. It was found that the PolSAR data were suitable to differentiate between the tussock and non-tussock tundra. The average classification accuracies of these classes were higher for the PolSAR data than for the optical data in supervised and unsupervised classification. Both data were suited to characterize the open substrate, the sparse vegetated areas and the wetlands.

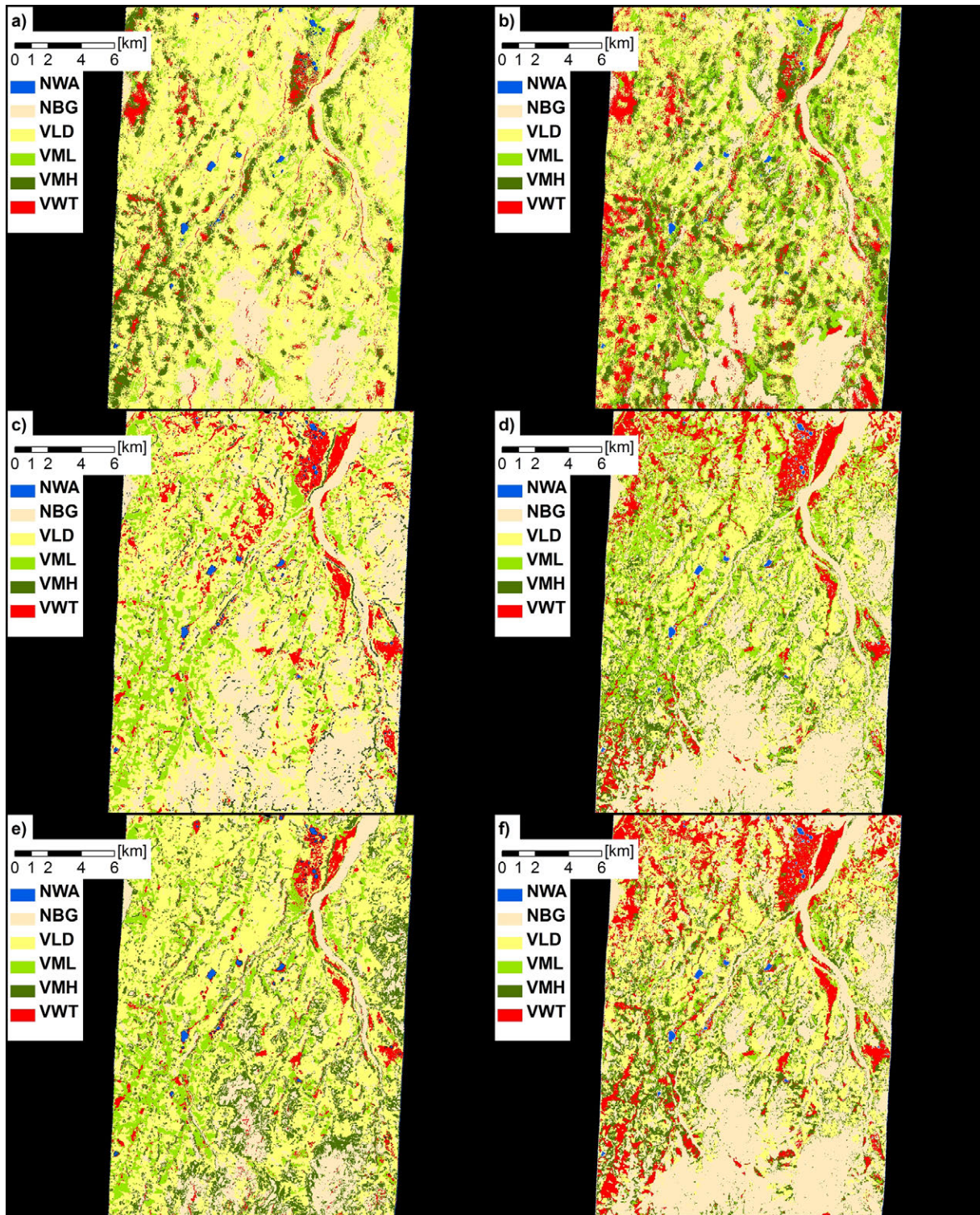


Figure 4.66: Banks Island (BIS) classification results for: a) unsupervised classification of co-polarized TSX, b) supervised classification of co-polarized TSX, c) unsupervised classification of L-8, d) supervised unsupervised classification of L-8, e) unsupervised classification of of co-polarized TSX and L-8 and f) supervised classification of co-polarized TSX and L-8. Source: Own Figure.

## 4 Results

### 4.3.2.3 James Bay

The unsupervised land cover classification was processed for the test site of the James Bay. The data used were co-polarized TSX and L-8 data (see Section 2.2). No land cover reference data were available for the site and the assessment of the classification results remained preliminary, qualitative and was based on the visual interpretation of high resolution airborne photography. All of the data were processed as described in Section 3.1.1.3. The PolSAR data were filtered with the Non-Local Means filter specified in Section 3.1.1.2 and with respect to the findings of Section 4.1.1. Prior to the land cover classification the water bodies of the test sites were masked based on the vector data of NWT-Geomatics (2014). The optical data of L-8 and TSX were manually registered and the estimated average location error was again less than 20 m. The data were finally sampled to a geometric resolution of 30 m using the pixel aggregate function of ENVI 5.1.

The FKM-ML was applied once to the L-8 data and once to the TSX data. The results of these unsupervised classifications are shown in Figure 4.67. Figure 4.67.a shows the false color composite of L-8. The image indicated the exposed bedrock of the hills and the vegetated ground very clearly. Figure 4.67.b shows the span of the TSX data. In contrast to the optical imagery, the differences between vegetated and non-vegetated ground were less obvious. The unsupervised classification results of the L-8 data showed that the non-vegetated hill tops and bare substrates of the intertidal zone were grouped as single classes (4.67.c). The wetlands at the mouths of Namapistikw, Sabascunica, Clergue and Torviens River (see Figure 2.12) were classified as class with comparable low greenness. The differences in the vegetation were mainly caused by the varying density of the spruces. Therefore at least four unsupervised classes could be distinguished that were related to the presence of spruce. The unsupervised classifier was capable to group the main land cover types in single classes.

In contrast to these findings, the unsupervised classification of the TSX data showed mainly the differentiation of the wetland and non-wetland vegetation (4.67.d). The wetlands were shown in red color and therefore with comparable high Alpha (T-Matrix) and double bounce values. The exposed and non-vegetated hill tops, as well as the bare ground of the intertidal, were shown in beige to blue colors and were characterized by comparable low Alpha values. The contrast of these classes was less clear compared to the L-8 classification. Beside this the TSX data were unsuited to highlight the differences in the vegetation, e.g. the varying density of the spruces.

The quantitative analysis will require more and particularly better documented reference data on the land coverage. The first findings indicated that the X-Band data had limited suitability for the land cover classification. The patterns of the spruce were not recognized in the PolSAR classification. However, the X-Band PolSAR data are likely useful for the characterization and classification of the wetland complexes and the bare ground substrates.



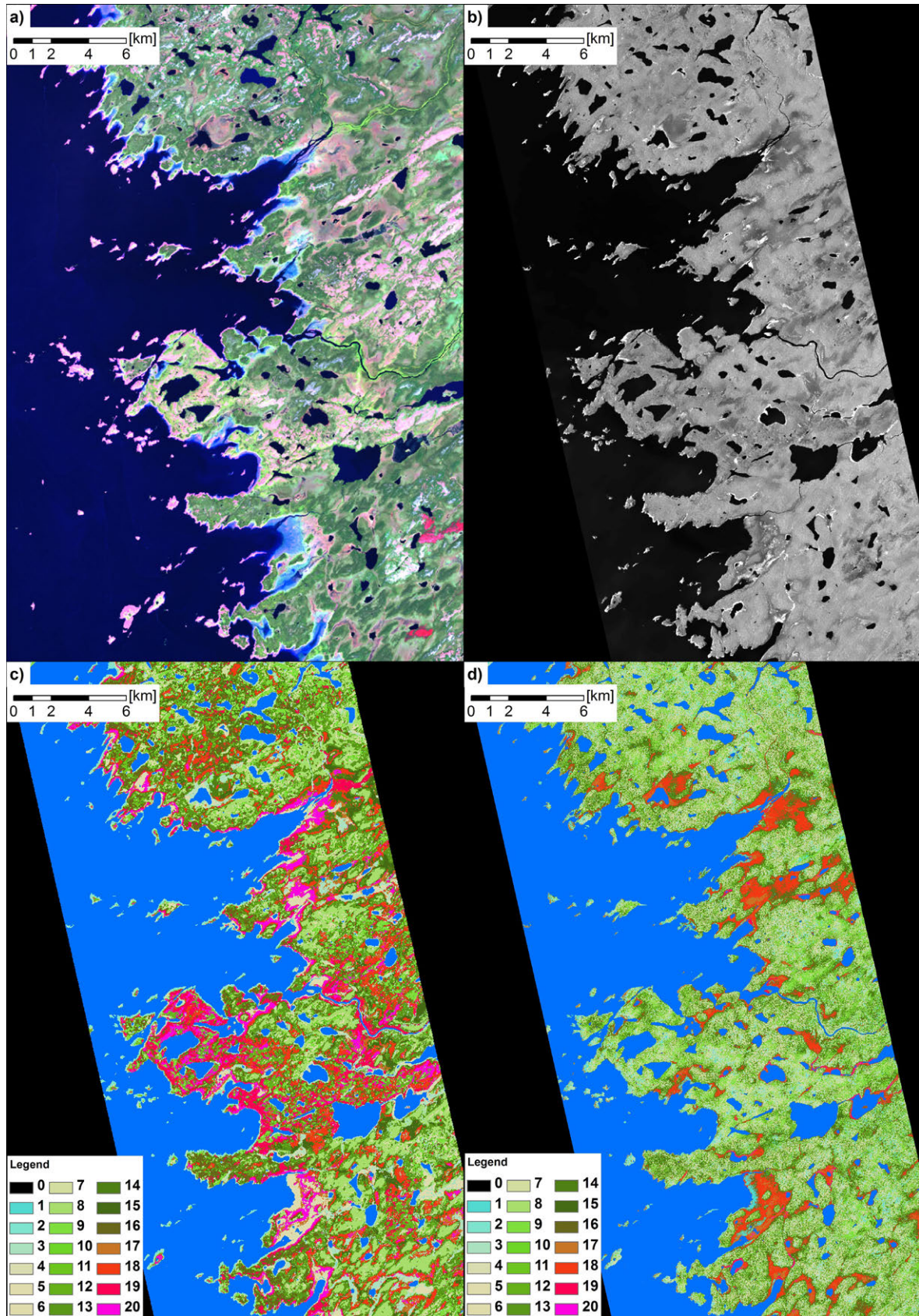


Figure 4.67: James Bay (JAB) unsupervised classification results: a) false color composite of L-8 (R=Band 7, B=Band 5, G=Band 4), b) span of co-polarized TSX, c) unsupervised classification of L-8 and d) unsupervised classification of co-polarized TSX. The water bodies were classified with the iterative water classifier based on the co-polarized TSX data. Source: Own Figure.

### 4.3.3 Terrain and Landform

The following section shows the results of the terrain and landform classification of the four test sites Caribou Hills of the Mackenzie Delta Region, northern Mackenzie Delta and Richards Island, northern Banks Island and James Bay. The following sections present the results of each individual site and are structured as follows. The first part of the section shows the selection of suitable TPI scales for the landform classification. The selection was based on the analysis of the TPI stack. The features analyzed were the change of the mean TPI, the change of the variance, the rate of variance changes between two adjunct scales or the direction of the TPI changes from scale to scale (see Section 3.1.3). The identification of thresholds for the classification of elevation and slope is shown afterward. The identification of suited thresholds was based on histogram analysis and Jenks-Natural-Breaks classification (see Section 3.2.2.1). The continuous landform classifications of different TPI scales are then shown in the following. The continuous classifications were processed as described in Section 3.2.4. The legend of all continuous classifications is the same and is shown in Figure 3.20. The elevation and slope thresholds used for the continuous classification followed the specifications of Barsch & Liedtke (1985). Therefore the elevation thresholds used were: 5, 10, 15, 20, 50, 100, 150, 200, 250 and 300 m. The slope threshold used were: 1°, 2°, 5°, 7°, 10°, 15°, 20°, 25°, 30°, 45° and 60°. With respect to the findings of Section 4.2 the TPI thresholds used for the classification were: -1.0, -0.5, -0.25, 0.0, +0.25, +0.5, +1.0. Therefore the continuous classification has 880 potential classes. These continuous landform classifications are drawn for each test site for six different scales, respectively, different estimation window sizes of the TPI.

The second part of each section shows the Nested-Means landform classification of Iwahashi & Pike (2007) and the TPI based landform classification of Weiss (2001) (see Section 4.3.3). Both classifications were processed in SAGA GIS 2.1.2. The Nested-Means Classification was processed with an estimation window size of 21x21 pixels (which is equal to SAGA GIS's radius of 10 pixels). The number of classes was set to 16. The landforms are therefore classified using the slope, texture and convexity. The thresholds were automatically set using the histogram information. The TPI based landform classification was processed with standard settings for all test sites. The first TPI radius was set to 100 m. This corresponds to an estimation window size of 15x15 pixels for the TDX IDEM data and an estimation window size of 7x7 pixels for the GDEM data. The second radius was set to 1000 m and corresponds to estimation window sizes of 153x153 pixels (TDX IDEM) and of 65x65 pixels (GDEM). The other thresholds were set internally and were 5° for the slope and -1.0 and +1.0 for the TPIs according to Weiss (2001), Jenness (2006). These two landform classifications are compared in the following to the discrete landform classifications of two selected TPI scales (see Section 4.3.3).

These discrete landform classifications were processed with the following settings: The number of elevation, slope and TPI classes was set to three and therefore the final classifications had 27 classes. The elevation and slope thresholds were estimated with the Jenks-Natural-Breaks classification. The TPI thresholds were set to -0.5, 0.0 and +0.5 with respect to the findings of Section 4.2. Finally, the discrete landform classifications were interpreted and the classes were manually merged and grouped - based on the specifics of the test site. The results and key findings of this section are summarized at the end of Section 4.3.3.4 on Page 238.

#### 4.3.3.1 Mackenzie Delta Region - Caribou Hills

The TPI stack of the test site Caribou Hills (see Section 148) was analyzed to identify scales that were suited to describe the landform ensemble of the site. Figure 4.68.a shows the development of the mean values of the TPI with increasing scale (estimation window size). It was observed that the mean was slightly negative for all scales up to a maximum of about -0.014. The mean values showed variations for the different estimation window sizes (scales) and the plot showed two turning points of the graph at 200 m and 2000 m. The first location showed the turning from decreasing to increasing TPI values, the second location showed the turning from increasing to decreasing TPI values. No turning points were identified for the average variance of the stack (Figure 4.68.b). This average variance was increasing with increasing scale and indicated a higher variation of the TPI values. The rate of change (see Section 3.2.4) showed two turning points at locations 200 m and 300 m (Figure 4.68.c) and indicated meaningful changes of the local variance at these scales. The frequency of positive TPI changes (Figure 4.68.d) indicated two turning points of the TPI with increasing scale. Between scales of 75 m and 500 m the TPI changes were negative. From scales 500 m to 1300 m the changes were positive and from scales 1300 m to 3000 m the changes were again negative.

With respect to these observations, four scales were identified to be meaningful for the characterization of the test site Caribou Hills: A first one with scales less than 500 m, a second one with scales greater than 500 m and less than 1300 m, a third one with scales greater 1300 m and less than 2000 m and finally the scales greater 2000 m. Therefore the continuous classifications were processed for TPI scales of 100, 500, 1000, 1500, 2000 and 3000 m. Figure 4.70 shows that the differences between the continuous classifications were maximal between the 100, 500, 1000 and 3000 m scales. That corresponds to the findings of the TPI stack analysis.

The analysis of the histogram of the elevation showed that meaningful elevation changes took place between the sea level and about 20 m, between 20 m and 50 m, between 50 m and 70 m, between 70 and 110 m and above 110 m (Figure 4.69.a). The histogram showed four major peaks and the identified levels can be related to the alluvial low lands and the delta, the steep proterozoic transition, the pleistocene to holocene uplands and the paleogen to neogen Caribou Hills. The histogram of the slope did not show any significant breaks of the histogram (Figure 4.69.b). The frequency of slopes less than 5° was high, medium for slopes between 5° and 10° and low for slopes greater 10°. The slope thresholds identified by Jenks-Natural-Breaks classification were therefore nearly equally spaced and indicated slope values of 1°, 3°, 5°, 8° and 12° as reasonable breaks and classes.

With respect to these findings, the discrete landform classifications were processed with elevation breaks of 20 m and 100 m and slope breaks of 3° and 10° and for two TPI scales of 250 m and 2000 m. These scales were chosen since they were identified to represent meaningful breaks in the histogram of the stack and also showed reasonable results in the visual analysis. The breaks of a single TPI were fixed to -0.5 and +0.5. The discrete classifications are shown in Figure 4.71. Both showed that the chosen elevation breaks classified the low alluvial delta complex (blue colors), the holocene to pleistocene uplands (green colors) and the neogen to paleogen Caribou Hills (brown colors). The classes of slopes less than 3° highlighted the flat plains of the delta, the plain mid and top-slopes of the upland and the flat lake surfaces.

#### 4 Results

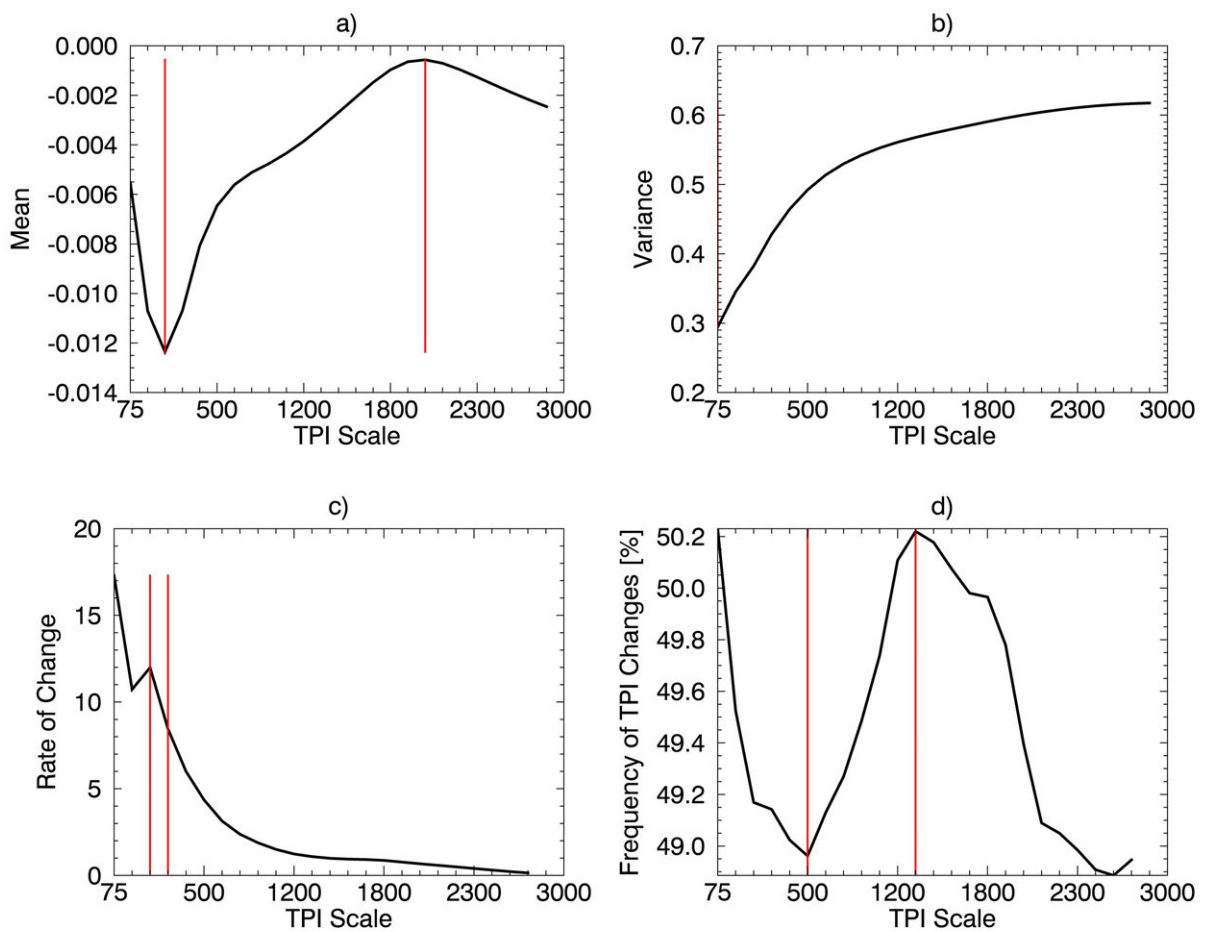


Figure 4.68: Selection of suitable TPI scales for the test site Caribou Hills for scales ranging from 75 m to 3000 m: a) mean, b) variance, c) rate of change and d) the frequency of positive TPI changes. The red lines indicate turning points. Source: Own Figure.

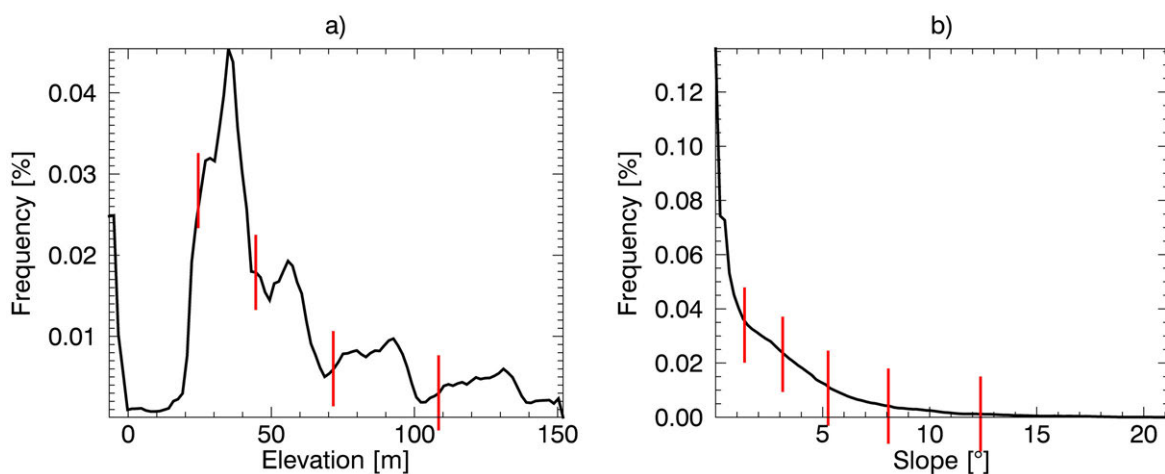


Figure 4.69: Selection of suitable elevation and slope thresholds for test site Caribou Hills using Jenks-Natural-Breaks classification: a) histogram of the elevation and b) histogram of the slope. The red lines indicate potential class thresholds. Source: Own Figure.

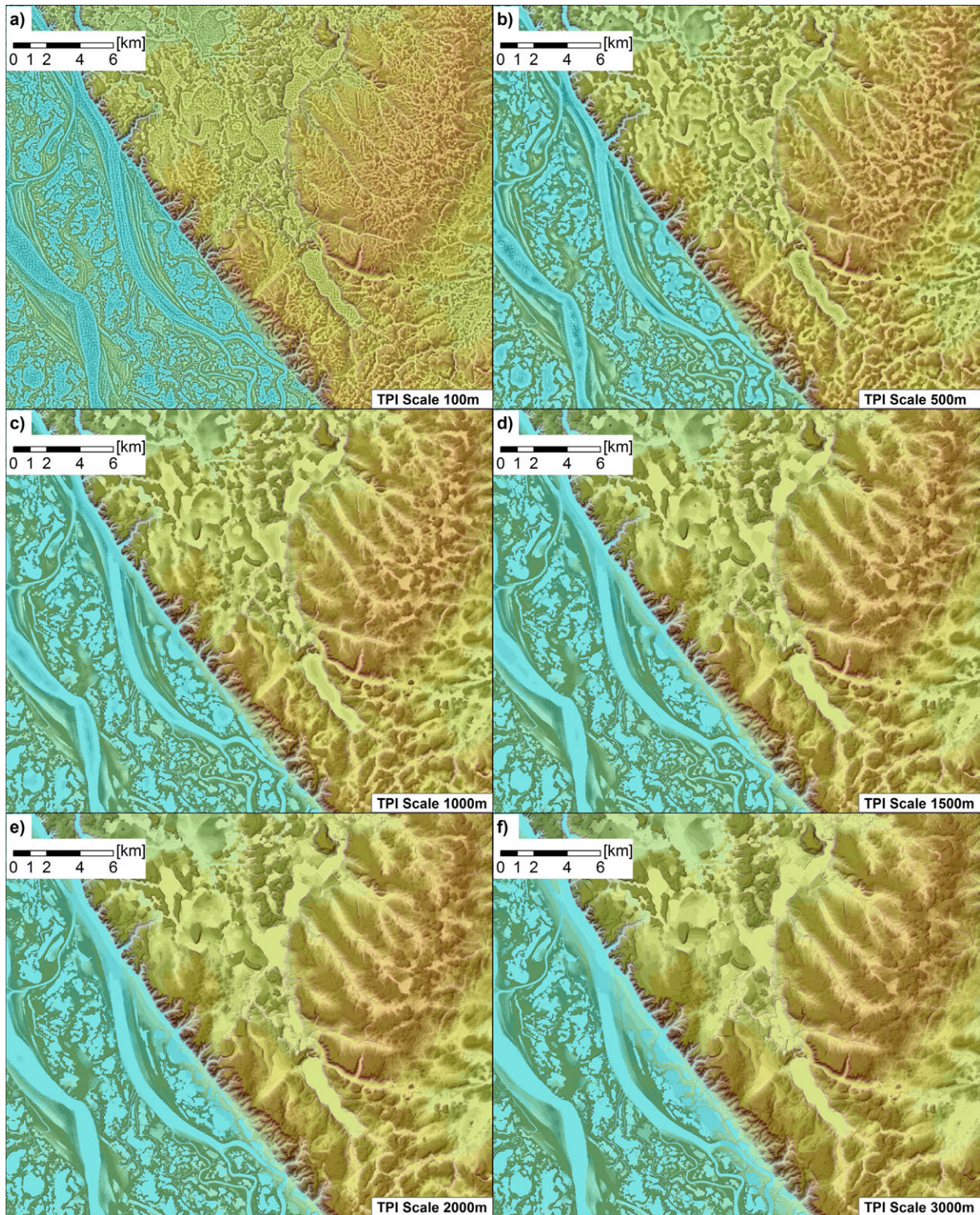


Figure 4.70: Continuous morphometric landform classification of the test site Caribou Hills for TPI scales of: a) 100 m, b) 500 m, c) 1000 m, d) 1500 m, e) 2000 m and f) 3000 m. The legend is shown in Figure 3.20 and the thresholds of elevation and slope were set in accordance to Barsch & Liedtke (1985). TDX IDEM with a spatial resolution of 13 m. Source: Own Figure.

4 Results

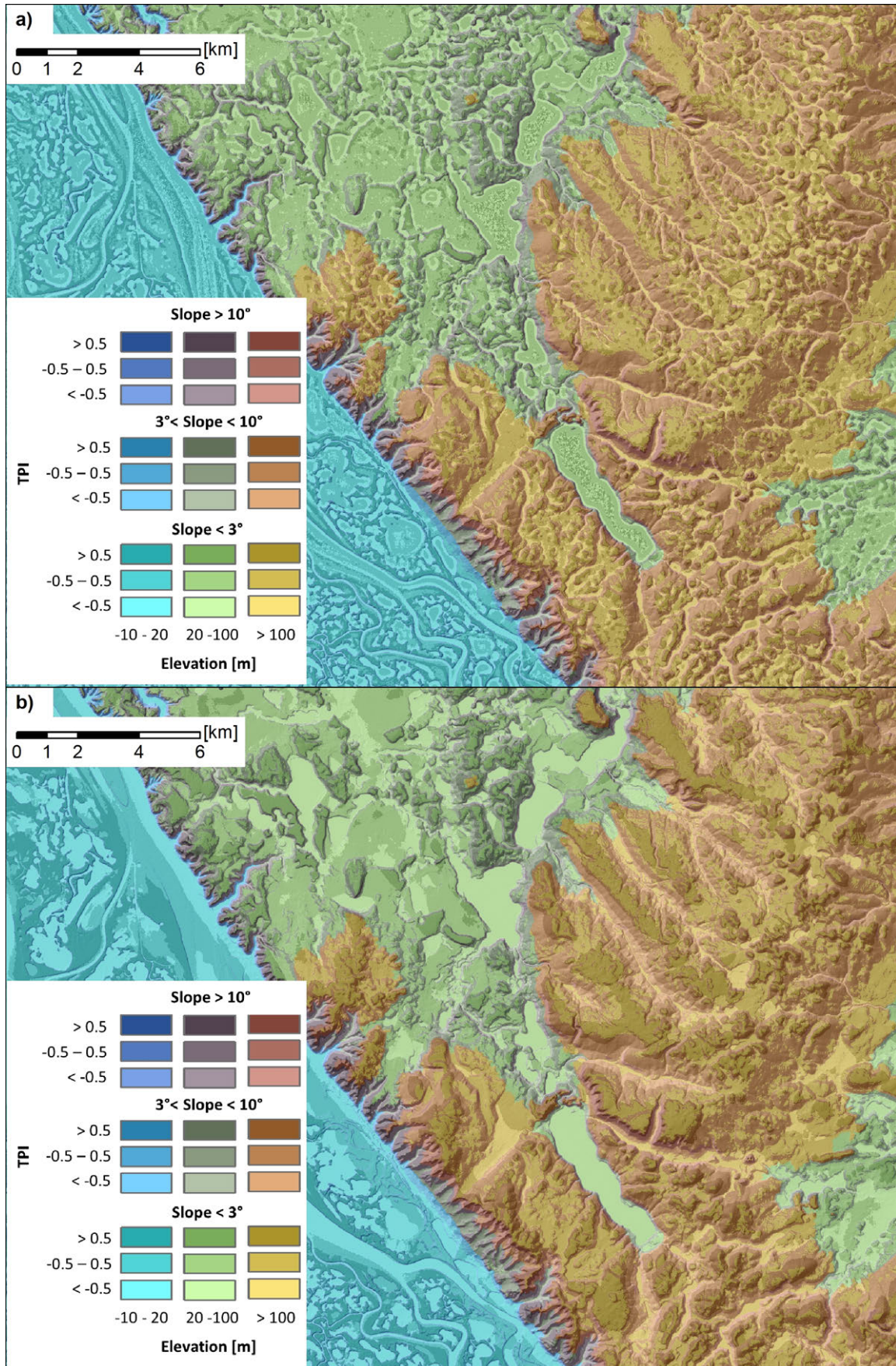


Figure 4.71: Discrete morphometric landform classifications of the test site Caribou Hills: a) morphometric landform classification based on elevation, slope and TPI (250 m) and b) morphometric landform classification based on elevation, slope and TPI (2000 m). TDX IDEM with a spatial resolution of 13 m. Source: Own Figure.

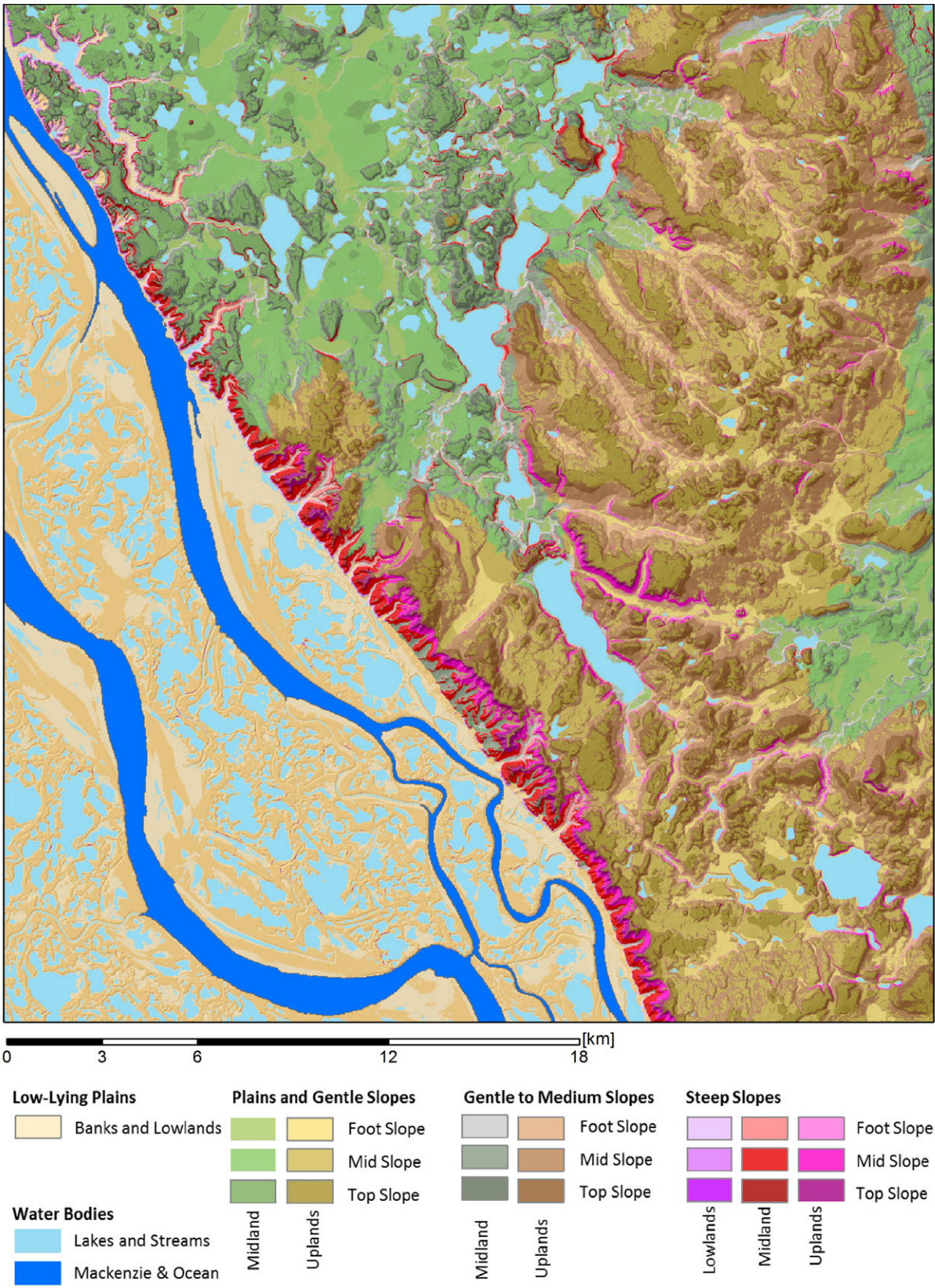


Figure 4.72: Discrete morphometric landform classification of the test site Caribou Hills based on a TPI scale of 2000 m and elevation and slope. Source: Own Figure.

## 4 Results

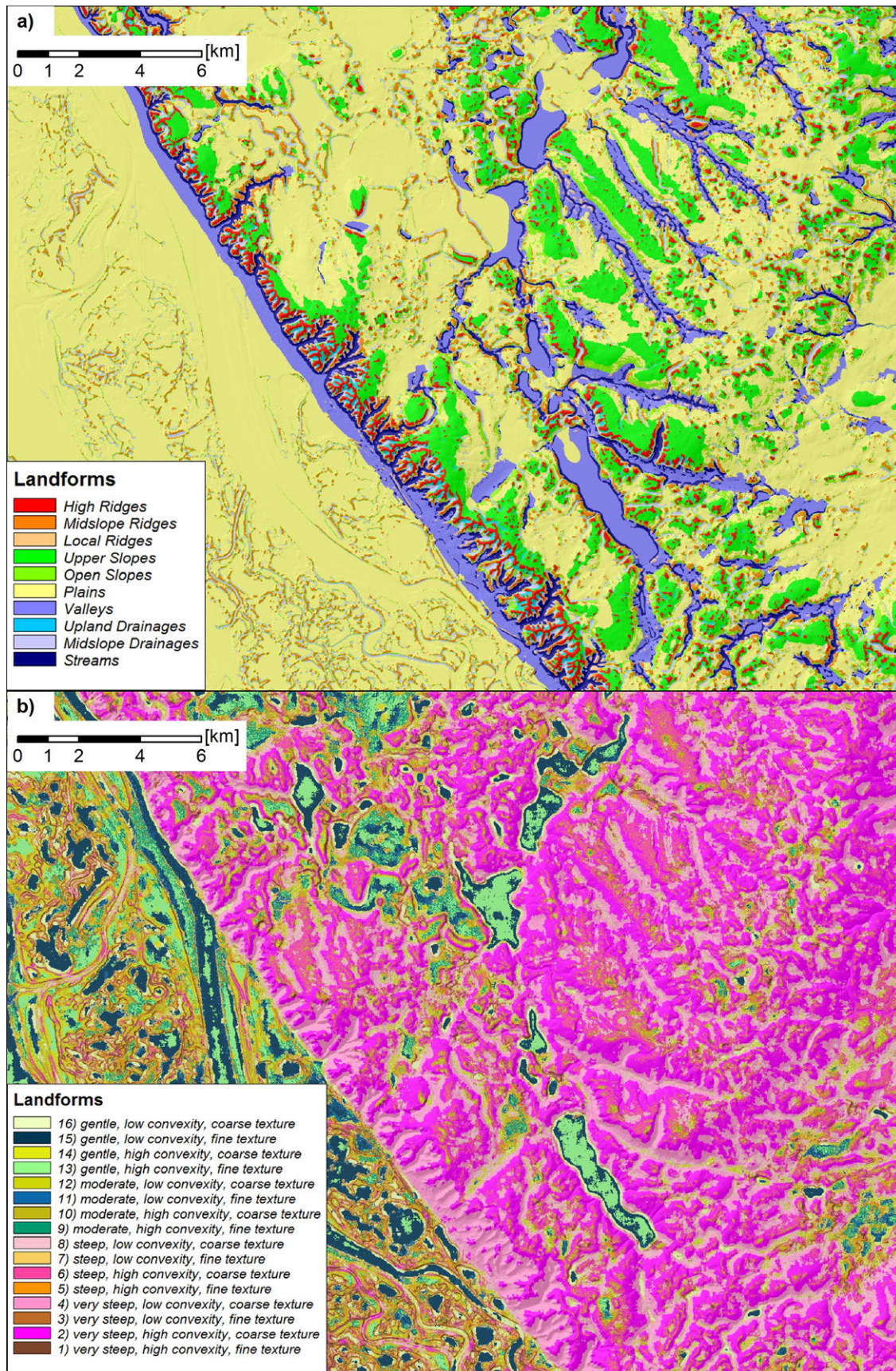


Figure 4.73: Morphometric landform classifications of the test site Caribou Hills: a) SAGA GIS standard TPI landform classification with TPI scales of 200 m and 2000 m and b) SAGA GIS standard Nested-Means landform classification with a estimation window size of 11x11 pixels. TDX IDEM with a spatial resolution of 13 m. Source: Own Figure.



The gentle to medium slopes ( $3^\circ$  to  $10^\circ$ ) indicated the flanks of the river and channels and the mid slopes of the Caribou Hills. The slope values greater  $10^\circ$  were present at the cliffs of the proterozoic formation and along the valleys of the Caribou Hills. The steep slopes were also present at some of the lake shores. The differences between the TPI scales of 250 m and 2000 m were mainly related to the local and regional landform features, e.g. the classification of local or regional peaks and valleys. This is visible along the eastern top-slopes of the proterozoic formation, for example. The small TPI scale of 250 m highlighted the local peaks and exposed tops, whereas the TPI scale of 2000 m grouped these forms to one class with regional relevance. Figure 4.72 shows the same classification with TPI scale of 2000 m and with more distinct colors. In addition, the different TPI classes of the alluvial delta complex were merged and water bodies were overlaid. The classification further highlights the shoulders and flanks of the valleys of the Caribou Hills and the separation of the top-slopes and open slopes. The legend provides a qualitative naming of the morphometric classes. This classification showed that the approach of threshold divided variables provided a clear regional overview on the landforms and the topographic features - even though the classification approach was simple and missed and multivariate analysis of the land surface parameters. Figure 4.73 shows the Nested-Means and the TPI based land cover classification. It was obvious that the content of information of the landform classifications varies significantly. The TPI based classification (Figure 4.73.a) showed that most areas of the delta and of the uplands were classified as plains. That meant that TPI values of both scales were between -1.0 and +1.0 and that the slope was less than  $5^\circ$ . The plain to gentle sloped ridges and top-slopes of the uplands and of the Caribou Hills were classified as open slopes. In addition, most of the lakes, the valleys of the Caribou Hills and the foot-slopes of the proterozoic formation were classified as Valleys. Some isolated spots along the cliff showed the class Upland drainage and Midslope Ridges. The local peaks along the eastern side of the cliff were classified as High Ridges.

The Nested-Means Classification classified the uplands and the Caribou Hills as Very Steep surface with coarse texture and varying convexity, in contrast to the TPI based classifications that classified the uplands as flat Plains. The plain banks of the Delta complex and the lake surfaces were classified as gentle sloped areas with fine texture in the Nested-Means Classification. Both classifications indicated that internal thresholds of the classifications did not reflect reasonable thresholds to separate actual landforms. Especially the TPIs of the TPI based classification showed only little variation and the thresholds of -1.0 and +1.0 were unsuited for the classification. Along with this the classifications did not provide a reasonable regional grouping of the landforms. All classifications that used the TPI to delineate landform classes showed the systematically miss-classification of regions close the proterozoic formation (see Section 4.2.3).

#### 4.3.3.2 Mackenzie Delta Region - Northern Delta

The TPI stack of the test sites Northern Mackenzie Delta was analyzed and showed that all of the mean TPI values of the different scales were negative. The mean was decreasing rapidly for scales between 75 m to 500 m. The values were then increasing up to a scale of 1000 m. The scales between 1000 m and 3000 m showed a gentle decrease of the mean TPI - without a turning point of the graph (4.74.a).

The average variance showed a rapid change between scales of 75 m and 500 m and a local maximum at a

#### 4 Results

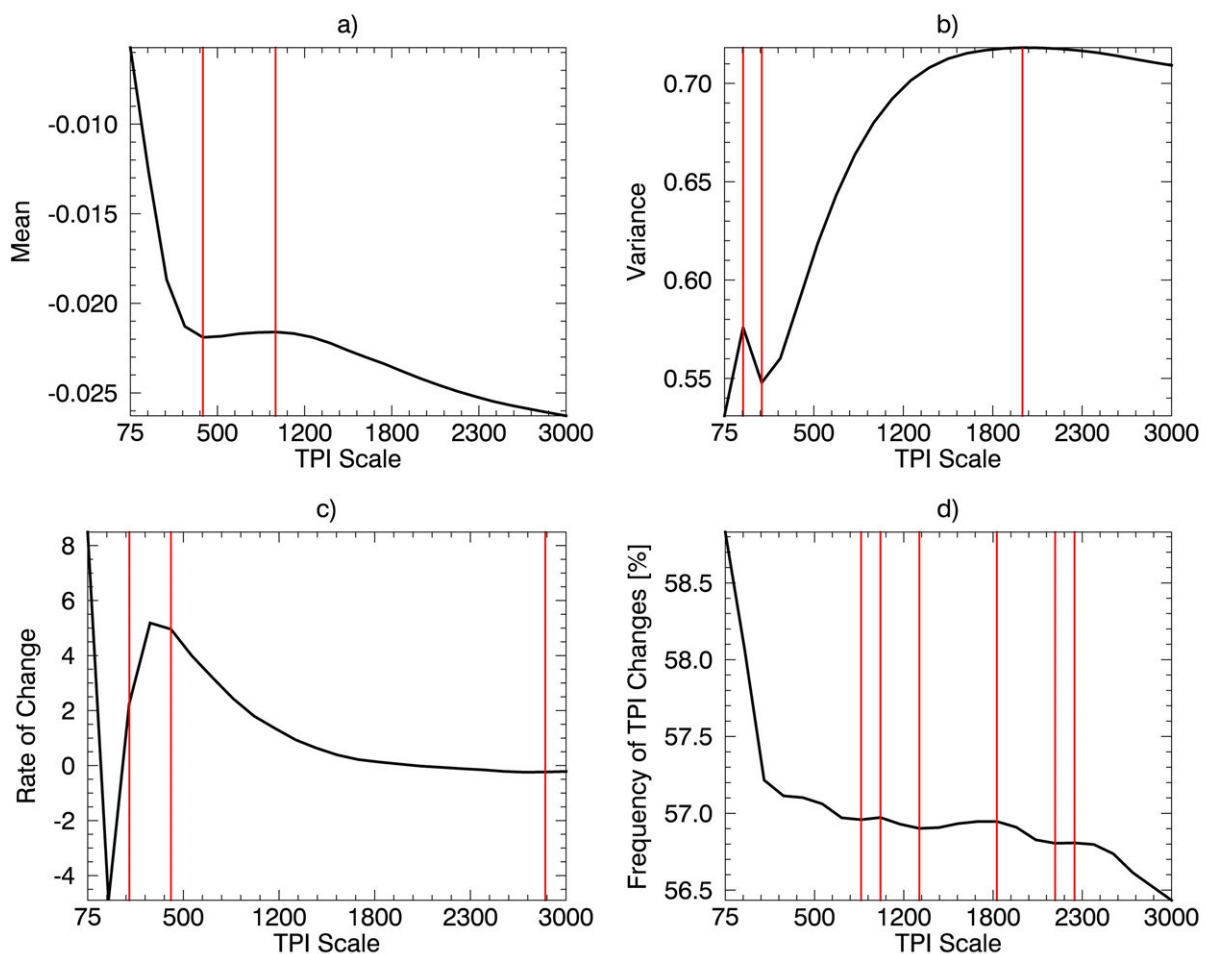


Figure 4.74: Selection of suitable TPI scales for Northern Mackenzie Delta for TPI scales ranging from 75 m to 3000 m: a) mean, b) variance, c) rate of change and d) the frequency of positive TPI changes. The red lines indicate turning points. Source: Own Figure.

scale of 200 m. The average variance was then increasing up to a scale of 2000 m (4.74.b). The graph of the rate of change had two turning points at scales of 100 m and 500 m (4.74.c). The TPI changes between the scales were positive but the frequency of these changes was decreasing with increasing estimation window size. The graph showed a nearly constant level between scales of 800 m and 2300 m with six local turning points (4.74.d).

Therefore four scales were identified that were meaningful for the characterization of the test site's landforms. These were the scales lower than 500 m, scales between 500 m and 1000 m, between 1000 m and 2000 m and scales greater than 2000 m. The continuous classifications of the Northern Delta were processed for TPI scales of 100, 500, 1000, 1500, 2000 and 3000 m and are shown in Figure 4.76. The most significant differences between the images were visible for scales of 100 m, 500 m and 2000 m. These scales were potentially best suited for the landform classification. In contrast, it was observed that scales greater 2000 m were very similar. This was in accordance to the observation that the spacing between the hills and the valleys of the inland was less than 2000 m. For this reason the TPI values did not show any meaningful changes with higher scale - but a high correlation and redundancy of the TPIs.

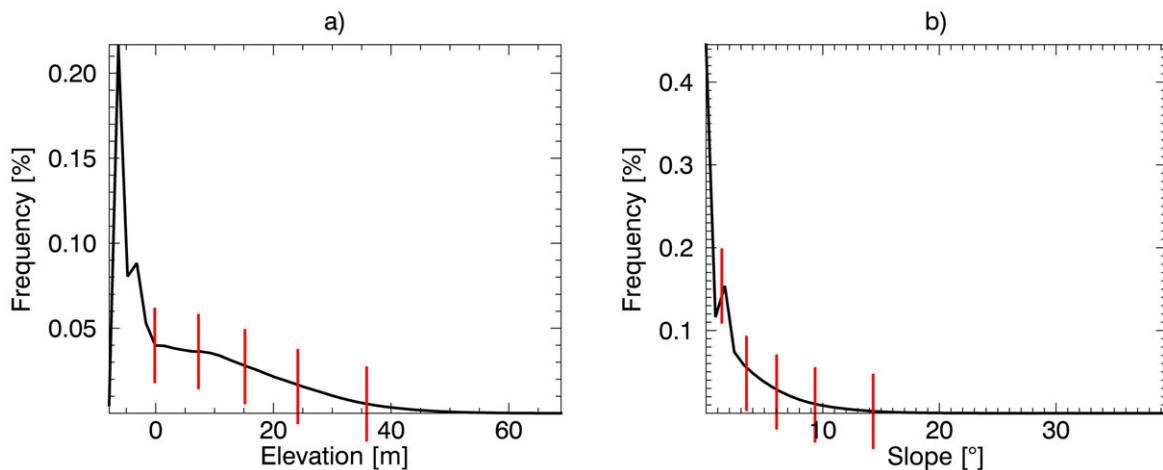


Figure 4.75: Selection of suitable elevation and slope thresholds for Northern Mackenzie Delta using Jenks-Natural-Breaks classification: a) histogram of the elevation and b) histogram of the slope. The red lines indicate potential class thresholds. Source: Own Figure.

The analysis of the elevation showed that a majority of the area lies above the sea level but lower than 0 m elevation (due to the WGS85 ellipsoid). These were the lowlands of the delta and the sea surface. The graph showed a plateau between 0 m and 10 m elevation that was related to the coast land and the upper shore zone. The hinterland showed elevation values higher than 10 m (4.75.a) up to maximum elevation of 70 m. The histogram of the slope did not show any significant variation of the frequencies but a discontinuity at 3° (Figure 4.75.b). The majority of the surface was plain with a slope less than 3°. Only few areas showed slopes greater 10°. These were the steep flanks of the hills and the eroding tundra cliffs of the shore.

With respect to these findings, the discrete landform classifications were processed with elevation breaks of 0 m and 10 m and slope breaks of 3° and 10° and for the two TPI scales of 250 m and 2000 m. The breaks of a single TPI were again fixed to -0.5 and +0.5. The discrete landform classification of the scale of 250 m is shown in Figure 4.77.a and of the scale of 2000 m in Figure 4.77.b. Both clearly showed the arrangement of the elevation units. The alluvial was low and plain to gentle slopes were classified (blue colors). The inland valleys and plains were situated on higher elevation and were classified with green color. The landform-classes of the upland of central Richards Island were shown in brown color. The distribution of the slope classes showed that steep slopes were mainly bounded to the northern and southern flanks of the inland hills, to the eroding tundra cliffs of the eastern and northern shore and to the small pingo features. The differences in the scales were again related to local and regional TPI features, e.g. to local or regional peaks and valleys.

Figure 4.78 shows the same classification with a scale 2000 m and with more distinct colors. The TPI classes of the alluvial delta complex were merged and water bodies were overlaid. The legend provides a qualitative naming of the morphometric classes. The merging and coloring was the same as done for the test site Caribou Hills (compare Figure 4.72). The classification showed to be suited to for the detection of the landform arrangement as noted above. (Section 4.2.3.2).

#### 4 Results

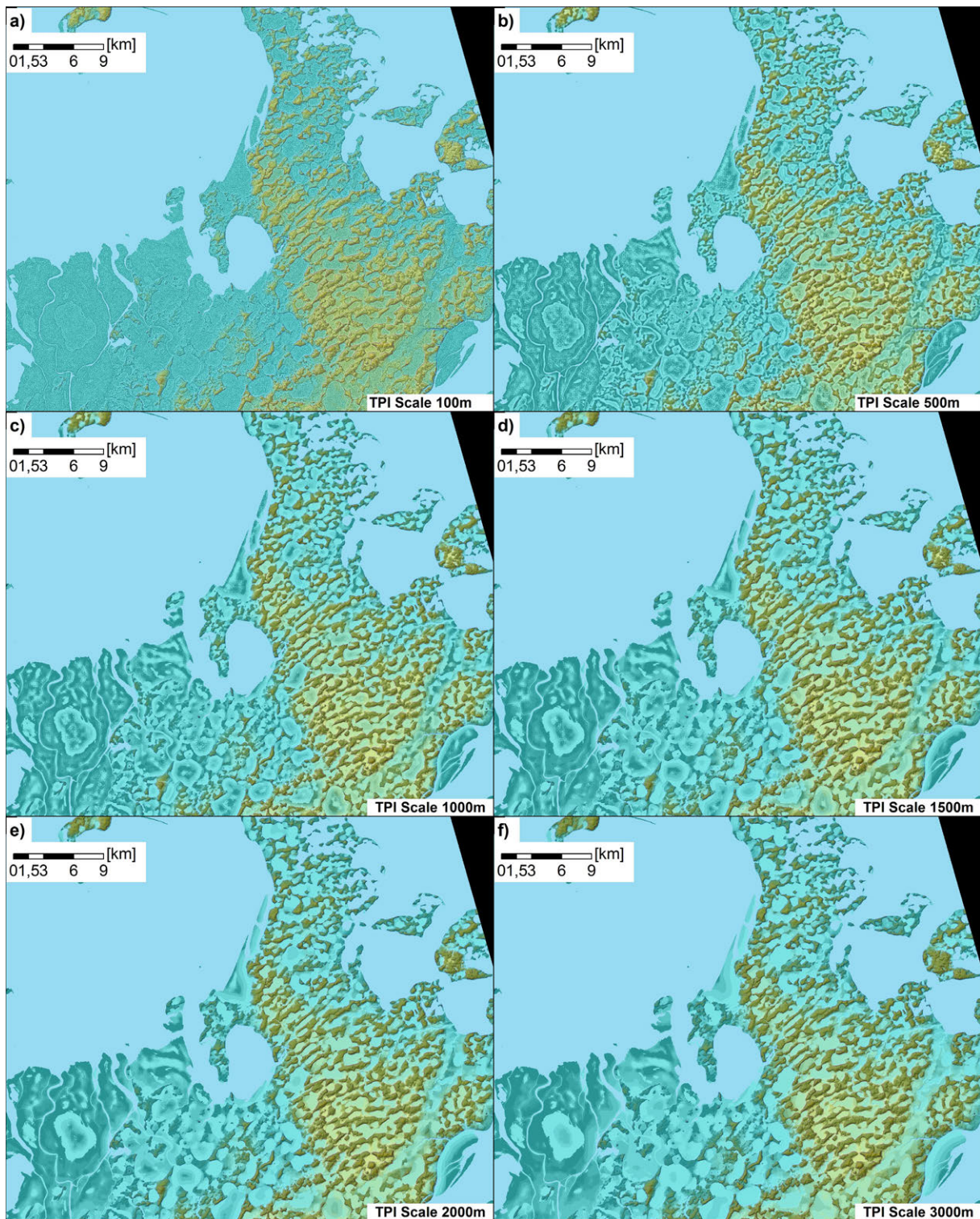


Figure 4.76: Continuous morphometric landform classification of the Northern Mackenzie Delta for TPI scales of: a) 100 m, b) 500 m, c) 1000 m, d) 1500 m, e) 2000 m and f) 3000 m. The legend is shown in Figure 3.20 and the thresholds of elevation and slope were set in accordance to Barsch & Liedtke (1985). Data Source: TDX IDEM with a spatial resolution of 13 m.

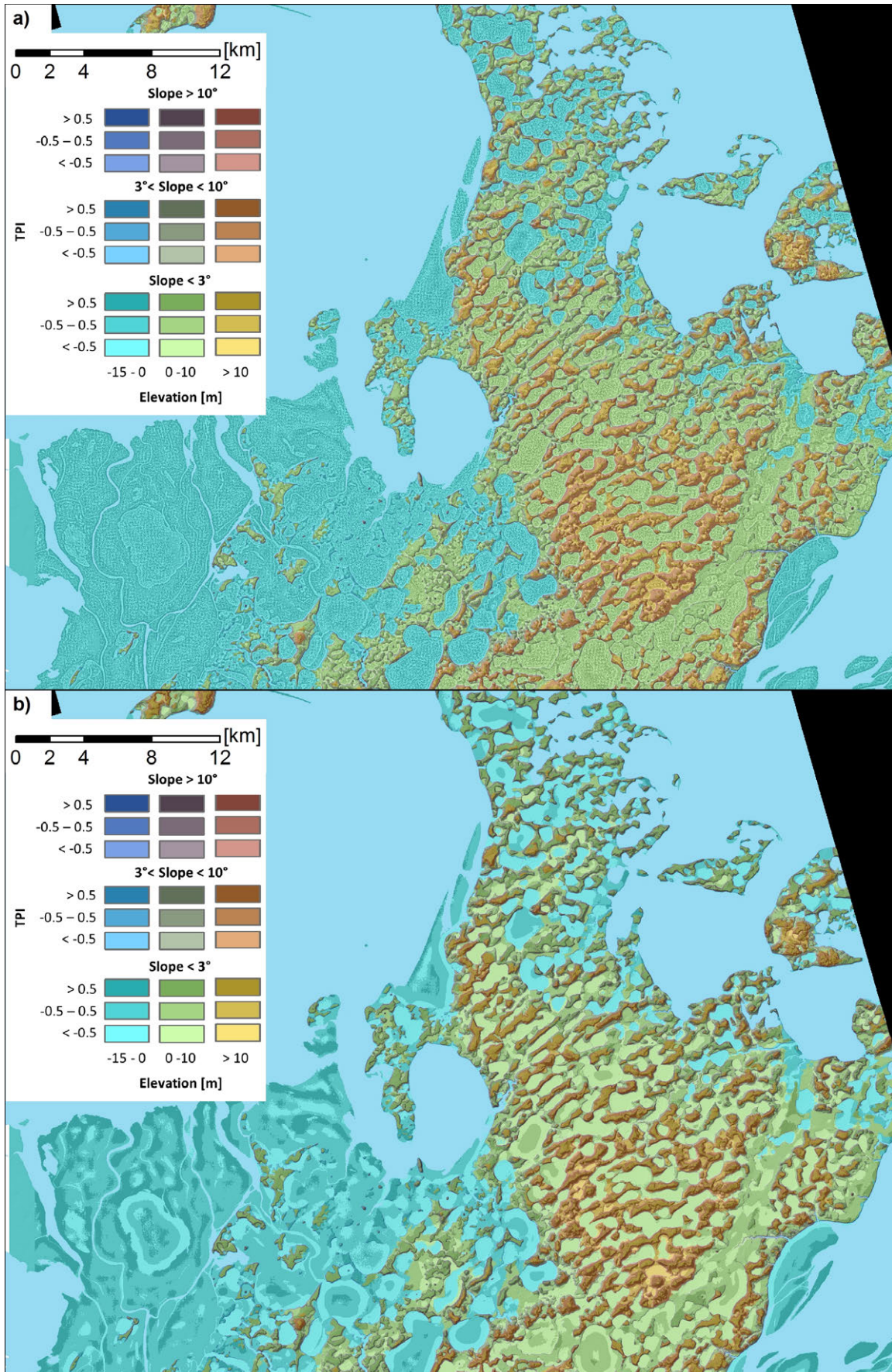


Figure 4.77: Morphometric landform classifications of the Northern Mackenzie Delta based on elevation, slope and: a) TPI (100 m) and b) TPI (2000 m). TDX IDEM with a spatial resolution of 13 m. Source: Own Figure.

4 Results



Figure 4.78: Landform classification of Northern Mackenzie Delta based on a TPI scale of 1500 m and elevation and slope. Source: Own Figure.



Figure 4.79: Landform classification of Richards Island based on a TPI scale of 1500 m and elevation and slope. Source: Own Figure.

## 4 Results

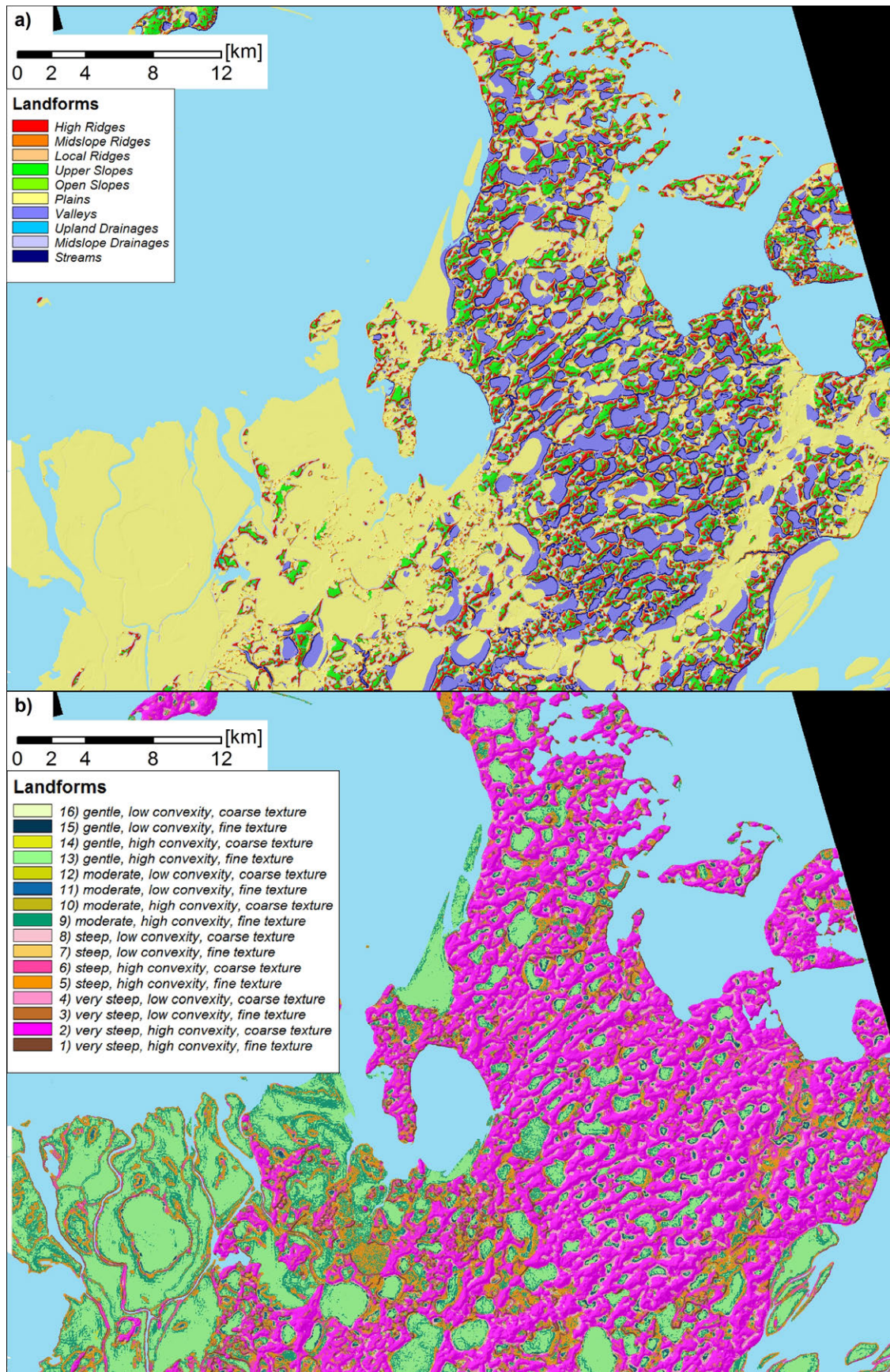


Figure 4.80: Morphometric landform classifications of the Northern Mackenzie Delta: a) SAGA GIS standard TPI landform classification with TPI scales of 200 m and 2000 m and b) SAGA GIS standard Nested-Means landform classification with a estimation window size 11x11 pixels. TDX IDEM with a spatial resolution of 13 m. Source: Own Figure.



In addition, it gave clear information on the morphometry of the coastal zone and was useful to detect the eroding tundra cliffs, the beach zone and the mudflats. Figure 4.79 shows a high resolution subset of this discrete classification that was calculated with a scale of 2000 m. The subset was located at the south-eastern part of Richards Island and showed the estuary of the Mackenzie East Channel. The classes of the Steep Slopes clearly highlighted the boundary between the ice-bearing permafrost bodies and the low lying ice-free wetland complexes and banks of the river mouth. The boundary is characterized by steep erosion cliffs. The different colors of the class Steep Slope highlighted the extent and position of the slope position and elevation. Furthermore, the subset indicated the hill-and-valley sequences of the central part of Richards Island and showed that the northern and southern flanks of the hills were comparable steep. The TPI further highlighted the valley that follows the main direction of the fault system (north-west direction). This valley is indicated in the classification by low TPI and slope values. The aerial photography of this region are shown in Figure 2.6 on Page 31 and show the wetlands of the East Channel, the steep erosion cliffs and the hilly tundra of the uplands.

The Nested-Means Landform and the TPI based Landform classification were processed for the Northern Delta data with standard setting of SAGA GIS (see Section 4.3.3.1). It was found that the TPI based landform classification (Figure 4.80.a) was suited to distinguish between the three main elevation levels that were connected to the three extensive landforms. These were the plains of the delta complex, the flat valleys and lakes of the inland and the Upper and Open Slopes of the hills. The northern and southern steep slopes of these hills were classified as high and mid-slopes ridges. The comparison of the discrete landform classification and the TPI based landform classification showed a high correspondence - with respect to the arrangement of the landform classes. In contrast, it was observed that the Nested-Means Landform classification (Figure 4.80.b) did not provide a reasonable grouping of the landform units. The hills and valleys of the inland, as well as the steep sloped of the northern and southern flanks, were classified as Very Steep landforms. Again it was obvious that the internal thresholds of this classification did not reflect reasonable thresholds to separate actual landforms.

#### 4.3.3.3 Banks Island

The same analyzes conducted for the test sites Caribou Hills and the Northern Delta were done for the high arctic test site Banks Island. As described in Section 4.2.3.3 this site has a higher topographic variation and higher relief energy. The analysis of the TPI stack showed that at least three scales were suited to characterize the landforms based on the TPI (Figure 4.81): a first one ranging from a scale of 75 m to about 400 m, a second one ranging from 400 m to 1600 m and the scales greater 1600 m. These scales were identified by the analysis of the mean, variance, rate of change and the frequency of positive TPI changes (Figure 4.81). The mean values of the stacks showed a fast decrease of scales ranging from 75 m to 1600 m and an increase of scales of 1600 m to 3000 m (Figure 4.81.a). This indicated two suitable scales. The range of the lower scales (75 m to 1600 m) was divided in two parts at a scale value of about 400 m. This break was indicated by the rate of change (Figure 4.81.c) and the frequency of positive TPI changes (Figure 4.81.d). The graph of the variance did not indicate turning points but a first one at a scale of 100 m. This turning point was likely related to a systematic effect and small sample size (see Dragut et al. (2011)).

4 Results

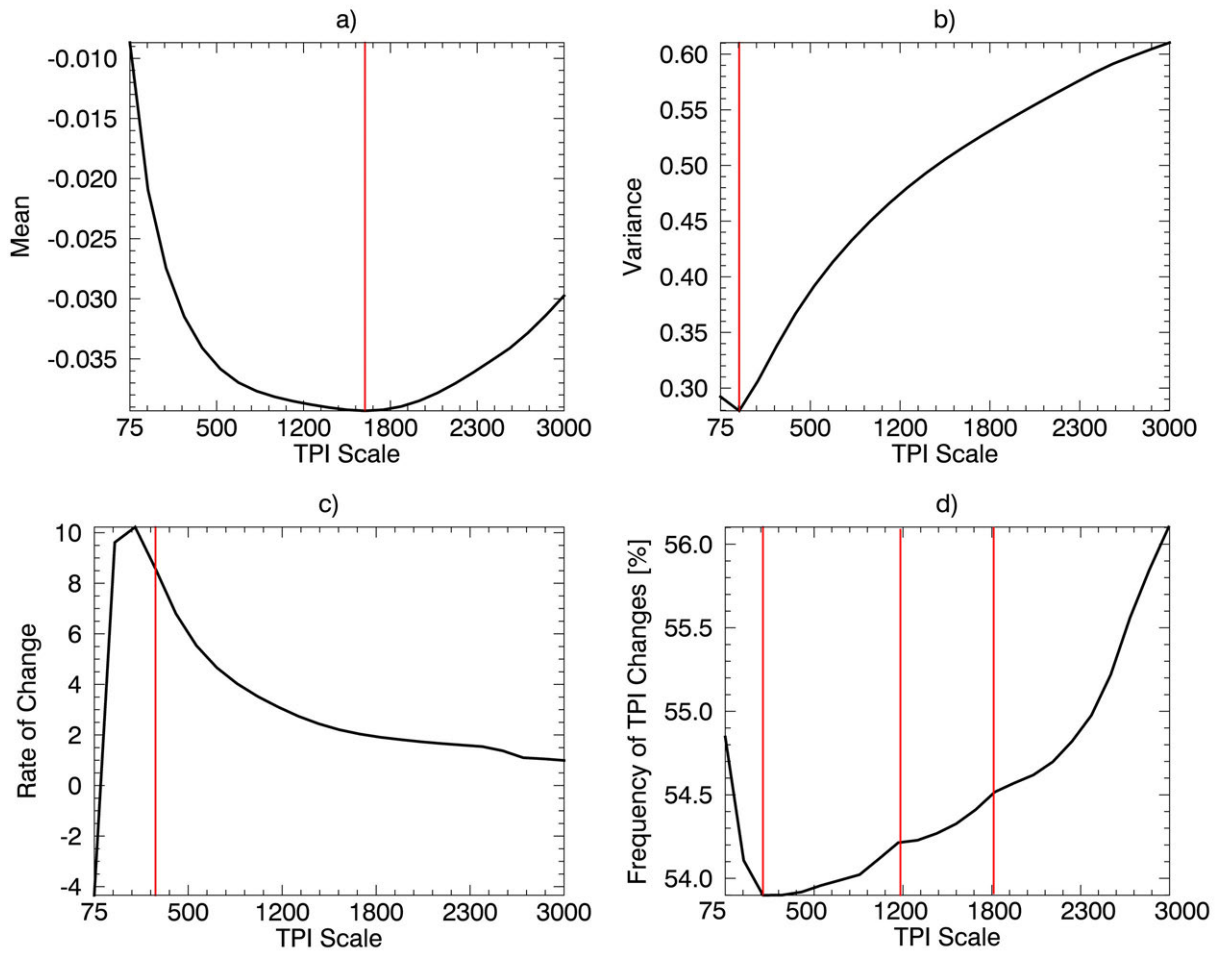


Figure 4.81: Selection of suitable TPI scales for Northern Banks Island for TPI scales ranging from 75 m to 3000 m: a) mean, b) variance, c) rate of change and d) the frequency of positive TPI changes. The red lines indicate turning points. Source: Own Figure.

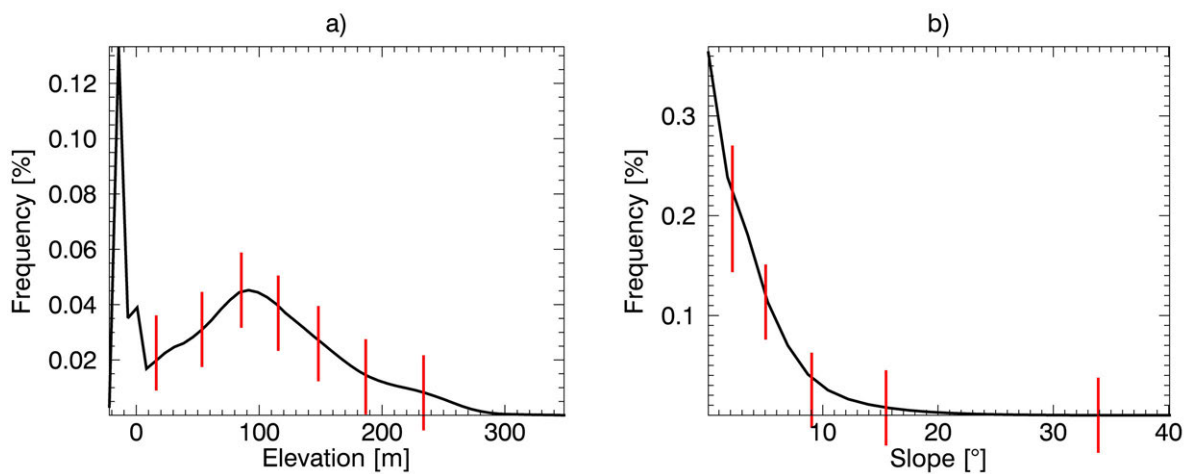


Figure 4.82: Selection of suitable elevation and slope thresholds for Northern Banks Island using Jenks-Natural-Breaks classification: a) histogram of the elevation and b) histogram of the slope. The red lines indicate potential class thresholds. Source: Own Figure.

The average variance was again increasing with increasing scale and indicated a higher variation of the TPI values. The discrete landform classifications with different TPI scales are shown in Figure 4.84.

The analysis of the histogram of the elevation showed that three levels were present: a first one from the sea level to about 15 m, a second one from 15 m to 100 m and a third one with elevation values greater 100 m (Figure 4.82.a). These units could be interpreted as (1) the coastal zone and the lowlands, (2) the valleys, river beds and plains of the hinterland and (3) the hills, peaks and ridges of the upland. The histogram of the slope showed that the test site was steeper than the sites of the Mackenzie Delta and higher frequencies of slope values greater  $5^\circ$  were observed (see 4.2.3.3 and Figure 4.82.b). Meaningful breaks were found for slope values of  $3^\circ$ ,  $5^\circ$ ,  $10^\circ$ ,  $15^\circ$  and  $35^\circ$ . The breaks of  $3^\circ$  and  $10^\circ$  were chosen as thresholds for the discrete classification in order to make the landform classifications of Banks Island comparable to the classifications of the Caribou Hills and the Northern Delta.

With respect to these findings, the discrete landform classifications were processed with elevation breaks of 15 m and 100 m, slope breaks of  $3^\circ$  and  $10^\circ$  and for two TPI scales of 250 m and 2000 m. The two chosen scales represented the first and the third scale that were identified to be suitable to characterize the landforms of the test site. The breaks of a single TPI were again fixed to -0.5 and +0.5 as done before for the test sites of the Caribou Hills and the Northern Delta. The two classifications are shown in Figure 4.84. As observed before the differences in the scales were related to local and regional TPI features, e.g. to local or regional peaks and valleys.

Figure 4.85 shows the same classification of TPI scale 2000 m with more distinct colors and the legend provides a qualitative naming of the morphometric classes. The new coloring was the same as the one of the test sites Caribou Hills and Northern Delta (compare Figure 4.78 and Figure 4.72). It was found that the classification gave detailed information on the distribution of the steep slopes, plains and primary valleys of Woon and Eames River on both investigated scales. Especially, the classes of steep slopes showed a good differentiation in two ways: (1) The colors clearly showed the elevation level and therefore if the form was present at the shore, the hinterland or the upland. (2) The TPIs of both scales gave information on the relative location of the slope position itself, i.e. top, mid or foot-slope position. The TPI estimated on a small scale further showed the comparable small river beds and valleys of the hills and the hinterland as single classes. The TPI estimated on a large scale showed the first-order arrangement of the landform elements and highlighted forms that are in relation to the drainage network and the geological structure.

The comparison of these classifications to the Nested-Means and the TPI based landform classification showed that these two standard classification techniques did not provide the same quality and detail on the morphology. The TPI based classification (Figure 4.86.a) showed primary the classes Plains, Upper and Open Slopes and the class Valley for some isolated medium sized valleys of the upland. The classes High Ridges and Midslope ridges were present for some spots in the south-west of the test sites. The classification did not show the arrangement of the landforms and it did not provide an overview on the landform arrangement. The Nested-Means Landform classification (Figure 4.86.b) highlighted three units of the test sites: (1) These were the hills and valleys that were classified as very steep and steep with coarse texture. The differentiation of valleys and peaks was realized in the classification based on the convexity feature. (2) The elements of the second unit were the gentle sloped and low convex river beds of the Woon and the Eames River.

#### 4 Results

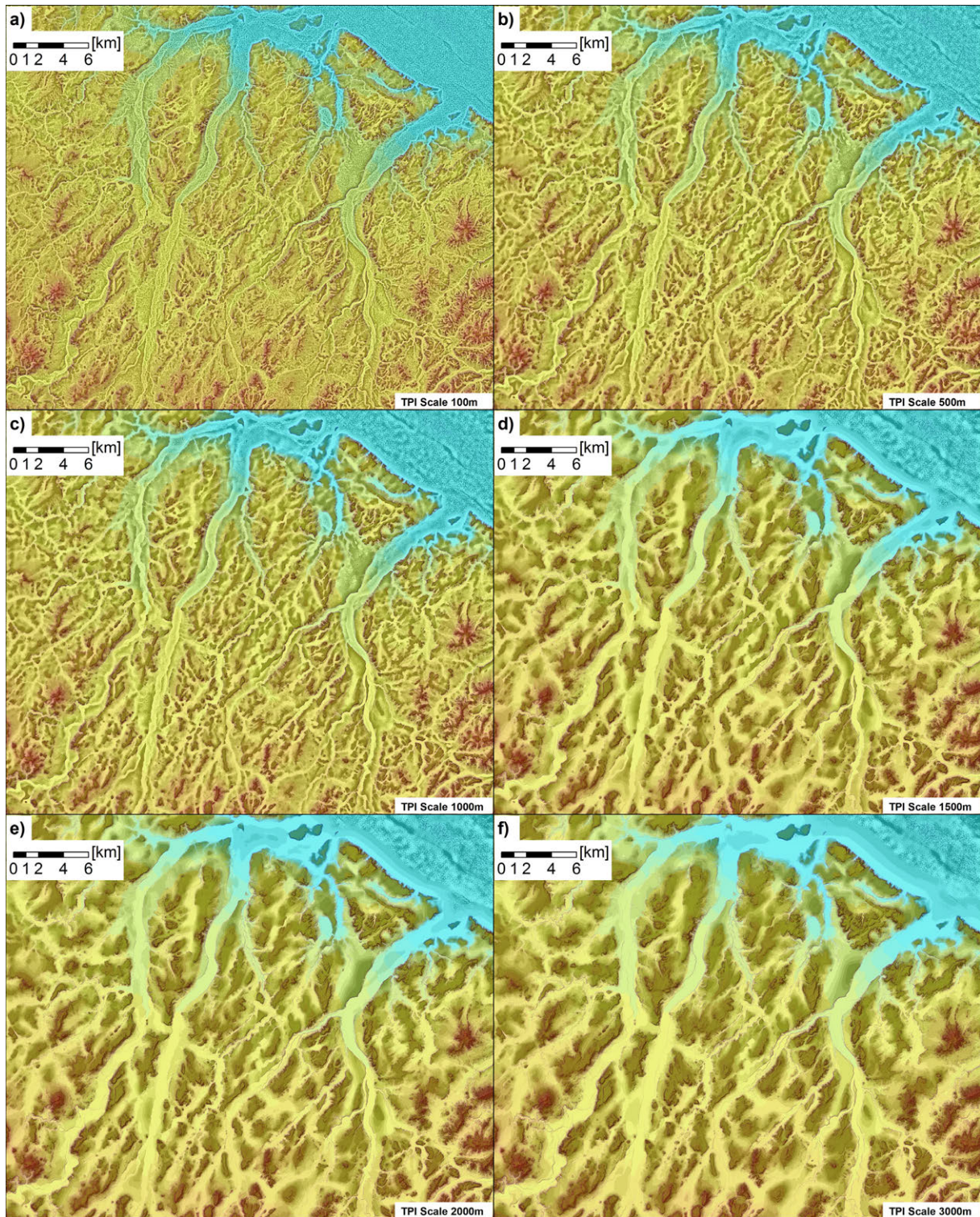


Figure 4.83: Continuous morphometric landform classification of Northern Banks Island for TPI scales of: a) 100 m, b) 500 m, c) 1000 m, d) 1500 m, e) 2000 m and f) 3000 m. The legend is shown in Figure 3.20 and the thresholds of elevation and slope were set in accordance to Barsch & Liedtke (1985). TDX IDEM with a spatial resolution of 13 m. Source: Own Figure.

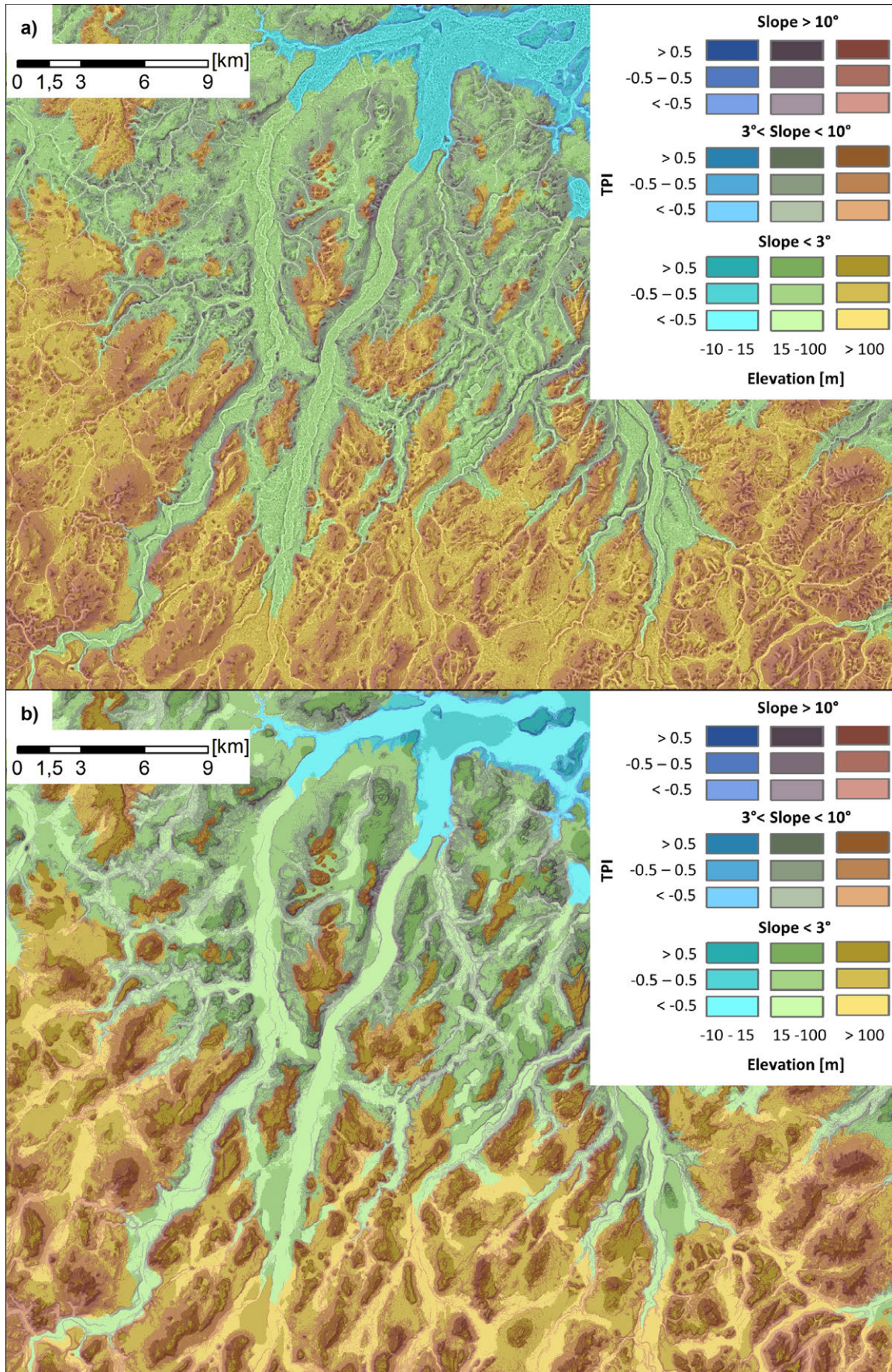


Figure 4.84: Morphometric landform classifications of the Northern Banks Island based on elevation, slope and: a) TPI (100 m) and b) TPI (2000 m). TDX IDEM with a spatial resolution of 13 m. Source: Own Figure.

4 Results

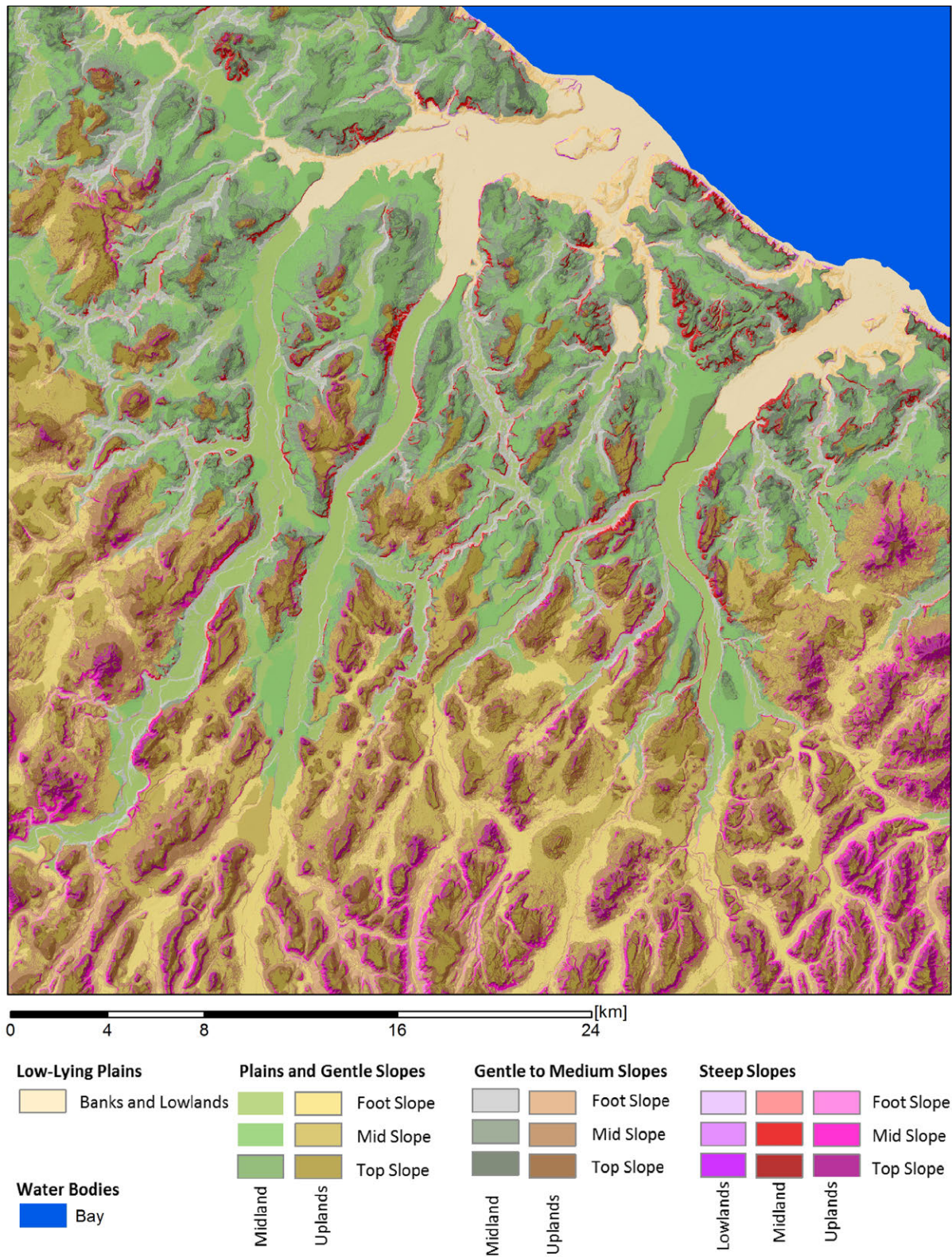


Figure 4.85: Landform classification of Northern Banks Island based on a TPI scale of 2500 m and elevation and slope. Source: Own Figure.

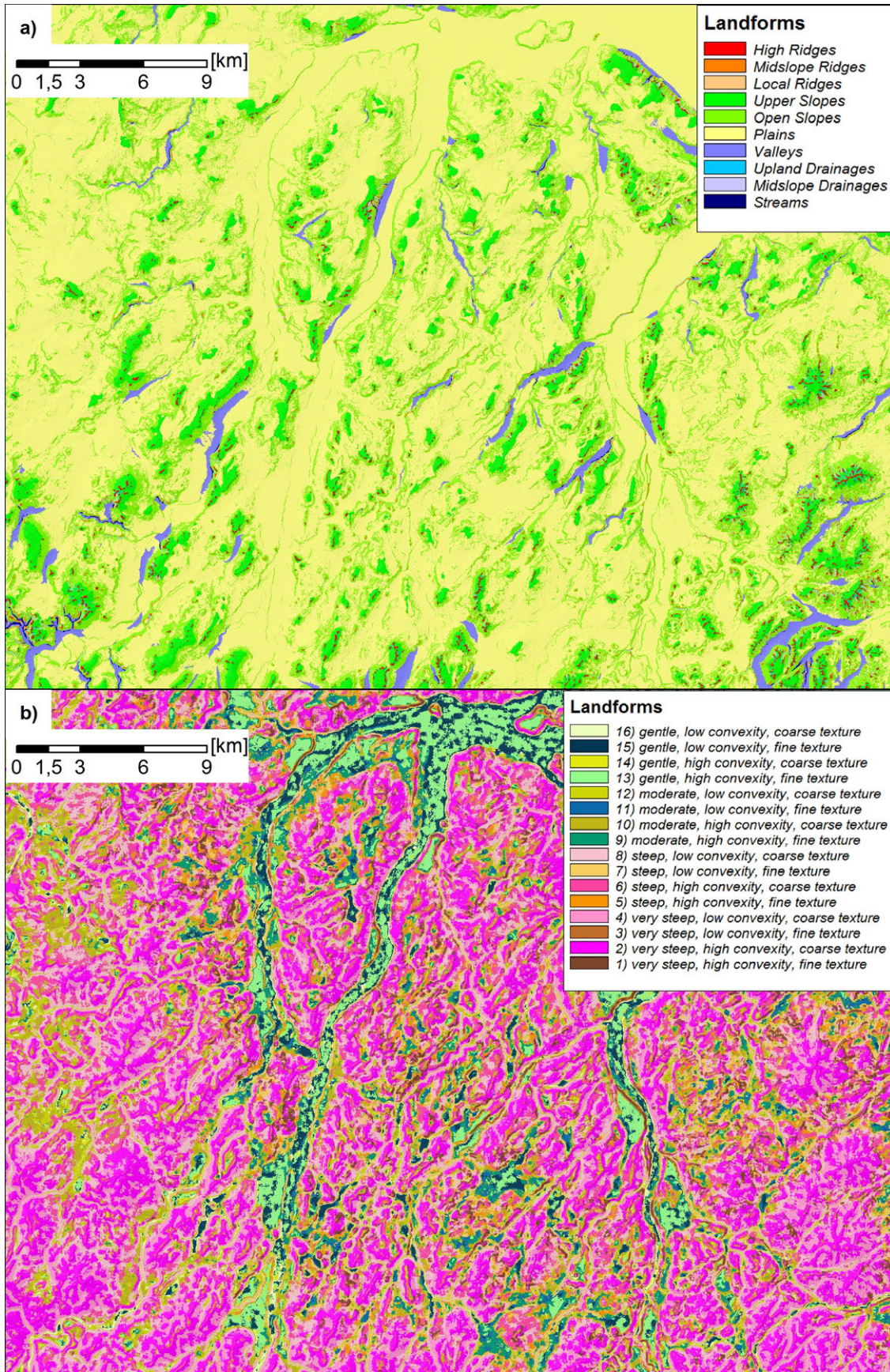


Figure 4.86: Morphometric landform classifications of Northern Banks Island: a) SAGA GIS standard TPI landform classification with TPI scales of 200 m and 2000 m and b) SAGA GIS standard Nested-Means landform classification with a estimation window size of 11x11 pixels. TDX IDEM with a spatial resolution of 13 m. Source: Own Figure.

## 4 Results

(3) The third unit showed the classes gentle to medium sloped with varying texture and convexity. These classes showed the mid-slope positions of the mid- and uplands and smaller valleys of the southwestern hills. However, again it was obvious that the internal thresholds of the Nested-Means and the TPI based landform classification did not reflect reasonable thresholds to separate actual landforms. In addition, it was observed that all classifications that used the TPI to delineate landform classes showed the systematical blurring of the regions close the northern shore and this was most obvious for the large scales (see Section 4.2.3).

### 4.3.3.4 James Bay

The analysis of the TPI stack of the test site James Bay showed three suited TPI scales: These were the scales from 75 m to 500 m, from 500 m to 1500 m and scales greater 1500 m. The scale of 500 m was identified as turning point in the graph of the mean, the variance, the rate of change and the frequency of positive TPI changes (Figure 4.87). The scale of 1500 m was a turning point in the graphs of mean and the frequency of positive TPI changes. Again it was observed that the variance was increasing with increasing scale and a higher range of TPI values was present with higher scales. The graph of the frequency of positive TPI changes showed additional turning points at scales of 1000 m and three turns around a scale of 2500 m. The discrete landform classifications of the test sites James Bay were therefore realized as before with scales of 100 m, 500 m, 1000 m, 1500 m, 2000 m and 3000 m. The visual analysis of these classifications showed that the selected TPI scales gave maximum contrast among the continuous landform classifications and that the differences between scales greater than 2000 m were small (Figure 4.89).

The Jenks-Natural-Breaks classification indicated breaks of the elevation at levels of 5, 10, 20, 30 45 and 50 m (4.88.a). The histogram showed that most parts of the site were leveled less than 10 m and less than 20 m. These breaks therefore reflected meaningful breaks for the discrete landform classification and were used for the classification. The comparison of the discrete classification and the elevation map of the James Bay (see Figure 2.12) showed that these classes were in correspondence to the lowlands close to the coast, respectively, the plains close to the mouths Namapistikw, Sabascunica, Clergue and Torviens River, to the midlands between the coast and the hills of the uplands and the uplands itself. The histogram of the slope showed a continuous decrease of the slope values between 1° and 10° (4.88.b) and no significant discontinuities or breaks. The identified thresholds were therefore nearly equally spaced. Again it was chosen to use the breaks of 3° and 10° for the classification in order to make the discrete classification comparable to the classifications of the other test sites.

Figure 4.90 shows the discrete landform classifications that was processed with elevation breaks of 10 m and 20 m, slope breaks of 3° and 10°, TPI scales of 250 m and 2000 m and single TPI breaks of -0.5 and +0.5. As noted above the breaks of the elevation gave a reasonable grouping of the elevation: The coastal, mid- and up-lands were clearly distinguished and corresponded to the description of the test site (see Section 4.2.3.4). The distribution of the steep slopes was bounded to the hills of the upland. Along with this the TPI of a scale of 2000 m highlighted the relative slope positions (foot-, mid- and top-slope) more pronounced than the valleys and ridges landforms. The TPI of a scale of 250 m showed a high noise contribution. This noise is hindering an analysis of the relative topographic position on small scale.



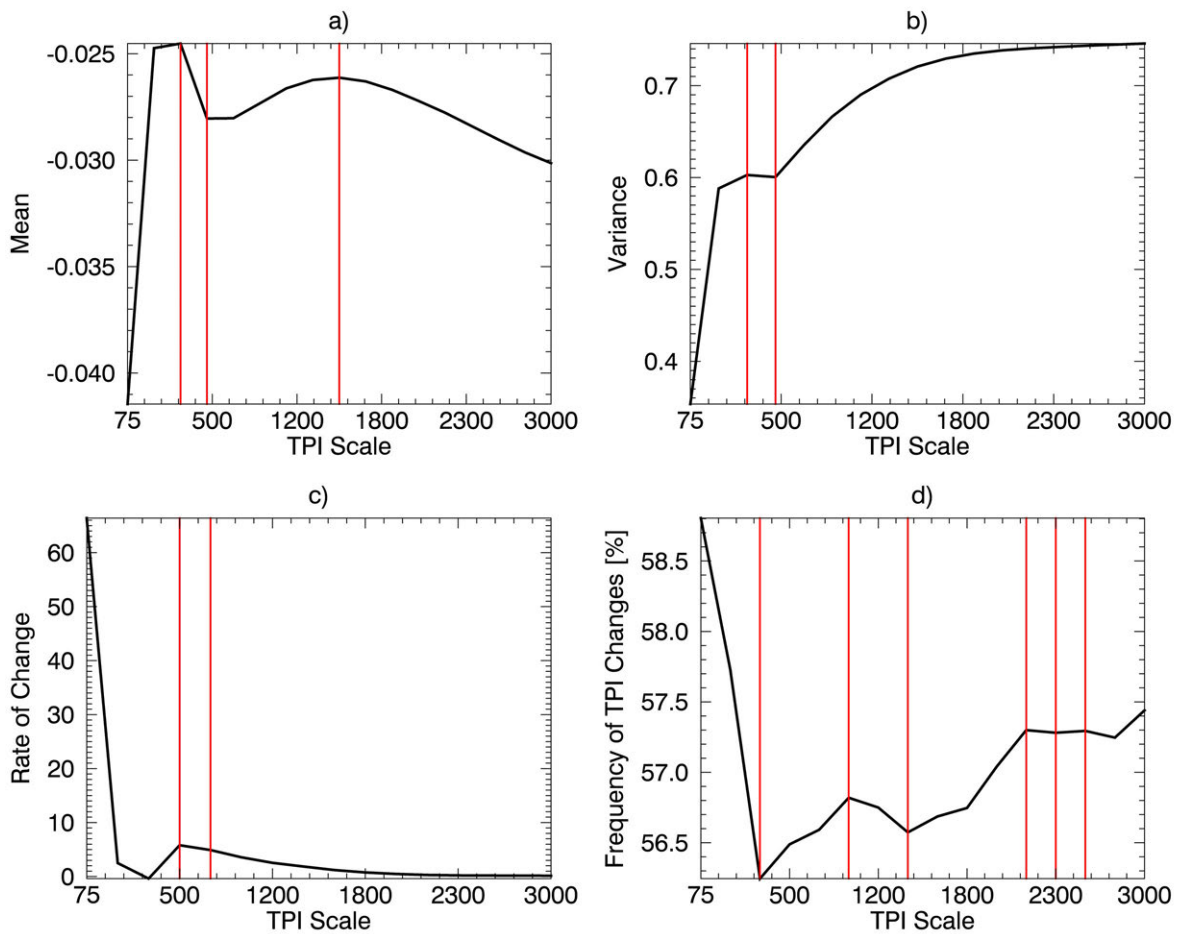


Figure 4.87: Selection of suitable TPI scales for James Bay for TPI scales ranging from 75 m to 3000 m: a) mean, b) variance, c) rate of change and d) the frequency of positive TPI changes. The red lines indicate turning points. ASTER GDEM with spatial resolution of 31 m. Source: Own Figure.

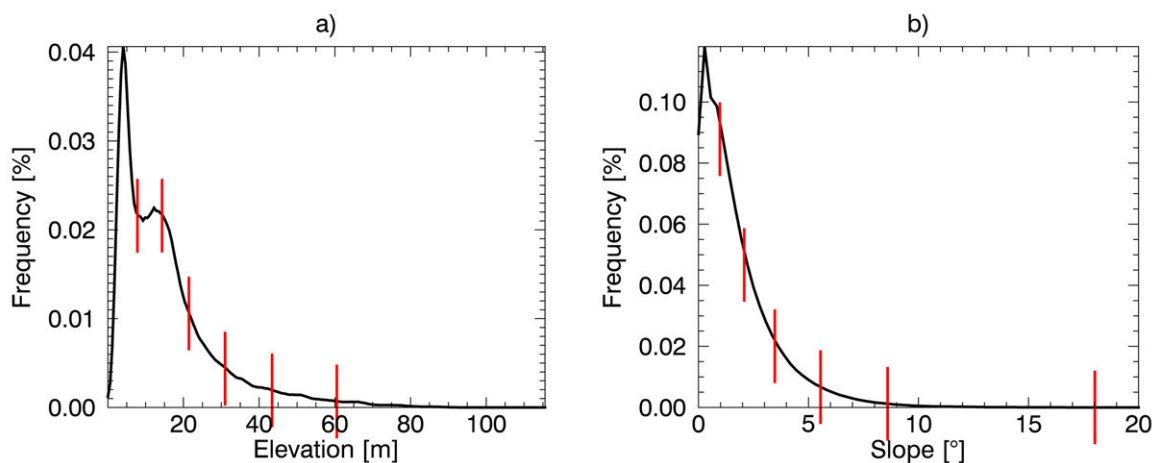


Figure 4.88: Selection of suitable elevation and slope thresholds for James Bay using Jenks-Natural-Breaks classification: a) histogram of the elevation and b) histogram of the slope. The red lines indicate potential class thresholds. ASTER GDEM with spatial resolution of 31 m. Source: Own Figure.

#### 4 Results

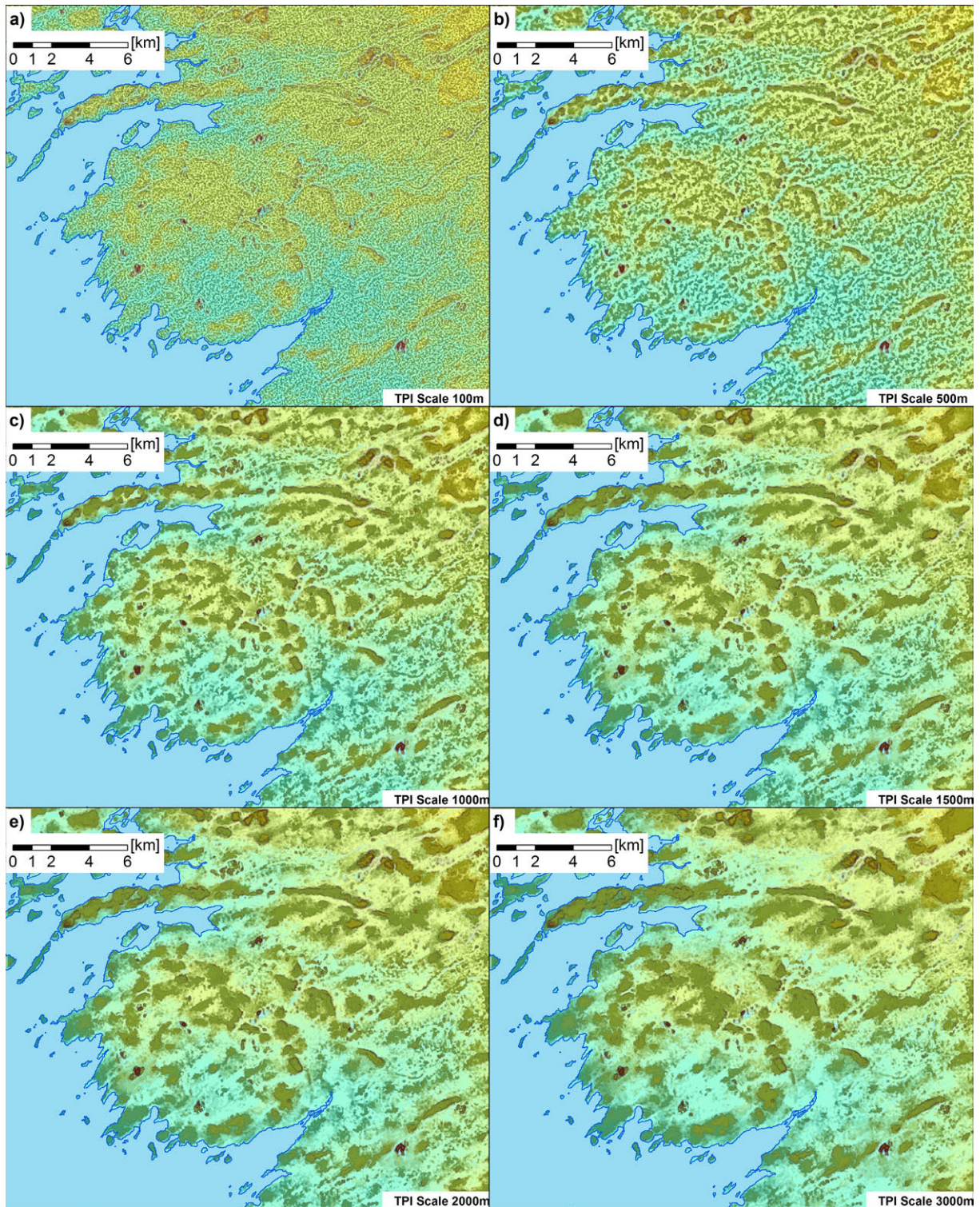


Figure 4.89: Continuous morphometric landform classification of James Bay for TPI scales of: a) 100 m, b) 500 m, c) 1000 m, d) 1500 m, e) 2000 m and f) 3000 m. The legend is shown in Figure 3.20 and the thresholds of elevation and slope were set in accordance to Barsch & Liedtke (1985). TDX IDEM with a spatial resolution of 13 m. Source: Own Figure.

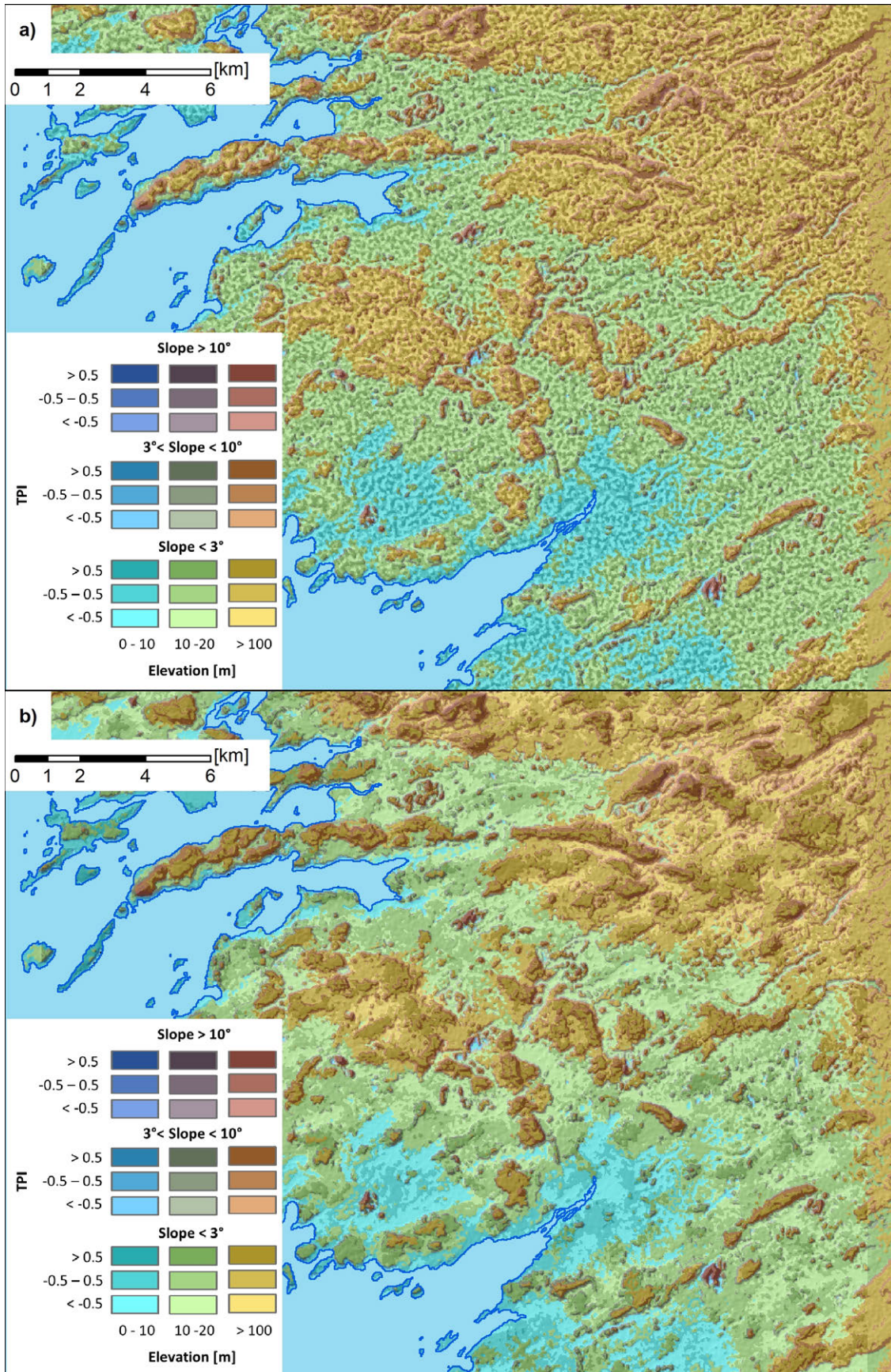


Figure 4.90: Morphometric landform classifications of James Bay: a) morphometric landform classification based on elevation, slope and TPI (250 m) and b) morphometric landform classification based on elevation, slope and TPI (2000 m). Source: Own Figure.

## 4 Results

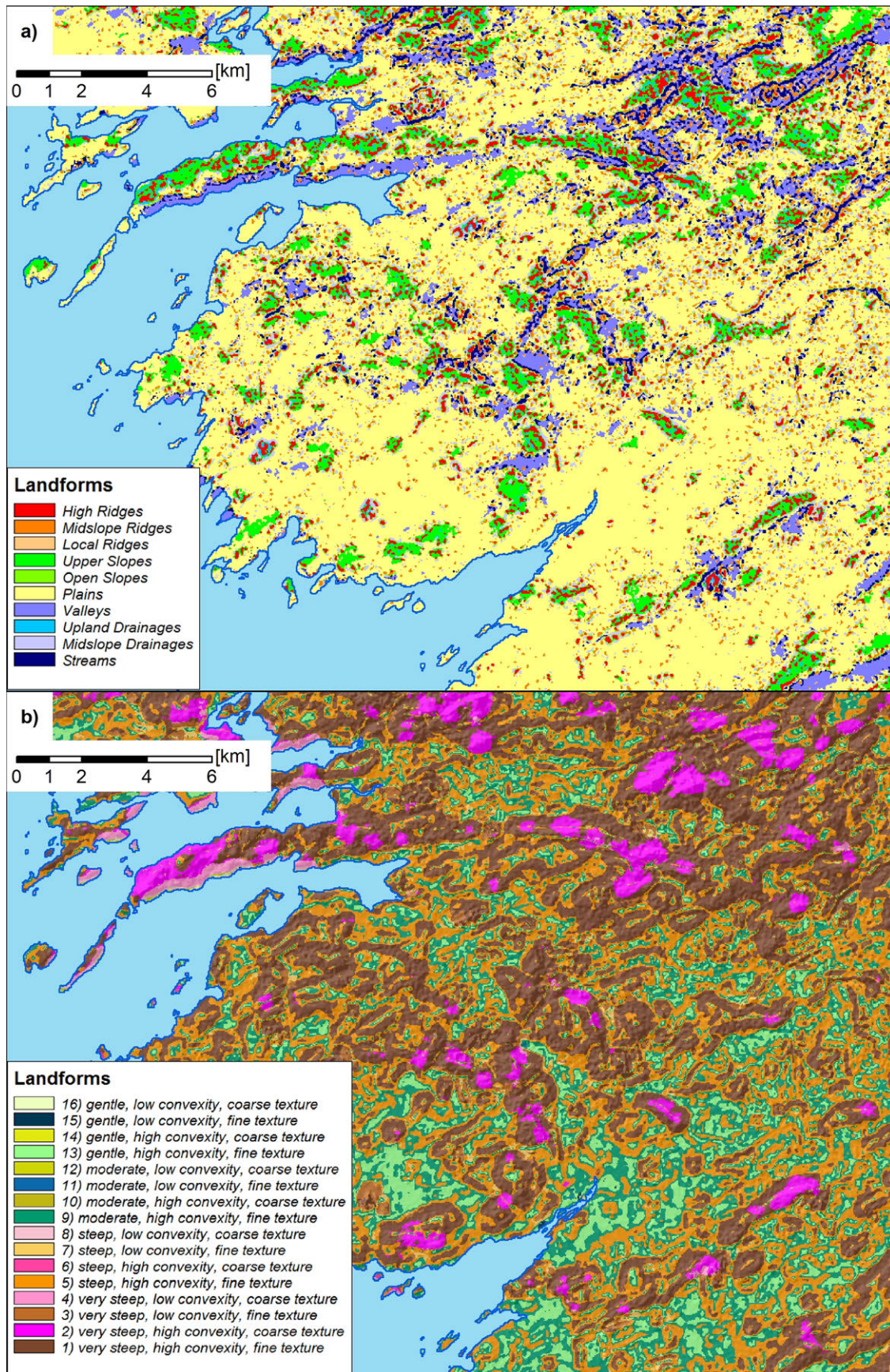


Figure 4.91: Morphometric landform classifications of James Bay: a) SAGA GIS standard TPI landform classification with TPI scales of 200 m and 2000 m and b) SAGA GIS standard Nested-Means landform classification with a estimation window size of 11x11 pixels. Source: Own Figure.

The comparison of this classification with the Nest-Means Landform classification and the TPI based landform classification showed that the level of detail was comparable to the standard landform classifications processed in SAGA GIS. The TPI based approach classified extensive areas of the site as Plains. This was reasonable with respect to the low slope values (Figure 4.91.a). The hills of the uplands were classified as Upper and Open Slopes and the main tops and ridges were detected. The local tops were highlighted as High and Midslope Ridges. This corresponded to the classes of the discrete landform classification. The valleys of the uplands in north-east of the test site were classified as valleys. The Nested-Means classification provided a more complete picture on the landforms of the test sites and showed three units (Figure 4.91.b). These were the gentle sloped and fine textured lowlands, the steep to very steep low and high convex hills and mid-slopes and the very steep coarse and high convex hills and ridges of the uplands.

The intermediate TanDEM-X and the ASTER GDEM digital elevation models were used for the landform classification of the test sites Caribou Hills, the Northern Mackenzie Delta, the north of Banks Island and the James Bay. Three different classification algorithms were applied and compared. These were the Nested-Means landform classification of Iwahashi & Pike (2007), the Topographic Position Index (TPI) based landform classification of Weiss (2001) and the developed landform classification approach. These approaches were applied to digital elevation models of the intermediate TanDEM-X (Caribou Hills, Northern Mackenzie Delta, Banks Island) and the ASTER GDEM (James Bay). The developed classification approach required the definition of elevation, slope and TPI thresholds and the selection of the TPI scale, respectively, the estimation window size of the TPI. The thresholds of the continuous classification were set in accordance to Barsch & Liedtke (1985). The thresholds of the discrete classification were defined by the analysis of the TPI stack and the histograms of elevation and slope. Appropriate scales and estimation window sizes of the TPI were found by the analyses of the statistics of the TPI stack: The turning points of the graphs of the mean, variance, rate of change and frequency of positive TPI changes were suited to indicate scales that showed significant changes of the size of the landforms. The thresholds that were used to classify the elevation and the slope were defined by the Jenks-Natural-Breaks algorithm. It was shown that this algorithm provided appropriate thresholds for the classification of the landforms. The comparison and evaluation of the final landform classifications showed that the continuous and discrete landform classifications provided a reasonable grouping of similar forms. The level of detail depended on the used scale and therefore on the estimation window size of the TPI: Large scales facilitated the classification of landforms with regional relevance - small scales facilitated the classification of landforms with local relevance. It was shown that the threshold divided classification of elevation, slope and TPI was suited to provide an initial classification of the surface morphology. Such classifications were especially useful to identify landforms that depend on the slope and the slope position, e.g. cliffs, exposed tops, or valley shoulders. The TPI based landform classification and the Nested-Means landform classification showed only limited suitability. The thresholds of these approaches were defined internally and the analysis revealed that the found thresholds did not reflect reasonable breaks to separate actual landforms. Furthermore, all classifications that used the TPI to delineate classes showed a systematical miss-classification when elevation changes took place on short distance. It was furthermore shown that TPI thresholds of -1.0 and +1.0 were unsuited for the classification. Relevant changes and differences in the landforms were observed in the value range from -0.5 to +0.5.



---

## Interpretation and Discussion

### 5.1 Methodological Concepts

The following sections discuss the main considerations, the interpretation and the developed methodological concepts. These were the Non-Local Means filtering of PolSAR and DEM data, the Two Component Decomposition of co-polarized PolSAR data and the unsupervised classification of radar and/or optical data. The final conclusions are provided in Section 6.

#### 5.1.1 Non-Local Means Filtering

The Non-Local Means filtering was shown to be an efficient method for processing PolSAR imagery. The developed Non-Local Means methodology was able to operate efficiently for two reasons: (1) the estimation window size of the patch window was fixed to a small size, and (2) the filtering was applied to already multilooked and processed imagery. The visual inspection of the NLM filtered PolSAR data revealed that the developed method was capable of enhancing image interpretation. The Non-Local Means filtering was able to preserve boundaries between land cover units and was able to smooth the appearance of extensive land cover units. In order to achieve this, the Non-Local Means filter required the parametrization of the parameter  $h$ , which is used to regulate the power of the filtering. The optimized filtering, with respect to the speckle filter evaluation indices Preservation of Mean, Speckle Reduction Index and the Edge Enhancement Index, was realized with a parameter  $h$  in the range from 0.02 to 0.03. This was observed for both sigma nought calibrated TSX and R-2 imagery. The following analyses demonstrate that when the parameter  $h$  is set to a value of 0.025 there is a positive effect on image interpretation and classification.

The parametrized Non-Local Means filter was quantitatively identified to be better suited for filtering PolSAR images (i.e. preserving edges) than the frequently used Boxcar and Lee filters. The speckle reduction was found to be as effective as the Boxcar filter with a window size of 7x7 pixels. The edge preservation was as efficient as the Lee Filter with a window size of 3x3 pixels. As stated previously, the Non-Local Means filtering was able to preserve boundaries between differing land cover units. In addition,

## 5 Interpretation and Discussion

Non-Local Means filtering was shown to produce less blurring of these boundaries. Boundary preservation is of high importance when mapping land cover classes. A blurring of class boundaries and edges will hinder the interpretation of any classification, whether supervised or unsupervised. The Non-Local Means filtering was shown to be efficient at increasing the classification accuracy. The reduction of image noise and the aggregation of pixels had a positive influence on the separability of classes and as a result classification accuracy increased by approximately about 10%.

Experimental results have shown that the Non-Local Means filter also provides reasonable results when applied to elevation data. The elevation data used for this test were the raw data of the TDX IDEM. However, it should be noted that these data do not show the final and smoothed end product. The IDEM data were acquired during the winter of 2012, grainy variations, that are likely the result of speckle and of rough ice-surfaces, appear throughout the imagery. The Non-Local Means filter was able to remove this grainy texture and preserve the land surface elevations and topography. Initial results show promise; however, further research will be needed to fully explore the filtering of DEM data with a Non-Local Means methods.

Within the recently published literature, Non-Local Means filtering has been shown to be a fast and robust method for filtering PolSAR data (Section 1.2). The Non-Local Means approach can be applied to any detected PolSAR product and can therefore be considered user-friendly. Nevertheless, the shown approach suffers from a lack of statistical distribution modeling and parametrization. Further investigations will be needed to implement statistical models or methods in the approach. Such a successful implementation will help to automatically estimate the filtering parameter  $h$  in order to avoid any manual interaction.

### 5.1.2 Two Component Decomposition

The results of the correlation and scatterplot analyses showed that features double bounce and odd bounce of the Two Component Decomposition (co-polarized data) can be interpreted similarly as the features double bounce and odd bounce of the Three Component Decomposition (quad-polarized data). This was found to be true for the land cover classes that showed dominant double or odd bounce scattering (e.g. bare ground and wetland classes). The correlations between Two- and Three Component Decomposition features were weaker for land cover classes that showed a high contribution of volume scattering (e.g. shrub lands). The correlation between the Two Component Decomposition features and the volume scattering of the Three Component Decomposition was found to be weak to moderate. Furthermore, it was observed that the features of the decompositions had a low correlation among themselves and could therefore be interpreted as independent orthogonal scattering mechanisms. These observations were made and confirmed for two independent test sites (Section 4.1.2) and further substantiated by the analysis of the Two and Three Component features (Section 4.2.1.3).

With respect to these results, the Two Component Decomposition has a high applicability for co-polarized data and offers a way to apply the frequently used Freeman-Durden or Yamaguchi Decomposition Model. The Two Component Decomposition generates polarimetric features that facilitate the interpretation of the co-polarized signal in terms of the scattering processes involved. As shown, the features were sensitive to specific land cover types and thus helped to characterize the PolSAR signal of the tundra land cover types. The double bounce feature was shown to be of value for the identification and classification of



water bodies and wetland vegetation. The co-polarized model is not adjusted to the volume contribution of a scatterer due to the missing HV or VH information. The double/odd bounce feature will therefore not show a double/odd bounce in the conventional sense. These tests were conducted on natural tundra landscapes and it is not known if similar results will be observed for agricultural or urban land cover types, or for that matter, all other non-natural targets.

### 5.1.3 Unsupervised Classifier

The unsupervised classifier FKM-ML was shown to be an efficient method for classifying dual- or quad-polarized SAR data, multispectral optical data, and combined PolSAR and multispectral data. The classifier was capable of handling data from all sources and was therefore more flexible compared to the standard PolSAR classification techniques such as Lee's approach (Lee et al. (2004)), or the Wishart K-Means classification (Lee, Grunes, Ainsworth, Du, Schuler & Cloude (1999)). A comparison between the standard PolSAR classifiers, the standard unsupervised classifiers, and the FKM-ML classifier showed that the FKM-ML had high classification accuracy that was comparable to the Wishart K-Means classification. Both classifiers were shown to be the best classification techniques among all tested unsupervised classifiers.

The final step of the FKM-ML classification was the iterative Maximum Likelihood classification. It was observed that iterative Maximum Likelihood classification converged for all classifications. This indicated that the necessary model assumptions were reasonable, e.g. the assumption that the distribution of a class can be modeled by a multivariate normal distribution. The Maximum Likelihood classification offers the opportunity to derive continuous land cover classifications and to assess the quality of the model.

The FKM-ML was applied to all of the test sites using the various combinations of multispectral and PolSAR data. The results of the accuracy assessments indicated that the FKM-ML technique was capable of detecting the underlying class structures of the feature space. This was demonstrated through the high classification accuracies of the wetland and bare ground classes. The detection of a class with a high level of confidence requires that the position of the class within the feature space be distinct. It was observed that the performance of FKM-ML was poor for the vegetation classes of sparse vegetated, mixed and shrub dominated tundra for many classifications of the PolSAR data. It was shown that only some of PolSAR data were sensitive to the differences of these classes and therefore the feature space positions of sparse vegetated, mixed, and shrub dominated tundra were very similar. Because of this it was observed that FKM-ML was not capable of differentiating these classes. The comparison of the unsupervised FKM-ML to the supervised Maximum Likelihood classification showed that FKM-ML was capable of classifying the land cover classes with satisfactory accuracy. The absolute classification accuracies of the unsupervised classification were lower but in many cases showed the same trends. In addition, it was observed that classes that demonstrate a high level of supervised classification accuracy have, in general, a high potential to be classified with a high level of confidence with an unsupervised classifier.

The analysis revealed that FKM-ML classification of big data stacks was possible but the technique was not able to make full use of the available information. For example, this was shown for the East Channel and Delta Island test sites. The accuracy assessment of the unsupervised FKM-ML indicated that classification accuracies of C-HH/VV and L-8 were higher than C-Quad and L-8. In contrast, the

## 5 Interpretation and Discussion

supervised classification indicated the C-Band Quad and L-8 data were best suited for the classification of all quad- and dual-polarized C-Band data. It was observed that the FKM-ML showed systematic errors in the classifications of the Banks Island test site - the classification accuracies of the VMH and VMD classes were less than 50%. It was not clear if these systematic errors were caused by the FKM-ML operation itself or by the class merging. The FKM-ML showed a good transferability to other sites and had capacity to map large areas, e.g. as shown for the test sites Banks Island, or the entire Mackenzie Delta Region.

## 5.2 Land Surface Characterization

The following sections provide the interpretation and discussion of the findings made for the characterization of land coverage and land surface morphology by means of radar, multispectral, and DEM data. The final conclusions are provided in Section 6.

### 5.2.1 Polarimetric Synthetic Aperture Radar Data

It was shown that the PolSAR data were sensitive to generalized tundra land cover classes at each of the test sites. The X-Band intensities, HH and HV, were particularly sensitive to classes of wetland and bare ground, showing distinct ranges of intensity values. In addition, both polarizations showed an increase in intensity with increasing vegetation coverage and shrub density. The differences between low and mixed tundra were more pronounced for the HV polarization. The VV polarization was shown to be less sensitive to differences in land cover compared to the other polarizations. The penetration depth of the X-Band is low and therefore it is sensitive to small physical variations in these land cover types. It was observed that the intensities of C-Band data showed similar characteristics to the X-Band data, while the HH and HV polarizations were more sensitive to differences in land cover than the VV polarization. Compared to the X-Band, the differences of the land cover classes were less pronounced and the data ranges were more similar. This is likely caused by the longer wavelength of the C-Band. Small differences, such as the difference between sparse vegetated and mixed tundra, were tense. The HV polarization of the C-Band was more sensitive to the differences between mixed and shrub dominated tundra. The C-Band was shown to be sensitive to these types of vegetation and the statistics showed a better separation between these two classes compared to the X-Band.

The analysis of the Entropy/Alpha Decomposition features showed that the features of the co-polarized data were very similar to the features of the quad-polarized data. The observed differences were very small since the characteristics were nearly identical. These findings are in line with those of Sugimoto et al. (2013). Further, it was shown that the co-polarization information was meaningful for the characterization of tundra land cover and that the cross-polarized information provided little benefit. It was further observed that the C- and X-Band features of the co-polarized data were very similar as both showed clear positions of the bare ground and wetland land cover types. These observations were in accordance to the considerations of Section 3.1.1.1. The differences between the X- and C-Band were again related to the tundra vegetation classes. The intensities of the co-polarized X-Band data were more sensitive to the difference of spares and mixed vegetation while the C-Band data were more sensitive to the difference between mixed tundra and shrub dominated tundra. The reason for these differences was again the

different penetration depths of the electromagnetic waves. The Entropy/Alpha decomposition of the cross-polarized data showed low sensitivity to the different land cover types. The differences between Entropy and Alpha for the different land cover types were small and only noticeable for bare ground (C-Band) and wetland vegetation (X-Band). The HH/HV combination was shown to be more sensitive than VV/VH polarization.

The characteristics of the Two and Three Component Decomposition features were in accordance to the considerations of Section 3.1.1.1. Similar to the analysis of the intensities and of the Entropy/Alpha Decomposition features, a high sensitivity of the C-Band features were observed for the land cover classes. In general, the double bounce features of both Two and Three Component Decompositions were most sensitive to differences in the land cover, showing low values for bare ground, increasing values for increasing shrub density, and highest values for wetland vegetation. The X-Band double bounce of the Two Component Decomposition was identified to be most sensitive to the characteristics of the low tundra vegetation which is in accordance to the prior stated relation of wavelength, penetration depth, and vegetation height. Along with this, the double bounce feature of the C-Band (Two and Three Component Decomposition) and the volume scattering feature of the C-Band (Three Component Decomposition) showed sensitivity to vegetation height and density. The findings made here for the three test sites, which include Richards Island, Tuktoyaktuk and East Channel, were in accordance to the previous findings made for the entire area of Richards Island (Ullmann et al. (2014)).

Features X- and the C-Band showed similar characteristic as both were identified to be sensitive to wetland vegetation and bare ground. The major differences were related to the separation of the different vegetation types. The longer wavelength of the C-Band was sensitive to taller vegetation such as shrubs. The shorter wavelength of the X-Band was more sensitive to the low-lying vegetation formations and sparse vegetated substrate. The HV channel was only acquired for the Tuktoyaktuk test site. A more meaningful evaluation of the X-Band HV Channel and of the X-Band volume scattering data will require the analysis of additional test sites.

The intensity of the dual-polarized L-Band data was shown to be of little value for characterizing land cover classes. It was also shown that the intensity ranges of all classes were very similar. It is likely that the long wavelength was able to penetrate the entire canopy of the low-lying vegetation, and therefore it was hypothesized that the signal was influenced primarily by the ground surface beneath the vegetation layers, and by the sub surface layers themselves. These observations were in accordance to the considerations of Section 3.1.1.1. In contrast, the analysis of the L-Band Entropy/Alpha Decomposition features showed more sensitivity. Entropy and Alpha values increased if the percentage of vegetation cover and shrub density increased. It was not clear if these variations were directly influenced by the different land cover types or soil moisture regimes. An investigation into this point will require additional reference data, such as the measurement of moisture at and below the surface. An important point also remained unclear: the reference data were not well suited to differentiate the grain sizes of the bare ground substrates. It is likely that the L-Band data will be of value to characterize grain size, since L-Band data is presumptively sensitive to grain sizes in the range of block to pebble size.

The usage of L-Band data for the characterization of tundra land cover is limited; however, the L-Band data may provide meaningful information on near ground conditions. In particular, it is of high interest to estimate soil moisture (Park et al. (2010)). As well, it will be desirable to use L-Band data for

## 5 Interpretation and Discussion

interferometric applications. Since the penetration is high it is likely that the signal will show high coherence values if the moisture regime of the soil is stable over time. The application of L-Band data for the estimation of the active layer heave and subsidence was previously demonstrated by Brisco et al. (2009), Short et al. (2011, 2014). L-Band interferometry of tundra landscapes shows promise and will become even more important when systems like ALOS 2 or TanDEM-L are operational.

The influence of the incidence angle on the separability of classes was evaluated for two test sites. It was found that the differences between shallow and medium incidence angles were small and that the classes' intensities had very similar characteristics. The intensities of data acquired with steep incidence angle were higher and the class positions were slightly different. The influence on the separability was evaluated using the Jefferys Matusita Distance and Bhattacharyya Distance and none of these features indicated a favorable incidence angle for the class separation. These inconclusive results are likely related to the poor quality of the reference data and the missing information on the shrub-lands. The influence of the incidence angle on the characteristics of PolSAR features were recently discussed by Banks et al. (2014) for the land cover of Richards Island and Tuktoyaktuk. Banks et al. (2014) found that shallow angles were better suited for the classification of the land cover classes.

### 5.2.2 Digital Elevation Model Data

The TDX IDEM data were shown to be of value for the characterization of the morphology of the test sites. The landform elements could be detected based on the elevation information if these were bounded to certain elevation levels. For example, this was shown for the structural landforms of the test sites that occupy the Mackenzie Delta region, e.g. the Caribou Hills that are situated on higher terrain. The TDX IDEM data were found to be highly sensitive to elevation changes of less than one meter and the DEM provided accurate topographic information with a low noise contribution. In contrast, the GDEM data showed a high noise contribution. This led to a grainy texture and random elevation changes with an amplitude of more than one meter. Both DEMs were suited to show the arrangement of the landform units on local and regional scale, such as peaks, ridges or valleys. In addition to this, the slope feature was identified to be meaningful for the characterization of discontinuities, e.g. cliffs, plains or ridges. The slope feature of the Northern Mackenzie Delta test site was shown to be suitable to characterize the morphology of the shore zone. In addition, the high quality of the TDX IDEM revealed in the aspect feature. The aspect of the different test sites were shown to be of value for detecting the orientation of the landform units and the pattern of the drainage system.

The analysis of the TPI of small, medium, and large scales showed that the large scales were best suited for characterizing first-order and higher-ranking landforms such as primary valleys, ridges, and hills. The TPIs derived from the medium scale were shown to be useful for characterizing the regional drainage systems, the top, mid and foot slopes, and secondary landforms. The TPIs calculated from the small scale estimation windows were suited for the characterization of local forms. A grainy and noisy texture of the small-scale TPIs was observed due to the small sample size and the small estimation window size. This was especially true for the GDEM data. In contrast, the small scales were better suited for the characterization of relief with high topographic variation and less suited for the characterization of relief with low topographic variation (e.g. flat areas and plains of the Mackenzie Delta). The extensive flat

surfaces showed a noisy texture on all investigated scales. However, the flat surfaces were smooth and had a constant range of TPI values if the extent of the flat area was smaller than the size of the estimation window. This was shown, for example, over the lakes of the Mackenzie Delta test sites. The thermokarst lakes were clearly visible in the TPI when the size of the estimation window was increased. This was particularly true for the TDX IDEM data. The results were less clear for the GDEM data.

The way in which TPI was estimated led to the problem of systematic blurring. This blurring was observed when rapid elevation changes take place over short distances. The signal of the peak (high elevation) was visible as long as the peak was part of the sample that was used to calculate the TPI. This effect could be illustrated and identified with the analysis of the TPI stack. The profiles of all sites showed a ramp (systematically changes of the TPI values) throughout all TPI scales if such a rapid elevation change took place. For example, this was visible for the proterozoic formation of the Caribou Hills and the coastal zones of the Northern Delta and Northern Banks Island. Even though TPI was a useful feature to characterize the relative position of a location, it was not suited to be used alone for the characterization of the landforms. The TPI values of different elevation levels showed the same range of values due to their normalization and standardization. The TPI therefore facilitated the interpretation but not with respect to deriving actual elevation or slope. An assignment of landforms will therefore require information on the elevation in order to separate various landforms based on their distinctive elevation levels.

Further analysis of the TPI stacks showed the evolution of the TPI values for different scales. It was shown that many of the scales had a high redundancy and were highly correlated. The analysis of the TPI stack was therefore essential to select less correlated scales that were suitable for characterizing the landscape. As shown for the test sites, about two to four of such scales were identified to be meaningfully different. The analysis of the stack further showed that important TPI variations also took place in a value range between -0.5 and +0.5. That was of importance for the TPI based landform classification (see Section 4.3.3). In this context Reu et al. (2011) noted similar observations. The TPI variations with relevance for the landform characterization take place between values in the range from -1 to +1 and should therefore be considered for the landform classification.

Visual analysis provided no evidence that the data were sensitive to sub-pixel, micro topographic variations that are caused by the presence of near surface permafrost. The characterization and detection of these features, e.g. polygonal ice wedge polygons, hummocks and tussocks, will be of value for the assessment and characterization of near-surface properties. It is likely that these features might be detectable with higher resolution DEM - as it was shown for example by Jones et al. (2012, 2013) and Chasmer et al. (2014). Nevertheless, the precise information of the TDX DEM is of great importance for an area-wide characterization of the polar land surface morphometry. The elevation and the topographic features provide accurate information for the morphometric characterization and the morphological interpretation. The analysis of DEM for Arctic research is of importance (Rees (2012)) and the TDX IDEM is capable of providing the most accurate area-wide information on topography - an even better quality than the ASTER GDEM (Janoth et al. (2012), Li, Shi, Li, Muller, Drummond, Li, Li, Li & Liu (2013)).

### 5.2.3 Multispectral Data

It was observed that the multispectral data of Landsat-8 had the highest sensitivity to the land cover classes among all evaluated data. The positions of bare ground, tundra vegetation, and tundra wetland vegetation were clearer and more distinct compared to the PolSAR data. The characteristics of the land cover units were in accordance to the assumptions of surface reflectance. It was observed that the problem of low spectral contrast of tundra vegetation classes is present. It was found that wetlands had a low reflectance, a low spectral contrast, and therefore a low signal. With respect to these findings the area-wide accurate classification of wetlands will be more accurate if optical and SAR (PolSAR) data will be used in synergistic way. The reflectance of mixed and shrub dominated tundra were very similar and were therefore also difficult to be classified by supervised or by unsupervised classification techniques.

Nevertheless, increases in greenness and NDVI were observed with increases to the percentage of vegetation cover and shrub density. Perhaps this makes these features suitable for the estimation of biophysical parameters, which could then be used to track the land cover changes that are expected with ongoing warming of the arctic land surface (e.g. increasing of the shrub density). The comparison of these two features showed that the NDVI had a lower applicability than the greenness for the characterization of tundra vegetation classes. The NDVI values of the sparse, mixed, shrub dominated tundra and wetland all had similar value ranges. This was observed for the classes for all the test sites in the Mackenzie Delta and Banks Island. The features of the tasseled cap transformation, e.g. the greenness, were better suited for land surface characterization and showed a more distinct position of the classes. This was especially true for the differentiation of wetland and non-wetland vegetation. These findings support the application of the greenness feature for the estimation of the shrub density. The recent findings of Olthof & Fraser (2007), Fraser et al. (2011), Olthof & Fraser (2014), Fraser et al. (2014) showed the application of the greenness and multispectral data for the long term monitoring and change detection of tundra landscapes. It was shown that the characteristics of the high arctic tundra formations of Banks Island were indifferent for both PolSAR and optical data.

## 5.3 Land Surface Classification

The following sections provide a brief summary and discussion of the results of the water body, land cover, and land surface morphology classifications. The final conclusions are provided in Section 6.

### 5.3.1 Water Bodies

The iterative water classification was shown to be a fast and effective method to derive a water mask from PolSAR data. A comparison between the water mask and the reference data demonstrated a high level of confidence and the classification accuracies were in the order of 90%. The larger water bodies, such as major inland lakes and wide river channels, were safely detected. Using the iterative water classification and TanDEM-X elevation model it was possible to delineate the entire shoreline of the Mackenzie Delta Region. The smaller water bodies, such as creeks and small inland lakes, were not classified with the same level of accuracy due to the spatial resolution of twelve meter. However, this spatial resolution was shown to be detailed enough to classify primary water bodies.

The misclassification of pixels was observed for areas with very low double bounce (volume scattering) intensities, such as smooth mudflats and shadowed areas. The misclassification of pixels led to an overestimation of the number of water bodies. A potential solution to this problem will be to classify the shadowed areas prior to the classification of water bodies by modeling the local incidence angle. In order to accomplish this, it will be necessary to bring together knowledge of the acquisition geometry and a high resolution DEM, e.g. the TDX IDEM. The classification of shadowed areas will avoid misinterpretation of the water mask and thus help to manually enhance the classification results.

The above approach will require the definition of a threshold to derive the water mask from the water probability map. This threshold will have to be determined by the user and therefore the classification will not operate in an automated way. A way around this will be to automatically estimate this threshold. For example, a threshold may be defined with the Otsu algorithm. This algorithm has been shown to be an effective threshold estimator for binary classifications (e.g. Li, Du, Ling, Zhou, Wang, Gui, Sun & Zhang (2013)). In addition, the definition of a Constant False Alarm Rate model may overcome the need for user-based interaction in the modeling process. The implementation of a Constant False Alarm Rate will require finding an adequate probability density function for the water probability feature. Constant False Alarm Rate models are frequently used to determine thresholds for SAR and PolSAR based ship/target detection (Estable et al. (2009), Brekke & Anfinson (2011)).

The developed algorithm is very flexible since it can be applied to any kind of PolSAR data. For cross-polarized data this approach can be applied using the HV and VH polarizations. For co-polarized data, the double bounce feature of the Two Component Decomposition can be used. For quad-polarized data the classification can be initiated using the volume scattering or the double bounce of the Three Component Decomposition or the HV polarization channel.

The application of the iterative water classification has shown to be of high value for subsequent classifications. It should be noted that the water surfaces can occupy several positions in the features space depending on the roughness of the water surface, e.g. calm or rough surfaces. The detection of water bodies prior to an unsupervised classification has positive effect on the classification of the remaining classes and is recommended for any unsupervised land cover classification.

#### 5.3.2 Land Cover

The results of this research show that a number of tundra-based land cover types can be detected through the use of PolSAR data and unsupervised classification techniques. The unsupervised classification of PolSAR data is of special interest due to the lack of land cover reference data, remoteness of the area, and frequent cloud cover. As was previously discussed, it was shown that (1) X- and C-Band data were sensitive to the user defined tundra-based land cover classes of the test sites and (2) an accurate unsupervised classification of wetland and bare ground classes could be achieved to a high degree of confidence using the unsupervised FKM-ML and supervised Maximum Likelihood classifications. An analysis of classification accuracies for the PolSAR data indicated that the separation and classification of the land cover types was best realized with quad-polarized data followed by co- and cross-polarized C- and X-Band data. Among the cross-polarized data, the HH/HV-polarized data were shown to be better suited for the land cover classification than the VV/VH-polarized data. This was indicated by higher

## 5 Interpretation and Discussion

classification accuracies for the HH/HV data. The L-Band data were shown to be less sensitive to the defined land cover classes: consequently, classification accuracies were low. The X-Band data were identified to be most sensitive to the characteristics of the sparse vegetated and mixed vegetated tundra. These classes had comparably high classification accuracies. Along with this the high sensitivity of the C-Band data for the shrub lands was also proven by the accuracy assessment. The classification accuracies of this class were high compared to X- and L-Band.

It was shown that the PolSAR data alone were not capable of classifying the generalized land cover types with a satisfactory accuracy. As for the unsupervised classification, it was observed that only the wetland and bare ground classes were accurately classified when co-polarized or quad-polarized C- or X-Band data were used. The observations made for the Mackenzie Delta and Banks Island test sites were in accordance with the results from previous research Banks et al. (2012), Ullmann et al. (2014). The accuracies of the vegetation classes were low and in most cases less than 60%. This indicated that although the PolSAR data were sensitive to the differences in vegetation types (respectively the vegetation coverage and the shrub density), the separation within the feature space was not sufficient for an accurate unsupervised or supervised classification. The application of PolSAR data for classification was therefore limited and restricted to the bare ground and wetland classes. This was shown for all test sites within the Mackenzie Delta and Banks Island. Up to date information for these two classes is relevant to coastal environmental monitoring, including pre- and post-disaster environmental assessments.

The accuracy assessment showed that a sufficiently accurate land cover classification was achieved using the multispectral data of Landsat-8. This supports the findings of recent publications (Olthof & Fraser (2007), Fraser et al. (2011)). It was demonstrated that the spectral data give information on the composition and distribution of the land cover types over time (Olthof & Fraser (2014)). In this research, it was shown that the classification accuracies of all generalized land cover classes were high to moderate and that the spectral information was crucial to differentiate between the different tundra vegetation formations of the Mackenzie Delta test sites, e.g. between mixed tundra and shrub dominated tundra. The classification accuracies of the unsupervised and supervised classification were higher than 80% and on average higher than any classification of the PolSAR data. As shown in Section 4.2.2 the spectral information was sensitive to classes sparse vegetated, mixed and shrub dominated tundra. The analysis of the Banks Island test site showed that the optical data offered a better separation of the land cover classes than the PolSAR data. However, the differentiation of the tussock and non-tussock tundra was difficult with optical data alone since both had similar spectral signatures (see Section 4.3.2.2).

The highest classification accuracies were observed when PolSAR and multispectral data were combined. It was shown that spectral reflectance and the polarimetric signal offered complementary information on the land cover classes of interest. This was especially true for the sparse vegetated tundra classes of the Mackenzie Delta Region, and the tussock and non-tussock dominated tundra of Banks Island. Neither multispectral nor polarimetric data showed high classification accuracy when used alone for land cover classification. In contrast, the accuracies were higher when PolSAR and Landsat-8 data were combined. This indicated that the PolSAR data provided information on the structure and roughness of the land cover. This supports the findings of Banks et al. (2014), which noted a substantial increase of the classification accuracies of land cover types of the test sites Richards Island and Tuktoyktuk when PolSAR and multispectral SPOT data were combined.



A classification with a high level of confidence was possible when the polarimetric information was added to the multispectral data. It was possible to achieve absolute classification accuracies of more than 95% for the bare ground and wetland classes. The effect was also positive for the classification of shrub dominated and mixed tundra. In total, the average increment of the classification accuracy was more than +5%. This result was observed for both the unsupervised and supervised classification, indicating that the class positions of the combined feature space were more distinct and therefore better suited to be classified. The accurate unsupervised or supervised classification of tundra vegetation will therefore require the usage of spectral information. The PolSAR data provide information on the structure of the vegetation but results here indicated that this information alone is not sufficient to clearly differentiate between different types of tundra vegetation and best results were obtained when spectral information on the land cover were included in the classification. Among the different combinations of PolSAR and multispectral data, the quad-polarized data followed by the co-polarized and cross-polarized data of the C- and X-Band were found to be best suited for the classification. This order was the same as the one found by the analysis of the scattering characteristics and was also confirmed by the analysis of the separability distances (Jefferys Matusita and Bhattacharyya Distances).

Concerning the assignment of unsupervised classes to land cover classes, some general issues remain. The unsupervised classes were assigned to land cover classes using the available reference data. In such circumstances, a minimum amount of land cover reference information is required. It is unlikely that a sufficient amount of reference data will be available for large (and remote) areas of interest. For this reason, it is recommended to base the assignment of the unsupervised classes on expert knowledge.

#### 5.3.3 Terrain and Landform

The TDX IDEM data were used to classify the land surface morphology and the approach used the features of elevation, slope and topographic position index. The continuous and discrete landform classifications were processed and compared to the TPI based landform classification (Weiss (2001)) and the Nested-Means landform classification (Iwahashi & Pike (2007)).

The continuous landform classifications showed that differences between the landform classifications were maximal when the identified scales were used. The classifications were suitable for giving an overview of the arrangement of the landforms of the sites. The high number of classes makes this kind of imagery unsuitable for landform classifications. Therefore, a possible application of this imagery is the support of (semi-) manually mapping. The selection of suitable TPI scales was qualitative and therefore did not make use of any quantitative methods. Along with this the selection of the scales that were actually used for the classifications were chosen manually and it was not reasonable at this point - with respect to the high number of the turning points - to involve automated decision rules for the selection of suitable scales. In contrast, the automated selection of elevation and slope thresholds based on the Jenks-Natural-Breaks algorithm showed promising results, even though the thresholds used were selected manually. The chosen TPI breaks of -0.5 and +0.5 were shown to provide a good grouping of the relative elevation (slope) positions.

The discrete landform classification derived with the estimated thresholds of elevation and slope and the chosen TPI thresholds showed a high applicability for all of the chosen sites. The classifications based on

## 5 Interpretation and Discussion

a large TPI scale were able to provide a reasonable overview of the arrangement of the landforms - as was shown for the test site of the Caribou Hills. The inclusion of the elevation in the classification was shown to have positive effect on the delineation of forms and units that are bounded to certain altitude levels. This was especially useful for the characterization of shoreline features. The front shore, the intertidal range, and back shore could be separated with this method. The slope and the TPI values provided further information on the morphology of the shore with different levels of details - depending on the chosen TPI scale. Since the thresholds used in the discrete landform classification were fixed throughout the classification process, this method of classifying the landforms had a high level of transferability. The application of this area-wide method shows promise. Nevertheless, it will require comprehensive expert knowledge and future investigations to select meaningful thresholds.

In contrast, the TPI based landform classification and the Nested-Means landform classification showed limited suitability for the classification of landforms at each of the test sites - that is to say, if they are applied with the standard settings. The automated selected thresholds of the Nested-Means classification were often unsuitable for landforms in accordance to their actual morphometric values; specifically, to separate actual landforms. This was true since the selection of the threshold was based on the sample statistics of the test site; therefore, this will vary with the chosen extent. This makes this approach unsuitable for homogenous and area wide classifications. The utilization of this approach will require the adjustment of the thresholds in order to make them independent from the actual extent of the site.

The differences between TDX IDEM and GDEM were related to the high noise level of the GDEM data. The classification results were smoother and gave a better regional overview for the TDX IDEM data. The higher resolution of the TDX IDEM data was better suited for distinguishing small landscape features. Beside this, the higher spatial resolution was able to provide a more robust estimation of the TPI values - especially for small scales. A comparison between the GDEM to the TDX IDEM remained incomplete since no direct comparison of the same site was investigated.

The methods used to select the suitable TPI scales for the landform classification were shown to be helpful tools for the analysis of the TPI stack. The mean values of the stack, as well as the frequency of the positive TPI changes, were used to identify turning points in the graphs that were believed to indicate significant changes in the size of the landform elements. In contrast, the variance and the rate of change did not provide clear indication of suitable scales. Further investigations are needed here for the automated selection of the thresholds, which was also discussed by Dragut et al. (2011) in terms of multi-scale object-based analysis. It will be a way forward to involve more than one TPI in the classification or to work with the statistical moments of the TPI stack, e.g. mean, standard deviation or skewness. Similarly, the TPI stack analysis and the discrete and continuous classification should be tested in an object-based classification approach. A general issue of the landform classification is the lack of reference data that can be used to assess the accuracy.

---

## Conclusions and Outlook

### 6.1 Summary and Conclusions

The ecosystem of the Arctic is affected by the recently changing environmental conditions and the Northern Hemisphere has undergone a significant climatic change over the last decades. It was observed that the land coverage of the Arctic ecosystems is changing due to the warming. The measurements of satellites have proven that a phenological response to the warming is apparent. Between 1982 and 2012 a substantial greening took place for more than thirty percent of the Arctic landmass. As well, the change of the vegetation composition was revealed in a proliferation of the shrub lands. A further visible indicator of the change is the actual degradation of permafrost that manifests, for example, in the formation of thermokarst lakes, the expansion of existing lakes via thawing and lateral erosion and the active layer destabilization and mobilization. It has been demonstrated that valuable information on the earth's surface can be collected by the use of remotely sensed data. The remote sensing of the Arctic's land surface was predominantly carried out by the usage of optical sensors so far. But the application of optical data encounters problems in the arctic environment, which are for example the frequent cloud cover, the solar geometry, the fragmentation of land cover boundaries, the fast changing spectral characteristics and the low spectral contrast of the land cover types. Contrary, the imaging of Synthetic Aperture Radar is not affected by the cloud cover and the acquisitions of radar systems are independent from solar illumination due to the active sending of the electromagnetic pulses. But compared to the optical sensors the interpretation of Synthetic Aperture Radar data is more challenging and less intuitive. The interpretation of the signal is based on the physical structure and the dielectric properties of the target and not on its spectral properties. The Synthetic Aperture Radar systems are capable to provide three-dimensional information on the topography of the land surface. The radar interferometry is a way to generate information on the elevation and the recent TanDEM-X Mission is an example for the application of area-wide interferometry. The digital elevation model of this mission has a spatial resolution of less than 15 m, a global coverage and an accuracy of less than one meter.

It is of interest to explore, how Synthetic Aperture Radar and digital elevation model data can contribute to

## 6 Conclusions and Outlook

the collection of meaningful land surface information of the polar regions and how they compare to optical remote sensing systems. The objectives of this work were the evaluation of dual- and quad-polarized Synthetic Aperture Radar data of contemporaneous systems for the characterization and classification of tundra land cover. Another objective was to identify the potential of high resolution digital elevation models for the characterization of the surface morphology and to classify generalized landforms. The study was conducted for selected sites of the Mackenzie Delta Region (Canada), for northern Banks Island (Canada) and of the east shore of the James Bay (Canada). The imagery used were polarized Synthetic Aperture Radar data of the satellites TerraSAR-X, TanDEM-X, Radarsat-2 and ALOS PALSAR - as well as multispectral data of the Landsat 8 satellite. In situ collected land cover reference data were available for the assessment. The up-to-date analysis of the radar data made the implementation of newly developed algorithms necessary. These were the Non-Local Means filtering of polarimetric data, the decomposition of co-polarized Synthetic Aperture Radar data and the unsupervised classification of radar and optical data.

**Non-Local Means Filtering** - The analysis of the developed Non-Local Means filter revealed that this kind of image filtering was better compared to standard filtering techniques. The filter showed a high capability to preserve the image values and also showed an enhancement of the edges and a meaningful reduction of the speckle effect. This supported not only the suitability of the data for interpretation but also the image classification. The accuracies of supervised classifications based on Non-Local Means filtered images were in average about +10% higher than the accuracies of supervised classifications based on unfiltered images. The usage the Non-Local Means filter is therefore recommended for any application that involves radar data in the analysis. The shown approach is also capable to handle already processed single-polarized, dual-polarized or quad-polarized radar data and radar data products, e.g. digital elevation models, but required manual parametrization.

**Decomposition of co-polarized Radar Data** - Further it was shown that the power decomposition of co-polarized radar data provided similar features as the established power decomposition of the quad-polarized data. The correlation of the co- and quad-polarized features double bounce and odd bounce was high for land cover classes that show distinct surface or double bounce scattering, e.g. bare ground and wetlands. The correlation was low for vegetation classes and showed no correlation with the volume scattering features of the quad-polarized data. The application of the co-polarized decomposition generated polarimetric features that facilitated the interpretation of the signal and the features were found to be useful to identify the type of scattering. The co-polarized model is not adjusted to the volume contribution of a scatter and this has to be considered when interpreting these features. A usage of the co-polarized data is beneficial and most reasonable for regions of natural land coverage without anthropogenic disturbance and for low vegetation formations that cause only little volume scattering, such as tundra vegetation.

**Unsupervised Land Cover Classification Approach** - The developed unsupervised classification technique offered an approach that is capable to handle any kind of polarized radar data and/or optical data in the same way. This approach is therefore especially useful for benchmarking and comparative analysis. It will not necessarily provide the most accurate classification. Nevertheless it was shown that among the different standard classification techniques this classifier and the K-Means Wishart classifier showed the best classification performance. The technique only requires a minimum of user interaction and showed good performance for land cover classes that have distinct class positions. It was observed and discussed

that this classifier is not capable to differentiate between classes with similar feature space positions. Further it was necessary to manually set the number of desired classes and the technique therefore needed manual initialization. But it did not require any land cover reference data for the training.

**Polarimetric and Multispectral Signatures** - The evaluation of the Synthetic Aperture Radar data revealed that the X- and C-Band data had the highest sensitivity to the investigated generalized land cover classes. The X-Band data showed higher sensitivity to the low tundra formations, the C-Band data were more sensitive to the medium and high tundra formations. The L-Band data showed only little sensitivity to these types of vegetation, but were sensitive to classes bare ground and wetland. As a result of this evaluation and discussion it can be concluded that the X- and C-Band data are suited for the characterization of the tundra land cover. The rather small vegetation of the tundra ecosystem requires the usage of short wavelengths. It was found that the X-Band is sensitive to these small vegetation formations and therefore suited to characterize sparse vegetated communities with low shrub density. The C-Band is less sensitive to sparse vegetated tundra but it was more sensitive to shrub density and best suited to characterize the shrub dominated tundra. The L-Band data were less suited for the characterization of the land cover since the characteristics of all classes were similar.

It was found that the analyzed features of the Entropy/Alpha Decomposition (Entropy, Alpha of Covariance-Matrix and Alpha of Coherency-Matrix) and of the Power Decomposition (double bounce, single bounce, volume scattering) were useful for the characterization of the investigated generalized tundra land cover types for all frequencies. The decomposition features were more sensitive and better suited for the interpretation of the signal than the intensity data. The comparison of different polarizations revealed that the HH and HV polarization channels were better suited for the characterization than the VV polarization. The co-polarization was identified to be most meaningful for the characterization of tundra land cover, followed by the HH/HV-polarization, and the VV/VH-polarization. The quad-polarization showed the highest sensitivity to land cover and only minor disparity to the co-polarized information. As the data of X- and C-Band were sensitive to the increasing shrub density and the vegetation fraction, the features of co- and quad-polarized data may be used in future for the estimation of bio-physical parameters, however, this will required comprehensive future investigations.

The analysis of the Landsat 8 multispectral data was performed using the in situ land cover data as reference. The features analyzed were the Normalized Difference Vegetation Index, the brightness, greenness and wetness of the tasseled cap transformation, the reflectance of red and the reflectance of near-infrared light. The boxplot analysis of the land cover reference data showed that Normalized Difference Vegetation Index and the greenness of the tasseled cap transformation were best suited to characterize the land cover. Both features showed increasing values for increasing vegetation density and coverage. In addition, they were suited to differentiate between bare and vegetated ground. Therefore the spectral information was of high value for the differentiation of land cover types, which is in line with recent findings. However, the results of this work were less clear for the high-arctic environment of Banks Island and future investigations are needed.

**Land Cover Classification of Tundra Environment** - The water bodies were the first land cover class that was derived using the polarimetric radar data. This was done to facilitate the land cover classification. The detection of water bodies prior to unsupervised classification has a positive effect on the classification of the remaining classes and is recommended for any unsupervised land cover classification. The

## 6 Conclusions and Outlook

classification of water bodies was performed by polarimetric X- and C-Band radar data using the double bounce feature of the Power Decomposition. The results showed that using the double bounce feature for the characterization of the water was sufficient since the water surface did not cause a double bounce signal. The water classifications had in average overall classification accuracies of more than 90% - for both co-polarized TerraSAR-X data and quad-polarized Radarsat-2 data. Wrong assignments were related to an overestimation of the water bodies. This overestimation was observed for areas of low double bounce, such as beaches, mudflats and shadowed areas. The intermediate digital elevation model of TanDEM-X Mission was used to finally differentiate between inland water bodies and the ocean and to delineate the shoreline.

The classification of the other land cover classes was done in unsupervised and supervised ways. Various data combinations of radar and/or multispectral data were tested. It was shown that the accurate land cover classification of tundra vegetation required the usage of spectral information. The radar data gave information on the structure of the vegetation but results indicated that this information alone is not sufficient to clearly differentiate between different types of tundra vegetation. Best results were obtained when spectral information was added. Including radar data in the classification led to a benefit of up to +15% accuracy. The quad-polarized data were found to be best suited for the classification, followed by the co-polarized and cross-polarized data of the C- and X-Band, and L-Band data. Therefore a combination of shortwave radar and multispectral data is favorable. The unsupervised classification of radar, optical, and combined radar and optical data showed an average of absolute classification accuracies of about 65%, 75% and 80%. The corresponding supervised classification showed accuracies of about 75%, 85% and 90%. It was further observed that radar data were suited to classify two classes on a high level of confidence - especially, if X- and C-Band data were combined in a multi-frequency analysis. These were the classes wetland and bare ground. Further, the X-Band data were found to be meaningful for the differentiation of tussock and non-tussock tundra at the test site of northern Banks Island. Therefore the integration of polarimetric X- and C-Band data is meaningful for accurate land cover classification of an Arctic environment. Co-polarized data are especially promising for this task since its polarimetric information is sensitive to the type of land cover, of value in the classification, and as co-polarized data provide a higher spatial resolution than the quad-polarized data. The combination of polarimetric radar and multispectral data has a high applicability for mapping the land surface properties of the Arctic environment. This is for example of value for the damage assessment in case of oil-spill disasters. As well, the land cover maps are of importance to evaluate the land cover changes over time, e.g. to map the succession of the vegetation or to estimate the extent and impact of tundra fires. The radar data provided significant information for these tasks. Therefore an integration of this remote sensing technique for actual and upcoming research is recommended.

**Morphometric Characterization and Landform Classification** - The basic topographic features of digital elevation model - such as elevation, slope or the relative Topographic Position Index - were analyzed in this work on multiple spatial scales. This initial investigations were done for four test sites using the intermediate digital elevation model of the TanDEM-X Mission and ASTER GDEM data. It was shown that the elevation, slope and aspect offer important information on the arrangement of the landscape elements and that the actual values of these features can be used for a quantification of the landforms and the morphometry of the surface. It was shown that Topographic Position Indices calculated

with small estimation windows were suited for the characterization of local forms. The Topographic Position Indices estimated with medium windows were identified to be useful to characterize the regional arrangement of landforms, e.g. the drainage system or the slope position. The Topographic Position Indices estimated with large windows were suited to characterize first-order and higher-ranking landforms, e.g. primary valleys, ridges, or peaks. It was found that the small scales were better suited for relief with high variation and less suited for relief with low topographic variation. The Topographic Position Indices estimated with medium and large windows showed robust values and high applicability for all test sites. The extensive flat surfaces showed a noisy texture on all scales investigated and therefore the feature was less suited for the characterization of this form. It was observed that a systematic blurring of the Topographic Position Index values was present if rapid elevation changes took place. The high spatial resolution of the intermediate digital elevation model was important to derive robust and reliable topographic features values on all investigated scales.

In addition, the digital elevation models were used for initial landform classification. This classification was based on the features elevation, slope and a selected Topographic Position Index. The classification was carried out in two ways: (1) A discrete classification with a manageable number of classes and (2) a quasi continuous classification with a very high number of classes. The preliminary results showed that the discrete landform classification provided a reasonable grouping of the arrangement of the landform ensemble. The technique was identified to be suited to give a qualitative overview of the landforms in the study area. The continuous classification showed to be a fast and suitable way to display several topographic features in one single image and that these classifications will support the interpretation and (semi-) manual mapping of geomorphometrical and geomorphological relevant units. The high resolution intermediate digital elevation models of the TanDEM-X Mission were again of high value for all investigated sites. The information on the elevation was very accurate and no discontinuities of the data were found. The vertical spacing of some decimeters was of importance to conduct a reliable analysis of terrain with low topographic variation, e.g. in the flat delta of the Mackenzie. Therefore this highly accurate and detailed elevation information will help to come to a better radiometric calibration of spectral and polarimetric signals of other sensors. The data of the TanDEM-X Mission will have a strong impact on any research that deals with the topography or morphometry of the Arctic land surface. The up to now unrivaled spatial resolution of this truly Pan-Arctic elevation model is highly suited for terrain, morphometric and geomorphologic analysis and an integration of this data in current and up-coming research projects is recommended.

**Summary** - Given the stated objectives it can be concluded that the polarimetric X-, C- and L-Band radar data can be used to characterize generalized land cover types of the tundra environment. (1) It was shown that the recent advances in radar data processing, such as the polarimetric decomposition of co-polarized data and the Non-Local Means speckle filtering advance the characterization and classification of the land cover. In addition to this, it was proven that the polarimetric radar data facilitated the characterization of tundra land cover types based on their physical structure due to their polarimetric characteristics and that they gave complementary (synergistic) information to the multispectral reflectance data. (2) The radar data were shown to be suited to classify some user-defined generalized types of tundra land cover - which were the classes wetland and bare ground. However, it was illustrated that the accurate land cover classification of tundra vegetation required the usage of spectral information. The unsupervised techniques lead to

## 6 Conclusions and Outlook

promising results and accurate classifications without integrating in situ reference information on the Arctic land cover. The unsupervised techniques therefore helped to overcome limitations that are caused by limited accessibility, circumference and missing reference. (3) The analysis of the digital elevation model data of the TanDEM-X showed a high potential for the characterization of the surface morphology. The basic and relative topographic features displayed a high relevance for the quantification of the morphology. (4) Further, these data were of value for the initial classification of the surface morphology and to delineate landforms. Therefore these classifications will assist the delineation of geomorphological units and an area-wide mapping is feasible. Such applications have potential to identify locations of actual and future activity and to monitor the Arctic land surface dynamics.

### 6.2 Outlook and Perspectives

Additional research is needed on the application of radar and digital terrain model for the characterization and classification of Arctic Environment. The following tasks should be subject of future investigations. Research is needed concerning the registration of optical and PolSAR data. In this work the PolSAR data and the optical data were manually registered which is a time consuming process. An automated registration will be necessary to come to a fully automated processing chain. Also it is of interest which benefits a high resolution digital elevation model will show on the orthorectification of multispectral, hyperspectral and other PolSAR data. It is believed that accurate topographic information will enhance the quality of the registration, orthorectification and radiometric accuracy. In future the data of the TanDEM-X Mission may be used operationally for the registration and orthorectification of satellite data of the Arctic to enhance the position accuracy.

Another research need is to extend the analysis on the land cover characterization and classification with quad-polarized X- and L-Band data and to conduct the analysis for other Arctic test sites. The results of this study indicated that the quad-polarized data X-Band data will likely have a very high potential for mapping the Arctic's low tundra vegetation. Currently no space borne system operationally acquires data in this mode. However, TerraSAR-X and TanDEM-X satellites offered the acquisition of quad-polarized data as experimental products mode during the DRA campaign (dual-receive-antenna, DLR (2006)). For a comprehensive and comparative study of the radar scattering characteristics a transfer of this approach to other sites is necessary. In this context, the classification of the land cover may be tested using multi-temporal satellite imagery and/or an object-based approach. The data base may be extended using data of the recently launched Sentinel-1 (C-Band) or ALOS PALSAR 2 (L-Band).

Further, the evaluation of PolSAR features should be carried out with more detailed reference data and more land cover classes for selected test sites. It should be tested if the sensitivity of the X- and C-Band to the small tundra vegetation is sufficient high to correlate the scattering with biophysical vegetation parameters, e.g. the shrub density, or the biomass. It will further be of interest to relate the PolSAR features to the grain size of bare substrates and to the moisture conditions. It is imaginable that PolSAR data facilitate the characterization of the surface roughness and moisture regime - as it was shown by Banks et al. (2014) for Tuktoyaktuk and Richards Island.

In addition, the water classification technique should be applied in time series analysis to estimate the fraction of the seasonal open water surface. The importance of this task was shown by Morgenstern et al.



(2011). A possible application will be the detection of the onset and offset of the freezing and thawing of the lakes and rivers. These dates are indicators for changing environmental conditions (Sobiech & Dierking (2013)). As well, the classification technique may be of value to monitor the water level of rivers and lakes.

It is of interest to combine high resolution optical and radar data for land cover classification applications of selected areas and hot spots of the environmental change. The contemporaneous radar sensors offer resolutions of less than five meters and since 2013 TerraSAR-X and TanDEM-X sensors are capable to acquire single-polarized images with a spatial resolution of less than one meter (Staring-Spotlight Mode). A possible scenario will be the usage of co-polarized data of the Spotlight or High-Resolution Spotlight mode of TerraSAR-X and multispectral RapidEye or Pléiades satellite imagery. These data may be applied for detailed analysis of selected areas, e.g. to monitor active erosion processes, to map small scale land cover changes, or to give near-real-time information in case of environmental disasters. In addition, these high resolution data may be applied to monitor remote infrastructure and to identify surface movements via differential interferometry, e.g. as shown by Short et al. (2014).

Concerning the analysis of digital elevation models it should be tested if more advanced feature extraction techniques and multivariate analysis provide better features for the characterization of the land surface morphology and of the landforms. Exemplary, the application of hydrographic modeling allows deriving parameters that are in relation to the drainage network and the depth contour line. The application of parametric unsupervised classification techniques allows integrating several topographic features in the classification process. Such techniques will presumptively allow more accurate classifications and a more distinct differentiation of the classes. A further task is the integration of the land cover and landform classifications. The synergistic usage of these remotely sensed products will require an elaborated conceptual approach and a defined framework. Nevertheless, it is imaginable to use these data for the classification of shoreline types when combining information on the coverage and morphology, for example.

Also it will be an advance to store the remote sensing data, the extracted meaningful features and the classification products in a regularly updated GIS-Database. Such a database will be of value for decision making, planning activities and near-realtime geographical analysis. On top of that it will also allow relating the spatio-temporal information of the remote sensing data to other ecosystem variable that are relevant for the indication of the environmental change. The continuous acquisition of remote sensing imagery of the Arctic Environment will not only help to quantify and understand today's situation but will also give future researchers insights on past processes and on the reasons for our decisions.



---

---

## Bibliography

- ACIA (2005), 'Arctic Climate Impact Assessment Report', *Cambridge University Press*, pp. 1–1042.
- Ainsworth, T., Kelly, J. & Lee, J. (2008), 'Polarimetric analysis of dual polarimetric SAR imagery', *Synthetic Aperture Radar (EUSAR), 2008 7th European Conference on*, pp. 1–5.
- Allen, D., Michel, F. & Judge, A. (1988), 'The permafrost regime in the Mackenzie Delta, Beaufort Sea region, N.W.T. and its significance to the reconstruction of the palaeoclimatic history', *Journal of Quaternary Science*, **Vol. 3**(1), pp. 3–13.
- Amante, C. & Eakins, B. (2009), 'ETOPO1 1 arc-minute global relief model: Procedures, data sources and analysis. NOAA technical memorandum NESDIS NGDC-24', *National Geophysical Data Center; NOAA*.
- An, W., Yi, C., Jiang, Y. & Hongji, Z. (2010), 'Fast alternatives to H/alpha for polarimetric SAR', *Geoscience and Remote Sensing Letters, IEEE*, **Vol. 7**(2), pp. 343–347.
- Anisimov, J.N., O., Constable, A., Hollowed, A., Maynard, N., Prestrud, P. and Prowse, T. & Stone, J. (2014), 'Polar regions.', *In: Climate Change 2014: Impacts, Adaptation, and Vulnerability. Part B: Regional Aspects. Contribution of Working Group II to the Fifth Assessment Report of the Intergovernmental Panel on Climate Change. Cambridge University Press, Cambridge, United Kingdom and New York*, pp. 1567–1612.
- Anisimov, O., D.G. Vaughan, T., Callaghan, C., Furgal, H., Marchant, T., Prowse, H., Vilhjalmsson & Walsh, J. (2007), 'Polar regions (Arctic and Antarctic)', *Climate Change 2007: Impacts, Adaptation and Vulnerability. Contribution of Working Group II to the Fourth Assessment Report of the Intergovernmental Panel on Climate Change. M.L. Parry, O.F. Canziani, J.P. Palutikof, P.J. van der Linden and C.E. Hanson, Eds. Cambridge University Press, Cambridge*, pp. 653–685.
- ASF (2014), 'Alaska Satellite Facility. Seasat mission', *URL: <https://www.asf.alaska.edu/seasat/>*.
- ASI (2014), 'Italian Space Agency. COSMO-SkyMed website for institutional and scientific users', *URL: <http://www.cosmo-skymed.it>*.
- Astrium (2011), 'Astrium officially presents the PAZ satellite in Spain', *Astrium, June 7, 2011*, *URL: <http://www.astrium.eads.net/en/presscentre/astrium-officially-presents-the-paz-satellite-in-spain.html>*.
- Banks, S., King, D., Merzouki, A. & Duffe, J. (2014), 'Assessing RADARSAT-2 for mapping shoreline cleanup and assessment technique (SCAT) classes in the Canadian Arctic', *Canadian Journal of Remote Sensing*, **Vol. 40**(3), pp. 243–267.
- Banks, S. N., King, D. J., Merzouki, A., Duffe, J. & Solomon, S. (2011), 'Assessing Radarsat-2 polarimetric SAR for mapping shoreline cleanup and assessment technique (SCAT) classes in the Canadian

## Bibliography

- Arctic', *Proceedings 32nd Canadian Symposium on Remote Sensing, 13.-16. June, 2011, Sherbrooke, Quebec*, pp. 1–8.
- Banks, S., Ullmann, T., Duffe, J., Roth, A., King, D., Demers, A., Hogg, A., Schmitt, A., Baumhauer, R. & Dech, S. (2012), 'Multi-frequency analysis of high resolution quad-pol Radarsat-2 and dual-pol TerraSAR-X data for land cover classification in Arctic coastal ecosystems, Mackenzie Delta, Beaufort Sea', *Geoscience and Remote Sensing Symposium (IGARSS), 2012 IEEE International*, pp. 3548–3551.
- Barsch, D. & Liedtke, H. (1985), 'Geomorphological mapping in the Federal Republic of Germany: Contributions to the GMK-priority', *Institut fuer Physische Geographie der Freien Universitaet Berlin*, pp. 1–94.
- Bishop, M., James, A., Shroder, J. & Walsh, S. (2012), 'Geospatial technologies and digital geomorphological mapping: Concepts, issues and research', *Geomorphology*, **Vol. 137**(1), pp. 5–26.
- Boerner, W. M. (2008), 'Basic concepts in radar polarimetry', *PolSARpro V3.0 - Lecture Notes*, pp. 1–100.
- Bologaro-Crevenna, A., Torres-Rodríguez, V., Sorani, V., Frame, D. & Arturo Ortiz, M. (2005), 'Geomorphometric analysis for characterizing landforms in Morelos State, Mexico', *Geomorphology*, **Vol. 67**(3-4), pp. 407–422.
- Bonfils, C., Phillips, T., Lawrence, D., Cameron-Smith, P., Riley, W. & Subin, Z. (2012), 'On the influence of shrub height and expansion on northern high latitude climate', *Environmental Research Letters*, **Vol. 7**(1), pp.1–9.
- Brekke, C. & Anfinsen, S. (2011), 'Ship detection in ice-infested waters based on dual-polarization SAR imagery', *Geoscience and Remote Sensing Letters, IEEE*, **Vol. 8**(3), pp. 391–395.
- Brisco, B., Short, N., Budkewitsch, P., Murnaghan, K. & Charbonneau, F. (2009), 'SAR interferometry and polarimetry for mapping and monitoring permafrost in Canada', *Proceedings of 4th International Workshop on Science and Applications of SAR Polarimetry and Polarimetric Interferometry - PolInSAR 2009, 26 - 30 January 2009, Frascati, Italy*, pp. 1–4.
- Buades, A., Coll, B. & Morel, J. (2005), 'A review of image denoising algorithms, with a new one', *Multiscale Modeling and Simulation*, **Vol. 4**(2), pp. 490–530.
- Burn, C. R. & Kokelj, S. V. (2009), 'The environment and permafrost of the Mackenzie Delta Area', *Permafrost and Periglacial Processes*, **Vol. 20**, pp. 83–105.
- Burn, C. R. & Zhang, Y. (2010), 'Sensitivity of active-layer development to winter conditions north of treeline, Mackenzie Delta area, western Arctic Coast', *Geo2010 Calgary Conference, Canadian Geotechnical Conference*, **Vol. 63**, pp. 1458–1465.
- Burrough, P., Gaans, v. & MacMillan, R. (2000), 'High-resolution landform classification using fuzzy k-means', *Fuzzy Sets and Systems*, **Vol. 113**(1), pp. 37–52.
- Canty, M. (2006), 'Image analysis, classification and change detection in remote sensing: With algorithms for ENVI/IDL', *Taylor & Francis*, pp. 1–472.
- Chasmer, L., Hopkinson, C., Veness, T., Quinton, W. & Baltzer, J. (2014), 'A decision-tree classification for low-lying complex land cover types within the zone of discontinuous permafrost', *Remote Sensing of Environment*, **Vol. 143**(0), pp. 73–84.

- Chenier, R. & Hemmingway, C. (2014), 'Updating CHS charts with remote sensing data radar and optical approach', *Canadian Hydrographic Association - 2014 Conference* .
- Chorley, R., Dunn, A. & Beckinsale, R. (1964), 'The history of the study of landforms', *Methuen. London* , **Vol. 1**, pp. 1–678.
- Christiansen, H. H. AMD Etzelmueller, B., Isaksen, K., Juliussen, H., Farbrot, H., Humlum, O., Johansson, M., Ingeman-Nielsen, T., Kristensen, L., Hjort, J., Holmlund, P., Sannel, A. B. K., Sigsgaard, C., Akerman, H. J., Foged, N., Blikra, L. H., Pernosky, M. A. & Odegard, R. S. (2010), 'The thermal state of permafrost in the nordic area during the international polar year 2007-2009.', *Permafrost Periglacial Processes*, pp. 156–181.
- Clark, P. & Lea, P. (1992), 'The last interglacial-glacial transition in North America', *Geological Society of America. Geological Society of America Special Paper*, pp. 31–52.
- Cloude, S. (1997), 'An entropy based classification scheme for land applications of polarimetric SAR', *IEEE Transactions on Geoscience and Remote Sensing* , **Vol. 35(1)**, pp. 68–78.
- Cloude, S. (2007), 'The dual polarization entropy/alpha decomposition: a PALSAR case study', *POLin-SAR2007 Workshop (2007). European Space Agency (ESA)*, pp. 1–6.
- Cloude, S., Goodenough, D. & Chen, H. (2012), 'Compact decomposition theory', *Geoscience and Remote Sensing Letters, IEEE* , **Vol. 9(1)**, pp. 28–32.
- Cloude, S. & Pottier, E. (1996), 'A review of target decomposition theorems in radar polarimetry', *IEEE Transactions on Geoscience and Remote Sensing* , **Vol. 34(2)**, pp. 498–518.
- Cloude, S. R. (2010), 'Polarisation: applications in remote sensing', *Oxford University Press*, pp. 1–449.
- Collingwood, A., Treitz, P., Charbonneau, F. & Atkinson, D. (2014), 'Artificial neural network modeling of high arctic phytomass using synthetic aperture radar and multispectral data', *Remote Sensing* , **Vol. 6(3)**, pp. 2134–2153.
- Congalton, R. G. & Green, K. (2008), 'Assessing the accuracy of remotely sensed data: Principles and practices', *CRC Press*, pp. 1–177.
- Corns, I. G. W. (1974), 'Arctic plant communities east of the Mackenzie Delta', *Canadian Journal of Botany* , **Vol. 52(7)**, pp. 1731–1745.
- Crosetto, M. & Perez Aragues, F. (2000), 'Radargrammetry and SAR interferometry for DEM generation: Validation and data fusion', *SAR Workshop: CEOS Committee on Earth Observation Satellites. Working Group on Calibration and Validation, Proceedings of a Conference, 26.29. October 1999, Toulouse, France*, pp. 1–6.
- CSA (2013), 'RADARSAT constellation mission', *Canadian Space Agency. URL: <http://www.asc-csa.gc.ca/eng/satellites/radarsat/default.asp>* .
- CSA (2014a), 'RADARSAT-2 mission', *Canadian Space Agency. URL: <http://www.asc-csa.gc.ca/eng/satellites/radarsat2>* .
- CSA (2014b), 'RADARSAT mission', *Canadian Space Agency. URL: <http://www.asc-csa.gc.ca/eng/satellites/radarsat1/default.asp>* .
- Cui, Y., Yamaguchi, Y., Yang, J., Park, S.-E., Kobayashi, H. & Singh, G. (2012), 'Three-component power

## Bibliography

- decomposition for polarimetric SAR data based on adaptive volume scatter modeling', *Remote Sensing*, **Vol. 4**(6), pp. 1559–1572.
- Deledalle, C.-A., Denis, L., Tupin, F., Reigber, A. & Jaeger, M. (2015), 'NL-SAR: A unified nonlocal framework for resolution-preserving (Pol)(In)SAR denoising', *Geoscience and Remote Sensing, IEEE Transactions on*, **Vol. 53**(4), pp. 2021–2038.
- Deledalle, C.-A., Tupin, F. & Denis, L. (2010), 'Polarimetric SAR estimation based on non-local means', *Geoscience and Remote Sensing Symposium (IGARSS), 2010 IEEE International*, pp. 2515–2518.
- Demers, A.-M., Banks, S., Duffe, J., Carriere, M., Torontow, V., Chaudhary, B. & Laforest, S. (2013), 'eSPACE: Emergency spatial pre-SCAT for arctic coastal ecosystem', *Radar Conference (RADAR), 2013 IEEE*, pp. 1–6.
- Demers, A.-M., Duffe, J. & Laforest, S. (2011), 'Use of radar and optical data to support emergency and wildlife management in case of an oil spill in Canada's northern coastal ecosystem: Case study of James Bay', *34th International Symposium on Remote Sensing of Environment. The GEOSS Era: Towards Operational Environmental Monitoring, 10.-15. April, 2011 Sydney, Australia*, pp. 1–3.
- DLR (2006), 'TerraSAR-X ground segment experimental product description, TX-GS-DD-3302. v. 1.7', *Deutsches Zentrum fuer Luft- und Raumfahrt, Cluster Applied Remote Sensing, TerraSAR-X Ground Segment*, pp. 1–11.
- DLR (2007), 'TerraSAR-X ground segment level 1b product format specification, TX-GS-DD-3307. v. 1.3', *Deutsches Zentrum fuer Luft- und Raumfahrt, Cluster Applied Remote Sensing, TerraSAR-X Ground Segment*, pp. 1–257.
- DLR (2010), 'TerraSAR-X ground segment basic product specification document, TX-GS-DD-3302. v. 1.7', *Deutsches Zentrum fuer Luft- und Raumfahrt, Cluster Applied Remote Sensing, TerraSAR-X Ground Segment*, pp. 1–109.
- DLR (2013), 'TanDEM-X ground segment DEM products specification document, TD-GS-PS-0021, v.3', *Deutsches Zentrum fuer Luft- und Raumfahrt, Cluster Applied Remote Sensing, TanDEM-X Ground Segment*, pp. 1–43.
- DLR (2014), 'TanDEM-X science service system.', *Deutsches Zentrum fuer Luft- und Raumfahrt*, URL: <https://tandemx-science.dlr.de/>.
- Dong, Y., Milne, A. & Forster, B. (2000), 'A review of SAR speckle filters: texture restoration and preservation', *Geoscience and Remote Sensing Symposium, 2000. Proceedings. IGARSS 2000. IEEE 2000 International*, **Vol. 2**, pp. 633–635.
- Dragut, L. & Blaschke, T. (2006), 'Automated classification of landform elements using object-based image analysis', *Geomorphology*, **Vol. 81**(3-4), pp. 330–344.
- Dragut, L. & Eisank, C. (2011), 'Object representations at multiple scales from digital elevation models', *Geomorphology*, **Vol. 129**(3-4), pp. 183–189.
- Dragut, L. & Eisank, C. (2012), 'Automated object-based classification of topography from SRTM data', *Geomorphology*, **Vol. 141-142**(0), pp. 21–33.
- Dragut, L., Eisank, C. & Strasser, T. (2011), 'Local variance for multi-scale analysis in geomorphometry', *Geomorphology*, **Vol. 130**(3-4), pp. 162–172.

- Duguay, C., Pultz, T., Lafleur, P. & Drai, D. (2002), 'RADARSAT backscatter characteristics of ice growing on shallow sub-arctic lakes, Churchill, Manitoba, Canada', *Hydrological Processes* , **Vol. 16**(8), pp. 1631–1644.
- Ehsani, A. & Quiel, F. (2008), 'Geomorphometric feature analysis using morphometric parameterization and artificial neural networks', *Geomorphology* , **Vol. 99**(1-4), pp. 1–12.
- El-Garouani, A., Alobeid, A. & El-Garouani, S. (2014), 'Digital surface model based on aerial image stereo pairs for 3D building', *International Journal of Sustainable Built Environment* , **Vol. 3**(1), pp. 119–126.
- Environment-Canada (2014), 'Canadian climate normals', URL: <http://climate.weather.gc.ca> .
- Epstein, H., Myers-Smith, I. & Walker, D. (2013), 'Recent dynamics of arctic and sub-arctic vegetation', *Environmental Research Letters* , **Vol. 8**(1), 1–6.
- ESA (2011), 'ERS mission', *European Space Agency*. URL: <https://earth.esa.int/web/guest/missions/esa-operational-eo-missions/ers> .
- ESA (2012), 'ENVISAT mission', *European Space Agency*. URL: <https://earth.esa.int/web/guest/missions/esa-operational-eo-missions/envisat> .
- ESA (2014a), 'PolSARpro - polarimetric SAR data processing and educational tool - polarimetry-tutorial', *European Space Agency*. URL: <https://earth.esa.int/web/polsarpro/polarimetry-tutorial> .
- ESA (2014b), 'Sentinel-1 mission', *European Space Agency*. URL: <https://earth.esa.int/web/guest/missions/esa-operational-eo-missions/sentinel-1> .
- Esch, T., Schenk, A., Ullmann, T., Thiel, M., Roth, A. & Dech, S. (2011), 'Characterization of land cover types in TerraSAR-X images by combined analysis of speckle statistics and intensity information', *Geoscience and Remote Sensing, IEEE Transactions on* , **Vol. 49**(6), pp. 1911–1925.
- ESRI (2014), 'ArcGIS help - ArcGIS resources', URL: <http://resources.arcgis.com> .
- Estable, S., Teufel, F., Petersen, L., Knabe, S., Saur, G. & Ullmann, T. (2009), 'Detection and classification of offshore artificial objects in TerraSAR-X images: First outcomes of the DeMarine-DEKO project', *OCEANS 2009 - EUROPE*, pp. 1–8.
- ESWG (1996), 'A national ecological framework for Canada', *Centre for Land and Biological Resources Research, Research Branch, Agriculture and Agri-Food Canada. Ecological Stratification Working Group and Ecological Stratification Working Group (Canada) and Center for Land and Biological Resources Research (Canada) and Canada. State of the Environment Directorate*, pp. 1–132.
- Evans, I. (2012), 'Geomorphometry and landform mapping: What is a landform?', *Geomorphology* , **Vol. 137**(1), pp. 94–106.
- FOC (2012), 'Fisheries and-Oceans Canada. Hudson Bay and James Bay - geology and physiography. report 314704.', URL: <http://www.dfo-mpo.gc.ca/Library/314704-Ch3.pdf>, pp. 1–22.
- Forbes, D. (2011), 'State of the arctic coast 2010 - scientific review and outlook', *International Arctic Science Committee, Land-Ocean Interactions in the Coastal Zone, Arctic Monitoring and Assessment Programme, International Permafrost Association. Helmholtz-Zentrum, Geesthacht, Germany*, pp. 1–180.

## Bibliography

- Fraser, R., Olthof, I., Carriere, M., Deschamps, A. & Pouliot, D. (2011), 'Detecting long-term changes to vegetation in northern Canada using the Landsat satellite image archive', *Environmental Research Letters* , **Vol. 6**(4), pp. 1–9.
- Fraser, R., Olthof, I., Kokelj, S., Lantz, T., Lacelle, D., Brooker, A., Wolfe, S. & Schwarz, S. (2014), 'Detecting landscape changes in high latitude environments using Landsat trend analysis: 1. visualization', *Remote Sensing* , **Vol. 6**(11), pp. 11533–11557.
- Freeman, A. & Durden, S. (1998), 'A three-component scattering model for polarimetric SAR data', *Geoscience and Remote Sensing, IEEE Transactions on* , **Vol. 36**(3), pp. 963–973.
- Gao, G. (2010), 'Statistical modeling of SAR images: A survey', *Sensors* , **Vol. 10**(1), pp. 775–795.
- Geldsetzer, T. & Yackel, J. J. (2009), 'Sea ice type and open water discrimination using dual co-polarized C-band SAR', *Canadian Journal of Remote Sensing* , **Vol. 35**(1), pp. 73–84.
- GeoBase (2003), 'Canadian digital elevation data', *URL: <http://www.geobase.ca>* .
- GeoBase (2009), 'Land Cover, circa 2000 vector data product specifications', *Centre for Topographic Information Earth Sciences Sector Natural Resources Canada*, pp. 1–21.
- Gratto-Trevor, C. (1996), 'Use of Landsat TM Imagery in determining important shorebird habitat in the outer Mackenzie Delta, Northwest Territories', *ARCTIC* , **Vol. 49**(1), pp. 11–22.
- Grosse, G., Schirrmester, L., Kunitsky, V. & Hubberten, H.-W. (2005), 'The use of CORONA images in remote sensing of periglacial geomorphology: an illustration from the NE Siberian coast', *Permafrost and Periglacial Processes* , **Vol. 16**(2), pp. 163–172.
- Grosse, G., Schirrmester, L. & Malthus, T. (2006), 'Application of Landsat-7 satellite data and a DEM for the quantification of thermokarst-affected terrain types in the periglacial Lena-Anabar coastal lowland', *Polar Research* , **Vol. 25**(1), pp. 51–67.
- Gruber, S. (2012), 'Derivation and analysis of a high-resolution estimate of global permafrost zonation', *The Cryosphere* , **Vol. 6**(1), pp. 221–233.  
**URL:** <http://www.the-cryosphere.net/6/221/2012/>
- Guissard, A. (1994), 'Mueller and kennaugh matrices in radar polarimetry', *IEEE Transactions on Geoscience and Remote Sensing* , **Vol. 32**(3), pp. 590–597.
- Hall-Atkinson, C. & Smith, L. C. (2001), 'Delineation of delta ecozones using interferometric SAR phase coherence Mackenzie River Delta, N.W.T., Canada', *Remote Sensing of Environment* , **Vol. 78**, pp. 229–238.
- Harper, J. R. (1990), 'Morphology of the Canadian Beaufort Coast', *Marine Geology* , **Vol. 91**, pp. 75–91.
- Hartmann, D., Klein Tank, A., Rusticucci, M., Alexander, L., Broennimann, S., Charabi, Y., Dentener, F., Dlugokencky, E., Easterling, D., Kaplan, A., Soden, B., Thorne, P., Wild, M. & Zhai, P. (2013), 'Observations: Atmosphere and surface', In: *Climate Change 2013: The Physical Science Basis. Contribution of Working Group I to the Fifth Assessment Report of the Intergovernmental Panel on Climate Change - Stocker, T.F., D. Qin, G.-K. Plattner, M. Tignor, S.K. Allen, J. Boschung, A. Nauels, Y. Xia, V. Bex and P.M. Midgley (eds.)*. Cambridge University Press, Cambridge, United Kingdom and New York, NY, USA, pp. 159–254.



- Hartmann, J. & Sachs, T. (2012), 'Airborne measurements of methane during POLAR 5 campaign AIRMETH in 2012 with links to raw data files.', *Alfred Wegener Institute, Helmholtz Center for Polar and Marine Research, Bremerhaven* .
- Hein, A. (2010), 'Processing of SAR data: Fundamentals, signal processing, interferometry', *Springer*; pp. 1–291.
- Hengl, T. & Reuter, H. (2009), 'Geomorphometry: Concepts, software, applications', *Elsevier. Developments in soil science*, pp. 1–772.
- Hese, S., Grosse, G. & Poecking, S. (2010), 'Object based thermokarst lake change mapping as part of the ESa data user element (DUE) permafrost', *GEOBIA 2010: Geographic Object-Based Image Analysis, 29.June - 2.July 2010, Ghent, Belgium*, pp. 1–5.
- Hill, P., Blasco, S., Harper, J. & Fissel, D. (1991), 'Sedimentation on the Canadian Beaufort Shelf', *Proceedings of the Canadian Continental Shelf Seabed Symposium* , **Vol. 11**, pp. 821–842.
- Hill, P., Hequette, A., Ruz, M. & Jenner, K. (1991), 'Geological investigations of the Canadian Beaufort Sea Coast. Geological Survey of Canada, open file 2387', *Natural Resources Canada*, pp. 1–365.
- Huang, Y. & Genderen, J. L. (1996), 'Evaluation of several speckle filtering techniques for ERS-1 and 2 imagery', *International Archives of Photogrammetry and Remote Sensing* , **Vol. XXXI, Part B2**, pp. 1–6.
- Hughenoltz, C. & Sanden, v.-d. J. (2001), 'Polarimetric SAR for geomorphic mapping in the intertidal zone, Minas Basin Bay of Fundy, Nova Scotia', *Natural Resources Canada & Canadian Center for Remote Sensing*, pp. 1–28.
- IPPC, van Oldenborgh, G., Collins, M., Arblaster, J., Christensen, J., Marotzke, J., Power, S., Rummukainen, M. & Zhou, T. (2014), 'Atlas of global and regional climate projections', *In: Climate Change 2013: The Physical Science Basis. Contribution of Working Group I to the Fifth Assessment Report of the Intergovernmental Panel on Climate Change [Stocker, T.F., D. Qin, G.-K. Plattner, M. Tignor, S.K. Allen, J. Boschung, A. Nauels, Y. Xia, V. Bex and P.M. Midgley (eds.)]. Cambridge University Press, Cambridge, United Kingdom and New York, NY, USA*, pp. 1311–1393.
- Irvin, B., Ventura, S. & Slater, B. (1997), 'Fuzzy and isodata classification of landform elements from digital terrain data in Pleasant Valley, Wisconsin', *Geoderma* , **Vol. 77(2-4)**, pp. 137–154.
- Iwahashi, J. & Pike, R. (2007), 'Automated classifications of topography from DEMs by an unsupervised nested-means algorithm and a three-part geometric signature', *Geomorphology* , **Vol. 86(3-4)**, pp. 409–440.
- Janoth, J., Gantert, S., Koppe, W., Kaptein, A. & Fischer, C. (2012), 'TerraSAR-X2 - mission overview', *Geoscience and Remote Sensing Symposium (IGARSS), 2012 IEEE International*, pp. 217–220.
- JAXA (1992), 'Japan Aerospace Exploration Agency - about JERS', *URL: <http://www.eorc.jaxa.jp/JERS-1/en/>* .
- JAXA (2006), 'Japan Aerospace Exploration Agency - about ALOS - PALSAR', *URL: [eorc.jaxa.jp](http://eorc.jaxa.jp)* .
- JAXA (2014), 'Japan Aerospace Exploration Agency - about ALOS-2 project', *URL: [eorc.jaxa.jp](http://eorc.jaxa.jp)* .
- Jeffries, M., Morris, K. & Liston, G. (1996), 'A method to determine lake depth and water availability

## Bibliography

- on the North Slope of Alaska with spaceborne imaging radar and numerical ice growth modelling', *ARCTIC*, **Vol. 49**, pp. 367–374.
- Jenks, G. F. (1967), 'The data model concept in statistical mapping', *International Yearbook of Cartography*, pp. 189–190.
- Jenness, J. (2006), 'Topographic position index (TPI) v. 1.2 - TPI online documentation', pp. 1–42.
- Jensen, J. (2007), 'Remote sensing of the environment: An earth resource perspective', *Prentice Hall PTR*, pp. 1–608.
- Jensen, J. R. (1995), 'Introductory digital image processing: A remote sensing perspective', *Prentice Hall PTR - Second Edition*, pp. 1–544.
- Jones, B., Grosse, G., Hinkel, K., Arp, C., Walker, S., Beck, R. & Galloway, J. (2012), 'Assessment of pingo distribution and morphometry using an IfSAR derived digital surface model, western Arctic Coastal Plain, Northern Alaska', *Geomorphology*, **Vol. 138**(1), pp. 1–14.
- Jones, B., Stoker, J., Gibbs, A., Grosse, G., Romanovsky, V., Douglas, T., Kinsman, N. & Richmond, B. (2013), 'Quantifying landscape change in an arctic coastal lowland using repeat airborne LiDAR', *Environmental Research Letters*, **Vol. 8**(4), 1–10.
- Kaeaeb, A. (2008), 'Remote sensing of permafrost-related problems and hazards', *Permafrost and Periglacial Processes*, **Vol. 19**, pp. 107–136.
- Kankaku, Y., Osawa, Y., Hatooka, Y. & Suzuki, S. (2010), 'Overview of advanced land observing satellite-2 (ALOS-2) mission.', *Proceedings of the International Archives of the Photogrammetry, Remote Sensing and Spatial Information Science, Kyoto, Japan, 9-12 August 2010*.
- Kozlenko, N. & Jeffries, M. (2000), 'Bathymetric mapping of shallow water in thaw lakes on the North Slope of Alaska with spaceborne imaging radar', *ARCTIC*, **Vol. 53**(3), pp. 306–316.
- Kramer, H. (2002), 'Observation of the earth and its environment: Survey of missions and sensors', *Springer. Engineering online library* pp. 1–1510.
- Laidler, G. & Treitz, P. (2003), 'Biophysical remote sensing of arctic environments', *Progress in Physical Geography March*, **Vol. 27**, pp. 44–68.
- Lantuit, H., Atkinson, D., Overduin, P., Grigoriev, M., Rachold, V., Grosse, G. & Hubberten, H. (2011), 'Coastal erosion dynamics on the permafrost-dominated Bykovsky Peninsula, north Siberia, 1951-2006', *Polar Research*, **Vol. 30**(0), pp. 1–21.
- Lantuit, H. & Pollard, W. (2008), 'Fifty years of coastal erosion and retrogressive thaw slump activity on Herschel Island, southern Beaufort Sea, Yukon Territory, Canada', *Science Direct - Geomorphology, 2008*, **Vol. 95**, pp. 84–102.
- Lantz, T. & Kokelj, S. (2008), 'Increasing rates of retrogressive thaw slump activity in the Mackenzie Delta region, N.W.T., Canada', *Geophysical Research Letters*, **Vol. 35**(6), pp. 1–5.
- Lantz, T., Marsh, P. & Kokelj, S. (2013), 'Recent shrub proliferation in the Mackenzie Delta uplands and microclimatic implications', *Ecosystems*, **Vol. 16**(1), pp. 47–59.
- Lara, M. J., Villarreal, S., Johnson, D. R., Hollister, R. D., Webber, P. J. & Tweedie, C. E. (2012), 'Estimated change in tundra ecosystem function near Barrow, Alaska between 1972 and 2010', *Environmental Research Letters*, **Vol. 7**(1), pp. 1–10.

- Larsen, J., Anisimov, O., Constable, A., Hollowed, A.B. AND Maynard, N., Prestrud, P., Prowse, T. & Stone, J. (2014), 'Polar regions.', *In: Climate Change 2014: Impacts, Adaptation, and Vulnerability. Part B: Regional Aspects. Contribution of Working Group II to the Fifth Assessment Report of the Intergovernmental Panel on Climate Change - Barros, V.R., C.B. Field, D.J. Dokken, M.D. Mastrandrea, K.J. Mach, T.E. Bilir, M. Chatterjee, K.L. Ebi, Y.O. Estrada, R.C. Genova, B. Girma, E.S. Kissel, A.N. Levy, S. MacCracken, P.R. Mastrandrea, and L.L. White (eds.)* Cambridge University Press, Cambridge, United Kingdom and New York, NY, USA, pp. 1567–1612.
- Larter, N. C., Raillard, M., Epp, H. & Nagy, J. A. (2009), 'Vegetation mapping of Banks Island with particular reference to Aulavik national park', *Northwest Territories. Environment and Natural Resources. File Report No. 138*, pp. 1–45.
- Lawrence, D. M., Slater, A. G., Romanovsky, V. E. & Nicolsky, D. J. (2008), 'Sensitivity of a model projection of near-surface permafrost degradation to soil column depth and representation of soil organic matter', *Geophysical Research Letters* , **Vol. 113F02011**, pp. 1–14.
- Lawrence, D. M., Slater, A. G., Tomas, R. A. & Holland, M. M. AMD Deser, C. (2008), 'Accelerated Arctic land warming and permafrost degradation during rapid sea ice loss', *Geophysical Research Letters* , **Vol. 35, L11506**, pp. 1–6.
- Lee, J. & Grunes, M. (1992), 'Classification of multi-look polarimetric SAR data based on complex wishart distribution', *Telesystems Conference, 1992. NTC-92., National* , **Vol. 7**, pp. 21–24.
- Lee, J., Grunes, M., Ainsworth, T. L., Du, L., Schuler, D. L. & Cloude, S. R. (1999), 'Unsupervised classification using polarimetric decomposition and complex wishart classifier', *IEEE Transactions on Geoscience and Remote Sensing* , **Vol. 37(5)**, pp. 2249–2258.
- Lee, J., Grunes, M. & De-Grandi, G. (1999), 'Polarimetric SAR speckle filtering and its implication for classification', *Geoscience and Remote Sensing, IEEE Transactions on* , **Vol. 37(5)**, pp. 2363–2373.
- Lee, J., Grunes, M., Pottier, E. & Ferro-Famil, L. (2004), 'Unsupervised terrain classification preserving polarimetric scattering characteristics.', *IEEE T. Geoscience and Remote Sensing* , **Vol. 42(4)**, pp. 722–731.
- Leichtle, T. (2013), 'Crop classification based on multi-polarized, multi-temporal and multi-frequency RADARSAT-2 and TerraSAR-X data for the RAMSAR site Upper Rhine', *Master Thesis - Karl-Franzens-University of Graz*, pp. 1–153.
- Lemke, P. & Jacobi, H. (2011), 'Arctic climate change: The ACSYS decade and beyond', *Spring. Atmospheric and Oceanographic Sciences Library*, pp. 1–464.
- Li, P., Shi, C., Li, Z., Muller, J., Drummond, J., Li, X., Li, T., Li, Y. & Liu, J. (2013), 'Evaluation of ASTER GDEM using GPS benchmarks and SRTM in china', *International Journal of Remote Sensing* , **Vol. 34(5)**, pp. 1744–1771.
- Li, W., Du, Z., Ling, F., Zhou, D., Wang, H., Gui, Y., Sun, B. & Zhang, X. (2013), 'A comparison of land surface water mapping using the normalized difference water index from TM, ETM+ and ALI', *Remote Sensing* , **Vol. 5(11)**, pp. 5530–5549.
- Lingli, Z., Jie, L., L., P. & Z., L. (2014), 'Characteristics analysis and classification of crop harvest patterns by exploiting high-frequency multipolarization SAR data', *IEEE Journal of Selected Topics in Applied Earth Observations and Remote Sensing* , **Vol. 7(9)**, pp. 3773–3783.

## Bibliography

- MacDonald, G. (1987), 'Postglacial vegetation history of the Mackenzie River basin', *Quaternary Research* , **Vol. 28**, pp. 245–262.
- Mackay, R. & Dyke, L. (1990), 'Geological features of the Mackenzie Delta Region, N.W.T.', *Scientific Report No. 1. Science Institute of the Northwest Territories*, pp. 1–16.
- MacMillan, R., Pettapiece, W., Nolan, S. & Goddard, T. (2000), 'A generic procedure for automatically segmenting landforms into landform elements using DEMs, heuristic rules and fuzzy logic', *Fuzzy Sets and Systems* , **Vol. 113**(1), pp. 81–109.
- Markon, C. & Derksen, D. (1994), 'Identification of tundra land cover near Teshekpuk Lake, Alaska using SPOT satellite data.', *ARCTIC* , **Vol. 4.3**, pp. 222–231.
- May, I., Ludwig, R. & Bernier, M. (2011), 'Using TerraSAR-X imagery for the monitoring of permafrost dynamics in Northern Quebec', *4. TerraSAR-X Science Team Meeting, Oberpfaffenhofen, 14. - 16. February 2011*, pp. 1–8.
- McNemar, Q. (1947), 'Note on the sampling error of the difference between correlated proportions or percentages', *Psychometrika* , **Vol. 12**, pp. 153–157.
- METI-NASA (2011), 'Ministry of Economy, Trade, and Industry (METI) of Japan and the United States National Aeronautics and Space Administration (NASA). ASTER Global Digital Elevation Map', *URL: <http://asterweb.jpl.nasa.gov>* .
- Moon-Kyung, K., Kwang-Eun, K., Seong-Ju, C. and Hoonyol, L. & Jae-Hee, L. (2010), 'Filtering effect in supervised classification of polarimetric ground based SAR images', *Korean Journal of Remote Sensing* , **Vol. 26**(6), pp. 705–719.
- Morgenstern, A., Grosse, G., Günther, F., Fedorova, I. & Schirmer, L. (2011), 'Spatial analyses of thermokarst lakes and basins in Yedoma landscapes of the Lena Delta', *The Cryosphere* , **Vol. 5**(4), pp. 849–867.
- Myers-Smith, I., Forbes, B., Wilking, M., Hallinger, M., Lantz, T., Blok, D., Tape, K., Macias-Fauria, M., Sass-Klaassen, U., Lévesque, E., Boudreau, S., Ropars, R., Hermanutz, L., Trant, A., Collier, S. L., Weijers, S., Rozema, S., Rayback, S., Schmidt, N., Schaepman-Strub, G., Wipf, S., Rixen, C., Ménard, C., Venn, S., Goetz, S., Andreu-Hayles, L., Elmendorf, S., Ravolainen, V., Welker, J., Grogan, P., Epstein, H. & Hik, D. (2011), 'Shrub expansion in tundra ecosystems: dynamics, impacts and research priorities', *Environmental Research Letters* , **Vol. 6**(4), pp. 1–15.
- Naito, A. & Cairns, D. (2011), 'Relationships between Arctic shrub dynamics and topographically derived hydrologic characteristics', *Environmental Research Letters* , **Vol. 6**(4), pp. 1–8.
- Nakamura, K., Wakabayashi, H., Uto, S., Naoki, K., Nishio, F. & Uratsuka, S. (2006), 'Sea-ice thickness retrieval in the Sea of Okhotsk using dual-polarization SAR data', *Annals of Glaciology* , **Vol. 44**(1), pp. 261–268.
- NASA (2013a), 'National Aeronautics and Space Administration (NASA). Landsat Program. US Geological Survey (USGS).', *Landsat 8 Scene Mackenzie Delta: LC80640112013214LGN00* .
- NASA (2013b), 'National Aeronautics and Space Administration (NASA). Landsat Program. US Geological Survey (USGS).', *Landsat 8 Scene James Bay: LC80190232013267LGN00* .

- NASA (2013c), 'National Aeronautics and Space Administration (NASA). Landsat Program. US Geological Survey (USGS).', *Landsat 8 Scene Banks Island: LC80600072013186LGN00* .
- NASA (2014), 'National Aeronautics and Space Administration (NASA). Homepage of ICESat & iCESat-2 Project', URL: <http://icesat.gsfc.nasa.gov/> .
- Nguyen, T.-N., Burn, C. R., King, D. J. & Smith, S. L. (2009), 'Estimating the extent of near-surface permafrost using remote sensing, Mackenzie Delta, Northwest Territories', *Permafrost and Periglacial Processes* , **Vol. 20**, pp. 141–153.
- NOAA (2014), 'National Oceanic and Atmospheric Administration. National Climate Data Center.', <http://www.ncdc.noaa.gov/> .
- Nolan, N. & Prokein, P. (2003), 'Evaluation of a new DEM of the Putuligayuk watershed for Arctic hydrological applications', *Permafrost, Phillips, Springman & Arenson*, pp. 833–838.
- Nuth, C. & Kääb, A. (2011), 'Co-registration and bias corrections of satellite elevation data sets for quantifying glacier thickness change', *The Cryosphere* , **Vol. 5**(1), pp. 271–290.
- NWT-Geomatics (2014), 'Northwest Territories (NWT) Centre for Geomatics', <http://geomatics.gov.nt.ca> .
- Nyoungui, A. N., Tonye, E. & Akono, A. (2002), 'Evaluation of speckle filtering and texture analysis methods for land cover classification from SAR images', *International Journal of Remote Sensing* , **Vol. 23**(9), pp. 1895–1925.
- Olthof, I. & Fraser, R. H. (2007), 'Mapping northern land cover fractions using Landsat ETM+', *Remote Sensing of Environment* , **Vol. 107**(3), pp. 496–509.
- Olthof, I. & Fraser, R. H. (2014), 'Detecting landscape changes in high latitude environments using Landsat trend analysis: 2. Classification', *Remote Sensing* , **Vol. 6**(11), pp. 11558–11578.
- Owens, E. H. (2010), 'Primary shoreline types of the Canadian north (draft), for eSPACE project', *Environment Canada, Montreal, Canada*, pp. 1–60.
- Park, S.-E., Yamaguchi, Y., Singh, G. & Bartsch, A. (2010), 'Spatio-temporal monitoring of permafrost regions using SAR remote sensing.', *In Proceedings of the International Archives of the Photogrammetry, Remote Sensing and Spatial Information Science, Kyoto, Japan, 9-12 August 2010*, pp. 1–4.
- Parrilli, S., Poderico, M., Angelino, C., Scarpa, G. & Verdoliva, L. (2010), 'A nonlocal approach for SAR image denoising', *Geoscience and Remote Sensing Symposium (IGARSS), 2010 IEEE International*, pp. 726–729.
- Pisaric, M. F. J., Thienpont, J. R., Kokelj, S. V., Nesbitt, H., Lantz, C., Solomon, S. & Smol, J. P. (2011), 'Impacts of a recent storm surge on an Arctic delta ecosystem examined in the context of the last millennium', *Proceedings of the National Academy of Sciences of the United States of America*, pp. 1–6.
- Prima, O., Echigo, A., Yokoyama, R. & Yoshida, T. (2006), 'Supervised landform classification of northeast Honshu from DEM-derived thematic maps', *Geomorphology* , **Vol. 78**(3-4), pp. 373–386.
- Re, D., Bourgeois, J., Bats, M., Zwertvaegher, A., Gelorini, V., Smedt, P., Chu, W., Antrop, M., Maeyer, P., Finke, P., Meirvenne, M., Verniers, J. & Crombe, P. (2013), 'Application of the topographic position index to heterogeneous landscapes', *Geomorphology* , **Vol. 186**(0), pp. 39–49.

## Bibliography

- Rees, W. G. (2012), 'Assessment of ASTER global digital elevation model data for arctic research', *Polar Record*, **Vol. 48**, pp. 31–39.
- Regmi, P., Grosse, G., Jones, M., Jones, M. & Anthony, K. (2012), 'Characterizing post-drainage succession in thermokarst lake basins on the Seward Peninsula, Alaska with TerraSAR-X backscatter and Landsat-based NDVI data', *Remote Sensing*, **Vol. 4**(12), pp. 3741–3765.
- Reu, J., Bourgeois, J., Smedt, P., Zwertvaegher, A., Antrop, A., Bats, M., Maeyer, P., Finke, P., Meirvenne, M., Verniers, J. & Crombé, P. (2011), 'Measuring the relative topographic position of archaeological sites in the landscape, a case study on the Bronze Age barrows in northwest Belgium', *Journal of Archaeological Science*, **Vol. 38**(12), pp. 3435–3446.
- Richards, J. A. (2009), 'Remote sensing with imaging radar', *Springer. Signals and Communication Technology*, pp. 1–361.
- Rignot, E., Mouginot, J. & Scheuchl, B. (2011), 'Ice flow of the Antarctic ice sheet', *Science*, **Vol. 333**(6048), pp. 1427–1430.
- Rignot, E., Way, J., Williams, C. & Viereck, L. (1994), 'Radar estimates of aboveground biomass in boreal forests of interior Alaska', *IEEE Transactions on Geoscience and Remote Sensing*, **Vol. 32**, pp. 1117–1124.
- Romanovsky, V. E., Smith, S. L. & Christiansen, H. H. (2010), 'Permafrost thermal state in the polar northern hemisphere during the international polar year 2007-2009: a synthesis', *Permafrost Periglacial Processes*, **Vol. 21**, pp. 106–116.
- Roth, A., Huber, M. & Kosmann, D. (2004), 'Geocoding of TerraSAR-X data', *International Archives of the Photogrammetry, Remote Sensing and Spatial Information Sciences, isprs Proceedings, XXXV, Part B, Comm. 3, 20th Congress of isprs, Istanbul, 12. - 23.July 2004*, pp. 1–5.
- Rune-Lauknes, T., Christiansen, H., Eckerstorfer, M. & Larsen, Y. (2013), 'InSAR detection of permafrost landform dynamics at Kapp Linné central Svalbard', *EGU General Assembly Conference Abstracts*, **Vol. 15**, 8612.
- Saadat, H., Bonnell, R., Sharifi, F. Mehuys, G., Namdar, M. & Ale-Ebrahim, S. (2008), 'Landform classification from a digital elevation model and satellite imagery', *Geomorphology*, **Vol. 100**(3-4), pp. 453–464.
- Salehi, M., Sahebi, M. & Maghsoudi, Y. (2014), 'Improving the accuracy of urban land cover classification using Radarsat-2 PolSAR data', *Selected Topics in Applied Earth Observations and Remote Sensing, IEEE Journal of*, **Vol. 7**(4), pp. 1394–1401.
- Sanden, J. v. d., Drouin, H., Hicks, F. & Beltaos, S. (2009), 'Potential of RADARSAT-2 for the monitoring of river freeze-up processes.', *Proceedings of the 15th Workshop on River Ice, St. John, NL, Canada, 14-17 June 2009*, pp. 364–377.
- Sang-Hoon, H., Kyung-Yup, L. & Youn-Soo, K. (2011), 'KOMPSAT-5 SAR application', *3rd International Asia-Pacific Conference on Synthetic Aperture Radar (APSAR)*, pp. 1–2.
- Schattler, B., Kahle, R., Metzig, R., Steinbrecher, U. & Zink, M. (2011), 'The joint TerraSAR-X / TanDEM-X ground segment', *Geoscience and Remote Sensing Symposium (IGARSS), 2011 IEEE International*, pp. 2298–2301.

- Scheuchl, B., Hajnsek, I. & Cumming, I. (2002), 'Sea ice classification using multi-frequency polarimetric SAR data.', *Proceeding of the Geoscience and Remote Sensing Symposium (IGARSS), Toronto, ON, Canada, 24-28 June 2002*, pp. 1914–1916.
- Schmitt, A. (2009), 'Änderungserkennung in multitemporalen und multipolarisierten radaraufnahmen', *Ph.D. Dissertation, Karlsruher Institut für Technologie (KIT)*, pp. 1–360.
- Schmitt, A., Wendleder, A. & Hinz, S. (2015), 'The Kennaugh element framework for multi-scale, multi-polarized, multi-temporal and multi-frequency {SAR} image preparation', *{ISPRS} Journal of Photogrammetry and Remote Sensing*, **Vol. 102**, pp. 122–139.
- Schmitt, A. & Wessel, B. (2010), 'Introducing partial polarimetric layers into a curvelet-based change detection', *Synthetic Aperture Radar (EUSAR), 2010 8th European Conference on*, pp. 1–4.
- Schneider, J., Grosse, G. & Wagner, D. (2009), 'Land cover classification of tundra environments in the Arctic Lena Delta based on Landsat 7 ETM+ data and its application for upscaling of methane emissions', *Remote Sensing of Environment*, **Vol. 113(2)**, pp. 380–391.
- Shan, Z., Wang, C., Zhang, H., & An, W. (2012), 'Improved four-component model-based target decomposition for polarimetric SAR data', *Geoscience and Remote Sensing Letters, IEEE*, **Vol. 9(1)**, pp. 75–79.
- Shan, Z., Wang, C., Zhang, H. & Chen, J. (2011), 'H-alpha decomposition and alternative parameters for dual polarization SAR data', *PIERS Proceedings, Suzhou, China, September 12-16, 2011*, pp. 1386–1390.
- Shawn, J., R., Stephen, D. D. & Elliot, R. (1999), 'A terrain ruggedness index that quantifies topographic heterogeneity', *Intermountain Journal of Science*, **Vol. 5(1-4)**, pp. 23–27.
- Short, N., Brisco, B., Couture, N., Pollard, W., Murnaghan, K. & Budkewitsch, P. (2011), 'A comparison of TerraSAR-X, RADARSAT-2 and ALOS-PALSAR interferometry for monitoring permafrost environments, case study from Herschel Island, Canada', *Remote Sensing of Environment*, **Vol. 115(12)**, pp. 1–16.
- Short, N., LeBlanc, A.-M., Sladen, W., Oldenborger, G., Mathon-Dufour, V. & Brisco, B. (2014), 'RADARSAT-2 D-InSAR for ground displacement in permafrost terrain, validation from Iqaluit Airport, Baffin Island, Canada', *Remote Sensing of Environment*, **Vol. 141(0)**, pp. 40–51.
- Smith, S. L., Burgess, M. M. & Nixon, F. M. (2001), 'Response of active-layer and permafrost temperatures to warming during 1998 in the Mackenzie Delta, Northwest Territories and at Canadian forces station Alert and Baker Lake, Nunavut', *Geological Survey of Canada. Current Research 2001-E5*, pp. 1–10.
- Sobiech, J., Boike, J. & Dierking, W. (2012), 'Observation of melt onset in an arctic tundra landscape using high resolution TerraSAR-X and RADARSAT-2 data', *Geoscience and Remote Sensing Symposium (IGARSS), 2012 IEEE International*, pp. 3552–3555.
- Sobiech, J. & Dierking, W. (2013), 'Observing lake- and river-ice decay with SAR: advantages and limitations of the unsupervised k-means classification approach', *Annals of Glaciology*, **Vol. 54(62)**, pp. 65–72.
- Solomon, S. (2005), 'Spatial and temporal variability of shoreline change in the Beaufort-Mackenzie region, northwest territories, Canada', *Geo-Marine Letters*, **Vol. 25**, pp. 127–137.

## Bibliography

- Stepinski, T. & Bagaria, C. (2009), 'Segmentation-based unsupervised terrain classification for generation of physiographic maps', *Geoscience and Remote Sensing Letters, IEEE* , **Vol. 6**(4), pp. 733–737.
- Stettner, S., Morgenstern, A., Guenther, F., Fedorov, I., Chetverova, A. & Rost, T. (2014), 'Characterizing thermo-erosionallandforms in Siberianice-rich permafros. morphometric investigations using high resolution satellite imagery and digital elevation models', *EUCOP4 Conference, 18-21 June 2014, Evora, Portugal*, p. 1.
- Stow, D. A., Hope, A., McGuire, D., Verbyla, D., Gamon, J., Huemmrich, F., Houston, S., Racine, C., Sturm, M., Tape, K., Hinzman, L., Yoshikawa, K., Tweedie, C., Noyle, B., Silapaswan, C., Douglas, D., Griffith, B., Gensuo, J., Epstein, H., Walker, D., Daeschner, S., Petersen, A., Zhou, L. & Myneni, R. (2004), 'Remote sensing of vegetation and land-cover change in arctic tundra ecosystems', *Remote Sensing of Environment* , **Vol. 89**(3), pp. 281–308.
- Strozzi, T., Grosse, G., Daanen, R. & Jones, B. (2012), 'Debris flows in the Brooks Range, Alaska, observed with satellite SAR interferometry', *ESA DUE Permafrost, Final Workshop February 15-17, 2012, Potsdam, Germany* .
- Sugimoto, M., Ouchi, K. & Yang, C.-S.-S. (2013), 'On the eigenvalue analysis using HH-VV dual-polarization SAR data and its applications to monitoring of coastal oceans', *Proceedings of SPIE* , **Vol. 8724**, pp. 1–8.
- Thanh, N. T., Wehrens, R. & Buydens, L. (2005), 'Clustering multispectral images: a tutorial', *Chemo-metrics and Intelligent Laboratory Systems* , **Vol. 77**, pp. 3–17.
- Tinkler, K. (1985), 'A short history of geomorphology', *Croom Helm*, pp. 11–317.
- Torres, L. & Frery, A. (2013), 'SAR image despeckling algorithms using stochastic distances and nonlocal means', *CoRR*, pp. 1–6.
- Touzi, R., Boerner, W., Lee, J. & Lueneburg, E. (2004), 'A review of polarimetry in the context of synthetic aperture radar: concepts and information extraction', *IEEE Transactions on Geoscience and Remote Sensing* , **Vol. 30**(3), pp. 380–407.
- Turner, J. & Marshall, G. (2011), 'Climate change in the polar regions', *Cambridge University Press*, pp. 1–448.
- Ulaby, F., Long, D., Blackwell, W., Elachi, C. & Sarabandi, K. (2014), 'Microwave radar and radiometric remote sensing', *University of Michigan Press*, pp. 1–1116.
- Ullmann, T., Schmitt, A., Roth, A., Duffe, J., Dech, S., Hubberten, H.-W. & Baumhauer, R. (2014), 'Land cover characterization and classification of arctic tundra environments by means of polarized synthetic aperture X- and C-band radar (PolSAR) and landsat 8 multispectral imagery - Richards Island, Canada', *Remote Sensing* , **Vol. 6**, pp. 8565–8593.
- USGS (2010), 'United States Geological Survey. about SRTM mission', *URL: <http://srtm.usgs.gov/index.php>* .
- Vaughan, D., Comiso, J., Allison, I., Carrasco, J., Kaser, G., Kwok, R., Mote, P., Murray, T., Paul, F., Ren, J., Rignot, E., Solomina, O., Steffen, K. & Zhang, T. (2013), 'Observations: Cryosphere', *In: Climate Change 2013: The Physical Science Basis. Contribution of Working Group I to the Fifth Assessment Report of the Intergovernmental Panel on Climate Change [Stocker, T.F., D. Qin, G.-K. Plattner,*



- M. Tignor, S.K. Allen, J. Boschung, A. Nauels, Y. Xia, V. Bex and P.M. Midgley (eds.)). Cambridge University Press, Cambridge, United Kingdom and New York, NY, USA, pp. 317–382.
- Verhagen, P. & Dragut, L. (2012), 'Object-based landform delineation and classification from DEMs for archaeological predictive mapping', *Journal of Archaeological Science*, **Vol. 39**(3), pp. 698–703.
- Vincent, J.-S. (1982), 'The quaternary history of Banks Island, N.W.T., Canada', *Geographie physique et Quaternaire*, **Vol. 36**, pp. 209–232.
- Weiss, A., D. (2001), 'Topographic position and landforms analysis', *Poster Presentation at the ESRI Users Conference 2001*, p. 1.
- Wentao, A., Cui, Y. & Yang, J. (2010), 'Three-component model-based decomposition for polarimetric SAR data', *Geoscience and Remote Sensing, IEEE Transactions on*, **Vol. 48**(6), pp. 2732–2739.
- Wessel, B., Marschalk, U., Gruber, A., Huber, M., Hahmann, T., Roth, A. & Habermeyer, M. (2008), 'Design of the DEM mosaicking and calibration processor for TanDEM-X', *Synthetic Aperture Radar (EUSAR), 2008 7th European Conference on*, pp. 1–4.
- Wiken, E. (1986), 'Terrestrial Ecozones of Canada', *Environment Canada, Lands Directorate. Ecological Land Classification Series*, pp. 1–26.
- Wilson, J. P. & Gallant, J. C. (2000), 'Terrain Analysis: Principles and Applications', *John Wiley and Sons*, pp. 1–479.
- Wolfe, S. A., Dallimore, S. R. & Solomon, S. M. (1998), 'Coastal permafrost investigations along a rapidly eroding shoreline, Tuktoyaktuk, N.W.T.', *Geological Survey of Canada, Contribution Series 1998234. Permafrost : Seventh International Conference*, pp. 1125–1131.
- Woodhouse, I. (2005), 'Introduction to Microwave Remote Sensing', *Taylor and Francis*, pp. 1–370.
- Xu, L., Myneni, R. B., Chapin, F. S., Callaghan, T. V., Pinzon, J. E., Tucker, C. J., Zhu, Z., Bi, J., Ciais, P., Tommervik, H., Euskirchen, E. S., Forbes, B. C., Piao, S. L., Anderson, B. T., Ganguly, S., Nemani, R. R., Goetz, S. J., Beck, P. S. A., Bunn, A. G., Cao, C. & Stroeve, J. C. (2013), 'Temperature and vegetation seasonality diminishment over northern lands', *Nature Climate Change*, pp. 581–586.
- Yamaguchi, Y., Moriyama, T., Ishido, M. & Yamada, H. (2005), 'Four-component scattering model for polarimetric SAR image decomposition', *Geoscience and Remote Sensing, IEEE Transactions on*, **Vol. 43**(8), pp. 1699–1706.
- Yamaguchi, Y., Sato, A., Sato, R., Yamada, H. & Boerner, W.-M. (2010), 'Four-component scattering power decomposition with rotation of coherency matrix', pp. 1327–1330.
- Zink, M., Krieger, G., Fiedler, H. & Moreira, A. (2007), 'The tanDEM-X mission: Overview and status', pp. 3944–3947.





## **Appendix**

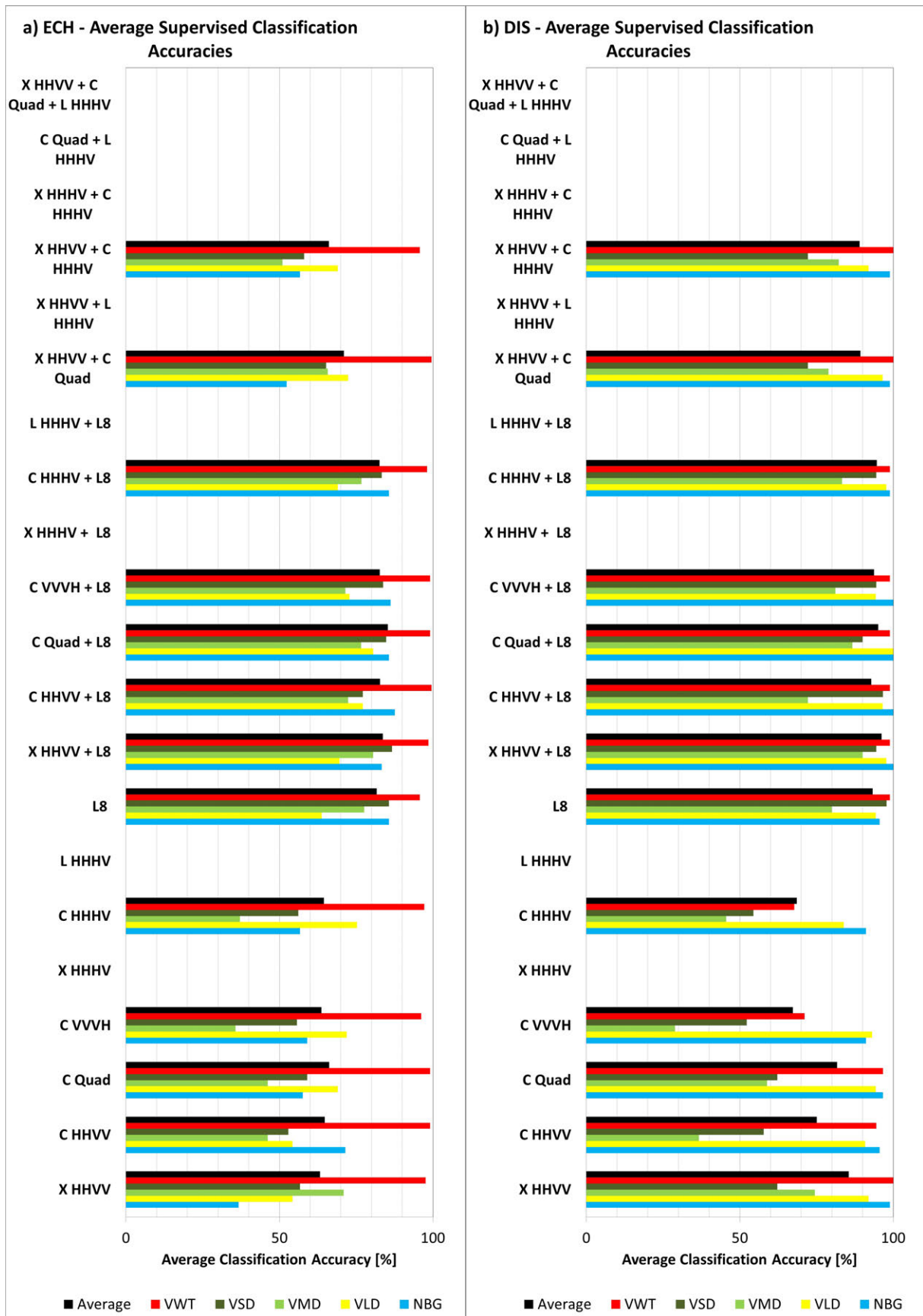


Figure A1: Supervised classification accuracies of the test sites: a) East Channel (ECH) and b) Delta Islands (DIS).

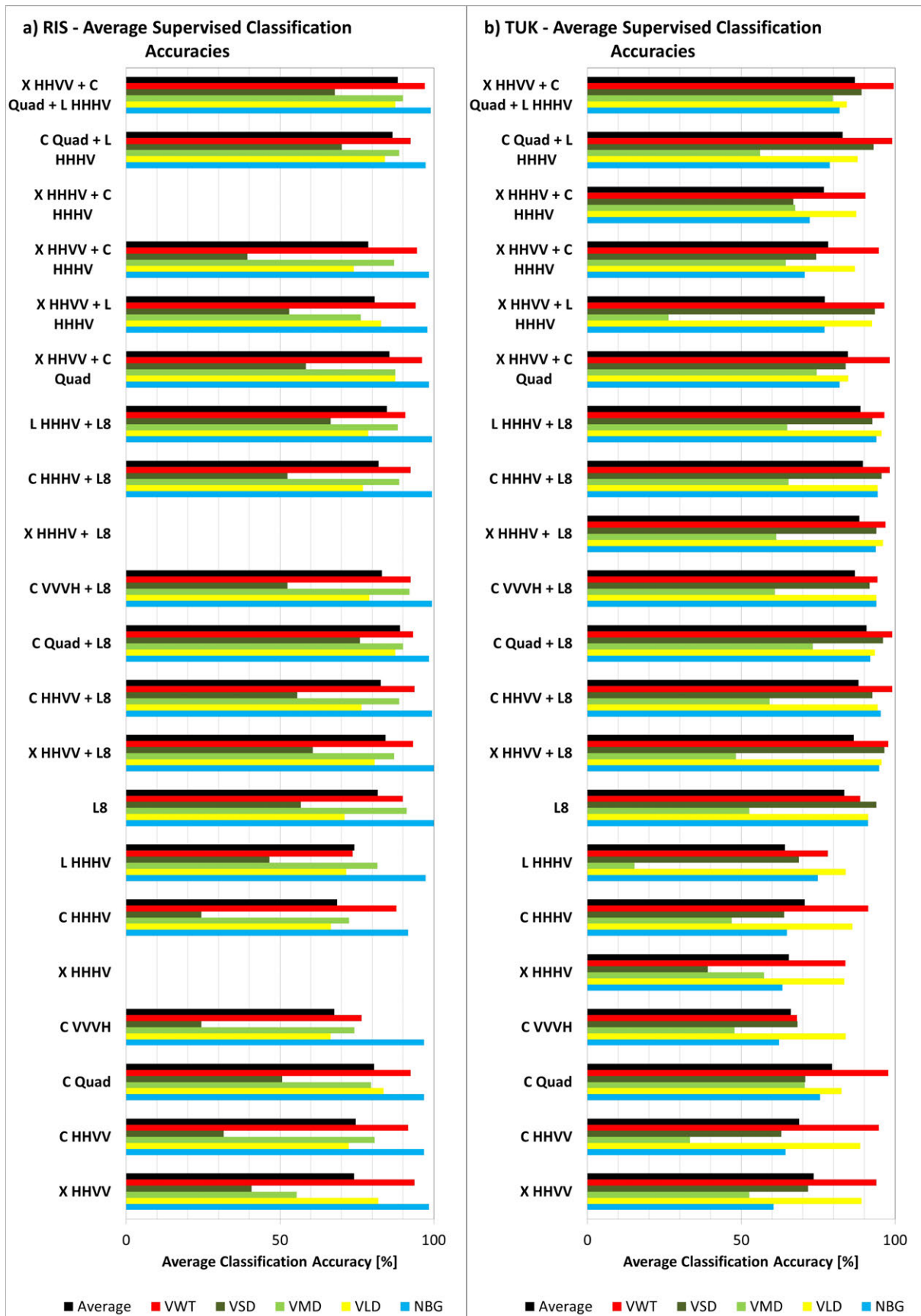


Figure A2: Supervised classification accuracies of the test sites: a) Richards Island (RIS) and b) Tuktoyaktuk (TUK).

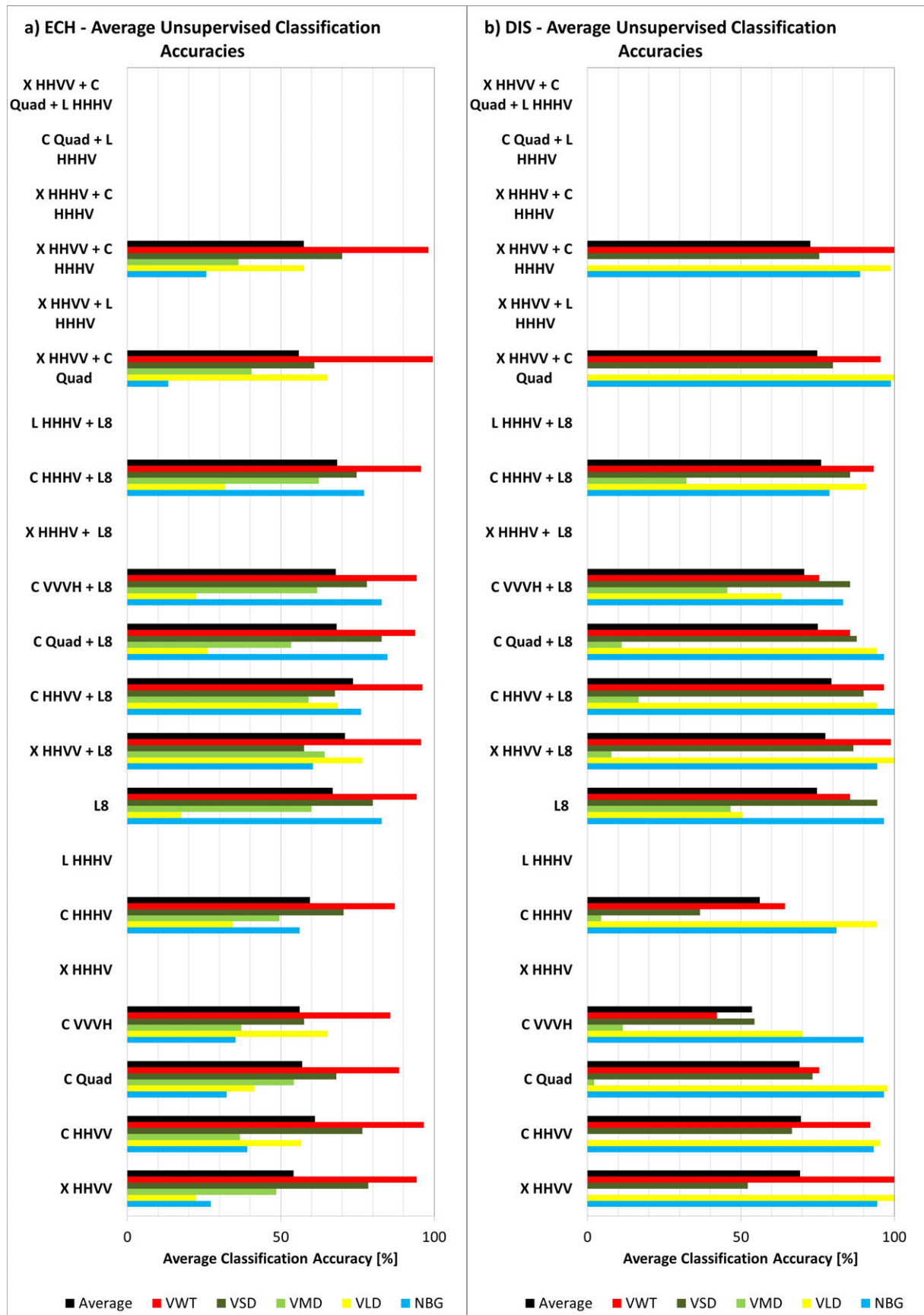


Figure A3: Unsupervised classification accuracies of the test sites: a) East Channel (ECH) and b) Delta Islands (DIS).

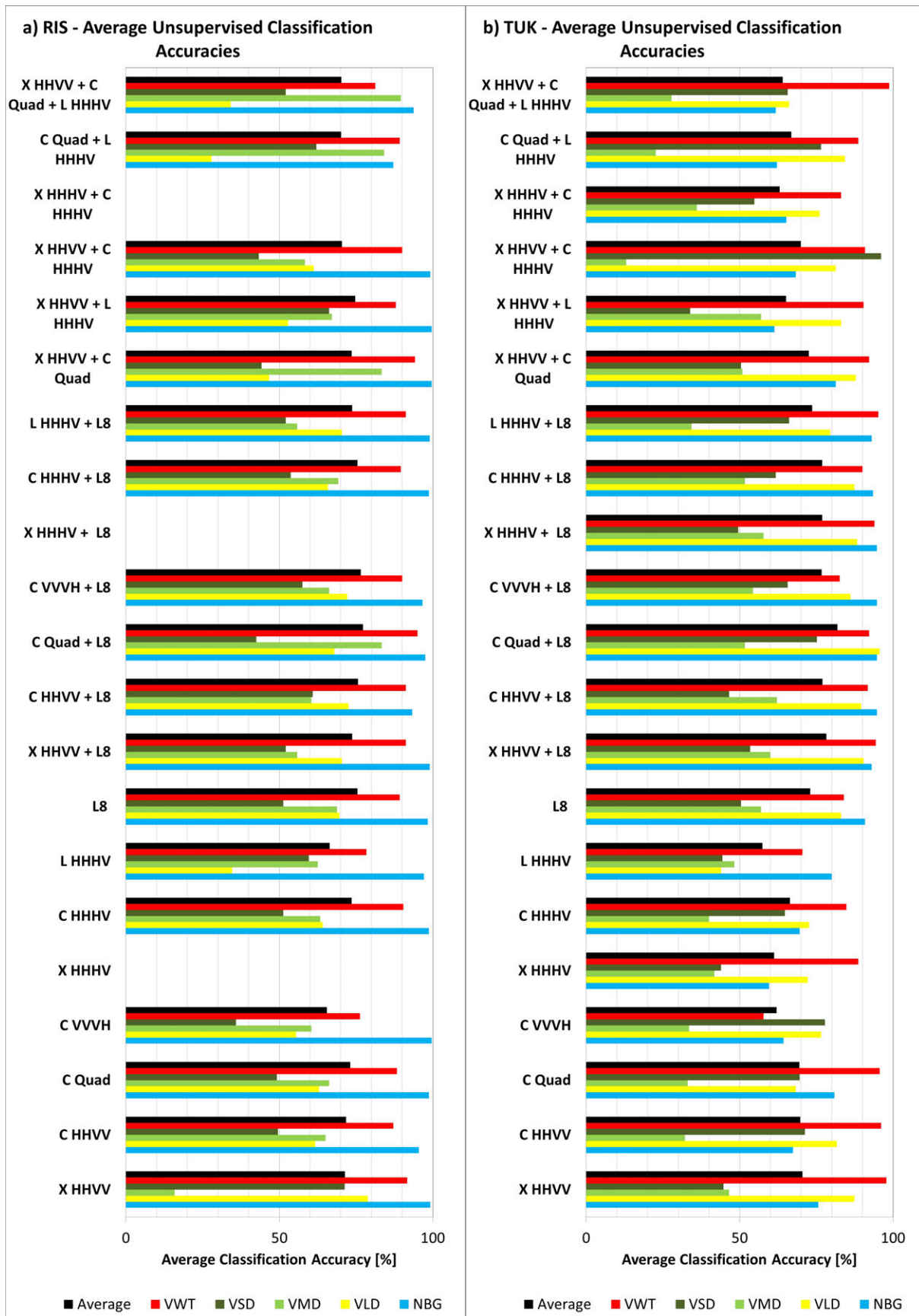


Figure A4: Unsupervised classification accuracies of the test sites: a) Richards Island (RIS) and b) Tuktoyaktuk (TUK).

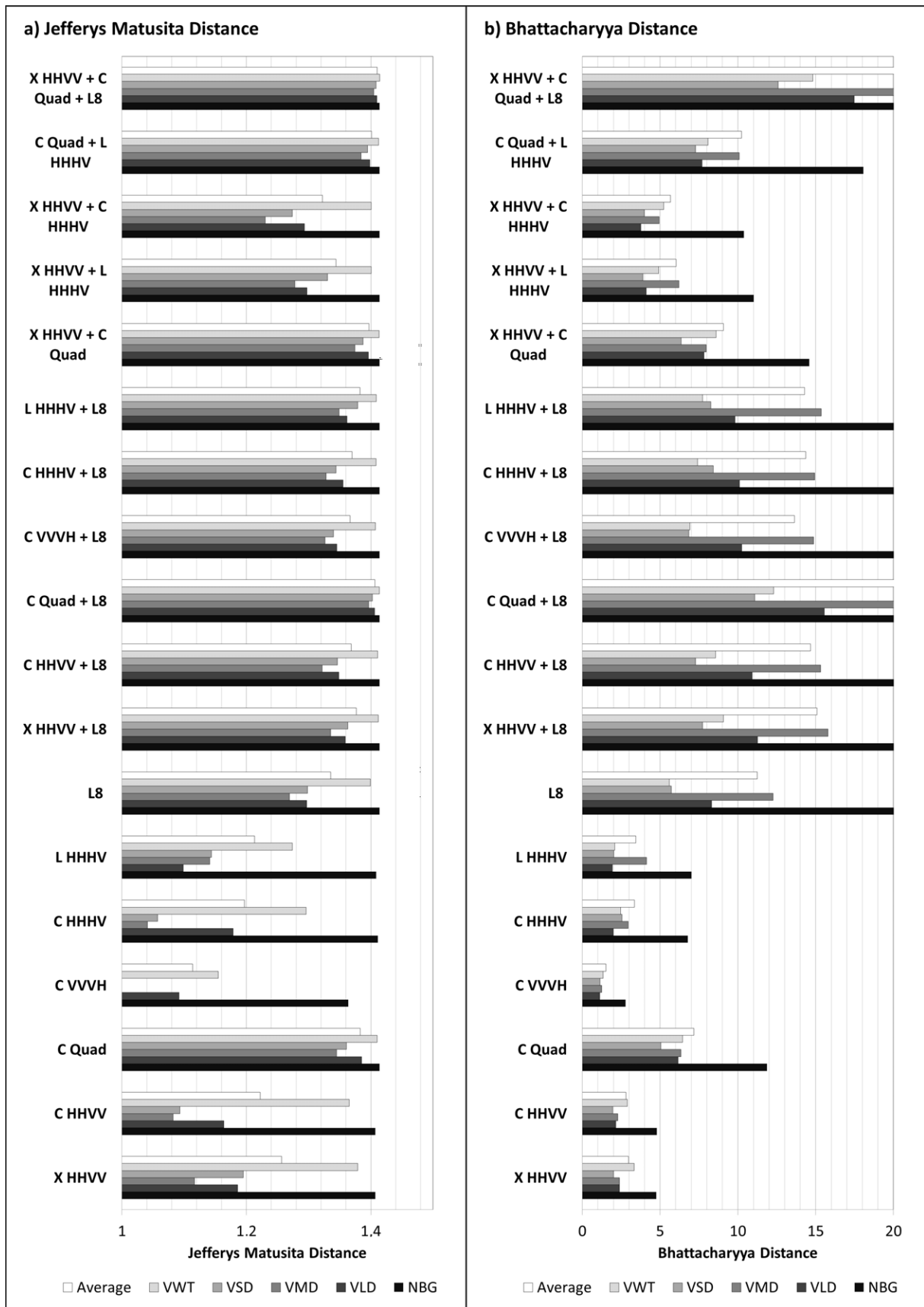


Figure A5: Separability distances of the test sites Richards Island (RIS): a) Jefferys Matusita Distances and b) Bhattacharyya Distances.



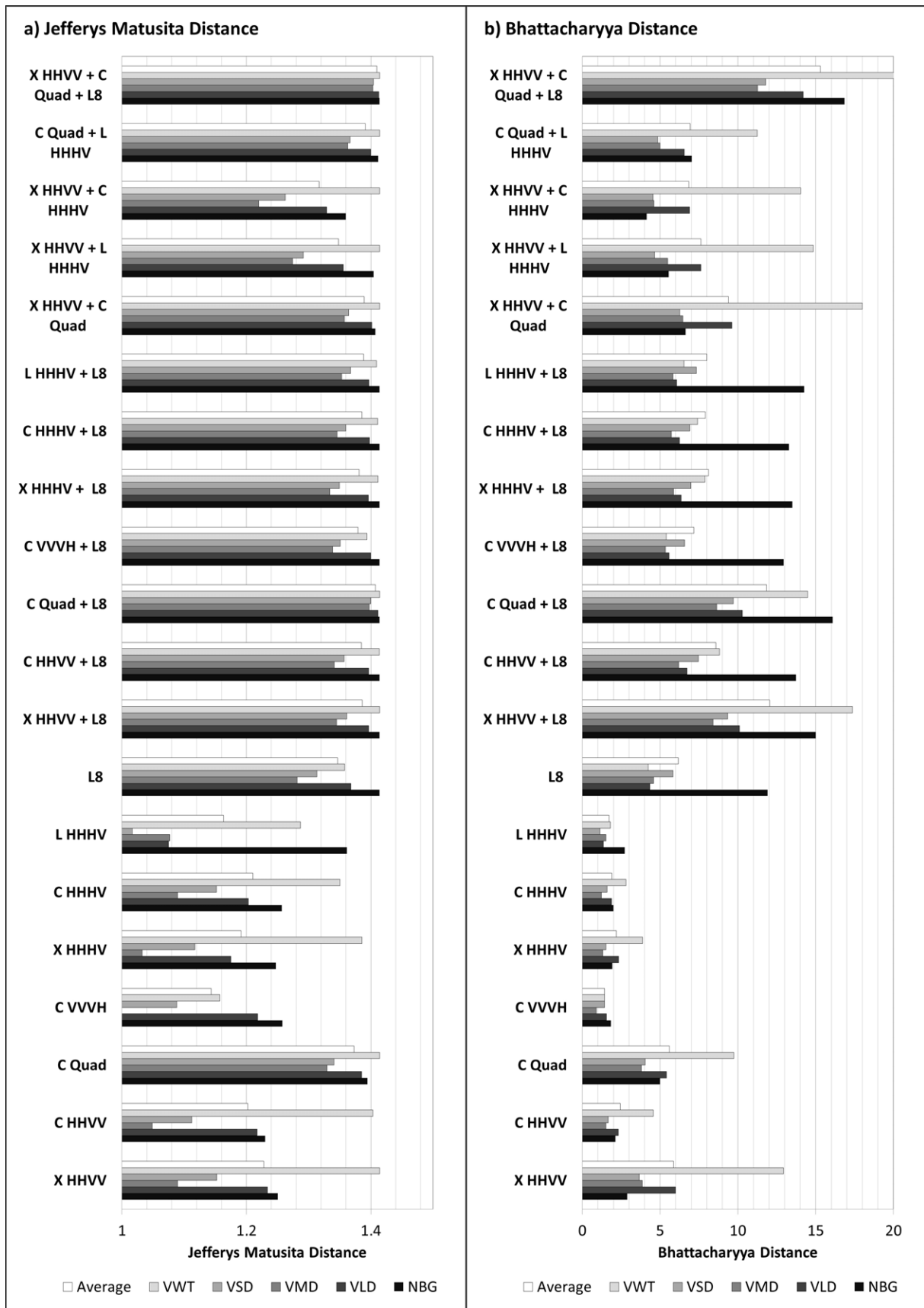


Figure A6: Separability distances of the test sites Tuktoyaktuk (TUK): a) Jefferys Matusita Distances and b) Bhattacharyya Distances.







---

---

## Index

- A Priori, 88
- Accuracy Assessment, 97
- Acquisition modes, 55
- ALOS, 49
- ALOS DGEM, 50
- Alternative Entropy/Alpha Decomposition, 72  
60
- Aspect, 84
- Azimuth, 55
  
- Back Scatter Alignment, 59
- Banks Island, 32
- Bare Substrate, 39, 43
- Boxcar Filter, 74
- Brightness, 81
  
- Caribou Hills, 20
- Classification, 87, 89, 93, 98
- Coefficient of Variation, 74
- Coherency Matrix, 63
- Convexity, 84
- Covariance Matrix C, 61
- Curvature, 84
  
- Database, 38
- Decomposition, 66, 69, 70, 72
- Digital Elevation Model, 81
  
- Ecosystems, 27
- Eigendecomposition, 66
- Enhanced Lee Filter, 74
- Entropy/Alpha decomposition, 69, 70
- Entropy/Alpha segmentation, 89
- Entropy/Alpha/Anisotropy segmentation, 90
  
- Fast Calculation of Topographic Position Indices (TPIs), 85
- Forward Scatter Alignment, 59
- Fuzzy Logic, 88
  
- Geocoding, 80
- Geometric Terrain Correction, 80
- Greenness, 81
  
- Image Classification, 87
- Image Filtering, 72
- In situ Data, 38
- Incidence angle, 54  
60
  
- James Bay, 36
  
- K-Means Wishart, 90
- Kennaugh Matrix, 64
  
- Land Cover, 89
- Landform, 98
- Landsat, 51
- Lee Filter, 74
- Lee Terrain Classification, 90
  
- Mackenzie Delta Region, 20  
60
- Mahalanobis Distance, 88
- Matrix Representations, 59
- Maximum Likelihood Classification, 88
- Mixed non-Tussock Tundra, 44
- Mixed Tussock Tundra, 44
- Modified TPI and Nested-Means Landform Classification, 99

## *Index*

- Multi-Looking, 73
- Multispectral Data, 80
- NDVI, 81
- Nested-Means Landform Classification, 99
- Non-Local Means Filter, 74
- Number of Looks, 73
- Overall Evaluation Index, 79
- Pauli Vector, 63
- Permafrost, 24
  - 60
- Polarimetric Decompositions, 66
- Polarimetry, 57
- Power Decomposition, 66
- Preservation of Edges, 78
- Preservation of Mean, 78
- Processing Chain, 79
- Pulse-repetition-frequency, 55
- R-2, 48
- radar cross section, 59
- Radar Equation, 59
- Range, 54
- Range Doppler, 80
- Reduction of Speckle, 78
- Reflectance, 81
- Remote Sensing Data, 47
- Richards Island, 20
- Scansar, 55
- Search Window, 75
- Sigma Lee Filter, 74
- Sinclair Matrix, 60
- Single-Look, 73
- Single-Look Complex, 79
- Single-look Slant Range Complex, 79
- Slantrange, 54
- Slope, 84
- Southern Arctic ecozone, 30
- Span, 66
- Speckle, 56, 72, 73
- Speckle Filtering, 72
- Speckle Filters, 74
- Spotlight, 55
- Stripmap, 55
- Supervised Classification, 87
- Taiga Cordillera, 30
- Taiga Plains, 30
- Tasseled Cap Transformation, 81
- TDX, 47, 50
- Terrain, 98
- Texture, 84
- Top of Atmosphere Correction, 81
- Topographic Position Index (TPI), 84
- Topographic Position Index (TPI) based Landform Classification, 99
- TSX, 47
- Tuktoyaktuk Peninsula, 20
- Tundra, 39, 43
- Two Component Decomposition, 67
- Two-Component Decomposition, 66
- Unsupervised Classification, 89
- Vegetation, 27
- Water, 39, 43
- Water Bodies, 93
- Wetlands, 39, 44
- Wetness, 81
- Wishart classifier, 90
- Yamaguchi Decomposition, 66

---

---

## Affidavit

Erklärung nach der Ordnung für Promotionsverfahren an den Graduiertenschulen der Julius-Maximilians-Universität Würzburg (University of Würzburg Graduate School) vom 15. Mai 2006. Versicherung nach § 38 Abs. 2 Satz 2 Nr. 4 und Erklärung nach § 38 Abs. 2 Satz 2 Nr. 5 der Promotionsordnung: An Eides statt wird die Eigenständigkeit der erbrachten wissenschaftlichen Leistungen versichert. Die Dissertation wurde selbstständig angefertigt und übernommene Inhalte sind eindeutig gekennzeichnet. Die Gelegenheit zum Promotionsvorhaben ist nicht kommerziell vermittelt worden. Keine Person oder Organisation wurde eingeschaltet, die gegen Entgelt Betreuer bzw. Betreuerinnen für die Anfertigung von Dissertationen sucht. Fernerhin wird erklärt, dass die Dissertation weder vollständig noch teilweise schon einmal einer anderen Fakultät mit dem Ziel vorgelegt worden ist, einen akademischen Grad zu erwerben. Der Bewerber hat nicht versucht früher akademische Grade zu erwerben und hat auch keine weiteren akademischen Grade erworben.

---

Würzburg, 26.02.2015, Tobias Ullmann

I declare that this dissertation is the product of my own work, that it has not been submitted before for any degree or examination in any other university, and that all the sources I have used or quoted have been indicated and acknowledged as complete references. I hereby confirm that my thesis entitled "Characterization of Arctic Environment by Means of Polarimetric Synthetic Aperture Radar (PolSAR) Data and Digital Elevation Models (DEM)" is the result of my own work. I did not receive any help or support from commercial consultants. All sources and / or materials applied are listed and specified in the thesis. Furthermore, I confirm that this thesis has not yet been submitted as part of another examination process neither in identical nor in similar form

---

Würzburg, 26.02.2015, Tobias Ullmann